

Cambridge University Press

978-1-107-64323-9 — MRI from Picture to Proton

Donald W. McRobbie , Elizabeth A. Moore , Martin J. Graves , Martin R. Prince

Frontmatter

[More Information](#)

MRI from Picture to Proton

Third Edition

Cambridge University Press
978-1-107-64323-9 — MRI from Picture to Proton
Donald W. McRobbie , Elizabeth A. Moore , Martin J. Graves , Martin R. Prince
Frontmatter
[More Information](#)

MRI from Picture to Proton

Third Edition

Donald W. McRobbie

South Australian Medical Imaging, Adelaide, Australia

Elizabeth A. Moore

Global MR R&D, Royal Philips, the Netherlands

Martin J. Graves

Cambridge University Hospitals, Cambridge, UK

Martin R. Prince

Weill Cornell Medical College, New York, USA



CAMBRIDGE
UNIVERSITY PRESS

Cambridge University Press

978-1-107-64323-9 — MRI from Picture to Proton

Donald W. McRobbie , Elizabeth A. Moore , Martin J. Graves , Martin R. Prince

Frontmatter

[More Information](#)

CAMBRIDGE UNIVERSITY PRESS

University Printing House, Cambridge CB2 8BS, United Kingdom

Cambridge University Press is part of the University of Cambridge.

It furthers the University's mission by disseminating knowledge in the pursuit of education, learning and research at the highest international levels of excellence.

www.cambridge.org

Information on this title: www.cambridge.org/9781107643239

DOI: 10.1017/9781107706958

© Donald W. McRobbie, Elizabeth A. Moore, Martin J. Graves and Martin R. Prince 2003, 2007, 2017

This publication is in copyright. Subject to statutory exception and to the provisions of relevant collective licensing agreements, no reproduction of any part may take place without the written permission of Cambridge University Press.

First published: 2003

Second edition 2007

Third edition 2017

Printed in the United Kingdom by Clays, St Ives plc

A catalogue record for this publication is available from the British Library

Library of Congress Cataloguing in Publication data

Names: McRobbie, Donald W., 1958-, author. | Moore, Elizabeth A. (Scientist), author. | Graves, Martin J., author.

Title: MRI from picture to proton / Donald W. McRobbie, Elizabeth A. Moore, Martin J. Graves.

Description: 3rd edition. | Cambridge ; New York : University Printing House, Cambridge University Press, 2016. | Preceded by MRI from picture to proton / Donald W. McRobbie . . . [et al.]. 2nd ed. 2007. | Includes bibliographical references and index.

Identifiers: LCCN 2016008139 | ISBN 9781107643239 (pbk.)

Subjects: | MESH: Magnetic Resonance Imaging

Classification: LCC RC78.7.N83 | NLM WN 185 | DDC 616.07/548-dc23 LC record available at <http://lccn.loc.gov/2016008139>

ISBN 978-1-107-64323-9 Paperback

Cambridge University Press has no responsibility for the persistence or accuracy of URLs for external or third-party internet websites referred to in this publication, and does not guarantee that any content on such websites is, or will remain, accurate or appropriate.

.....

Every effort has been made in preparing this book to provide accurate and up-to-date information which is in accord with accepted standards and practice at the time of publication. Although case histories are drawn from actual cases, every effort has been made to disguise the identities of the individuals involved. Nevertheless, the authors, editors and publishers can make no warranties that the information contained herein is totally free from error, not least because clinical standards are constantly changing through research and regulation. The authors, editors and publishers therefore disclaim all liability for direct or consequential damages resulting from the use of material contained in this book. Readers are strongly advised to pay careful attention to information provided by the manufacturer of any drugs or equipment that they plan to use.

Cambridge University Press

978-1-107-64323-9 — MRI from Picture to Proton

Donald W. McRobbie , Elizabeth A. Moore , Martin J. Graves , Martin R. Prince

Frontmatter

[More Information](#)

I would like to acknowledge the following, with thanks: Dr Marc Agzarian, Gregory Brown, Patrick Revel,
Kathryn McClintock

DWMcR

Dedicated to inspirational friends throughout the MRI world (you know who you are).

EAM

To my family, friends and colleagues.

MJG

We could not have completed this without the support of CUP's editorial staff, particularly Kirsten Bot
and the late Richard Marley.

Cambridge University Press

978-1-107-64323-9 — MRI from Picture to Proton

Donald W. McRobbie , Elizabeth A. Moore , Martin J. Graves , Martin R. Prince

Frontmatter

[More Information](#)

Contents

Glossary x

- 1 **MR: What's the Attraction?** 1
 - 1.1 It's not Rocket Science, but I Like It 1
 - 1.2 A Brief History of Medical Imaging 1
 - 1.3 How to Use this Book 5

- 2 **Early Daze: Your First Week in MR** 11
 - 2.1 Introduction 11
 - 2.2 Welcome to the MR Unit 11
 - 2.3 Safety First 14
 - 2.4 Safety Second: Additional Practical Guidelines 17
 - 2.5 The Patient's Journey 21
 - 2.6 MRI Radiographer's Blog ... A Few Years On 23

- 3 **Seeing is Believing: Introduction to Image Contrast** 26
 - 3.1 Introduction 26
 - 3.2 Introduction to the T-Words 27
 - 3.3 T₂-Weighted Images 27
 - 3.4 FLAIR Images 28
 - 3.5 T₁-Weighted Images 28
 - 3.6 T_{1w} Images Post-Gd 29
 - 3.7 STIR Images 30
 - 3.8 PD-Weighted Images 32
 - 3.9 Gradient-Echo Images 35
 - 3.10 More About Contrast Agents 37
 - 3.11 Angiographic Images 38
 - 3.12 Diffusion-Weighted Images 39

- 4 **Lost in the Pulse Sequence Jungle?** 41
 - 4.1 Introduction 41
 - 4.2 Anatomy of a Pulse Sequence 41
 - 4.3 Take Me for a Spin (Echo) 43
 - 4.4 The Other Branch of the Tree: Gradient Echo 49
 - 4.5 Echo Planar Imaging 54
 - 4.6 The Pulse Sequence Traveller 54

- 5 **The Devil's in the Detail: Pixels, Matrices and Slices** 55
 - 5.1 Introduction 55
 - 5.2 From Analogue Signal to Digital Image 55
 - 5.3 Matrices, Pixels and an Introduction to Resolution 58
 - 5.4 Slices and Orientations 61
 - 5.5 Displaying Images 61
 - 5.6 What do the Pixels Represent? 63
 - 5.7 From 2D to 3D 64

- 6 **What You Set is What You Get: Basic Image Optimization** 67
 - 6.1 Introduction 67
 - 6.2 Looking on the Bright Side: What are we Trying to Optimize? 67
 - 6.3 Trading Places: Resolution, SNR and Scan Time 72
 - 6.4 Ever the Optimist: Practical Steps to Optimization 76

- 7 **Improving Your Image: How to Avoid Artefacts** 81
 - 7.1 Introduction 81
 - 7.2 Keep Still Please! Motion Artefacts 81
 - 7.3 Lose the Fat! 88
 - 7.4 Digital Imaging Artefacts 92
 - 7.5 Susceptibility and Metal Artefacts 96
 - 7.6 Equipment Artefacts 98
 - 7.7 What's Causing this Artefact? 101

- 8 **Spaced Out: Spatial Encoding** 102
 - 8.1 Introduction 102
 - 8.2 Anatomy of a Pulse Sequence 102
 - 8.3 From Larmor to Fourier via Gradients 103
 - 8.4 Something to get Excited About: The Image Slice 106
 - 8.5 In-Plane Localization 110
 - 8.6 Consequences of Fourier Imaging 117

Cambridge University Press

978-1-107-64323-9 — MRI from Picture to Proton

Donald W. McRobbie , Elizabeth A. Moore , Martin J. Graves , Martin R. Prince

Frontmatter

[More Information](#)

Contents

8.7 Speeding It Up	120	13.3 One Tree, Many Branches: FIDs, Echoes and Coherences	207
8.8 3D FT	121	13.4 Ultra-Fast GE Imaging	218
9 Getting in Tune: Resonance and Relaxation	124	14 The Parallel Universe: Parallel Imaging and Novel Acquisition Techniques	225
9.1 Introduction	124	14.1 Introduction	225
9.2 Spinning Nuclei	124	14.2 Groundwork	225
9.3 Measuring the Magnetic Moment	127	14.3 Making SENSE: Parallel Imaging in Image Space	227
9.4 Relaxation Times	129	14.4 SMASH Hits: Parallel Imaging in k-Space	230
9.5 Creating Echoes	132	14.5 Undersampling by Simultaneous Multi-Slice Excitation	236
9.6 Relaxation Time Mechanisms	135	14.6 Image Quality in Parallel Imaging	237
9.7 Gadolinium-based Contrast Agents	141	14.7 k-t BLAST	240
10 Let's Talk Technical: MR Equipment	144	14.8 Non-Cartesian Acquisition Schemes	242
10.1 Introduction	144	14.9 Compressed Sensing	248
10.2 Magnets	144	15 Go with the Flow: MR Angiography	251
10.3 Gradient Subsystem	149	15.1 Introduction	251
10.4 Radiofrequency Transmit Subsystem	154	15.2 Effect of Flow in Conventional Imaging	251
10.5 RF Receiver Subsystem	158	15.3 Non-Contrast MR Angiography	255
10.6 Computer Systems	162	15.4 Contrast-Enhanced MRA	263
10.7 Siting and Installation	163	15.5 Susceptibility-Weighted Imaging	267
10.8 Other Types of MRI Systems	164	16 A Heart to Heart Discussion: Cardiac MRI	269
11 Ghosts in the Machine: Quality Control	166	16.1 Introduction	269
11.1 Introduction	166	16.2 Patient Set-up	269
11.2 The Quality Cycle	166	16.3 Morphological Imaging	272
11.3 Signal Parameters	169	16.4 Functional Imaging	273
11.4 Geometric Parameters	173	16.5 Myocardial Perfusion	282
11.5 Relaxation Parameters	177	16.6 Myocardial Viability	284
11.6 Artefacts	178	16.7 Myocardial Tissue Characterization	286
11.7 Spectroscopic QA	179	16.8 Coronary Artery Imaging	286
11.8 Temporal Stability	179	17 It's Not Just Squiggles: In Vivo Spectroscopy	288
11.9 Other Specialist QA	181	17.1 Introduction	288
Part II The Specialist Stuff		17.2 Some Basic Chemistry	288
12 Acronyms Anonymous I: Spin Echo	185	17.3 Single-Voxel Spectroscopy	291
12.1 Introduction	185	17.4 Processing of Single-Voxel Spectra	295
12.2 Conventional Spin Echo	185	17.5 Chemical Shift Imaging	297
12.3 RARING to Go: Fast Spin-Echo Techniques	186	18 To BOLDly Go: fMRI, Perfusion and Diffusion	303
12.4 The Extended Family of TSE	191	18.1 Introduction	303
12.5 Combining Gradient and Spin Echoes	200	18.2 Diffusion Imaging	303
13 Acronyms Anonymous II: Gradient Echo	207		
13.1 Introduction	207		
13.2 Image Formation in Gradient Echo	207		

Cambridge University Press

978-1-107-64323-9 — MRI from Picture to Proton

Donald W. McRobbie , Elizabeth A. Moore , Martin J. Graves , Martin R. Prince

Frontmatter

[More Information](#)

Contents

18.3 Perfusion Imaging	311	20.3 Gradient Effects	347
18.4 Dynamic Contrast Enhancement: Permeability Imaging	316	20.4 Static Field Effects	351
18.5 Brain Activation Mapping Using the BOLD Effect	319	20.5 MR Exposures and Pregnancy	352
19 Making it Count: Quantitative MRI	326	20.6 Occupational Exposure	352
19.1 Introduction	326	20.7 Contrast Agent Safety	354
19.2 Relaxation Times	326	20.8 So is MRI Safe?	356
19.3 Diffusion Parameters	334	21 Where Are We Going Now?	358
19.4 Tissue Perfusion and Permeability	335	21.1 Introduction	358
19.5 Fat Quantification	335	21.2 7 Tesla Systems	358
19.6 MR Elastography	338	21.3 Hyperpolarization	360
19.7 Accuracy, Precision, and Diagnostic Confidence	341	21.4 MR-PET	362
20 But is it Safe? Bio-effects	345	21.5 MR-LINAC	363
20.1 Introduction	345		
20.2 Radiofrequency Effects	345		
		Appendix: maths revision	365
		Index	369

Glossary

See also: Liney G (2011) *MRI from A to Z*, 2nd edition. London: Springer-Verlag.

Acronym/symbol	Term	Explanation
γ	Gyromagnetic ratio	A constant which relates the precessional frequency of a nucleus to the external magnetic field B_0 . For ^1H $\gamma = 2.68 \times 10^8$ radians s^{-1} .
μ	Magnetic moment	Microscopic magnetic field originating from nuclear spin.
α	Flip angle	The angle through which magnetization M is tipped, or flipped, by an RF B_1 pulse.
ω_0, f_0	Larmor frequency	The precession frequency of the nuclear spins, or the resonance frequency for nuclear magnetic transitions.
ΔB	Inhomogeneity	Non-uniformity (of a magnetic field), expressed in parts-per-million (ppm).
τ_c	Correlation time	The average time between molecular collisions, part of the relaxation mechanism of protons.
χ_m	Susceptibility	Property determining the magnetization of a material in an external magnetic field.
180°	180° pulse	An RF (radiofrequency) pulse which flips the magnetization through 180° . May be used either for inversion or refocusing.
2D FT	Two-Dimensional Fourier Transform	The process whereby the data from frequency and phase-encoded MR signals is converted to a two-dimensional image.
3D FT	Three-Dimensional Fourier Transform	A volume-based Cartesian image acquisition which utilizes two phase-encode directions.
4D-TRAK	4D-Time-Resolved Angiography using Keyhole	Method for time-resolved CE-MRA (Philips)
90°	90° pulse	An RF (radiofrequency) pulse which flips the magnetization through 90° . Usually used for excitation, but can also act as a refocusing pulse.
ARC	Auto-calibrating Reconstruction for Cartesian sampling	A k-space-based parallel imaging method that uses auto-calibration, related to GRAPPA (GE Healthcare).
ASL	Arterial Spin Labelling	A method to assess tissue perfusion using endogenous water as a contrast agent.

Cambridge University Press

978-1-107-64323-9 — MRI from Picture to Proton

Donald W. McRobbie , Elizabeth A. Moore , Martin J. Graves , Martin R. Prince

Frontmatter

[More Information](#)

Glossary

(cont.)

Acronym/symbol	Term	Explanation
ASSET	Array Spatial Sensitivity Encoding Technique	An image-based parallel imaging method related to SENSE (GE Healthcare).
B	Magnetic field	Magnetic flux density or induction, measured in tesla (T).
B_0		The main (static) magnetic field, e.g. 1.5 T.
B_1		The alternating radiofrequency magnetic field used to rotate the net magnetization.
BASG	Balanced SARGE	A fully rewound GE imaging sequence (Hitachi).
bFFE	Balanced FFE	A fully rewound GE imaging sequence (Philips).
BLADE	BLADE	A hybrid Cartesian/radial acquisition method that can partly correct for patient motion (Siemens; 'BLADE' is not an acronym, it is a tradename). See also PROPELLER.
BLAST	Broad-use Linear Acquisition Speed-up Technique	A method for the acceleration of dynamic images (Philips).
BOLD	Blood Oxygen Level Dependent	Effect of deoxygenated blood on MR signals.
BRAVO	BRAin VOlume imaging	IR-prepared fast 3D gradient echo for isotropic brain imaging (GE Healthcare).
BSI	Blood Sensitive Imaging	Method for non-contrast MR angiography based on 3D TSE (Hitachi).
bSSFP	Balanced Steady-State-Free-Precession	An alternative generic name for fully rewound GE sequences.
b-TRANCE	Balanced Triggered Angiography Non Contrast Enhanced	Method for non-contrast MR angiography based on fully rewound GE (Philips).
BW, RBW	Bandwidth, receive bandwidth	The range of frequencies contained in a pulse or signal. The range of frequencies that may be detected by the MR receiver.
CARE Bolus	Combined Applications to Reduce Exposure Bolus	Method for fluoro-triggered contrast-enhanced MR angiography (Siemens).
CE-MRA	Contrast Enhanced Magnetic Resonance Angiography	Methods for acquiring MR angiograms using an injection of gadolinium-based contrast agent.
CENTRA	Contrast ENhanced Timing Robust Angiography	Centric k-space method for time-resolved CE-MRA (Philips).
CHESS	CHEmical Shift Selective	Chemical excitation or saturation of either water or fat ^1H nuclei based upon differences in the Larmor frequency of each chemical species.
CIA	Contrast Improved Angiography	Method for non-contrast MR angiography based on 3D TSE (Toshiba).
CISS	Constructive Interference in the Steady State	A fully rewound GE imaging sequence with two acquisitions and phase-cycling to reduce banding artefacts (Siemens).

Cambridge University Press

978-1-107-64323-9 — MRI from Picture to Proton

Donald W. McRobbie , Elizabeth A. Moore , Martin J. Graves , Martin R. Prince

Frontmatter

[More Information](#)**Glossary**

(cont.)

Acronym/symbol	Term	Explanation
CLEAR	Constant LEvel AppeRance	Post-processing filter to reduce signal inhomogeneities caused by coil sensitivity (Philips).
CP	Carr–Purcell sequence	Sequence containing a series of $90^\circ - 180^\circ - 180^\circ - \dots$ pulses, resulting in an echo train of length ETL.
CPMG	Carr–Purcell–Meiboom–Gill sequence	Similar to CP but with a 90° phase difference between the excitation and refocusing pulses. Even-numbered echoes are corrected for inaccuracies in the refocusing pulses.
CS	Compressed sensing	Rapid image acquisition technique applicable to sparse data sets.
CUBE		3D TSE sequence with variable refocusing flip angles (GE Healthcare; Cube is not an acronym, it is a trademark).
DCE	Dynamic Contrast Enhanced	A dynamic $T_1 w$ method used to monitor the signal changes as a contrast agent passes through tissue.
DESS	Double Echo Steady State	A form of GE imaging sequence that combines two different types of gradient-echo signals to form one image (Siemens).
DIET	Delayed Interval Echo Train	A TSE imaging sequence with an echo spacing designed to maintain J-coupling, thus with reduced fat signal compared to other TSE sequences (Toshiba).
DIR	Double Inversion Recovery	Method to suppress the signal from flowing blood, also known as black or dark-blood preparation. Alternatively, a dual inversion prepulse used with 3D TSE to null two tissues, typically CSF and grey matter in brain imaging.
Dixon		TSE or GE techniques for producing separate water and fat images, named after the inventor.
DRIVE	DRIVen Equilibrium	90° RF pulse added to end of FSE echo train to restore longitudinal magnetization (Philips).
DRKS	Differential Rate K-space Sampling	Centric k-space method for time-resolved CE-MRA (Toshiba).
DSC	Dynamic Susceptibility Contrast	A dynamic $T_2^* w$ method used to monitor the signal changes as a contrast agent passes through tissue.
DSV	Diameter Spherical Volume	Spherical region with this diameter over which B_0 uniformity is measured.
DTI	Diffusion Tensor Imaging	Method to determine the anisotropy of tissue diffusion.
EPI	Echo Planar Imaging	A pulse sequence that allows rapid MR acquisition, where k-space is collected following a single excitation pulse.
ESP	Echo SPacing	The time interval between refocusing pulses in a TSE sequence.

Cambridge University Press

978-1-107-64323-9 — MRI from Picture to Proton

Donald W. McRobbie , Elizabeth A. Moore , Martin J. Graves , Martin R. Prince

Frontmatter

[More Information](#)

Glossary

(cont.)

Acronym/symbol	Term	Explanation
ETL	Echo Train Length	The number of echoes acquired following a single initial excitation.
FASE	Fast Advanced Spin Echo	A multiple spin-echo sequence that uses a segmented k-space (Toshiba). SuperFASE is a variant with very short echo spacing. See also TSE.
FBI	Fresh Blood Imaging	Method for non-contrast MR angiography based on 3D TSE (Toshiba).
FE	Frequency Encoding	A process using a frequency encode gradient to determine the position of MR signal during its acquisition.
FFE, TFE	Fast Field Echo, Turbo Field Echo	A GE imaging sequence (Philips). See also T1-FFE, bFFE, T2-FFE. TFE is a fast version of FFE.
FID	Free Induction Decay	MR signal following a single RF excitation pulse.
FIESTA	Fast Imaging with Enhanced Steady sTate Acquisition	A fully rewound GE imaging sequence (GE Healthcare).
FIESTA-c	Fast Imaging with Enhanced Steady sTate Acquisition Cycled phases	A fully rewound GE imaging sequence with two acquisitions and phase-cycling to reduce banding artefacts (GE Healthcare). See also CISS.
FIR	Fast Inversion Recovery	A TSE imaging sequence with an inversion prepulse, used for FLAIR or STIR (Hitachi).
FISP, TrueFISP	Fast Imaging with Steady Precession	A rewound GE imaging sequence (Siemens). The fully rewound version is called TrueFISP.
FLAIR	Fluid Attenuated Inversion Recovery	An SE-based imaging sequence used to null the signal from cerebrospinal fluid (CSF) based upon its longitudinal relaxation time T_1 .
FLASH	Fast Low Angle SHot	A spoiled GE imaging sequence using RF spoiling (Siemens). Turbo-FLASH is a fast version of FLASH.
FLUTE	FLUoro TriggEred	Method for fluoro-triggered contrast-enhanced MR angiography (Hitachi).
fMRI	Functional Magnetic Resonance Imaging	Method to investigate signal changes based upon the BOLD contrast mechanism.
f_N	Nyquist frequency	The minimum frequency required to accurately sample (digitize) a signal.
FOV	Field Of View	The size of the region to be imaged.
FSBB	Flow Sensitive Black Blood	Method for susceptibility-weighted imaging (Toshiba).
FSE	Fast Spin Echo	A multiple spin-echo sequence that uses a segmented k-space. See also TSE.
FWHM	Full Width at Half Maximum	A measure of slice width or thickness.
GE	Gradient Echo	A pulse sequence which creates a signal at time TE by refocusing using gradients. Alternatively, the signal itself at time TE.

Cambridge University Press

978-1-107-64323-9 — MRI from Picture to Proton

Donald W. McRobbie , Elizabeth A. Moore , Martin J. Graves , Martin R. Prince

Frontmatter

[More Information](#)**Glossary**

(cont.)

Acronym/symbol	Term	Explanation
GMN	Gradient Moment Nulling	A method to eliminate the phase shifts due to moving spins. Also known as flow or velocity compensation.
GRAPPA	GeneRalized Auto-calibrating Partial Parallel Acquisition	A k-space-based parallel imaging method that uses auto-calibration (Siemens).
GRASE	Gradient and Spin Echo	A pulse sequence that acquires both spin and gradient echoes within a single TSE-type readout.
GRE	Gradient Recalled Echo	A rewound GE imaging sequence (GE Healthcare).
G_x, G_y, G_z	Gradients	Magnetic field gradients, or linear variations in B_z along orthogonal directions x , y and z , measured in mT m^{-1} .
HASTE	Half-Fourier Acquired Single shot Turbo spin Echo	A single shot TSE imaging sequence that also uses half-Fourier data acquisition and reconstruction. See also SS-TSE.
IDEAL	Iterative Decomposition of water and fat using Echo Asymmetry and Least-squares estimation	A technique for producing separate water and fat images (GE Healthcare). See also Dixon.
IFIR	Inhance inFlow Inversion Recovery	Method for non-contrast MR angiography based on fully rewound GE (GE Healthcare).
iPAT	Integrated Parallel Imaging Techniques	An alternative name for parallel imaging techniques (Siemens).
IR	Inversion Recovery	A pulse sequence that initially inverts M_0 and measures its longitudinal relaxation after inversion time TI.
ISCE	Inclined Slab for Contrast Enhancement	Linear flip angle variation used in 3D-MRA to reduce saturation effects in slice-encoding direction (Toshiba). See also TONE.
JET		A hybrid Cartesian/radial acquisition method that can partly correct for patient motion (Toshiba; JET is not an acronym, it is a tradename). See also PROPELLER.
LAVA	Liver Acquisition with Volume Acceleration	3D T_1 w GE with fat suppression used for dynamic liver imaging (GE Healthcare). See also THRIVE, VIBE.
M	Magnetization	The magnetic field vector produced in a material when placed in an external magnetic field, with units amperes per meter (A m^{-1}).
M	Gradient moment	The time integral of a gradient waveform.
M_0	Equilibrium Magnetization	Equilibrium magnetization formed from the vector sum nuclear magnetic moments when placed in an external magnetic field B_0 .
MAVRIC	Multi-Acquisition with Variable Resonances Image Combination	Method based on 3D TSE to reduce artefacts when imaging in the presence of metal implants (GE Healthcare). Also a generic term.

Cambridge University Press

978-1-107-64323-9 — MRI from Picture to Proton

Donald W. McRobbie , Elizabeth A. Moore , Martin J. Graves , Martin R. Prince

Frontmatter

[More Information](#)

Glossary

(cont.)

Acronym/symbol	Term	Explanation
MEDIC	Multi-Echo Data-Image Combination	Method that combines multiple gradient echoes to improve image quality and contrast (Siemens).
MERGE	Multi-Echo Recombined Gradient Echo	Method that combines multiple gradient echoes to improve image quality and contrast (GE Healthcare).
mFFE	Multi-echo FFE	Method that combines multiple gradient echoes to improve image quality and contrast (Philips).
MIP	Maximum Intensity Projection	An image processing operation used in MR angiography to produce 2D projection images from 3D raw image data.
mIP	minimum Intensity Projection	An image processing operation used in susceptibility-weighted angiography to produce 2D projection images from 3D raw image data.
MOTSA	Multiple Overlapping Thin Slab Acquisition	A technique for acquiring multiple 3D slabs for 3D non-contrast MRA, avoiding saturation effects.
MPR	Multi-Planar Reformat	An image processing operation used to produce new 2D slices at arbitrary orientations from 3D raw image data.
MP-RAGE	Magnetization-Prepared Rapid Acquisition by Gradient Echoes	IR-prepared fast 3D gradient echo for isotropic brain imaging (Siemens). Also a generic term.
MRA	MR Angiography	Imaging of blood vessels, usually arteries.
mSENSE	Modified SENSitivity Encoding	An image-based parallel imaging method related to SENSE using auto-calibration (Siemens).
MT	Magnetization Transfer	Excitation of the bound fraction of nuclei using an off-resonance B_1 pulse.
MultiVane	MultiVane	A hybrid Cartesian/radial acquisition method that can partly correct for patient motion (Philips); MultiVane is not an acronym, it is a trademark. See also PROPELLER.
M_{xy}	Transverse magnetization	Component of M in the xy plane. M_{xy} produces the signal.
M_z	Longitudinal magnetization	Component of M in the z axis, static field direction, denoted M_z .
NATIVE	Non-contrast MR of ArTerles and VEins	Methods for non-contrast MR angiography (Siemens). NATIVE-SPACE is based on 3D TSE; NATIVE-TrueFISP is based on fully rewound GE.
NATURAL	NATural Uniformity Realization ALgorithm	Post-processing filter to reduce signal inhomogeneities caused by coil sensitivity (Hitachi).
NC-MRA	Non-Contrast Magnetic Resonance Angiography	Methods for acquiring MR angiograms without using exogenous contrast agent.
NEX	Number of EXcitations	Number of signal averages (GE Healthcare). See also NSA.
NMR	Nuclear Magnetic Resonance	The basic phenomenon underlying MRI.

Cambridge University Press

978-1-107-64323-9 — MRI from Picture to Proton

Donald W. McRobbie , Elizabeth A. Moore , Martin J. Graves , Martin R. Prince

Frontmatter

[More Information](#)**Glossary**

(cont.)

Acronym/symbol	Term	Explanation
NSA	Number of Signal Acquisitions	Number of signal acquisitions averaged to improve signal-to-noise ratio (SNR). See also NEX.
O-MAR	Ortho-Metal Artefact Reduction	Method based on multi-slice TSE to reduce artefacts when imaging in the presence of metal implants (Philips). See also SEMAC.
PACE	Prospective Acquisition CorREction	Technique for updating scan geometry in real time based on detecting motion by navigators (Siemens).
PBSG	Phase Balanced SARGE	A fully rewound GE imaging sequence with two acquisitions and phase-cycling to reduce banding artefacts (Hitachi).
PC	Phase contrast	A non-contrast MRA technique that relies on the phase shift caused by spins moving through a magnetic field gradient.
PD	Proton density	The MR signal intensity in the absence of relaxation, related to number of hydrogen nuclei per unit volume, equivalent to M_0 .
PE	Phase Encoding	A process using a phase-encode gradient to encode the MR signal in terms of spatial frequencies.
PEAKS	PEak Arterial K Space	Centric k-space method for time-resolved CE-MRA (Hitachi).
PEAR	Phase-Encoded Artefact Reduction	Reordered phase-encoding to reduce respiratory motion artefacts (Philips). See also ROPE.
PERRM	Phase-Encode Reordering to Reduce Motion	Reordered phase encoding to reduce respiratory motion artefacts (Hitachi). See also ROPE.
PNS	Peripheral nerve stimulation	Peripheral nerve stimulation is a bio-effect caused by rapidly time-varying magnetic fields.
ppm	Parts Per Million	A measure of the chemical shift between metabolites. Alternatively a measure of field inhomogeneity.
Promo	Prospective Motion correction	Technique for updating scan geometry in real time based on detecting motion by navigators (GE Healthcare).
PROPELLER	Periodically Rotated Overlapping Parallel Lines with Enhanced Reconstruction	A hybrid Cartesian/radial acquisition method that can partly correct for patient motion (GE Healthcare). Also a generic term.
PSIF		A time-reversed GE imaging sequence with improved T_2 w contrast (Siemens; PSIF is not an acronym, it is 'FISP' backwards).
PURE	Phased array UnifoRmity Enhancement	Post-processing filter to reduce signal inhomogeneities caused by coil sensitivity (GE Healthcare).
r_1, r_2	Relaxivity	The relaxivity of a contrast agent determines its shortening effect on relaxation times.

Cambridge University Press

978-1-107-64323-9 — MRI from Picture to Proton

Donald W. McRobbie , Elizabeth A. Moore , Martin J. Graves , Martin R. Prince

Frontmatter

[More Information](#)

Glossary

(cont.)

Acronym/symbol	Term	Explanation
R ₁ , R ₂ or R ₂ [*]	Relaxation rate	Reciprocal of relaxation time.
RADAR	RADial Acquisition Regime	A hybrid Cartesian/radial acquisition method that can partly correct for patient motion (Hitachi). See also PROPELLER.
RAPID, RAPID-3D	Rapid Acquisition through Parallel Imaging Design	An image-based parallel imaging method related to SENSE (Hitachi).
rb	Rheobase	The minimum threshold for a physiological response to a stimulus.
RESTORE		90° RF pulse added to end of FSE echo train to restore longitudinal magnetization (Siemens; RESTORE is not an acronym, it is a trademark).
ROPE	Respiratory-Ordered Phase Encoding	Reordered phase encoding to reduce respiratory motion artefacts.
RSSG	RF Spoiled SARGE	A spoiled GE imaging sequence using RF spoiling (Hitachi).
SAR	Specific Absorption Rate	The RF power per unit mass deposited in tissue in W kg ⁻¹ .
SARGE	Steady state Acquisition Rewound Gradient Echo	A rewound GE imaging sequence (Hitachi).
SE	Spin echo	A pulse sequence which creates a signal at time TE by refocusing from two RF pulses, usually a 90° followed by a 180°. Alternatively, the signal itself at time TE.
SEMAC	Slice Encoding for Metal Artefact Correction	Method based on multi-slice TSE to reduce artefacts when imaging in the presence of metal implants.
SENSE	SENSitivity Encoding	Technique for parallel imaging based upon image-space unwrapping (Philips). Also a generic term.
SMASH	SiMultaneous Acquisition of Spatial Harmonics	Technique for parallel imaging based upon k-space calculations.
SORS-STC	Slice-selective Off-Resonance Sinc Pulse Saturation transfer contrast	Method for magnetization transfer imaging (Toshiba).
SPACE	Sampling Perfection with Application of optimized Contrasts using different flip angle Evolution	3D TSE sequence with variable refocusing flip angles (Siemens).
SPEEDER	SPEEDER	An image-based parallel imaging method related to SENSE (Toshiba; 'SPEEDER' is not an acronym, it is a trademark).
SPGR	SPoiled GRadient echo	A spoiled GE imaging sequence using RF spoiling (GE Healthcare). FSPGR is a fast version of SPGR.
SPL	Sound Pressure Level	Acoustic noise, often measured with reference to the response of the human ear in decibels, dB(A).
SR	Slew Rate	The maximum gradient amplitude divided by its minimum rise time in T m ⁻¹ s ⁻¹ .

Cambridge University Press

978-1-107-64323-9 — MRI from Picture to Proton

Donald W. McRobbie , Elizabeth A. Moore , Martin J. Graves , Martin R. Prince

Frontmatter

[More Information](#)**Glossary**

(cont.)

Acronym/symbol	Term	Explanation
SS	Slice Selection	A process using a slice-select gradient at the same time as a narrow-bandwidth RF pulse to excite a slice of tissue.
SS-TSE	Single Shot Turbo Spin Echo	A single shot TSE imaging sequence that also uses half-Fourier data acquisition and reconstruction. See also HASTE.
SSP	Sloped Slab Profile	Linear flip angle variation used in 3D-MRA to reduce saturation effects in slice-encoding direction (Hitachi).
STIR	Short TI Inversion Recovery	An IR-based imaging sequence used to null the signal from fat based upon its longitudinal relaxation time T_1 .
SWAN	T2-Star Weighted ANgiography	Method for susceptibility-weighted imaging (GE Healthcare).
SWI	Susceptibility-Weighted Imaging	Method for susceptibility-weighted imaging (Siemens).
SWIp	Susceptibility-Weighted Imaging with phase difference	Method for susceptibility-weighted imaging (Philips).
T_1	Spin-lattice relaxation time	Spin-lattice relaxation time, also known as longitudinal relaxation time. Characterizes the recovery of the longitudinal magnetization M_z towards M_0 .
T_1-FFE		A spoiled GE imaging sequence using RF spoiling (Philips).
T_2	Spin-spin relaxation time	Spin-spin relaxation time, also known as transverse relaxation time. Characterizes the decay of transverse magnetization M_{xy} to zero.
T_2^*	Apparent Spin–spin relaxation time	Apparent spin–spin relaxation time. Characterizes the decay of the free induction signal to zero.
TA		Acquisition or scan time.
TE	Echo time	Time to the peak MR signal from the initial excitation.
TFE	Turbo Field Echo	A fast GE imaging sequence (Philips). See also FFE.
THRIVE	T_1 High Resolution Isotropic Volume Excitation	3D T_1 w GE with fat suppression used for dynamic liver imaging (Philips). The eTHRIVE variant (enhanced THRIVE) uses asymmetric k-space ordering. See also LAVA, VIBE
TI	Inversion Time	See IR (inversion recovery).
TIGRE	T_1 GRadient Echo with RF fat saturation	3D T_1 w GE with fat suppression used for dynamic breast and abdomen imaging (Hitachi).
Time-SLIP	Time-Spatial Labelling Inversion Pulse	Method for non-contrast MR angiography based on fully rewound GE (Toshiba).
TOF	Time of Flight	Non-contrast MRA technique that relies on the in-flow of unsaturated spins.

Cambridge University Press

978-1-107-64323-9 — MRI from Picture to Proton

Donald W. McRobbie , Elizabeth A. Moore , Martin J. Graves , Martin R. Prince

Frontmatter

[More Information](#)

Glossary

(cont.)

Acronym/symbol	Term	Explanation
TONE	Tilted Optimized Non-saturating Excitation	Linear flip angle variation used in 3D-MRA to reduce saturation effects in slice-encoding direction (Philips, Siemens). Also a generic term.
TR	Repetition time	Repetition time of an MR pulse sequence. Time between successive excitations.
TRANCE	TRiggered Angiography Non Contrast Enhanced	Method for non-contrast MR angiography based on 3D TSE (Philips).
TRAQ	Time-Resolved AcQuisition	Method for time-resolved CE-MRA (Hitachi).
TRICKS	Time-Resolved Imaging of Contrast Kinetics	Method for time-resolved CE-MRA (GE Healthcare).
TRSG	Time-Reversed SARGE	A time-reversed GE imaging sequence (Hitachi).
TSE	Turbo Spin Echo	A multiple spin-echo sequence that uses a segmented k-space.
TWIST	Time-resolved angiography WIth Stochastic Trajectories	Method for time-resolved CE-MRA (Siemens).
UTE	Ultra-short TE	Ultra-short TE sequence capable of measuring the bound fraction of nuclei.
VASC ASL	VASCular Arterial Spin Labelling	Method for non-contrast MR angiography based on fully rewound GE (Hitachi).
VASC FSE	VASCular Fast Spin Echo	Method for non-contrast MR angiography based on 3D TSE (Hitachi).
VCG	Vector CardioGram	Method for ECG gating that helps reduce T-wave mistriggering.
v_{enc}		The maximum velocity that can be uniquely encoded in phase-contrast MR angiography.
VIBE	Volume Interpolated Breath-hold Examination	3D T_1 w GE with fat suppression used for dynamic liver imaging (Siemens).
VIBRANT	Volume Image Breast Assessment	3D T_1 w GE with fat suppression used for dynamic breast imaging (GE Healthcare).
VIEW	Volume Imaging with Echo Weighting	3D TSE sequence with variable refocusing flip angles (Philips).
WFS	Water–Fat Shift	The spatial misregistration between water and fat in the frequency encoding direction (Philips).

MR: What's the Attraction?

1.1 It's not Rocket Science, but I Like It

How would you impress a stranger you meet at a party with your intelligence? You might claim to be a brain surgeon or a rocket scientist. Well Magnetic Resonance (MR) is not rocket science, it's better. MR involves an amazing combination of advanced science and engineering, including the use of superconductivity, cryogenics, quantum physics, digital and computer technology – and all within the radiology department of your local hospital. MR imaging has evolved from unpromising beginnings in the 1970s to become nowadays the imaging method of choice for a large proportion of radiological examinations and the 'jewel in the crown' of medical technology. A modern MRI scanner is shown in Figure 1.1.

So what is it? It is an imaging method based principally upon sensitivity to the presence and properties of water, which makes up 70–90% of most tissues. The properties and amount of water in tissue can alter dramatically with disease and injury, which



Figure 1.1 Modern superconducting MR system. Courtesy of Philips Healthcare.

makes MR very sensitive as a diagnostic technique. MR detects subtle changes in the magnetism of the nucleus, the tiny entity that lies at the heart of the atom. This is probing deeper than X-rays, which interact with the clouds or shells of the electrons that orbit the nucleus. MR is a truly powerful modality. At its most advanced, MR can be used not just to image anatomy and pathology but to investigate organ function, to probe *in vivo* chemistry and even to visualize the brain thinking.

In the early days, the scanners were the domain of the physicists and engineers who invented and built them, and the technique was called NMR imaging (NMR stands for nuclear magnetic resonance). The cynics may say that the technique really took off clinically when the 'N-word' was dropped. This was sensible as the term 'nuclear', although scientifically accurate, implied a connection with nuclear energy and, in the last of the Cold War years, resonated in the public's mind with the spectre of nuclear weapons.

Because of the diversity of sciences and technologies that gave birth to and continues to nurture MR, it is an extremely hard subject to learn. A lifetime is not enough to become expert in every aspect. Clinicians, technologists and scientists all struggle with the study of the subject. The result is sometimes an obscurity of understanding or a dilution of scientific truth resulting in misconceptions. This is why we have chosen to write this book. Our aim is to introduce you to MR as a tool – rather like learning to drive a car. Once you are confident on the road, we can then start to learn how the engine works.

1.2 A Brief History of Medical Imaging

Radiology began after the accidental discovery of 'X-rays' by Roentgen in 1895. At about the same time (1896) Becquerel and the Curies were discovering radioactivity and radium and making possible the future development of nuclear medicine. Within a

couple of years most of the basic techniques of radiography were established, e.g. the use of fluorescent screens in 1896 by Pupin, contrast media reported by Lindenthal in the same year, even the principle of angiography. Early fluoroscopy entailed direct viewing from a fluorescent plate, i.e. putting your head in the main beam, a practice frowned upon today! Unfortunately radiation protection followed slightly too late for the pioneers of radiology. The next real technical break-through was the development of the image intensifier in the 1950s, but the basis of conventional radiography remained the same until the recent IT and digital revolutions. Computed tomography (CT) was a huge break-through, earning Hounsfield and Cormack the Nobel Prize for medicine and physiology in 1979. X-ray CT was unique in producing tomographic images or slices of the living human body for the first time and with a higher contrast than that achievable by conventional planar techniques. The combination of a moving X-ray gantry and the computing power necessary to reconstruct from projections made CT possible.

In nuclear medicine a similar evolution was occurring, from the development of the gamma camera by Anger in 1958 to tomographic imaging in the form of Single Photon Emission Computed Tomography (SPECT) and Positron Emission Tomography (PET), which is ongoing today. PET's clinical use is increasing, particularly in detecting metastases in oncology. Its ability to image minute concentrations of metabolites is unique and makes it a powerful research tool in the aetiology of disease and the effects of drugs.

Ultrasound was developed in the 1950s following the development of SONAR in World War II and was

unique in involving no ionizing radiation and offering the possibility of safe, non-invasive imaging. Its ability to image in real time and its sensitivity to flow, through the Doppler effect, have been key factors in its widespread role in obstetrics, cardiology, abdominal investigations and vascular imaging, real-time biopsy guidance and minimally invasive surgery.

As early as 1959, J. R. Singer at the University of California, Berkeley, proposed that NMR could be used as a non-invasive tool to measure *in vivo* blood flow. In 1971 Raymond Damadian discovered that certain mouse tumours displayed elevated relaxation times compared with normal tissues *in vitro*. This opened the door for a completely new way of imaging the human body, where the potential contrast between tissues and disease was many times greater than that offered by X-ray technology and ultrasound (Figure 1.2). At the same time, developments in cryogenics, or the study of very low temperatures, made the development of whole-body superconducting magnets possible. Damadian and his colleagues at the State University of New York, starved of mainstream research funding, went so far as to design and build their own superconducting magnet operating in their Brooklyn laboratory, and the first human body image by NMR is attributed to them. There is some dispute about who actually is the founder of modern Magnetic Resonance Imaging (MRI), but one thing is certain: Damadian coined the first MR acronym, namely FONAR (Field fOCused Nuclear mAgnetic Resonance). This set a trend, and you can see the development of the acronym family tree in Chapter 4!

In 1973, in an article in *Nature*, Paul Lauterbur proposed using magnetic field gradients to distinguish

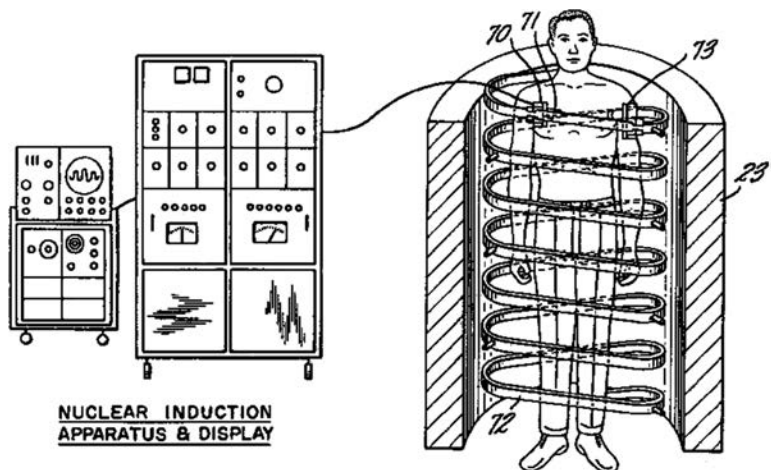


Figure 1.2 Raymond Damadian's 'Apparatus and method for detecting cancer in tissue'. US patent 3789832 filed 17 March 1972, issued 5 February 1974. Image from the US Patent and Trademark Office.

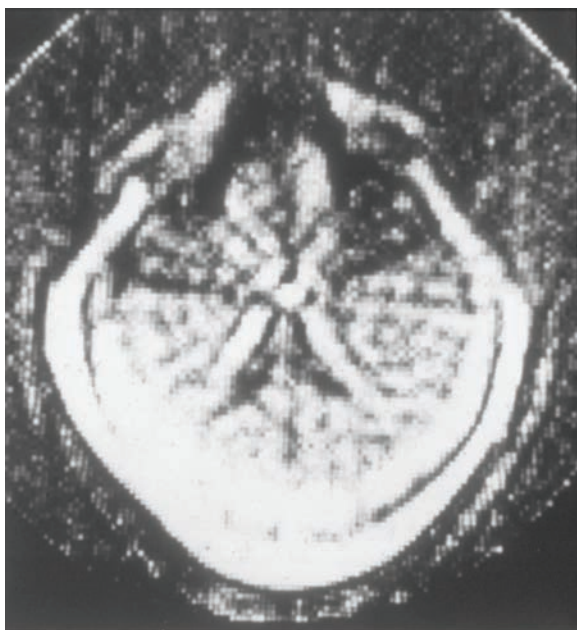


Figure 1.3 First ever human head image using MRI at 0.1 T from EMI Central Research Laboratories. For this image CT type 'back projection' was used. Courtesy of Ian Young.

between NMR signals originating from different locations, combining this with a form of reconstruction from projections (as used in CT). The use of gradients still forms the basis of all modern MRI as recognized by the Nobel Committee in 2003. Unfortunately, Lauterbur's brilliant invention was not accompanied by a brilliant acronym; he coined the obscure term 'zeugmatography', meaning imaging from a joining together (of the main field and the gradients). In contemporary MR terms Lauterbur can be said to have invented frequency encoding. While the term 'zeugmatography' sunk without a trace, fortunately the technique it described has gone from strength to strength.

Selective excitation, or the sensitization of tomographic image slices, was invented at the University of Nottingham, England in 1974 by Sir Peter Mansfield's group, a contribution also recognized by the 2003 Nobel Committee, while in 1975 Richard Ernst's group in Zurich invented two-dimensional Fourier transform imaging (2D FT). The first practical 2D FT imaging method, dubbed 'spin warp', was developed by Edelstein and Hutchison at the University of Aberdeen, Scotland in 1980. Many other researchers contributed to the early development of MR, and in this

short introduction it is impossible to do justice to them all (see Further reading). And what of the commercial development? EMI, the creators of X-ray CT through Sir Godfrey Hounsfield, were involved from very early on. Clow and Young produced the first published human head image in 1978 (Figure 1.3). EMI sold their research interest to Picker International, which became Marconi and is now part of Philips. The 'Neptune' 0.15 T superconducting system installed at the Hammersmith Hospital, London, was the first commercial clinical system. Elsewhere in Europe, Philips also dedicated substantial early investment (Figure 1.4). General Electric introduced high-field (1.5 T) systems around 1984. The technique developed rapidly through the late 1980s to become the method of choice for non-trauma neurological scanning. By 2015 there were in excess of 35 000 scanners worldwide.

The Spin Doctors: Nobel Laureates' Roll-Call (Figure 1.5)

In 1952 Edward Purcell (Harvard) and Felix Bloch (Stanford) jointly received the Nobel Prize for physics 'for their development of new methods for nuclear magnetic precision measurements and discoveries in connection therewith'. Of Purcell's discovery, the Boston Herald reported that 'it wouldn't revolutionize industry or help the housewife'. Purcell himself stated that 'we are dealing not merely with a new tool but a new subject which I have simply called nuclear magnetism. If you will think of the history of ordinary magnetism, the electronic kind, you will remember that it has been rich in difficult and provocative problems and full of surprises.' It seems that the Boston Herald misjudged the importance of NMR!

Bloch, a Swiss-born Jew and friend of quantum physicist Werner Heisenberg, quit his post in Leipzig in 1933 in disgust at the Nazi's expulsion of German Jews (as a Swiss citizen, Bloch himself was exempt). Bloch's subsequent career at Stanford was crammed with major contributions to physics and he has been called 'the father of solid state physics'.

Nicolaas Bloembergen, a Dutch citizen, was forced to hide from the Nazis for the duration of the War, reputedly living on boiled tulip bulbs, until becoming Purcell's first graduate student at Harvard two months after the discovery of NMR. With Purcell and Robert Pound he developed the theory of NMR relaxation, known now by their initials BPP. In 1981 he won a Nobel Prize for his work in laser spectroscopy. In 1991 Richard Ernst joined the MRI Nobel Laureates



Figure 1.4 0.15 T resistive magnet used by Philips in the early development of MRI. Courtesy of Philips Healthcare.

'for his contributions to the development of the methodology of high resolution nuclear magnetic resonance spectroscopy'. You could say Richard Ernst achieved the same trick twice: by his novel applications of 2D FT in both spectroscopy and imaging.

The 2003 Nobel Prize for physiology or medicine was awarded to Professor Paul Lauterbur and Sir Peter Mansfield 'for their discoveries concerning magnetic resonance imaging'. Peter Mansfield left school at 15 with no qualifications, aiming to become a printer. His scientific curiosity was sparked by the V1 and V2 flying bombs and rockets that fell on London in 1944, when he was 11. After working as a scientific assistant at the Jet Propulsion Laboratory and a spell in the army, he went back to college to complete his education, eventually becoming Professor of Physics at the University of Nottingham. He was knighted in 1993.

Paul Lauterbur is said to have been inspired to use field gradients to produce an image while eating a hamburger. His seminal paper 'Image Formation by Induced Local Interactions. Examples Employing Nuclear Magnetic Resonance' (*Nature* 242, 16 March 1973) was originally rejected. Thirty years later, *Nature* placed this work in a book of the 21 most influential scientific papers of the twentieth century.

Other Nobel Laureates associated with NMR include Norman Ramsey (1989), a spectroscopy pioneer who developed the theory of the chemical shift; Isidor Rabi (1944), Ramsey's PhD mentor, 'for his resonance method for recording the magnetic properties of atomic nuclei'; and Kurt Wüthrich (2002) for his development of NMR spectroscopy for determination of the three-dimensional structure of biological macromolecules in solution.

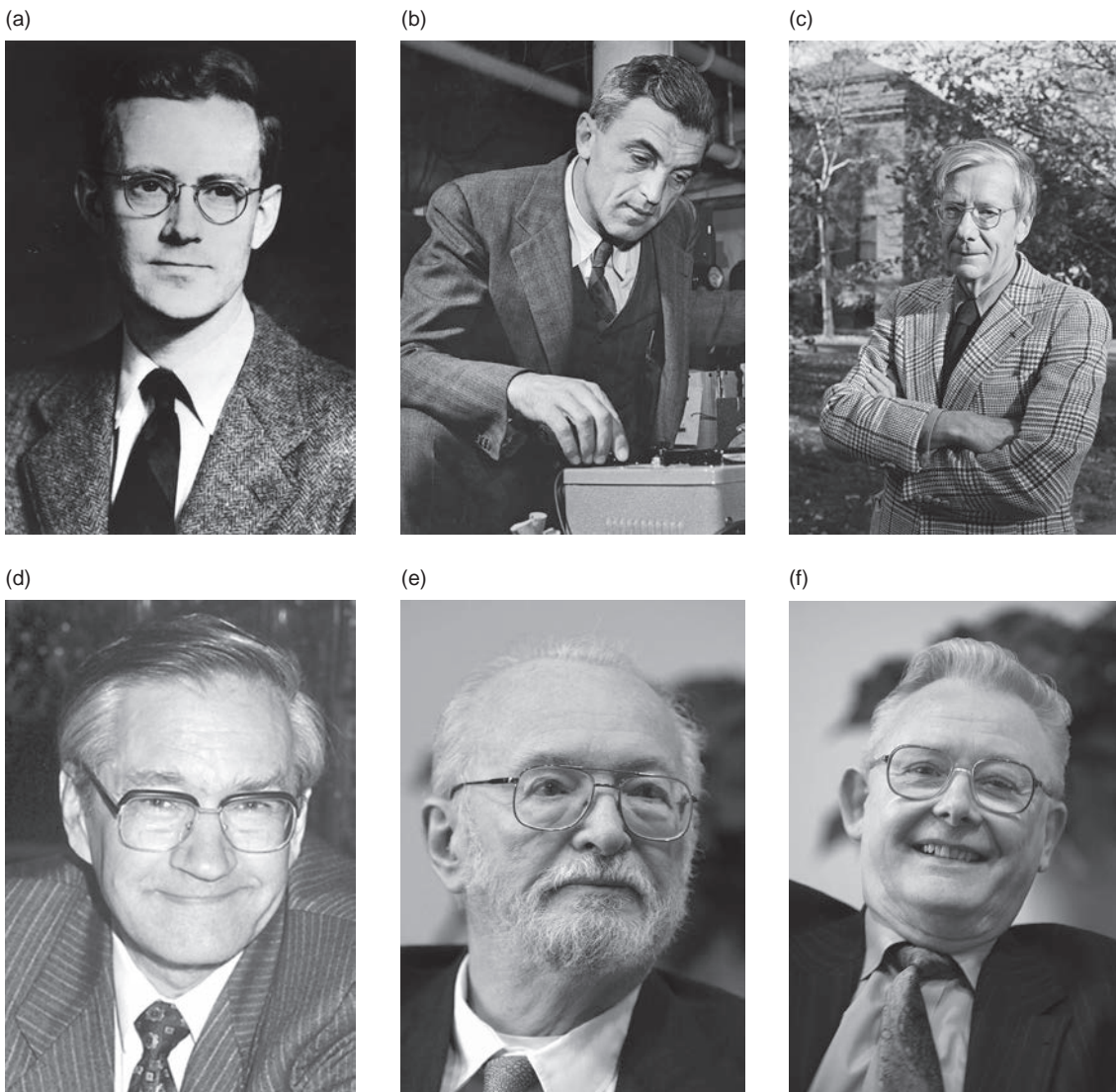


Figure 1.5 Nobel prize-winners in NMR: (a) Purcell 1912–1997, (b) Bloch 1901–1999, (c) Bloembergen b. 1920, (d) Ernst b. 1933, (e) Lauterbur 1929–2007 and (f) Mansfield b. 1933–2017. Images courtesy of Ullstein Bild/Getty Images; Bettman/Getty Images; Ira Wyman/Getty Images; the Nobel Museum; and Sven Nackstrand/Getty Images (x2) respectively.

Due to problems of low signal and high sensitivity to motion, body MR did not really take off until the 1990s. The key factors were the development of fast imaging techniques, particularly gradient echo, and phased array coil technology. The 1990s also saw the coming of age of earlier developments, namely cardiac MRI and Echo Planar Imaging (EPI). EPI, which is the fastest and one of the most cutting-edge methods, was actually one of the first imaging methods to be proposed, by Sir Peter Mansfield. EPI is now extensively used in neurological imaging through functional MRI (fMRI) and diffusion imaging.

MR development has since then exploded into new innovations and clinical applications explored throughout this book, some of which are illustrated in Figure 1.6.

1.3 How to Use this Book

Everyone starts MRI with the same basic problem: it's like nothing else they've learned in the past. All that knowledge you have about radioactive isotopes and film-screen combinations is useless to you now. Where do you start? Most MRI books start at the

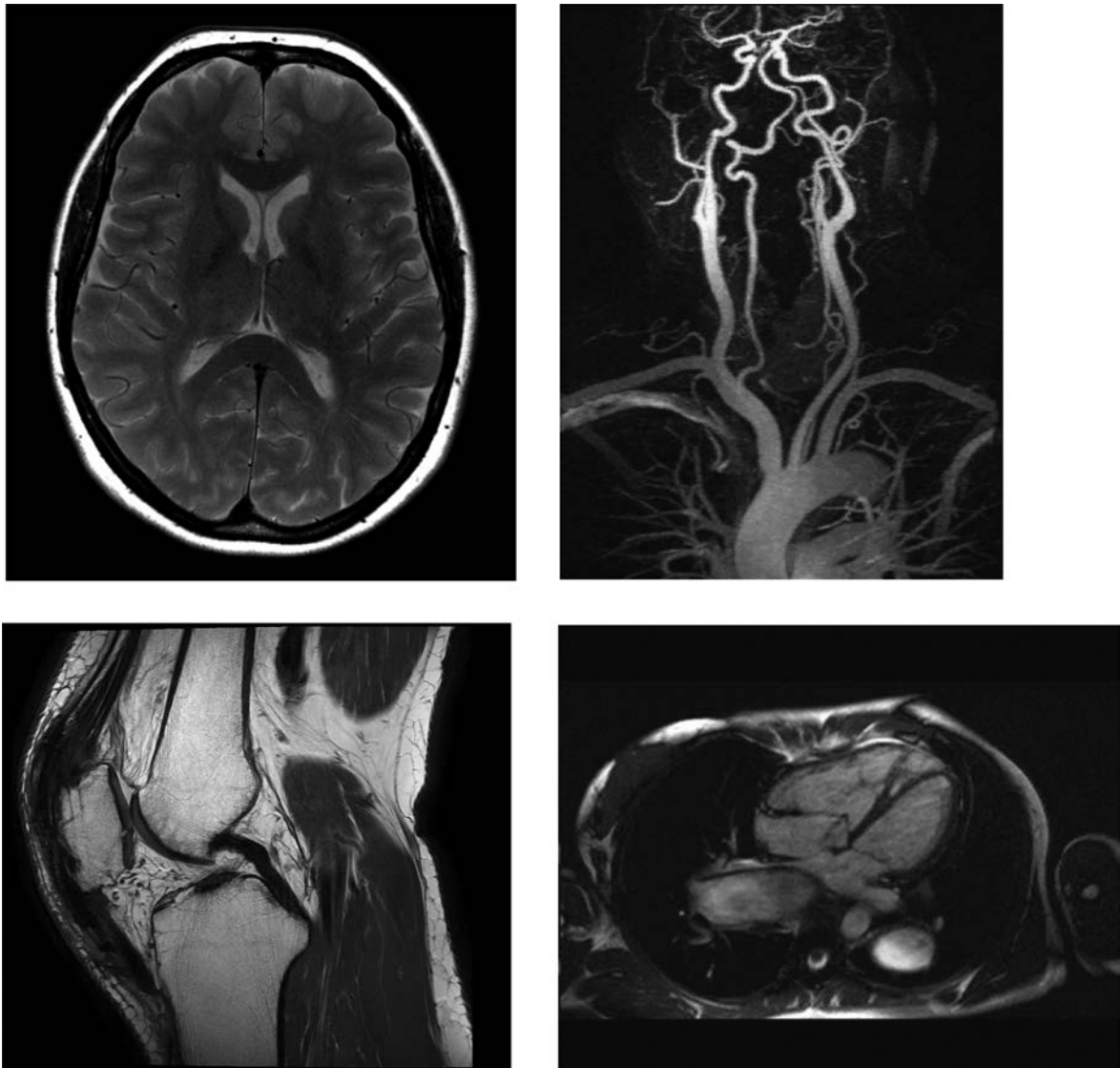


Figure 1.6 Diverse clinical applications of MRI.

beginning (a very good place to start, according to the song), and introduce protons, net magnetization, precession and the Larmor equation all in the first three pages. We think there is another way: starting at the end with the images that are produced, which is much more useful if you're already working in the MR unit. After all, you don't expect to understand how the internal combustion engine works before you learn to drive.

The book is divided into two parts. In Part I you will find everything you need to know about the basics of MRI, but presented in reverse order. We start with

things you can touch and look at: the equipment you find in an MR unit and what the images look like, using terms like 'T₁-weighted' simply as labels. Later on we talk about how the images are produced and finally we cover the underlying physics. By that stage you will be able to link these rather difficult concepts back to things which matter – the images.

Part II contains more advanced topics, such as cardiac MR and spectroscopy, in no particular order. You don't have to work right through Part I before you read these chapters; we just couldn't fit them neatly into the reverse order!

In all the chapters you will find the most basic information in the main text. Clinical boxes, shaded green, provide the clinical context as you go along. Yellow boxes are about trying things for yourself: simple (and not-so-simple) imaging experiments to run on your own scanner. Advanced boxes, shaded in blue, deal with various topics in more detail and are placed at appropriate places throughout the text.

If you're completely new to MR, we suggest you read straight through Part I, skipping all the advanced boxes. When you need to understand something a bit

better, re-read the chapter, this time taking in some of the boxes. And when you're ready for more advanced subjects like spectroscopy or fMRI, head over to Part II. The topics can seem to jump around a bit by splitting them up this way, but we think it is a good compromise, which allows us to include enough information for everyone, whether you are a new radiographer hoping to make a good impression in your new job, a radiologist interested in improving diagnostic image quality or a physicist studying for a postgraduate degree.

Further Reading

Christie DA and Tansey EM (eds) (1996) *Making the Human Body Transparent: The Impact of Nuclear Magnetic Resonance and Magnetic Resonance Imaging*. London: Wellcome Institute for the History

of Medicine. Available from: www.histmodbiomed.org/witsem/vol2 [accessed 8 January 2015].

Dawson M Joan (2013) *Paul Lauterbur and the Invention of MRI*. Cambridge, MA: MIT Press.

Mansfield P (2013) *The Long Road to Stockholm: The Story of Magnetic Resonance Imaging – An Autobiography*. Oxford: Oxford University Press.

Part

The Basic Stuff

Early Daze: Your First Week in MR

2.1 Introduction

In any first week of a new job or in a new environment, it takes a little time to become orientated and to find your way around. This chapter aims to ease those initial experiences so that you will feel more like a seasoned campaigner than a raw recruit. The following are your essential instructions:

- Magnet safety, especially from ferromagnetic projectiles, is paramount to the safe operation of any MR unit; do nothing to endanger the wellbeing of your patients and colleagues.
- The MRI unit should have clearly written policies and procedures for checking that patients and staff have no contraindications.
- Aside from the magnet itself, the coils are the main items of equipment that you will have to learn to handle (don't break them!), and learn how to position patients comfortably and effectively with them.
- Good patient cooperation is essential for safe and effective scanning; you will need good people skills.

The MR environment is a bit confusing at first, but you will soon feel at home. Enjoy the experience!

2.2 Welcome to the MR Unit

On your first day you will be asked to complete a staff safety questionnaire and should undergo a thorough safety induction. (Once you are MR trained you will find yourself doing strange things such as taking off your watch and emptying your pockets when you go into a CT room!) As part of your induction you will need to become familiar with your institution's MR safety policy or Local Rules. These will contain information about access to the controlled area or zones, local policy on implants, dealing with emergencies, staff roles and responsibilities, and other site-specific safety-related information.

2.2.1 The MR Suite

The MR suite will probably be arranged differently from the remainder of the imaging department. It may have its own dedicated reception, administration, waiting and patient-handling areas. Security will be high on the staff's agenda and the suite usually has its own lockable doors. The preoccupation with security and the 'separateness' of the MR suite is principally to prevent anyone introducing ferromagnetic items into the vicinity of the magnet, where the outcome could be disastrous.

MR accommodation may comprise:

- facilities for patient management: reception, waiting areas, changing facilities, toilets, anaesthesia and recovery area, counselling room;
- facilities for staff: reception/office, administration office, reporting rooms;
- MR system: the MRI scanner room (magnet/examination room), computer/technical room and operator's console/host computer;
- dedicated storage areas: trolley bay, general store, resuscitation trolley bay, cleaner's store.

An example of a typical MRI suite layout is given in Figure 2.1.

The MRI *scanner room*, or *magnet room* or *examination room* is a restricted access or controlled access area. See Box 'Zonal Defence: Control and Access' for further details. The MR system is actually distributed between three of the rooms in the suite: the magnet room which houses the *magnet* and *coils*, an air-conditioned technical (computer) room which is full of supporting electronics and electrical plant, and the control room which contains the MR console.

You will spend most time in the control room at the MR scanner console: where you enter patient details, select and customise scan acquisition parameters, view and post-process images, archive images and send them to the Picture Archiving

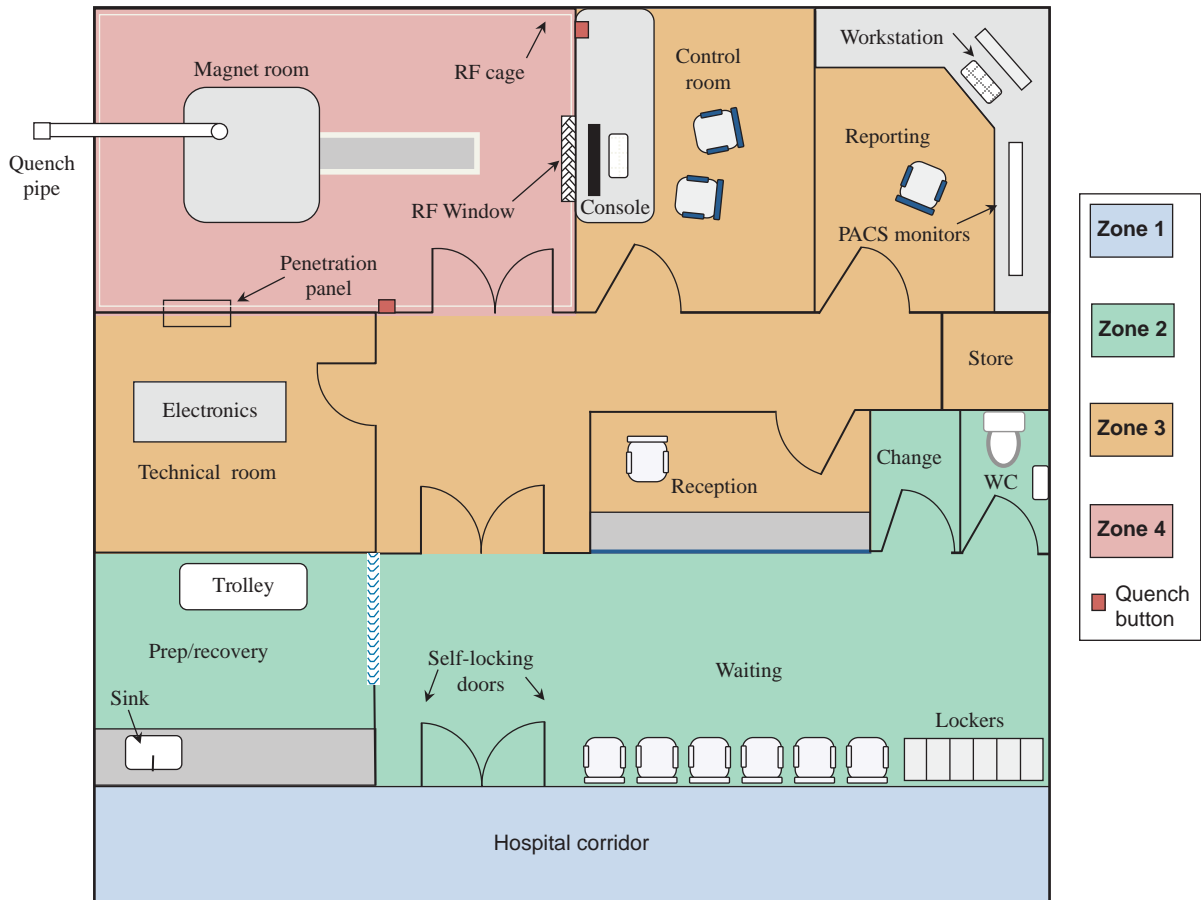


Figure 2.1 Typical MR imaging suite, showing Zones I to IV as defined by the ACR, and the controlled access area as defined by MHRA. Access to Zones III–IV and the controlled areas is strictly controlled.

and Communications System (PACS). As a trained member of MR staff you will have access to the magnet room (Zone IV) but others will not. See Box ‘Can I Go In?’.

Zonal Defence: Control and Access

The American College of Radiology (ACR) expert panel on MR safety recommends the designation of various zones for ensuring safe practice in MR units.

- **Zone I:** areas that are accessible to the general public, generally outside the MR environment completely.
- **Zone II:** the interface between the publicly accessible area (Zone I) and the areas where strict control and supervision are required (Zones III, IV). Patients may be screened in Zone II and will generally be under supervision.

- **Zone III:** a restricted access zone under the control of designated MR personnel (i.e. you!), physically demarcated from areas of greater access, with secure access only.
- **Zone IV:** the magnet or MR examination room itself.

These zones are indicated in Figure 2.1 through shading. In the UK, the Medicines and Healthcare products Regulatory Agency (MHRA) defines the ‘MR Environment’ as that which encloses the entire 0.5 mT fringe field contour, to ensure no active implant malfunction. It recommends physical demarcation, secure and restricted access to the MR Controlled Area (similar to ACR Zones III and IV). This guidance is consistent with that from the International Commission on Non-Ionising Radiation Protection (ICNIRP) and other national bodies (see Further reading).

Can I Go In?

Strict limitations are required as to which staff have access to the MR environment. The ACR designates personnel into various categories:

- *Non-MR personnel* includes all patients, visitors and non-MR staff.
- *Level 1 MR personnel* are members of staff who have received a basic level of MR safety education, sufficient to ensure their own safety in the MR environment.
- *Level 2 MR personnel* have more extensive MR safety training, relating to the hazards to patients, and would include MR technologists/radiographers and radiologists. As you are reading this book, it is assumed that you aspire to be a Level 2 staff member.

It is helpful to designate an MR Safety Officer who supervises day-to-day safety in the unit, and the MR Safety Expert who has more extensive knowledge for special or novel cases. The Institute of Physics and Engineering in Medicine (IPEM) has published guidance on the role, knowledge base and skills of the MR Safety Expert.

2.2.2 The Magnet

The magnet is the heart of the MR system. The size of an MR system is expressed in terms of its operating magnetic field strength. The scientific name of field strength is magnetic flux density or induction, and its unit is the *tesla* (T). You may also come across the *gauss* (G) as a measure of field strength. One tesla equals 10 000 gauss, i.e. 1 G equals 0.1 mT (millitesla). The Earth's magnetic field is approximately 0.05 mT (0.5 G).

The principal types of magnet used in MRI are:

- *superconducting magnets* – typically with fields of 1.5 or 3 T;
- *permanent magnets* – capable of sustaining fields up to about 0.3 T;
- *electromagnets* – capable of fields up to about 0.6 T.

The main field usually points horizontally along the bore (the opening where the patient goes). For superconducting and permanent magnets the magnetic field is *always* present; electromagnets are electrically powered and can have their field switched off; however, it is safer to assume that it is always on.

Superconducting magnets require liquid helium as a *cryogenic* cooling fluid. A sudden loss of superconductivity results in a magnet *quench* where the windings heat up, the field collapses in less than one minute and large amounts of helium boil off as gas. Accidental quenches are a rare occurrence in modern systems. In an emergency a quench can be initiated deliberately. In normal operation, small amounts of helium 'boil off' and are released into the atmosphere outside. The helium level is usually maintained by the manufacturer's service personnel. Figure 1.1 shows a typical superconducting system.

2.2.3 Radiofrequency Coils

The MR *signals* that provide the diagnostic information are produced within the patient's tissue in response to *RadioFrequency* (RF) pulses. These are generated by a *transmitter coil* which surrounds the whole or a part of the body. A *body coil* is usually built into the construction of the magnet. For imaging the head or extremities, smaller transmitter coils are sometimes used.

The MR signals produced in the body are detected using a *receive coil*. The MR signals are very weak and are sensitive to electrical interference. Electromagnetic shielding is built into the magnet room (known as a Faraday cage) to minimize this interference. It is important to keep the magnet room door closed during scanning to maintain the effectiveness of the shielding.

All MR systems have a head coil and integral body coil. Other coils you may encounter include those for the spine, neck, knee, wrist, shoulder, breast, Temporo-Mandibular Joint (TMJ), abdomen, and also peripheral vascular and other general-purpose flexible coils. You can actually use any coil to obtain an image provided it encompasses the anatomical region of interest, but specialist coils, which fit closer and are smaller, usually do a better job.

Some coils are called *arrays* or *matrix coils*. This generally means they will produce better images than a non-array version of the same sort of coil. Array coils have multiple elements and you may have to select which of them you wish to scan with. Array coils allow the use of *parallel imaging* to reduce scan time.

You must store coils carefully. They are the one part of the MR system most prone to failure due principally to excessive or careless handling. Be



Figure 2.2 Examples of coils: (a) head coil, (b) knee coil, (c) shoulder coil, (d) torso coil. Courtesy of Siemens Healthcare.

careful when connecting or disconnecting the coils: all the MR signals have to go through the coil connectors, so treat them with due respect. Examples of coils are shown in Figure 2.2.

2.2.4 Imaging Gradients

The localization of the MR signals in the body to produce images is achieved by generating short-term variations in magnetic field across the patient. These are commonly referred to as the *gradients*. The strength of steepness of the gradient is measured in milli-tesla per metre (mT m^{-1}) and the magnitude of the gradient magnetic field is in the region of tens of mT , much smaller than the main B_0 field. There is one set of *gradient coils* for each direction, x , y , z , built

into the bore of the magnet. The gradients are applied repeatedly in a carefully controlled *pulse sequence*. They generate loud tapping, clicking or higher pitched beeping sounds during scanning, like a loudspeaker. Ear protection is usually required for the patient or anyone remaining in the room during scanning – you can hear the gradients, even though you can't see them!

2.3 Safety First

Although MRI has no known long-term or harmful biological effects, the MRI environment is potentially very hazardous to both patients and staff if metal objects get pulled into the magnet bore. It is imperative that any person responsible for their own safety

or the safety of patients undergoing an MRI investigation is aware of the risks associated with taking metallic objects into the vicinity of an MRI magnet.

2.3.1 Will I Feel Anything? Bio-Effects

Unlike other medical imaging modalities, such as X-rays and CT, MRI is non-ionizing, and there is no evidence that it can cause cancer or any other disease. Biological effects of magnetic field exposures are examined in more detail in Chapter 20.

As staff you will be primarily exposed to only the static field. There are no known hazardous bio-effects for this, although some mild sensory effects may be experienced around high-field magnets. Your patients will be exposed to the main static field, the imaging (time-varying) gradient fields and RF fields. In extreme cases, the gradients can induce *peripheral nerve stimulation*. This may be alarming or annoying, but it is not harmful. The main effect of RF is the heating of tissue; however, the scanner does not let you exceed certain values of RF exposure or Specific Absorption Rate (SAR) – see Box ‘Modes and Options’. Sometimes you may need to alter the scan parameters to keep within the permitted values. Care is required to avoid the potential for RF burns when electrodes for physiological monitoring are used in the scanner. See Box ‘Burning Issues’.

Modes and Options

The international standard for the safety of MR equipment intended for medical diagnosis is the International Electrotechnical Commission (IEC) 60601-2-33. IEC 60601-1 is the general standard for the safety of medical electrical equipment. An important aspect of the IEC standard is the establishment of three operating modes:

- *normal mode* – requires only routine monitoring of the patient, the usual mode of operation;
- *first-level controlled mode* – requires medical supervision and a medical assessment of the risk versus benefit for the patient having the scan;
- *second-level controlled mode* – requires an approved human studies protocol. Security measures, e.g. a lock or password, are provided to prevent unauthorized operation in this mode.

These modes confine the SAR and imaging gradients to certain levels, considered further in Chapter 20.

The **Fixed Parameter Option: Basic** (FPO:B) was developed jointly by MRI equipment manufacturers

and implant manufacturers, and implemented as IEC TS10974. When available, the FPO:B will restrict the scanner’s RF and imaging gradient output to levels that are within the conditions for that device, if it has been manufactured to comply with the standard. Not all active devices will comply, and great care is still needed for implanted cardiac devices and deep brain and other neurological stimulators.

Burning Issues

There is a small risk of patients receiving burns through the coupling of RF energy into wires or cables, such as those used for **ElectroCardioGram** (ECG) triggering, that are touching the patient. Care must be exercised in ensuring that cables are not formed into loops, that dry flame-retardant pads are placed between cables and the patient and that any unnecessary cables are removed from the patient prior to imaging. All cables should also be inspected every time before use to ensure that there is no damage to the insulation. Furthermore, only ECG cables specifically deemed MR safe should be used. Insulating pads should be placed between the patient’s legs, if bare, and against their shoulders and upper arms if touching the side of the bore.

The MR scanner is very noisy during operation, often exceeding safety guidelines. It is recommended that all patients and any other person in the room during scanning are given ear-plugs and/or ear-defenders to reduce their exposure to acoustic noise.

Potential hazards of working with cryogens include asphyxiation in oxygen-deficient atmospheres, cold burns, frostbite and hypothermia. Additionally there is the possibility of inducing asthma in susceptible persons if cold gas is inhaled. Resist the temptation to touch the feed pipes just after a helium fill to see how cold they get! Contact with cryogens should be restricted to fully trained engineering staff.

Adverse reactions to common MR contrast agents, injected into the patient to provide better diagnostic information, are rare. However, for proper safety, there should be a ‘crash trolley’ in the MR suite with appropriate resuscitation equipment and drugs, ideally made of non-magnetic material so that it can be taken into the magnet room in an emergency. It is recommended that a trained physician is nearby

whenever Gd-based agents are being used. Restrictions on the use of contrast agents may apply during pregnancy and for nursing mothers. Hazards associated with contrast agents are considered in Chapter 20.

2.3.2 Beware: Strong Magnetic Field

The primary hazard associated with the static magnetic field arises from forces on ferromagnetic objects. The magnetic field extends beyond the physical covers of the scanner, referred to as the *fringe field* – see Figure 2.3. The strength of the fringe field decreases rapidly with distance, but this *static field spatial gradient* is responsible for the attractive force. If a ferromagnetic object, e.g. one containing iron or steel, is introduced, it will experience a force. If sufficiently close, this can turn the object into a dangerous projectile. Items such as scissors could become deadly and even a coin could inflict serious damage or injury. The bigger the object, the stronger the force involved. There has been one known death of a patient caused by an oxygen cylinder being inappropriately taken too close to the magnet. The location of the maximum value of the spatial gradient, and therefore the greatest attractive force, is usually close to the *bore entrance*, around the rim.

Even in the absence of a static field change, any ferromagnetic object will twist with a force considerably greater than its mass in an attempt to align its long axis with the static magnetic field lines of force. This twisting force is called *torque* (see Box ‘Force Fields’). It will be greatest within the magnet bore.

This ability to twist objects and to turn them into high-velocity projectiles presents a major risk to both staff and patients within an MRI unit. In modern MRI systems the stray field may decrease very rapidly with distance: an object that does not appear to demonstrate ferromagnetic properties as you approach the magnet may suddenly be torn from your grasp or pocket as you take one further step closer. By the time you feel it, it’s already too late, so be very careful at all times!

Some MR sites employ either hand-held or static metal detectors. It is important to know whether any device employed in your institution detects all metals, or (preferably) only ferromagnetic ones. It is also essential to appreciate that such devices are simply tools to supplement MR safety practice and should never replace thorough screening of the patient by a person competent to do so. The key to MR safety in this respect is to be acutely vigilant at all times. Metallic objects taken into the bore of a magnet may at worse cause serious injury or death and at best may produce unwanted artefacts on the images.

In the vast majority of MRI systems (those with superconducting or permanent magnets), the magnetic field is *always present*, even when the electrical power is switched off. Therefore *everyone* entering the magnet room should be carefully screened, using a checklist and/or detailed questioning, to ensure they do not have any contraindications to MRI either internally or about their person. This includes the patient’s relative(s), friend(s) or other staff who may enter the MR scanner room to assist the patient.

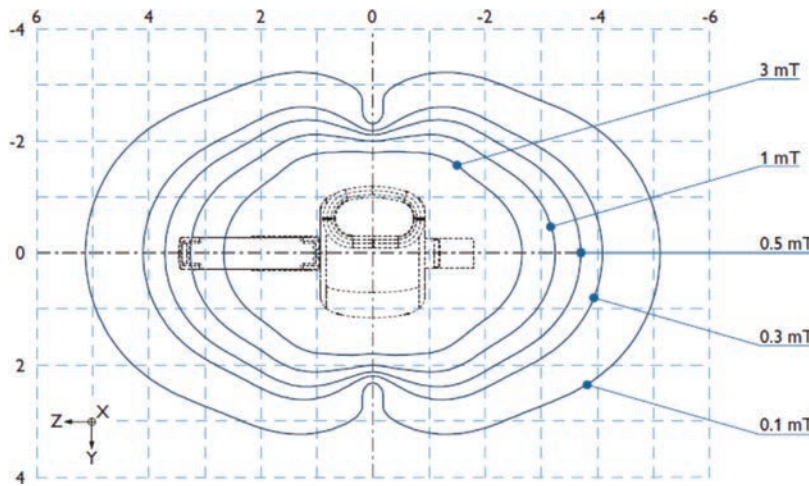


Figure 2.3 Fringe field contours for a typical actively shielded 1.5 T MRI magnet. Courtesy of Philips Healthcare. Each square represents 1 m². The field contours will be three-dimensional.

The fringe field can also interfere with the operation of nearby equipment, as detailed in Table 2.1.

Force Fields

The translational force (F) on an unsaturated object volume V with magnetic susceptibility χ is proportional to the product of the static field (B) and its spatial gradient:

$$F \propto \chi V B \cdot \frac{dB}{dz}$$

where dB/dz is the rate of change of B with position (z). F gets stronger the closer you are to the opening of the magnet bore. Once a ferromagnetic object becomes saturated, i.e. fully magnetized, the maximum force is simply proportional to the fringe field gradient dB/dz .

If an object is elongated in any way it will experience a twisting force or torque (T) aligning it with the field proportional to the square of the static field. The force depends upon the angle the object makes with the field direction

$$T \propto \chi^2 V B^2$$

An elongated ferromagnetic object may experience a torque even in a uniform field. This is extremely important for implanted objects, e.g. aneurysm clips.

It may be necessary for a patient to be moved quickly from the scanner room, either for an emergency procedure, such as resuscitation, or because of a situation related to equipment failure, for example in

the event of a magnet quench. Local safety rules will detail the evacuation procedures for various emergencies. As a general rule, when a patient needs resuscitating or other emergency treatment, the priority is to get the patient out of the scanner room as quickly as possible. This is because arriving emergency personnel, who may not understand the dangers of the strong magnetic field, can unintentionally make matters worse by bringing MR-unsafe ferromagnetic equipment (stethoscopes, laryngoscopes, oxygen tanks, metal crash carts, etc.) into the scanner room. Remember that not all clinical staff have your level of knowledge of MR safe behaviour.

2.4 Safety Second: Additional Practical Guidelines

Implanted ferromagnetic items such as vascular aneurysm clips may also experience these forces and torques. There has been at least one reported death of a patient scanned with a ferromagnetic aneurysm clip that moved, rupturing the blood vessel, as they were moved into the magnet. Similar hazards arise with patients who may have metallic foreign bodies located in high-risk areas such as the eye. Alternatively, the function of Active Implanted Medical Devices (AIMDs) such as pacemakers or cochlear implants may be severely impaired by the static magnetic field and persons with pacemakers are normally excluded from the 0.5 mT fringe field. The same rules apply to any pieces of medical equipment that may also need to be taken into the room; for example, a pulse oximeter for monitoring a sedated patient. Devices such

Table 2.1 Maximum fringe field values and minimum distances to avoid interference on device operation

Fringe field (mT)	Item	Minimum distance (m)		Minimum distance (m)	
		1.5 T	3 T	On axis	Radially
10	Oxygen monitors, laser imager	2.2	1.6	2.6	1.8
3	Magnetic media, LCD displays	2.8	2.0	3.3	2.2
1	Computer hard disks, X-ray tubes	3.4	2.2	4.3	2.7
0.5	Conventional pacemakers	4.0	2.5	4.6	2.6
0.2	CT scanners	4.9	3.0	5.6	3.2
0.1	Gamma cameras, image intensifiers, PET scanners	5.6	3.3	6.8	3.9
0.05	Linear accelerators	6.8	3.9	8.2	4.6

as these must be designed to operate safely within the MR environment. Older devices labelled as 'MR compatible' may have a maximum operating proximity to the magnet and care must be taken that the device is not moved any closer.

This book is not intended to give comprehensive advice on the MR safety of medical devices, since this is covered in great detail in specialized books and on the internet (see Further reading at the end of this chapter), but the following provides a general overview. You must check your institutional policies to know which patients you may scan and what additional checks are required to do so.

2.4.1 Contraindications and Caution

MRI examinations are usually contraindicated for patients with:

- conventional cardiac pacemakers or implanted cardiac defibrillators;
- abandoned cardiac leads;
- cochlear implants.

MRI examinations require particular caution in the following cases:

- patients with implanted *surgical clips* or other potentially ferromagnetic material, particularly in the brain;
- patients with *AIMDs*, e.g. neuro-stimulators, MR conditional cardiac placements, ingested endoscopic cameras;
- patients who have engaged in occupations or activities that may have caused the accidental lodging of *ferromagnetic materials*, e.g. metal-workers, or anyone who may have embedded metal fragments from military duties;
- *neonates* and *infants*, for whom data establishing safety are lacking;
- patients with *tattoos*, including permanent eye-liner;
- patients with compromised *thermoregulatory systems*, e.g. neonates, low-birth-weight infants, certain cancer patients;
- patients with *prosthetic heart valves*;
- *pregnant patients*: although no MRI effects have been found on embryos and fetal MRI is performed in specialist centres, many units still avoid scanning pregnant women during the first trimester. The unknown risk to the fetus must be weighed against the alternative diagnostic tests, which may involve ionizing radiation.

The screening process should identify any of these issues. Aspects relating to the safety of gadolinium-based contrast agents are considered in Chapter 20.

2.4.2 Dealing with Implants

A passive implant is one that has no requirement for electrical power, e.g. a titanium hip joint. The usual conditions for these relate to magnetic forces (attraction and torque) and RF heating (SAR). Box 'Good Metal, Bad Metal' contains information about the magnetic properties of common metals.

Active implants or AIMDs are those that utilize electrical power, either through in-built power supply (batteries) or through coupled external supply (e.g. using RF energy). Examples include pacemakers, neuro-stimulators such as deep brain stimulators or vagal nerve stimulators. Active implants pose the additional risks of malfunction, modification of their operating mode, inhibition, unintended stimulation or permanent damage. Also there are increased risks of excessive heating in any internal leads. Active implant conditions will also often include a maximum imaging gradient slew rate ($T\ m^{-1}\ s^{-1}$).

In every case, be aware of local practice and policies and check that your scanner and protocol satisfies the conditions before introducing the patient to the magnet environment. Be wary of such statements as 'I've had a scan before and it was fine', as all scanner models are different; an uneventful previous scan does not necessarily mean that a particular device is safe in all other scanners.

A system for categorizing the risk from implants has been developed by the American Society for Testing and Materials (ASTM), regulated by the Food and Drug Agency (FDA) in the USA, and incorporated into the standards of the International Electrotechnical Commission (IEC). This categorizes implants and other devices as either *MR safe*, *MR conditional* or *MR unsafe*. The internationally recognized symbols for each category are shown in Figure 2.4.

MR safe means that the device or object poses no additional risk in the MR environment. For example, it may be that it is non-metallic. It may, however, result in image quality degradation if it is within or close to the imaging Field Of View (FOV).

MR conditional forms by far the largest group of implanted medical devices. Patients may be scanned safely subject to compliance with certain specified



Figure 2.4 MR symbols as defined by standard ASTM F2503 and IEC 62570:2014.

conditions. These usually include the maximum static field strength (T), the maximum static fringe field gradient ($T\ m^{-1}$ or $G\ cm^{-1}$) and the maximum time-averaged SAR. See Box ‘Working Conditions’ for an example of MR conditions and further explanation. Sometimes other conditions apply – for example, an anatomical or positional restriction, or a specific coil to be used. Remember that even if you comply with all the MR conditions, metal objects will cause image artefacts in the region of the implant.

MR unsafe devices or objects must never be introduced into the MR environment.

Working Conditions

Typically the wording on MR conditions may contain something like the following:

'Non-clinical testing has demonstrated that the Company X Implant model number Y can be scanned under the following conditions:

*Static magnetic field of 3 tesla or less
Spatial gradient of $720\ G\ cm^{-1}$ ($7.2\ T\ m^{-1}$)
Maximum whole-body-averaged specific absorption rate (SAR) of $2.0\ W\ kg^{-1}$ for 15 minutes of scanning.'*

The static field condition is easy to interpret, although note that not all implants have been tested at 3 T.

The second and third conditions often cause confusion. The maximum spatial gradient refers to the static fringe field spatial gradient. The condition means that the device has exhibited a magnetic force less than the force due to gravity in the stated fringe field gradient. Note that units quoted vary and that $1\ T\ m^{-1}$ equals $100\ G\ cm^{-1}$. Plots of fringe field gradients are shown in Figure 2.5. Each manufacturer presents this information in different ways, so it is important that you understand how to interpret it for your scanner.

The SAR condition relates to potential heating (in a non-clinical test phantom). Note that 15 minutes is

the time per sequence, and does not relate to the maximum time you can scan. In the USA, SAR used to be averaged over a 15 min period, whereas, elsewhere under the IEC guidelines, SAR is calculated over every 6 min period. Often the SAR limitation condition restricts scanning to the Normal Mode (see Box ‘Modes and Options’).

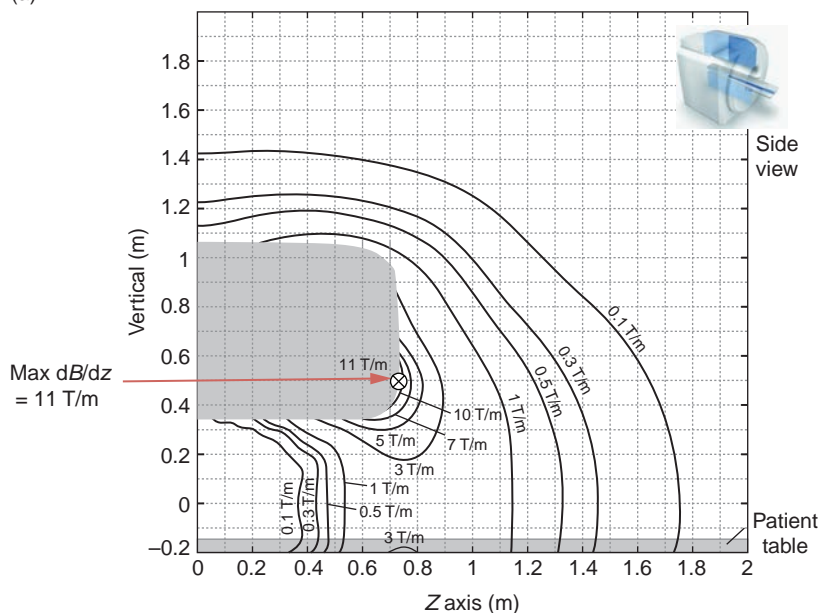
Good Metal, Bad Metal

There are three major categories of magnetic properties for materials, each characterized by their magnetic susceptibility, often denoted by the Greek letter χ .

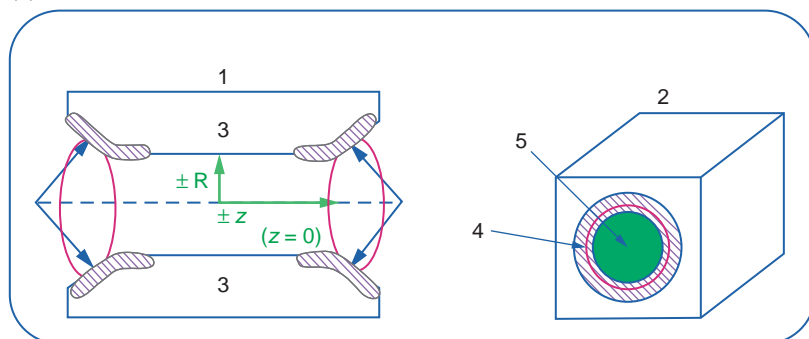
- *Diamagnetic* materials have a small, negative susceptibility. This means that the force, although tiny, is repulsive. Water and most biological tissues are diamagnetic with values less than 10^{-5} (0.00005).
- *Paramagnetic* materials have a slightly larger and positive susceptibility. Example materials are oxygen molecules and ions, such as gadolinium. Values range from 10^{-5} to 10^{-2} . The attractive forces on paramagnetic or even weakly ferromagnetic materials are small.
- *Ferromagnetic* materials have large positive χ . For example, iron has values in the range 1000–10 000 depending upon how it is produced. Some stainless steels are ferromagnetic. The large susceptibility means that magnetic forces and torques will be very strong. Some metals used for implants, e.g. 316LV or surgical stainless steel, titanium, and some metal alloys, e.g. cobalt-chromium-molybdenum alloy, nitinol, are only weakly or non-ferromagnetic. These would not be expected to be displaced in the magnet, especially after six weeks from implantation.

Figure 2.6 shows the range of materials in the susceptibility spectrum.

(a)



(b)

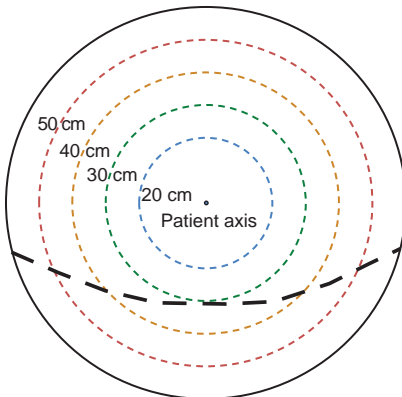
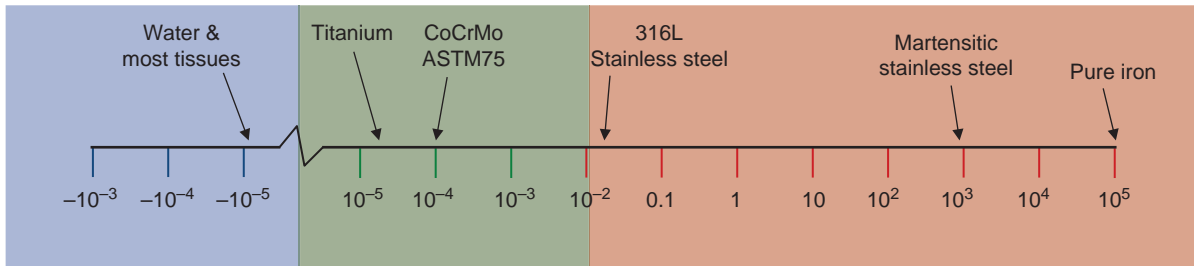


Parameter	Radial location R (m)	Location along Z (m)	B(T)	Grad (B) (T/m)	Max (B) * grad (B) (T ² /m)
Peak B	0.35	0.64	3.9	7.2	28.2
Peak gradient	0.51	0.92	0.92	12.4	22.6
Peak product	0.36	0.73	3.6	10.7	38.7

Figure 2.5 Static fringe field gradients (a) Contour plots for a Siemens Aera 1.5 T scanner. The plot shows one quadrant with the origin (0,0) being the isocentre of the magnet. (b) Diagram and table showing maximum values of dB/dz and its product with B for the GE Healthcare MR750w 3 T scanner. (c) Iso-gradient surfaces from a Philips Achieva and Intera 1.5 T scanners. Each contour represents a cylinder with the maximum spatial gradient indicated. For ease of interpretation, the patient couch is also shown.

(c)

Achieva and Intera 1.5T		
	T/m	Gauss/cm
On patient axis	2.5	250
Cylindrical shape of 20 cm diameter	2.6	260
Cylindrical shape of 30 cm diameter	2.8	280
Cylindrical shape of 40 cm diameter	3.1	310
Cylindrical shape of 50 cm diameter	3.6	360

**Figure 2.5** (cont.)**Diamagnetic**

- Susceptibility small, negative
- water, most organic molecules
- 'non-magnetic'

Paramagnetic

- Susceptibility small, positive
- ions, metal salts, O₂, Gd
- affect relaxation times

Ferromagnetic

- Susceptibility large, positive
- e.g. iron
- 'magnetic'

Figure 2.6 Magnetic susceptibility spectrum.

2.5 The Patient's Journey

Patient cooperation is essential for obtaining high-quality images, and their initial chat with MR staff can make all the difference. All patients require counselling to explain the nature of the examination and must complete a questionnaire to assess their suitability and safety for being scanned. This should take place in an appropriate quiet and private place. During this interview you should also follow your institutional identity policy, confirming you have the right patient and body region to be scanned. Pay particular attention where 'left' or 'right' is specified on the request form as this is a common source of

error. Sometimes it's helpful to mark the area to be scanned with a vitamin E or cod liver oil capsule to ensure correct positioning. This is useful when you are scanning someone with a moveable 'lump', especially the ones which are there one minute and gone the next!

Patients need to remove all metallic objects, jewellery, watches and credit cards, which can be stored in lockers. Locker keys should be non-magnetic to be safe in the magnet room. Local policy will determine whether patients should undress and wear a gown for the examination. The inconvenience and extra prep time should be balanced against the

common problem of ‘finding’ metal in items of clothing, e.g. in zips and underwires, when the patient is in the magnet. Non-ambulatory patients will be transferred to non-ferromagnetic, MR-safe trolleys or wheelchairs prior to being taken into the MRI examination room. Many MR systems incorporate removable patient couch systems or table-tops to allow for efficient and comfortable moving of bed-bound patients.

The patient will usually be weighed before entering the scanner. This is required to enable the scanner to operate with a safe level of RF exposure (see Chapter 20). On some scanners, the patient’s height may also be required for the SAR calculation. Patient details will be registered on the scanner either manually or from a Hospital or Radiology Information System (HIS/RIS) worklist.

Choose the coil most suitable for the examination. This should completely cover the area to be scanned. Position the patient on the couch as appropriate to the examination and ensure their comfort before positioning any additional coils that are required. Ensure the patient does not provide unnecessary conduction loops, for example, by clasping their hands together, or crossing their ankles. Insulating padding to prevent their thighs touching is also recommended. Ensure that the patient inserts ear plugs appropriately or wears ear defenders. Give them the hand-held alarm button, and position any other comfort devices such as mirrors or headphones. Maximizing patient comfort and relieving anxiety is essential to the success of the examination.

Use the scanner’s positioning lights or lasers to indicate (or ‘landmark’) the centre of the region to be scanned. Select the desired position. Then ensuring the patient is comfortable, move the scan region to the magnet iso-centre (usually carried out automatically on a single button press). It is important to ensure the scan region is positioned at the isocentre as this is the location or ‘sweet spot’ where the magnetic field is most uniform (or homogeneous) and will produce the best image quality. ‘Landmarking’ on the region of interest allows the scanner to place this anatomy at the very centre of the magnet (the *isocentre*). This is the ‘sweet spot’ with the best magnetic field uniformity or *homogeneity*, thereby ensuring highest image quality. After landmarking the initial scan position using the laser light guides, the couch is moved into the centre of the magnet.

As the couch moves into the scanner the patient may show signs of claustrophobia, or may not fit, especially in older 60 cm bore scanners. Reposition the arms if necessary to fit comfortably and place thin pads between the

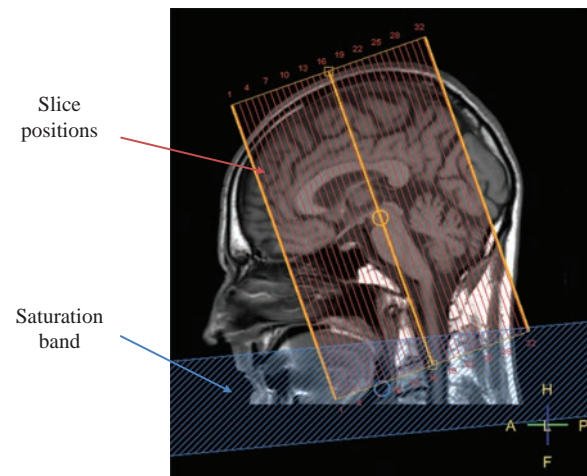


Figure 2.7 Quick localizer or scout scan for planning. Slice positions are shown as lines. A regional saturation band is also shown.

elbows and the scanner. In exceptional cases you may need to ask the patient to put one or both arms above their head, to fit the bore. Be sure to scan these patients as quickly as possible, and bring them out of the magnet to rest the arms by the side if you have delays. Once the patient is comfortably positioned at the isocentre, staff can leave the scanner room, making sure to close the door properly to prevent external RF interference.

Initially a set of localiser or positioning scans is performed (Figure 2.7). These give a quick, low-resolution, overview which is then used to plan the diagnostic scans on the region of anatomy under investigation. The positioning of slices and saturation bands is usually prescribed graphically using these scout scans. The diagnostic scans or sequences can often be queued to run automatically, leaving you free to do other tasks on the console such as post-processing or archiving.

All patients need to be observed during the examination, either through the observation window from the control room or by closed-circuit TV. An intercom enables two-way audible communication between the patient in the magnet and the control room. At some point during the examination, the administration of an MR *contrast agent*, usually a gadolinium compound, to the patient may be required. Since gadolinium alters the image contrast, gadolinium-enhanced imaging is always performed towards the end of the examination. Local policy may allow a radiographer or nurse to give this injection; however the radiologist always has medical responsibility for the patient.

During an MRI examination, the patient may be fully conscious (this is the norm), naturally asleep (e.g. for infants), sedated or anaesthetized. In the latter instances they may require life support and physiological monitoring, e.g. ECG and pulse oximetry. There is a small risk of patients receiving burns through the coupling of RF energy into wires or those used for ECG monitor or triggering, that are touching the patient. Care must be exercised in ensuring that cables are not formed into loops, that dry flame-retardant pads are placed between cables and the patient and that any unnecessary cables are removed from the patient prior to imaging. All cables should also be inspected every time before use to ensure there is no damage to the insulation. Furthermore, only ECG cables specifically deemed MR safe should be used.

After the examination the patient will be escorted from the magnet room and will need to retrieve their personal possessions. If the patient feels unwell due to the contrast agent injection or claustrophobia, it is advisable to have them remain in the MR unit where they can be observed to ensure their well-being before leaving. The reading or reporting of the scans by a

radiologist usually occurs later, often via PACS where the radiologist returns his/her findings to the referring physician. The patient will usually have a follow-up appointment with the physician to discuss the diagnosis and follow-up tests or treatment.

That completes the patient journey, as far as their MRI is concerned. Now it's over to your journey. In the next section we take a look into the life of an imaginary radiographer.

2.6 MRI Radiographer's Blog ... A Few Years On

A scarily all-true but slightly tongue-in-cheek description of the typical working pattern in a busy MRI unit, with apologies to other better known diarists. For Emma's earlier adventures, please see older editions of the book. Note, we as authors do not necessarily condone Emma's behaviour or level of MR knowledge.

See also

- Let's talk technical: MR equipment: Chapter 10
- But is it safe? Bio-effects: Chapter 20.

MONDAY			
Weight	+0.2kg from what I was expecting (you didn't think I was going to reveal my true weight, did you?)	Helium level	79.3%
Alcohol level	5 units (it was the weekend after all)	B ₀ exposure	5.2 mT-hours (time-weighted average)
Twitter followers	C	Tweets/retweets	C
<p>I found my old diary, so in keeping with the times, I decided to start a blog.</p> <p>It's been a while. Not such a newbie to MRI. Older, wiser, less naive. Not drinking so much. Not exactly fitter, or healthier. Completely adapted to the MR environment, I empty my pockets every time I go near an x-ray room! Better safe than sorry.</p> <p>Sorted my Twitter profile name (Yes, am going to be a Modern Person, a social medium, a Twit?). It's @EM_are_1. Genius! Was inspired by the IT help-desk call centre person who once asked when our network was down, 'How do you spell MRI?' ROFL.</p>			
TUESDAY			
Weight	still plus 0.0 kg, or maybe I should say minus 0.0 kg	Helium level	79.3% (zero boil-off scanner, but old habits die hard)
Alcohol level	2 units (good for a Monday night)	B ₀ exposure	7.3 mT-hours
Twitter followers	C	Tweets/retweets	1 (see below)

@Em_are_1: Hello twittersphere

Worked on new 3 T scanner! Very exciting. Tried to get visual phosphenes by shaking my head madly round the back of the magnet but got told off by colleague who said, 'Don't do that, Em, you're upsetting the patients, and you'll get mag lag.'

'Mag lag?' I replied. 'What's that?'

'OMG! You've forgotten?' she shrieked. 'You've got it already!'

Hmm, I don't believe this 'mag lag' business. I think I'll see what Picture to Proton has to say about it. (author's note: see Chapter 20)

WEDNESDAY

Weight	plus 0.1 kg	Helium level	79.3%
Alcohol level	3 units (on target for the week)	B_0 exposure	23 mT-hours (on account of - see below)
Twitter followers	0 (where are you all? I'm interesting!)	Tweets/retweets	1

OMG MRI incident! No one hurt, thank goodness. Was scanning an old codger. We'd gone through the MR safety check. Pacemaker? No. Aneurysm clip? No. Recent surgery? No. Etc, etc.

'Have you got anything in your pockets,' I asked. 'Cards, money?'

'Only Paper Money?' He replied.

'Good', I say. So I position him on the table, head first, and am just putting him in the scanner when...

ZIP! WHAM! A shower of shiny objects flashes past my ear as a pocketful of coins embed themselves into the magnet, our lovely new (not quite so) shiny 3 T magnet. I checked he was all right and took him out, saying, 'I thought you said you had no money in your pockets?' I was quite shaken.

'Yes, paper money,' he said unperturbed, as if this was a daily occurrence, 'you know, for my daily newspaper.'

Took ages to pry the coins off. And scratches all over our lovely scanner.

Later on I tweeted @Daily_News how stupid are you're readers?

THURSDAY

Weight	plus 0.3 kg (the MR scales over-weigh - it's a safety feature)	Helium level	78.9%
Alcohol level	9 units (price you pay for cyber-celebrity/MR safety anxiety)	B_0 exposure	5.2 mT-hours
Twitter followers	151	Tweets/retweets	10,093

Got trolled by 10,092 Daily News readers on Twitter. How stupid am I? This one's typical (and polite, relatively):

@Em_are_1 you're profile sucks Em_am_!! #grammar #init

I blame the iPhone auto-spell. Still, at least I picked up some followers, but I don't want them to follow me if they think I'm an idiot.

So the new scanner ... I was concerned about the patients heating up because it was going to the First Level almost all the time. And I am a bit disappointed by the image quality. So I called the applications specialist. 'You said a hundred percent more SNR,' I accused.

There was a long pause. 'Erm ... We said a hundred percent more SAR, not SNR.'

Really? Can one letter make that much difference? Time for another MR physics course?

Authors' note: theoretically twice the SNR (for the same bandwidth and T_1/T_2) and four times the SAR.

FRIDAY			
Weight	minus 0.2kg (sometimes I do believe the MR scales)	Helium level	78.9%
Alcohol level	0 units (post hangover dry night)	B ₀ exposure	3 mT-hours
Twitter followers	152	Tweets/retweets	2 (thank goodness! I've had my fill of virality)
<p>Browsing through Twitter, I saw a patient had just published his scans on Instagram. What's wrong with these Gen-Y people? Oh I see ... meniscal tear! At least he didn't put a sepia filter on the images (#hipsterScan).</p> <p>Tweet of the day: so I went in for a #MRI scan for my shoulder, and they diagnosed me with claustrophobia! #medicalgenius</p> <p>Scanned a patient with an MR Conditional pacemaker this afternoon. Scary! And Fridays are meant to be relaxing!</p> <p>Monitored his ECG. Hated the way the scanner interference looked like violent arrhythmias! And the cardiac tech was happily chatting about his holidays, like a hairdresser, all nonchalantly. Relieved when the patient walked out smiling. He didn't seem worried at all. It's great for the patients, but it sure does add an edge to MR safety. Must remember to search Twitter with hashtag #MRIsafety.</p>			
SATURDAY			
Weight	Don't care. It's the weekend.	Helium level	Don't care. It's the weekend.
Alcohol level	Ditto	B ₀ exposure	Ditto
Twitter followers	155 (up three!)	Tweets/retweets	2
<p>What a week! But Sunday is my fun day. Still undecided about the MRI course. Maybe I'll just buy the new edition of <i>MRI from Picture to Proton</i>. I see they're on Twitter too...</p> <p>@MRI_P2P I love that diary thing you do. I wish I could be in it. #dreamscometrue</p>			

Further Reading

American College of Radiology Expert panel on MR Safety (2013) 'ACR guidance document on MR safe practices: 2013'. *JMRI* 37:501–530.

American Society for Testing and Materials (2013) 'Standard practice for marking medical devices and other items for safety in the magnetic resonance environment'. www.astm.org/Standards/F2503.htm [accessed 10 December 2013].

Institute for Magnetic Resonance Safety, Education and Research (2013) www.mrisafety.com [accessed 9 December 2013].

Institute of Physics and Engineering in Medicine (2013) 'Scientific safety advice to magnetic resonance imaging units that undertake human imaging'.

www.ipem.ac.uk/Portals/0/Documents/Publications/Policy%20Statements/IPEM_MRSafety_Expert_PolicyStatement_04102013_SK.pdf [accessed 27 July 2014].

International Commission on Non-Ionising Radiation Protection (2004) 'Medical magnetic resonance (MR) procedures: protection of patients'. *Health Physics* 87:197–216

International Electrotechnical Commission (2013) 'Medical electrical equipment – Part 2-33: particular requirements for the safety of magnetic resonance equipment for medical diagnosis edition: 3.1'. IEC 60601-2-33. www.iec.ch/webstore [accessed 22 March 2015].

Medicines and Healthcare products Regulatory Agency (MHRA) (2014) *Safety Guidelines for Magnetic Resonance Imaging Equipment in Clinical Use*. London: MHRA.

Netherlands Working Group on MR Safety (2008) 'Using MRI safely: practical rules for employees'. www.ismrm.org/smrt/files/20081210_Dutch_Guidelines_on_MR_Safety.pdf [accessed 23 March 2016].

Shellock FG (2015) *Reference Manual for Magnetic Resonance Safety 2015*. Salt Lake City, UT: Amirsys Inc. (New edition published annually.)

Shellock FG and Crues JV (eds) (2013) *Magnetic Resonance Procedures: Health Effects and Safety*. Los Angeles, CA: Biomedical Research Publishing.

Seeing is Believing: Introduction to Image Contrast

3.1 Introduction

In this chapter you will learn what MR images can show, and get an introduction to the different types of contrast that can be produced. We will use a very simple classification of the body tissues, which will be good enough to describe the basic appearances:

- fluids – CerebroSpinal Fluid (CSF), synovial fluid, oedema;
- water-based tissues – muscle, brain, cartilage, kidney;
- fat-based tissues – fat, bone marrow.

Fat-based tissues have some special MR properties, which can cause artefacts. Artefacts are disturbances in the image, which can be misinterpreted as pathology or can hide the real anatomy. Fluids are different from other water-based tissues because they contain very few cells and so have quite distinct appearances on images. (Flowing fluids are rather complicated and their appearance depends on many factors including their speed; they are dealt with in detail in Chapter 15.) Pathological tissues frequently have either oedema or a proliferating blood supply, so their appearance can be due to a mixture of water-based tissues and fluids.

Various tissues have different signal intensities, or brightness, on MR images. The differences are described as the image contrast, and allow us to see the boundaries between tissues. For example, if a tumour is bright and brain tissue is a darker shade of grey, we can detect the extent of the tumour (Figure 3.1a). MRI allows us to produce a wide range of contrasts by using different imaging techniques (known as *pulse sequences*) and by controlling the timing of the components that make up the sequences. So it is also possible to make the tumour dark and brain tissue brighter (Figure 3.1b). Note that this is quite separate from changing the window and level: that can make the whole image darker or brighter, but the tumour will always be darker than the brain tissue. Compare this with CT images. CT contrast depends only on the attenuation of X-rays by the tissues (measured in Hounsfield units). In CT we can produce ‘soft tissue’ or ‘bony’ windows by changing the reconstruction algorithm, but bone will always be the brightest tissue and grey matter will always be darker than white matter.

In this chapter we will show:

- the basic labels that are used to describe images: T_1 , T_2 , proton density and so on;

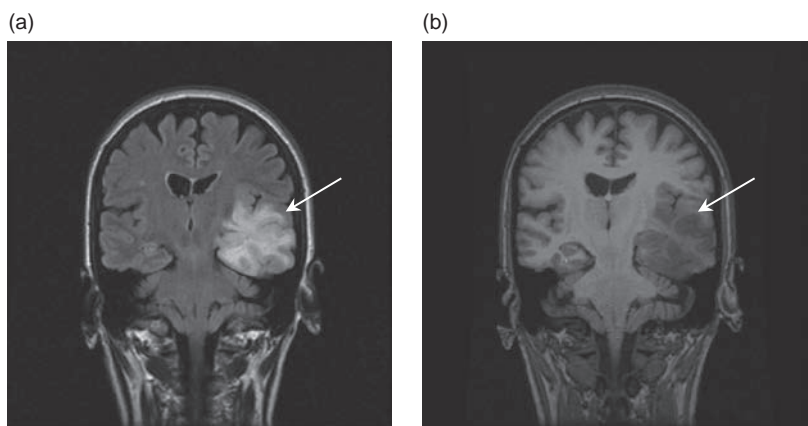


Figure 3.1 (a) Coronal image of the brain showing a tumour (arrow). In this image the tumour is bright against the darker grey of the normal brain tissue. (b) The same slice with a different pulse sequence, this time showing the tumour darker than the surrounding brain.

- we can achieve different contrasts with the basic spin-echo and gradient-echo pulse sequences, by changing the TR and TE times and, in gradient echo, the flip angle;
- STIR and FLAIR sequences are available for suppressing fat or CSF respectively, leaving a ‘T₂-weighted’ appearance in the remaining tissues;
- injected contrast agents can improve image contrast by enhancing signal intensity in tumours;
- there are two special scans, MR angiography and MR diffusion imaging, which are important in many basic exams, and they will be explained here.

Clinical Exam 1: Simple Brain

All MR exams consist of a survey followed by at least two more scans with different image contrasts. Many exams contain four or more scans; each new contrast provides different information about the anatomy and pathology, and helps to improve diagnostic confidence in the result.

A very simple brain exam might contain a T₂w image and a FLAIR, with T₁w images pre- and post-Gd. (Here, ‘Gd’ is shorthand for an injected contrast agent containing gadolinium, Gd. More about that later.) The T₂w and FLAIR images are both sensitive to fluid collections; the FLAIR images show CSF as a black signal, which helps to distinguish periventricular lesions. T₁w images have better contrast between **Gray Matter** (GM) and **White Matter** (WM), which helps to show mass effect or effacement of GM/WM boundaries. The Gd contrast agent leaks into the brain tissue wherever the blood-brain barrier is impaired, and gives a bright enhancing signal on T₁w images after injection. This gives further delineation between pathological tissue and oedema.

In Figure 3.3, both images are shown in the transverse plane, so you can easily see how the different contrasts affect the appearance of the normal anatomy and pathology. However, radiologists can get even more information by acquiring the images in different planes, e.g. coronal or sagittal, and mentally building a 3D overview of the patient’s condition while reading the images.

3.2 Introduction to the T-Words

All these strange acronyms beginning with ‘T’ – what language is this? Like any other field of medicine (or science), MRI has its own jargon which can be confusing at first. Table 3.1 introduces you to the main words, with a short description. We won’t explain all

Table 3.1 Overview of important MRI terms

Term	Description
T ₁	A property of a tissue, called <i>spin-lattice relaxation time</i>
T ₂	A property of a tissue, called <i>spin-spin relaxation time</i>
T ₂ *	A property of a tissue in a magnetic field, called <i>apparent spin-spin relaxation time</i>
PD	A property of a tissue, called <i>proton density</i> (closely related to water content)
TR	A timing parameter for a scan, called <i>repetition time</i>
TE	A timing parameter for a scan, called <i>echo time</i>
TI	A timing parameter for a scan, called <i>inversion time</i>
<i>a</i>	A parameter for a scan, called <i>flip angle</i>
T ₁ w	Description of image contrast, dependent mainly on T ₁ of tissues
T ₂ w	Description of image contrast, dependent mainly on T ₂ of tissues
T ₂ w*	Description of image contrast, dependent mainly on T ₂ * of tissues
PDw	Description of image contrast, dependent mainly on PD of tissues

the detail yet, because it can be overwhelming. For now, just use these terms as labels.

3.3 T₂-Weighted Images

T₂-weighted (T₂w) images are one of the most important MR images, because they are sensitive to fluid collections. Since many pathological tissues have high capillary density, or excess fluid accumulations, these images provide confirmation of the preliminary diagnosis and show the extent of the disease. So, for example, the meniscal tear in the knee shows up well because the synovial fluid in the tear is brighter than the cartilage (Figure 3.2). T₂w contrast can be produced by either Spin-Echo (SE) or some Gradient-Echo (GE) sequences. (GE sequences actually produce T₂*-weighting, not T₂-weighting: the image appearance is similar, but there are important differences which we will explain later.) SE T₂ images require long TR and long TE, so they have a long scan time (this is because the scan time depends directly on the TR).

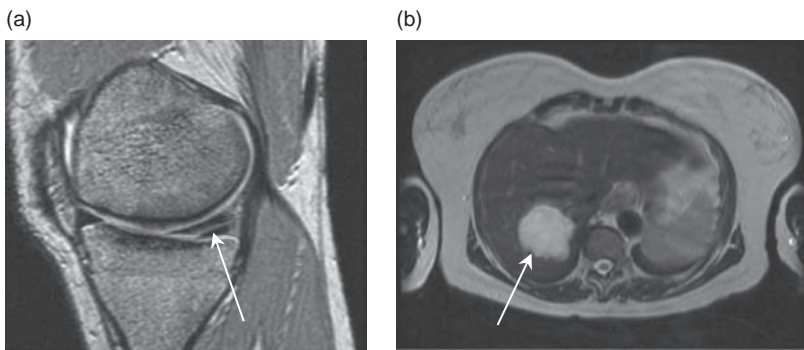


Figure 3.2 T_2 -weighted pathology images. (a) Sagittal image of meniscal tear (arrow) and (b) axial liver scan showing haemangioma.

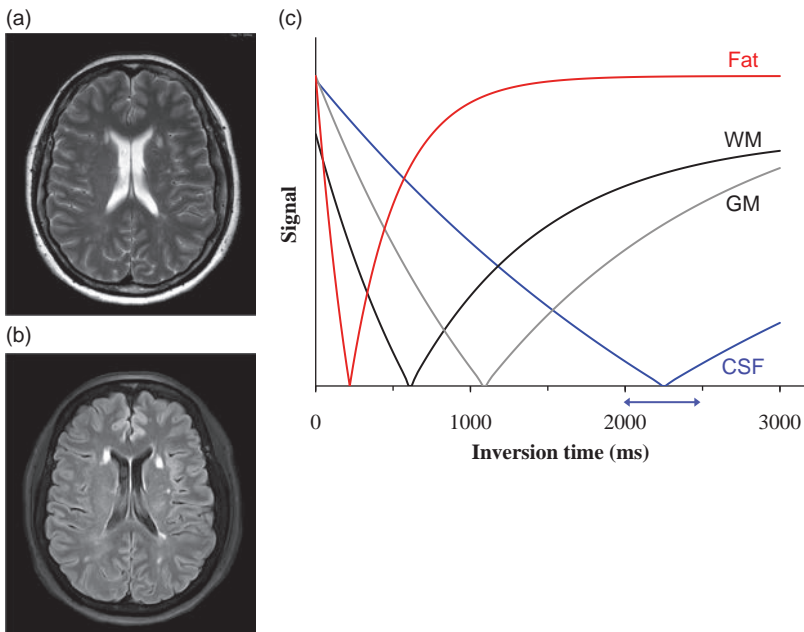


Figure 3.3 (a) SE T_2 w and (b) FLAIR images in a patient with multiple sclerosis (MS). Notice that the lesions are better seen when the CSF signal is suppressed. (c) Inversion recovery curves showing the range of null point for CSF.

On T_2 w images tissues with long T_2 relaxation times are brighter than those with short T_2 s. For brain and spine imaging, T_2 w images are usually acquired with the spin-echo pulse sequence. For liver, where a breath-hold is needed, the T_2 w images can be acquired using gradient echo which is faster – but remember that this is actually T_2^* w, not T_2 w (see Section 3.9 for more information).

3.4 FLAIR Images

The very high signal of CSF in brain T_2 w images can give problems for the radiologist to identify periventricular lesions. It is possible to remove the CSF signal, known as ‘nulling the signal’, by choosing an Inversion Recovery (IR) sequence instead of spin

echo, and carefully setting the inversion time (TI). This combination of IR with a certain TI to null CSF is known as FLAIR (FLuid Attenuated Inversion Recovery (Figure 3.3a,b)). Because of the long spin-lattice relaxation time T_1 of CSF, there is a wide range of TIs which will give reasonably good fluid suppression, typically between 1800 and 2500 ms depending on the magnet’s field strength (Figure 3.3c). Be aware that all tissues with T_1 s similar to CSF will be suppressed, and FLAIR is not recommended after gadolinium injection because of the variable effects on T_1 s.

3.5 T_1 -Weighted Images

T_1 -weighted (T_1 w) images can be produced using either SE or GE sequences. Unlike T_2 w images, where

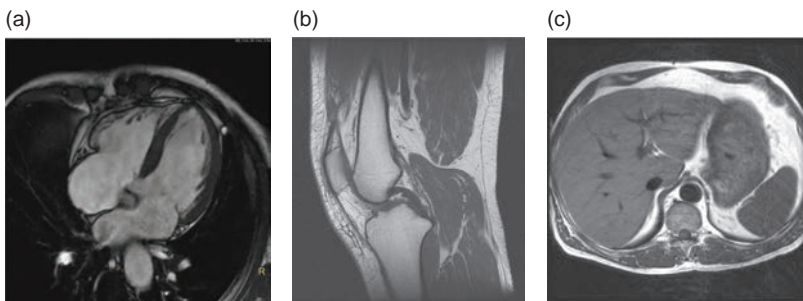


Figure 3.4 T₁-weighted images of normal anatomy. (a) Oblique 'four-chamber' view of the heart, (b) sagittal knee, (c) axial liver.

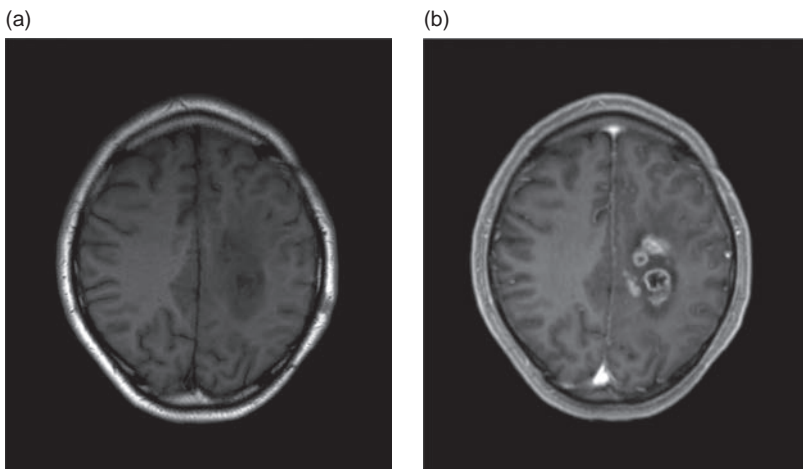


Figure 3.5 (a) Pre-Gd and (b) post-Gd SE T₁ images of a high-grade glioma.

long T₂ tissues have a bright signal, on T_{1w} images the longest T_{1s} have the darkest signal. Tissues with short T_{1s} appear brighter. T_{1w} images are usually quite fast to acquire, because they have short repetition times (TR). T_{1w} images often have excellent contrast: static fluids, e.g. synovial fluid, are very dark, water-based tissues are mid-grey and fat-based tissues are very bright. The appearance of flowing fluids (e.g. blood) depends on the speed of flow and the sequence parameters. T_{1w} images are often known as 'anatomy scans', as they show most clearly the boundaries between different tissues (Figure 3.4).

3.6 T_{1w} Images Post-Gd

Although MRI is extremely flexible in creating different image contrasts, just by manipulating the pulse sequence and timing parameters, there is still a role for injected contrast agents. The most commonly used contrast agents are based on gadolinium (Gd), a metallic element with a strong paramagnetic *susceptibility* (refer back to Section 2.4.2 for definition of different

magnetic properties). When a Gd contrast agent is injected into the body, it starts in the veins and arteries but rapidly leaves the blood vessels into the extracellular fluid spaces (with a half-life of around 10 min), and is then gradually excreted via the kidneys. The total body dose has a half-life of around 90 min in subjects with normal kidneys, and can be considered completely eliminated after 24 h. It has the effect of shortening the T₁ of tissues where it accumulates, so the most useful images to acquire post-Gd are T₁-weighted. We normally keep exactly the same parameters for the scan pre- and post-Gd, so that comparison between the images is easier. It's especially important to keep the same window/level on the two scans – although it can be very difficult to do this!

Since Gd reduces the T_{1s}, the affected tissues will have higher signals on the post-Gd T_{1w} images. For example, highly vascular tumours will become brighter and where the blood-brain barrier is disrupted gadolinium will leak into the region and enhance that area (Figure 3.5).

Technical Interlude for the Curious

We have already introduced several new concepts which deserve some extra explanation. This box will give you some basic info to help you through the next sections.

MR images are produced using a repeating series of RF and gradient pulses, known as a *pulse sequence* or simply *sequence*. All sequences have a *repetition time TR*, and an *echo time TE*, which control the sequence timing. All sequences have an *excitation* RF pulse which disturbs the body's protons and creates a signal in the RF coils. The signal can be detected by forming either a *spin echo (SE)* or a *gradient echo (GE)*. SE sequences have a second RF pulse for *refocusing* the signal echo, and this extra pulse corrects the signal for B_0 inhomogeneities. GE sequences use gradient pulses to create the echo, which can be much faster than SE, but has sensitivity to B_0 inhomogeneity. A useful variant of SE is the *inversion recovery (IR)* sequence, which starts with a 180° pulse to invert the protons' magnetization. The delay between the inversion pulse and the excitation pulse is called the *inversion time (TI)*. By setting TI to a particular fraction of the T_1 of a tissue it is possible to *null* the signals from that tissue. The important fraction is $0.693 \times T_1$.

T_1 and T_2 are fundamental properties of all tissues. They describe the two kinds of *relaxation* which allow the protons to get back to their equilibrium condition. T_1 is known as *spin-lattice* or *longitudinal* relaxation time and is always longer than T_2 . T_2 is known as *spin-spin* or *transverse* relaxation time. Through many experiments in the last 30 years, we have good knowledge of the T_1 and T_2 times for body tissues.

Clinical Exam 2: Spine

The spine may be examined either for neurological problems, or for **MusculoSkeletal (MSK)** indications. Sagittal scans are the most important because they show the whole area within one set of images. Spine exams always include T_1w and T_2w scans in the sagittal plane. We will then acquire a stack of T_2w images in an oblique transverse plane through areas of particular interest, for example a prolapsed disk.

For neuro indications, it's important for the transverse T_2w images to show the internal anatomy of the spinal cord, and GE T_2^*w is usually best for this. For MSK, it's usually more important to be able to trace the nerve roots as they exit the spinal canal, and SE T_2w is often better for this.

A third type of contrast, called STIR, is often used in the sagittal plane. STIR stands for *Short TI Inversion Recovery*, so it is another IR sequence like FLAIR. However, in this case the TI is chosen to null fat signals, which have much shorter T_1 s than CSF. Using short TI, fluids with long T_1 s give a high signal, so the STIR appearance is approximately T_2w with fat suppression'.

Spine imaging in modern wide-bore scanners is very simple for patients. The receive RF coil lies underneath the patient couch, and a shaped head-neck coil offers support for the cervical spine. The majority of spine exams are performed with the patient head-first into the scanner. However it is possible to do lumbar spine exams with the patient feet-first, a configuration which can help some claustrophobic patients to feel more comfortable.

3.7 STIR Images

You will often hear people ask for STIR (Short TI Inversion Recovery) images, especially for spine and for musculoskeletal imaging (Figure 3.6). STIR images have very low signal from fat but still have high signal from fluids, i.e. they can be thought of as a 'fat-suppressed T_2w ' imaging technique. However, bear in mind that STIR images will suppress all tissues with the same T_1 as fat, so they should not be used after gadolinium contrast injection when there may be T_1 changes in the pathology as well as in normal tissues.



Figure 3.6 STIR image of bone marrow changes in spine.

STIR is a type of IR sequence, like FLAIR, except that we choose to null fat-containing tissues instead of CSF. The appropriate TI depends on the T_1 of the tissue and should be about 70% of the T_1 . For example, fat has a T_1 of 220 ms at 1.5 T, so if we set TI to 150 ms, the signal from fat can be suppressed. You may need to adjust the TI slightly either side of this value to achieve the best fat suppression, since TE and TR also have an impact on nulling the signal. At other field strengths TI will be different, e.g. fat T_1 is approximately 380 ms at 3.0 T, so STIR sequences require a TI of around 260 ms.

There are other methods for removing or reducing the signal from fat, and STIR is not always the best choice. See Section 7.3.3 for a more detailed explanation and evaluation of the strengths and weaknesses of fat suppression techniques.

Clinical Exam 3: Knee or Shoulder

After brain and spine exams, musculoskeletal (MSK) referrals are the most common in many MR centres. Since the size and location of the main joints are very different, there are often dedicated RF receive coils for each area. However, the sequence choices are fairly similar, since we are typically looking for detailed information about the joint structures.

STIR is sometimes used in larger joints to achieve a fat-suppressed T_2 w appearance. Proton-density-weighted (PDw) imaging is very useful in knee and shoulder, especially when using an alternative method to suppress fat. T_1 w images may be used pre- and post-Gd if there is a history of surgery.

Many patients have joint replacements, and these often contain large amounts of metal. You should always carefully check the type of implant, to see if it is safe to scan. If it is safe, you may find that the large amounts of metal create strong artefacts in the images. There are new imaging sequences available on some scanners to minimize this effect: see Chapter 7 for details.

Positioning patients for MSK exams is a question of personal preference and RF receive coils available. Shoulders, hips, knees and ankles are straightforward, using a supine position. Elbows and wrists, however, are tricky in conventional 60 cm-bore systems. Often the ‘superman’ position is needed, with the patient lying semi-prone with the affected arm stretched above their head, in order to get the coil into a good position. It is difficult for many patients to hold this position, which may limit the exam time to around 20 min. In wide-bore systems

these joints can be imaged with the patient lying supine with the arm by their side, often with enough space to move their body slightly off-centre and allow the elbow/wrist coil to be more central in the scanner.

Technical Details: SE Sequence

As we have seen, it is possible for SE sequences to produce images with T_1 w, T_2 w or PDw, just by changing the timing parameters. Suppose you need to change one of these parameters during an exam, for example to keep scan time low. How do you make sure the timing will still produce the required contrast? You need to learn some technical details about the SE sequence and practise using it.

In some ways the SE sequence is simple to understand: it has just two RF pulses, one for excitation and one to refocus the echo. The repetition time TR is the time between two consecutive excitation pulses, and TE is the time between excitation and the signal echo. In its simplest form, the TE is twice the time between the excitation and refocusing pulse.

We can image the brain using a fixed (long) TR, and vary the TE from 10 ms to 100 ms. The series of images is shown in Figure 3.7a. If we measure the signal of GM, WM and CSF on each of these images, we can plot the signals against TE on a graph (Figure 3.7b). Notice that the longer TEs have the maximum contrast – the most difference between signals – even though they have lower **Signal-to-Noise Ratio (SNR)** overall. These are the T_2 w images which are so common in MRI.

Next we can image the same brain with a fixed (short) TE, and vary the TR from 50 ms to 1000 ms. This series of images is shown in Figure 3.8a and the corresponding signal curves are shown in Figure 3.8b. This time we see that the maximum contrast occurs at shorter TRs, although again the overall SNR is low. These are the T_1 w images.

If we want to acquire PDw images, we need to minimize the effects of both T_1 and T_2 . That means we should use the longest possible TR and shortest TE. These images will have high SNR, as you can see from the curves in Figure 3.7 and Figure 3.8.

Suppose we go a bit crazy, and image the brain with short TR and long TE – what does an image look like with both T_1 and T_2 weighting? See Figure 3.9 for an example. It has extremely low SNR, and we now cannot be sure what a high signal intensity means: is it a short- T_1 tissue, or a long- T_2 tissue? This is not helpful for the radiologist, so make sure you don’t do it!

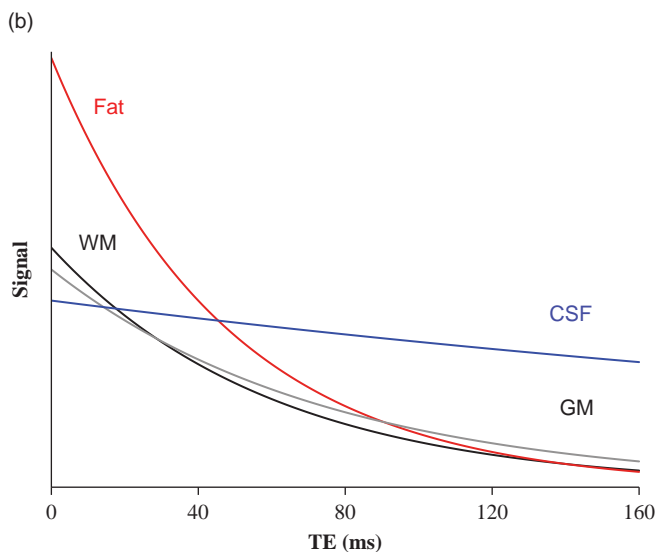
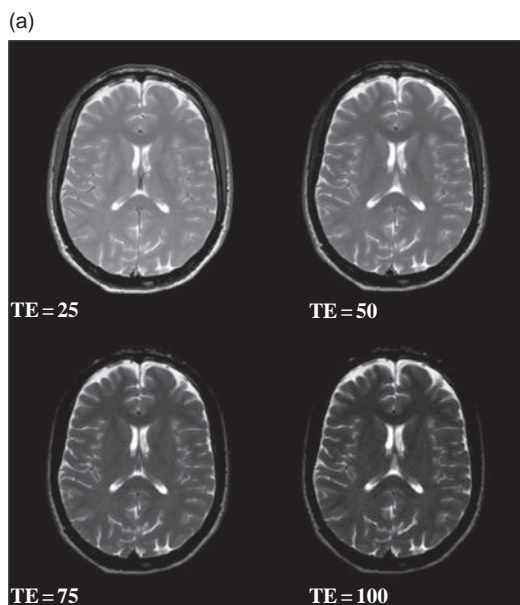


Figure 3.7 (a) SE brain images with TR = 1500 ms and various TE. (b) Signal intensity for brain tissues plotted against TE.

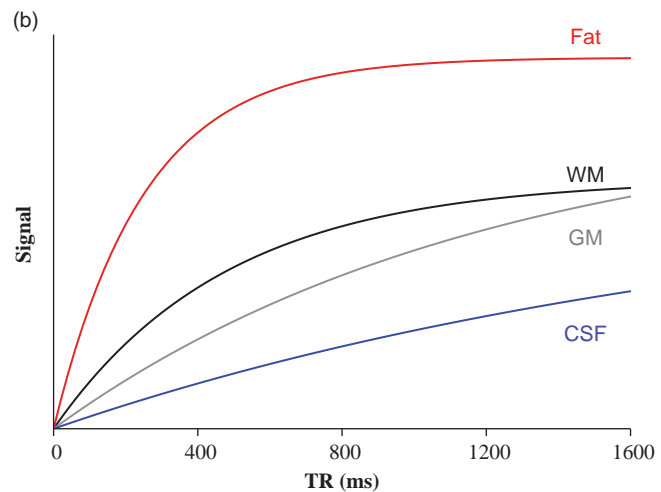
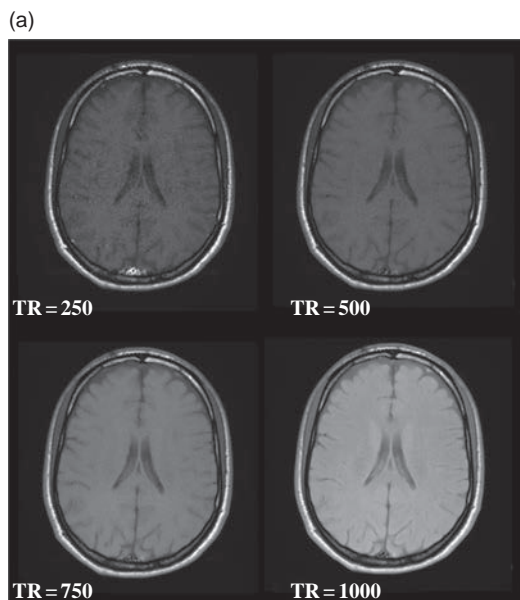


Figure 3.8 (a) SE brain images with TE = 10 ms and various TR. (b) Signal intensity of CSF, grey and white matter, and subcutaneous fat plotted against TR.

3.8 PD-Weighted Images

We have already introduced two fundamental properties of tissues in the body: T_1 and T_2 relaxation, which are used to create contrast in MR imaging. The

third important property is the proton density, PD. Proton density is essentially the water content of the tissues, and so it does not vary much, ranging from 75% to 85% in most organs. Although this limited

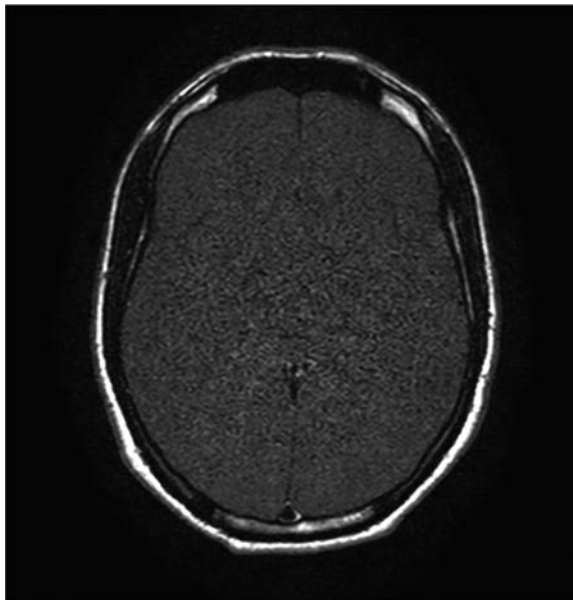


Figure 3.9 Image of the brain acquired with short TR (150 ms) and long TE (80 ms).

range means that PD scans are rather ‘grey’, i.e. lack contrast, compared with T₁w or T₂w scans, they have some useful clinical applications; for example, in the knee you can distinguish articular cartilage from the cortical bone and menisci (Figure 3.10). PDw images can be produced either with SE or GE sequences; however, for musculoskeletal imaging it is usual to stick to SE.

Try It for Yourself 1: Contrast on Spin-Echo Images

One of the best learning experiences is to produce MR images yourself with different timings to see the effect on contrast. For ethical reasons it is better to use a phantom than to scan one of your friends; fill leak-proof bottles with cooking oil (representing fat signals) and water. If you can find an out-of-date bottle of gadolinium contrast, use it to change the T₁ and T₂ of more bottles of water; you only need 0.1–0.2 ml per litre of water. Arrange the bottles within the head coil or knee coil, do a localizer scan and then start playing. Make sure you only change one parameter at a time, keeping all the others constant.

A few hints (some scanners have little tricks which can catch you out):

- Don’t use fast spin echo (turbo spin echo), use the conventional spin echo without an echo train.



Figure 3.10 Sagittal PD-weighted image of the knee.

- Short TRs or long TEs don’t allow many slices: check how many you can get before you set up the long TRs and short TEs. You need to scan slices at exactly the same locations to get a proper comparison of contrast.
- Don’t be stingy with the slice width, you’re not looking for high resolution here. Go for 10 mm.
- Make sure you keep the same receiver gains for all the scans. Check your manufacturer’s system manual to see how to do this. This will allow you to measure the signal intensity within regions on the images, and then plot curves similar to the ones in this chapter.

Technical Details: IR Sequence

We already mentioned that the IR sequence is a variant of SE, with an extra *inversion* RF pulse at the start. As the name suggests, this first pulse tips all the protons upside-down. From this position, they return back towards equilibrium via T₁ relaxation. When the excitation pulse is applied, some of the protons may still be in the negative direction, some will be positive (almost back to equilibrium) and some may be at exactly zero. Their position depends on the T₁ of the tissues. Tissues which are at zero will not give any signal in the imaging sequence; they are said to be nulled.

(a)

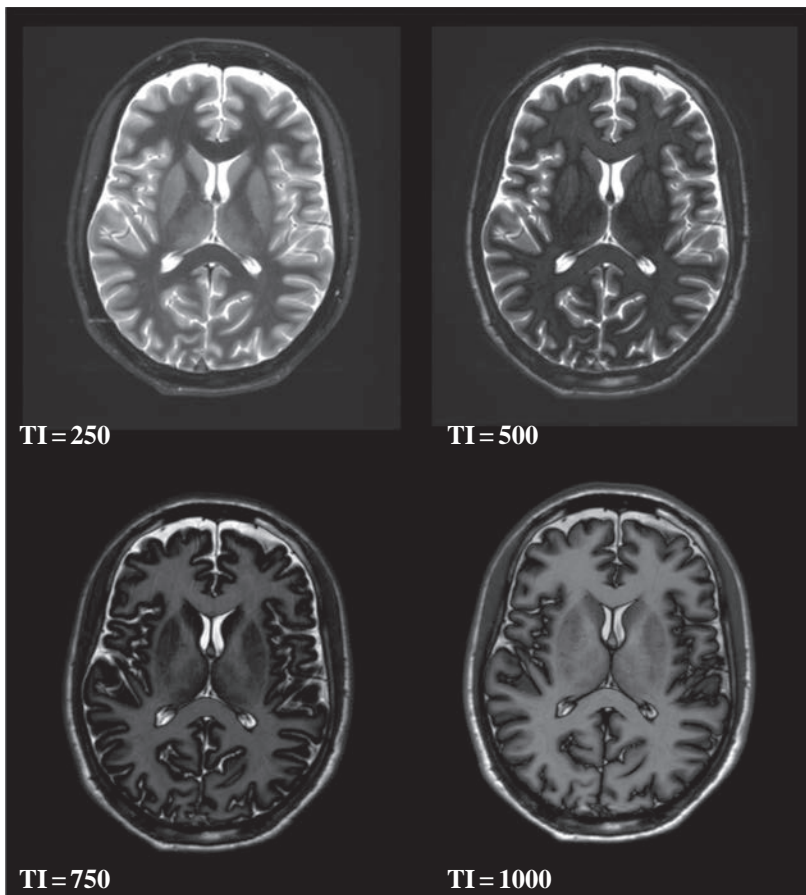
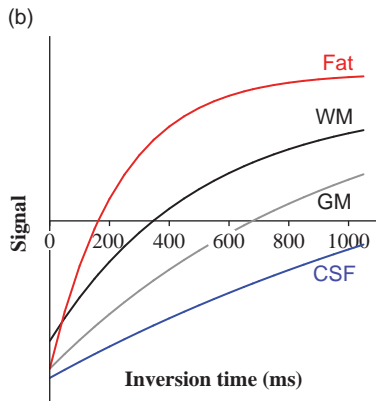
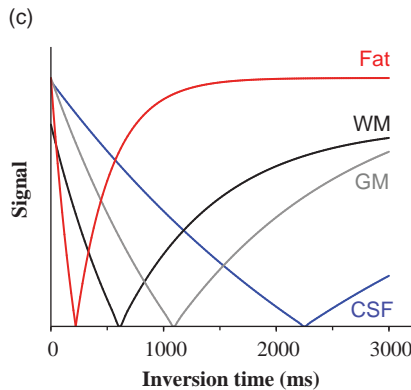


Figure 3.11 (a) Inversion recovery images at various TI with TR = 8000 ms and TE = 10 ms. (b) Signal curves plotted from these images. The curve for fat indicates the appropriate TI for a STIR image. (c) Inversion recovery curves showing magnitude signals (as most commonly used in scanners) with only positive values.

(b)



(c)



Using the brain example again, the sequence of images in Figure 3.11a shows a fixed TR of 8000 ms, a fixed TE of 10 ms and TI varying from 100 ms to 3000 ms. By plotting the signal values against TI

(Figure 3.11b), you can see how tissues change from negative to positive, and by selecting the right TI we can make a fat-suppressed image (STIR) or a CSF-suppressed image (FLAIR).

Normally MR images don't show negative and positive signals; they are simple *magnitude* images where the signal brightness only shows the size of the MR signal, not its direction (whether it is positive or negative). If we re-plot the same image series using magnitude signals only, the curves show a characteristic dip to zero before rising back up again (Figure 3.11c).

3.9 Gradient-Echo Images

The gradient-echo (GE) sequence is extremely versatile, allowing for T_1w , T_2^*w and PDw images. For the beginner, the first problem is that there are lots of different GE sequences with different names – how do you know which one to choose? There are important differences between these sequences, so we will eventually have to explain which is which (see Chapter 13). In this chapter, we will simply tell you the appropriate sequence for the main manufacturers.

Although the sequence choice is important, the choice of excitation *flip angle*, α , is much more important to determine the contrast in the images. GE sequences generally use small flip angles for excitation, often less than 90° , which is normally used in SE sequences. They also have very short TRs

compared with SE, between 15 ms and 250 ms. Looking back at Figure 3.8b, we would expect to have very little SNR (Signal-to-Noise Ratio) with such short repetition times. However, by reducing the excitation flip angle to e.g. 30° , we can avoid this signal loss. A 30° excitation RF pulse leaves most of the protons in their equilibrium position, aligned with the main magnetic field. This means that full relaxation can be achieved in a very short time (typically less than 500 ms). So even with a short TR, using $\alpha = 30^\circ$ will avoid T_1w in the images, leaving either PD or T_2^*w (depending on the chosen echo time).

Alternatively, using $\alpha = 50^\circ$ or higher affects more of the protons, leaving fewer in the equilibrium position, and we can create more T_1 weighting. (The exact choice of α depends on which GE sequence you are using; please read Chapter 13 to understand this complex subject.) You can see the effect of changing α on the signal intensities of brain tissues in Figure 3.12. Notice that intermediate values of α give contrast that is not good for either T_1 or PD.

In daily practice, GE scans give us flexibility to increase the TR to allow extra slices, or reduce it to save scan time. When we do this, we have to maintain the T_1w contrast by adjusting the flip angle to match the TR.

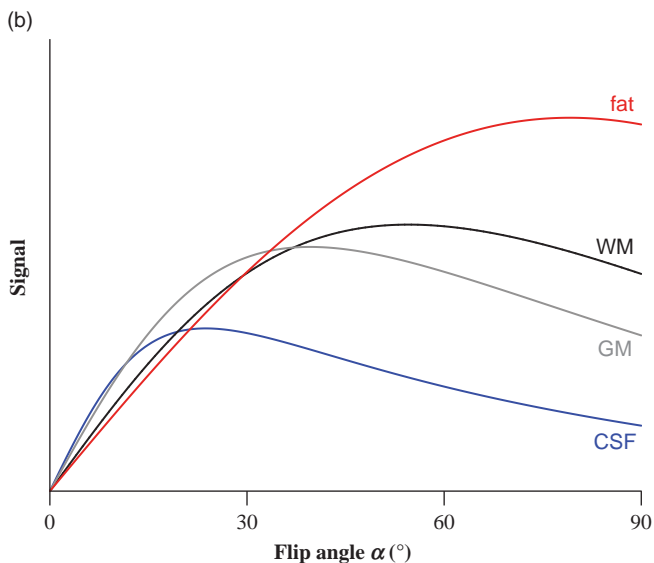
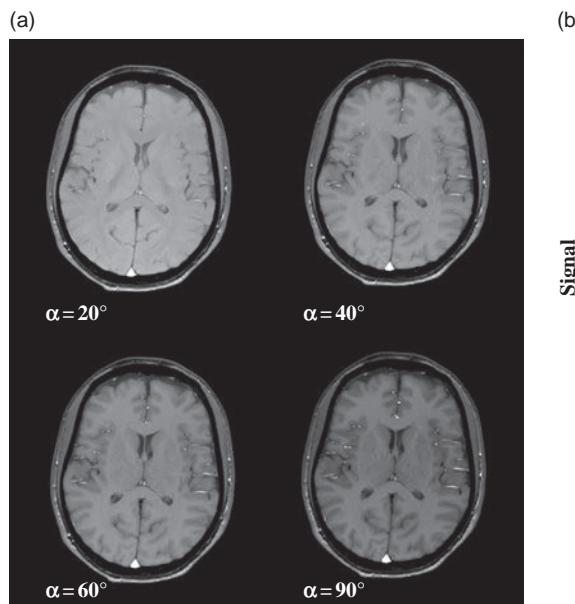


Figure 3.12 (a) GE images with fixed TR (150 ms) and TE (4.6 ms) and various flip angles α . (b) Signal intensity of brain tissues plotted against α .

3.9.1 Gradient-Echo T₁-Weighted Images

Using the information in the previous section, you can already suggest the timing parameters needed to get T_{1w} GE images. A short echo time, a flip angle of at least 50°, and a TR of . . . well, it doesn't matter does it? You can set the TR as short as you like, to achieve a very short scan time – but be careful that you don't make it so short that you have no SNR left! See Chapter 6 for more practical hints about optimizing contrast etc. We promised to tell you which GE sequence to select. On GE Healthcare systems, choose SPGR; on Philips, choose T1-FFE; and on Siemens, choose FLASH (see Table 4.2). By the way, throughout this book we shorten gradient echo to GE, and refer to the manufacturer as GE Healthcare.

One interesting variant with T_{1w} GE images is the possibility to acquire *in-phase* and *out-of-phase* images. This refers to the choice of echo times, which determines whether water and fat signals are either in phase with each other, or out of phase. In-Phase (IP) means that both sets of protons are in the same direction, while out-of-phase means that they point in opposite directions. Out-of-Phase (OP) images have a characteristic dark line which seems to outline the organs, just like a child's drawing with a black outline. This is due to the interface between the water-based organs and the intra-abdominal fat, giving OP signals for the water and fat in these voxels. This technique allows a radiologist to detect if there is diffuse fatty infiltration in the liver or other organs, since the OP images will show a darker signal than the IP images.

Clinical Exam 4: Liver

Liver MR imaging is becoming more and more common, and it introduces some new challenges for the radiographer. Most scans are done with breath-holding, to avoid motion artefacts as the liver moves with respiration. This means that all scan times have to be reduced to less than 25 s, and preferably closer to 15 s. Spin-echo sequences are too slow for this, so gradient echo is frequently used for liver imaging. Breath-holding in inspiration is easier for the patient and can be held for longer, but expiration breath-holds offer more consistent liver positioning between scans, so expiration is usually the preferred method.

A typical examination would include T₂*w images, T_{1w} images acquired in- and out-of-phase, a fat-suppressed T_{1w} 3D image, and a dynamic series

of T_{1w} scans acquired before and after an injection of Gd. Focal liver lesions react to Gd in different ways, and it is important to see both the uptake and wash-out of the contrast agent in order to characterize the lesions. Images are mostly acquired in the transverse plane, or the coronal plane.

Positioning patients for liver MRI takes longer than spine or MSK imaging. Before you even get the patient into the scanner room, coach them with the breath-holding instructions, as expiration breath-holding may be new for them. A respiratory belt or device may be necessary for any non-breath-hold scans, and this should be positioned according to the manufacturer's instructions. Liver imaging requires an RF receive coil to be placed over the patient's body. The patient lies supine and can be entered into the scanner either head-first or feet-first. Finally, make sure that the patient can hear you clearly when you talk through the intercom, so that they can follow the breath-holding instructions.

3.9.2 Gradient-Echo T₂*-Weighted Images

Looking back at Section 3.3, you may have noticed the strange notation (*) next to the T_{2w}. This is linked to the fact that GE sequences cannot correct for the effects of magnetic field non-uniformities. A perfectly uniform magnetic field simply can't be produced, and even if it could the patient would make it imperfect due to *susceptibility* effects (see Box 'Good Metal, Bad Metal' in Chapter 2). Susceptibility is a term used for low-level magnetic field variations, introduced by anatomy such as sinuses or intestines containing air, or dense cortical bone, or iron-rich blood breakdown products.

These inhomogeneities affect the relaxation of tissues after an RF pulse, making the spin–spin relaxation time appear shorter. We call this the *apparent spin–spin relaxation time* T₂*, or simply *apparent* T₂*. It turns out that the effect of the B₀ non-uniformity can be separated from the fundamental T₂ of the tissues, and Chapter 9 will provide much more information about these relaxation processes. For now, it is enough to remember that T₂* is always shorter than T₂.

If we consider a range of tissue T₂s all in the same imperfect magnetic field then we can say that the tissue T₂*s will stay in the same relationship to each other. So CSF with T₂ longer than grey matter will also have a T₂* longer than the T₂* of GM. The basic contrast in GE T₂*w images is therefore the same as in

SE T_2^* scans (fluids are bright, other tissues are mid-grey). As usual, we tend to be a bit lazy when describing the image contrast, so you might hear the phrase ‘gradient echo T_2^* s’. This is accepted as MRI jargon, because the image contrast is very similar to that of spin-echo T_2 s. But do keep in mind that magnetic field non-uniformities will have an effect on all the signals; the scans are actually ‘gradient echo T_2^* s’.

To produce GE T_2^* images, select GRE sequences on GE Healthcare systems; choose T2-FFE on Philips; and FISP on Siemens scanners. You need to keep α small to avoid T_1 weighting, and TR can be short for rapid scanning or long enough for multiple slices. The TE is increased to achieve T_2^* weighting, although the TE is always short compared with the TEs used in spin-echo sequences.

By now you can probably work out for yourself how to get a gradient echo PD image. You need to use the same type of sequence as you did for a GE T_1^W image, setting the TR to be as short as possible (for a 3D scan) or long enough to get the required number of slices. Since we don’t want any T_2 decay, the echo time must be short, and α must be small to avoid creating T_1 contrast. GE PDw images are not often used in clinical practice, so we won’t spend any more time on them.

Try It for Yourself 2: Contrast on Gradient-Echo Images

Using your oil and water bottles again, try changing TR, TE and α to see the effect on contrast. You need to use different GE sequences to show T_1 or T_2^* contrast: refer back to the last two sections. As before, there are pitfalls to avoid:

- Short TRs and long TEs don’t allow many slices: check first how many you can get.
- Keep all the other scanning parameters the same.
- Keep the same receiver gains for all the scans within a set (e.g. for several different TEs).

Measure the signal intensity within regions on the images, and then plot curves.

3.10 More About Contrast Agents

You have already been introduced to gadolinium-based contrast agents in Section 2.5. Gadolinium is very common in MR exams, and there are several different preparations available in the market. There are variations in concentration and dosage, so be sure to familiarize yourself with the manufacturer’s information sheet at your institution.

Gd contrast agents are rapidly passed from the arterial system into the extravascular space. From there, they are excreted to the veins and eventually filtered out in the kidneys. In tissues with abnormal vascularity, Gd tends to pool in the extravascular space. The exception to this principle is in the brain, where Gd remains intravascular *except* where the blood-brain barrier is disrupted.

Since gadolinium is paramagnetic, it alters the local magnetic field in areas where it accumulates. Not enough to be measurable, but enough to affect the relaxation times of the tissues. In particular, the tissue T_1 is reduced, and this leads to *higher* signal on T_1^W images after Gd injection.

Other paramagnetic metals have been developed as MRI contrast agents. For a while, Super-Paramagnetic Iron Oxide, known as SPIO contrast agents, were available for liver MRI. The effect of a SPIO agent is to *reduce* the T_2 of tissues in which it accumulates, causing lower signal intensities on T_2^W or T_2^* images post-contrast. Since SPIO agents are taken up by healthy Kupffer cells, the signal of normal tissue is reduced, leaving pathological tissues with a relative signal enhancement post-injection. However, many SPIO formulations have been discontinued due to disappointing sales in many countries. The only agent left in the market is Lumirem® (Guerbet), available in some European countries and marketed as a rectal or oral agent to delineate the bowel lumen. Manganese is another paramagnetic metal which has been developed as an MR contrast agent. It behaves in a similar way to Gd agents, by reducing the T_1 of tissues where it accumulates. However, like the SPIO agents, sales were poor compared with Gd and there are currently no approved formulations in the market.

Why Doesn't Gadolinium Affect T_2 ?

The real answer is that gadolinium *does* affect T_2 as well as T_1 . The precise effect of contrast agents depends on their concentration in the tissue concerned, and also on the imaging sequence being used. Remember that although images are described as T_1^W , T_2^W , etc., the signals have contributions from all the magnetic properties of the tissues concerned – T_1 , T_2 , PD, susceptibility, and so on. At very high concentrations and in sequences with longer TEs, gadolinium may actually reduce the signal intensity of the tissue due to shortening of T_2 .

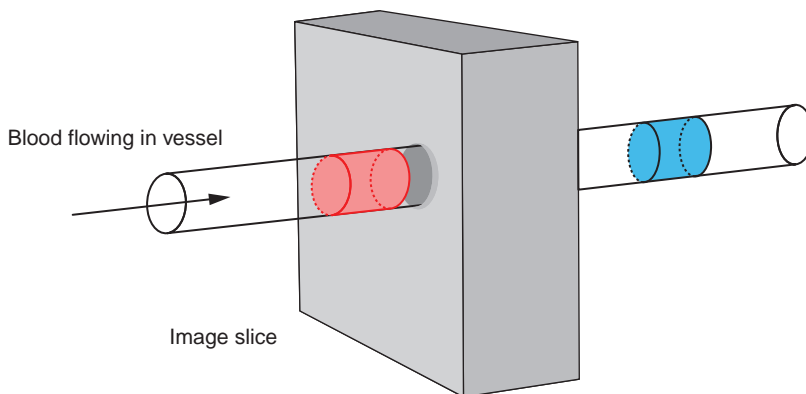


Figure 3.13 The time-of-flight or in-flow effect. The blood vessel is shown crossing through the imaging slice. When the sequence is repeated, the previously excited blood (coloured blue) has moved on and the bolus within the slice (coloured red) has fully relaxed magnetization M_0 .

Clinical Exam 5: Advanced Brain

Some neurological conditions are linked with the neurovascular system, so angiography is an important technique in MR. For example, MRI is used in the diagnosis of **Arterio-Venous Malformations** (AVMs), to monitor aneurysms, and to investigate acute stroke in some specialist centres. **MR Angiography** (MRA) sequences are mainly based on gradient echo, and may include imaging during an injection of Gd contrast agent. MRA is capable of detecting small aneurysms and vascular stenosis, and can also be sensitive to thrombosis. When high resolution is needed, MRA scans can be quite long (5–6 min).

In many neuropathologies, we use a scan called **Diffusion-Weighted Imaging** (DWI). This scan is sensitive to the tiniest movements of water protons, rather than the bulk flow properties seen in the vascular system. DWI is particularly used in the characterization of focal brain lesions, and can also be used to determine the age of a stroke infarct. DWI is typically a very fast scan, less than a minute, but it is also one of the noisiest scans because it uses very strong gradient pulses to create the diffusion sensitivity. Patients may be alarmed by the noise and may also feel the scanner vibrating during the DWI.

3.11 Angiographic Images

When we were describing T_1 w imaging, we mentioned that flowing fluids, such as blood, do not behave like other static fluids, like synovial fluid. You may have noticed that the signal within vessels is very high on GE images and can also cause artefacts. How can a long- T_1 fluid give a high signal on T_1 -weighted images? It is because the blood is flowing.

Consider a blood vessel passing through the imaging slice (Figure 3.13). During the repetition

time of the sequence, the little plug or ‘bolus’ of blood within the slice flows out of the slice and is replaced by a new bolus. This blood has not been tipped by the RF pulse, so when the next pulse is applied the blood has its full equilibrium signal. Thus, it will give a high signal even though TR is short and the T_1 of blood is long. This process repeats itself during each TR, so each bolus of flowing blood always gives a high signal. This is known as the ‘in-flow’ or ‘time-of-flight’ effect.

We can exploit the high signal of flowing blood in **MR Angiography** (MRA) using a variety of techniques to suppress almost all the signal in static tissues. The three most important sequences are ‘time-of-flight MRA’ (also known as ‘in-flow MRA’), ‘phase-contrast MRA’, and ‘contrast-enhanced MRA’, which uses a very rapid imaging sequence during the injection of gadolinium. All three MRA sequences leave the blood vessels as the main high-signal structures against a dark background. Using a special kind of computer processing technique called ‘Maximum Intensity Projection’ (MIP), we can produce images which show the blood vessels (Figure 3.14), with a 3D effect when they are shown in a movie loop.

Warning: MRA is Not as Simple as it Looks!

MRA seems to be an easy technique for producing angiographic images without subjecting the patient to a risky intra-arterial procedure or ionizing radiation. However, it is not without problems. For example, time-of-flight sequences may not distinguish freshly thrombosed clots from flowing blood (because the methaemoglobin is starting to affect the MR signal), stenoses may be exaggerated in terms of length and severity, and very slow-flowing blood may disappear altogether. All these pitfalls will

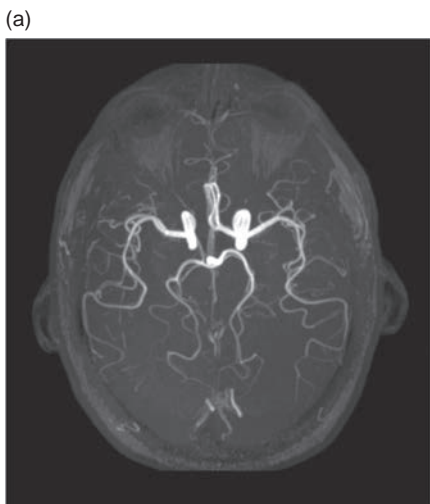


Figure 3.14 MR angiograms of (a) the Circle of Willis and (b) an aortic coarctation.

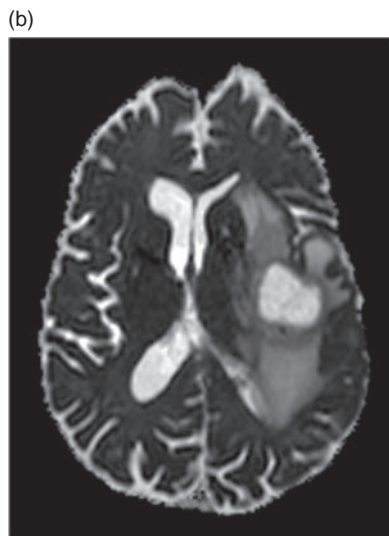
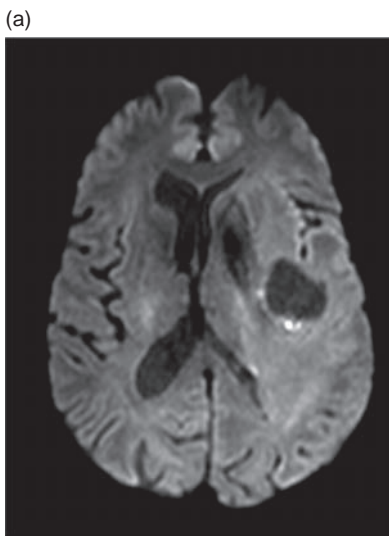


Figure 3.15 (a) DW images of brain tumour, with the lesion showing high signal. Notice that the CSF is not completely dark due to T_2 shine-through effect. (b) ADC map of the same slice, showing bright signal for CSF and mixed signal for the lesion.

be explained in detail in Chapter 15, along with ways of avoiding them. In spite of these potential problems, MRA is a common and very useful imaging technique which you will undoubtedly use regularly.

3.12 Diffusion-Weighted Images

Diffusion is a random process by which molecules move gradually within their environment. In MRI we are interested in the diffusion of water molecules, which changes in certain pathological conditions. For example in tumours which are rapidly proliferating, the local cell density becomes very high and the

extracellular space becomes restricted. The protons in the extracellular space demonstrate reduced diffusion compared with normal tissues.

Diffusion-Weighted Imaging (DWI) is almost always performed using a spin-echo Echo Planar Imaging (EPI) scan, which will be explained in Chapter 12. The diffusion sensitivity comes from a pair of very strong gradient pulses, one on either side of the refocusing RF pulse. These gradients have a large amplitude and duration, which means that they force the TE to be rather long, e.g. 80 ms. This means the DW images are also rather T_2 -weighted, a phenomenon known as ' T_2 -shine-through'. We can separate the T_2w effect from the diffusion effect by acquiring a

non-DW image as well as the DWI, and then combining these two images mathematically. The result is known as the ADC (Apparent Diffusion Coefficient) map, and this will be explained in more detail in Chapter 18.

Bulk fluids like CSF are dark on DW images, while normal brain tissue has an intermediate signal level. Restricted diffusion, such as we see in stroke or tumours, shows up as high signal intensity on DWI (Figure 3.15a). On the ADC images, the opposite is true: CSF shows up as very high signal (high diffusion) while restricted diffusion is dark (Figure 3.15b).

Diffusion is also widely used in body imaging, for example breast, liver or prostate. Focal tumours in

these organs also tend to have high cell densities and show the same high signal on DWI as brain tumours or strokes. However, the EPI technique introduces geometric distortions which are particularly bad in these body areas, so it is rather difficult to achieve high-quality imaging.

See also:

- Details of T_1 , T_2 and T_2^* , including the effects of gadolinium: Chapter 9.
- Gradient-echo sequences: Chapter 13.
- Fat suppression techniques: Section 7.3.
- MR angiography: Chapter 15.
- EPI and diffusion: Chapters 12, 18.

Further Reading

Bushong SC and Clarke G (2014)
Magnetic Resonance Imaging: Physical and Biological Principles, 4th edn. St. Louis, MI: Mosby, chapter 7.

Hashemi RH and Bradley WG Jr (2010) *MRI: The Basics*, 3rd edn. Baltimore, MD: Lippincott, Williams & Wilkins, chapters 4–6.

Rinck PA (2007) *Magnetic Resonance in Medicine*, 5th edn. Berlin: ABW Wissenschaftsverlag GmbH, chapter 10.

Lost in the Pulse Sequence Jungle?

4.1 Introduction

In Chapter 3 we saw how the image appearance can be manipulated by altering sequence parameters such as TR, TE, TI and flip angle to give T_1 -weighted or T_2 -weighted contrast. If only that was all there is to MRI! Unfortunately there are literally hundreds of pulse sequences. Every year at MR conferences around the world scores of new pulse sequences are launched and, in the tradition of the MR scientific community, all sport stylish acronyms.

Now, the trouble with acronyms is that despite sounding memorable and snappy (e.g. FLASH, HASTE, DIET, BRAVO, RESOLVE, etc.) it's virtually impossible to remember what they stand for, and therefore what they are designed to do. Moreover, MR manufacturers have the tendency to use different names for the same things (manufacturer conversion information is given in the tables of this chapter and the acronyms are spelled out in the Glossary). While the end-point of an acquisition can be expressed in terms of T_1 or T_2 weighting, there are numerous ways of achieving this – few destinations but many routes. So if you are lost in the pulse sequence jungle with a bewildering variety of sequence species, and cannot see the wood for the trees, this chapter is for you.

You will see that:

- there are two major pulse sequence families: spin echo (SE) and gradient echo (GE);
- gradient-echo sequences are generally faster;
- there are ways of speeding up spin echo;
- sequences generally exploit T_1 or T_2 contrast;
- gradient-echo sequences are good for studies with gadolinium-based contrast agents, particularly in the body or for bright fluid imaging, for example in cardiac studies.

4.2 Anatomy of a Pulse Sequence

A pulse sequence has several functions. These include generating suitable contrast between tissues (Chapter 3), forming an image, having an appropriate scan time, for example, within a breath-hold, and avoiding artefacts, e.g. motion, flow. You'll get a lot more detail in later chapters. For now, be aware that there will always be *RF pulses* and *gradients*, one of which will always be a read or *Frequency-Encode* (FE) gradient. There will almost always be one or two sets of *Phase-Encode* (PE) gradient pulses and some form of *slice selection* or slab selection. Every sequence also contains the basic timing parameters: TR, measured in milliseconds (ms), and TE (also in ms) are shown in Figure 4.1. TR is the repetition time between the acquisition of different lines of the raw data, or between excitations (making the signal). TE is the time that each signal or echo is measured following its initial generation or excitation.

4.2.1 Examinations, Sequences and Parameters

In the scanner's user interface, whole examinations are grouped together according to body part and clinical application or pathology (and sometimes coil). An *examination* or a *program* consists of a list of *sequences* to carry out the examination. Examples of standard examinations are given in clinical boxes in Chapter 3.

Each sequence within the examination, for example T_1 -weighted, T_2 -weighted, diffusion-weighted, will contain default *parameters* such as orientation, number of slices, slice width, number of signal acquisitions or averages, and the timing parameters: TR, TE, TI (where applicable). These have been either pre-selected by the manufacturer or customized on site to give images of the desired diagnostic quality and utility. Common sequence parameters are shown in Figure 4.2. Each

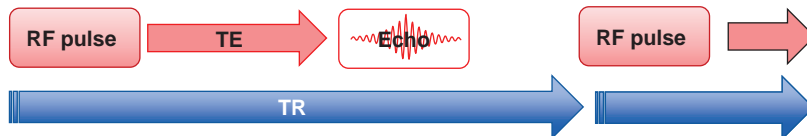


Figure 4.1 Basic sequence structure. The time between repeated RF excitations is TR. TE is the time after the RF excitation that the echo signal is measured.

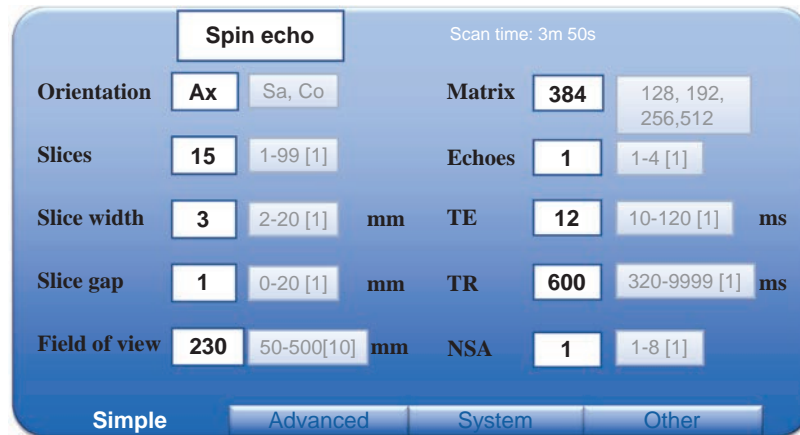


Figure 4.2 Sequence parameters shown in a mock-up of a user interface. The selected parameter values are in bold type, the possible range in grey and the incremental changes permitted shown in brackets. A user interface will usually consist of a number of pages or cards or tabs, shown along the bottom or top of the page.

parameter will have a default value and a range of user-selectable values. Sometimes the parameters are arranged on different *tabs* or *cards*.

In the next two chapters we will learn much more about making parameter changes. For now we will only concern ourselves with a basic subset of parameters: TR, TE, TI, Echo Train Length (ETL), 2D or 3D, and scan time. Scan time is determined by TR, along with the number of lines (N_{PE}) in the image and Number of Signal Averages (NSA, called NEX on GE Healthcare systems):

$$\text{Scan time} = \text{TR} \times N_{PE} \times \text{NSA}$$

For example, using the values shown in Figure 4.2, the prescribed scan time would be $[(600 \text{ ms} \times 384 \times 1) \div 1000]$ seconds, or 3 min 50 s.

Additionally, various other features may be added to the basic sequence structure to ensure that scans are diagnostic. These are listed in Box ‘Sequence Options’ and explored more deeply in later chapters.

Sequence Options

In addition to providing the basic image contrast, sequences often incorporate features to avoid certain artefacts or to reduce unwanted signals. These can include:

- *spatial saturation*, to remove unwanted artefact-producing signals (e.g. from breathing). Usually

there will be a choice of several saturation bands, all freely selectable in space;

- *fat suppression* or saturation;
- *magnetization transfer saturation* to improve contrast, or reduce background signal intensity in cerebral angiography;
- *magnetization preparation*, e.g. inversion pulses as the start of the TR period;
- *magnetization restoration*, e.g. driven equilibrium pulses at the end of the TR period.

These are repeated within every TR period so, referring to Figure 4.3, reduce the time available for each slice and also the number of slices possible.

4.2.2 The Pulse Sequence Family Tree

A great deal of the variety of MR sequences arises from the need to generate particular types of image contrast and also to speed up MR acquisitions. It’s a complicated family, but like human families with maternal and paternal branches, there are basically two types of sequence: spin echo (SE) and gradient echo (GE). Helpfully there are also two basic contrast mechanisms: T_1 and T_2 , but like real families there is often a hidden complexity to sequence characteristics and contrast behaviour. Figure 4.4 shows the generic pulse sequence family tree for spin echo, with an indication of acquisition speed and type of contrast achievable.

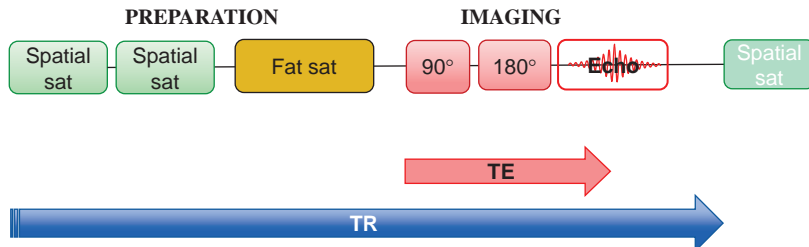


Figure 4.3 Sequence options. These must all fit within the TR period.

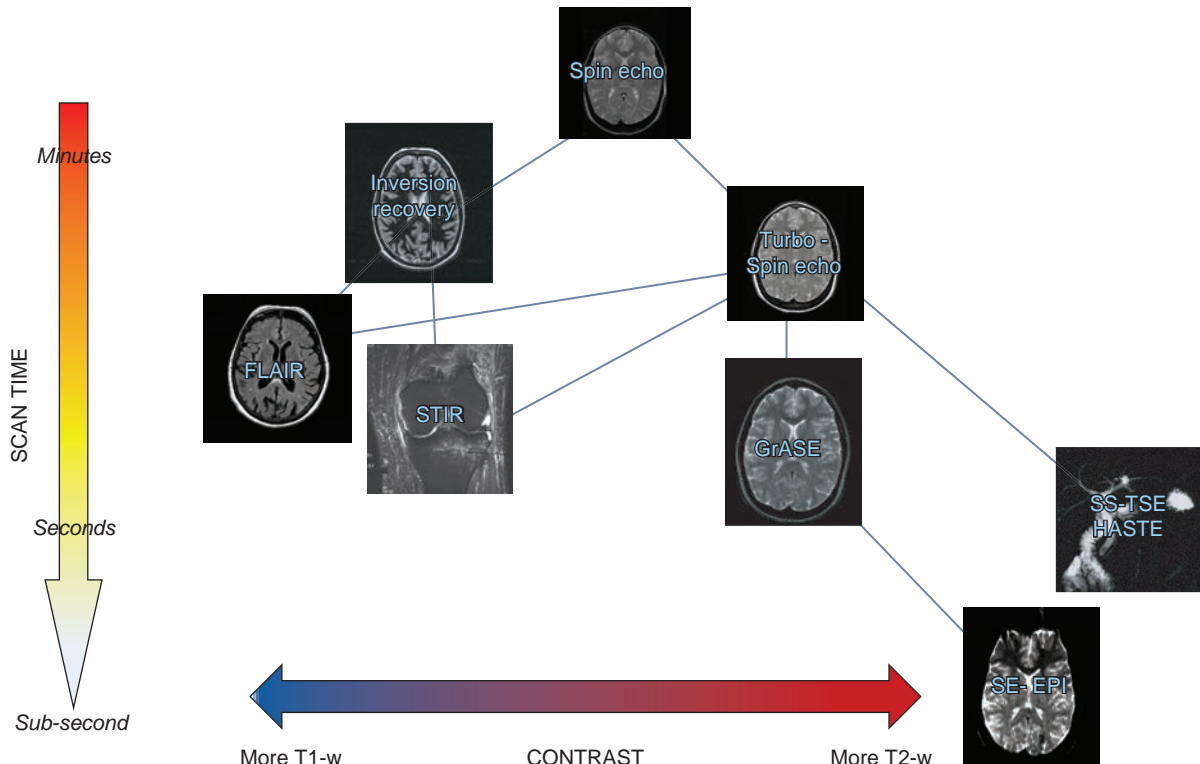


Figure 4.4 Pulse sequence family tree: spin-echo branch. Acquisition time is indicated vertically, with indicative contrast behaviour shown horizontally.

In terms of increasing speed and complexity the spin-echo branch of the family contains Turbo or Fast Spin Echo (TSE/FSE), turbo GRAdient And Spin Echo (GRASE), single-shot TSE or HAlf-Fourier Single-shot Turbo spin Echo (HASTE) and Spin-Echo Echo Planar Imaging (SE-EPI). Other variants of spin echo include FLuid Attenuated Inversion Recovery (FLAIR) and Short TI Inversion Recovery (STIR). These sequences are usually applied in two dimensions, i.e. in slices or sections, as in CT. Three-dimensional fast/turbo spin-echo sequences have recently become viable. These can provide high-resolution, isotropic images suitable for Multi-Planar Reformats (MPR). The commercial names of these sequences are shown in Table 4.1.

4.3 Take Me for a Spin (Echo)

Spin echo is the standard, vanilla-flavour MR pulse sequence and, rather like ice-cream, we find that it is now often surpassed by more exotic flavours although it remains the standard sequence for T_1 -weighted brain imaging. It also forms the basis of the SE sequence family tree, with its parameters TR and TE respectively controlling the T_1 and T_2 weighting of the image.

The advanced Boxes ‘Magnetization and the Meaning of Life’ and ‘Making a Spin Echo’ show the origin of the MR signal and how the echo is formed, but you can just as easily leave the details of how the echo is made until later (Chapter 9). Consider for now that to

Table 4.1 Spin-echo sequences manufacture comparison chart. The acronyms are defined in the Glossary

Generic name	GE Healthcare	Hitachi	Philips	Siemens	Toshiba
Spin echo	SE	SE	SE	SE	SE
RARE	FSE	FSE	TSE	TSE	FSE
IR-RARE	FSE-IR	FIR	IR-TSE	Turbo-IR, TIR	Fast IR
Short TI inversion recovery	STIR	STIR	STIR	STIR	Fast STIR
Long TI inversion recovery for CSF suppression	FLAIR	FLAIR	FLAIR	Turbo-dark fluid	Fast FLAIR
Single-shot RARE	SS-FSE SSFSE-IR		SS-TSE	SS-TSE HASTE	DIET, FASE, SuperFASE
Gradient and spin echo (GRASE)			GRASE	TGSE	
RARE driven equilibrium (90° flip back)	Fast Recovery FSE	DE-FSE	DRIVE	RESTORE	T ₂ plus FSE
3D RARE with variable flip angle	CUBE	isoFSE	VISTA, 3D-VIEW	SPACE	3D mVOX
Radial FSE	PROPELLER	RADAR	MultiVane	BLADE	JET
Echo planar imaging	EPI	EPI	EPI	EPI	EPI

make an MR signal we have to put in a pulse of (radio-frequency) energy and that, analogous to ultrasound, the tissue responds by generating an ‘echo’ which can be detected by the scanner through the MR coil (Figure 4.5). The time between the initial (excitation) pulse and the detection of the echo is called ‘echo time’ or TE, while the time between successive excitation pulses is the repetition time, TR. As we saw in Chapter 3, TR controls the T₁ contrast, while TE controls the T₂ contrast. Spin-echo sequences have the advantage that the image appearance is solely dependent upon the properties of the tissue, and not significantly influenced by the quality of the magnetic field, or inhomogeneity, in the scanner.

Magnetization and the Meaning of Life

When the patient is placed within the bore of the magnet, they become very, very slightly magnetic (Figure 4.6). For example, in a 1.5 T scanner, the average induced magnetic field, or magnetization of a typical adult head, is around 20 microtesla

(μT) – less than half the earth’s magnetic field and 75 000 times less than the scanner’s magnetic field. This magnetic field points in the direction of, or aligns with, the direction of the scanner’s field, along the head-foot or z axis.

In order to measure this tiny magnetization, it is necessary to tilt it away from the z axis. This is achieved by applying a radiofrequency (RF) pulse at the resonant or Larmor frequency f_0 given by

$$f_0 = \gamma \cdot B_0$$

where B_0 is the scanner’s magnetic field measured in tesla, γ (pronounced ‘gamma bar’) is the gyromagnetic ratio, a constant equal to approximately 42 MHz T⁻¹, and f_0 is expressed in megahertz (MHz).

Once tipped away from the B_0 direction (z), the magnetization M can be detected by an appropriately set-up coil. The signal detected is proportional to the transverse, or xy component of M, denoted M_{xy} . The maximum signal is achieved following a pulse which tilts or flips M through 90 degrees. This is called a 90° pulse.

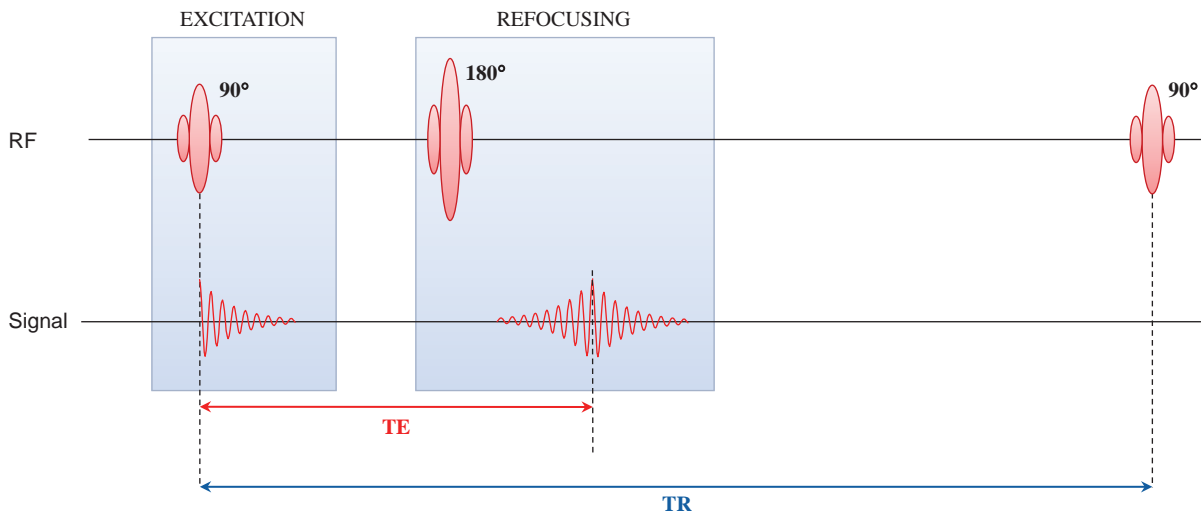


Figure 4.5 Simple spin-echo sequence (showing only RF pulses).

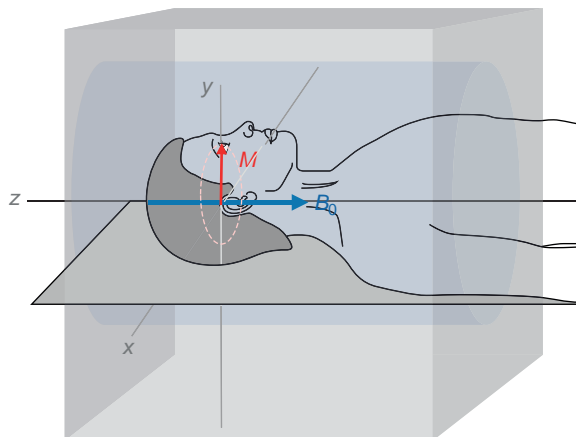


Figure 4.6 The patient's magnetization when placed in the magnet. This is flipped into the transverse plane (xy) to make a signal.

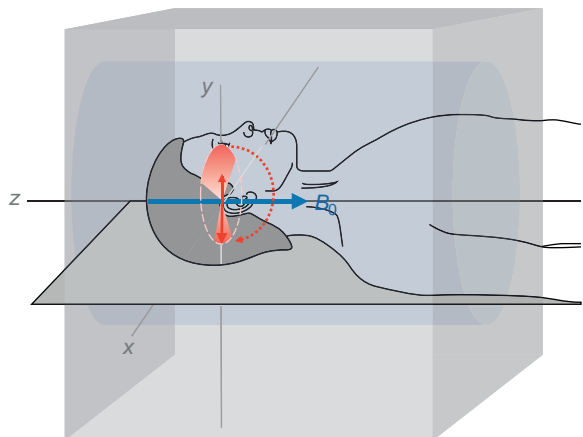


Figure 4.7 The formation of a spin echo.

Making a Spin Echo

Once created, the signal does not last very long (typically a few tens of milliseconds). It reduces or decays because transverse magnetization M_{xy} in different positions within the scanner experience slightly different magnetic fields – and thus produce signals at slightly different frequencies. This is equivalent to parts of M_{xy} diverging or fanning out in the xy -plane (Figure 4.7), where some of

M_{xy} has lower frequencies (or a phase lag) and other parts have higher frequencies (phase advance).

By applying a 180° or refocusing pulse the effect of the spread of frequencies can be reversed. The 180° pulse twists the 'fan' of magnetization vectors about the x axis, in such a way that parts which had the largest phase lag (slowest), now have the greatest phase advance. Similarly, parts which were

most advanced (fastest) are now moved to a position where they are most retarded. In this way, after a time TE equal to double the time between the two RF pulses, all the transverse magnetization coincides along the x axis and a signal maximum, the spin echo, is obtained. Thereafter the dephasing, or signal decay, occurs again and the echo fades away. Spin echo corrects for signal loss due to static field inhomogeneities, with any signal decay indicating the true transverse or T_2 relaxation behaviour of the tissue.

Spin echo formation is often considered in terms of the 'runners on the track' analogy. In this a group of contestants start a race on the sound of a gun (the 90° pulse). Having different levels of fitness and ability they all spread out. When the gun is fired again (a 180° pulse) they all have to double back the way they came. In this way the slowest runners, who have the least far to go, and the fastest who have covered more ground, all arrive back at the start together (making the echo).

4.3.1 Turbo Spin Echo: The Work Horse

In order to make an image, the basic pulse-echo sequence has to be repeated (for as many times as there are lines in the image). As we are using TR to control the image contrast we therefore don't have proper control of the scan time: we cannot reduce it by shortening TR as that will affect the image appearance. In Turbo or Fast Spin Echo (TSE, FSE), multiple signal echoes are collected following each excitation pulse (Figure 4.8) and therefore the scan time can be reduced by the Turbo Factor (TF) or Echo Train Length (ETL). Thus for an ETL or TF of 8, the scan time is reduced by eight times. In practice echo train lengths vary from 3 to 256. The generic name for this type of SE sequence is Rapid Acquisition with Relaxation Enhancement (RARE). We will refer to it as TSE.

TSE has become the standard sequence for T_2 -weighted imaging. It produces excellent T_2 contrast by the combination of long TR (to avoid T_1 effects) and variable TE to control the extent of T_2 weighting. In Chapter 12 we shall see how this is achieved in practice, but for now we can think of it as an SE used for T_2 -weighting. Example images of SE-type sequences are shown in Box 'Brain Sequences'.

Brain Sequences

Here, we look at the sequences within a typical brain examination. These are for illustrative purposes only. Actual clinical sequences and parameters used will depend upon the diagnostic question and your institutional protocols.

Scan	Sequence	Typical parameters	Comments
Axial T_1 w	SE (Figure 4.9a)	Short TR (400–700 ms). Short TE (<15 ms). 20–30 slices, 3–5 mm slice, FOV 230 mm, matrix 320 × 256.	The short TR gives good T_1 weighting. The sequence can be used pre-contrast, demonstrating sub-acute haemorrhage and infarct necrosis. Post-contrast it shows ring-enhancing lesions such as lymphoma, glioblastoma and necrotic metastases.
Coronal T_2 w	TSE (Figure 4.9b)	Long TR (>4000 ms). Long TE (>80 ms). Turbo factor ~ 11–15. Slices etc. as above	TSE is used to mitigate the time penalty of a long TR, required for good T_2 weighting. Good for detection of tumours, infarct, inflammation and infection.
Axial T_2 w	FLAIR (Figure 4.9c)	Very long TR (>8000 ms). Long TE (>80 ms). TI ~ 2400 ms. Slices etc. as above.	Nulls signal from CSF, enables detection of small lesions with elevated T_2 including MS plaques.
Axial DWI	Spin echo EPI (Figure 4.9d)	b-factor 500–1000, TR and TE as required. 20 slices, 5 mm. Matrix 128 × 128.	Lower-resolution scan with diffusion weighting. Detection of hyper-acute stroke. Distinguishes acute ischaemia from chronic infarct.

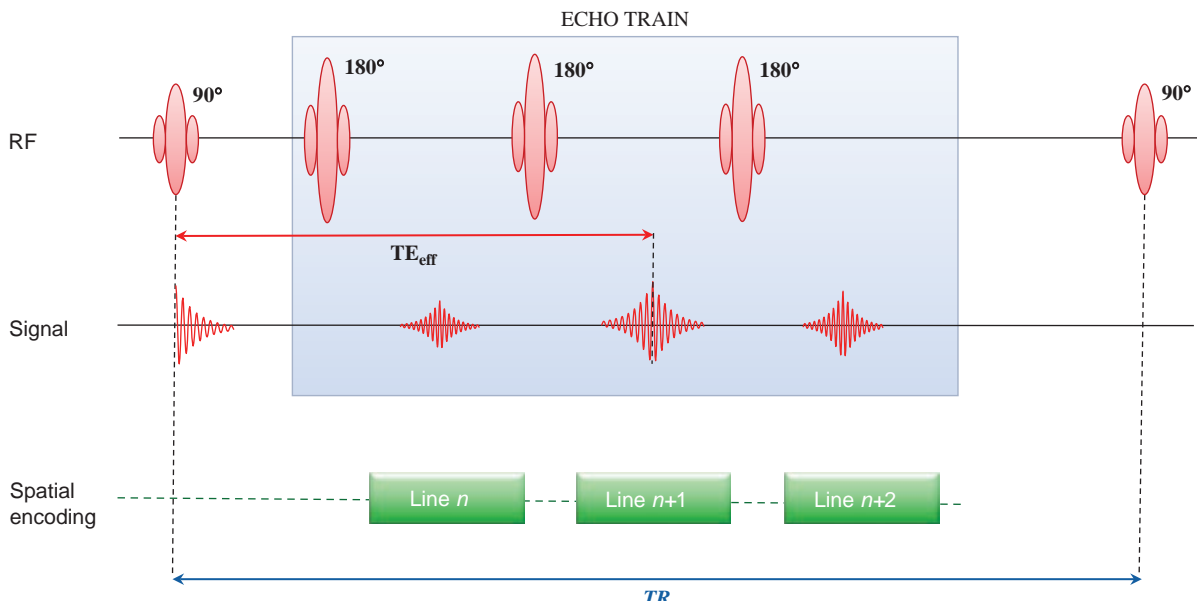


Figure 4.8 Basis of turbo spin echo. Several lines of data (in this example, three) are acquired for every TR period, reducing the overall scan time by the echo train length or turbo factor.

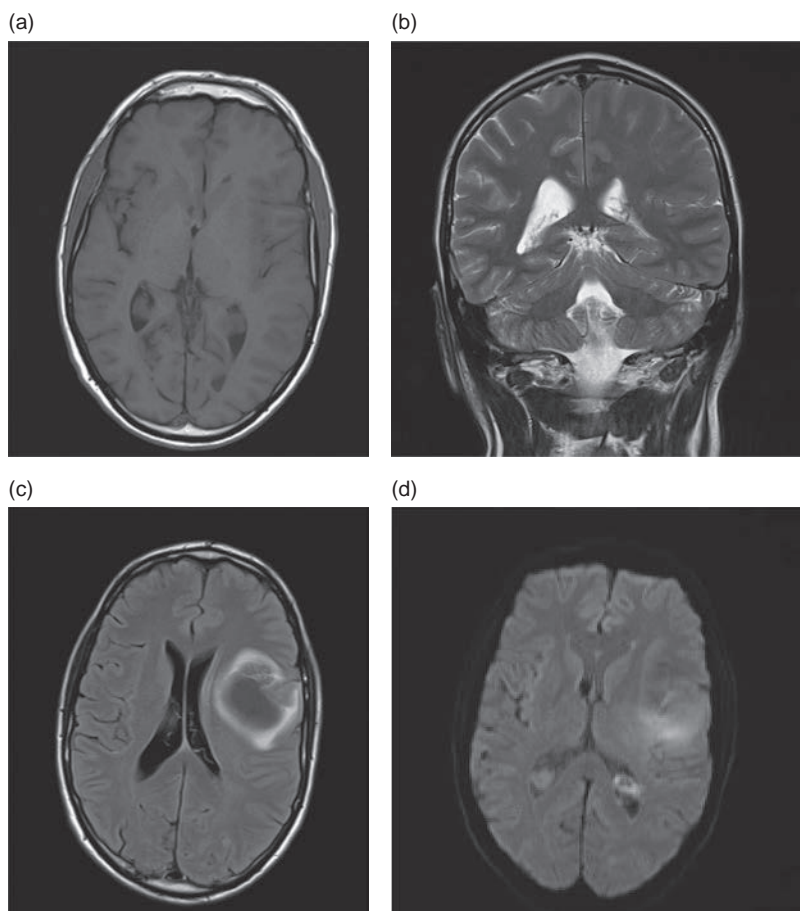


Figure 4.9 SE type images (a) T₁-weighted SE, (b) T₂-weighted TSE, (c) FLAIR with T₂-weighting, (d) DWI-EPI. See Box 'Brain Sequences' for details.

4.3.2 TSE Variants

A number of parameter options are available to further refine the use of TSE sequences. One of these is to add an *inversion pulse* before the excitation. This sequence is called Inversion Recovery (IR) and results in very strong T_1 weighting. IR may also be used to remove unwanted signals from the image, such as fat as in STIR or cerebrospinal fluid as in FLAIR. To achieve this, an additional parameter TI, the inversion time between the initial 180° pulse and the 90° excitation pulse, is set. Because the value of TI determines the ability of the sequence to null signals from either fat or CSF, it should not usually be altered from the default value in the protocol.

Another option, particularly useful in T_2 w imaging, is to use an RF pulse to speed up the recovery of the signal, thereby enabling a reduction in TR. This so-called *driven equilibrium* pulse is a 90° pulse applied after the MR signal has been acquired and just before the next excitation pulse. Figure 4.10 shows how these options add to a basic TSE sequence.

Some TSE sequences can acquire the whole image with a very long echo train following a single excitation pulse. These may be called HASTE or Single-Shot FSE/TSE (SS-TSE). These sequences are very useful for imaging fluid structures, e.g. the biliary system in **MR Cholangio-Pancreatography** (MRCP) examinations. TSE can operate in either two-dimensional (2D) or three-dimensional (3D) mode. The 3D mode enables high-resolution 3D images to be acquired, and may be called CUBE, 3D-VIEW or SPACE on your scanner.

One of the downsides of TSE is its sensitivity to movement artefacts. To reduce this, radially acquired TSE can be used. Sometimes known as PROPELLER, MultiVane, BLADE or JET, the sequence offers more limited image contrast, primarily T_2 , but proves almost immune to patient movement.

Knee Sequences

Here we look at the sequences within a typical knee examination. These are for illustrative purposes only. Actual clinical sequences and parameters used will depend upon the diagnostic question and your institutional protocols.

Scan	Sequence	Typical parameters	Comments
Sagittal PDw (Figure 4.11a)	TSE	Long TR >2000 ms. Short TE <30 ms. 20–30 × 3 mm slices, FOV 160 mm, matrix 320 × 256.	Good for visualizing anterior/ posterior cruciate ligaments and anatomical overview: muscle, cartilage, bone marrow, fat.
Coronal T_2 w fat sat (Figure 4.11b)	TSE with fat sat and driven equilibrium pulse	Intermediate TR >1000 ms. Long TE >80 ms. Turbo factor ~11–15. Slices and FOV as above.	Fat sat removes bone marrow signal, and enables assessment of bone bruises. Good for evaluating menisci and cartilage.
Coronal STIR (Figure 4.11c)	STIR (TSE)	Long TR >4000 ms. Short TE <20 ms. TI ~140 ms. Slices and FOV as above.	STIR nulls the fat. Can be used in place of TSE fat sat. Gives 'appearance' of T_2 - weighting.
Axial or sagittal T_1 w or PDw GE (Figure 4.11d)	3D FLASH with water excitation or fat sat or DESS ¹	Short TR <20 ms. Short TE <10 ms. Small flip angle <40°. FOV as above, slices 1–2 mm.	Enables semi- quantitative investigation of chondral cartilage integrity and thickness. Can view in multiple planes.

¹ See Section 13.3.4.

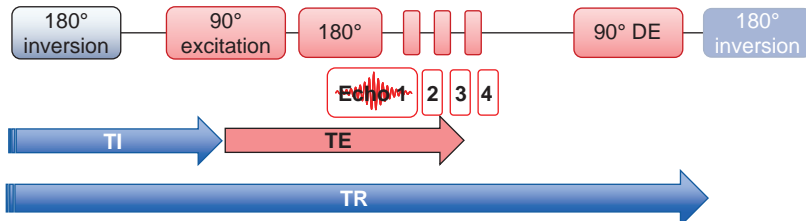


Figure 4.10 TSE variants. An inversion pulse with its timing parameter T_1 can be added to the beginning of the TR period to control T_1 weighting or null CSF or fat. A driven equilibrium magnetization restoration pulse can be added at the end of the TR period to enhance the recovery of the magnetization (signal) and allows a shorter TR.



Figure 4.11 (a) PD-TSE, (b) TSE with fat sat and DRIVE, (c) Coronal STIR (d) 3D DESS.

4.4 The Other Branch of the Tree: Gradient Echo

The family on the gradient-echo side is somewhat more complex: spoiled or incoherent gradient echo, rewound or coherent gradient echo and time-reversed GE plus some hybrid sequences, most with options for 2D or 3D acquisition (shown in Figure 4.12). Contrast tends to be T_1 - or T_2^* -weighted and

sometimes a mixture of T_1 and T_2 . The sequences in this branch will commonly be used for MR angiography, contrast studies, breath-hold imaging and high-resolution 3D imaging. EPI is the ultimate in terms of scanning speed, collecting a whole slice in under 100 ms. In this chapter we will introduce the most popular forms of gradient echo: spoiled GE and rewound GE, and their offspring. Table 4.2 shows the commercial names for these sequences.

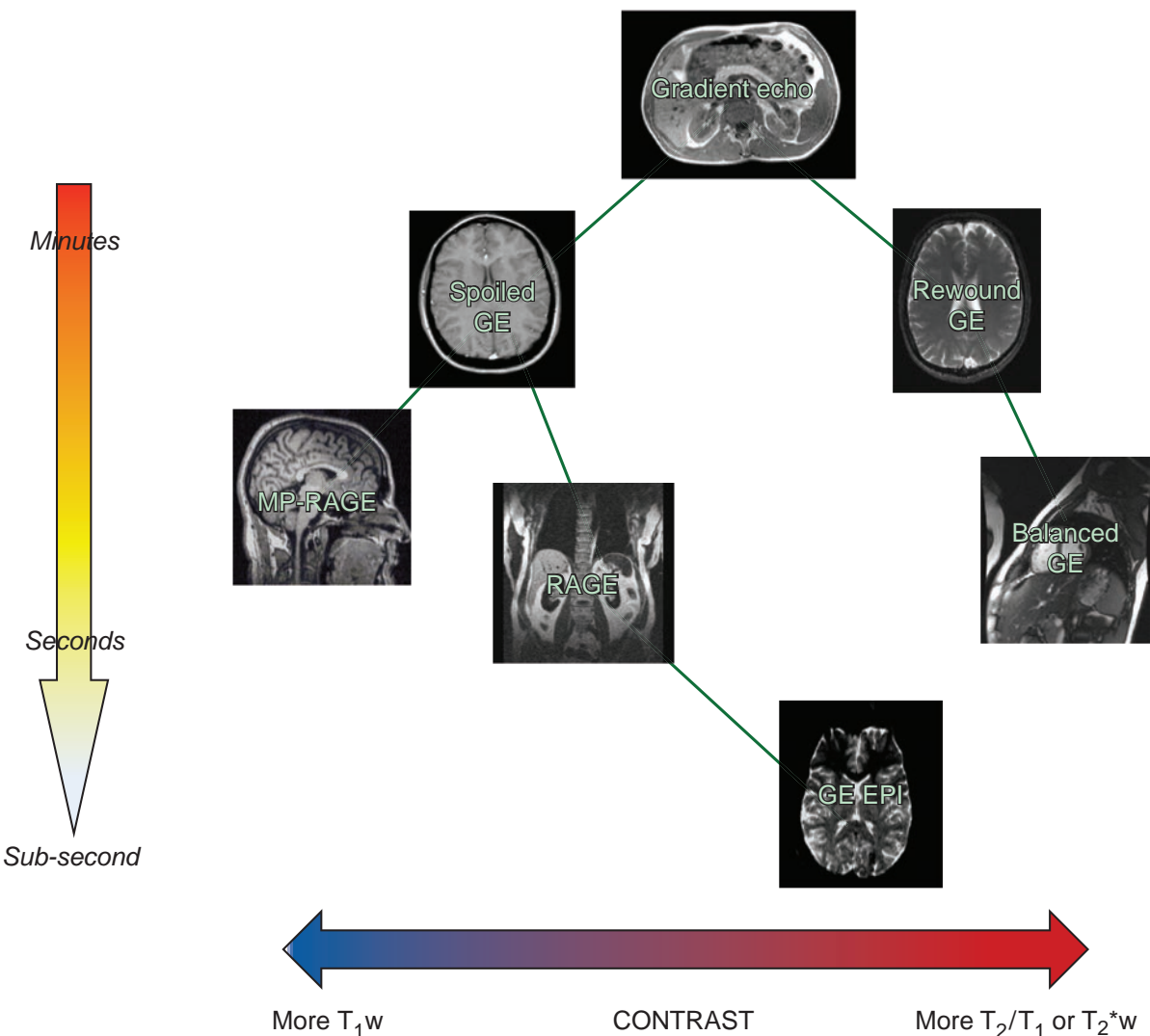


Figure 4.12 Pulse sequence family tree: gradient-echo branch. Acquisition time is indicated vertically, with indicative contrast behaviour shown horizontally.

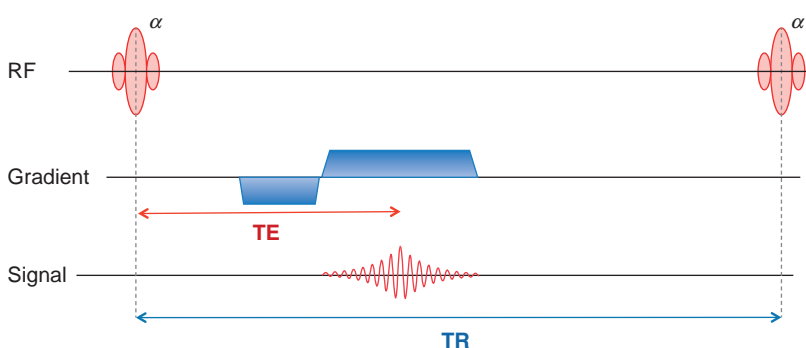
4.4.1 Making the Grade: Gradient Echo

Gradient Echo (GE) or Gradient Recalled Echo (GRE) was originally conceived of as a way of reducing scan time, by reducing TR without adversely affecting the T_1 contrast of the image. In GE a new parameter, the flip angle, α (alpha) is introduced. As we saw in Chapter 3, this mainly controls the T_1 appearance of the image. As in spin echo, an echo signal is detected in the coils. However, one major difference is that this

echo is produced by a magnetic field gradient rather than by a refocusing RF pulse. This results in the signal existing for a much shorter time than in SE, and this limits the maximum value of TE that can be used, and consequently the T_2 weighting that may be achieved. Rather, in GE we say that the signal is T_2^* -weighted. Figure 4.13 shows a simplified GE sequence with the timing parameter. Box ‘Making a Gradient Echo’ explains how the echo is formed, but you can leave the details of this till later if you wish.

Table 4.2 Gradient-echo sequences and sequence names

Generic name	GE Healthcare	Hitachi	Philips	Siemens	Toshiba
Spoiled gradient echo	SPGR	RSSG	T1-FFE	FLASH	FE
Rewound gradient echo	GRE	SARGE, SG	FFE	FISP	FE/PFI
Fully rewound gradient echo	FIESTA	BASG	bFFE	TrueFISP	True SSFP
Phase-cycled rewound gradient echo	FIESTA-c, COSMIC	PBSG		CISS	
Time reversed gradient echo		TRSG	T2-FFE	PSIF	SSFP
Multi-echo combined GE	MERGE		mFFE	MEDIC, DESS	
2D ultrafast GE	FGRE, FSPGR	RGE	TFE	Turbo-FLASH	Fast FE
3D ultrafast GE	BRAVO	MP-RAGE	3D TFE	MP-RAGE	3D Fast FE
Volume interpolated 3D-GE	LAVA	TIGRE	THRIVE	VIBE	QUICK 3D
Echo planar imaging	EPI	EPI	EPI	EPI	EPI

**Figure 4.13** Simple gradient-echo sequence (showing only 1 gradient).

Making a Gradient Echo

In gradient echo, the transverse magnetization M_{xy} is artificially dephased by introducing a deliberate and controlled linear variation in magnetic field across the imaging field of view (FOV). This is applied in the form of a gradient pulse, usually of a few milliseconds' duration (Figure 4.14). This changes the resonant frequency across the FOV and will result in a very rapid dephasing of different parts of the transverse magnetization M_{xy} and loss of measurable signal.

If the effect of the gradient is reversed, by changing the algebraic sign of the pulse, parts of M_{xy} that were in a lower magnetic field now find themselves in a higher field, and vice versa, with the result that at some point in time, the echo time TE, they will

all be aligned again, forming the peak of the gradient echo. The relaxation behaviour of signal in gradient echo is determined by T_2^* (pronounced 'tee two star') which includes the T_2 properties of the tissue, but also is degraded by the effects of the static field imperfections or inhomogeneities and differences in tissue composition.

T_2^* differs from T_2 in that it relates not just to the tissue properties, but also to the quality of the magnetic field or inhomogeneity of the scanner. This latter property often dominates the signal characteristics, hence the shorter TE (compared with SE).

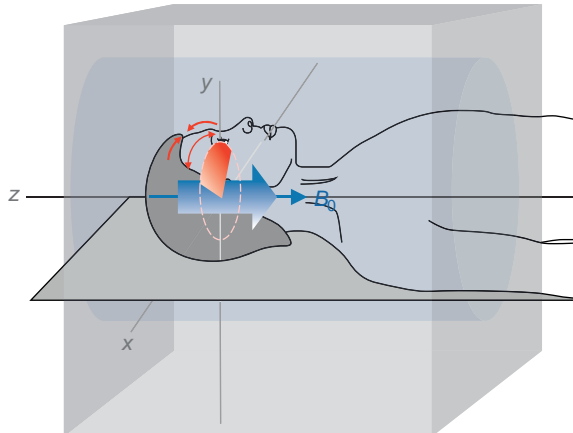


Figure 4.14 Making a gradient echo.

4.4.2 Spoiled Gradient Echo

Gradient-echo sequences can be used to give fast T_1 -weighted sequences in either 2D or 3D. They are particularly suited to dynamic gadolinium contrast enhanced studies (see Box ‘Abdomen Sequences’). Depending upon your scanner, the basic T_1 -weighted (or spoiled) gradient-echo sequence may be called FLASH, T_1 -FFE, or SPGR. Note, however, that these are all basically the same thing. The marketing department of the scanner company wants you to think that they have a unique feature (and sometimes they do, but not in this instance!).

Just as GE does not compensate for inhomogeneity in the scanner’s static magnetic field (denoted ΔB_0 , pronounced ‘delta bee nought’), neither does it correct for inhomogeneities in tissue composition, e.g. between water and fat. This may

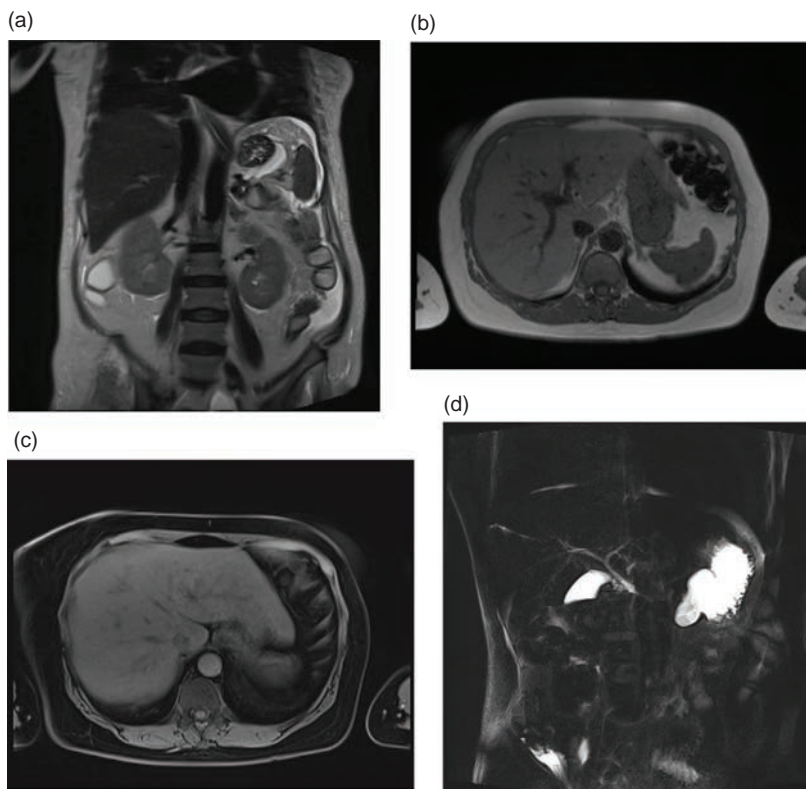


Figure 4.15 Sequences used in the abdomen: (a) HASTE, (b) 2D FLASH (c) 3D-VIBE (d) thick slab MCRP using HASTE.

result in the signals from water and fat either combining or cancelling each other. For this reason it is important not to change TE in gradient echo without careful consideration on its effect on the image appearance. In the abdomen, in-phase (IP) and out-of-phase (OP) imaging can be useful to delineate intra-organ fat.

4.4.3 Rewound Gradient Echo

The other common type of gradient echo is called rewound (or refocused) gradient echo. This is partway between a proper spin-echo and a gradient-echo sequence, and the contrast is generally a mixture of T_2 - and T_1 -weighted. We shall see later (Chapter 13) that the image contrast often favours a bright fluid appearance, which makes the sequence popular for angiography or cardiac applications. Rewound GE sequences may be called FISP, FFE or GRE. The sequence may be performed in 2D or 3D, and the short TR makes it particularly suitable for 3D scanning.

A particular variant of this sequence is the balanced version, also called True-FISP, balanced FFE or FIESTA. These are especially popular for bright-blood cardiac imaging where blood is bright in contrast to the darker myocardial muscle. In balanced gradient echo, TE may not be independently set from TR, but is always equal to exactly half the value of TR. The images may suffer from artefacts around the edges of the field of view.

4.4.4 Ultrafast GE Sequences

Just as in SE, there is a limit to how fast we can run gradient-echo sequences and still obtain enough signal with suitable contrast to make a diagnostic image. This restricts the shortest useful TR, and thus the shortest scan time achievable. If we were to use a very short TR, with a small flip angle, the image would have a very flat (proton density) appearance and would appear very noisy with low signal intensity. However, we can use pre-pulses to improve SNR and contrast, e.g. to re-introduce T_1 weighting we would add an inversion pulse at the start of the sequence. These sequences carry the generic name RAGE (Rapid Acquisition Gradient Echo). RAGE sequences are useful for very fast T_1 -weighted imaging, for example, in dynamic Gd-based contrast studies in the abdomen. T_2 -weighted versions are also possible, although they are less common. RAGE can be optimized for fast 3D breath-hold abdominal examinations, and may be called VIBE, LAVA or THRIVE.

Abdomen Sequences

Here we look at the sequences you might encounter in abdominal imaging. These are for illustrative purposes only. Actual clinical sequences and parameters used will depend upon the diagnostic question and your institutional protocols.

Scan	Sequence	Typical parameters	Comments
Coronal T_2 SS-TSE (Figure 4.15a)	HASTE or SS-TSE	Moderate TR >1000 ms. Long TE >100 ms. 30 × 5 mm slices, FOV 400 mm, matrix 256 × 192.	Quick sequential scanning, not overly affected by movement due to acquisition of a whole slice per shot. Bright T_2 w indicates cysts, hepatocellular carcinoma (HCC) and metastases.
Axial T_1 w (Figure 4.15b)	2D Spoiled GE	Short TR <200 ms. Short TE e.g. 4.2 ms (IP), 2.1 or 6.3 ms (OP) at 1.5 T. Slices and FOV as above.	Spoiled GE is used to obtain T_1 w within a breath-hold. Acquired in- and out-of-phase. Useful to discriminate adenoma or fatty infiltration due to cirrhosis.
Axial T_1 w volume (Figure 4.15c)	VIBE, THRIVE, LAVA, etc.	Very short TR <10 ms. Very short TE <3 ms. 60 × 3 mm slices, FOV 400 mm, matrix 320 × 224.	Acquired as a 3D T_1 -weighted volume. Can be timed to give arterial, venous and equilibrium phases in the liver. Early enhancement for HCC, hepatic adenoma and cholangiocarcinoma. Metastases show persistent enhancement.
MRCP (Figure 4.15d)	T_2 w HASTE/SS-TSE or 3D-TSE	Long TR >4000 ms. Very Long TE >500 ms. For 2D use thick slices >50 mm. For 3D use thin slices (<3 mm). Very high turbo factor >128.	Very long TE ensures only fluid signal in the biliary system is visible. Thick slabs are acquired as obliques. Thin slices can be viewed as MIP.

4.5 Echo Planar Imaging

There are two points in the family tree where spin echo and gradient echo are linked, hybrid sequences which cannot be classified as just one or the other. The first is GRASE, which we have placed in the spin-echo branch, even though it is a true hybrid sequence generating both spin echoes and gradient echoes. The reason for this is that the contrast which GRASE generates is closer to a spin-echo or TSE contrast, i.e. T_2^* -weighted rather than T_2 -weighted.

The other sequence is echo planar imaging (EPI), which can exist either as a hybrid SE-EPI or as a pure gradient echo version. EPI is used in applications such as perfusion, diffusion or functional MRI, where extreme acquisition speed in a single shot is required. Spin-echo EPI is used for DWI, while gradient echo EPI (or simply EPI) is used for perfusion and fMRI. Scan times can be less than 100 ms, thus freezing all physiological motion. Generally these are applied with a relatively low spatial resolution and the images suffer from particular artefacts (considered further in Chapters 12 and 13). On their own they are seldom diagnostic, but lend themselves to further image processing to produce quantitative

maps of diffusion, perfusion or brain oxygenation (Chapter 18).

4.6 The Pulse Sequence Traveller

Needing to choose a pulse sequence? At this point we refer you back to Figure 4.4 and Figure 4.12, but this time you should view it more as a route map than a family tree. First, decide your destination – T_1 , T_2 or PD weighting, etc. Then decide how you want to get there and how fast you want to go. Finally, think about potential pitfalls; for example, what artefacts you might encounter, or what limitations there are on resolution or slice number. Remember that as in real travel, when visiting different countries, different languages are spoken. You can think of Table 4.1 and Table 4.2 as your pulse-sequence phrase book. Bon voyage!

See also:

- Getting in Tune: Resonance and Relaxation: Chapter 9.
- Acronyms Anonymous I: Spin Echo: Chapter 12.
- Acronyms Anonymous II: Gradient Echo: Chapter 13.
- Glossary – for explanation of sequence acronyms.

Further Reading

Brown MA and Semelka RC (1999)
 'MR imaging abbreviations, definitions and descriptions: a review'. *Radiology* 213:647–662.

Elster AD and Burdette JH (2001)
Questions and Answers in Magnetic Resonance Imaging, 2nd edn.
 London: Mosby-Yearbook,
 chapters 5 and 12. Also on the web

at <http://mri-q.com> [accessed 23 March 2015].

Liney G (2011) *MRI from A to Z*, 2nd edn. London: Springer-Verlag.

The Devil's in the Detail: Pixels, Matrices and Slices

5.1 Introduction

MR images are like photographs or plain digital X-radiographs; they are made up of thousands of tiny squares known as *pixels* (a contraction of ‘picture elements’) or *voxels* (‘volume elements’). CT images are also made up of pixels, as are Digital Subtraction Angiograms (DSAs). The common link between MR, CT and DSA is that all these images are acquired digitally, by a computer. However, all the original data start out as analogue signals, either a voltage in an RF receive coil (for MR), or a scintillation in a photodiode (CT) or image-intensifier (DSA). The process of converting signals from analogue to digital can introduce artefacts in the final image, and it’s important to understand the process. In this chapter we show:

- that the analogue MR signal is digitized in order to create the image, and data can be misrepresented due to the digitization process;
- the organization of the image as pixels in a matrix with phase and frequency encoding directions;
- the relationship between the image matrix and the physical field of view, and how each pixel represents the MR signal from a small volume of tissue;
- the size of the voxel can be calculated from the FOV and matrix, which defines the resolution in MR images;
- that MR images can be acquired as either multi-slice two-dimensional scans, or as a three-dimensional volume, each of which has advantages and disadvantages.

5.2 From Analogue Signal to Digital Image

The MR signal is detected by the receive coils, and is simply a voltage induced in the coil. This is just the same as your high-school physics lessons; when you

move a magnet through an electrical coil, you generate a voltage in the coil. If the magnet moves quickly back and forth through the coil, you can generate an alternating voltage. If we add up all the tiny magnetic fields of the protons in the body, they become a measurable magnetic field, which is also changing very quickly because the protons are spinning. So the MR signal in the receive coils is an analogue voltage.

The *analogue* MR signal is described as *continuous*, which means it has a value (an electric voltage) at every point in time, no matter how closely you zoom in. So we can measure the signal every second, or every millisecond, or every microsecond: no matter how small the time interval, the signal always has a value (Figure 5.1a). Because it is analogue, it also varies smoothly; whether we use a meter working in volts, millivolts or microvolts, there is a continuously changing voltage.

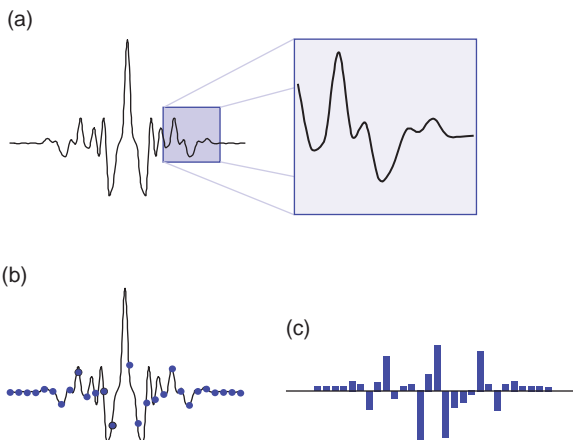


Figure 5.1 (a) The MR signal in the receive coil is a continuously changing voltage; no matter how closely we zoom in, it still varies smoothly. (b) When it is digitized, there are gaps between sample points due to the Analogue-to-Digital Converter’s (ADC) performance. (c) Digital data are stored as integers, so the digitized MR signal has a stepped appearance.

When the signal is digitized (by an Analogue-to-Digital Converter, or ADC), the changing voltage is represented as a series of numbers. The ADC makes a measurement of the voltage, calculates the appropriate number and stores the *digital* value in the computer. Although this happens very quickly, each conversion takes a certain length of time, so the ADC can only measure the signal at certain time intervals (Figure 5.1b). The digital data are described as sampled because there are gaps between the measured values. Since the computer can only store whole numbers (integers), so the signal also changes from being continuous to stepped or *discrete* data (Figure 5.1c).

Another advantage of digital data is that they can be transmitted over fibre-optic cables, whereas the analogue voltage is normally carried on standard copper wires. The copper wires are always shielded to protect them from other signal sources, but shielding is not perfect and extra noise is introduced. There are also losses due to resistive heating of the copper; although this is a tiny amount of heat, the MR signal is also very tiny, so we need to avoid losses and noise interference. Fibre-optic cables avoid the problem of interference completely, and losses are minimal. So, the sooner we digitize this tiny signal, the better! In many modern MR scanners, the ADC is mounted on the magnet, or even in the coil itself. Fibre-optic cables then carry the signal into the technical room to the reconstruction computer.

The Nyquist Theorem

An ADC can work at different speeds, defined as its sampling rate or sampling frequency, denoted f_s . If f_s

is high, there is only a small gap between signal measurements, known as the sample period, T_s . T_s and f_s are related mathematically:

$$T_s = \frac{1}{f_s}$$

So if f_s is low, there is a larger T_s and you can see that there is a chance that the digitized signal will miss some of the real MR signal (Figure 5.2a). Mathematicians and engineers have done a lot of theoretical work on this problem and have found a rule to characterize it, called the *Nyquist theorem* (Henry Nyquist was an engineer working for AT&T in the 1920s). According to Nyquist, the highest frequency signal that can be accurately digitized at a certain sampling frequency f_s is equal to half of the sampling frequency. This is known as the Nyquist frequency f_N , and we can write

$$\text{Nyquist frequency} = \frac{1}{2} \times \text{sampling frequency}$$

or

$$f_N = \frac{1}{2} \cdot f_s$$

Let's look carefully at various frequency signals all digitized at the same frequency f_s . First, a signal with frequency lower than f_N (Figure 5.2b) is accurately digitized and the reconstructed signal made by 'joining the dots' clearly has the same frequency as the original. What about a signal at exactly the Nyquist frequency (Figure 5.2c)? Now the digital samples occur at every peak and trough and again the reconstructed signal represents the correct frequency. However, if the signal frequency is higher than f_N , you can see that the digital samples miss some of the peaks and troughs (Figure 5.2d). When

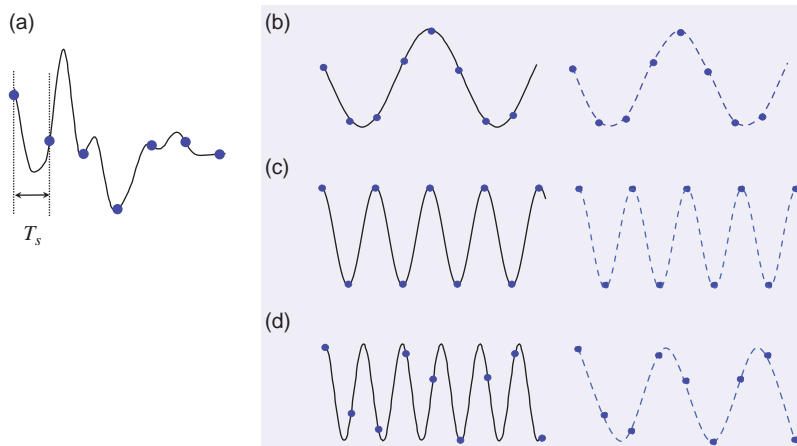


Figure 5.2 (a) The sample period (T_s) is the time between digitized sample points on the MR signal. If T_s is too big, information may be lost. (b) Digitization of a frequency lower than the sampling frequency, f_s . (c) Digitization of a signal at the Nyquist frequency f_N . (d) Signals at frequencies higher than f_N are aliased and the digital frequency appears to be low.

you connect up the reconstructed samples (shown by the blue line), the frequency appears to be much lower instead of the correct high frequency. This is known as aliasing; we say that for any f_s , all frequencies higher than the Nyquist frequency f_N are aliased as low frequencies.

You can see a good visual example of aliasing by watching an old Western film: look at the spokes on the wagon wheels as they start to move. When the wheels are turning slowly the individual frames of the film are fast enough to show the motion accurately. As the wagon gets faster and the wheels turn more quickly, the spokes appear to slow down, stop still and then they seem to turn backwards! This is because the wheel has gone through more than one complete turn between each frame, i.e. the frequency of the spokes is higher than the sampling frequency (or frame rate) of the film.

The Receive Bandwidth and Oversampling

The MR signal is centred at an RF frequency (which we will see later is fixed by the strength of the main magnetic field), but it contains a range of different frequencies that encode information about the location of various tissues (see Section 8.5.3). This centre RF frequency can be removed from the signal before it is digitized, leaving the *receive bandwidth* of the signal, which is typically several kilohertz (kHz) wide. However, many modern scanners use technology known as 'direct digitization' (see Box 'Direct Digitization') and in this case the centre frequency is removed after digitization. The end result is the same: a digitized signal centred at zero with a receive bandwidth of several kHz. Most of the signal-to-noise and contrast information is in the low frequencies, while the higher frequencies contain information about resolution in the image (see Box 'An Easy Introduction to k-Space'). Electronic noise is distributed evenly across the whole bandwidth (Figure 5.3). High receive bandwidths have a worse signal-to-noise ratio than low receive bandwidths simply because they include more noise. More noise gives an increased 'graininess' in the final images. However, low receive bandwidths cause chemical shift artefacts (see Section 7.3); advice about choosing the right bandwidth for your images is given in Chapter 6.

Earlier we learned that frequencies higher than f_N will be aliased and appear as low frequencies. In order to avoid this corruption of the spatial information, we use either an electronic (analogue) or digital filter to

remove all the MR signals with frequencies higher than f_N . This is known as a *low-pass filter* because it allows low-frequency signals to pass through. Its cut-off frequency, defined by f_N , is set to match the receive bandwidth (RBW). In reality, filters tend to attenuate signals close to the cut-off frequency, i.e. the signals have reduced intensity. If we look at the effect of the filter on all frequencies, we would see a sloping edge at the cut-off (Figure 5.4a), known as 'filter roll-off'.

Does this matter? No it doesn't on most modern scanners because digital filters have much sharper cut-offs, except at very high receive bandwidths. However, the MR signal contains all sorts of information about the tissues in the body, and its height is very important. The filter roll-off makes it look as if the number of protons fades away at the edges of the field of view – like a soft-focus filter on a photograph. That's not very useful for a diagnostic scan! To get round the problem, we can use a technique called *oversampling*.

Direct Digitization

At the end of the twentieth century, analogue-to-digital converters (ADCs) were limited to relatively low digitization rates, and most scanners had a maximum rate of around 1 MHz. However, there have been huge technology advances in the last 15 years, and today it's possible to get an ADC which works at 80 MHz. This means the MR signal can be digitized directly for 1.5 T, 64 MHz: the same ADC can be used for a 3 T scanner, which means it will be aliased to 48 MHz. After digitization, the central frequency can be subtracted digitally instead of using an analogue demodulation, which is prone to phase errors. For more detail on the technology, turn to Chapter 10.

Frequency oversampling means that the ADC runs at double the required frequency. The Nyquist frequency is therefore doubled, and the filter cut-off frequency is also doubled. The filtered digital signal still has a roll-off edge, but we can now discard all the information above our original required frequency (Figure 5.4b). The remaining signals are accurately represented and have no attenuation due to the filters. Older systems with analogue filters will automatically use frequency oversampling, but on modern scanners it is not always necessary. Phase oversampling is similar in principle but it is always controlled by the operator because it has a direct effect on the scan time; it will be fully explained in Section 7.4.3.

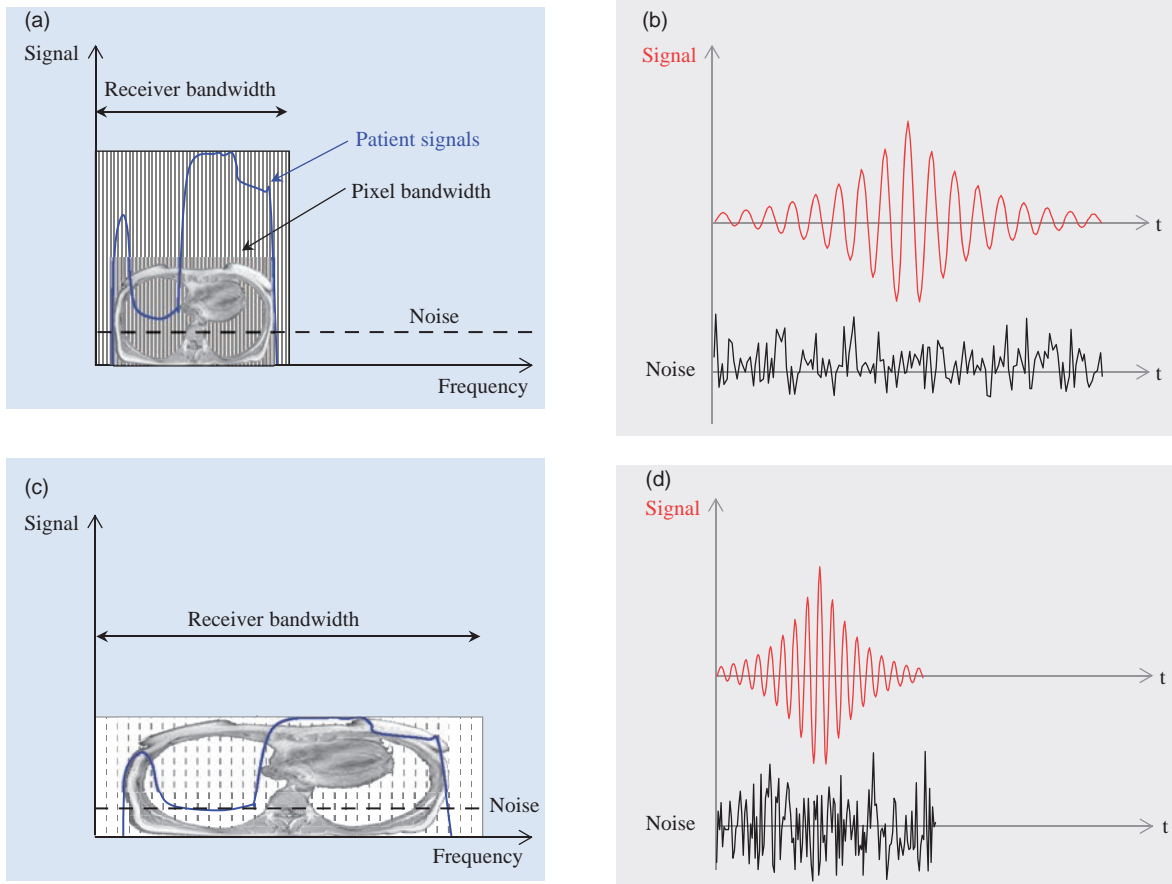


Figure 5.3 Signal and noise in the receive bandwidth. (a) The patient's signals in a narrow bandwidth and (b) the corresponding echo signal and noise. (c) and (d) as (a) but with a wider receive bandwidth; more noise gets into each pixel.

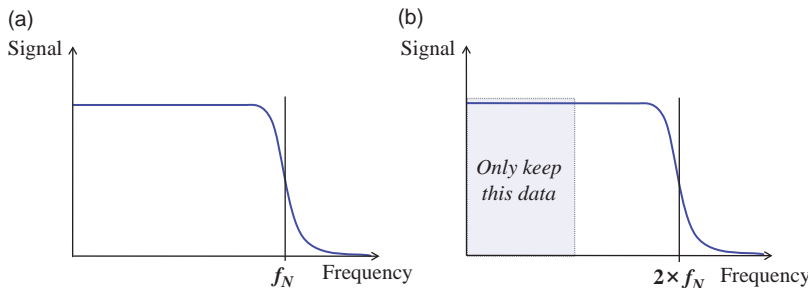


Figure 5.4 (a) The filter at the Nyquist frequency (f_N) has a sloping edge, which distorts the MR signal. (b) By frequency oversampling we can create a sharp cut-off at the original Nyquist frequency.

5.3 Matrices, Pixels and an Introduction to Resolution

Let's start this section with a few simple definitions. The pixels in MR images are organized into rows and columns in a *matrix* (plural 'matrices'). Each pixel in the reconstructed image can be thought of as a

location in the computer memory or hard disk, containing a number which represents the signal intensity. Although most images look square, the matrix doesn't have to be square, in other words it doesn't have to have equal numbers of rows and columns. You will have already come across some typical matrix sizes for MR; for example, 256×128 ,

256×192 , 512×256 and 512×384 , but there are many others in common use.

The image matrix is conventionally shown in the following order: frequency-encode matrix, phase-encode matrix, number of slices (for 3D scans). Don't worry for now what frequency and phase encoding actually mean, that will be covered in Chapter 8. You will often hear people refer to the 'frequency-encode axis' and 'phase-encode axis': these are the two dimensions of the image. Bear in mind that the images have a third dimension too, the slice thickness. The matrix not only controls the final image size, it is also used for the raw data space, and defines how the scanner samples the signals. The raw data matrix is also known as k-space. Each time the sequence is repeated a full line of data in the frequency-encode direction is acquired (e.g. 256 or 512 points). The phase-encode gradient is changed for each repetition and each line has a different position in the phase-encode direction. Thus, as the sequence is acquired, k-space is filled row by row in the raw data matrix. Once the raw data matrix is full it is reconstructed into the final image using a clever piece of maths called a Fourier transform. Notice that when you set the phase-encode matrix, you define how many times the sequence must be repeated (how many rows there are in k-space) and therefore how long the scan will take to acquire. The frequency-encode matrix doesn't have an effect on the scan time, which is why we often have a larger matrix in the FE direction.

Rather confusingly, the FE and PE directions are not always the same. For example, frequency encoding may be either the horizontal or the vertical direction of the displayed image, and it may be along any one of the three anatomical axes (superior-inferior SI, right-left RL or anterior-posterior AP) or even an oblique direction. There may be an annotation on the image for the FE direction; check your manufacturer's manual if you're not sure where it is. If it's not labelled, you can usually recognize the PE axis by looking for ghost signals from motion, as these always go across the PE direction.

An Easy Introduction to k-Space

Many people get very worried about understanding k-space, but don't panic – it's really quite easy. You probably know that the raw data have to be processed or 'reconstructed' before you can see the final image. Simply, you can think of k-space as the 'raw data space' which is used to store the digitized MR signals during data acquisition (Figure 5.5a). When k-space is full (at the end of the scan) the data can be reconstructed to produce the image (Figure 5.5b). The clever bit is that k-space contains lots of information about the real space that it represents, although it's in a coded form. For now we will just look at the basic features of k-space.

When you set the frequency- (FE) and phase-encoding (PE) matrix, you are controlling the k-space

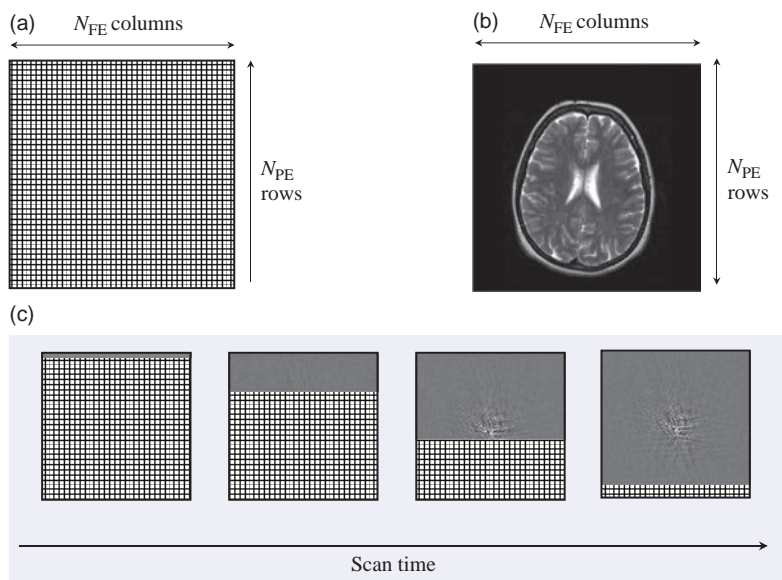


Figure 5.5 (a) k-space is raw data space. The computer reserves a section of memory to hold the digitized raw data during the scan, which has the same number of rows and columns as (b) the final image. (c) During a conventional SE or GE scan k-space is filled with raw data, one line per TR.

(raw data) matrix size and hence the size of the final image. Conventionally we show the FE direction as columns (left-right) in k-space, and the PE direction as rows (top-bottom). So if you choose 256 for frequency encoding, each MR echo will have 256 sample points, thus requiring 256 columns in the k-space matrix for temporary storage. When you set the PE matrix, you control how many echoes have to be acquired and thus how many rows are needed in k-space. So every digitized sample point has its own unique location in k-space, which you can imagine as rows and columns of little boxes, each with its own number.

Although both k-space and (image) space have the same matrix size, the pixels do not correspond directly with each other. That means the information in the bottom left pixel in k-space does not contain the raw information for the bottom left pixel in the image. This is because the reconstruction processing uses a Fourier transform (which will be fully discussed in Chapter 8). Instead, *data in the middle of k-space contain all the signal-to-noise and contrast information for the image, and data around the outside contain all the information about the image resolution (edges and boundaries)*. You can see this if we take a set of raw data and reconstruct just the middle (Figure 5.6a) or just the outside (Figure 5.6c).

We can use this information in practical ways to design new pulse sequences or to re-order the data acquisition, avoiding artefacts. k-space is linked mathematically to image space, and we will deal with this in Section 8.6.1.

Choosing Anatomical Axes for Frequency and Phase Encoding

You will probably notice after working in MR for a while that the scanner automatically selects the directions for frequency and phase encoding depending on the orientation of the scan and the part of the body. Although it seems confusing at first, it is worthwhile learning what the system is doing.

The principle is to set up frequency encoding on the longest anatomical axis on the scan, in order to minimize the number of phase encoding steps on the shortest axis. To work it out for yourself, you need to imagine the final image and decide which axis has anatomy extending outside the field of view (FOV). For example, on a coronal head scan, the right-left direction is contained within the FOV, while the superior-inferior direction has anatomy below the bottom of the FOV (the rest of the body!). So the default frequency-encode direction for this scan is

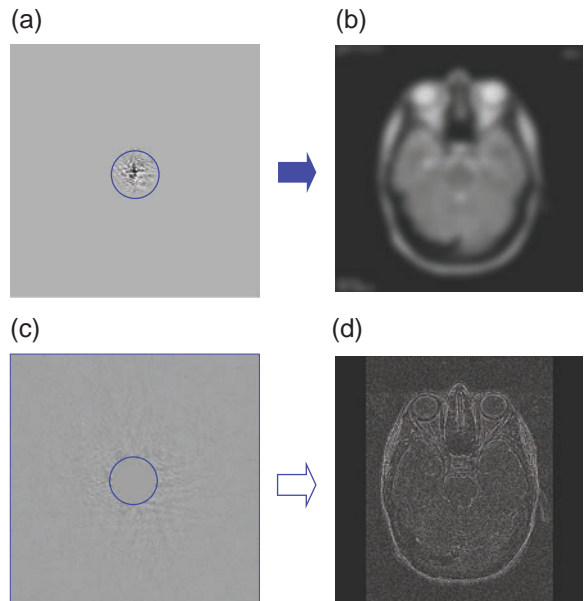


Figure 5.6 Signal and resolution information in k-space. (a) By reconstructing only the data from the middle of k-space we get all the signal and contrast information (b), but it is very blurred. (c) If we erase the middle of k-space and just reconstruct the outside data we can see where the tissue boundaries are (d), but the signal-to-noise ratio is very low and we have no contrast information. Clearly we need both parts of k-space to get a useful MR image!

superior-inferior (Figure 5.7a): if you put frequency encode along right-left, you will get artefacts (Figure 5.7b). If you are not sure, use a hard window to reveal motion ghosts, which are always along the phase-encode direction (Figure 5.7c).

It is sometimes useful to swap the frequency- and phase-encode directions from this default, for example to avoid flow artefacts in the phase-encoding direction on sagittal spines. Check on your own scanner how to change the PE direction, and make sure you know how the default direction is set for different scans.

When you set the Frequency-Encoding (FE) matrix, it makes no difference to the scan time (although it might affect the number of slices possible). The Phase-Encoding (PE) matrix, however, has a direct effect on the scan time. Thus a PE matrix of 256 takes twice as long to acquire as a 128 PE matrix. To get the best possible resolution, we should ideally use a square matrix (256×256 or 512×512), but we have to strike a balance between resolution and scan time, so the phase matrix is often reduced. As a general rule you should not

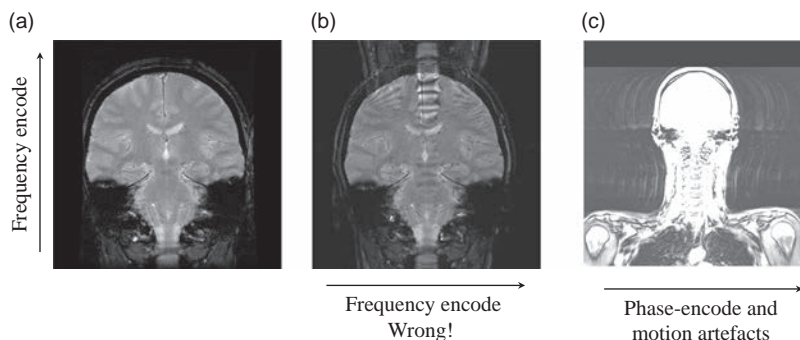


Figure 5.7 Coronal head scan showing frequency encoding on the SI axis (a) and the RL axis (b) – you can see what happens if it's wrong! (c) Motion artefacts show you the phase-encoding axis (with hard windowing to reveal the ghosts).

make the PE matrix less than half the FE matrix, because it makes the pixels too pencil-like. Chapter 6 has more information on optimizing parameters to get the best signal-to-noise ratio, resolution and scan time.

Obviously the size of the voxel is very important since it determines both the image resolution and the signal-to-noise ratio in the image. We can calculate the voxel size in all three dimensions from the field of view (FOV), matrix and slice thickness, all of which are parameters that you can control. We have to calculate the size in the frequency- and phase-encode directions separately, because we usually have different matrix sizes in those directions. So,

$$\text{FE pixel size} = \frac{\text{FE field of view}}{\text{FE matrix}}$$

$$\text{PE pixel size} = \frac{\text{PE field of view}}{\text{PE matrix}}$$

$$\text{Slice pixel size} = \text{slice thickness}$$

The FOV is often square, which makes things a little simpler than they appear. For example, with a 32 cm FOV, a matrix of 256 (FE) \times 192 (PE) and a slice thickness of 4.5 mm, we can define the voxel size as $1.25 \times 1.67 \times 4.5 \text{ mm}^3$. Note that in this book we always use the order FE \times PE \times slice when quoting voxel sizes (or just FE \times PE for pixel size); some manufacturers and textbooks use a different order.

5.4 Slices and Orientations

We've introduced the idea of slice thickness as an important part of the voxel size. From working in the MR unit, you already know that MR can produce slices in any direction – axial, coronal, sagittal, obliques and even double obliques. For comparison, CT produces only axial scans, although if you tilt the gantry you can

get obliques and even coronals. But to get coronals e.g. for sinuses, you have to position the patient prone with their head in a rather uncomfortable position and the gantry tilted to its maximum. Actually CT has caught up with MR now that multi-detector helical scanners are the norm; effectively they acquire an axial 3D block which is then reformatted into other orientations.

Getting back to MR, let's take a look at how the slice orientation is defined relative to the scanner. With a standard cylindrical MR system, B_0 is along the bore, and we conventionally define this as the z direction. This corresponds to the superior-inferior axis of the patient (the foot-head direction). By convention, the horizontal axis across the bore is known as X and the vertical axis as Y, corresponding to the right-left and anterior-posterior directions respectively. When we select an axial slice, we are creating images perpendicular to the Z direction. Sagittal images are perpendicular to the X direction, and coronal images are perpendicular to the Y direction. Figure 5.8 shows the principle anatomical axes and corresponding images of the head.

5.5 Displaying Images

We have seen that the MR image is a matrix of pixels containing numbers, which is held in the computer memory or disk that represent the MR signal intensity. They are not much good to us on the computer hard disk – we want to look at the images. When the computer displays an image on the screen, it takes the pixel values and displays them as different intensities on the display screen. Display systems usually have 12- or 16-bit depth (4096 or 32 768 grey levels respectively). However, the human eye can only distinguish about 200 grey levels, so it makes more sense to compress the range of values in the image into relatively few grey levels. To achieve this a Look-Up Table (LUT) is used to link the pixel values to the screen brightness. The

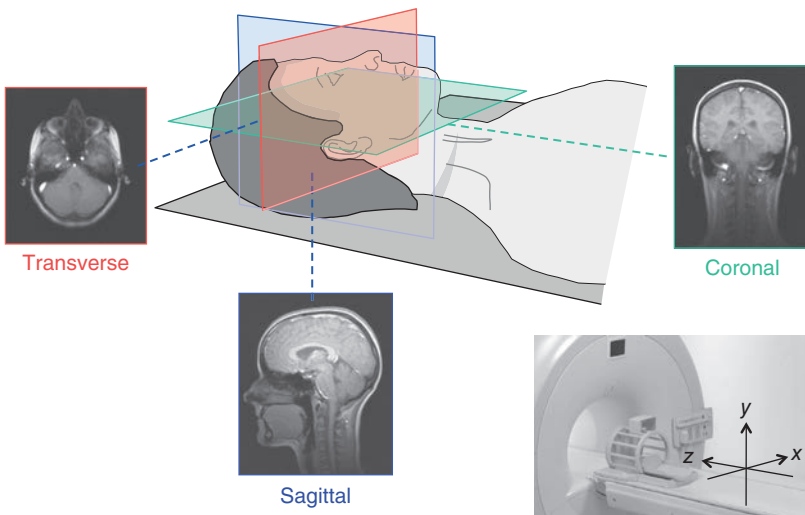


Figure 5.8 The use of physical gradient axes to select the principal slice orientations. By combining physical gradients, oblique and double oblique views are also possible.

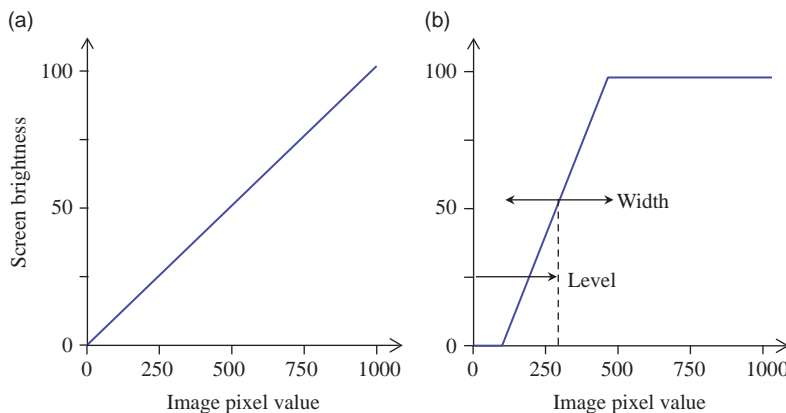


Figure 5.9 (a) A simple look-up table (LUT) scaling the pixel values (0–1000) to the screen brightness controls (0–100%). (b) Reducing the window width changes the LUT to make noise pixels very dark, and to bring out the detail in the mid-intensity pixels.

maximum pixel value in the image is found during the reconstruction process and is stored in the image *header* – the data tacked on to the front of the image file which holds all the information about the acquisition, including the patient's details. So it is quite straightforward to calculate an LUT to scale the pixel values to grey levels (Figure 5.9a). In this example, the highest pixel value has the brightest screen intensity, zero-valued pixels are black, and everything in between is scaled accordingly.

DICOM: A Common Language Leading to Misunderstanding?

DICOM (Digital Imaging and Communications in Medicine) is a standardized format for storing, viewing, and transferring medical images. It has been

developed over several decades, by groups representing all manufacturers, for all digital medical images. Updates are published, reflecting changes in radiology practice. For every image, there is a 'header' which contains all the necessary information about the image, from the obvious (patient's name, date of scan, imaging sequence used, etc.) to the not-so-obvious (e.g. what orientation was the image last displayed, the date when the scanner was last serviced).

Each piece of information is called an element, and each element has a tag, a keyword, plus some other details which are not so important here. The tag is a numerical code consisting of two bytes, usually shown as two four-digit hexadecimal numbers. The keyword describes what the element represents, and most of them are human-readable – so you can often

guess what the element holds. The header of each image has the tag followed by the value for this particular image, then the next tag with its value, etc., until all the necessary information is recorded. Then the image file stores the actual image data, in an order defined within the header. Clever: as the receiving computer reads the file, it learns exactly how to read the image data so that it can be displayed properly.

There is, however, a slight problem with the DICOM standard. Manufacturers are allowed to define private elements for themselves, as many as they like. And although they usually do use all the public elements properly to share common information, this is not always the case. If we think of DICOM as a language, each manufacturer speaks a slightly different dialect! This means that there is always room for misinterpretation when data are sent between devices by different manufacturers. However, in this DICOM Tower of Babel, there is one comfort: every manufacturer publishes a DICOM Conformance Statement, usually easily found on their website. The conformance statement describes exactly how the DICOM header is implemented for this particular scanner and software release, and can help to unravel the misunderstandings.

While this is simple, it rarely shows the image in the sort of detail necessary for diagnostic imaging. Often there are only a few high-value pixels, so the whole image looks very dark. We can improve things if the LUT has a steeper slope, so that all pixel values above a certain level are displayed at maximum brightness. On the other hand, it is also helpful to make the background noise as dark as possible, and this is done by setting all pixel values below the noise level to have minimum brightness (Figure 5.9b). This type of modification to the LUT is known as setting the window width and level.

The *window width* is the range of pixel values which are displayed across the screen's brightness range, while the *level* is the central value of the window width. Reducing the window width increases the contrast of the displayed image, while moving the level up or down makes the whole image darker or brighter respectively (Figure 5.10). This aspect of changing the displayed image is very similar to that used in CT and DSA. However, remember that you are only changing the displayed pixel intensities, not the values in the underlying MR image.

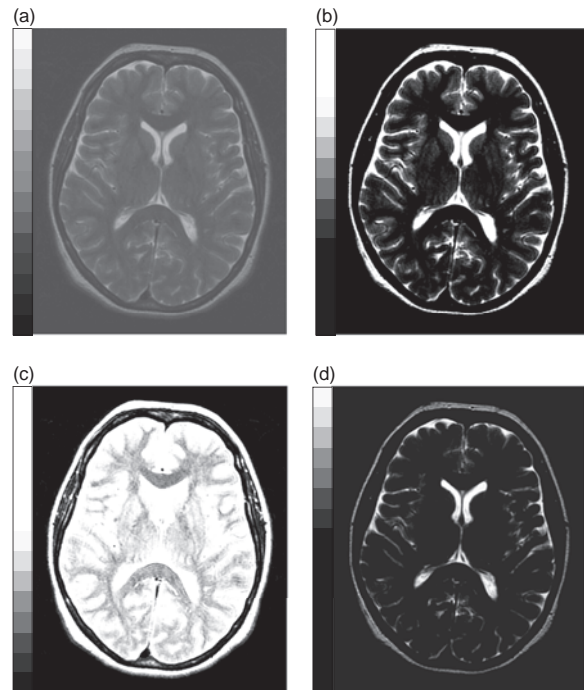


Figure 5.10 The effect of changing the window width and level on the displayed image. (a) A wide window and (b) a narrow window. (c) A low window level makes the image very bright; (d) a high level makes it much darker. The greyscale bar on the left of each image shows how the LUT is changed.

5.6 What do the Pixels Represent?

We have been talking about pixels and matrices in a rather abstract way. Let's see how they correspond to the physical reality of the patient being scanned. What does the number in each pixel actually mean? We know that it is calculated during image reconstruction, and we have already said that it represents the MR signal intensity. In fact, it represents the signal from just a small volume of tissue within the patient's body, known as a voxel (a contraction of 'volume element'). You can imagine the front face of the voxel as the pixel which is displayed on the scanner (Figure 5.11a). The third direction is determined by the slice thickness of the image.

So if we could chop up the patient into slices of the right width, cut each slice into the appropriate number of rows and columns (Figure 5.11b), and then measure the MR signal from just one of the resulting voxels, that is the number held in the computer. The higher the MR signal, the higher the number. The computer then uses this number to control the brightness of the

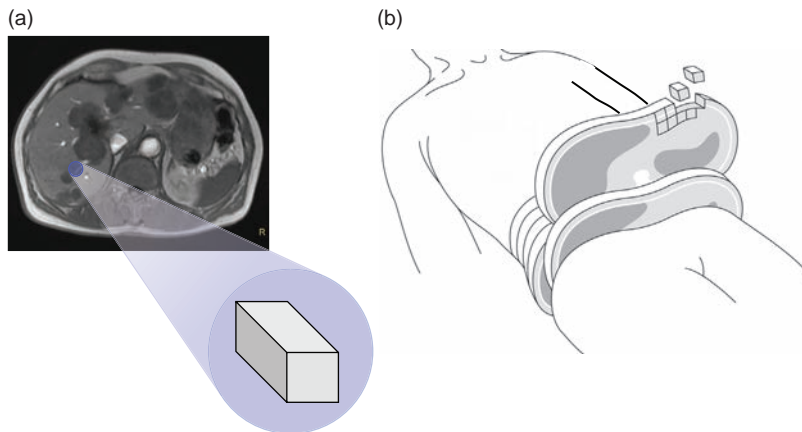


Figure 5.11 The relationship between pixels on the screen and the patient being scanned. (a) The pixel on the screen is just the front face of a three-dimensional voxel within the patient. (b) Chopping up the patient into voxels!

corresponding pixel on the image display screen (previous section). Thus the larger the number, the brighter the displayed pixel on the screen. Working backwards, we can say that the brightness of the pixel on the (two-dimensional) screen represents the MR signal intensity from the three-dimensional volume of tissue in the patient, and we are just seeing the front face of the voxel.

The actual signal intensity depends on many factors, including the sequence timings and the intrinsic T₁, T₂ and PD of the tissues. If you scanned the same patient using the same parameters on a different scanner (even if it was made by the same manufacturer) you wouldn't necessarily get exactly the same pixel values in the images. Compare this with CT scans, where the pixel values are in Hounsfield units, and we get pretty much the same values for each patient, even between scanners.

Partial Volume Effects

If we chopped up a patient into 5 mm slices and sub-divided each slice into 256 × 256 pixels, would each voxel contain just one type of tissue? That would depend on which part of the body was being scanned and the relative size of the voxels. If we were imaging the thorax, we might expect most of the voxels to contain only lung, cardiac muscle or intercostal muscle. However, at the boundaries, where the lung is next to the mediastinum or rib cage, there will be some voxels which contain a mixture of tissues. If we imagine the same situation in the head, there will be many voxels that contain both grey and white matter, and around the cerebellum they would also

include contributions from CSF. The signal from such mixed voxels will be the weighted sum of the signals from the various tissues.

Let's now take this imaginary situation to two extremes. First let's consider the effect of very small voxels, e.g. $0.25 \times 0.25 \times 3.00 \text{ mm}^3$. In a head scan many of the voxels will contain just one tissue and the intensity is an accurate representation of the tissue structure (Figure 5.12a). Now let's consider a more usual scan, i.e. voxels $1 \times 1 \times 3 \text{ mm}^3$. The same slice location (Figure 5.12b) will have a mixture of tissues within each voxel and it is obvious that fine structures cannot be resolved. This is known as the partial volume effect and it is a critical limiting factor of all digital imaging techniques. We cannot completely avoid partial volume effects as very small voxels take a long time to acquire (the scan in Figure 5.12a took 8 min 23 s compared with 2 min 5 s for Figure 5.12b), and have low signal-to-noise ratio. We have to reach a compromise between resolution, signal-to-noise ratio and scan time, as described in Chapter 6 in more detail.

5.7 From 2D to 3D

As you now know, each image is a 2D representation of a 3D slice of the patient. You should always remember that your image has depth, due to the slice thickness. MR and CT images are known as cross-sectional imaging techniques to distinguish them from plain X-radiographs and DSA, which are both projection techniques where the final image has lost the 3D information about the patient.

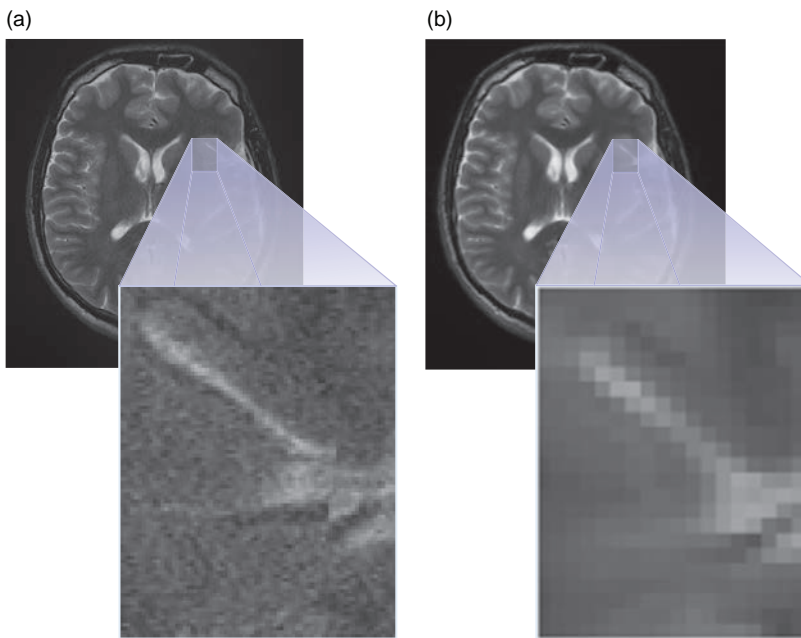


Figure 5.12 (a) High-resolution head scan with $0.25 \times 0.25 \times 3.00 \text{ mm}^3$ voxels. (b) The same slice position with $1 \times 1 \times 3 \text{ mm}^3$ voxels showing the partial volume effect.

Since we have to repeat the imaging sequence many times to produce an image, and because we set the TR to get the appropriate image contrast (as described in Chapter 3), scan times tend to be relatively long. If we were just producing one slice per scan, it would take all day to get enough information! Fortunately we can use most of the wasted time during the TR to image other slices.

Suppose we have a TR of 600 ms and a TE of 20 ms, to give T₁-weighted images. It takes about 30 ms to excite one slice, generate the spin echo and collect the data. That leaves $600 - 30 = 570$ ms before we have to re-excite that slice for the next TR. While it's waiting, the scanner excites a second slice and collects the data from its echo, taking another 30 ms. This process can be repeated, exciting new slices and collecting data, until it's time to re-excite the first slice (Figure 5.13). So during each TR, the scanner excites and collects echoes from many slices. The signals of different slices do not interfere with each other, thanks to the way slice selection works usually with a small gap between adjacent slices (see Section 7.4.2). A simple calculation ($600 \div 30$) shows us that we can get 20 slices within the TR. So for the same scan time as one slice, we can image up to 20 slice locations. This is known as *multi-slice* imaging.

Due to imperfections in the RF pulses we usually have to introduce a slice gap to separate the slices. This is measured as the distance between the slice edges, although sometimes it can be defined as the

separation between slice centres (Figure 5.14) – you just need to know which definition is used by your system. We generally try to keep the slice gap to a minimum, since tissues in the gap are not imaged at all. If the gap is too big, there is the possibility of completely missing a small pathological feature.

Falling Into the Gaps

Different manufacturers have different ways of setting the gap between slices in a multi-slice sequence. GE Healthcare systems let you set the edge-to-edge slice gap in millimetres.

Siemens scanners use a distance factor, which is the edge-to-edge gap as a percentage of the slice width. So if you have a slice width of 5 mm and you want a 1 mm gap, you set a distance factor of $(1 \div 5) \times 100\% = 20\%$. A 3 mm slice with a gap of about 0.5 mm would be achieved with a distance factor of 15%, and so on.

In Philips systems you also set the slice gap, the edge-to-edge distance between the slices. The system default is a gap of 10% of the slice thickness, but it's always shown in millimetres.

True 3D scanning, rather than 2D multi-slice imaging, requires a different kind of imaging technique, with phase encoding in the slice direction as well as in-plane. For every slice encode, we must acquire all the in-plane phase encodes. So the scan

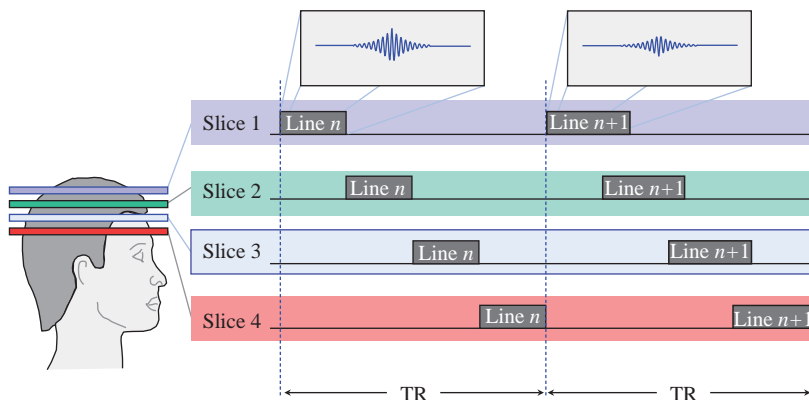


Figure 5.13 Multi-slice imaging. Once the spin echo has been collected, the scanner has plenty of time to excite other slices and collect their data, before starting to repeat the sequence with the first slice.

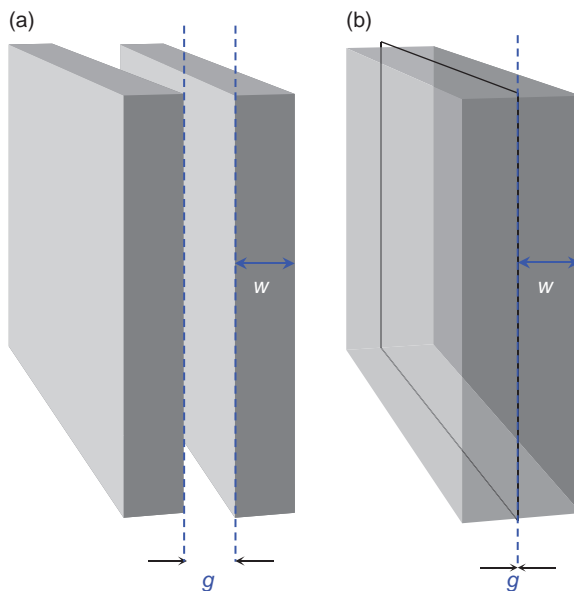


Figure 5.14 Definition of slice-to-slice separation: (a) distance factor 100%; (b) contiguous slices (distance factor = 0%).

time gets multiplied by the selected number of slices (sometimes called *partitions*) in the 3D volume. The majority of 3D scans are acquired with gradient-echo sequences with a very short TR, using the flip angle α to control the amount of T_1 weighting. Turbo spin

echo can also be used for 3D imaging, using some extra tricks with flip angles to manage the power deposition, blurring and contrast. 3D TSE sequences often have a special name from the manufacturer; see Chapter 12 for more details on these.

Although slow to acquire, 3D scans have a few advantages over multi-slice 2D imaging. For example, it's possible to define very thin slices with no slice gaps (contiguous slices), and, if the voxels are nearly isotropic, the resulting volume can be reformatted on a workstation to produce images in any orientation. Signal-to-noise ratio (SNR) is also higher compared with 2D scans, by a factor of $\sqrt{N_{\text{slice}}}$ where N_{slice} is the number of slices in the 3D volume. This extra SNR compensates for the high-resolution voxels (which reduce SNR), so 3D scans are a good choice when very high resolution is required, and when it is important not to miss anything in the slice gaps. We will discuss this technique in more detail in Section 8.8.

See also:

- How frequency- and phase-encoding gradients work: Chapter 8.
- k-space and Fourier transforms: Section 8.6.
- 3D imaging: Section 8.8.
- Optimizing image resolution and signal-to-noise ratio: Chapter 6.

Further Reading

Brown MA and Semelka RC (2010) *MRI: Basic Principles and Applications*, 4th edn. Hoboken, NJ: Wiley-Blackwell, chapter 5.

Elster AD and Burdette JH (2001) *Questions and Answers in Magnetic Resonance Imaging*, 2nd edn. London: Mosby-Yearbook, chapter 4. Also on the web at <http://mri-q.com> [accessed 23 March 2015].

Hashemi RH and Bradley WG Jr (2010) *MRI: The Basics*, 3rd edn. Baltimore, MD: Lippincott, Williams & Wilkins, chapters 12 and 13.

What You Set is What You Get: Basic Image Optimization

6.1 Introduction

We have seen that MRI is a digital, truly three-dimensional imaging modality of great flexibility with respect to image contrast and geometry. However, one of the downsides of this flexibility is a greater complexity in terms of the choice of scanning parameters. This aside, does MR have any other weaknesses? Yes it does: in general scan times are not negligible and there is a certain tendency towards artefacts (which we will investigate in the next chapter). However, most MR people would probably agree that the fundamental limitation in MRI is the signal-to-noise ratio (SNR). This is dependent on many factors, but unlike X-ray imaging, there is no radiation dose or milliampere-seconds (mAs) that can be increased to improve image quality. Good image quality depends upon making good scanner parameter choices. There are many parameters to tweak, buttons to press and dialogue boxes to click, and one way to learn about how each affects image quality would be to spend a lifetime tweaking! Alternatively, you could read this chapter which investigates the influence of various acquisition parameters and the practical trade-offs between SNR, contrast-to-noise, spatial resolution and scan time. You will see that:

- signal intensities and contrast are determined by the timing parameters TR and TE (also inversion time (TI) and flip angle (α) where appropriate);
- SNR is proportional to the voxel volume;
- signal scales with size parameters (field of view, slice width), and noise scales with averaging parameters (number of signal averages, phase-encode matrix size, frequency-encode matrix size) with an ‘inverse square root relationship’ (some parameters affect both);
- an appropriate choice of receive coil helps SNR;
- resolution is not usually the limiting factor;
- good Contrast-to-Noise Ratio (CNR) is essential for diagnostic-quality images;

- parameter juggling is often required to get a suitable scan time.

Knowledge of this chapter should enable you to predict the effect of changing the basic scan parameters: TR, TE, bandwidth, matrix, FOV, slice thickness and number of excitations (NSA) or Number of signal EXcitations (NEX). Fundamental aspects of image quality will be discussed in Chapter 11.

6.2 Looking on the Bright Side: What are we Trying to Optimize?

This section introduces the basic parameters: contrast, SNR, contrast-to-noise ratio (CNR) and resolution. These are illustrated in Figure 6.1. Simple mathematical definitions are given in Box ‘Here’s the Maths Bit’.



Figure 6.1 Definitions of contrast, signal-to-noise ratio (SNR) and contrast-to-noise ratio (CNR). See Box ‘Here’s the Maths Bit’ for mathematical definitions.

Here's the Maths Bit

Mathematically we can define contrast as

$$C = \frac{S_A - S_B}{S_A + S_B}$$

where S_A and S_B are signal intensities for tissues A and B. Refer to Figure 6.1. Signal-to-noise ratio (SNR) is defined as

$$\text{SNR} = \frac{\text{signal}}{\text{noise}}$$

Contrast-to-noise ratio (CNR) is defined for tissues A and B as

$$\text{CNR}_{AB} = \frac{S_A - S_B}{\text{noise}}$$

In the simplest terms, spatial resolution of the voxels is related to the field of view (FOV) and matrix thus

$$\Delta x = \frac{\text{FOV}}{N_{FE}} \quad \Delta y = \frac{\text{FOV}}{N_{PE}} \quad \Delta z = \text{slice width}$$

6.2.1 Contrast

Contrast was introduced in Chapter 3 in terms of the image appearance, or relative brightness of different tissues and pathology. Image contrast arises (or doesn't) when tissues generate MR signals which have different intensities because of their physical properties, i.e. T_1 and T_2 relaxation times and proton density. You can refer to Figure 6.2 or Box 'Try It for Yourself 3: Predicting Contrast Appearance' to estimate the relative MR signals for a given tissue (if you know its T_1 and T_2). Mathematical expressions are given in Box 'Signal Calculator'.

Try It for Yourself 3: Predicting Contrast Appearance

Let's take two easily obtained substances: a saline bag and some cooking oil. The T_1 and T_2 of the saline are probably about 2000 ms and 1500 ms, and for the oil 200 ms and 180 ms. If we use a spin-echo (SE) sequence with $TR = 600$ ms and $TE = 20$ ms, what will we see?

Looking at Figure 6.2a, we have a ratio TR/T_1 of 0.3 and 2.5 for the saline and oil. For the oil the ratio of TE/T_2 is 0.1 so we should use the darkest of the grey curves. For saline TE/T_2 is 0.02. The blue curve is for TE/T_2 of zero, and as this is the closest value to the calculated ratio for saline, we should use the blue curve.

To calculate the oil signal, read off the value on the MR signal axis corresponding to TR/T_1 of 2.5 using the top grey curve. This gives about 0.83. For

the saline, using the blue curve and the x axis value of 0.4, we get 0.28.

So we predict that oil will be brighter than water and that the contrast will be

$$C = \frac{0.83 - 0.28}{0.83 + 0.28} = 0.48$$

Now do the experiment on your scanner. Choose a single 5 mm slice which includes both substances and use a spin echo (not turbo or fast spin echo) with $TR = 600$ ms and $TE = 20$ ms. It doesn't matter what resolution you choose (256×256 will do fine). Check that the oil is indeed brighter and use regions of interest to measure the mean signal intensities in each container and calculate the contrast.

As a further test, using Figure 6.2a, how should you change TR to make the saline and oil closer to the same signal intensity? Looking at Figure 6.2b, for inversion recovery, what value of TI should you use to get zero signal from the oil? How will this look in the image? Try it for yourself to check your predictions.

One point to note using these graphs and the maths is that although they let you predict the changes to image appearance when you vary the parameters (TR , TE , TI), they do not include any tissue differences in proton density. Nor do they give you absolute values, but they do serve as a guide for predicting the image contrast.

Signal Calculator

To calculate the relative signal strength in terms of relaxation effects, use the following equations for the sequence-dependent relaxation factor F . If you don't like the look of the maths, you can use Figure 6.2 instead.

Spin Echo

$$F_{SE} \propto \left[1 - \exp\left(\frac{-TR}{T_1}\right) \right] \cdot \exp\left(\frac{-TE}{T_2}\right)$$

provided $TE \ll TR$.

Inversion Recovery

$$F_{IR} \propto \left[1 - 2\exp\left(\frac{-TI}{T_1}\right) + \exp\left(\frac{-TR}{T_1}\right) \right] \cdot \exp\left(\frac{-TE}{T_2}\right)$$

also provided $TE \ll TR$; or if $TR > 5 \times T_1$ this simplifies to

$$F_{IR} \propto \left[1 - 2\exp\left(\frac{-TI}{T_1}\right) \right] \cdot \exp\left(\frac{-TE}{T_2}\right)$$

Gradient Echo

$$F_{GE} \propto \frac{\sin \alpha \cdot (1 - \exp(-TR/T_1)) \cdot \exp(-TE/T_2^*)}{1 - \cos \alpha \exp(-TR/T_1)}$$

for a ‘spoiled’ gradient echo (possibly called ‘SPGR’, ‘FLASH’ or ‘T1-FFE’ on your scanner). This will probably be the gradient-echo (GE) sequence you encounter most often. Other types of GE contrast are considered in Chapter 13.

6.2.2 SNR and CNR

In using the term ‘signal’ in this chapter we mean the pixel or voxel brightness in the image. This is related to the MR signal (i.e. what we measure from the coils). In any acquisition there is a finite amount of signal available dependent upon the MR characteristics of the tissue and the pulse sequence chosen. In Chapter 5 we considered the image as being made up of a number of voxels, each with a particular volume.

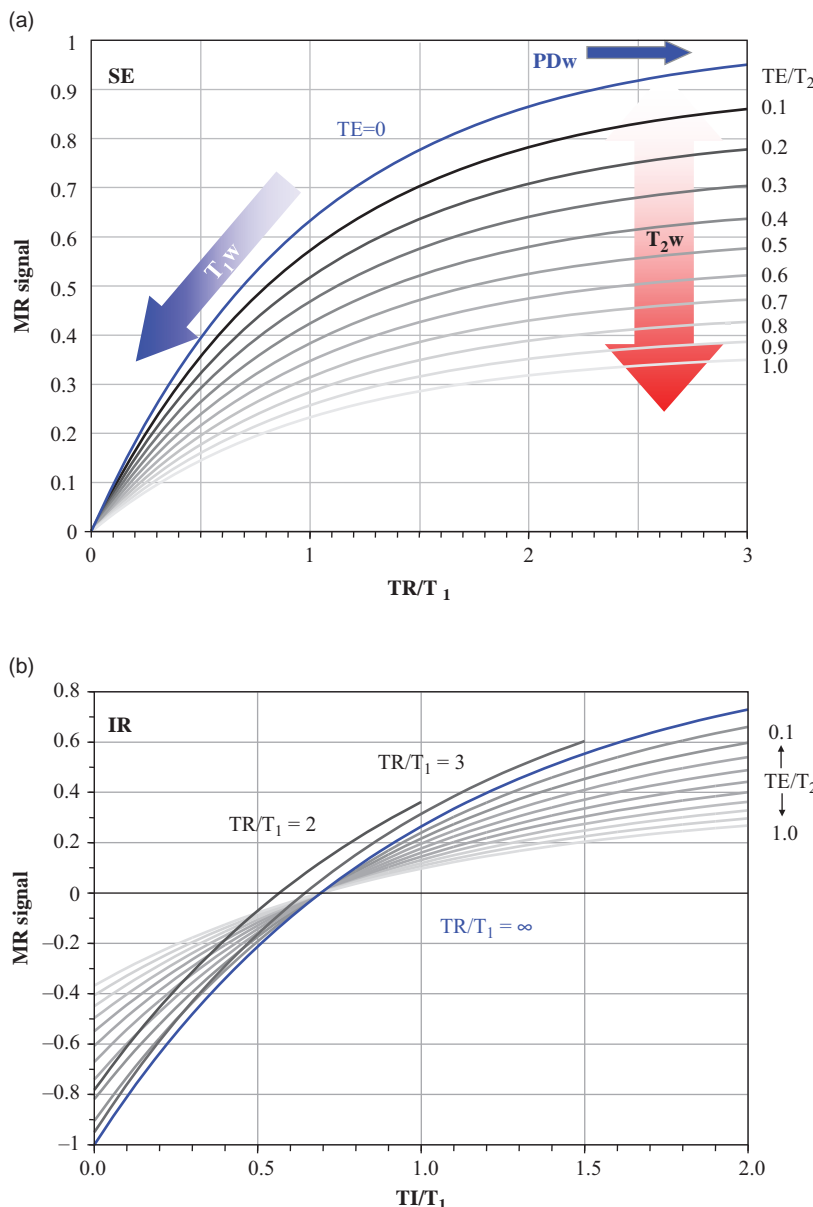
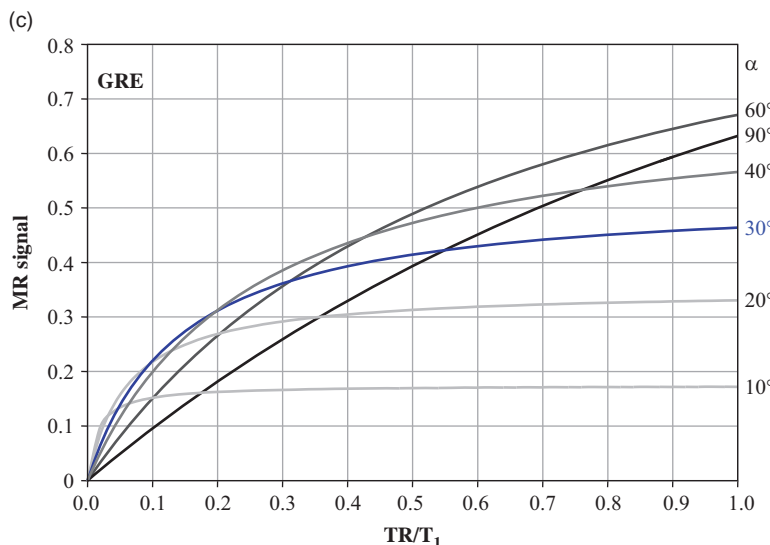


Figure 6.2 Normalized contrast behaviour. To use these graphs work out the ratio of tissue TR/T₁ and TE/T₂ or TI/T₁. Choose the nearest curve and read off the notional signal value. (a) Spin echo – blue line is for TE = 0. (b) Inversion recovery – blue line is for TE = 0, TR = ∞. The curves for TR/T₁ = 2 and 3 assume TE = 0 or that T₂ is very long. (c) Gradient echo (spoiled) all assuming TE = 0 or a long T₂.

Figure 6.2 (cont.)



Since the MR signal that is returned from the patient during the scan has to be divided amongst the voxels that make up the image, the fundamental factor influencing the size of the signal is the number of protons within each voxel.

By ‘noise’ we don’t mean the banging of the gradients (acoustic noise), but random differences in pixel values which give images a grainy, mottled look (like quantum mottle in a radiograph). Usually this noise originates mainly from the patient’s tissues (see Box ‘Who’s Making All That Noise?’).

In an MR image the individual voxels that make up the image will contain a mixture of signal and noise. The ratio of signal intensity in the image to noise level is the SNR. Images with a poor SNR will appear fuzzy. An important aspect of image optimization is to ensure that there is a high enough SNR for the images to be diagnostically useful. Low SNR may result in missing small details or the obscuring of subtle contrast changes. For this reason we often speak of a *contrast-to-noise ratio* (CNR). CNR is arguably the most important aspect of image quality. Ways of measuring image quality are considered in Chapter 11.

Who’s Making All That Noise?

The noise comes from random fluctuations in electrical current. It therefore is called electronic noise, and exists in all electrical conductors. This

obviously includes the MR coils with which we measure the signal, but it also includes the electrically conducting tissues of the patient. Human tissue contains many ions such as sodium, potassium and chloride which are electrically charged atomic particles carrying electrical currents within the body, e.g. in nerve conduction. These currents generate fluctuating magnetic fields which induce a noise voltage in the coil. The most effective way to reduce this noise is to use a small or dedicated anatomy coil. Where large fields of view are essential, array or matrix coils are usually best (see Section 10.5.2).

In the example of Figure 6.3 we see how the contrast and CNR are affected by the choice of slice thickness. If the slice is too thick, we get a good SNR but the contrast is reduced by a partial volume effect (mixing of the signals of the lesion and background). If the slice is too thin, the CNR may be too low to visualize the detail clearly.

Which is More Important, Resolution or SNR/CNR?

Certain applications such as MR angiography work best with higher resolution, but in general you need a certain SNR whatever the resolution. How much? As a rule-of-thumb an SNR higher than 20:1 offers little image quality advantage to the observer and excess

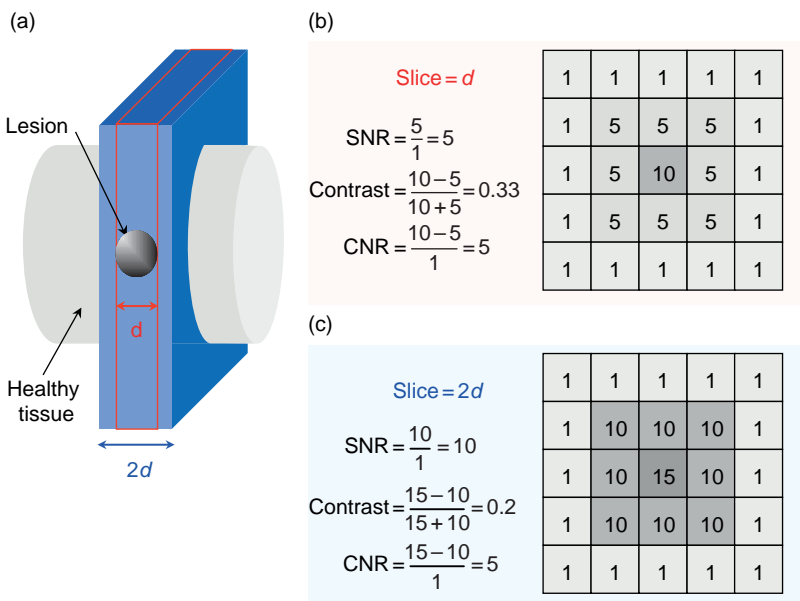


Figure 6.3 Contrast and CNR (a) example of changing slice thickness for a small lesion. The optimal contrast is obtained for a slice width less than or equal to the lesion diameter d . (b) Simulated pixel values for a small lesion with slice thickness d and calculated SNR, contrast and CNR. The lesion has a signal value of 10, surrounding tissue 5 and background noise 1. (c) Pixel values and image quality calculated values when the slice thickness is $2 \times d$. SNR is better, but contrast is down.

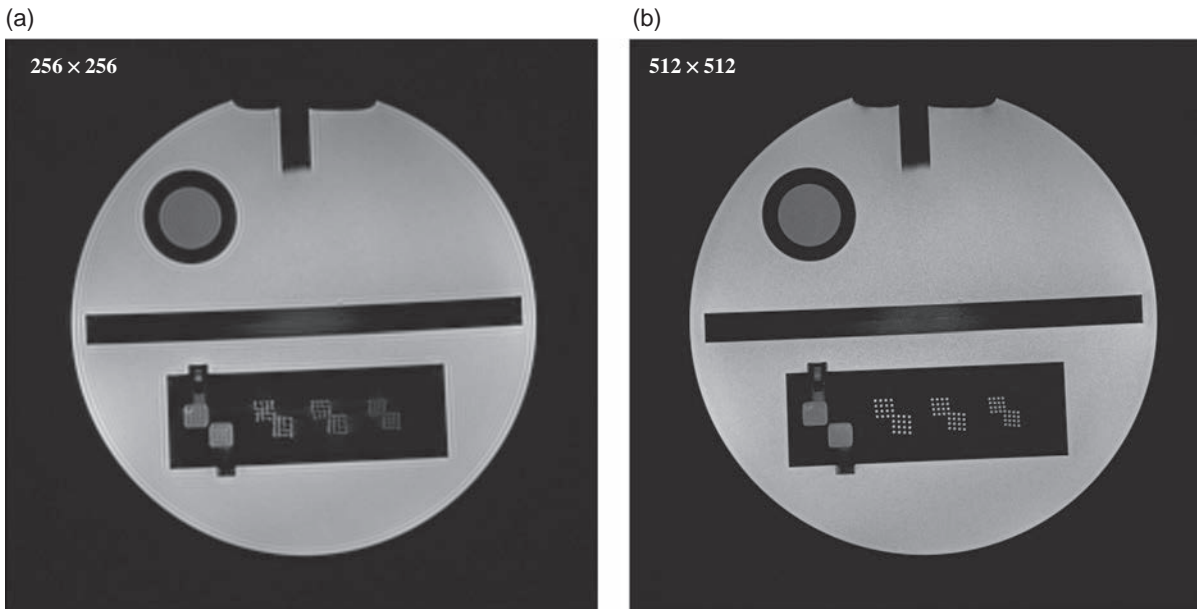


Figure 6.4 Effect of doubling the matrix, for the same FOV on the ACR phantom. The image in (b) has double the scan time of (a).

SNR would be best converted to either a larger matrix or reduced scan time. If SNR is adequate, high-resolution images will always look better but the diagnostic advantage of say 1024 matrix over 512 has not yet been established. Figure 6.4 shows the effect of different matrix sizes on image quality.

6.2.3 Resolution

The other important property of the images is *spatial resolution*. In MR we need to consider both the in-plane resolution, which may be different in each axis, and the through-plane resolution or slice width. Generally the latter is the largest dimension and is usually the more critical in visualizing a lesion.

6.3 Trading Places: Resolution, SNR and Scan Time

Just as compromises are common in real life, so too in MRI. Here we look at the trade-offs between the image quality parameters. For the mathematically minded, it's all in Box 'A Complicated Relationship: Resolution and SNR'.

A Complicated Relationship: Resolution and SNR

The signal is proportional to the voxel volume and the appropriate sequence-specific relaxation factor (given in Box 'Signal Calculator').

$$\text{signal} \propto \Delta x \cdot \Delta y \cdot \Delta z \cdot F_{\text{sequence}}$$

where Δx and Δy are the in-plane pixel dimensions and Δz is the slice width. F_{sequence} is the appropriate sequence-dependent factor from Box 'Signal Calculator'.

The noise is related to the receive bandwidth and 'averaging parameters':

$$\text{noise} \propto \frac{\sqrt{BW}}{\sqrt{NSA \cdot N_{PE} \cdot N_{FE}}}$$

where BW is the bandwidth across the whole image. In terms of the 'bandwidth per pixel' (bw) we can write

$$\text{noise} \propto \frac{\sqrt{bw}}{\sqrt{NSA \cdot N_{PE}}}$$

Putting this together with the signal equation we get

$$\text{SNR} \propto \frac{\Delta x \cdot \Delta y \cdot \Delta z \cdot F_{\text{sequence}} \cdot \sqrt{NSA \cdot N_{PE} \cdot N_{FE}}}{\sqrt{BW}}$$

where BW is the total receiver bandwidth. In terms of the field of view (FOV), we can say

$$\text{SNR} \propto \frac{\text{FOV}_{FE} \cdot \text{FOV}_{PE} \cdot \Delta z \cdot F_{\text{sequence}} \sqrt{NSA}}{\sqrt{BW \cdot N_{FE} \cdot N_{PE}}}$$

For systems which utilize the 'bandwidth per pixel' concept we get the following equation:

$$\text{SNR} \propto \frac{\Delta x \cdot \Delta y \cdot \Delta z \cdot F_{\text{sequence}} \cdot \sqrt{NSA \cdot N_{PE}}}{\sqrt{bw}}$$

A good rule of thumb is that if the scanning time is held constant, the achievable SNR is directly proportional to the voxel volume. So reducing the matrix from 256×256 to 128×128 and doubling NSA (to keep the same scan time) while maintaining the bandwidth per pixel will quadruple the SNR.

6.3.1 Resolution and SNR

Generally MRI resolution is pixel limited. That means that the smallest object or detail you can visualize in the image has the dimensions of a single pixel. So for a 256 matrix and a 25 cm FOV details of the order of 1 mm should be visible. In this, MR is quite distinct from digital radiography, computed tomography (CT) and ultrasound, where other processes (focal spot size, blurring, detector aperture, etc.) affect the ultimate resolution.

Three factors determine whether a particular detail or structure can be visualized in the image. Clearly there needs to be contrast between the structure and its surroundings. Second, if the resolution is insufficient, information about the object will not be transferred into the image by the image-formation process. Third, if the SNR or CNR is too low, the details of the structure may be obscured by image noise. You can get a feel for the effect of these parameter changes in Box 'Try It for Yourself 4: FOV and Matrix Size'.

Try It for Yourself 4: FOV and Matrix Size

To see the effect of field of view (FOV) and matrix size, you need a phantom with some fine structure, preferably with a range of sizes between 0.2 and 2 mm. These are commercially available, but you can make one of your own with a selection of plastic hair combs with different size 'teeth', including one designed to remove head lice (don't be embarrassed to buy this, you're going to use it for a scientific experiment!). Use a fairly deep plastic container and fill it with water, adding 1–2 ml of old gadolinium contrast to reduce T_1 , and a few drops of detergent to break down the surface tension. Put the combs in the bottom, making sure there are no air bubbles trapped between them.

Put the container in the head or knee coil, and perform a localizer scan. Use a T_1 -weighted spin-echo sequence and keep the receiver gain constant in order to be able to measure changes in SNR related to the other parameters. Select a coronal slice at the bottom of the container, with a slice width of about 5 mm so that you can see the effect of various matrix sizes. Then start changing FOV and matrix size. Be sure to change only one parameter at a time, keeping all others constant.

An important stage in image optimization therefore is to decide on the trade-off required between the voxel size required for an adequate SNR and the

requirement for the voxel size to be small enough to permit the visualization of small anatomical or pathological details. Figure 6.4 shows images acquired on the ACR phantom with different resolution – 256×256 and 512×512 . Clearly the 512 image (b) has greater spatial detail, but at the cost of more noise. Which do you prefer? Which is optimized?

6.3.2 Resolution and Scan Time

Spatial resolution in the frequency-encoding (FE) direction comes ‘free’ in terms of scan time (but not in terms of SNR) if the matrix is increased while keeping the FOV constant. To change the phase-encoding (PE) matrix, we have to acquire more lines of data, which takes time.

$$\text{Scan time} = \text{NSA} \times \text{TR} \times N_{\text{PE}}$$

In terms of the image slice, reducing the slice width will reduce the anatomical coverage unless slice gaps are increased. It is important to realize that changing the ratio of slice–slice increment to slice width in MRI is not like the ‘pitch’ in spiral CT. In MR the gaps are real gaps – and small lesions occurring exactly in a gap will be missed. The number of slices obtainable, in standard 2D mode, will be determined by the sequence timing parameters, particularly TR.

High-Resolution Brain Scan

Your radiologists have requested more spatial resolution from your brain scans in order to see smaller lesions, e.g. infarcts, MS plaques and micro haemorrhages. What do you change? Let’s start from your existing 256×256 matrix. The simplest thing to do is to double the matrix to 512×512 . Depending upon your MR system, this will give you either 50% or 35% of the SNR of your original protocol. Images are shown in Figure 6.5. The improved spatial resolution is evident, but is the increased level of noise acceptable (they are sure to complain about it)? The easiest way to improve SNR is to increase NSA. However this would take a four- to eight-fold increase, leading to a clinically unacceptable scan time – and you have already doubled the scan time by increasing N_{PE} .

To reduce the scan time you can increase the parallel imaging reduction factor or increase the turbo factor. The former will further erode SNR – so we don’t recommend it, except in small, fractional amounts (e.g. a few tenths) if your scanner allows this. The latter is feasible provided the longer echo

train length does not introduce blurring or hit SAR limits. In practice you may have to settle for an intermediate resolution of e.g. 512×384 , reducing the PE matrix slightly.

This example is also considered in Box ‘Try It for Yourself 5: Predicting SNR’.

6.3.3 Predicting the Effect on Image Quality

The relationships between SNR, CNR and spatial resolution are quite complicated, not the least in that many user-controllable scanner parameters affect them. How can we get our heads round what is going on sufficiently to predict the effect of parameter changes on image quality and, indirectly, diagnostic potential? It is clear that SNR and resolution are related. Throw in contrast and CNR and you have a recipe for confusion. One way is to understand the maths! Alternatively you could consider parameters as falling into two categories: *size parameters* determine how much signal is produced, *averaging parameters* reduce noise. Some parameters are a combination of both. Size parameters bear a linear relationship with SNR; averaging parameters have an inverse square-root relationship.

Field of view and slice width are size parameters only. They only affect the signal. Increasing them increases the signal and the SNR. Of course they affect resolution but fortunately that is intuitive. So doubling the slice width doubles the SNR. Halving the FOV while keeping the same matrix will quarter SNR, as we have changed two dimensions, the FOV in the phase-encoding direction and in the frequency-encoding direction.

Signal averaging (NSA or NEX) is an averaging parameter. It does not affect resolution and reduces the noise. Going from $\text{NSA} = 1$ to $\text{NSA} = 4$ will double SNR. NSA obviously affects scan time. The effect of signal averaging is illustrated in Figure 6.6. The image in (c) took four times longer to acquire than the one in (a) and twice that in (b). You have to ask yourself, is averaging worth the time?

N_{PE} and N_{FE} are combination parameters. They affect resolution and hence voxel volume, with a linear effect on signal. With standard two-dimensional Fourier transform (2D FT) MRI the acquisition of multiple ‘lines’ of data can be considered as a kind of averaging; therefore, they also affect the noise. So if we double N_{PE} we halve the

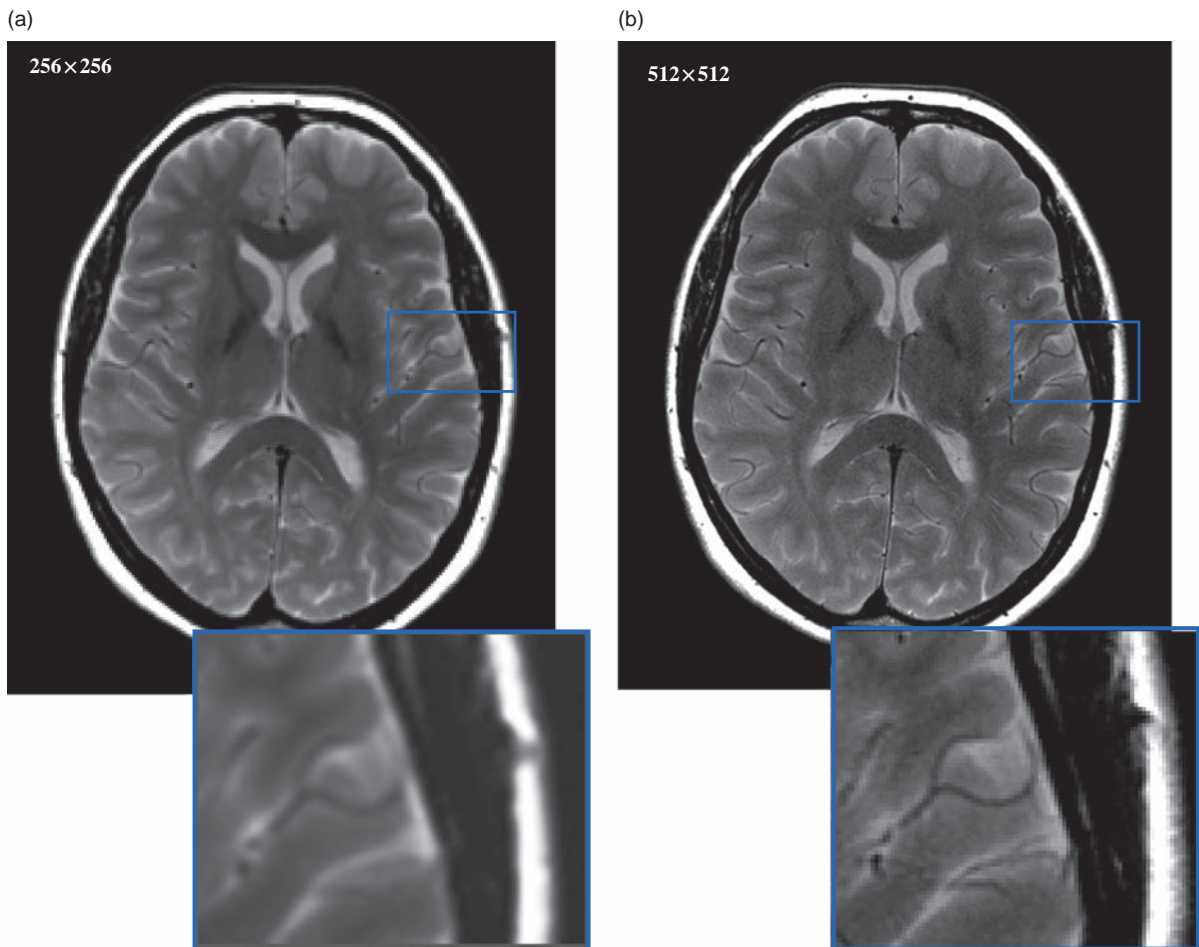


Figure 6.5 Effect of resolution on image quality. (a) 256 matrix (b) 512 matrix. The higher spatial resolution results in greater image noise (lower SNR).

number of protons in a voxel, producing half the signal, but we reduce the noise by $\sqrt{2}$ – so the net effect on SNR is a reduction of approximately 30% ($1 \div \sqrt{2}$).

Changing N_{FE} affects the noise, but the effect depends upon what happens to the ‘bandwidth’ and field of view. It is a classic result of electronic theory that noise is proportional to the square root of total bandwidth (\sqrt{BW}). If the total bandwidth does not change, increasing N_{FE} has the same effect as increasing N_{PE} : doubling the FE matrix while maintaining FOV gives a two-fold reduction in signal (because the voxel size has halved), but a $\sqrt{2}$ reduction in noise, and hence a $\sqrt{2}$ reduction in SNR. However, on systems which define bandwidth in hertz per pixel, the noise is unaffected

but the signal and therefore the SNR will be reduced by half.

These inter-parameter dependencies are not obvious, so in Box ‘Try It for Yourself 5: Predicting SNR’ we present a ‘paper app’ for predicting the effect of parameter changes on SNR – the ‘SNR abacus’, illustrated in Figure 6.7.

Try It for Yourself 5: Predicting SNR

You can look at the maths in Box ‘A Complicated Relationship: Resolution and SNR’ to predict the effect of changing parameters on image quality. Alternatively you can use the ‘SNR abacus’ in Figure 6.7. Working from left to right, each arrow indicates the effect of doubling or halving the

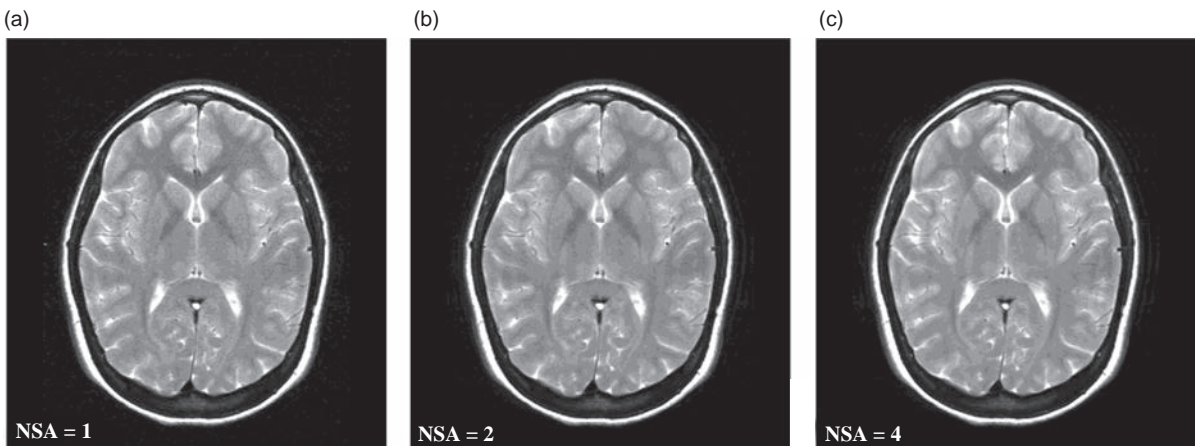


Figure 6.6 Effect of signal averaging (a) NSA = 1; (b) NSA = 2; (c) NSA = 4. Scan times increased proportionately. Image SNR improves with increasing NSA.

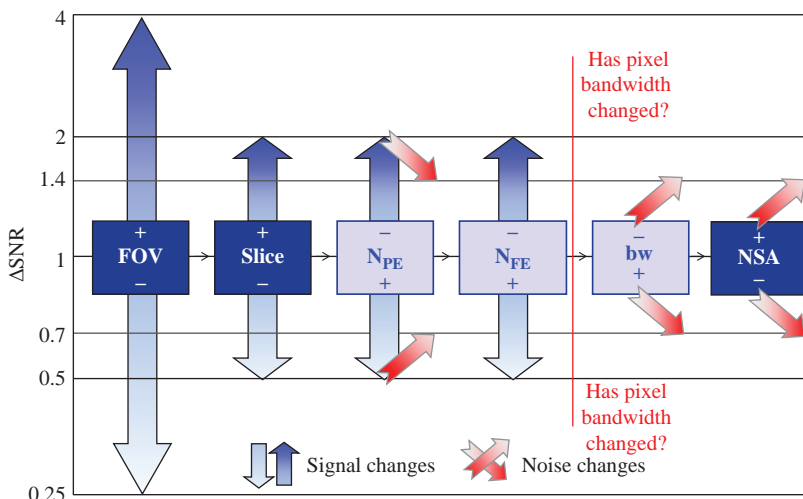


Figure 6.7 ‘SNR abacus’ showing how parameter changes affect SNR, when each parameter value is either doubled or halved. To use the abacus, start at the left and work towards the right. For each parameter change follow the arrows to calculate the effect on SNR. To predict the overall effect on SNR multiply all the SNR changes together. Note that the arrow directions indicate the effect on SNR. An increase in either signal or noise is represented by the shading in the arrows, with a deeper colour indicating an increase in either signal or noise.

parameter in each box. Read off the values on the left for the effect on SNR. Then multiply up for each parameter change.

Here is an example. Suppose you double the matrix size, keeping FOV and slice width unchanged. The first two boxes have no effect (FOV and slice are unchanged). Doubling N_{PE} halves the signal but lowers the noise – with an overall SNR reduction of 0.7.

Doubling N_{FE} will halve the signal and the SNR. However, you need to consider what happens to the bandwidth. If the total bandwidth (BW) does not change, then the effect of doubling N_{FE} will be to halve the bandwidth per pixel (bw) and SNR will

improve by $\sqrt{2}$. This will not affect systems which use a constant bandwidth per pixel.

As N_{PE} has increased, let’s keep scan time the same by halving NSA, reducing SNR by a further $\sqrt{2}$ (0.7). Table 6.1 summarizes what has happened.

Starting from the same original image, let’s try halving the FOV and doubling the NSA, but keep all other parameters unchanged. What do you get? You can now try it for yourself on the scanner using any phantom. Actually most scanners will do this calculation for you while you change the parameters, so you don’t even have to do the scans – but do it anyway, it’s good for your soul!

Table 6.1 Example of doubling the matrix for the same FOV on SNR

Step	SNR (constant BW)	SNR (constant bw)
FOV unchanged	× 1	× 1
Slice unchanged	× 1	× 1
Double N_{PE}	× 0.7	× 0.7
Double N_{FE}	× 0.5	× 0.5
Check bandwidth per pixel....	× 1.4 (bw halved)	× 1.0 (bw unchanged)
NSA unchanged	× 1	× 1
TOTAL (multiplied)	0.5	0.35

6.3.4 2D Versus 3D

We have seen from the simple example in Section 6.2.2 that too thin a slice can ruin the CNR. What if we really want very thin slices, e.g. for multi-planar reformatting? The solution is to acquire a 3D volume instead of multiple 2D slices. How this works is described in Section 8.8. The scan time is increased to

$$\text{Scan time} = \text{NSA} \times \text{TR} \times N_{PE1} \times N_{PE2}$$

where N_{PE2} is the number of ‘slices’ or partitions. Since these are acquired sequentially, TR must be reduced using one of the sequences described in Chapter 13. The signal is reduced since the slice or ‘partition’ thickness is often very small. However, a reduction in the noise is achieved by using the extra dimension of phase encoding. Box ‘3D Maths’ contains ... er, the maths.

3D Maths

The maths for 3D is the same as for 2D, except that we have an extra ‘combination’ term N_{PE2} .

$$\text{SNR} \propto \frac{\Delta x \Delta y \Delta z \cdot F_{\text{sequence}} \cdot \sqrt{\text{NSA} \cdot N_{PE1} \cdot N_{PE2}}}{\sqrt{bw}}$$

or on systems which use the total bandwidth instead of bandwidth per pixel:

$$\text{SNR} \propto \frac{\Delta x \Delta y \Delta z \cdot F_{\text{sequence}} \cdot \sqrt{\text{NSA} \cdot N_{FE} \cdot N_{PE1} \cdot N_{PE2}}}{\sqrt{BW}}$$

6.4 Ever the Optimist: Practical Steps to Optimization

Optimization is a complicated subject. Our golden rules for image optimization are:

- 1 Set the required image contrast by choice of pulse sequence and basic timing parameters TR and TE (and α for gradient echo). In general for T_1 contrast using spin echo, a TR with a value intermediate to the tissue T_1 values of interest will produce the optimum contrast. The same is true for the choice of TE in terms of T_2 contrast.
- 2 Adjust for the desired geometry – slice, FOV, resolution (pixel size), remembering that this will involve a compromise with SNR.
- 3 Adjust for acceptable SNR. The chances are that your radiologist will be demanding more spatial resolution, higher matrix, etc., so your SNR will probably suffer. Some of the desired geometric changes may have to be scaled back or NSA increased.
- 4 Check your scan time. This may have exploded from a couple of minutes to hours if you are not careful! Do what it takes to get a clinically acceptable scan time.

Optimization will invariably lead to some compromises. However, other unforeseen pitfalls may also arise. Figure 6.8 summarizes which parameters affect others (but refer to Figure 6.7 for how they do so). Usually SNR ultimately limits what you can do. Some further practical advice is given below.

6.4.1 Check Your Slices

If you cannot get enough slices you may have to run the scan as two batches or *concatenations*, i.e. the slices are split into two or more blocks and the scans are run consecutively. To get sufficient coverage without increasing the number of slices, you could increase the slice thickness (at a cost of resolution loss and possible reduced contrast due to partial volumes), or increase the slice separation or gap (at a risk of missing a small lesion). If you are only one or two slices short, an increase in TR may help, but you will be changing the contrast which may have undesirable consequences. Bear in mind that any extra sequence options such as saturation bands (Section 7.2.5) and fat suppression (Section 7.3.3) will all add to the time required to acquire each slice and should be used sparingly if scan time is a major constraint.

Adapting a Protocol for Paediatric Scanning

In this example let's suppose that you are taking an adult brain protocol and modifying it for use in neonates. Let's suppose that the adult FOV is 23 cm and we need to reduce this to 17 cm. It doesn't seem that much but for the same matrix will only have about half the SNR. However, there is no effect on scan time. Assuming that the baby is asleep, or the child under general anaesthetic, we can get away with longer scan times. The only way to restore the SNR in this case is to increase NSA, and consequently the scan duration, by up to four times. In the case of a neonatal brain, the long relaxation times (longer than for adults) will be less susceptible to T_2 blurring than for adults and so the turbo factor (ETL) in TSE can be increased. Figure 6.9 shows adult and paediatric T_2 -weighted brain scans from the protocols shown in Table 6.2. Note that the immature brain requires longer TR to give reasonable contrast on account of the longer T_1 .

Table 6.2 Example scan parameters for the adult and paediatric brain examinations shown in Figure 6.9

	Unit	Adult	Paediatric
TR/TE/ETL	ms	2850/105/10	4650/118/15
FOV	cm	23	17
Matrix		320×256	320×288
Slice thickness	mm	5	3
Pixel bandwidth	Hz/pixel	150	190
Scan time	minutes: seconds	2:25	3:20

6.4.2 How to Boost SNR

Above all, make sure you *choose the best coil*. The simple rule of thumb is that ideally the receive coil should encompass the whole of the anatomical region of interest and no more. Smaller coils 'see' less noise. Array coils allow the MR receiver to see more useful anatomy without picking up more noise.

The easiest way to improve SNR is to increase the number of signal averages (NSA). This also increases the scan time, so this may not be the most time-efficient way of improving the SNR. Five methods to improve SNR that do not affect scan time are listed below:

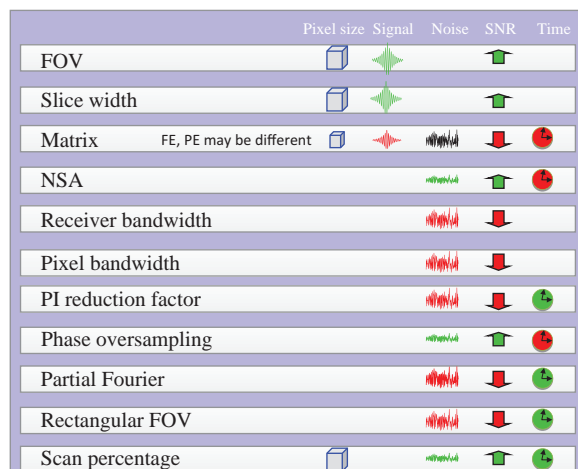


Figure 6.8 Interdependency of parameter changes. For an increase in the value of the listed parameter, beneficial image quality improvements are shown in green, detrimental in red.

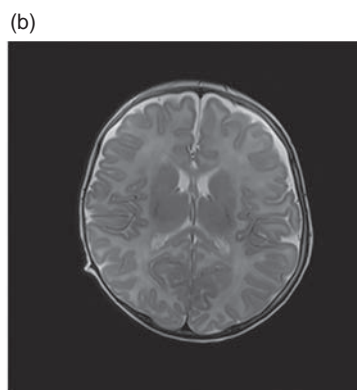


Figure 6.9 (a) Adult and (b) paediatric brain scans.

Increase the slice thickness

This improves the SNR in direct proportion to the slice thickness with no time penalty at all. But be aware of the effect on image contrast from partial volumes. If thin slices are essential, you should consider a 3D acquisition.

Increase the FOV

Increasing the FOV without changing the matrix size makes the in-plane pixels bigger, giving more signal without changing the noise. Spatial resolution is, of course, reduced and the desired part of the image will appear smaller, surrounded by more empty background. However, as you would normally match the FOV to the anatomy, this option may not be a terribly useful one.

Reduce the bandwidth

Reducing the bandwidth reduces the noise by a factor proportional to the square root of the reduction, e.g. halving the bandwidth reduces the noise by a factor of 1.4. The way this is done in practice depends on your scanner (see Box ‘Adjusting the Bandwidth: A Scanner Guide’). The side-effect of reducing the bandwidth is an increase in the chemical shift, which may create an unwelcome artefact (see Section 7.3.1). Where chemical shift artefact is not a concern, the lowest bandwidth achievable is usually a good starting point. Your TE will determine the limit on how low you can set the bandwidth.

Adjusting the Bandwidth: A Scanner Guide

Some systems (e.g. General Electric) have the total MR receiver bandwidth in kilohertz (kHz) as a user-adjustable parameter. So to improve SNR you simply reduce the receiver bandwidth. For others (e.g. Siemens with Syngo software) the bandwidth per pixel is selectable.

For older Siemens scanners bandwidth is not adjustable. Instead, each pulse sequence has a bandwidth per pixel in hertz, given as the last number in the sequence name following the letter ‘b’, e.g. se15_b130 has a pixel bandwidth of 130 Hz. So you must select the appropriate pulse sequence from the list.

For other scanners (e.g. Philips) the pixel bandwidth is presented as the ‘water–fat shift’ (WFS). The meaning of this is explained in Section 7.3.1. To improve SNR on these systems you must increase the water–fat shift.

Select a pre-processing filter

Filtering of the MR signals prior to reconstruction improves SNR at a cost of reducing spatial resolution. Effectively we reduce the magnitude of the high spatial frequencies, where the noise is most apparent (because the signal here is low); in doing so, we attenuate genuine high spatial frequency information and thus reduce the resolution. Some manufacturers may apply filtering by default, in which case you are probably not told that it is happening, or as a user-selectable option. When should you filter? Basically, never, if you can avoid it. You would do better to reduce the number of phase-encode steps, which would improve SNR and save scan time. An exception to this is for certain so-called segmented sequences, e.g. fast or turbo spin echo where filtering reduces ringing artefacts (Chapter 12).

6.4.3 Check Your Scan Time Again

Even where scan time is not a major issue, shorter scans improve patient cooperation and reduce the opportunity for movement-related artefacts. They also improve your throughput. If the scan time is too long, a few tricks are available to help reduce it. One of the easiest ways is to reduce TR, but this will affect the contrast. The next easiest way is to reduce the number of phase-encode steps. Three ways of doing this are:

- 1 rectangular FOV;
- 2 partial Fourier;
- 3 reduced matrix.

How they work will be considered in Chapter 8, but they are illustrated in Figure 6.10. Using a higher reduction factor in parallel imaging will also help, but remember all time-saving techniques will reduce your SNR.

Scan Time Reduction in Abdominal Scanning

Let’s suppose that your sequence lasts 20 s – and that’s too long for your patient. You don’t want to change either the matrix or TR as that will affect the diagnostic quality of the images. If you just need a minor reduction – say 10–20% in breath-hold time – then consider partial Fourier of 6/8 (0.75) or 7/8 (if available) which will maintain resolution but with a 5–10% loss in SNR; this is usually acceptable. Alternatively, using 80–90% scan reduction (phase

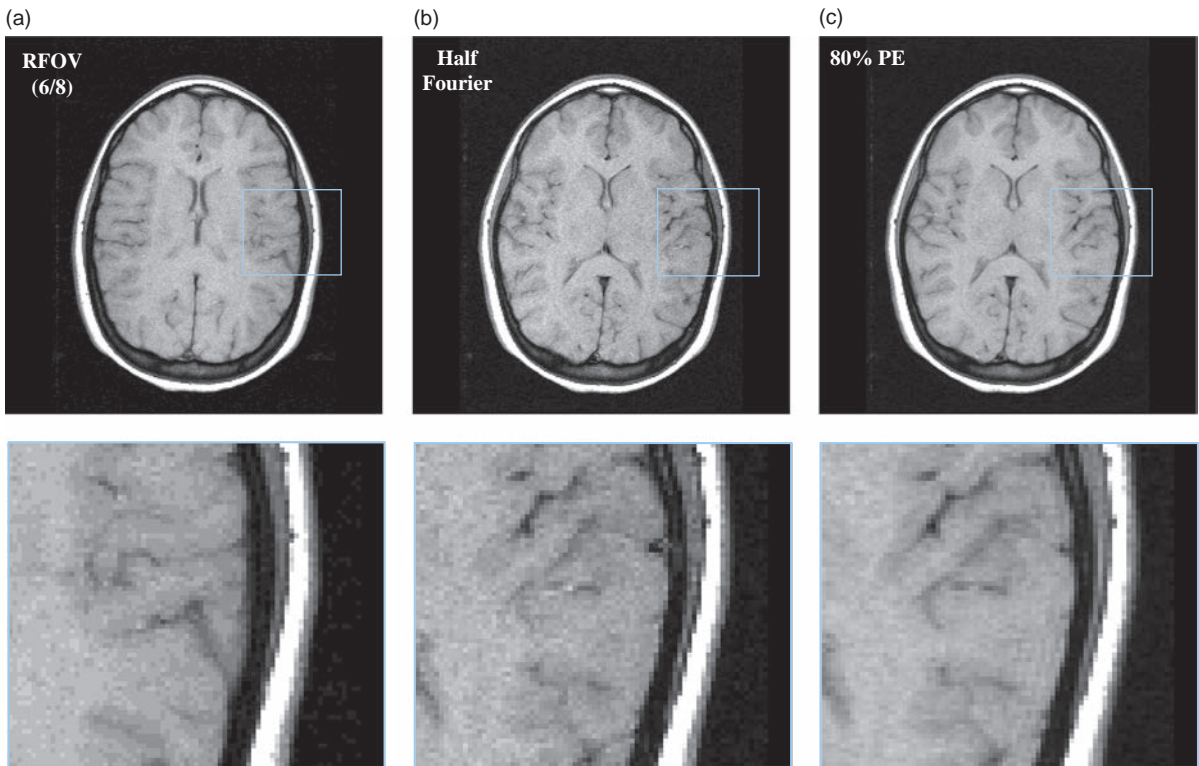


Figure 6.10 Images showing (a) rectangular field of view (RFOV): scan time 1 min 39 s, (b) half Fourier: scan time 55 s, (c) reduced matrix (80%), scan time 1 min 20 s. Full acquisition scan time would have been 2 min 8 s (spin echo, TR = 500 ms, TE = 15 ms). The half Fourier image is noisier, while the reduced matrix has less noise but reduced spatial resolution.

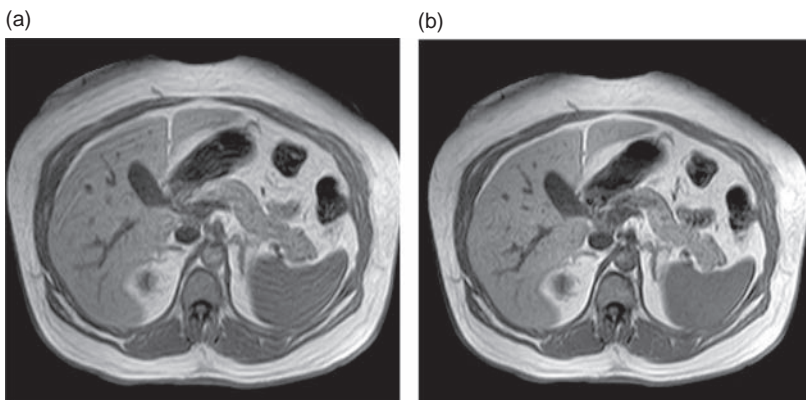


Figure 6.11 (a) Image from patient unable to maintain breath-hold. (b) Parallel imaging is used to reduce breath-hold time and respiratory movement artefact.

resolution) will maintain SNR but with a minor loss of resolution. A combination of 7/8 Fourier and 90% scan percentage would also work. Alternatively, on a Philips scanner you could use parallel imaging (SENSE) with a reduction factor of 1.1 to 1.2 without changing any of the other sequence parameters. This

would give the desired reduction in scan time with a small but negligible loss in SNR but no loss in resolution.

However, let's say your patient is really sick and can barely manage a 10 s breath-hold. If NSA is greater than 1 then reduce it. If NSA = 1 already, then

parallel imaging with a reduction factor of two or slightly more will get your scan time down to the required 10 s but with an SNR loss of about 30%. Figure 6.11 shows how this helps the overall image quality where the loss in SNR is more than compensated by the reduction in movement artefact.

6.4.4 Tweaker's Charter

Usually your scanner's protocols will be well set-up and optimized so off-the-cuff 'tweaking' will not be required. Remember that making seemingly

innocuous parameter changes can have an adverse effect on the diagnostic quality of the images. This chapter is not a licence to tweak, but instead provides the theoretical and practical knowledge for when you do have to optimize a protocol, or when the specifics of the patient requires that some minor parameter modifications are made.

See also:

- Image artefacts: Chapter 7
- Spatial encoding using gradients: Chapter 8
- Parallel imaging: Chapter 14.

Further Reading

Brown MA and Semelka RC (2010) *MRI: Basic Principles and Applications*, 4th edn. Hoboken, NJ: Wiley-Blackwell, chapter 6.

Elster AD and Burdette JH (2001) *Questions and Answers in Magnetic Resonance Imaging*, 2nd edn. London: Mosby-Yearbook, chapter 4. Also on the web at <http://mri-q.com> [accessed 23 March 2015].

Hashemi RH and Bradley WG Jr (2010) *MRI The Basics*, 3rd edn. Baltimore, MD: Lippincott, Williams & Wilkins, chapter 17.

Improving Your Image: How to Avoid Artefacts

7.1 Introduction

As we all know, real life is far from perfect and MRI is just as disappointing in some ways! MR scanners do not have absolutely uniform magnetic fields, the gradients don't produce exactly the pulse shapes programmed by the pulse sequence and patients don't keep still. These problems, and many others, produce artefacts in MR images. An artefact is defined as any feature in an image which misrepresents the object in the field of view (FOV). This could be a bright signal lying outside the body, or lack of signal where there should be something. It might also be a distortion in the image, so that a straight line appears curved, or a certain area is artificially magnified or reduced. A large group of MR artefacts appear as 'ghost' images, where a faint copy of the anatomy appears in the image displaced in one direction or another.

In this chapter we will describe the most common artefacts encountered in MRI, along with ways to avoid or minimize them. The causes of artefacts can be broadly divided into four groups: motion, inhomogeneity, digital imaging artefacts, and hardware-related artefacts:

- *Motion artefacts* appear as ghosts along the phase-encode direction, and are produced by physiological motion or involuntary movement by the patient.
- *Inhomogeneity artefacts* usually cause signal intensity changes and image distortions, and are due to hardware imperfections and to the susceptibility effects within the human body.
- *Digital imaging artefacts* have a variety of appearances, and include phase wrap-around artefacts and problems arising from approximations and errors in the encoding process.
- *Hardware-related artefacts* are less common these days, but RF interference and spike noise are still important to recognize.

7.2 Keep Still Please! Motion Artefacts

7.2.1 Gross Patient Motion

Probably the commonest cause of artefacts on images is patient motion, resulting in a range of ghosting effects depending on the severity of the motion. Continuous movement during the scan causes a generalized blurring, often making the scan useless (Figure 7.1), while a few twitches or only small movements may only cause a few subtle ghosts which may leave an acceptable image. Patients may move involuntarily if they are suffering from a movement disorder, or they may have difficulty understanding or remembering the instructions to keep still during the scan. In these cases it may be necessary to sedate the patient or even use a general anaesthetic in order to get a diagnostic scan.

More often patients become uncomfortable in the scanner and move to relieve pain or muscle cramps.

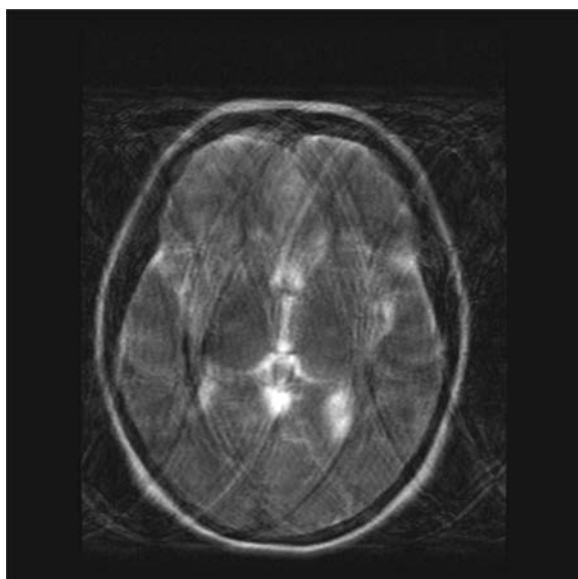


Figure 7.1 Gross motion artefacts due to the patient moving continuously throughout the scan.

Careful preparation for the scan should minimize the patient's discomfort. This should include a clear description of what they will hear and feel during the imaging, as well as using pads and immobilization straps to help them keep still. Immobilization often works particularly well with young babies who seem to like being well swaddled! Hearing protection is mandatory in many centres, especially for 3 T systems, but you need to make sure patients can still clearly hear you over the intercom – both for instructions and for reassurance during the exam.

If a scan is unacceptably degraded due to motion artefact, the only solution is to repeat the scan. Obviously it makes sense to check that the patient is as comfortable as possible and understands the need to keep still before starting the repeat scan. If the scan is a particularly long one it is also worthwhile trying to reduce the scan time to improve the chances of an image without movement artefact, so long as the reduced SNR or resolution is still acceptable for the radiologist. Even better, choose one of the special motion-control sequences available on all scanners (e.g. BLADE, MultiVane, PROPELLER, JET).

7.2.2 Respiratory Motion

Breathing motion causes ghosting on thoracic and abdominal imaging. Sometimes it is easy to recognize the strong ghosts of the chest wall (Figure 7.2).



Figure 7.2 Motion artefacts due to respiration.

The best way of avoiding respiratory artefacts is to reduce the scan time to less than 15 s, so that the scan can be acquired during a single breath-hold. The acquisition can also be split up so that packages of slices are acquired in separate breath-holds. The position of the liver and kidneys is more reproducible if the breath is held in expiration, so if multiple breath-holds are necessary, expiration is preferable. However, inspiration breath-holds can be maintained for longer, up to 25 s, and if you can achieve the whole scan in one breath-hold, it may be better to do it in inspiration. Careful coaching with the patient is needed before the examination starts so that they understand your instructions.

By using a special respiratory monitoring device, often known as a 'bellows' or 'respiratory belt', the MR system can detect the breathing motion. The device has a fixed-volume bellows arrangement strapped around the patient's chest and placed between the chest and the receive coil. The breathing motion causes a change in volume and hence air pressure within the device, which is detected and converted to an electrical signal that tracks respirations (Figure 7.3). This signal can be used either for *respiratory gating* or *triggering*, or respiratory compensation by phase re-ordering

Respiratory gating uses the bellows waveform to start the imaging sequence at a consistent place in each breathing cycle. As a result, each signal is acquired when the chest wall is in the same position, so there are no ghost images. Instead of a regular TR, the sequence now uses the interval between two consecutive triggers, which at a normal breathing rate of about 10–15 breaths per minute gives an effective TR of at least 4000 ms. This means that respiratory gating is only useful for PD or T₂-weighted imaging, and scan times may be very long.

Respiratory compensation, also called Respiratory-Ordered Phase Encoding (ROPE), uses the waveform from the bellows to reduce artefacts with breathing. As the name suggests, the phase-encode gradients are re-ordered to match the breathing motion, taking care to maintain the same contrast. To understand this, you need to understand k-space, so this might be a good time to check Box 'An Easy Introduction to k-Space' in Chapter 5. Remember that all the signal and contrast information is in the middle of k-space, which corresponds to the smallest phase-encoding gradients, while the large phase-encoding gradients fill the outer portions

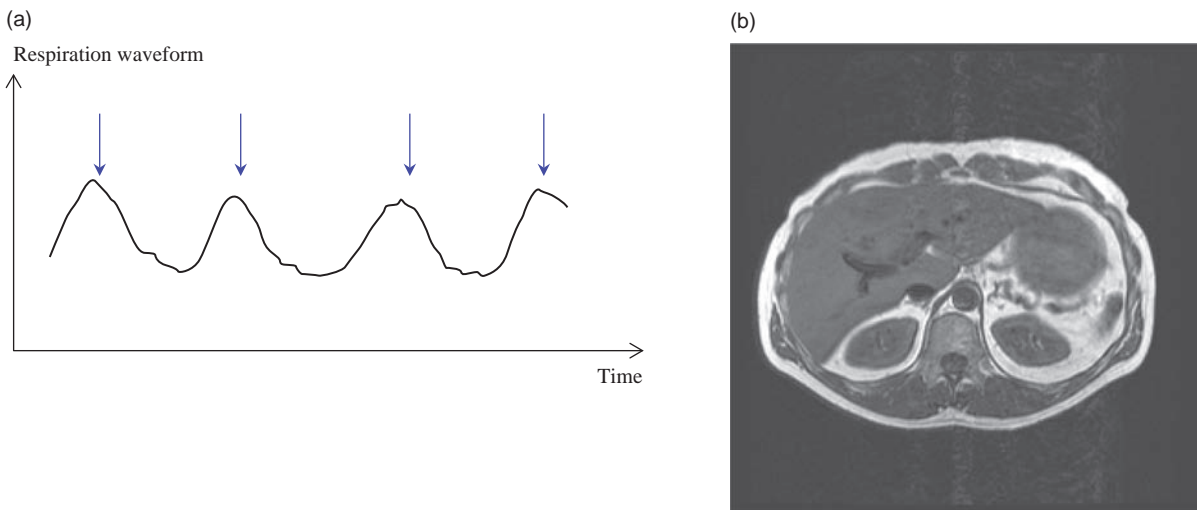


Figure 7.3 (a) The changing signal produced by respiratory bellows around a patient's chest. Respiratory gating triggers the scans so that all the acquisitions are synchronized to the same point in the cycle (small arrows). (b) Axial image of the abdomen acquired with respiratory-ordered phase encoding (ROPE).

of k-space and control the resolution of the image. In ROPE the order of the gradients is matched to the respiratory cycle (Figure 7.4a) so that neighbouring lines in k-space are acquired close together in the breathing cycle (Figure 7.4b). ROPE is an efficient way of removing the breathing artefacts and it has the advantage that it can be used for any type of image weighting, although it does tend to extend the scan time slightly since it needs to start by measuring and analysing the respiratory waveform for a couple of cycles. However, it is not available with all image sequences.

The last method to avoid respiratory motion is a technique called 'navigator echoes' (see Chapter 16 for full details). This method does not use the bellows; instead, a rapid 1D imaging method is used to monitor the position of the diaphragm. The navigator 'signal' is from a single column of voxels, which you might think is pretty useless. However, the strong contrast between the (dark) lung and the (brighter) liver shows up clearly. When a series of navigators is acquired while the patient breathes normally, the changing position of the diaphragm can be visualized by displaying the 1D images side-by-side (Figure 7.5). The boundary can be automatically detected by the scanner software, and controls the acquisition so that the image data are acquired when the diaphragm is within certain spatial limits, typically 2–4 mm.

So in total there are four different ways of avoiding respiratory artefacts. How do you choose

the right one for your application? We can start by saying that respiratory triggering, where the TR is effectively the length of the breathing cycle, has such a long scan time that it is rarely used. For cardiac imaging (see Chapter 16), the methods of choice are breath-hold for morphology and perfusion scans, and navigators for coronary arteries and high-resolution viability. In abdomen imaging, a breath-hold is usually the best choice, but ROPE can also be used with classic SE or GE sequences. Unfortunately ROPE cannot be used with fast spin-echo (TSE) sequences; the only choice is navigator or respiratory gating, which therefore means relatively long scan times for these sequences.

7.2.3 Cardiac Motion

The beating heart is a source of artefacts not only when imaging the heart itself, but also in exams like thoracic spine or liver (Figure 7.6). Avoiding the artefacts is achieved by synchronizing the sequence to the cardiac cycle, known as 'gating'. Special electrocardiogram (ECG) electrodes are attached to the patient's chest, in a similar way to normal cardiac monitoring electrodes. These electrodes are usually non-metallic to reduce artefacts on the images, and to avoid local skin heating. The ECG leads typically have high impedance (compared with low impedance in normal ECG monitoring); this reduces the chance of RF burns for the patient. You should never use ordinary ECG electrodes in an MR system.

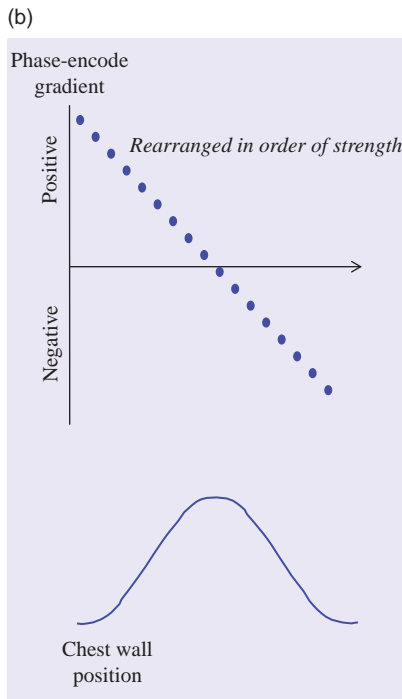
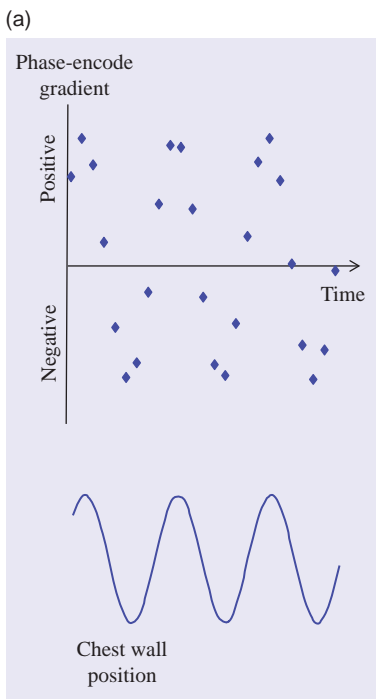


Figure 7.4 (a) Low-sort ROPE rearranges the phase-encoding order to match the respiratory cycle. (b) When the data are arranged in order of phase-encode gradient strength, neighbouring lines in k-space are close together on the respiratory waveform and it appears that the whole acquisition has taken place over one breathing cycle.

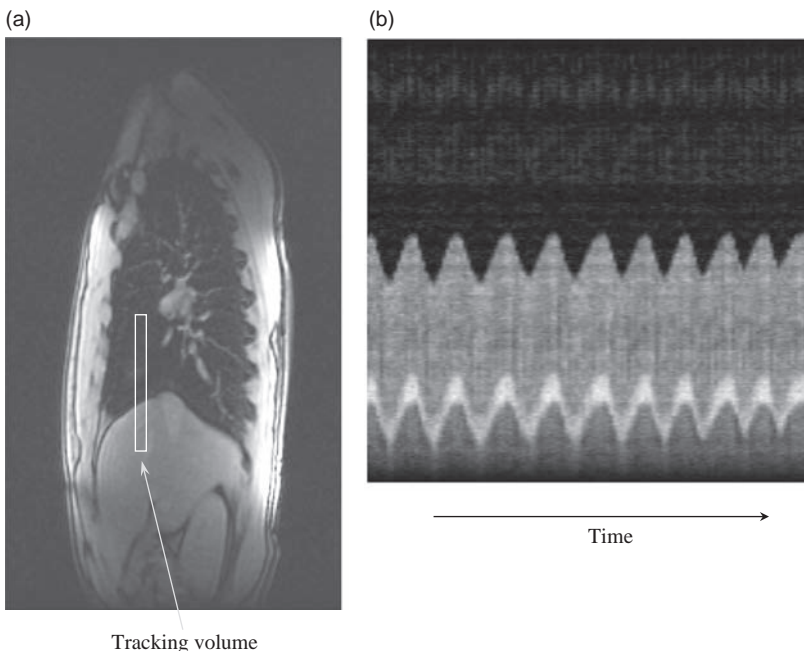


Figure 7.5 The navigator signal is frequency encoded in one direction, and the other direction becomes time.

The peak of the R wave is detected by the scanner and used to trigger the next phase-encoding acquisition (Figure 7.7a). In this way each line of data is acquired at the same point in the cardiac cycle, and

the ghosting is removed. The TR (and therefore the scan time) is determined by the heart rate, so at a typical HR of 75 beats per minute (bpm), TR will be 800 ms. This is an intermediate TR for spin echo,

neither short enough for T_1 weighting nor long enough for PD or T_2 w. It is possible to define the TR as 2 or more R-R intervals, which can extend the usable TR time. However, it is still necessary to avoid acquiring data during the QRS peak, so it slightly reduces the time-efficiency of the sequence.

Cardiac gating can also be achieved by detecting the arterial pulse of blood in the patient's finger or toe. In these areas the blood vessels are very close to the skin, and an infrared light detector can pick up the increased volume of blood as the arterial pulse reaches the extremity. The signal only shows the arterial peak, not the other portions of the cardiac cycle, but this is sufficient to provide a trigger for the MR sequence.

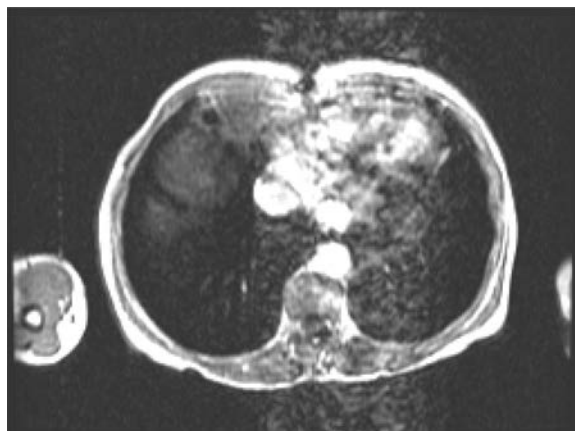


Figure 7.6 Motion artefacts due to cardiac motion.

This technique is known as peripheral pulse gating or photoplethysmographic gating (rather a technical mouthful!), or simply Peripheral Gating (PG). Peripheral gating is a useful way of removing pulsatility artefacts in the brain and cervical spine.

ECG or Peripheral Gating?

Both methods are available on most modern scanners. What are the advantages and disadvantages of the two techniques?

ECG gating is a more accurate gating method, since the R wave is usually sharp and should be easily detected by the scanner. But that does depend on a good connection of the electrodes to the patient. This is particularly important for cardiac imaging since it allows as many multi-slice images as possible to be scanned within the R-R interval. In a multi-slice gated sequence, not only is each slice at a different location, it is also at a different point in the cardiac cycle. During systole the heart moves within the chest and so slices acquired during systole may be spatially mismatched with slices in the rest of the cycle.

In contrast, peripheral gating only detects the arterial pulse and the peak is much broader than the ECG R wave (Figure 7.7c). Thus peripheral gating is not ideal for cardiac imaging because it results in variability of the trigger position. In addition, the trigger is delayed relative to systole due to the time it takes for the arterial blood to arrive in the finger or toe, typically about 500 ms. Bear in mind that the arterial delay for

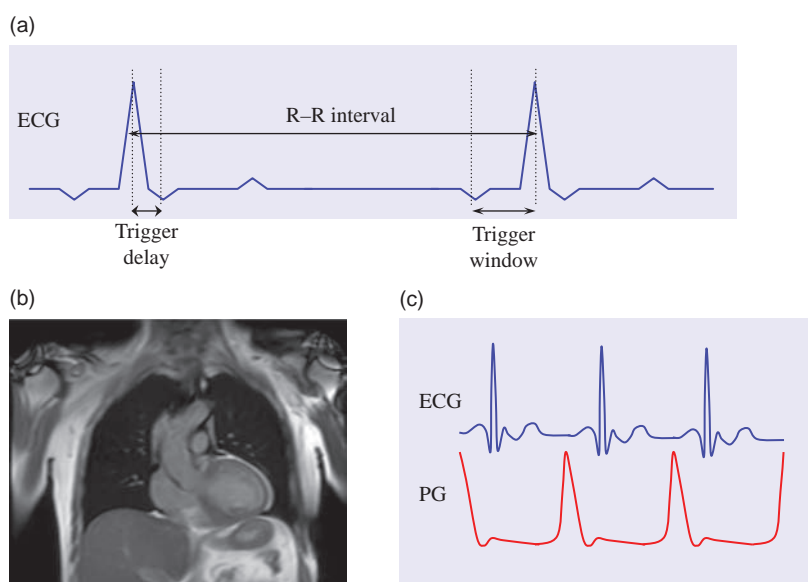


Figure 7.7 (a) The ECG waveform used to trigger the scan acquisitions to remove cardiac motion artefact, showing the effective TR (the R-R interval), the trigger delay and the trigger window. (b) Coronal view of the chest showing no artefact from cardiac movement. (c) Peripheral gating (PG) signal compared with ECG signal.

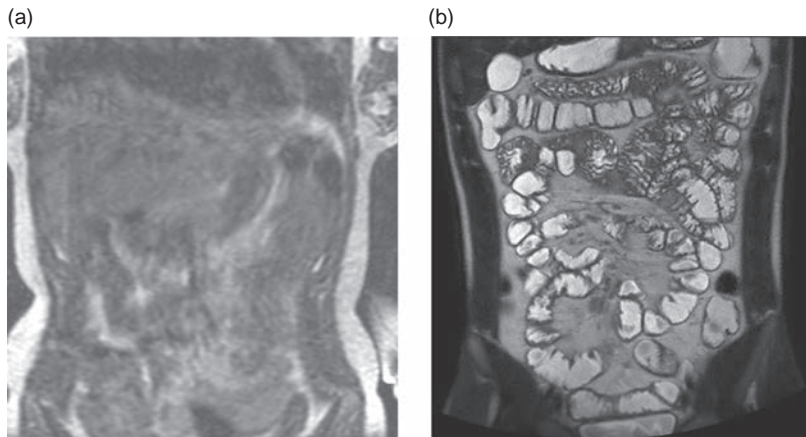


Figure 7.8 (a) Motion artefacts due to peristalsis. (b) Coronal enterography image acquired using single-shot TSE to 'freeze' the peristalsis motion.

the anatomy you are imaging may be different from that in the finger too, so there may be some residual ghosts. However, for the most common application, that of removing CSF pulsation artefact in neurological imaging, the delay times are actually quite similar, so peripheral gating is usually successful.

The advantages of peripheral gating are in the ease of preparing the patient and for safety. For ECG gating it is necessary for the patient to change into a hospital gown, and for electrodes to be carefully attached to the skin, including hair removal if necessary. In comparison, placing the peripheral trigger detector on one of the fingers is very easy and more comfortable for the patient.

Always follow the manufacturer's instructions when using ECG gating or peripheral gating.

7.2.4 Peristaltic Motion

Peristalsis causes a random continuous motion of the abdominal contents, and there is no physiological signal to trigger the MR acquisition. Acquiring multiple averages can reduce the ghost appearances, but for imaging the small or large bowel it is much more effective to use an antiperistalsis drug such as hyoscine butylbromide or glucagon. This has the effect of stopping the peristaltic motion for a short time (usually around 15–20 min) which is just long enough to acquire the required images. If a drug is not possible, then ultrafast pulse sequences such as HASTE (see Section 12.4.3) or Single-Shot Turbo Spin Echo (SS-TSE) can be used to acquire images fast enough to minimize the motion artefacts (Figure 7.8).

Clinical Exam: MR Enterography

Imaging the bowel wall is becoming an important MR exam in some regions, especially for diagnosis of Crohn's disease or irritable bowel syndrome. MR is considered equivalent to CT enterography for sensitivity and specificity, so the choice of technique is largely a matter for local (institutional) preference.

Patient preparation includes drinking a large volume of an enteral contrast agent, such as an aqueous solution of mannitol, or methyl-cellulose. This agent distends the bowel and provides a high-signal lumen, allowing for clear delineation of the bowel walls. Scanning is done with single-shot TSE sequences, or strong T_2^* w GE scans. It is also possible to acquire dynamic images with GE scans, to show peristalsis in certain segments of the bowel.

7.2.5 Motion Artefacts from Flowing Blood

Moving protons in blood vessels or the cerebrospinal fluid (CSF) cause a range of artefacts due to two effects. First, there is an in-flow effect which produces high signal within blood vessels on gradient-echo images, as new protons flow into the imaging slice during the TR. Second, there are velocity-induced phase effects, which reduce the blood signals and create ghost images of arteries or veins in the phase-encode direction (Figure 7.9a). Complete intra-voxel dephasing occurs in areas of turbulent flow, e.g. distal to a bifurcation, leaving a dark appearance. Depending on whether the scan is an MRA or not, these effects may cause problems.

To explain the in-flow effect, we will consider a blood vessel passing through an imaging slice (Figure 7.9b), and assume that the blood flow is

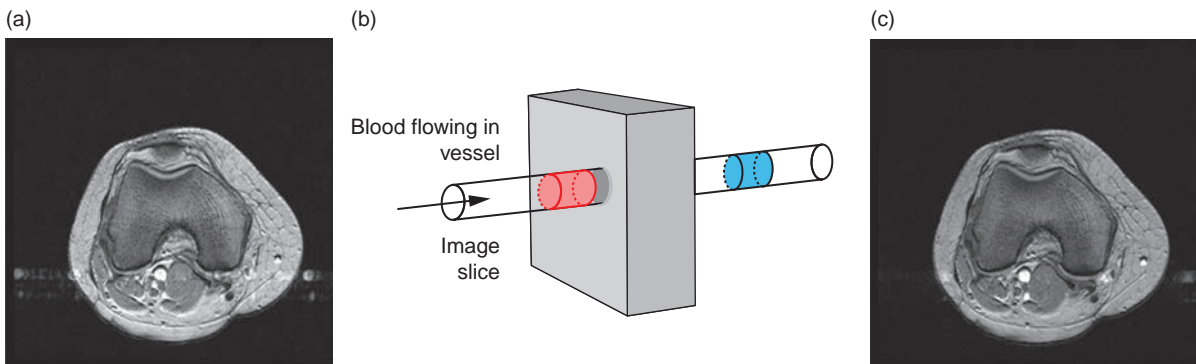


Figure 7.9 (a) Knee image showing artefact from flowing blood. (b) Blood vessel passing through an imaging slice. In a spin-echo sequence, the blood excited by the 90° pulse (coloured blue) moves on by the time the 180° pulse is applied (red-coloured bolus), and neither bolus produces a signal. In gradient-echo sequences, each bolus has fully relaxed magnetization M_0 when the excitation pulse is applied, and its signal is refocused by the gradients so that blood appears bright. (c) Axial knee image acquired with gradient moment nulling (flow compensation).

steady. In SE sequences, we use two RF pulses to create the echo, excitation followed by refocusing. Assuming the blood is moving fast enough, the bolus of blood within the imaging slice will be replaced by a second bolus of fresh, i.e. unsaturated, blood during the gap between the two pulses. The first bolus receives a 90° pulse but not the 180° , while the second receives only the 180° pulse. Since both a 90° and a 180° pulse are required to create a spin echo, neither bolus will produce an echo. There will be a signal loss within the blood vessel, giving spin-echo images a characteristic dark-blood appearance.

GE sequences only have an excitation pulse and the echo is formed using the gradients. So the excited bolus of blood always contributes a signal, provided it is still within the gradient volume. For the next and every subsequent slice there is a fresh bolus of blood within the slice, with fully relaxed magnetization. Thus, on GE images blood vessels have high intensity and can easily produce ghost images in the phase-encode (PE) direction, if the TR is not synchronized with the pulse rate. We can also take advantage of that very bright signal to create MR angiograms with the scan technique called ‘time-of-flight’ (TOF) – see Chapter 15 for all the details.

Apart from the in-flow or time-of-flight effects, phase-related artefacts arise because the blood protons are moving during the imaging gradients and so their resonant frequencies are continuously changing. When their frequencies change, they acquire phase differences compared with each other and with static tissue. When a voxel contains protons moving at different velocities, for example in a region

of turbulent flow, their signals will dephase rapidly and cause a signal dropout. More detail about flow-related phase effects can be found in Chapter 15.

To avoid flow artefacts, we frequently use *spatial saturation* slabs just outside the field of view or in the slice direction. Saturation slabs, also known as REgional Saturation Technique (REST) slabs or ‘pre-sat’, act exactly like slice selection. We apply a 90° pulse to all the tissues within the slab immediately before the RF excitation pulse for the imaging sequence, then apply a large gradient pulse to dephase the protons, leaving no signals from the tissues in the sat band.

Saturation bands can be used in many ways. They can be placed within the FOV, e.g. to saturate signal from the thoracic aorta for sagittal spines or reduce artefact from swallowing (Figure 7.10), or at the edges of the FOV, e.g. to reduce phase wrap on coronal shoulders. Placed above and/or below the image FOV, sat bands can remove arterial and/or venous blood flow; blood flowing from the sat band into the imaging slice will have no time to recover its equilibrium magnetization, so it will give no signal. Be sure to pay attention to the flow direction to make sure you put the sat band in the right place!

It is also possible to correct for velocity-induced flow dephasing effects using a technique called *gradient moment nulling*, also known as *gradient moment rephasing* or *flow compensation*. Extra gradient pulses are inserted into the pulse sequence, so that the velocity-induced phase shifts are corrected. For vessels with simple laminar flow, the vessel will appear on the final image without ghosting artefacts

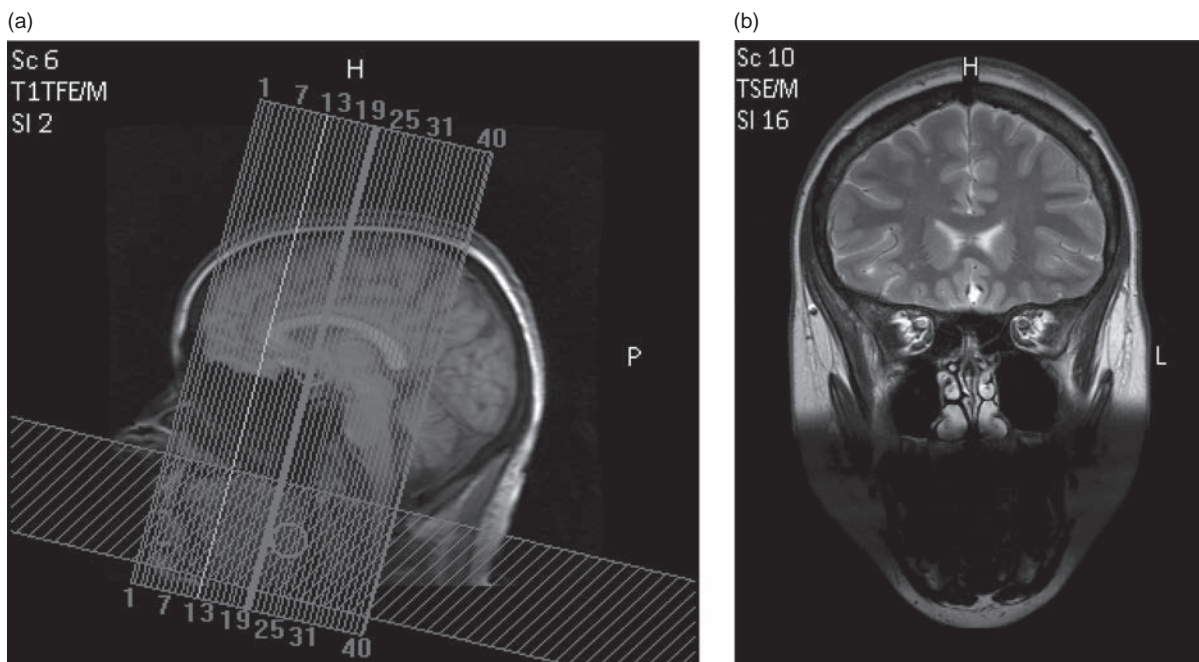


Figure 7.10 (a) Angled sat band within the FOV to eliminate artefacts from tongue movement and swallowing. (b) Resulting image.

(Figure 7.9c). The details of gradient moment nulling will be fully explained in Chapter 15.

7.3 Lose the Fat!

Fat is often a source of problems in MR imaging. It tends to have high signal intensity in all contrast weightings, potentially masking pathology. It also causes two types of artefact, known as chemical shift artefacts.

In Section 3.1 we sub-divided tissues into fat-based and water-based tissues. In all MR images we are detecting signals from protons (the nuclei of hydrogen atoms), but fat and water have very different structures. Water has only two hydrogen atoms and an oxygen atom, so it is a small molecule. Fat is made up of triglyceride chains, long backbones of 10–20 carbon atoms each with two hydrogen atoms on either side. Fat molecules are thus very large and each hydrogen atom is surrounded by many other atoms. The neighbouring electron clouds reduce the effective strength of the external magnetic field B_0 , so the hydrogen nuclei in fat have a lower Larmor frequency than those in water, which are not shielded. This difference is known as the chemical shift, which is quoted in parts per million (ppm), a unit which is independent of magnetic field strength. We can calculate the actual frequency difference by multiplying

the chemical shift in ppm by the resonant frequency in megahertz of protons at a particular magnetic field strength. For example, the chemical shift between fat and water is 3.5 ppm, and at 1.5 T protons have a Larmor frequency of 63.855 MHz, so the frequency difference is approximately 220 Hz; at 3 T it is approximately 440 Hz. If we look at the frequency spectrum from the human body we see two peaks, the larger one from water protons and the smaller one to the right (Figure 7.11a).

7.3.1 Chemical Shift Artefact

As we will see in Chapter 8, we use frequency encoding, i.e. we rely on the MR signal's frequency for spatial information. But fat naturally has a lower frequency than water, so the frequency encoding will be fooled into thinking that the fat is in a different position. Due to the frequency difference, the apparent position of fat signals is shifted by a number of pixels, but only in the frequency-encode direction. This appears as light and dark bands on opposite sides of a structure, or as an entire ghost image of the fat distribution in the anatomy (see Figure 7.11b). This is called the *chemical shift artefact* or *chemical shift misregistration artefact*. The severity of the pixel shift depends mainly on the receiver bandwidth used: the

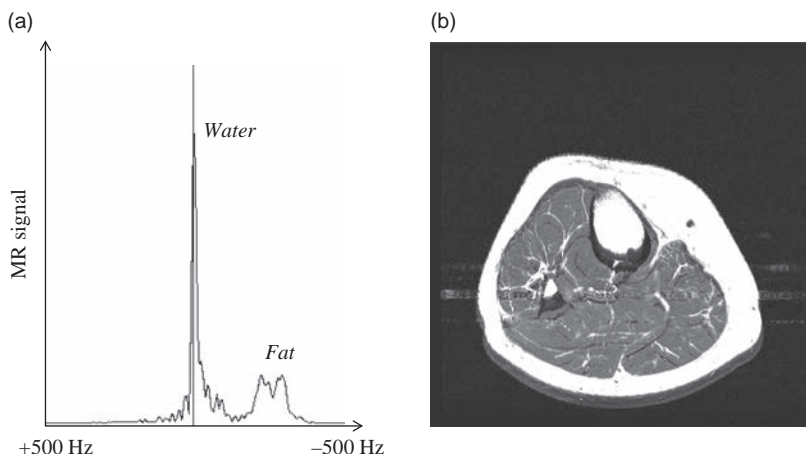


Figure 7.11 (a) Spectrum from the lower leg showing water and fat peaks with a separation of 3.5 ppm. (b) Chemical shift artefact in the lower leg.

lower the bandwidth the worse the problem. So to minimize the chemical shift artefact you should ideally use a higher bandwidth. However, increasing the bandwidth also reduces the signal-to-noise ratio in the image, so it is not always desirable. The chemical shift artefact occurs with both spin-echo and gradient-echo sequences.

How Many Pixels is it Shifted?

You need to know how much the fat signal is shifted with respect to the water in order to know if the chemical shift artefact is a problem. The severity of the chemical shift effect depends on two things: the field strength of the magnet and the receiver bandwidth used for imaging. Some manufacturers (e.g. Philips) quote the receiver bandwidth in terms of the number of pixels by which fat will be shifted; this is the easiest way for operators to minimize the artefact! Others (e.g. Siemens) use 'hertz per pixel' for the receive bandwidth; again this makes life easy as you just have to divide the chemical shift for your magnet field strength by the bandwidth. For example, at 1.5 T the chemical shift is 220 Hz, so if you choose a bandwidth of 100 Hz/pixel the fat signals will be shifted by about two pixels relative to water, whereas a bandwidth of 500 Hz/pixel will give a negligible shift of $220 \div 500 \approx 0.5$ pixels.

Lastly, some manufacturers quote the receiver bandwidth directly in kilohertz (e.g. GE Healthcare). Working out the chemical shift is a little more long-winded, so you might like to work it out for a range of bandwidths and either memorize them or have them in a handy notebook when you are at the console. It's important to know that the bandwidth

is quoted as ' \pm ' the value, which means you need to double it in your calculation, as shown below.

First, work out the bandwidth in hertz per pixel; multiply by 1000 to convert from kilohertz into hertz, then divide by the frequency matrix. At the moment 256 is the commonest frequency matrix (although 512 is becoming much more popular), so in this example we will use 256 and a bandwidth of ± 10 kHz:

$$\frac{10 \times 2 \times 1000}{256} = 78.2 \text{ Hz/pixel}$$

Now divide the chemical shift for your scanner's field strength by this number. We will use the example of 1.5 T, so

$$\frac{220}{78.2} = 2.8 \text{ pixels}$$

So at this field strength a ± 10 kHz bandwidth with a 256 frequency matrix gives a moderate chemical shift artefact. If the matrix is increased to 512, the shift will be more than five pixels and will be more of a problem.

7.3.2 Phase Cancellation Artefact

There is a second type of artefact, also caused by the chemical shift between fat and water, which only occurs with gradient-echo imaging. Some texts call this 'chemical shift of the second kind', 'black line' artefact, 'India ink' or the '*phase cancellation artefact*', which is the term we will use. The phase cancellation artefact appears as a black outline (Figure 7.12b), especially noticeable in the abdomen where water-based tissues are surrounded by peritoneal fat. It occurs in any voxel containing both fat and water, and depends on the fat-water chemical shift and the TE used.

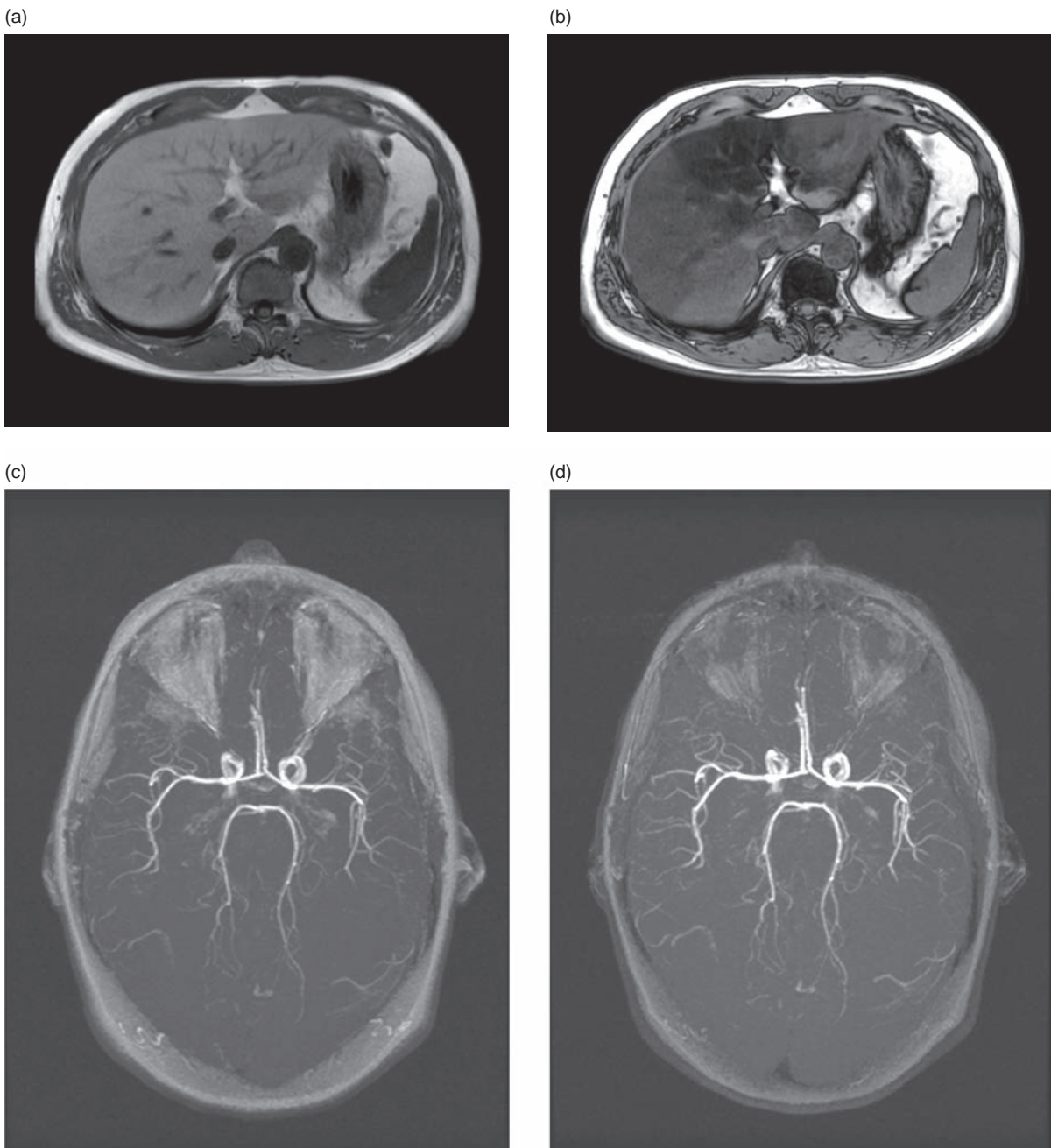


Figure 7.12 Phase cancellation artefact. (a) At a TE of 4.2 ms the fat and water signals are in phase and no phase cancellation artefact is seen. (b) At a TE of 2.1 ms, a black line appears at boundaries between fat and water, because the fat and water signals within the voxel are out of phase with each other. (c) Cranial time-of-flight (TOF) MR angiography with TE for fat and water in phase, and (d) out of phase. Notice how much the periorbital fat intensity is reduced.

Why does it occur? Immediately after the excitation pulse of the sequence, fat and water signals are in phase with each other, but due to the small difference in their Larmor frequencies they begin to dephase. If the echo is acquired when fat and water are exactly

out of phase, i.e. 180° to each other, voxels with a mixture of tissues will have a reduced signal since the fat signal subtracts from the water. This gives the characteristic dark outline at fat–water interfaces, due to all the mixed voxels around the edge. If

the TE is increased so that fat and water are back in phase with each other, the signals will add together instead of subtracting, and no black line occurs (Figure 7.12a).

So there are specific TEs in gradient-echo imaging which produce the phase cancellation artefact, and others which don't. Some manufacturers list 'in-phase' (IP) and 'out-of-phase' (OP) as options for the TE, which makes life easy! Acquiring both IP and OP images is common in liver or spleen imaging, since a signal loss in the OP image can indicate diffuse fatty infiltration in the water-containing organs. Phase cancellation artefact is not a problem in spin-echo imaging because the fat–water phase shift between the 90° and 180° pulses is inverted by the 180° pulse, so that at the echo time they are back in phase.

In-Phase and Out-of-Phase TEs

If your scanner doesn't show 'in-phase' and 'out-of-phase' as TE options, you need to work out some appropriate values. As with the chemical shift artefact, you might find it useful to keep this information in a handy notebook. We start with the chemical shift in hertz between fat and water, for example at 1.5 T the shift is 220 Hz. Fat and water are in phase immediately after the excitation pulse, but we can't acquire the signal immediately. The next time they are in phase will be 1/220 s later, i.e. 4.55 ms. So a TE of 4.55 ms or multiples thereof will have fat and water in phase, avoiding the black line artefact. Halfway between these two echo times fat will be exactly 180° out of phase with water, so a TE of 6.9 ms (or 2.3 ms if the gradients allow it) will give the phase cancellation artefact. To get a T_2^* -weighted gradient echo with in-phase TE, you may need to go to 22.7 or 27.3 ms, while an out-of-phase T_2^* -weighted TE would be halfway between these values at about 25 ms. At 3 T the values will be different, with IP TEs at multiples of $1/440 = 2.27$ ms and OP TEs halfway between these values.

7.3.3 MRI Liposuction: Removing Fat Signals

There are two easy ways of suppressing fat signals more or less completely. The first we have already met in Section 3.7: the STIR sequence which uses the inversion recovery pulse sequence with the TI set at the null point of fat. This technique depends on the T_1 of fat, which is considerably shorter than that of most other tissues. The TI varies slightly with field strength,

from approximately 150 ms at 1.5 T to 220 ms at 3 T. The initial ('inversion') 180° pulse inverts all the equilibrium magnetization, which then begins to recover towards the equilibrium value, M_0 , with T_1 recovery (see Figure 3.11). When the 90° pulse is applied at the null point of fat, fat-based tissues produce zero signal as they have nothing to tip into the xy plane. At an appropriate TE a refocusing 180° pulse is applied to generate a spin echo and create an image with no signal from fat. Since we use 'magnitude' reconstruction in MRI, all the other tissues give bright signals, with fluids (with the longest T_1 s) having the highest signal.

The alternative technique is frequency-selective *fat saturation*, often known simply as 'fat sat' or 'chem sat' (chemical sat). This takes advantage of the chemical shift between fat and water to excite only the fat protons. A narrow range of RF frequencies centred on the fat Larmor frequency is used (see Figure 7.13a) to give a 90° pulse to protons in fat, leaving the water protons unexcited. This is known as a CHESS (CHEmical Shift Selective) pulse. The imaging sequence is started immediately after the CHESS pulse, so that fat has no time to recover its longitudinal magnetization and the image is produced with a suppressed fat signal. Typically *crusher* gradients are applied immediately after the CHESS pulse to dephase the transverse fat magnetization, which otherwise tends to produce an echo due to its rapid relaxation. There has to be some compromise over the fat sat pulse; it needs a bandwidth wide enough to saturate all the fat protons, but shouldn't excite any water protons. Even though the chemical shift of 220 Hz (at 1.5 T) sounds quite large, the variation of main field homogeneity over the field of view can

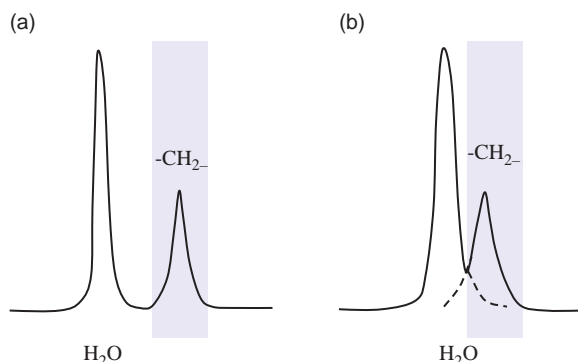


Figure 7.13 (a) Frequency-selective saturation uses a narrow-bandwidth RF pulse to excite only fat protons. (b) At low field strengths the peaks overlap, making it impossible to saturate all the fat without affecting the water protons.

easily reach this order of magnitude. In areas where the local B_0 is reduced by 220 Hz, the CHESS pulse will perfectly saturate the water signal instead of the fat signal. This annoying problem is called fat sat failure and can be found especially with off-centre or very large fields of view.

A slight modification of fat sat combines frequency-selective excitation with STIR. This is known as SPIR (SPectral Inversion Recovery) by Philips or SPECIAL (SPECtral Inversion At Lipid) by General Electric. A frequency-selective pulse is applied to the fat protons, followed by crusher gradients to dephase any signal produced in the transverse plane. At an appropriate TI (depending on field strength) the rest of the imaging sequence is started, producing an image with better fat suppression than the simple CHESS pulse.

Another variation is to use so-called ‘adiabatic’ RF pulses for fat suppression. These pulses are commercially known as SPAIR (SPectral Adiabatic Inversion Recovery) and are recommended for 3 T use, because they give more uniform fat suppression, especially over larger FOVs. They are tricky to explain, so we leave that for a later chapter (when you are ready, turn to Chapter 12).

Which is Better, STIR or Fat Sat?

If your scanner has a field strength of 1.5 T or higher, fat sat or SPIR/SPAIR is almost always better than STIR. At these fields it is possible to apply a good suppression pulse to just the fat, leaving the water protons unexcited, thanks to the higher chemical shift. Frequency-selective fat saturation pulses can be inserted before almost any pulse sequence, so the image contrast can be controlled independently of the fat suppression. In comparison, STIR can only produce a fat-suppressed ‘ T_2 -weighted’ appearance, not fat-suppressed PD.

However, fat sat can become unreliable at the edges of the imaging volume, causing both unsuppressed fat and suppressed water signal. This happens because of the large range of magnetic field non-uniformities which cannot be shimmed as easily as a smaller FOV in the centre of the magnet. Failing fat-sat is particularly a problem for shoulder, elbow and wrist imaging, where the anatomy cannot be brought to the isocentre. Adiabatic fat suppression (e.g. SPAIR) can help to avoid B_1 non-uniformities, but cannot help with main field non-uniformities. Under these circumstances STIR is still useful, because it is relatively independent of both B_1 and B_0 non-uniformities. Dixon-based methods are also useful, since the latest reconstructions offer very robust fat-sat.

Try It for Yourself 6: Chemical Shift Effects

The chemical shift artefacts and methods to avoid them are easily shown using a cooking oil and water phantom. Fill a deep plastic container one-third full with water, adding a drop of gadolinium to reduce the T_1 , then carefully pour on some cooking oil until the container is two-thirds full. The oil will float in a separate layer on top of the water, but you have to handle it carefully to avoid making a salad dressing at the interface! Put the container into the head coil or knee coil, do a localizer scan and start changing parameters one at a time. For instance, use several different receive bandwidths (water–fat shifts on Philips systems) to see the chemical shift artefact, or try gradient-echo scans with echo times for fat and water in and out of phase.

A couple of things to look out for:

- Use a T_1 -weighted spin-echo sequence to see the chemical shift effect, and make sure the frequency-encode direction is across the fat–water boundary, not parallel to it.
- To compare STIR and fat sat, use the fat sat with a T_2 -weighted spin-echo scan to get similar contrasts in the final images. Try both techniques at large and small FOVs (you might want to devise a larger phantom for the big FOVs).

7.4 Digital Imaging Artefacts

7.4.1 Partial Volume Artefact

Partial volume artefacts occur wherever a voxel contains a mixture of tissue types. Considering that a typical voxel is $1 \text{ mm} \times 1 \text{ mm} \times 4 \text{ mm}$, it is easy to see that in a structure as complex as the human body, most voxels in any given slice will have a mixture of tissues. We can consider this as a digital imaging artefact, since we are representing a lot of information in a relatively small number of voxels (yes, $512 \times 384 = 196\,608$ does sound like a lot, but it’s not enough!). Look back at Chapter 6 to learn how to optimize the resolution in your scan.

You cannot completely avoid partial volume effects, but you can minimize them by setting the appropriate voxel size for the anatomy and by choosing the correct oblique slice angle. For example, we would use 0.4 mm in-plane resolution for the Internal Auditory Meatus (IAM), because we know that the VIIIth cranial nerve is only about 2.5 mm in diameter and lesions may be only 1 mm in diameter. We also angulate ‘sagittal’ slices so that they are perpendicular

to the nerve, and set the slice thickness to 3 mm or less. Conversely 7 or 10 mm slices are appropriate for the liver, because it is a much larger organ and clinically significant pathology is likely to have a diameter of at least 7 mm.

7.4.2 Cross-Talk

A similar problem with multi-slice imaging is cross-talk between adjacent slices, also known as cross-excitation or (erroneously) cross-relaxation. Cross-talk appears as a reduced intensity on all but the first slice of a multi-slice set, which is often only detectable when comparing the end slices with their neighbours. It happens because the slices are not straight-edged, like a sliced loaf of bread, but have a curved profile (see Figure 7.14a) due to imperfections in the selective excitation pulse. The slice width is defined by the Full Width at Half Maximum (FWHM), so if the slice gap is too small the edges of the slice may overlap with its neighbours (Figure 7.14b). Tissue in the overlapping section is excited by both slices, and experiences a very short effective TR instead of the TR set by the user. It doesn't have time to relax between the pulses, so its signal intensity is reduced. A similar effect occurs with multi-angle oblique acquisitions, e.g. in the lumbar spine, where you may see horizontal black bands across neighbouring slices where the slices intersect.

The best cure for cross-talk is to use an interleaved slice order; excite the odd-numbered slices first, then go back and acquire the even-numbered slices. In this way, tissue in the imperfect slice edges will see a TR much closer to the required TR, instead of a very short TR. This is a default setting on many scanners, so you usually don't need to think about it. If you still see cross-talk effects, you should increase the slice gap, especially in IR sequences since the slice profiles are worse for 180° pulses. However, you should bear in

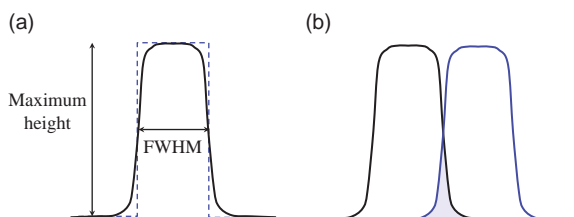


Figure 7.14 (a) The slice excitation profile, ideally rectangular (dotted line), is in reality a curved shape (solid line) whose full width half maximum (FWHM) defines the slice width. (b) When the slice gap is too small the edges of neighbouring slices overlap.

mind that large gaps reduce resolution, as tissues in the gap are not imaged at all. If very thin gaps or contiguous slices are required, it may be better to do a 3D acquisition.

Why isn't the Slice Profile Straight-Edged?

The reason for non-rectangular slice profiles is the nature of selective excitation. The frequency spectrum of the RF pulse, with the strength of the slice-select gradient, defines not only the slice width but also its profile. To get a perfectly rectangular excitation profile, where all protons within the slice receive exactly a 90° pulse and all protons outside the slice are unexcited, the amplitude of the excitation pulse must be a sinc ($\sin(x)/x$) function (Figure 7.15a and Appendix). However, a sinc function is infinitely long in the time domain, and we obviously have to truncate the pulse. In the simplest case, truncating the sinc corresponds to multiplying by a top-hat (see Figure 8.5 and Appendix) in the time domain, and the excitation profile becomes a rect function convolved with a sinc, with significant ripple at the edges of the slice (Figure 7.15b). A better approach is to apodize the sinc, i.e. multiply it by a smoothly varying function such as a Hanning or a Gaussian. The excitation profile then has much less ripple (Figure 7.15c), although its FWHM is slightly greater than the original width.

7.4.3 Phase Wrap-Around Artefact

The phase wrap-around artefact happens when the patient's anatomy continues outside the field of view (FOV) in the phase-encode direction. It causes the signal from the tissue outside the FOV to appear at the opposite side of the image in the phase-encode direction (see Figure 7.16a). The wrapped-in tissue can overlay the real anatomy being scanned potentially interfering with the diagnosis. Although it is most commonly seen in the phase-encode direction, it also occurs in the slice direction in 3D imaging (when the slice-select axis is also phase encoded) and causes the end slices of the volume to wrap into each other.

The best way to avoid phase wrap-around is to use *phase oversampling*, also called the 'no phase wrap' or 'foldover suppression' option. This technique increases the FOV in the phase-encode direction and also increases the number of phase-encode steps so that the pixel size remains the same. The simplest

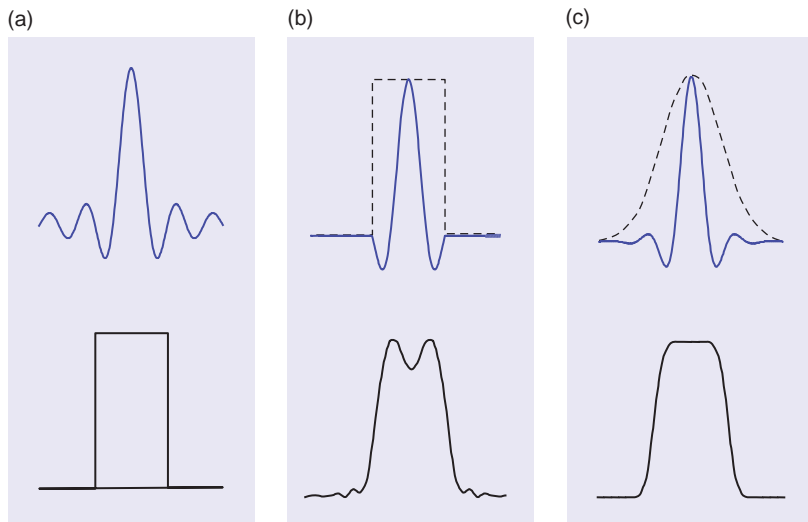


Figure 7.15 (a) The Fourier transform of a rectangle or top-hat (rect) function is a sinc ($\sin(x)/x$). (b) Simply truncating the sinc produces large ripples on the slice profile. (c) An apodized sinc RF pulse produces a cleaner excitation profile, although the FWHM is slightly wider.

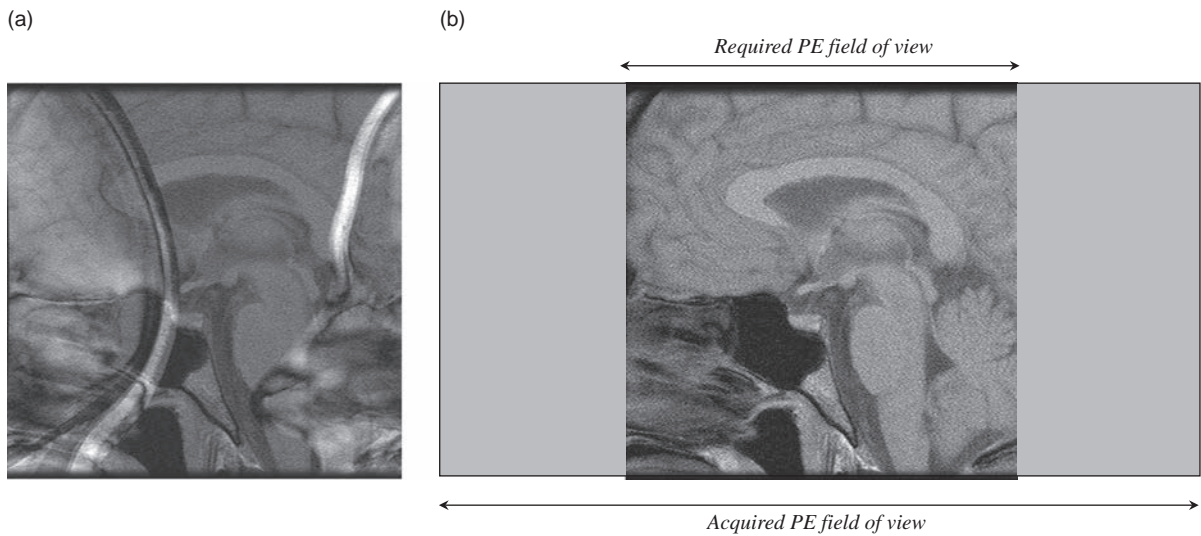


Figure 7.16 (a) Tissue outside the field of view (FOV) in the phase-encode direction wraps into the image. (b) With phase oversampling the reconstructed image is larger than the required FOV, and the computer just throws away the unwanted regions.

implementation of phase oversampling is to simply double the size of the phase-encode matrix (N_{PE}) and also double the acquired FOV, but many scanners allow phase oversampling to be specified as a percentage of the FOV, which optimizes the technique. The anatomy just outside the desired FOV is now properly phase encoded, and the unwanted edges can simply be cut off by the computer, leaving a clean image (Figure 7.16b). Increasing the phase-encode matrix usually extends the scan time, although some scanners adapt the number of signal averages to compensate for this. Suppose we have an FOV of 20 cm with a PE

matrix of 256 and two signal averages. When ‘no phase wrap’ is switched on, the FOV and PE matrix are doubled to 40 cm and 512 respectively. Using one signal average instead of two will maintain the original scan time, and the SNR stays the same. Refer also to Chapter 6 for optimization of scan time and resolution.

7.4.4 Gibbs' Artefact

Gibbs’ artefact, also known as *truncation* or *ringing* artefact, is another consequence of undersampling most often seen in the phase-encode direction, and

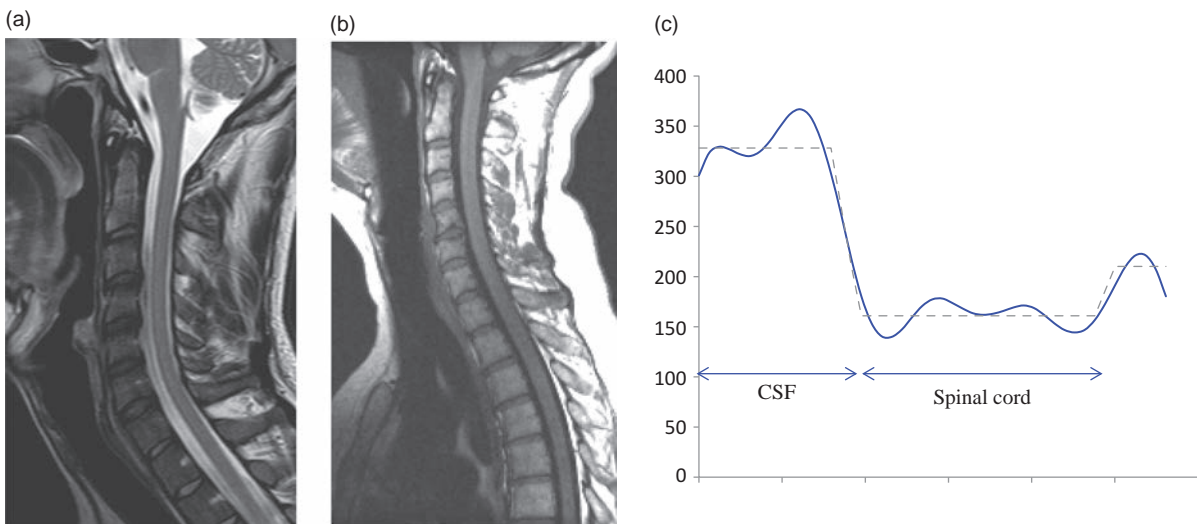


Figure 7.17 (a) A low phase-encode matrix can cause Gibbs' artefact, alternating light and dark bands near a high-contrast interface. (b) Increasing the phase-encode matrix avoids the artefact. (c) A line profile across the structure reveals the typical pattern of Gibbs' ringing.

it can also be seen in the slice direction in 3D scans. It is visible at high-contrast boundaries, where the intensity changes from bright to dark, and appears as a series of alternating light and dark lines superimposed on the image. The intensity of the lines fades away from the boundary, and they follow the contours of the interface. A common example is on T₁w or T₂w images of the cervical spine (Figure 7.17a), where it can mimic the appearance of syringomyelia.

Gibbs' artefact is caused by having the acquisition matrix too small, i.e. the pixel size is too large to accurately represent the high-contrast boundary. As a rule of thumb the phase-encode matrix should never be less than half the frequency-encode matrix. If the artefact reduces the diagnostic quality of the image the only solution is to repeat the scan with a larger phase-encode matrix (Figure 7.17b).

you increase the matrix size you probably won't be able to see it visually, but you can measure the pixel intensities across the boundary to see if it is still there: it shows up as 'ringing' on either side of the boundary (Figure 7.17 c).

7.4.5 Parallel Imaging Artefacts

Parallel imaging techniques, used to speed up acquisitions, can produce artefacts which are ghost-like or, in severe cases, phase-wrap-around (see also Chapter 14). These can arise when the reference image has uneven signal intensity, for example a bright fat signal, or if the patient has moved a lot between the reference image and the diagnostic scan. They are less likely when Auto-Calibration Scans (ACSSs) are used as part of the parallel imaging technique.

It's possible to misinterpret these faint ghosts as 'motion' artefacts. In order to decide if a ghost is due to parallel imaging or motion, you can measure the distance between the ghost and the main image, along the PE direction. In the example shown in Figure 7.18, this distance is 31 mm. Divide the FOV by this distance, e.g. $180 \div 31 = 5.8$. In this example, a parallel imaging factor of 6 was used, very close to the offset of the ghost within the FOV. So it is most likely that this is a parallel imaging artefact, not patient motion.

Another common artefact with parallel imaging is *noise break-through*, usually seen in the centre of the

Try It for Yourself 7: Phase Wrap and Gibbs' Artefacts

You can show the phase-wrap artefact with almost any phantom, although to see the Gibbs' artefact you need something with a sharp high-contrast boundary. Set up the phantom in the head coil or knee coil and scan a localizer. To show phase-wrap, set up a really small FOV in the middle of the phantom, or deliberately move it off-centre in the phase-encode direction. Gibbs' artefact is best seen with a very low matrix of 128–192 on a medium-sized FOV. When

image. It is usually found when the selected acceleration factor is too high to be supported by the receive coil. Signals which are the cross-over point of coil sensitivities have an inherent risk of being misplaced in the unfolded image, and this leads to increased noise appearance.

There are no special techniques to avoid parallel imaging artefacts. Most manufacturers impose limits

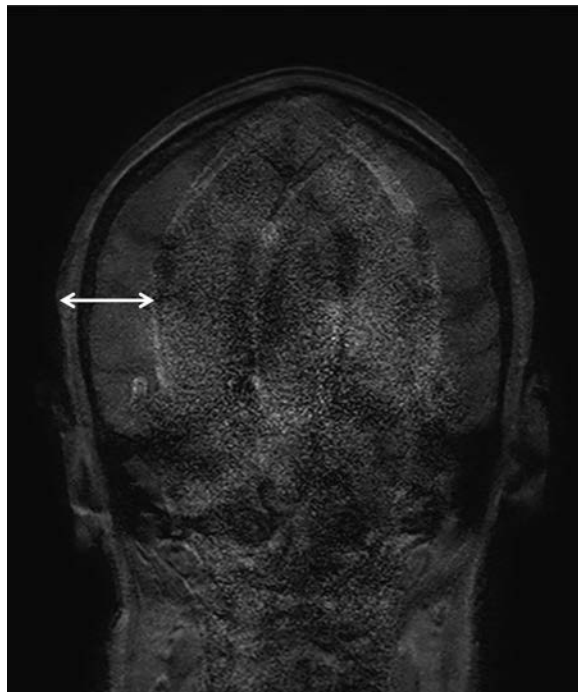


Figure 7.18 Parallel imaging ghost in coronal brain. The distance between ghosts (white arrow) is 31 mm, while the phase-encode FOV is 180 mm. A very high SENSE factor was used to demonstrate this ghost; at normal SENSE factors it is hardly visible.

on the maximum reduction factor which can be used with each receive coil, but you still can run into trouble. For example, when imaging the abdomen with a torso coil, a very large patient may have noise break-through artefact on axial images, whereas a thin patient with the same reduction factor would have no artefact.

7.5 Susceptibility and Metal Artefacts

Susceptibility and metal artefacts are closely related, having essentially the same appearance on images, except that susceptibility artefacts are more subtle than metal ones. Typically a metal artefact consists of an area of zero signal, often with a very high intensity rim on one or two edges (Figure 7.19a) and with neighbouring regions showing significant geometric distortion. The high-intensity areas are caused by signal pile-up; the frequencies of these signals are so disturbed by the local ferromagnetic material that they all end up in the same FE location. Susceptibility artefacts may just have reduced, rather than zero, intensity and may not show any geometric distortion (Figure 7.19b).

As described in Chapter 3, different tissues become magnetized to a different extent when placed in the scanner's magnetic field due to their susceptibility differences. These microscopic field changes increase the dephasing of protons around boundaries between these tissues, reducing the signal intensity of voxels in the area. Most metals have much higher susceptibilities than the body tissues, creating large magnetic field non-uniformities around the object. Since metals are good conductors, they also absorb energy from the RF excitation pulses very easily, and can pose a safety hazard if they heat up.

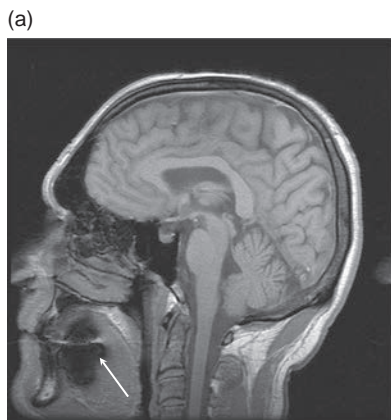


Figure 7.19 (a) Metal artefact from dental work on a spin-echo image. (b) Susceptibility artefact in the temporal lobes on a gradient-echo image.

Susceptibility Artifacts and Voxel Size

Magnetic susceptibility is defined as the extent to which any material becomes temporarily magnetized when it is placed in a large magnetic field (see Box 'Magnetization and the Meaning of Life' in Chapter 4). Among the body tissues, bone and air have the lowest susceptibility; most tissues have mid-range susceptibility, while iron-containing molecules such as haemoglobin and blood breakdown products have the highest. At the boundaries between these tissues, the slightly different magnetic fields within the tissues create micro-gradients which speed up the dephasing between protons on either side of the boundary. The phase change caused by susceptibility is given by

$$\Delta\phi = \gamma \cdot G_i \cdot \Delta r \cdot TE$$

where G_i is the internal magnetic field gradient, and Δr is the voxel size. This equation shows that susceptibility artefacts are worst with large voxels and at long TEs, and can be minimized by reducing TE or increasing the resolution. Often there is not just one simple boundary but many tiny boundaries on a microscopic level, for example in trabecular bone or the mastoid processes. Thus the T_2^* is reduced over a large area, giving the characteristic low signal of susceptibility artefacts. Also keep in mind that susceptibility acts in all three directions, so you can get artefacts extending over neighbouring slices.

RF Inhomogeneity Effects

Larger metallic implants also cause distortion of the radiofrequency field generated by the transmit coil. The implants tend to preferentially absorb RF energy, and thus neighbouring tissues don't receive a proper flip angle. The signals will be reduced and the artefacts are very similar to those produced by the susceptibility inhomogeneities. In practice you cannot separate the effects of RF and static field inhomogeneities just by looking at the images. Both gradient-echo and spin-echo sequences are affected by the RF inhomogeneity problem, and there is no way to avoid it.

Another common artefact caused by RF inhomogeneity is known as 'Moiré' fringes or 'zebra stripes' (Figure 7.20a). These effects are usually seen at the edges of large FOVs, especially where the patient's elbow or sides are very close to the transmitting body coil. Be aware that true-FISP-type sequences can also cause alternating stripes, because these scans are very sensitive to static field inhomogeneities ΔB_0 , but these tend to be thicker stripes and are not necessarily at the edges of the FOV. Don't confuse Moiré fringes with black-band artefacts!



Figure 7.20 Moiré fringes.

Because they are caused by inhomogeneities, metal and susceptibility artefacts are generally worse on gradient-echo images (Figure 7.19b) than spin-echo images, and they can be particularly marked on echo planar images. Spin-echo or TSE images may not show susceptibility artefacts at all. Susceptibility and metal artefacts can be minimized by using a high receiver bandwidth, or reducing the echo time (if T_{1w} or PDw contrast is required), but they cannot be completely avoided. If the images are severely degraded by metal artefacts, only (fast) spin-echo sequences should be used to acquire the data.

Metal artefacts also raise the question of safety for the patient, since the preferential absorption of RF can cause a local temperature rise. In this book we don't provide a list of MR compatibility for implants, as there are other texts and websites that can be consulted. Rather we hope to give you an understanding of the potential interactions between implants and the various fields used in imaging, which will help you to work out for yourself whether or not a particular implant is safe to scan. Chapters 2 and 20 include other aspects of safety advice.

In the last three years, new pulse sequence techniques have been developed which minimize the artefact around metal implants. They are based on TSE, and use extra phase encoding in the slice direction to collect information about signal displacements due to the metal. SEMAC (Slice Encoding for Metal Artefact

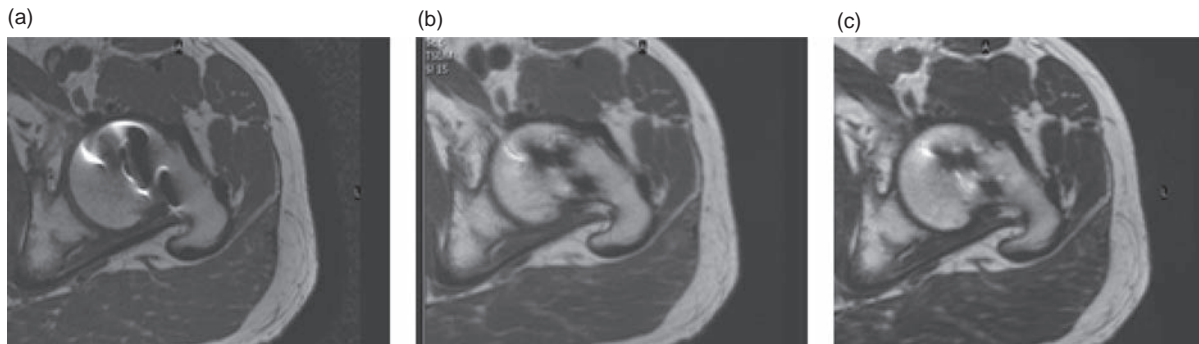


Figure 7.21 Metal-artefact-reduction scans on an example of hip screws. (a) High-bandwidth TSE; (b) SEMAC; (c) MAVRIC. Note that both SEMAC and MAVRIC offer similar reduction of artefact compared with conventional TSE, in this particular example.

Correction) is a 2D multi-slice technique with a small number of phase encodes per slice. By combining the information from all the slice phase encodes, the SEMAC scan generates an improved slice profile and resolves much of the artefact. MAVRIC (Multi-Acquisition Variable-Resonance Image Combination) is a 3DTSE method with a limited bandwidth used for excitation. Like SEMAC, MAVRIC is repeated with a small number of different bandwidths, to resolve the frequency displacements of the metal artefact. When these images are combined, the result has much lower artefact around the metal implant (Figure 7.21).

Both SEMAC and MAVRIC are time-consuming scans, because they use extra slice-encoding steps. Although both techniques can provide all types of image contrast, commercial availability is limited. At the time of writing, MAVRIC is only available as PDw, while SEMAC is being introduced with T₁w and STIR variants.

7.6 Equipment Artefacts

7.6.1 Zipper Artefact

The so-called zipper artefact, due to RF breakthrough, is probably the most common equipment artefact. It appears as a line of alternating light and dark pixels, sometimes two or three pixels wide, extending across the image in the phase-encode direction (see Figure 7.22). Occasionally there will be multiple zippers, regularly spaced across the image, but usually there is just one.

The cause of the zipper is external RF radiation finding its way into the magnet room and being picked up by the imaging coils. This may be due to a break in the RF-screened room – the metal shield built into the

walls, floor and ceiling of the scan room. In this case the artefact will be present on all images. It may also be a problem in the system itself, either as a result of a component fault, or static electrical discharges caused by dissimilar materials rubbing together (e.g. cable insulation lying next to the metal magnet container). In the latter case, it might only show up on certain images. In all cases, the manufacturer's engineers should be called first to investigate the problem, followed by the RF cabin supplier if needed.

A more common cause is patient monitoring equipment, especially if it relies on metallic leads or mains leads going through the waveguides into the scan room. (This is a guaranteed way to get zippers in your image, but sometimes you have no choice, you have to work with what you've got.) The leads pick up RF waves from the environment and carry them through the Faraday cage, then radiate them into the room where they are picked up by the RF imaging coils. Even if there are no leads going through the waveguides, the power supplies may generate RF noise while charging or when fully charged, which may also be picked up by the imaging coils if the equipment has defective RF shielding. These problems can be particularly difficult to track down. Although it is more expensive, all monitoring equipment used should be specially designed for use in the MR room – it saves a lot of heartache over zipper artefacts!

More RF Interference

Generally the zipper artefact is the result of external RF, which is not coherent with the phase-encode gradient and it thus appears across the whole image. In rare circumstances the RF may be coming from

faults within the MR system, in which case it may be coherent and will appear as a very intense spot at the centre of the image. Another rare possibility is RF being carried on the mains electricity, which creates a 50–60 Hz modulation and a regularly spaced series of fairly faint zipper artefacts. Providing the monitoring equipment has been eliminated as a possible cause, any of these problems needs investigation by the system engineers.

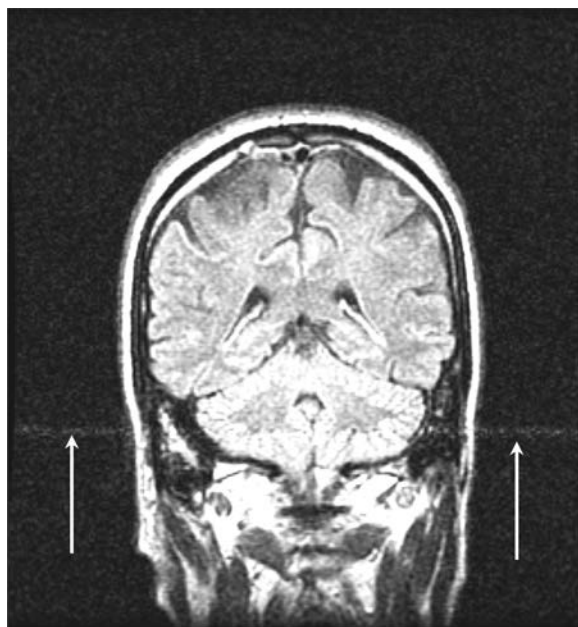


Figure 7.22 RF break-through artefact.

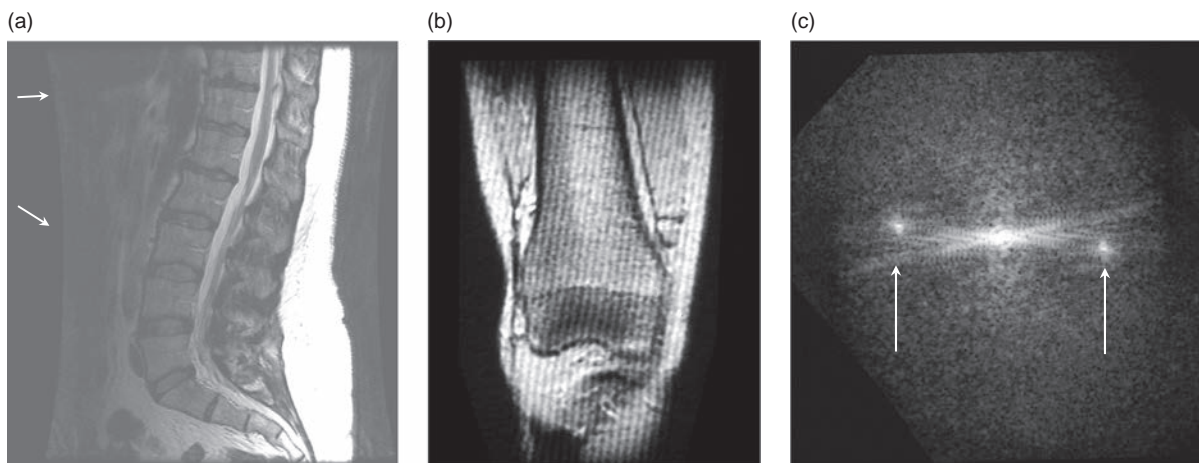


Figure 7.23 (a) Curved edges on a large FOV after compensation for gradient inhomogeneities. (b) Corduroy or herring-bone artefact is caused by (c) a noise spike in k-space.

7.6.2 Gradient Non-Linearity

The gradients only produce linear magnetic field gradients over a limited distance, and very large FOVs may include regions of gradient non-linearity; for example, whole-body or spine images. The effect of non-linearities is to distort the image, tending to compress the image information at the edges of the FOV. Many systems apply a correction to the images to stretch out the pixels, and on rectangular FOV a curved edge can be seen (Figure 7.23a). This is quite normal and also unavoidable.

7.6.3 Herring-Bone Artefact (Spike Noise)

The ‘herring-bone’ or ‘corduroy’ artefact is a regular series of high- and low-intensity stripes extending right across the image (Figure 7.23b). The intensity variation, the angle and the spacing of the stripes are all variable, and it often appears on just one or two images in a multi-slice set. It is caused by spike noise in the raw data (Figure 7.23c), whose Fourier transform (a series of spikes) is then convolved with all the image information. In theory the bad data points can be removed and the image reconstructed again, but usually the only solution is to re-scan the image. A single image with a corduroy artefact is probably just bad luck, but you are more likely to see problems with several different scans, especially diffusion-weighted images. Multiple bad data points in a single image give more severe artefacts which dramatically reduce SNR. This is a symptom of ‘spiking’ around the system, often caused

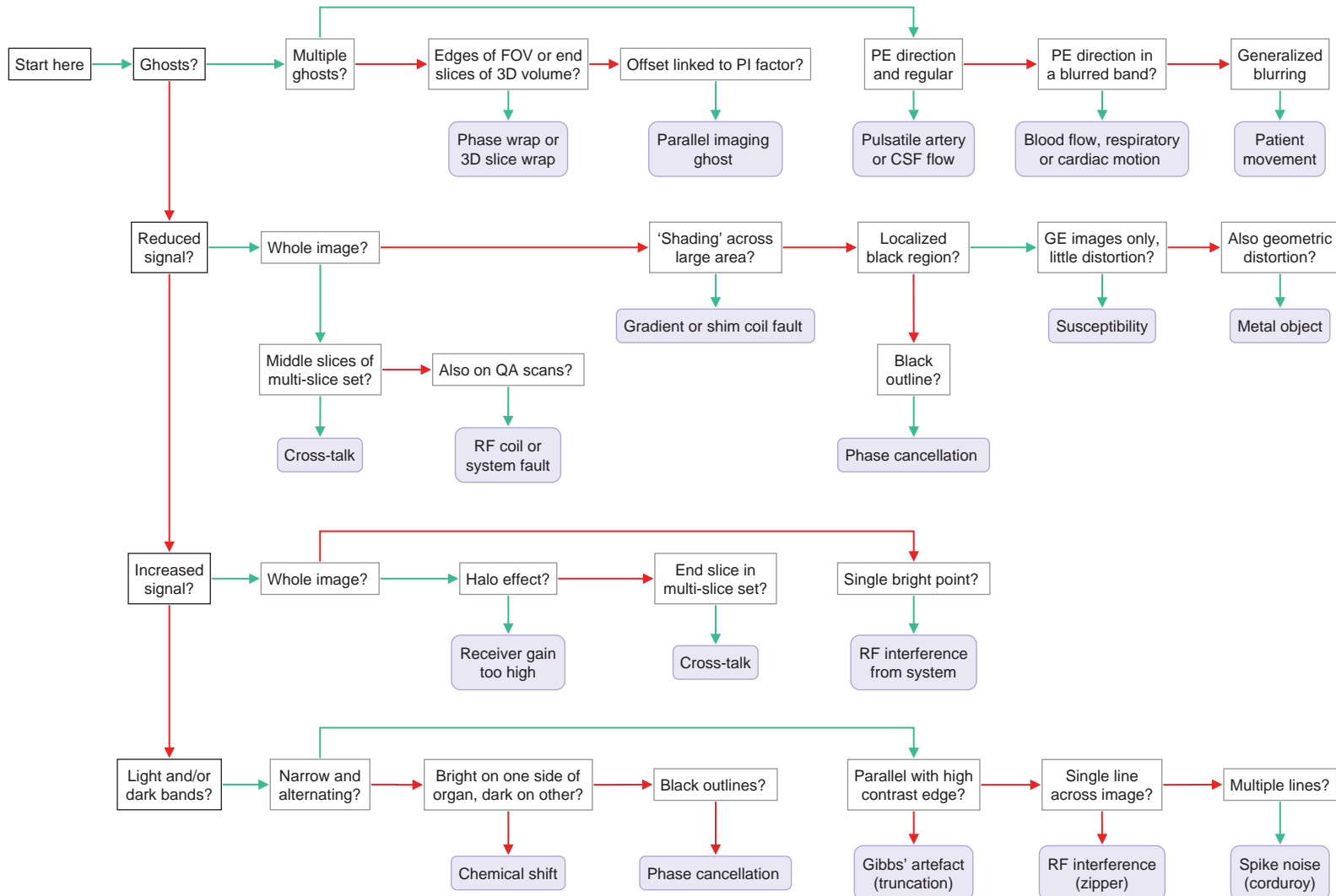


Figure 7.24 The artefacts flowchart. Start by identifying the symptoms on the degraded image, then ask yourself the questions in the boxes. Follow the green arrows if the answer is 'yes' and the red ones if it's 'no'. You should arrive at one of the blue boxes, which will tell you the most likely cause of your artefact.

by static electrical discharges when components rub against the metal of the magnet, particularly when humidity is low. It is recommended to call the service engineers to investigate the problem.

7.7 What's Causing this Artefact?

We hope the flow chart shown in Figure 7.24 will help you to decide the most likely cause of your artefact, but we can't guarantee it! Bear in mind that serious

system artefacts are less likely than patient motion or susceptibility effects.

See also:

- Flow appearances and MR angiography: Chapter 15
- Cardiac MRI: Chapter 16
- Safety of metal implants: Chapters 2 and 20
- Optimizing SNR and resolution: Chapter 6
- Phase encoding: Section 8.5.2

Further Reading

Brown RW, Cheng YCN, Haacke EM, Thompson MR and Venkatesan R (2014) *Magnetic Resonance Imaging: Physical Principles and Sequence Design*, 2nd edn. Hoboken, NJ: John Wiley & Sons, various chapters.

Elster AD and Burdette JH (2001) *Questions and Answers in Magnetic*

Resonance Imaging, 2nd edn. London: Mosby-Yearbook, chapter 4. Also on the web at <http://mri-q.com> [accessed 23 March 2015].

McRobbie D and Semple S (eds) (in preparation) *Quality Control and Artefacts in MRI*. York: Institute of Physics and Engineering in

Medicine. Available via www.ipem.ac.uk.

MR Technology Information Portal, artefacts section: www.mr-tip.com/serv1.php?type=art [accessed 8 May 2015].

Radiopaedia, <http://radiopaedia.org/articles/mri-artifacts> [accessed 8 May 2015].

Spaced Out: Spatial Encoding

8.1 Introduction

By now you are probably a regular user of the MR scanner and are familiar with the appearance of images (as seen in Chapter 3) produced from various common sequences (Chapter 4). You may have a feel for the digital nature of the images as pixels, voxels and slices (Chapter 5), how parameter changes affect them (Chapter 6) and the artefacts that may sometimes arise (Chapter 7). In a way, that concludes much of your basic hands-on training. In this chapter we begin to provide the theoretical basis for how the scanner produces images from MR signals. Chapter 9 will continue to develop the theory by looking at how the signals are made in the first place.

It should be stressed here that understanding image formation in MRI is neither simple nor obvious and most people struggle to conceptualize it. There are a number of ways of understanding this and what matters is that you find a way that makes sense to you. Persistent students also find that eventually the penny always drops, a light bulb inside their brain suddenly switches on and usually, like the current in a superconducting magnet (or the skill of bicycle riding), it becomes permanent.

An understanding of the image-formation process is helpful for obtaining the optimum diagnostic information from an examination, modifying or creating new protocols, recognizing common image artefacts and taking measures to overcome or avoid them. It will also help as a basis for understanding the pulse sequences considered in Chapters 12, 13 and beyond. It is not just theory. It is the heart and soul of MRI.

In this chapter you will see that:

- magnetic field gradients form the basis of MR signal localization;
- 2D slices are produced by the combination of an excitation RF pulse and simultaneous slice-select gradient;

- the in-plane MR signal is encoded in terms of the spatial frequencies of the object using phase-encoding and frequency-encoding gradients;
- we collect or sample every spatial frequency that can exist within the image before we Fourier transform these data (known as ‘k-space’) to produce the image directly;
- inadequate or erroneous k-space sampling leads to certain image artefacts.

8.2 Anatomy of a Pulse Sequence

You will have noticed that some scans take a long time to acquire and involve loud banging sounds from the scanner. Each sound is produced by gradient pulses applied to localize the MR signals in the body. In MR the static magnetic field B_0 ('B-nought') is constantly present. The gradients are not. They are applied in a controlled fashion to form a pulse sequence. An MR pulse sequence diagram is a simple means of showing how the RF and gradients are applied. The vertical axis represents pulse amplitude and the horizontal axis is time. Figure 8.1 shows

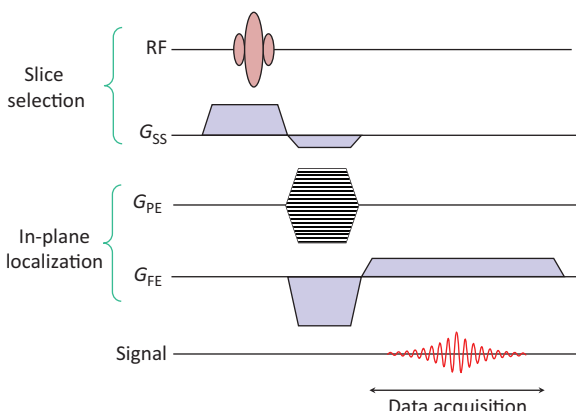


Figure 8.1 Basic gradient-echo MR imaging sequence. Amplitude is shown vertically, time horizontally. G_{SS} is the slice-selective gradient, G_{PE} the phase-encoding gradient and G_{FE} the frequency-encoding gradient.

the basic gradient-echo MR imaging sequence that we will use to illustrate the image-formation process. For the present we will only say what each bit does (how and why will follow).

First (top line), an RF pulse is applied simultaneously with a *slice-selective* gradient G_{SS} (line 2). The RF pulse stimulates the MR interactions in tissue which lead to the MR signal. By combining the RF *excitation* with a gradient the MR interactions are restricted to a two-dimensional plane, slab or slice. Any physical gradient G_x , G_y or G_z or combinations of these can be used for this purpose, allowing us to produce transverse, sagittal or coronal, oblique or double oblique slices.

Next, in line 3, *phase encoding* is applied in a direction orthogonal to the slice selection. This encodes the MR signal in the phase-encode direction. In line 4, the *frequency-encode* or readout gradient is applied in the third direction and finally line 5 shows the time when the MR signal is measured or *acquired*. Note that this is during the frequency-encode gradient but after the phase encoding. The whole sequence pattern has to be repeated for every ‘line’ of data, corresponding to a different value of phase-encode gradient until the data or *k-space* matrix is filled. A time period, TR, occurs between the application of one RF excitation and the next.

The total scan time is

$$\text{Scan time} = \text{NSA} \times \text{TR} \times N_{\text{PE}}$$

where NSA is the number of signal averages and N_{PE} the size of the phase-encoding matrix.

Once all the data are acquired, a two-dimensional Fourier transform is applied. This converts the data, already encoded as *spatial frequencies*, into an image. Reconstruction in MRI is generally simpler than in X-ray CT; most of the hard work has been done during the acquisition by the gradients.

Although this is the simplest possible MR imaging sequence, once you have grasped the purpose of each element, it is relatively easy to make the jump to more complicated sequences as they all have the same basic elements. We will describe three of the steps towards localization – slice selection, phase encoding and frequency encoding – in some detail. First, however, it is important to make sure you understand some underpinning principles.

8.3 From Larmor to Fourier via Gradients

The basic groundwork for this chapter is a knowledge of the Larmor equation to describe the behaviour of excited nuclei (or ‘spins’), an understanding of the effect of magnetic field gradients and familiarity with the concept of spatial frequencies. Mathematical skills that would be useful include an understanding of sine waves and an awareness of Fourier transforms (see Appendix). If you already know about sine waves you can skip to Section 8.3.1.

A purely sinusoidal signal or waveform has three basic properties: amplitude, frequency and phase. Amplitude describes how large the signal is, measured in real-world units like volts, or arbitrary ‘signal units’. Frequency, measured in hertz (Hz), describes how rapidly in time the instantaneous magnitude of the wave is changing: 1 Hz equals one cycle or rotation per second. Phase describes the instantaneous position within the cyclic variation in terms of an angle. It is measured in degrees or radians, and can vary from 0° to 360° (0 – 2π radians), thereafter repeating itself. It is sometimes helpful to think of a phase as the angle displayed on a ‘clockface’. See Appendix A.2.

8.3.1 Larmor Equation

Sir Joseph Larmor was an Irish physicist who died four years before the discovery of NMR, but who nevertheless predicted the relationship between the *precession* frequency of spins and the magnetic field strength (he also has a crater named after him on the moon). In a simple picture we can think of the spins as rotating at the *Larmor* or *resonance frequency*, which is also the frequency of the MR signal given by the equation

$$\text{Frequency} \approx 42 \times \text{magnetic field}$$

where frequency is in megahertz (MHz) and magnetic field is in tesla (T). The good news is that this is the only equation you need to know to understand spatial localization, although you do need to develop a thorough understanding of its consequences. The number 42 is called the *gyro-magnetic ratio* (which has the symbol γ , pronounced ‘gamma’) and is a property of the nucleus in question. Its value more exactly is 42.56 MHz T^{-1} for hydrogen (water or fat protons). Other nuclei (e.g. phosphorus) have a different value of gamma, but for most of MRI we only care about hydrogen.

So, if the magnetic field strength of the MR magnet is 1.5 T, the MR signal obtained has a frequency of

$$1.5 \text{ T} \times 42 \text{ MHz T}^{-1} = 63 \text{ MHz}$$

Similarly, at 3 T the Larmor frequency becomes 126 MHz. An RF pulse applied at 63 MHz in a 1.5 T MR system will result in MR signals of a periodic (sinusoidal) nature also at 63 MHz. These can be detected by a coil and receiver tuned, in the same manner as a transistor radio, to this frequency. The proportionality of field and frequency underlies all of the image-formation process.

Where's the Bar?

Conventionally, the Larmor equation is written as

$$\omega_0 = \gamma B_0$$

where ω_0 is the angular frequency of the protons ($\omega = 2\pi f$). Using this scheme gives γ a value of 2.67×10^8 radians s $^{-1}$ T $^{-1}$. We find this number unmemorable and angular frequencies are not as intuitively understandable as regular (scalar) frequencies. When the use of scalar frequency is helpful or important for understanding, we will use the symbol $\bar{\gamma}$ ('gamma bar'), which is equal to $\gamma/2\pi$ (i.e. 42 MHz T $^{-1}$). The use of gamma and gamma bar only affects the material in the advanced boxes. Beware, not all authors realize whether or not they are using the bar.

This signal alone is insufficient to produce an image of a patient lying within the magnet bore because we would have no way of assigning parts of the signal to where in the patient they originated. To achieve this localization we now need to introduce the concept of magnetic field gradients, or in short 'gradients'.

8.3.2 Gradients

In MRI the term 'gradient' refers to an additional spatially linear variation in the static field strength in the z direction, i.e. along B_0 . For example an ' x gradient' (G_x) will add to or subtract from the magnitude of the static field at different points along the x axis or x direction. Figure 8.2 shows representations of the main field (a) and the field plus an x gradient (b) with the total field represented by the spacing of the 'field lines'. Gradient field strength is measured in milli-tesla per metre (mT m $^{-1}$).

In Figure 8.2a all the protons (spins) experience the same field and have the same frequency. When a gradient is added (b) the magnetic field produced by the gradient adds to the main field B_0 . At the centre ($x = 0$) the total field experienced by the nuclei is simply B_0 , so these spins resonate at the Larmor frequency. As we move along the x direction, however, the total field either increases or decreases linearly and thus these protons resonate faster or slower depending upon their position. Faster or slower

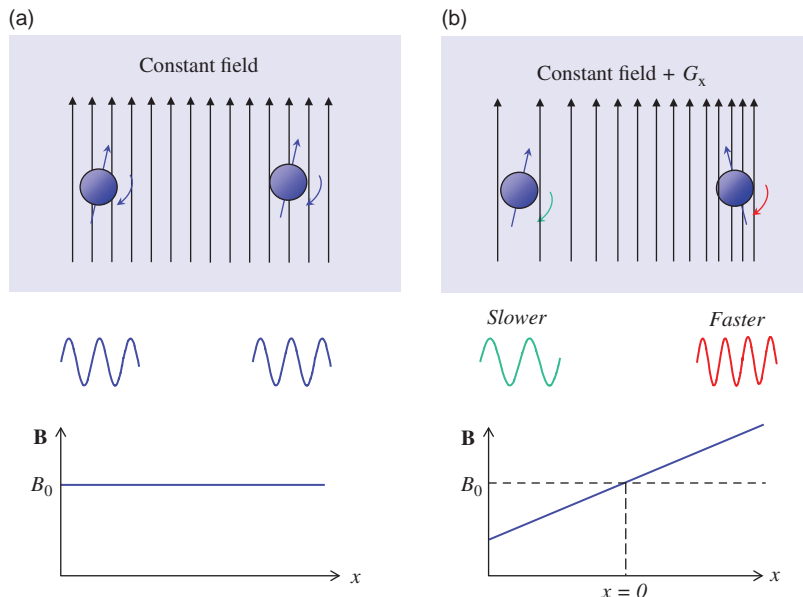


Figure 8.2 Effect of field gradient on nuclei. (a) B_0 only, all nuclei precess at the same frequency. (b) B_0 plus gradient G_x – precession frequency now depends upon position.

precession is detected as higher or lower frequencies in the MR signal, and so frequency measurements may be used to distinguish between MR signals at different positions in space. Gradients can be applied in any direction or orientation. Three sets of gradient coils – G_x , G_y and G_z – are included in the MR system. They are normally applied only for a short time as pulses. It is these three sets of gradients that give MR its three-dimensional capability.

The Effect of Gradients

Mathematically the three orthogonal spatial gradients of B_z are defined as

$$G_x = \frac{\partial B_z}{\partial x} \quad G_y = \frac{\partial B_z}{\partial y} \quad G_z = \frac{\partial B_z}{\partial z}$$

When a gradient (e.g. G_x) is applied, the total field in the z direction experienced by nuclei will be dependent upon the position in space, e.g.

$$B(x) = B_0 + x \cdot G_x$$

When a gradient is applied the Larmor frequency will depend upon the total z component of the magnetic field and thus becomes spatially dependent, e.g. for the x gradient.

$$f(x) = \gamma(B_0 + x \cdot G_x)$$

where we are using $\gamma \approx 42 \text{ MHz T}^{-1}$.

8.3.3 Dephasing and Rephasing

If we have a uniform distribution of water producing an MR signal and we apply a gradient G for a given time, what will happen to the MR signal? There will be variations in frequency of the MR signal, either faster or slower, depending upon position, as in Figure 8.2. The spins which are precessing faster, because of the action of a gradient, appear to move apart or dephase (see Figure 8.3), and those which are precessing slower dephase in the opposite direction. The combined effect is often thought of as a ‘fanning out’ due to dephasing. The speed at which this happens depends upon the gradient amplitude or strength. The total angle of dephasing depends upon the product of the gradient strength and its duration, also known as the gradient moment.

If we now apply another gradient with a reversed sign or polarity (i.e. negative amplitude) as shown in Figure 8.4, the signals which sped up before now will start to precess slower and the ones which had travelled

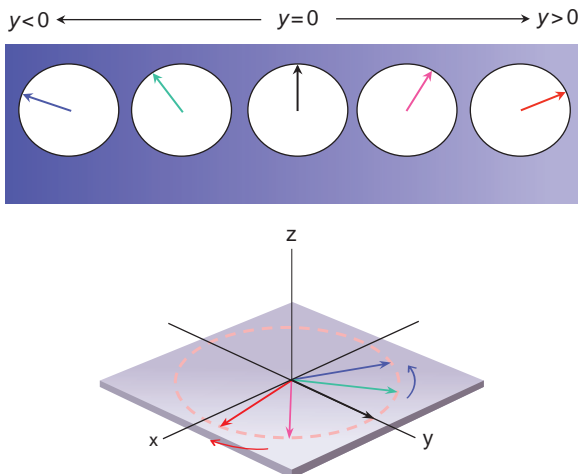


Figure 8.3 Effect of gradient on MR signal (transverse magnetization). Signal originating from different positions along the y -gradient axis will have a position-dependent phase change. These are shown as clock-face diagrams in the upper part of the figure. It is usual in the MRI literature to ‘collapse’ or superimpose these all on the same xyz -axes as in the lower portion.

with a slower rotation will now speed up. The spins will start to rephase until, when the gradient moments are equal, the components of the MR signal will all be pointing in the same, original direction. At this point in time we get a measurable MR signal, known as a gradient echo. Each gradient pulse is known as a lobe and is described as dephasing if it occurs first, or as rephasing if it corrects for an earlier dephasing.

Gradient Dephasing

In the rotating frame (see Box ‘My Head’s in a Spin!’) we can view the action of the gradient as a dephasing of components of transverse magnetization in the xy plane. The phase change at any time and place is

$$\phi(x, t) = \exp(iy \cdot x \cdot G_x \cdot t)$$

and it evolves for as long as the gradient is applied. Once the gradient is switched off, the accumulated phase changes remain encoded until the transverse magnetization decays to zero or further gradients are applied. A gradient echo results from the application of gradient of equal moment but with the opposite polarity. The echo time TE occurs for

$$\int_0^{TE} G^-(t) \cdot dt = - \int_0^{TE} G^+(t) \cdot dt$$

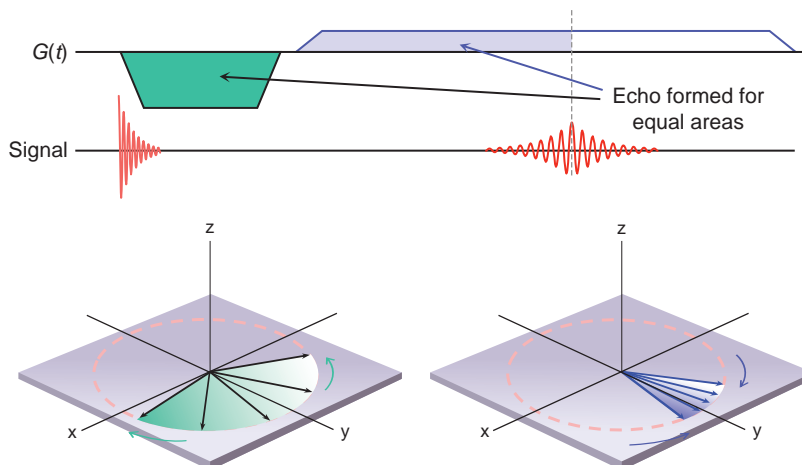


Figure 8.4 Rephasing of signal by a bipolar gradient to form a gradient echo.

where the plus and minus signs refer to the positive and negative lobes of the gradient waveform. Signal loss due to main B_0 field inhomogeneity is not restored. The MR signal decays exponentially with time constant T_2^* .

My Head's in a Spin!

What's the rotating frame? It's a set of xyz axes that rotates around the z axis at the Larmor frequency. In this frame of reference, a proton at exactly the Larmor frequency is static, which makes all the maths a bit more straightforward. We're not going to say any more than that for now, because it's easy to get confused. Once you have come to the end of this chapter and read the next (Chapter 9), you will realize that all along in this chapter we have been subversively operating in the 'rotating frame of reference'. You don't need to worry about this at all; in MR we tend to naturally adopt this frame of reference; after all, we live on one! The rotating frame is fully explained in Box 'The Rotating Frame of Reference' in Chapter 9.

8.3.4 Fourier Transforms

Joseph Fourier was a French mathematician who enjoyed a colourful life spanning science, politics and high society during the time of Emperor Napoleon Bonaparte. His lasting achievement was the invention of the *Fourier transform*, which entirely underpins the theory of MR imaging. Fourier's great idea was that any signal or waveform in time could be split up into a series of 'Fourier components', each at a different frequency. For example, the sound of a musical

instrument could be described either by the actual pressure waveforms it produced in the time domain, or by the appropriate magnitude of its constituent frequencies or its spectrum in the frequency domain. An acoustic signal, such as that produced by a musical instrument, is an example of a one-dimensional waveform, and when Fourier transformed gives a one-dimensional spectrum. In MR we use two- or three-dimensional Fourier transforms. Variables which relate to each other in their respective domains are called Fourier transform pairs. Examples are shown in Figure 8.5. One of the key features of the Fourier transform is that 'less is more': if a shape is small in one domain, its transform will be large in the other.

8.4 Something to get Excited About: The Image Slice

Slice selection or selective excitation is the process whereby MR signals are restricted to a two-dimensional plane or slab within the patient. The position, width and orientation of the slice can all be controlled by the operator.

8.4.1 Selective Excitation

In selective excitation we apply a specially designed RF excitation pulse at the same time as a gradient (the slice-selective gradient) as shown in the top two lines of the pulse sequence diagram in Figure 8.1. The designer RF pulse contains a narrow range of frequencies of RF, centred about the Larmor frequency. In technical terms we say it has a 'narrow bandwidth'. (Note that this is different from the receive bandwidth: the transmit bandwidth is not operator-controlled.)

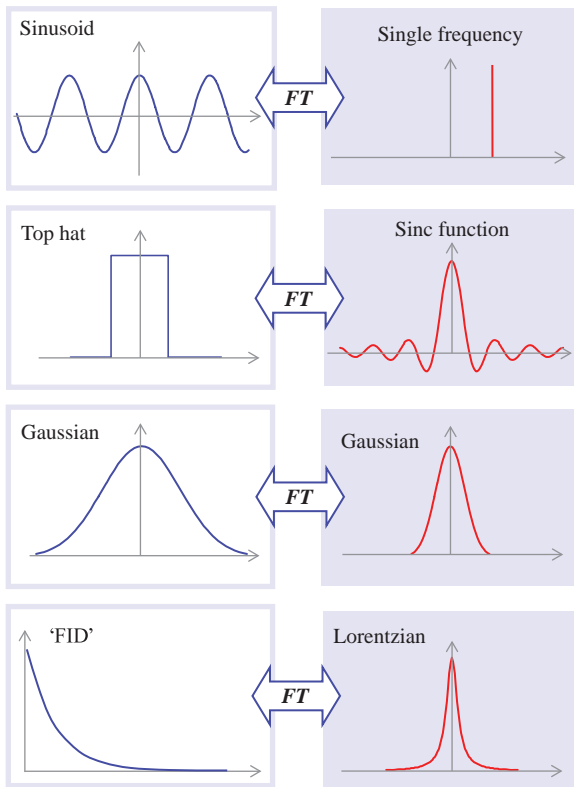


Figure 8.5 Spectra and waveforms (Fourier transform pairs). A narrow extent in one domain is equivalent to a wide extent in the other. FID stands for free induction decay.

In contrast, a simple block RF pulse which is simply switched on and then off again has a wide bandwidth because it is a sinc function in the frequency domain (see Figure 8.5).

The principle of slice selection is illustrated in Figure 8.6. The presence of the gradient causes the resonant frequency (required for producing MR signals) to vary with position in the gradient direction. At the isocentre where the additional value of the gradient is zero, the normal Larmor frequency will apply. Further away along the selection axis, either a higher or lower RF frequency will be needed. If the required frequency is present within the RF pulse's bandwidth then resonance will happen, i.e. protons will be excited. If the required frequency is not present within the RF pulse's bandwidth then nothing will happen. Thus, excitation for the production of signal can only take place at or close to the isocentre. If the slice-select gradient is applied along the z axis, the resultant slab of excited nuclei or slice will form a transverse plane.

In the advanced Box ‘Slice Selection Maths’ (which is for those who wish to know more about the maths), we show that the shape of the physical slice is related to the shape of the spectrum of the RF pulse. We could use Figure 8.5 to give an indication of the distribution of flip angle in the slice-select direction (the slice profile) for various RF waveforms. Commonly, a version of a ‘sinc’ or ‘sinx/ x ’ pulse (an apodized or truncated sinc) is used for the RF, which gives an approximately rectangular slice profile.

Slice Selection Maths

For a selective pulse the magnetic field gradient introduces a position-dependent spread Δf in the Larmor frequency about the carrier frequency f_0 such that

$$\Delta f(z) = \gamma \cdot z \cdot G_z$$

using the z gradient for excitation (to produce a transverse slice). Let us apply an amplitude-modulated RF 90° pulse with a form

$$B_1(t) = A(t) \cos(2\pi \cdot f_0 \cdot t)$$

where A is the pulse envelope or shape and f_0 is the ‘carrier’ frequency. Applying a result which will be derived in Section 9.3, the resultant flip angle will be (approximately)

$$\alpha(z) = \gamma \int A(t) \cdot \exp(i\gamma \cdot z \cdot G_z \cdot t) dt \\ = \gamma \int A(t) \cdot \exp(i2\pi \cdot \Delta f \cdot t) dt$$

The integral is the Fourier transform of $A(t)$, i.e. $a(z) = \gamma A(f)$. So the shape of the RF pulse’s spectrum determines the shape of the slice with regard to the selection direction (in this case z).

The position of the slice is given by

$$z = \frac{f_1 - f_0}{\gamma \cdot G_z}$$

where f_1 is the shifted carrier frequency. Thus for a slice shift of 100 mm, using a 5 mT m^{-1} gradient an RF carrier frequency shift of about 20 kHz is required. The slice width or thickness is given by

$$\text{slice width} = \frac{\text{RF bandwidth}}{\gamma \cdot G_z}$$

So for a 5 mm thickness with a 5 mT m^{-1} gradient the RF bandwidth needs to be approximately 1 kHz. This implies an RF pulse duration of the order of 1 ms.

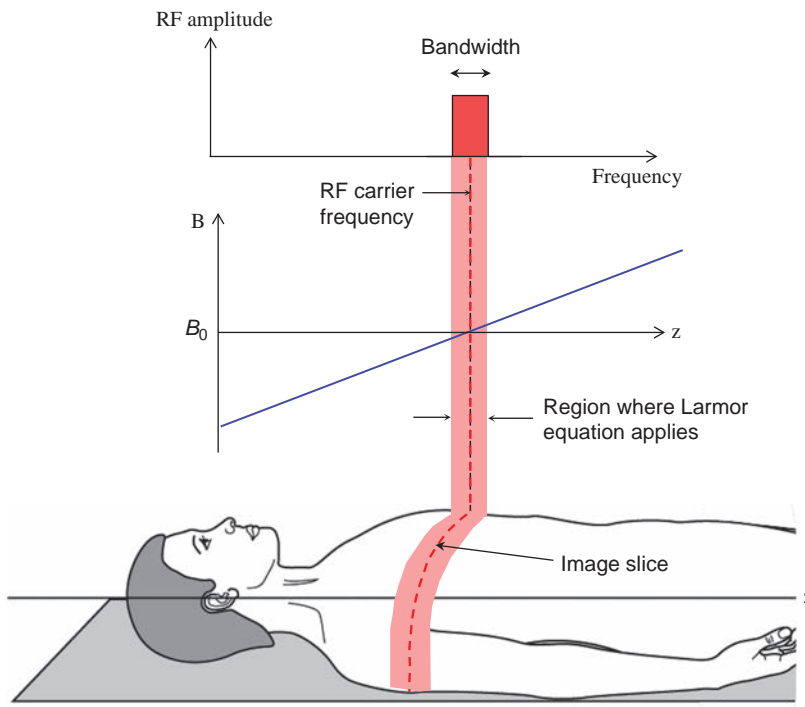


Figure 8.6 Selective excitation of an image slice by applying a shaped RF pulse and a field gradient at the same time.

8.4.2 What's Your Orientation? Manipulating the Slice

All features of the slice can be manipulated by adjusting the gradient or RF waveform properties, i.e. electronically, rather than having to move the patient as required in X-ray CT. These include position, orientation and thickness. Box 'Slice Selection Maths' contains a more mathematical description of these features.

First, the position of the slice can be varied simply by changing the basic (or carrier) frequency of the RF pulse but using the same gradient strength. The region which now fulfils the MR resonant condition will have moved. Second, the thickness of the slice can be controlled by changing either the shape of the designer RF pulse (changing its bandwidth) or the strength of the gradient. A stronger gradient will result in a thinner slice (Figure 8.7a). Alternatively, we can use a narrower RF pulse bandwidth. According to Fourier theory, this means using a longer duration RF pulse. Notice the 'less is more' principle again: you can have a thinner slice but it will take longer to excite (Figure 8.7b).

Third, the orientation of the slice can be varied by using a physically different gradient axis. The

selected slice is always orthogonal (perpendicular) to the gradient applied. So far we have assumed the application of G_{ss} in the z -axis, along the patient, giving a transaxial or transverse slice. If we use G_x as a slice-select gradient we get a sagittal slice. For a coronal slice we use G_y (as was shown in Figure 5.8). Oblique and double oblique slices can be created using combinations of G_x , G_y and G_z . See Box 'An Oblique View'.

An Oblique View

Oblique slices may be obtained by driving two orthogonal gradients in proportion to the sine and cosine of the angle required, e.g. to obtain a transverse slice rotated through an angle ϕ from the x axis requires the simultaneous application of

$$G_x = G_{ss} \cos \phi \quad G_y = G_{ss} \sin \phi$$

while the generation of a double oblique angulation of ϕ from x and θ from z requires the application of

$$G_x = G \sin \theta \cos \phi, \quad G_y = G \sin \theta \sin \phi, \quad G_z = G \cos \theta$$

(a)

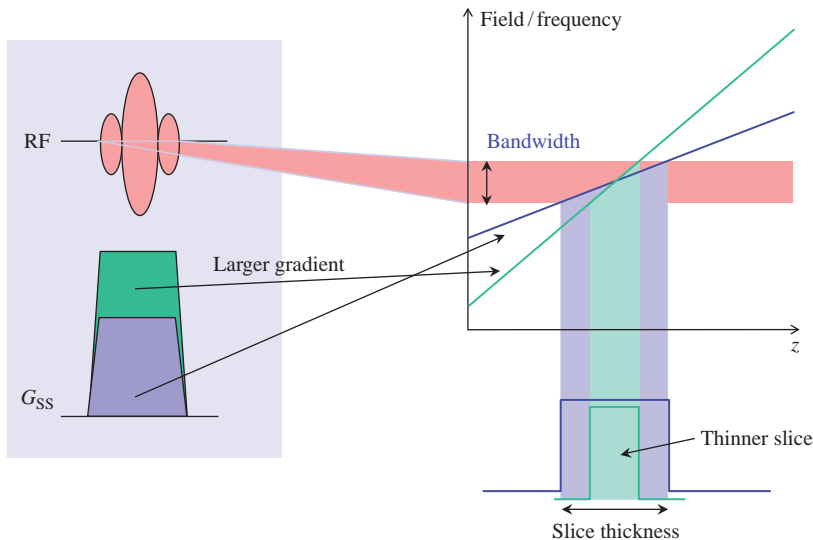
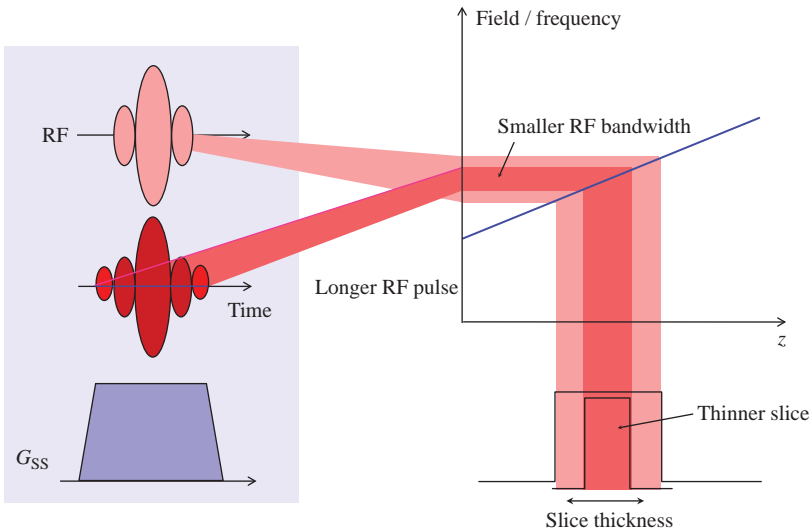


Figure 8.7 Dependence of slice thickness on (a) gradient strength and (b) RF transmit bandwidth. Larger gradient amplitude and longer RF pulses both result in thinner slices.

(b)



8.4.3 Multiple Slices

It doesn't take very long to excite a slice and collect its echo, typically much less than the TR needed to control the image contrast. We can use the 'dead time' within the TR period to acquire multiple interleaved slices (see Section 5.7). By applying a slice-select gradient and changing the central frequency of the RF pulse we can move the position of the slice (Figure 8.8). This is the standard means of image acquisition. A multi-slice interleaving scheme is shown in Figure 8.9. It is possible to acquire the slices in any order. Normally an 'interleaved' slice order is

used, e.g. for an eight-slice sequence acquiring the following positions in this order: 1, 3, 5, 7, 2, 4, 6, 8 (see Section 5.7).

8.4.4 Rephasing

In Figure 8.1 you will have noticed a negative portion of the slice-select gradient. This is necessary to rephase the MR signal in order to get the maximum possible signal. While the selective excitation process is occurring, the signal being generated is also being dephased by the gradient. We normally consider the action of the RF pulse to occur at its centre in time. In

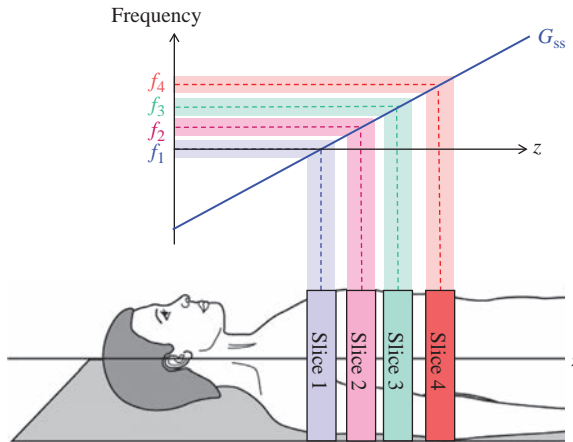


Figure 8.8 By changing the RF centre frequency, multiple slices may be acquired at different locations quite independently of each other.

this case, a rephasing gradient moment of half the slice-selection gradient is required to leave all the spins in phase throughout the slice.

8.5 In-Plane Localization

In MRI we use the gradients to measure the two- (or three-) dimensional spectrum of the object being imaged. This spectrum is what we call k-space and consists of an array or matrix of individual spatial frequencies. The next sections will explain the process conceptually. If you want (or need) the maths, check out Box ‘Encoding for 2D FT Imaging’, but you don’t need to in order to understand image formation.

Encoding for 2D FT Imaging

Following the excitation of a localized slice, frequency- and phase-encoding gradients are applied to manipulate the MR signal to encode spatial frequencies. The effect of a gradient G_{FE} applied along the x direction following the initial excitation on a discrete signal element ∂s is

$$\partial s(t) = \rho(x) \cdot \exp\left(\frac{-t}{T_2^*}\right) \cdot \exp(i\gamma \cdot x \cdot G_{FE} \cdot t) \cdot dx$$

where $\rho(x)$ is the proton density along x , and i is the square-root of -1 , denoting complex notation (see Appendix). This gradient is applied continuously during the signal acquisition (sampling). A dephasing

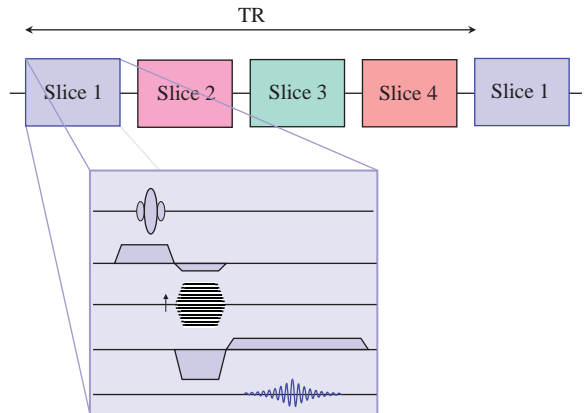


Figure 8.9 Multi-slice sequence. Different slices can be selected and lines of data acquired within each TR period. The expanded section is repeated for each slice position using a different RF carrier frequency.

gradient is usually applied prior to sampling in order to generate a symmetrical echo.

The phase encoding is applied (along the y direction for our example) through a gradient G_{PE} with a duration of τ prior to the signal measurement (sampling). The signal from a small element following the application of both gradients is

$$\begin{aligned} \partial s(t) = & \rho(x, y) \cdot \exp\left(\frac{-t}{T_2^*}\right) \cdot \exp(i\gamma \cdot x \cdot G_{FE} \cdot t) \\ & \cdot \exp(i\gamma \cdot y \cdot G_{PE} \cdot \tau) \cdot dx dy \end{aligned}$$

In words, this is

$$\text{signal} = \text{spin density} \times T_2^* \text{ decay} \times \text{phase change due to } G_{FE} \times \text{phase change due to } G_{PE}$$

The total MR signal is the integral of this with respect to x and y . In a complete MR acquisition the signal is sampled M times at intervals Δt , and the pulse sequence repeated N times, each time incrementing the PE gradient amplitude such that

$$G_{PE}(n) = \Delta G \cdot n \quad \text{for } n = \left(\frac{N}{2}\right) \text{ to } \left(\frac{N}{2} - 1\right)$$

Now define quantities k_{FE} and k_{PE} such that

$$\begin{aligned} k_{FE} &= \gamma \cdot G_{FE} \cdot \Delta t \cdot m \\ k_{PE} &= \gamma \cdot \Delta G \cdot n \cdot \tau \end{aligned}$$

The total signal S acquired in two dimensions time t and ‘pseudo-time’ $n \cdot \tau$ is found by integrating over x and y

$$S(m, n) = \iint \rho(x, y) \cdot \exp\left(\frac{-t}{T_2^*}\right) \cdot \exp(i2\pi \cdot x \cdot k_{FE}) \cdot \exp(i2\pi \cdot y \cdot k_{PE}) \cdot dx dy$$

which (except for the T_2^* term) is the form of an inverse Fourier transform of the spin density $\rho(x, y)$, i.e.

$$S(m, n) = \rho(k_{FE}, k_{PE})$$

Thus the 2D FT of the encoded signal results in a representation of the spin density distribution in two dimensions. An alternative way of viewing this is that the spatial frequency components are given by the discrete signal elements $S(m, n)$, the raw k-space data. Position (x, y) and spatial frequency (k_{FE}, k_{PE}) constitute a Fourier transform pair.

We have seen how the gradient-encoded MR signal represents the matrix of spatial frequencies. However, a glance at the maths shows that this equivalence is not exact – there is a term which depends upon T_2^* . This affects some spatial frequencies more than others and can lead to loss of resolution and blurring of the image. This is explored in Section 13.4.

8.5.1 Spatial Frequencies Demystified

The concept of spatial frequencies is not just a theoretical abstraction dreamt up to torment students of MRI. In real life the brain makes use of spatial frequencies to construct the visual images that you see.

Spatial frequencies may be hard to conceptualize but they are very natural and we'd all be in the dark without them!

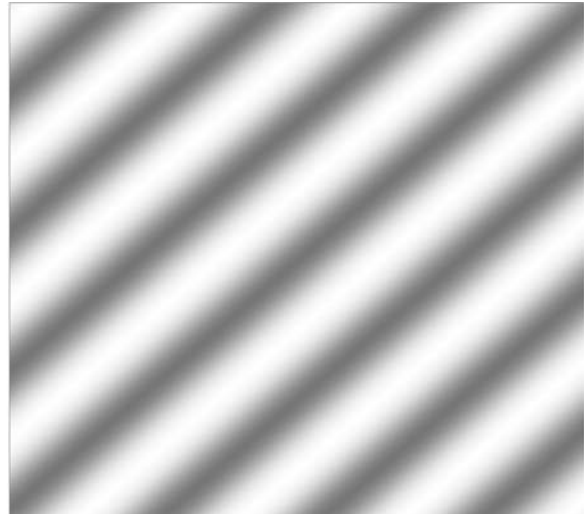
One of the easiest ways of understanding spatial frequencies is to think of a line-pair test object, such as those used for testing X-ray imaging systems. These consist of alternate light and dark bands or *line-pairs* of differing spacings (Figure 8.10). Suppose we have five line-pairs per centimetre. This means that five dark-light patterns are contained within a centimetre. The pattern of image brightness produced by this line-pair pattern is like a spatial frequency. In MR a spatial frequency is a periodic variation in signal spatial distribution or image brightness, measured not as line-pairs per centimetre but as ‘cycles per centimetre’ (which are very similar).

Applying the theory of Fourier, any image (not just MRI) may be decomposed into a spectrum of periodic (sinusoidal) brightness variations or spatial frequencies. In a digital image with a matrix of 256 × 256 pixels there are 256 × 256 possible spatial frequencies, allowing for positive and negative values. If we know the spatial frequencies we can calculate an image of the object that formed them. The purpose of MR localization by gradients is to manipulate the MR signal so that it gives all the spatial frequencies necessary to form an image. Each point of data or k-space is a spatial frequency component.

Figure 8.11 shows an image and its constituent spatial frequencies (k-space). If we remove the high



Figure 8.10 Spatial frequencies.



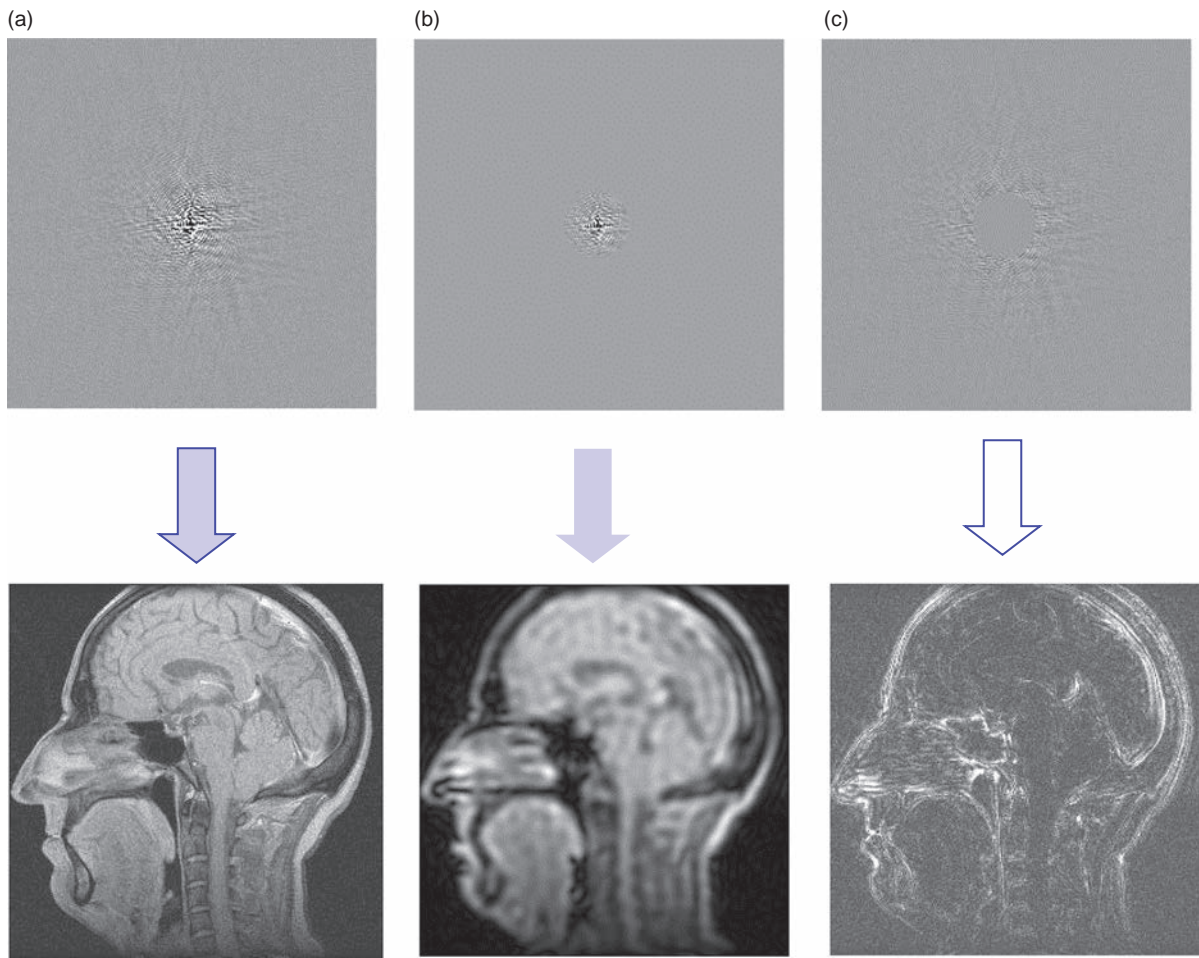


Figure 8.11 Images and their 2D spectra (k-space) showing: (a) reconstruction from all spatial frequencies; (b) low spatial frequencies, i.e. the centre of k-space only; and (c) high spatial frequencies, i.e. the edges of k-space only.

spatial frequencies we are left with an image which has the right brightness but no detail. Removing the low spatial frequencies leaves the image with details of edges and sharp features but low intensity elsewhere. So big objects have low spatial frequencies. Small objects or sharp edges have high spatial frequencies.

8.5.2 Totally Fazed: Phase Encoding

Most people find phase encoding the hardest part of MR image formation to understand, but gaining a conceptual grasp of it will pay dividends in terms of your overall understanding. Consider the following in conjunction with Figure 8.12, which shows the effect of the phase-encoding gradient on the transverse magnetization at three different locations and times.

Suppose we already have an MR signal with all the spins in phase. If we apply the phase-encode gradient (G_{PE}) at time A in the y direction, then the precession of the nuclei will speed up or slow down according to their position along the y axis. As we saw in Section 8.3.3, this causes the spins to dephase or fan out to a progressively greater degree for as long as the gradient is applied. When we switch off the gradient at time B , all the nuclei will revert to their original frequency or speed, but will keep their different phase angles. They are said to be *phase encoded*. The relative phase differences between signals in different locations remain until either another gradient is applied or the MR signal decays due to T_2 relaxation.

Figure 8.13 shows the phase encoding generated by three different gradient amplitudes on a column of

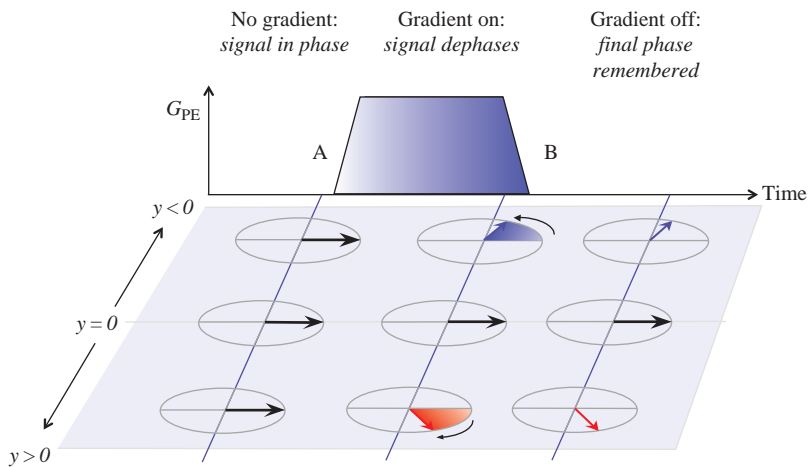


Figure 8.12 Phase encoding returns the signal to the Larmor frequency but with position-dependent phase changes.

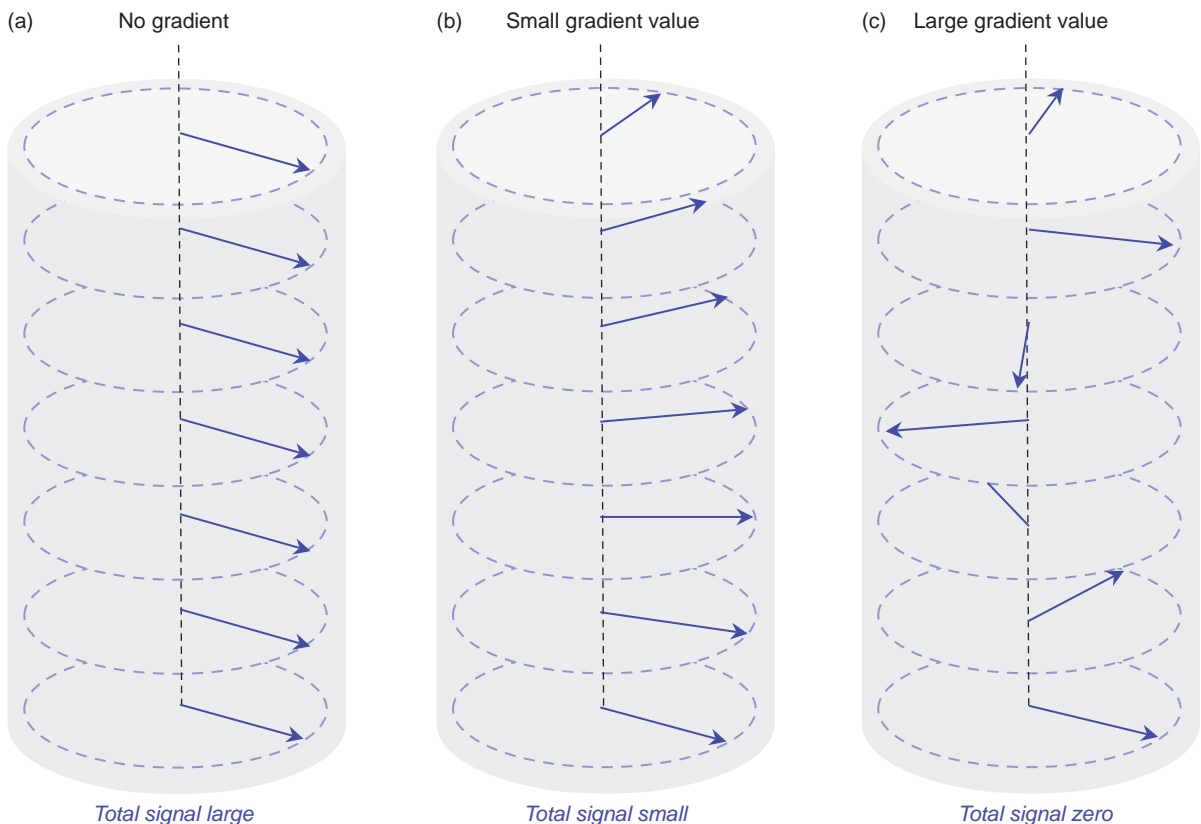


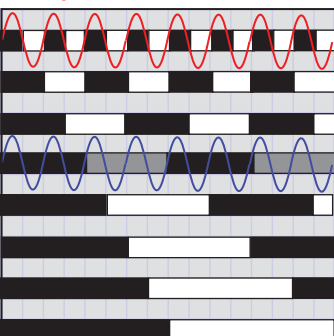
Figure 8.13 Effect of three different strengths of phase encoding on a uniform distribution of signal-producing material. The MR signal detected is given by the sum of all the vectors. (a) No gradient, (b) small gradient, (c) large gradient.

protons in the phase-encode axis. We see that without any applied gradient, the spins are all in phase and a large signal is obtained, but that the dephasing or twisting of the spins increases with gradient strength

until the dephasing is large enough for all the spins to cancel each other out and no signal is obtained.

How is this measuring spatial frequencies? Referencing to Figure 8.13, suppose we have a uniform

Example, k = 8



$$\begin{aligned}\text{Sum} &= 0+1+0+1+0+1+0+1+0+1+0+1+0+1 \\ &= 8\end{aligned}$$

Signal adds up constructively

$$\begin{aligned}\text{Sum} &= 0+0+0+0+1-1+1-1+0+0+0+0+1-1+1-1 \\ &\equiv 0\end{aligned}$$

Signal adds up destructively

Figure 8.14 Picking out a single spatial frequency with phase encoding step 8. Black represents an area which produces no signal (i.e. with zero proton density). Only one pattern results in any signal. This is spatial frequency or k value 8.

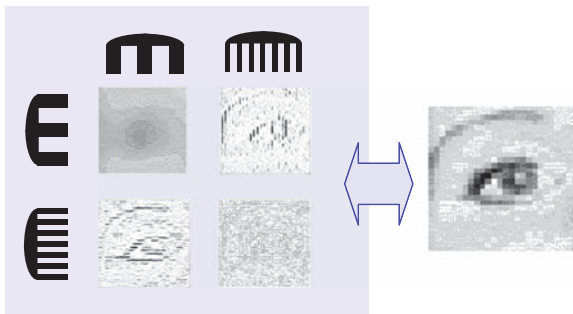


Figure 8.15 The ‘MR eye’: picking out spatial frequencies in two dimensions by applying spatial frequency ‘combs’ or filters. The thumbnails show the parts of the overall image selected by each comb. Like understanding MRI, the eye is not always obvious at first.

distribution of protons and we apply a sufficient phase-encode gradient to cause the phase of the spins to vary by 360° (2π radians or multiples of 2π). When we add up the MR signal from this column we get zero as the spins are evenly distributed throughout each direction. We can say that this object contains no information at the spatial frequency of one cycle per unit length.

Consider now a series of line-pair structures as in Figure 8.14 with alternating sections containing protons or nothing. Obviously only the sections containing protons can contribute to the signal. In the instance where $k = 8$ due to their distribution in space they are in phase and add up to give a net positive signal. That is to say, this particular value of phase-encode gradient is sensitive to objects containing the spatial frequency eight cycles per FOV. Looking at the other patterns in Figure 8.15, none of the lines add up to anything other than zero.

In general, however, an object (i.e. the patient) will have a range of spatial frequencies. Each value of phase encoding can be considered as a template or a

comb (technically, a filter) that only responds to one spatial distribution of MR signal or spatial frequency. To build up a whole picture, the entire range of possible spatial frequencies has to be interrogated. This is achieved by stepping through all the values of phase encoding (the 'ladder' in Figure 8.1), once per TR period. When no gradients are applied, we get a signal from the whole object, and this is referred to as the zero spatial frequency or zero k.

So the MR sequence consists of multiple repetitions of the excitation process followed by a different phase-encode gradient until all possible spatial frequencies are collected. You can think of each phase-encode step as being a filter or a comb, as in Figure 8.15. Once all these signals are collected, the application of a Fourier transform converts the spatial frequency distribution into a spatial distribution of the excited nuclei, i.e. an image of the patient.

8.5.3 Frequency Encoding

There is no reason why this phase-encode process should not be re-applied to obtain the full image in the other directions. The only practical difficulty is that for every value of G_{PE} (or spatial frequency in the PE direction, k_{PE}) we have to collect ALL the values of k_{FE} (apply all the G_{FE} gradient steps). This would take a long time, but it is possible, and three-dimensional imaging or three-dimensional Fourier transform (3D FT) does something similar. Fortunately there is a quicker, more convenient and conceptually simpler method of encoding the second in-plane direction: *frequency encoding*.

In frequency encoding we can acquire all the spatial frequency information needed from one MR signal following one RF excitation. In phase encoding we required one MR excitation (RF pulse) for every

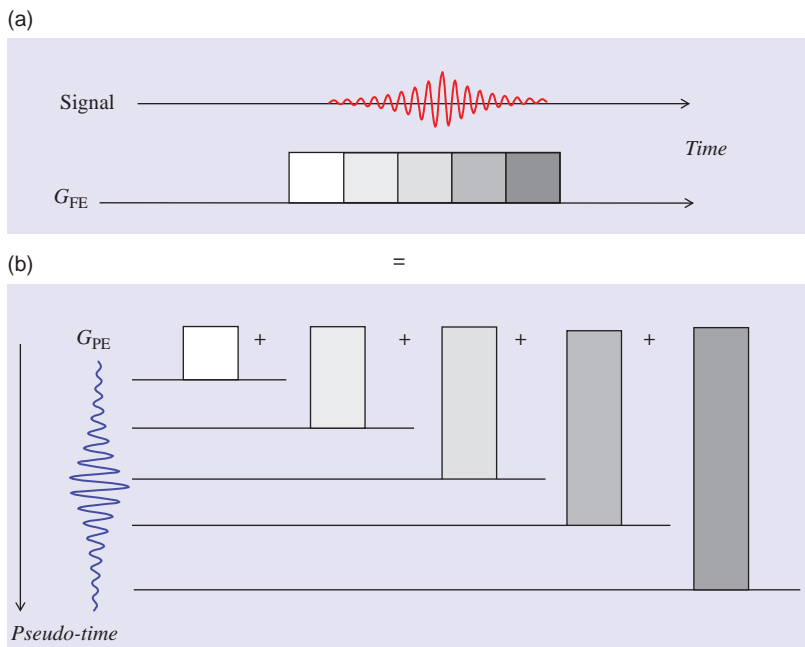


Figure 8.16 Equivalence of frequency encode acquired continuously in real time (a), and phase encode acquired step-wise in ‘pseudo-time’ (b).

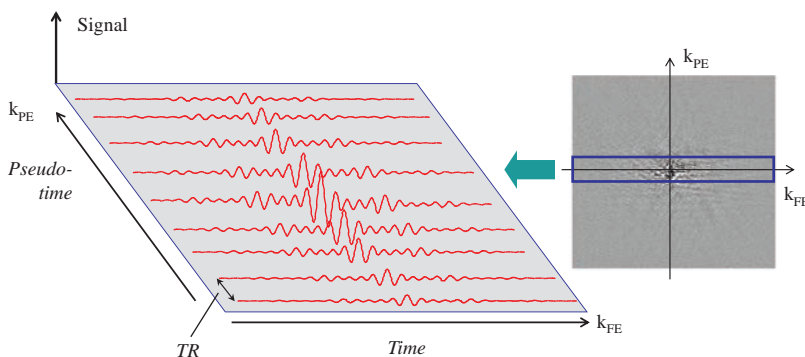


Figure 8.17 Central lines of k -space (magnified) showing the equivalence of phase and frequency axes. Signal strength is shown in the vertical direction in the magnified portion and as a greyscale in the thumbnail. Each PE line is separated by time TR.

line of data (i.e. every value of k_{PE}). For a 256-pixel image we thus required 256 MR excitations, and this will take $256 \times \text{TR}$ ms. Figure 8.16 shows a gradient being applied for a certain time, giving a certain gradient moment and phase change, after which the signal strength is measured. The next data point is measured after a different gradient step (and gradient moment and phase change). We then have data points corresponding to the strength of the MR signal after a whole range of gradient moments.

Suppose, however, that we apply a gradient continuously and measure or sample the MR signal at different time-points during the application of that gradient. At each point, the MR signal is affected by a different amount of gradient moment and has a

different amount of phase change. Each data point therefore reflects a different amount of ‘phase encoding’ and thus corresponds to a different spatial frequency. We can therefore collect all the spatial frequencies for that direction from the evolving MR signal in real time following a single RF excitation. This is analogous to the phase-encode acquisition which works in ‘pseudo-time’, with a sampling separated by TR, as shown in Figure 8.17. The resulting raw data matrix is sometimes referred to as k -space.

So if we can do frequency encoding all at once, why waste all that time with multiple excitations and phase encoding? The answer is that frequency is a scalar parameter, i.e. it is described by a single number. If we applied frequency-encoding gradients

in two directions at the same time we would have no way of knowing whether a particular frequency in the signal originated from one or the other (or both) of the applied gradients. By combining phase encoding and frequency encoding in two orthogonal directions we can collect all the spatial frequencies unambiguously that we need to make the image.

Another way of understanding frequency encoding, more usually considered in texts, is to consider the effect of G_{FE} on the frequency of the MR signal, illustrated in Figure 8.18. Because the frequency-encode gradient is present at the same time as the MR signal is being measured, the signal's frequency will now depend upon the position of the material from which it originated within the gradient field. It will not be a single sinusoid wave but a mixture of many frequency components. We then have a signal which is frequency encoded. It is easy to determine the frequency components; we simply perform another Fourier transform. Applied in one dimension this produces a spectrum which represents a one-dimensional projection of the object.

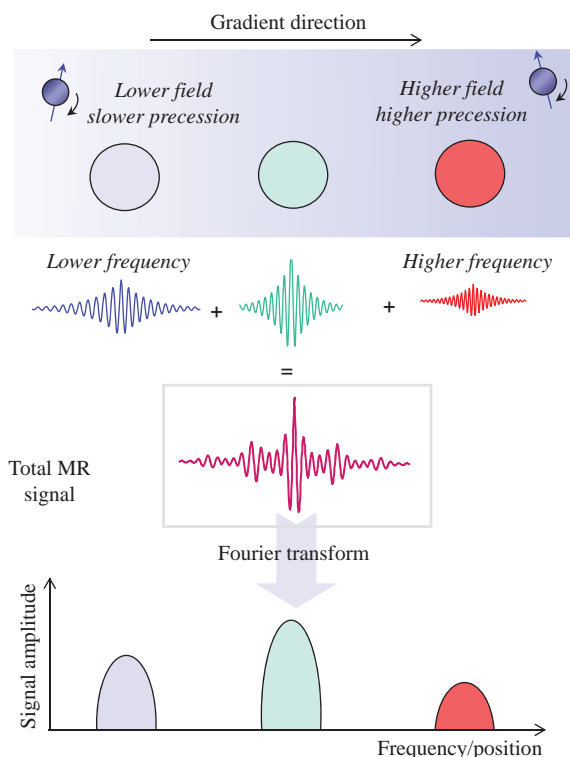


Figure 8.18 Alternative description of frequency encoding in terms of position-dependent frequency changes.

8.5.4 Spatial Encoding: A Musical Analogy

You can think of MRI in-plane localization in terms of playing a multi-stringed musical instrument such as a guitar. Suppose you wish to play every possible note (or frequency) distinctly, you first have to pluck a string. This is like the RF excitation. The sound it makes is like the MR signal. It is then relatively easy to play every note available on that string by running a finger up the fretboard. As one does this the length of the string is in effect shortened (this is like a gradient) and the pitch of the note (or frequency) changes. All the while the sound can be heard. This is like frequency encoding.

However, there are other strings. To hear them we have to pluck one of them (perform another RF excitation) and repeat the pitch-changing action. The action of changing to a different string is analogous to the operation of phase encoding in MRI.

8.5.5 2D FT Reconstruction

To reconstruct the image we do a 2D FT on the raw data matrix or k-space. Usually the image is then displayed as a ‘magnitude’ image. The result of the 2D FT is actually a complex image with ‘real’ and ‘imaginary’ parts, as shown in Figure 8.19, or with amplitude and phase (see the Appendix for a reminder about complex numbers). We usually combine these as a complex magnitude (this gets round some problems with the B_0 field) and the images only contain positive values. Sometimes a phase image can be optionally produced too.

Certain types of scan may require ‘real’ reconstruction, which allows the image to have positive and negative values. In this case the image background is mid-grey. Real-valued inversion recovery is an example of this (see Section 12.4.1).

8.5.6 Resolution and Field of View

For a 2D FT MR acquisition the resolution is normally pixel limited provided the signal-to-noise ratio (SNR) is adequate. So if the pixel size is 1 mm, then you should be able to see details of this size clearly. To increase the resolution for a fixed field of view (decrease the pixel size) you can do one of three things: increase the gradient strengths, increase the matrix or increase the sampling time (for the FE direction only). In practice, you cannot get arbitrarily small pixels as sooner or later you will run out of gradient power and SNR.

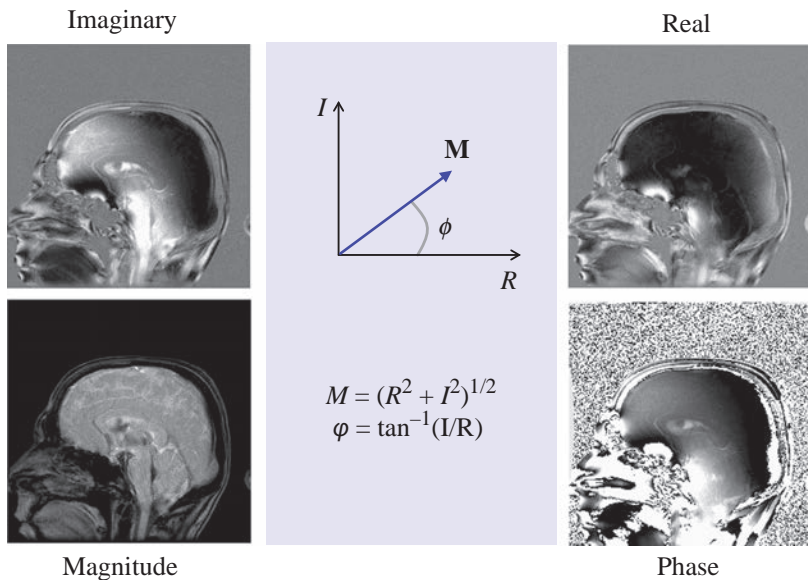


Figure 8.19 Reconstruction of a magnitude (M) image from real and imaginary parts following Fourier transformation. A phase (ϕ) image can also be calculated.

To decrease the field of view (zoom in) while maintaining the matrix size you can either increase the gradients or increase the sampling time (in the FE direction only).

Resolution and Field-of-View Maths

The maximum resolution is given by the pixel size

$$\Delta x = \frac{1}{\gamma \cdot G_{FE} \cdot M \cdot \Delta t} \quad \Delta y = \frac{1}{\gamma \cdot \Delta G \cdot N \cdot \tau}$$

The size of the image or the field of view (FOV) is given by the inverse of the minimum spatial frequency step

$$FOV_{FE} = \frac{1}{\gamma \cdot G_{FE} \cdot \Delta t} \quad FOV_{PE} = \frac{1}{\gamma \cdot \Delta G_0 \cdot \tau}$$

Notice that the Fourier transform principle of 'less is more' applies: it is the maximum size of the gradient which controls the pixel size, while the time between samples or phase-encode step size controls the FOV.

8.6.1 Adventures in k-Space

In simplest terms k-space is the raw data matrix which stores the already-encoded MR signals (Figure 8.17). We can think of the application of the gradients as defining a path or a trajectory through k-space, as shown in Figure 8.20. At time A, the application of the frequency- and phase-encoding gradients, the signal is at the centre of k-space (corresponding to a summation of the total MR signal from the object). The dephase portion of G_{PE} gradient combined with the maximal negative G_{PE} step moves it to the bottom left corner at time B. The read-out part of G_{FE} moves it along a line of k_{FE} from left to right. The peak of the gradient echo occurs on crossing the k_{PE} axis (time C). Provided the MR signal has totally decayed before the next excitation we will start at the centre again. This time G_{PE} moves us to the second bottom line of k-space. By the end of the scan we will have acquired N_{PE} gradient echoes, each corresponding to a different k_{PE} position. This gives us a full sample of the spatial frequencies in the image.

The pixel size is defined by the total length of the k-space axes. The FOV is determined by the separation of the k_{PE} lines and of the samples along each k_{FE} line as shown in Figure 8.21. We have already seen that the central portion of k-space determines the overall brightness or contrast of the image while the outer regions determine the fine detail (Figure 8.11).

8.6 Consequences of Fourier Imaging

The consequences of Fourier imaging relate to the properties of k-space, the determination of resolution and field of view and the generation of typical artefacts.

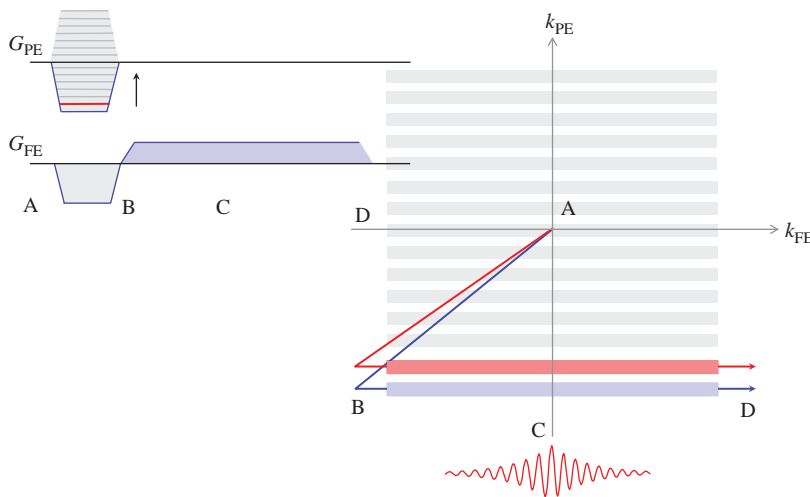


Figure 8.20 k-space path for a pair of frequency- and phase-encode gradients, showing echo formation. Following the RF pulse, and before the gradients are applied, the signal is at the centre of k-space. This means that it represents the total image brightness irrespective of spatial localization.

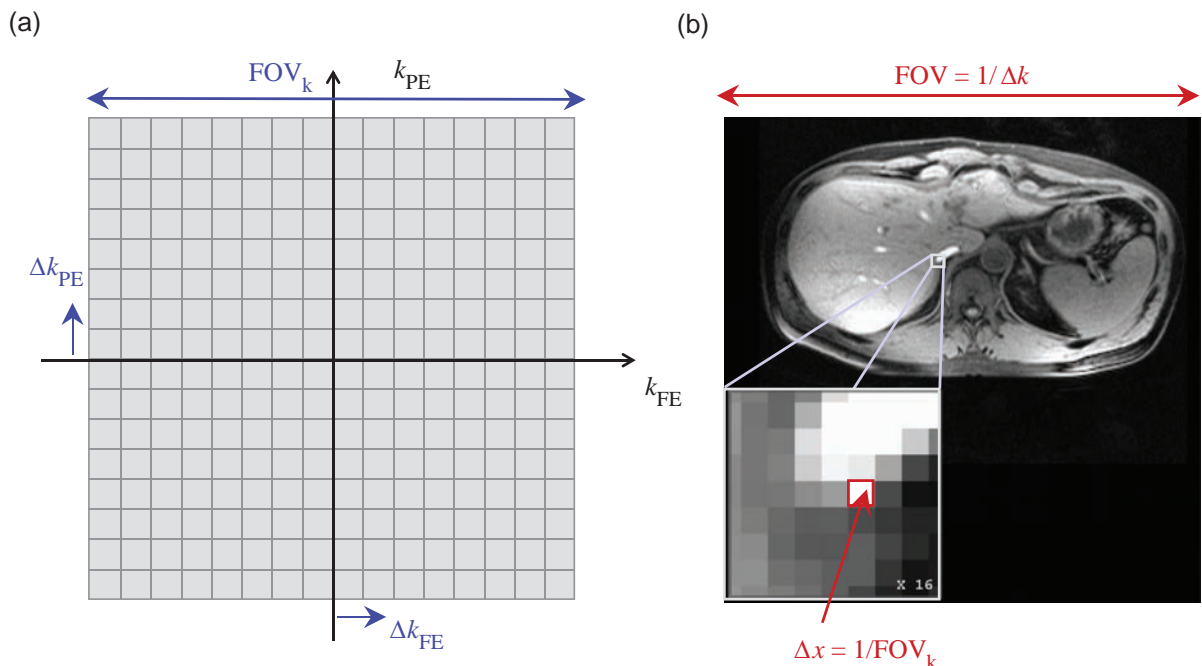


Figure 8.21 Relationship between (a) k-space and (b) image resolution and FOV.

k-Space Exploration

For a 2D object represented by the function $f(x, y)$, the spatial frequencies k_x, k_y are given by

$$F(k_x, k_y) = \iint f(x, y) \cdot \exp(i2\pi \cdot (x \cdot k_x + y \cdot k_y)) \cdot dx dy$$

and the object expressed in terms of the spatial frequencies is

$$f(x, y) = \iint F(k_x, k_y) \cdot \exp(-i2\pi \cdot (x \cdot k_x + y \cdot k_y)) \cdot dk_x dk_y$$

The functions f and F are a Fourier transform pair. The quantities x and k_x bear a reciprocal arrangement, i.e. small spatial objects (little x) have big k values and vice versa. Less is more again! Thus the highest spatial frequency represents the smallest object detectable (i.e. the pixel size)

$$\Delta x = \frac{1}{N\Delta k} = \frac{1}{FOV_k}$$

and the largest object (i.e. the field of view)

$$FOV_x = \frac{1}{\Delta k_x}$$

For example, in the phase-encode axis, if the maximum gradient strength is 8.6 mT m^{-1} applied for 0.7 ms with 256 steps

$$\Delta k = \frac{8.6}{128} \times 0.7 \times 42.56 = 2 \text{ m}^{-1}$$

(remember we step through G_{PE} from $-N/2$ to $N/2-1$) so the FOV is 0.5 m or 500 mm. (Hint: if you use units of mT m^{-1} , ms and use γ in MHz T^{-1} , you get k in m^{-1} .) Similarly,

$$FOV_k = 2 \times 8.6 \times 0.7 \times 42.56 = 512 \text{ m}^{-1}$$

The pixel size in mm is therefore

$$\Delta y = \frac{1000}{512} = 1.95 \text{ mm}$$

For a readout gradient of amplitude 5.87 mT m^{-1} and a total data sampling time of 2.048 ms

$$FOV_k = 42.56 \times 5.87 \times 2.048 = 512 \text{ m}^{-1}$$

giving the same pixel size $\Delta x = 1.95 \text{ mm}$. If 256 samples are taken (a sampling time of 8 μs) Δk will be 2 m^{-1} and the frequency-encode FOV will be 500 mm again.

The MRI image-formation process can be thought of as a sampling of k-space. If sampling conventions (i.e. the Nyquist criterion) are not fulfilled with regard to the spatial frequencies in the object, then artefacts will occur as shown in Section 8.6.2.

In a generalized form for an arbitrarily shaped gradient we can write

$$k = \gamma \cdot \int_0^t G(t) dt$$

which defines any k-space trajectory.

8.6.2 Artefacts

Fourier imaging is susceptible to specific artefacts, e.g. phase wrap and Gibbs' ringing (see Section 7.4). Aliasing occurs because the anatomy being scanned exceeds the FOV in the PE direction causing image wrap-around. In Fourier terms this means that the sampling interval Δk is insufficient. Phase encoding

will occur as in Section 8.5.2 and Figure 8.13, but as the gradient field is physically larger than the selected FOV, the twisting of the columns of vectors outside the FOV will be too tight. This will exceed the Nyquist criterion and is therefore interpreted erroneously. Phase-encode oversampling reduces the problem. Aliasing is not commonly a problem in the frequency-encode direction as the signal from outside the FOV is encoded as a real frequency which can be removed by electronic filtering.

Haunted by Fourier

It can be argued that the fundamental weakness of Fourier transform encoding and reconstruction is its susceptibility to modulation artefacts which produce 'ghost' replications of the image displaced relative to the true image and often aliased in the phase-encode direction. Any interaction which results in a modulation of either the frequency (FM) or amplitude (AM) of the MR signal will result in ghosting artefacts.

Consider a one-dimensional example of a signal $s_0(t)$ giving an image $i_0(\omega)$ by its FT

$$i_0(\omega) = \text{FT}\{s_0(t)\}$$

Suppose we have a temporal modulation of this signal such that

$$s = s_0(1 - m \cdot \cos \omega_m t)$$

where m is the modulation amplitude and ω_m is the modulation frequency (i.e. this is amplitude modulation or AM). We can then apply the Fourier modulation theory to predict the image in terms of modulation frequency ω

$$i(\omega) = i_0(\omega) + \frac{m}{2} i_0(\omega - \omega_m) + \frac{m}{2} i_0(\omega + \omega_m)$$

The encoding produces an equivalence between frequency (or 'pseudo-frequency') and position, giving a resultant image

$$i(y) = i_0(y) + \frac{m}{2} i_0(y - \Delta y) + \frac{m}{2} i_0(y + \Delta y)$$

This is a combination of the true image plus two shifted ghost images with intensity $m/2$. Converting the modulation frequency in terms appropriate to k-space (PE) we get a distance shift Δy given by

$$\Delta y = \frac{1}{p\Delta k}$$

$$\Delta y = \frac{FOV_{PE}}{p}$$

where p is the periodicity of the modulation in numbers of PE lines. In real time this becomes

$$\Delta y = \frac{FOV_{PE} \cdot TR}{T_m}$$

where T_m is the real time period of the modulation. The effect of signal averaging is to change the periodicity of the modulation relative to the phase-encode time scale. If $TR = T_m/n$ there will be n ghosts, separated by FOV/n .

Gibbs' artefact is a ringing of signal on sharp edges in the image. In k-space terms it is a truncation effect; that is, there are not enough k-values to represent the detail. In basic Fourier theory the transform of a sharp (high-frequency) detail will involve spectral components at all frequencies, theoretically extending infinitely over k-space. Obviously an infinite k-space is impossible. The ringing occurs because of the abrupt ending, or truncation, of k-space. Filtering the data by multiplying it by a smooth function prior to Fourier transformation helps to reduce ringing, at the cost of spatial resolution. The best remedy is more k-space samples, i.e. to increase the PE matrix.

Ghosting is slightly different in that it arises from a modulation, i.e. a variation in amplitude or time, of the MR signal over the lines of k-space (k_{PE}) possibly arising from physiological motion or equipment imperfections. The shift of the ghost images is inversely proportional to the period of the unwanted modulation. The fastest perceptible modulation is from one line to the next (period = $\Delta k/2$). This gives a ghost separation of half the FOV. Slower modulations, covering several TR intervals, will result in less shifted ghosts. The size (or depth) of the modulation determines the amplitude of the ghost images.

8.7 Speeding It Up

There are three things we can do to speed up the data acquisition which involve tricks in k-space: they are half Fourier, reduced matrix and rectangular field of view (RFOV). We also encountered these in Chapter 6. Some are illustrated in Figure 8.22, along with a fourth option, partial echo. Partial echo is like half Fourier but applied to frequency encoding (see Box 'Real or Imaginary').

8.7.1 Half Fourier

The most radical trick we can do is called 'half Fourier', 'halfscan' or 'half NEX', in which we only acquire slightly more than half the data, i.e. we omit half the phase-encoding gradient steps (either the positive or negative ones). In terms of k-space we acquire just the lower (or upper) half (Figure 8.22a) and then estimate the other half of the data using a mathematical trick called complex conjugate synthesis. This is a property of Fourier transform of 'real' functions. This produces a time saving of approximately 50%, does not significantly affect spatial resolution but loses about 30% in signal-to-noise ratio (SNR).

8.7.2 Reduced Matrix

Secondly, we can apply a reduced matrix, or reduced acquisition, i.e. just not bother to acquire the largest phase-encoded lines of data (k-space) (Figure 8.22c). Instead, we replace the omitted k-space data with zeros (zero-filling). The time saving will be proportional to the number of PE lines missed out. The

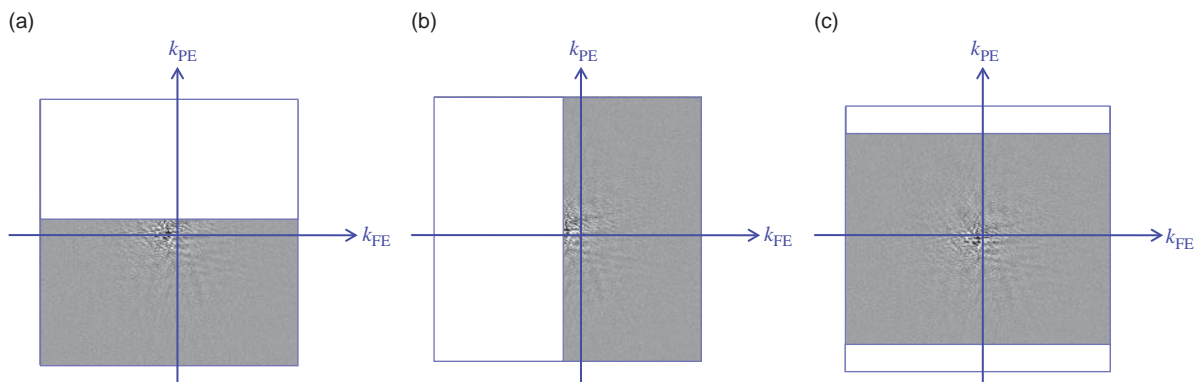


Figure 8.22 Fourier transform speed tricks: (a) half Fourier, (b) partial echo, which can be used to reduce TE and TR but does not reduce the number of PE lines, and (c) reduced matrix.

downside of this technique is a loss of spatial resolution in the phase-encode axis. Small improvements in SNR are made.

Real or Imaginary

A property of 'real' functions is that their Fourier transforms possess complex conjugate symmetry. In a perfect magnetic field we would expect the encoded MR signal to be real, i.e.

$$S(k_{\text{FE}}, k_{\text{PE}}) = S^*(-k_{\text{FE}}, -k_{\text{PE}})$$

where S^* denotes the complex conjugate of S (see Appendix A.4). We can say that signals in k-space have 180° rotational symmetry about the origin (zero), so that values in the top right-hand corner of k-space should be equal to those in the bottom left-hand corner.

This means we can synthesize one-half of k-space from the other, simply by making a copy of the acquired data and swinging it through 180° to fill the other half. In half-Fourier scanning we use this property to reduce the number of phase-encode steps. However, since the magnetic field is never perfect we actually have to collect slightly more than half the data in order to apply phase corrections to the synthesized part. Another application of complex conjugate symmetry is in partial or fractional echo techniques where up to about 40% of the k_{FE} data are not acquired directly, but synthesized (Figure 8.22b). Once again field imperfections prevent a reduction of exactly 50% in the data. Fractional echo is used in rapid imaging to reduce TE and TR.

A 'k-space shutter' is similar, except that it chops off the corners of k-space and thus affects resolution in both frequency and phase-encode directions. This offers no time saving in 2D scanning, but it can help in 3D acquisitions.

8.7.3 Rectangular Field of View

Finally, sometimes we can acquire a rectangular field of view. In the explanations above we have assumed a square field of view (FOV) with an equal matrix size in both directions, e.g. 256 × 256. Often the anatomical region to be scanned is not of similar dimensions in either axis of the image plane, so we can reduce both the phase-encode FOV and the PE matrix. Typical examples are for sagittal or coronal scanning of the knee or spine, where an unequal number of

phase-encode to frequency-encode points gives a more efficient coverage of space. To save time (and avoid phase wrap) we always choose the phase-encode axis to be the smaller of the two physical dimensions, i.e. for a sagittal spine we would choose posterior-anterior for phase encoding, while for a transverse head we would commonly choose left-right for the phase-encode direction.

In k-space the effect of a rectangular field of view is to 'space out' the lines in the PE axis (Figure 8.23). Only the field of view is affected as the value of k_{max} remains the same. A time saving of up to 50% is achievable with no resolution loss and only a slight loss of SNR.

It Looks Good, but is it Real?

'Zero-filling' is a very common feature of MRI. Since computers like to work in powers of 2, any non-square matrix (where $N_{\text{PE}} \neq N_{\text{FE}}$) must be filled up with zeroes before it can be Fourier-transformed. The zeroes are added at the edge of k-space, which corresponds to the high spatial frequencies. This means a smaller pixel size, which is equivalent to interpolating the pixels in the image. However, the zeroes do not contain any signal information about the high spatial frequencies, so it is not real data.

It is also possible for the user to decide to add extra zeroes to improve the apparent resolution of the final image. Remembering that the edge of k-space contains information about high spatial resolution, adding zeroes all around the edge of the acquired k-space can artificially reduce the pixel size. On GE Healthcare scanners these are the 'zip512' and 'zip1024' options, on Siemens it is the 'interpolate' box, and on Philips you set the reconstruction matrix independently from the scan matrix.

The extra zeroes contain no signal, but also no noise, so they have no effect on the SNR of the image. The acquired pixel resolution is unchanged but the displayed pixels are smaller. As with reducing the phase-encode matrix, the rule of thumb is that you shouldn't zero-fill by more than a factor of two.

8.8 3D FT

A fully three-dimensional technique may sometimes prove advantageous over two-dimensional multi-slice acquisition. The principle is simply to apply a second

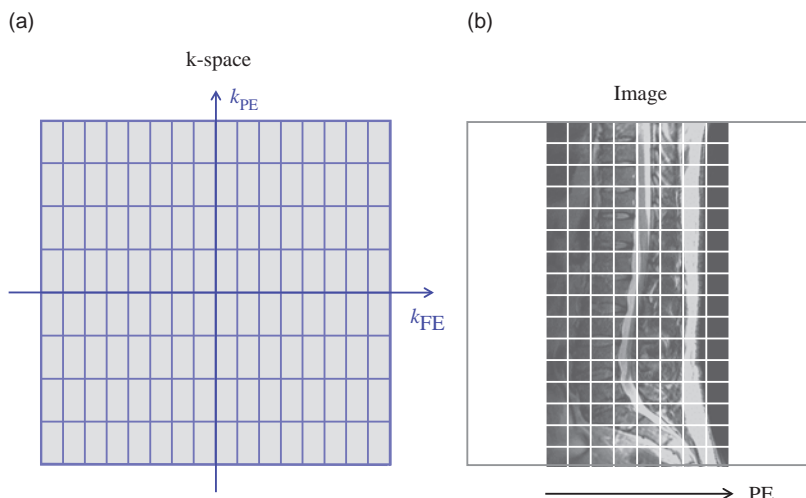


Figure 8.23 (a) k-space sampling for (b) rectangular FOV. Pixel size is maintained by keeping the same maximum and minimum k . The PE field of view is changed by altering the spacing between k_{PE} lines.

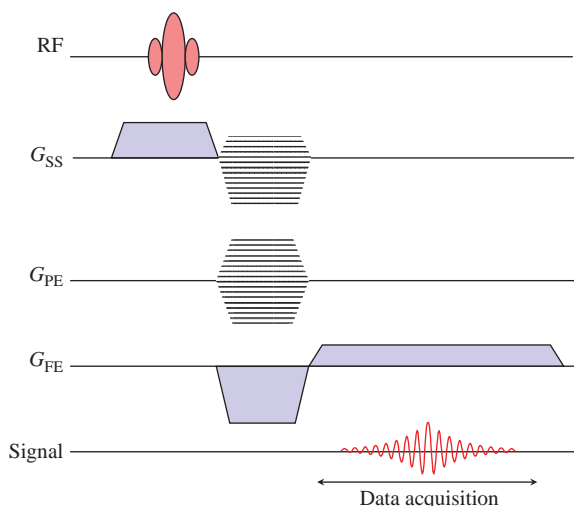


Figure 8.24 Simple 3D FT pulse sequence.

phase-encode axis, ensuring that for every gradient step in the new axis we apply the whole set of other axes steps: i.e. for a $L \times M \times N$ 3D matrix, we acquire

Further Reading

Bracewell RN (1999) *The Fourier Transform and its Applications*, 3rd edn. London: McGraw-Hill.

Brown RW, Cheng YCN, Haacke EM, Thompson MR and Venkatesan R

(2014) *Magnetic Resonance Imaging: Physical Principles and Sequence Design*, 2nd edn. Hoboken, NJ: John Wiley & Sons, chapters 9, 10 and 11.

Edelstein WA, Hutchison JMS, Johnson G and Redpath T (1980)

'Spin warp NMR imaging and applications to human whole-body imaging'. *Phys Med Biol* 25:751–756.

Elster AD and Burdette JH (2001) *Questions and Answers in Magnetic Resonance Imaging*, 2nd edn. London:

Mosby-Yearbook, chapter 4. Also on the web at <http://mri-q.com> [accessed 23 March 2015].

Kumar A, Welti D and Ernst RR (1975) 'NMR Fourier zeugmatography'. *J Magn Reson* 18:69–83.

Mansfield P and Maudsley AA (1977) 'Medical imaging by NMR'. *Br J Radiol* 50:188–194.

Twieg DB (1983) 'The k-trajectory formulation of the NMR imaging process with applications in analysis

and synthesis of imaging methods'. *Med Phys* 10:610–623.

A good explanation of spatial frequencies can be found at <http://7e.biopsychology.com/av10.04.html> [accessed 22 March 2015].

Getting in Tune: Resonance and Relaxation

9.1 Introduction

MRI involves three kinds of magnetic field: the main static field of the scanner (B_0), the gradients which are used for spatial localization, and the oscillating magnetic field of the RF pulses (B_1). There must be something in the body which has magnetic properties in order to interact with all these fields. So far we have deliberately avoided a detailed discussion of these properties, since we believe it's easier (and more useful practically) to understand the images first. However, the time has come to explore the protons which are essential for MRI, and on the way we will tackle some difficult concepts from quantum mechanics. We will discuss the relaxation mechanisms T_1 and T_2 in more detail. We will find that:

- hydrogen nuclei have a magnetic moment which interacts with the main field of the scanner;
- quantum mechanics controls the behaviour of the individual protons, but classical mechanics is used to describe the changes in a large collection of nuclei;
- excitation and relaxation of a collection of protons is described by the Bloch equations;
- spin–spin and spin–lattice relaxation mechanisms are due to dipole interactions, and relaxation times depend on molecular motions within the tissues;
- magnetization transfer can be observed between the bound and free water compartments in tissues;
- we can use contrast agents to modify the relaxation times of tissues, usually to create a brighter signal from pathological tissues.

9.2 Spinning Nuclei

At school, we all learned that atoms consist of electrons orbiting a central nucleus composed of neutrons and protons. As you probably know by now, MRI is derived from NMR, nuclear magnetic

resonance, so we're only interested in the nucleus. In particular we want to look at the nucleus of the hydrogen atom, because of its abundance in the human body in water and other molecules. The nucleus of the hydrogen atom is a single positively charged *proton*. Something you probably didn't learn at school is that all fundamental particles (protons, neutrons, etc.) spin on their own axes, and the hydrogen nucleus is thus a continuously rotating positive charge. Basic electromagnetism tells us that a moving charge (i.e. a current) has an associated magnetic field, and so the proton generates its own tiny field known as its magnetic moment.

9.2.1 Classical Mechanics Explanation of NMR

If the proton is placed in a strong external magnetic field, it experiences a turning force, known as a torque, which tries to align the proton's magnetic moment with the main field. This is similar to a compass needle which experiences a force in the earth's magnetic field and turns so that it is aligned with the direction of the field. However, the proton is constrained by the laws of quantum mechanics. Quantum Mechanics (QM) is a branch of physics which explains some rather odd behaviours of fundamental particles, which sometimes act like individual particles and sometimes act like waves. Classical Mechanics (CM), on the other hand, works for normal-sized ('macroscopic') bodies, and for large numbers of small particles where their quantum mechanical behaviour is averaged out. Although we will have to do a bit of QM to understand why the protons don't simply align with the field, we will find that CM is quite capable of explaining almost everything else (sigh of relief!).

Since it can't align exactly with the external field, the proton continues to experience a torque which makes it *precess* around the direction of the field. This

precession is analogous to the wobbling of a spinning top (gyroscope) tilted slightly off axis so that it experiences a torque due to gravity. If you've never seen this, it's worthwhile buying a gyroscope from any toy store and trying to make it precess. All serious MR specialists have a gyroscope!

The precessional frequency of the protons is found to be proportional to the external magnetic field, and is given by the Larmor equation

$$\omega_0 = \gamma B_0$$

where γ is a constant called the gyromagnetic ratio, and is equal to $2.7 \times 10^8 \text{ rad s}^{-1} \text{ T}^{-1}$. We use ω to denote angular frequencies which are vectors, but in everyday life we use scalar frequencies denoted f ; in these units the gyromagnetic ratio is 42.57 MHz T^{-1} . All the equations in this chapter use angular frequencies, but you could simply replace ω with f and use $\gamma = 42.57 \text{ MHz T}^{-1}$ to get the frequencies in megahertz. See Box 'Where's the bar?' in Chapter 8. So the protons in a magnetic field all precess at the same Larmor frequency. This is known as a *resonance* condition. So we have the two key components for MRI, a collection of magnets (protons) and a resonance condition.

Derivation of the Larmor Frequency: Classical Mechanics

We use vector notation in the boxes in this chapter because direction is important. Vectors are written in bold upright font, while their corresponding magnitudes are in italics, with subscripts to show component magnitudes where appropriate.

The magnetic moment μ is directly proportional to the angular momentum J

$$\mu = \gamma J$$

where γ is the gyromagnetic ratio. When this moment is in an external field B it experiences a torque and precesses about the field, its angular momentum changing according to the equation

$$\left| \frac{dJ}{dt} \right| = |\mu \times B| = |\gamma J \times B| = \gamma J B \sin \theta$$

where θ is the angle between the magnetic moment and the main field. From basic geometry (Figure 9.1) we can see that dJ is given by

$$dJ = J \sin \theta d\phi$$

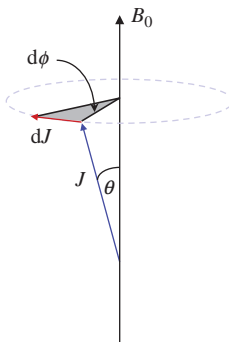


Figure 9.1 Geometric representation of the precession of the magnetic moment μ around the main field B_0 .

Combining these two results we can show that the precessional frequency is given by

$$\begin{aligned} \omega &= -\frac{d\phi}{dt} = -\frac{d\phi}{dJ} \cdot \frac{dJ}{dt} = \frac{1}{J \sin \theta} \cdot -\gamma J B \sin \theta \\ \therefore \omega_0 &= \gamma B_0 \end{aligned}$$

The minus sign, which we quietly dropped just before the last line, is there to make sure that ω_0 defines a clockwise rotation about the z axis. So the magnetic moment precesses clockwise about B_0 at an angular frequency of ω_0 or a scalar frequency of f_0 if you prefer to use $\gamma = 42.57 \text{ MHz T}^{-1}$.

9.2.2 Quantum Mechanics Explanation

So here's the QM bit. The proton's spin is said to be *quantized* in the presence of an external field, and the torque it experiences makes it precess in one of only two orientations, known in QM as 'spin states'. One state is almost aligned with the main field, and is known as *spin-up* or *parallel*. The other state is aligned almost opposite to the external field, known as *spin-down* or *anti-parallel* (see Figure 9.2). Since the magnetic moment is at an angle to the external field, the tip of its vector traces out a circle around the direction of the field (Figure 9.3), whichever orientation it is in.

How does the proton choose which orientation to precess in? It just depends on how much energy it has, since the anti-parallel direction requires slightly more energy than the parallel direction. Both states are stable, so protons are quite happy to stay in either position. However, protons can also swap between the two states simply by gaining or losing a certain amount of energy in the form of a photon (a packet of electromagnetic radiation). It turns out that the energy difference between the two states is directly

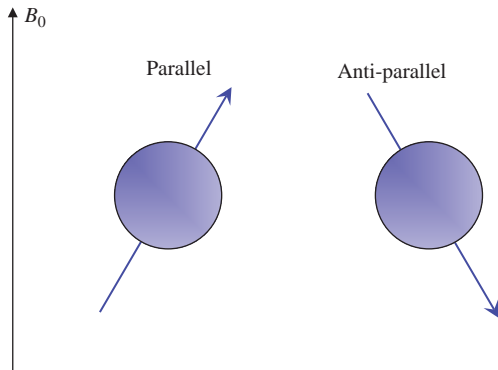


Figure 9.2 Two possible orientations for the proton in an external magnetic field.

proportional to the strength of the external magnetic field, and from QM we can calculate exactly what the energy difference is, and thus the frequency of electromagnetic radiation required. We will find that the frequency is the Larmor frequency, just as we found from classical mechanics,

$$\omega_0 = \gamma B_0$$

So we have a link between the classical and quantum mechanical pictures, showing that the precessional frequency of the proton in a magnetic field is the same as the frequency of radiation required to cause transitions between the two states.

In the human body there are many trillions of protons; after all, we are about 75% water. So although an individual proton obeys QM, we should expect to measure their average behaviour with CM. There is a statistical distribution of protons between the two states and we find that the lower-energy state is slightly favoured, so that there are more protons spinning parallel than anti-parallel. The ratio depends on both the main magnetic field strength and (inversely) on temperature. At body temperature (37 °C) and in a 1.5 T scanner, this works out at about 1.000004, which means that for every million protons in the spin-down direction there are a million-and-four protons in the spin-up direction.

Derivation of the Larmor Frequency: Quantum Mechanics

The magnetic moment of the proton is related to the quantized angular momentum

$$\mu = \gamma J = \gamma \hbar l$$

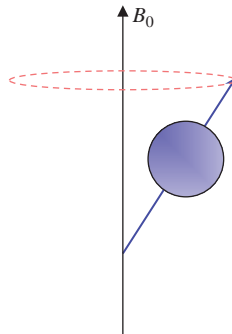


Figure 9.3 Precession of the magnetic moment.

where l is the spin angular momentum quantum number, equal to $\frac{1}{2}$ for protons, \hbar is Planck's constant divided by 2π and γ is the gyromagnetic ratio. In an external magnetic field there are $2l + 1$ possible values for the angular momentum, ranging from $l, l-1, \dots, 0, \dots, -(l-1), -l$. Thus for the proton there are only two possible states, with values of $\pm\frac{1}{2}$. The energy of each state (ϵ) is given by

$$\epsilon = \mu \cdot \mathbf{B} = \gamma \hbar l \cdot B$$

and thus we can calculate the energy difference as

$$\Delta\epsilon = (\gamma_{\frac{1}{2}} - \gamma_{-\frac{1}{2}})\gamma \hbar B = \gamma \hbar B$$

De Broglie's wave equation tells us that the frequency associated with this energy is

$$\Delta\epsilon = \hbar\omega$$

and so we can find the precessional frequency (using the subscript 0 to indicate the Larmor frequency and applied external field)

$$\begin{aligned}\hbar\omega_0 &= \gamma \hbar B_0 \\ \omega_0 &= \gamma B_0\end{aligned}$$

In equilibrium the protons are all out of phase with each other, so the tips of the magnetic moment vectors are evenly spread out around the circles (see Figure 9.4). Since there are so many protons, we can also make each vector represent the average magnetic moment of a large group of protons all precessing at exactly the same frequency, rather than an individual proton's magnetic moment. This is sometimes called an 'isochromat' of protons, but we will use the term 'spin'. This may seem like an unnecessary complication but it means that we can drop QM and just use CM from now on! The vector sum of all these spins is called the *net magnetization* M_0 , which is aligned exactly with the main field B_0 (conventionally shown as the z direction). M_0 is a measurable

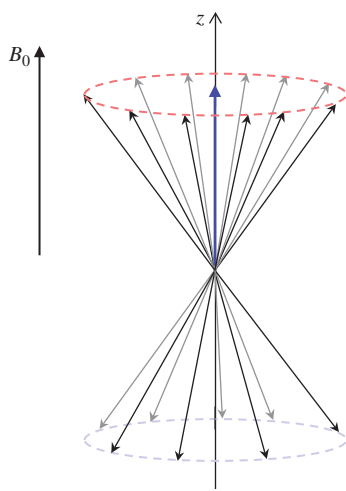


Figure 9.4 Average of many protons produces the net magnetization M_0 .

magnetization which can be calculated to be of the order of microtesla (μT).

9.3 Measuring the Magnetic Moment

As we've just seen, the magnetization in the body is very small (e.g. $1 \mu\text{T}$) compared to the main magnetic field (e.g. 1.5 T). It is virtually impossible to measure it while it is at equilibrium, lying parallel with B_0 . By tipping it through 90° into the xy plane (known as the transverse plane), M_0 now generates a significant signal which can be recorded using a detector which is sensitive to magnetic fields in the transverse plane.

Population of Energy States

Whether a proton is in the parallel or anti-parallel direction depends on its internal energy. For a large collection of protons, the number in each state is given by the Boltzmann distribution:

$$\frac{N_{\text{up}}}{N_{\text{down}}} = \exp\left(\frac{\Delta E}{k_B T}\right)$$

where k_B is the Boltzmann constant, $1.38 \times 10^{-23} \text{ J K}^{-1}$. Since $\gamma\hbar B_0 \ll k_B T$ at body temperature and clinical field strengths, we can write this as

$$\begin{aligned} \frac{N_{\text{up}}}{N_{\text{down}}} &= 1 + \frac{\gamma\hbar B_0}{k_B T} \\ \Rightarrow N_{\text{excess}} &= N_{\text{up}} - N_{\text{down}} = \frac{N_{\text{total}}}{2} \cdot \frac{\gamma\hbar B_0}{k_B T} \end{aligned}$$

This difference creates the net magnetization M_0 . If we replace N_{total} with proton density ρ we will get M_0 per unit volume. We also know that the magnetic

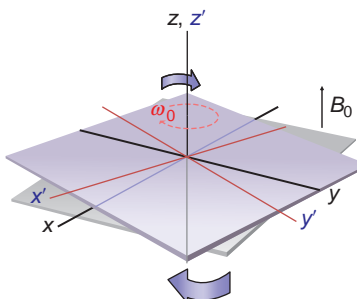


Figure 9.5 The rotating frame of reference. The coordinate system x' , y' , z' is considered to be rotating at the Larmor frequency in the same direction as the nuclear spins, which thus appear stationary.

moment of the proton has a magnitude of $\gamma/2\hbar$; thus we can calculate

$$M_0 = \frac{\rho\gamma^2\hbar^2 B_0}{4k_B T}$$

Now we can calculate that water contains 6.67×10^{22} protons ml^{-1} , so we can show that at body temperature and 1.5 T we get $M_0 \approx 0.02 \mu\text{T ml}^{-1}$. Assuming that the human head has a volume of approximately 1500 ml and is about 80% water, $M_0 \approx 20 \mu\text{T}$, which is small, but measurable!

The Rotating Frame of Reference

In order to explain the effects of RF pulses and relaxation mechanisms, it is helpful to use a rotating frame of reference. However, many people automatically think about the protons in a rotating frame, and may actually find it confusing to have it explained. Physicists should read this section, but others may like to skip it for now. Refer to the Appendix if you're unsure about vector notation and the cross product.

We choose a frame rotating at the Larmor frequency about the z axis, which is defined by the direction of B_0 (Figure 9.5). In the rotating frame, spins at exactly the Larmor frequency are stationary, while those at higher or lower frequencies gain or lose phase respectively. We can describe the motion of the magnetization \mathbf{M} in the new rotating frame as

$$\left(\frac{d\mathbf{M}}{dt}\right)_{\text{rot}} = \left(\frac{d\mathbf{M}}{dt}\right)_{\text{fixed}} - \boldsymbol{\omega} \times \mathbf{M}$$

where $\boldsymbol{\omega}$ is the frequency of the rotating frame. We already know that a magnetic moment precesses in an external field \mathbf{B} (see Box 'Derivation of the Larmor Frequency: Classical Mechanics'), with its motion described by

$$\left(\frac{d\mathbf{M}}{dt}\right)_{\text{fixed}} = \gamma\mathbf{M} \times \mathbf{B}$$

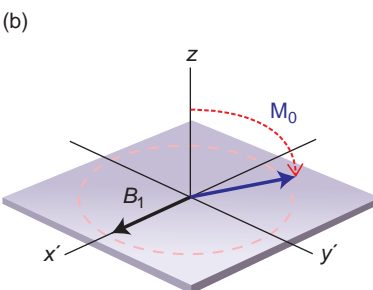
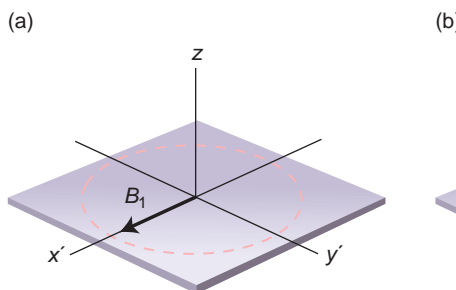


Figure 9.6 (a) The RF pulse produces a fixed magnetic field B_1 in the rotating frame. (b) M_0 precesses about B_1 until the RF is switched off.

Thus we can write

$$\begin{aligned} \left(\frac{dM}{dt} \right)_{\text{rot}} &= \gamma \mathbf{M} \times \mathbf{B} - \omega \times \mathbf{M} \\ &= \gamma \mathbf{M} \times \mathbf{B} + \gamma \mathbf{M} \times \frac{\omega}{\gamma} \\ &= \gamma \mathbf{M} \times \left(\mathbf{B} + \frac{\omega}{\gamma} \right) \end{aligned}$$

The term ω/γ represents a fictitious magnetic field which arises because of the rotation of the frame of reference, and thus $(\mathbf{B} + \omega/\gamma)$ is the effective magnetic field experienced by the spins. So the motion of the magnetization in the rotating frame can be described by the same equation as in the fixed frame. This allows us to add fields due to RF pulses and predict the motion of M_0 in those conditions, if necessary using an off-resonance rotating frame. Notice that if $\mathbf{B} = B_0$ and the frame rotates at $-\omega_0$, \mathbf{M} is stationary, i.e. in the basic frame rotating clockwise around z at the Larmor frequency M_0 is static. From now on we will always use x and y for the fixed laboratory frame, and x' and y' for the rotating frame. Since z and z' are aligned, we will just use z for this axis.

As you can probably guess, we tip M_0 into the transverse plane using a 90° RF pulse. What exactly is going on during the pulse though? Obviously the RF frequency used must be the Larmor frequency due to the resonance condition. The RF pulse creates a magnetic field within the transmit coil which is perpendicular to B_0 and oscillating at the Larmor frequency. In the rotating frame, this is a static field B_1 aligned along x' in the transverse plane (Figure 9.6a). M_0 moves away from the z axis until the RF pulse is switched off (Figure 9.6b). The motion of M_0 looks like a spiral since it is also precessing about the z axis (see Figure 9.7). The maths for this isn't much fun, but we can make it easier by subtracting or removing the ω_0 precession. A nice analogy for this is watching a fairground roundabout with horses going up and

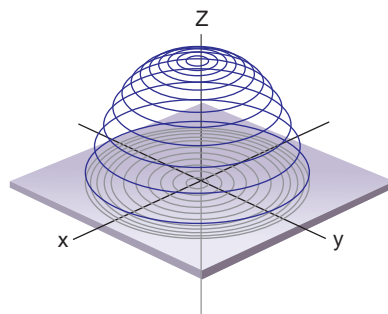


Figure 9.7 During the RF pulse M_0 spirals away from the z axis and down towards the transverse plane.

down. If you hop onto the roundabout and stand next to the horse, ignoring the outside world spinning backwards, the up-and-down motion is the only one you 'see'. Refer to Box 'The Rotating Frame of Reference' for the maths explanation.

For a simple RF pulse switched on and then off (known as a 'hard' pulse), the flip angle (α) is given by

$$\alpha = \gamma B_1 t_p$$

where B_1 is the strength of the RF magnetic field and t_p is the duration of the pulse. If M_0 ends up exactly in the transverse plane, $\alpha = 90^\circ$ and the RF pulse is called a 90° pulse. Leaving the RF on for twice as long (or doubling its strength) would turn M_0 through exactly 180° , and the pulse would then be called a 180° pulse. Since time is always a crucial factor in MRI, we tend to just change the strength of the pulse to produce different flip angles. The RF pulse has another important effect on the spins, bringing them all into phase. This means that they all point to the same position on the precession circle.

In the Rotating Frame Again

The RF wave is produced either linearly or circularly polarized (see Chapter 10), and creates a fixed magnetic field B_1 in the rotating frame (Figure 9.6a). (A linearly polarized wave can be considered as two counter-rotating circularly polarized waves. The one

which is in the clockwise direction produces B_1 , while the other is ignored.) The motion of M_0 in the rotating frame is given by

$$\left(\frac{d\mathbf{M}}{dt}\right)_{\text{rot}} = \gamma\mathbf{M} \times \left(\mathbf{B}_0 + \frac{\omega}{\gamma} + \mathbf{B}_1\right) = \gamma\mathbf{M} \times \mathbf{B}_1$$

provided $\omega = -\omega_0$, i.e. the frame is rotating clockwise at ω_0 . Thus the motion of M_0 will be to precess in the rotating frame about B_1 (Figure 9.6b). Note that the magnitude of B_1 is much smaller than B_0 , so the precession will be much slower, typically of the order of 100 Hz (cf. 63 MHz Larmor frequency at 1.5 T). The flip angle at the end of a pulse of duration t_p will be

$$\alpha = \gamma B_1 t_p$$

To produce a 90° pulse lasting 0.25 ms, for example, we need a B_1 of only 23 μT .

Paradoxes in QM

Some useful insights into excitation can be found by considering the quantized protons, rather than just the macroscopic magnetization. Unfortunately not all the concepts can be directly translated between QM and CM, so we will point out where the usefulness of QM stops, in our opinion at least.

When the population of protons is irradiated by an RF field, protons can flip between energy levels. Spin-up protons can absorb energy to jump into the spin-down position, while those in the spin-down state are stimulated into giving up an equal amount of energy to drop into the spin-up state, and there is an equal probability of each transition. Since in equilibrium there are more spin-up protons than spin-down, the net effect will be absorption of energy from the RF wave, causing the ‘temperature’ of the spin system to rise. The protons’ temperature is considered separately from the temperature of the surrounding tissues, known as the lattice, which will eventually come into equilibrium with the spins. We will come back to this idea when we consider spin-lattice relaxation.

Taking the simple idea of population difference and absorption of RF, it can be seen that the maximum absorption will be when all the spin-down protons have flipped into the spin-up position and vice versa. This is known as population inversion, and can be easily considered as a 180° pulse which flips the magnetization from z to $-z$. The definition of a 90° pulse can then be considered to be half that amount of energy, which is thought of as equalizing

the populations, leaving no magnetization along the z axis. Thus far the QM concepts seem to agree with our macroscopic observations, and they can be helpful up to this point.

However, we cannot take this picture much further, not least because pulses larger than 180° can be used and have a measurable effect on the spin system, which is difficult to reconcile with the idea that there is a maximum absorption of energy which causes population inversion. Also, from the Boltzmann distribution, we know that increasing temperature will decrease the population difference between the two states. Thus the magnetization should decrease monotonically to zero with increasing absorption of energy. It also means that population inversion would give the spins a negative temperature, which in turn places other thermodynamic constraints on the system.

This raises some strange paradoxes which are difficult to understand in everyday terms, and we would recommend that if you want to pursue these ideas you should consult some of the physics texts listed at the end of this chapter. The good news is that many people probably have rather confused internal ideas about MRI, mixing up the concepts of classical and quantum mechanics in all sorts of odd ways, but so long as you can correctly predict the effect of changing parameters such as TR, does it matter? We think probably not!

Having rotated M_0 into the transverse plane, we measure it by detecting the voltage it induces in a receive coil which is sensitive only to magnetization perpendicular to B_0 . In the laboratory frame M_0 is now precessing in the transverse plane (see Figure 9.8a), so the coil sees an oscillating magnetic field which induces a voltage varying at the Larmor frequency. The amplitude of the signal decays exponentially to zero in only a few milliseconds (Figure 9.8b), because the protons rapidly dephase with respect to each other. This signal is known as the Free Induction Decay (FID), a rather obscure term coined by one of the original NMR researchers. In the next section we will look in more detail at what happens after excitation.

9.4 Relaxation Times

Having excited the protons in order to flip them into the transverse plane, they begin to relax back to their

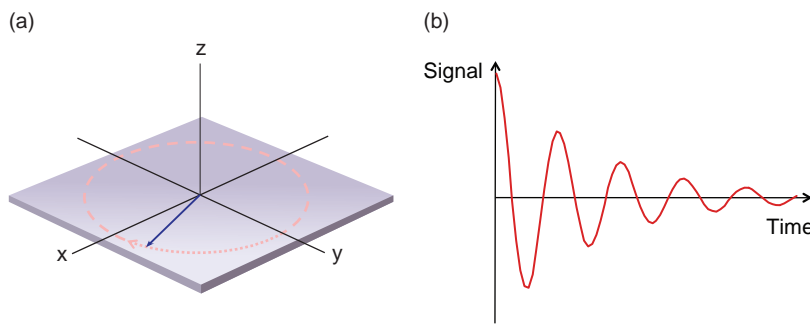


Figure 9.8 (a) Precession of the flipped magnetization in the transverse plane. (b) Signal induced in the receive coil – the Free Induction Decay (FID).

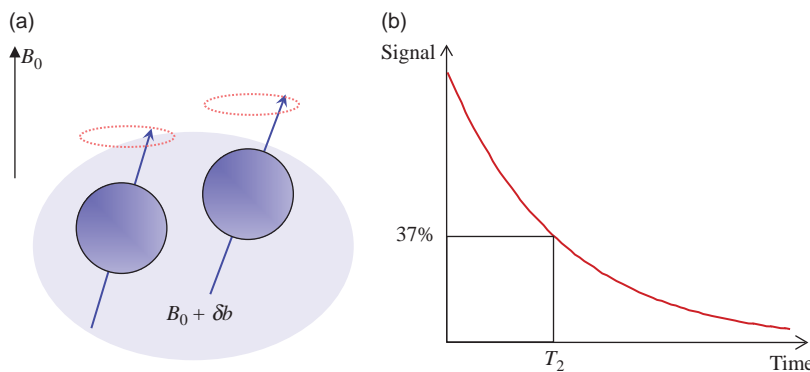


Figure 9.9 (a) As two protons come close together, they experience a change in magnetic field strength (δB) which changes their precessional frequency. (b) Because the interactions are random, the resultant transverse magnetization vector decays to zero exponentially. T_2 is the time taken for the transverse magnetization to drop to 37% of its initial size.

equilibrium position as soon as the RF pulse is switched off. There are two main features of the relaxation: a dephasing of the spins following their phase coherence after the pulse, and realignment along the z axis as they lose the energy they absorbed from the pulse.

The spins dephase because of small differences in their precessional frequencies. Thinking of the system in the rotating frame (rotating at the Larmor frequency), a slightly higher frequency will make spins dephase in the clockwise direction, while a lower frequency causes an anticlockwise phase angle. Anything that changes a spin's frequency from the Larmor frequency will add to the dephasing. For the FID, the dominant effect is the unavoidable inhomogeneity in the main magnetic field. A second effect is formed by the interactions between spins as they move around within the tissues. It is this interaction that we call *spin-spin relaxation*, characterized by the spin-spin relaxation time T_2 , which is independent of the magnet in which it is being measured and (for practical purposes) largely independent of field strength.

To understand T_2 , imagine a system of excited protons in a perfect magnetic field, free to move around in a random fashion. They all precess in the transverse plane, ignoring the relaxation back to the z axis for now. So long as they are evenly distributed around the volume, they are all precessing at the Larmor frequency and remain in phase in the rotating frame. However, if two protons come close together, each of them experiences a slightly higher or lower magnetic field, as the magnetic moment of the other proton adds or subtracts from the main field (Figure 9.9a). Their precessional frequencies change instantaneously to match the ‘new’ field, and each proton will dephase with respect to the Larmor frequency. When they move apart again they both return to the Larmor frequency, but the phase angles they acquire during the interaction are irreversible. Over time each proton will interact with many thousands of other protons, and the phase angles become larger and larger until all the protons are out of phase with each other. The vector sum of the magnetic moments, which is the signal we detect in the MR receiver, gradually decays from a maximum

Table 9.1 Selection of T_1 and T_2 values for tissues at 0.5 T, 1.5 T and 3 T. All values measured *in vivo* from human tissues

Tissue	T_1 (ms)		T_2 (ms)			
	0.5 T	1.5 T	3 T	0.5 T	1.5 T	3 T
White matter	520 ^f	560 ^a	832 ⁱ	107 ^b	82 ^c	110 ⁱ
Grey matter	780 ^f	1100 ^a	1331 ⁱ	110 ^b	92 ^c	80 ⁱ
CSF	–	2060 ^e	3700	–	–	–
Muscle	560 ^g	1075 ^d	898 ^h	34 ^g	33 ^g	29 ^h
Fat	192 ^b	200 ^b	382 ^h	108 ^b	–	68 ^h
Liver	395 ^b	570 ^e	809 ^h	96 ^b	–	34 ^h
Spleen	760 ^b	1025 ^e	1328 ^h	140 ^b	–	61 ^h

Notes:

- ^a Steinhoff S, Zaitsev M, Zills K, Shah NJ (2001). 'Fast T_1 mapping with volume coverage'. *Mag Reson Med* 46: 131–140.
- ^b Bottomley PA, Foster TH, Argersinger RE, Pfeifer LM (1984). 'A review of normal tissue hydrogen NMR relaxation times and relaxation mechanisms from 1–100 MHz: dependence on tissue type, NMR frequency, temperature, species, excision and age'. *Med Phys* 11: 425–448.
- ^c Pfefferbaum A, Sullivan EV, Hedges M, Lim KO (1999). 'Brain gray and white matter transverse relaxation time in schizophrenia'. *Psychiatr Res* 91: 93–100.
- ^d Venkatesan R, Lin W, Haacke EM (1998). 'Accurate determination of spin-density and T_1 in the presence of RF field inhomogeneities and flip-angle miscalibration'. *Mag Reson Med* 40: 592–602.
- ^e Bluml S, Schad LR, Stepanow B, Lorenz WJ (1993). 'Spin-lattice relaxation time measurement by means of a TurboFLASH technique'. *Mag Reson Med* 30: 289–295.
- ^f Imran J, Langevin F, Saint Jalme, H (1999). 'Two-point method for T_1 estimation with optimized gradient-echo sequence'. *Magn Reson Imag* 17: 1347–1356.
- ^g de Certaines JD, Henrikson O, Spisni A, Cortsen M, Ring PB (1993). 'In vivo measurements of proton relaxation times in human brain, liver, and skeletal muscle: a multi-centre MRI study'. *Magn Reson Imag* 11: 841–850.
- ^h de Bazelaire CM, Duhamel GD, Rofsky NM, Alsop DC (2004). 'MR imaging relaxation times of abdominal and pelvic tissues measured *in vivo* at 3.0 T: preliminary results'. *Radiology* 230: 652–659.
- ⁱ Wansapura JP, Holland SK, Dunn RS, Ball WS Jr (1999). 'NMR relaxation times in the human brain at 3.0 tesla'. *J Magn Reson Imaging* 9: 531–538.

immediately after the excitation pulse down to zero (Figure 9.9b). Since their motion is random, the dephasing is an exponential decay process, which we call spin–spin relaxation.

Although the transverse magnetization decays, there is no net loss of energy in spin–spin relaxation. To lose energy, the protons must interact with the surrounding tissues (Figure 9.10), known as the lattice, which can absorb the energy and disperse it via blood flow. As the protons lose the extra energy from the RF pulse, they gradually return to the equilibrium populations in the spin-up and spin-down states, so that eventually the magnetization along the z axis, M_z , is back to M_0 . This is known as *spin-lattice relaxation*, characterized by the spin-lattice relaxation time T_1 . Unlike T_2 , T_1 changes with field strength, getting longer as the field strength increases, and T_1 is always longer than T_2 . Table 9.1 shows some approximate values at 0.5 T, 1.5 T and 3

T (use these with caution – remember that *in vivo* measurements are often inaccurate).

Since we consider the net magnetization being flipped through 90° by the RF pulse, it is tempting to think of the relaxation processes as simply being the reverse, with M_0 slowly turning through -90° back to its equilibrium position. This would explain the gradual loss of transverse magnetization and recovery of the longitudinal magnetization. However, it would also imply that T_1 and T_2 must be equal to each other, and we know that this is not the case in biological tissues. Many textbooks do not make this clear enough, showing T_1 and T_2 curves without time scales so it is difficult to see that two separate processes are at work. T_2 dephasing happens quickly, so the transverse magnetization is zero after only a few hundred milliseconds. T_1 relaxation is much slower and it may take several seconds before M_0 is fully restored along the z axis.

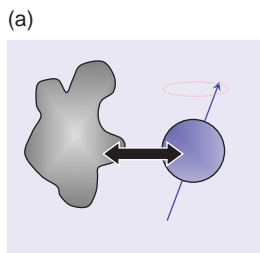


Figure 9.10 (a) The spins can transfer energy to the surrounding lattice, allowing them to relax back to equilibrium. (b) The process is random, so the recovery of M_z to M_0 is controlled by an exponential. T_1 is the time taken for the magnetization to recover to 63% of its equilibrium value.

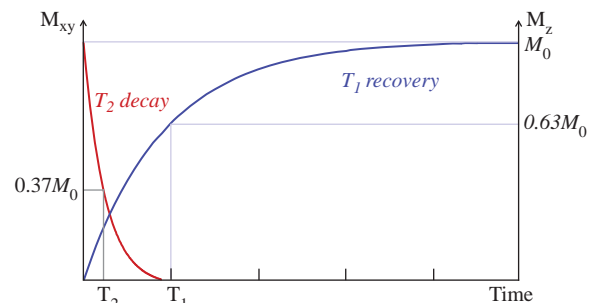


Figure 9.11 T_1 and T_2 relaxation occur simultaneously, but T_2 is much quicker than T_1 .

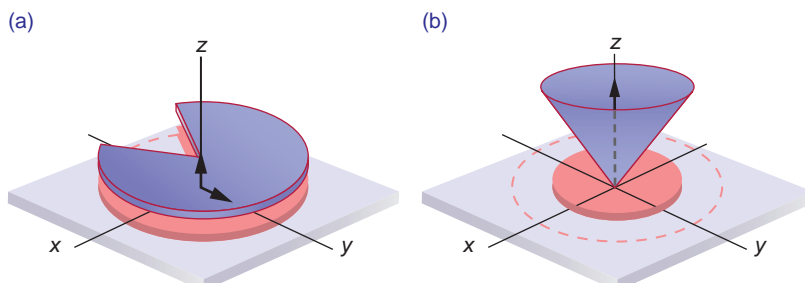


Figure 9.12 T_2 relaxation causes rapid fanning out of the protons in the transverse plane (a). T_1 is much slower, and can be thought of as an umbrella closing up (b).

If we plot both curves on the same graph for a tissue with $T_1 \approx 5 \times T_2$ (Figure 9.11) you can see the differences in the time scales for these two processes. Looking at Table 9.1 you can see that in most tissues T_1 is several times longer than T_2 . It is better to use a more specific mental picture in which the protons rapidly dephase like a fan opening up in the transverse plane, before folding up slowly towards the z axis like an umbrella closing (see Figure 9.12). Compare this with the simplistic idea of M_0 rotating back and forth between the z - and y -axes, and you will realize that too much simplification can be seriously misleading. Although the full picture takes a bit more effort to think about, it won't let you down!

9.5 Creating Echoes

In MRI we never measure the FID directly; instead we use two types of echo, gradient (GE) and spin echoes (SE). In each case the sequence starts with an RF excitation pulse, 90° in the case of SE and

smaller angles in GE. We will explain gradient echoes first.

In the GE sequence (Figure 9.13), we apply a negative gradient lobe immediately after the excitation pulse. This causes rapid dephasing of the transverse magnetization, much faster than the normal FID. After the negative lobe we apply a positive gradient, which simply reverses the magnetic field gradient. Spins that were precessing at a low frequency due to their position in the gradient will now precess at a higher frequency because the gradient will now add to the main field, and vice versa. Spins which were previously dephasing now begin to rephase, and after a certain time they will all come back into phase along the y' axis forming the gradient echo. However, the positive gradient only compensates for the dephasing caused by the negative gradient lobe, it does not refocus dephasing due to the main magnetic field inhomogeneities or spin-spin relaxation (which is explained in the next section). The height of the echo (S_{GE}) is thus determined by the FID decay curve which depends on T_2^* .

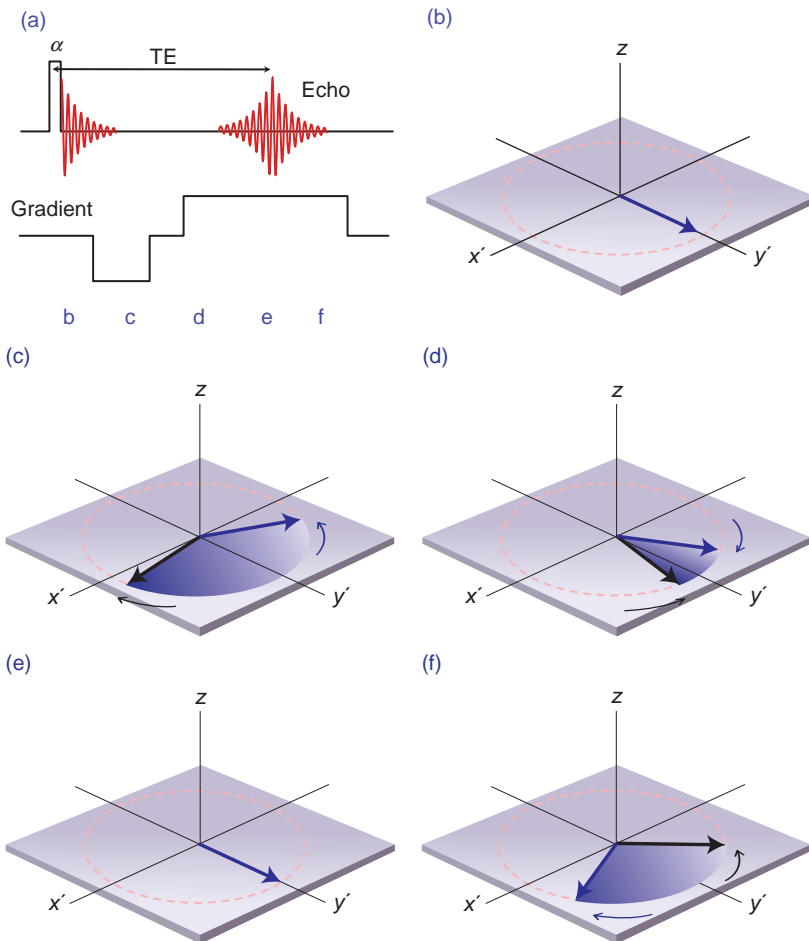


Figure 9.13 (a) Simple gradient-echo sequence. (b) Spins initially along the y' axis are rapidly dephased by the negative lobe (c). When the gradient is switched positive (d), the spins begin to rephase, forming an echo (e). If the gradient is left on (f) dephasing will occur again.

$$S_{GE} = S_0 \exp\left(-\frac{TE}{T_2^*}\right)$$

where S_0 is the initial height of the FID. T_2^* is a composite relaxation time which includes T_2 , inhomogeneities due to the main field and tissue susceptibility, and diffusion of the protons.

In the spin-echo sequence (Figure 9.14) we leave the spins to dephase naturally after the 90° pulse for a certain time. Then we apply a 180° pulse on the $+y'$ axis which flips all the spins through 180° about the y' axis. It does not change the precessional frequencies of the spins, but it does reverse their phase angles. Spins which were in a lower magnetic field strength will have been dephasing anticlockwise; the 180° pulse flips them over and they now appear to have been in a higher magnetic field and have dephased clockwise. Similarly, spins which were

dephasing clockwise will appear to have been in a lower magnetic field and dephased anticlockwise. Assuming that the spins do not move too far within the imaging volume, they will continue to experience the same magnetic field inhomogeneities and continue to dephase in the same direction. After a time equal to the delay between the 90° and the 180° pulse, all the spins will come back into phase along the $+y'$ axis, forming the spin echo. The phase-reversal trick means that the echo height will only depend on T_2 and diffusion, and not on the magnetic field inhomogeneities or tissue susceptibilities. Provided we keep the echo times fairly short, the diffusion component is negligible and we find that the signal S_{SE} is dependent on T_2 :

$$S_{SE} = S_0 \exp\left(-\frac{TE}{T_2}\right).$$

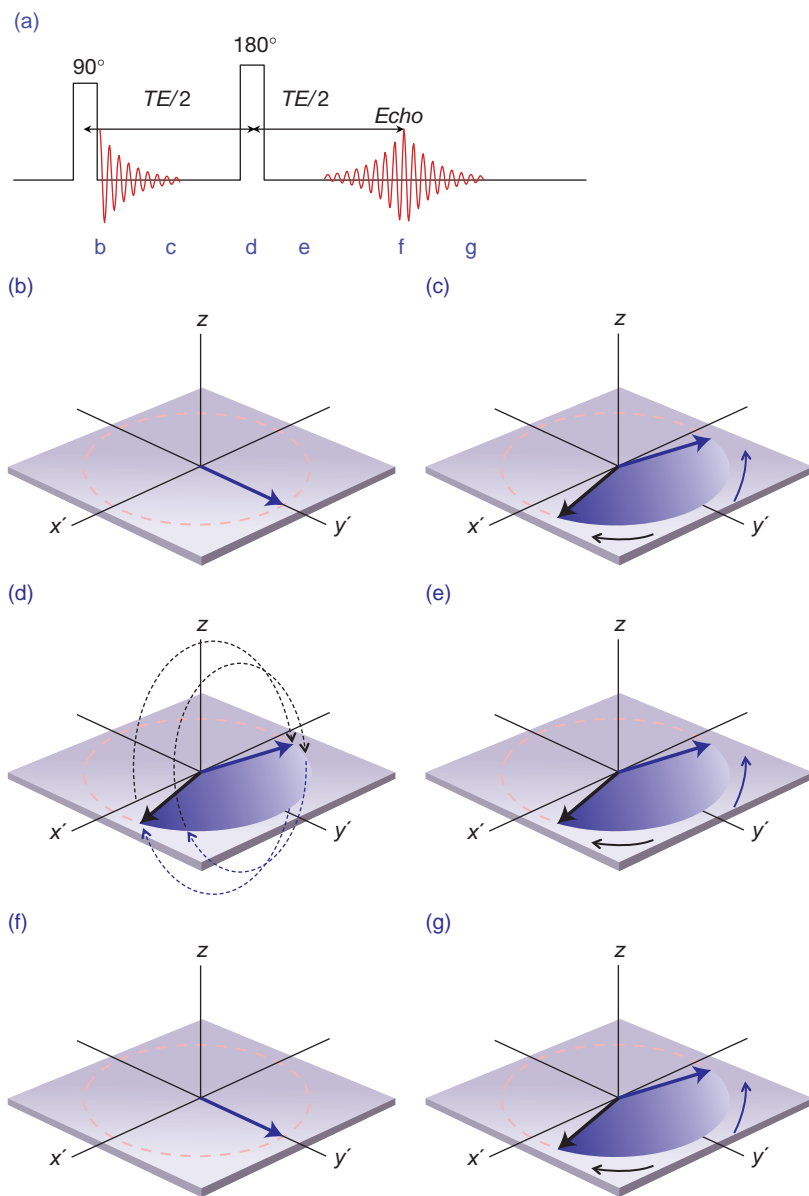


Figure 9.14 (a) Spin-echo pulse sequence. Spins initially in phase (b) dephase naturally (c) until the 180° pulse is applied (d). Immediately after the pulse their phases are reversed, but they continue to dephase in the same direction (e) forming an echo (f) and then dephasing again (g).

RF Phase Angles: Which Axis?

You may find that other texts show the 180° pulse on the $+x'$ axis so that the fan of dephasing protons is flipped a further 180° and creates a spin echo along the $-y'$ -axis, i.e. a negative echo (but then of course we take the magnitude for the final image intensity). Why have we done it differently? Well partly because we have found, over many years of giving lectures,

that people find the negative echo an extra complication, and we can avoid that just by putting the 180° pulse on $+y'$. Both forms create a spin echo of the same height, the only difference is in the direction of the vectors. It is also because multi-echo sequences always put the 180° pulses on $+y'$ instead of $+x'$, which partially compensates for imperfections in the RF pulse.

9.5.1 The 'Runners on a Track' Analogy (Slightly Reworked)

You may have come across this analogy to describe the spin echo in other textbooks or lectures. It is explained by saying that the runners all start at the same time (analogous to the 90° pulse exciting all the protons), but because they run at different speeds, after a while they are spread out along the track. The 180° pulse is like turning all the runners around at this point, so that they all have to run back to the starting point. Assuming they all continue to run at the same speeds, after an equal time they will all cross the starting point together – analogous to the protons coming back into phase to create the echo.

We can modify this slightly to explain the differences between spin echo and gradient echo, and also show why the echo heights depend on T_2 and T_2^* respectively. First, suppose that as well as running at different speeds, the runners get tired at different rates, so they tend to slow down. Also imagine that the track is not flat but rather lumpy, and that it is different in each lane. To explain the spin echo first, let the runners start together running in one direction; after a while they are spread out due to the differences in their running speeds and the track conditions in each lane. When the 180° pulse is applied the runners all turn around and run back towards the starting point, and magically the track conditions are reversed: the bad lanes become perfect, the good ones become difficult. So if the runners all go at the same speeds as before, the effects of the track will be evened out and they will all cross the starting point together. Since they get tired though, they don't manage to maintain their speeds, and in fact we only get some of them back at the same time.

To extend the analogy to gradient echo, the gradient reversal is the turning point instead of the 180° pulse. This time, however, the track conditions don't get fixed and the runners who had bad lanes to start with have to run back under the same conditions. As well as tiredness slowing them down, the lane conditions alter their performance. At the echo time, even fewer of the runners are back at the starting point. In this extended analogy, the runners' different tiredness rates are analogous to T_2 and the lane conditions are analogous to the magnetic field inhomogeneities.

9.6 Relaxation Time Mechanisms

The time difference between T_1 and T_2 is extremely important in all MR imaging or spectroscopy. We always use a repeated sequence of RF and gradient pulses, with a repetition time (TR). Consider the simple case of a repeated $90^\circ\text{-}TR\text{-}90^\circ\text{-}TR$ sequence; if TR is at least five times the longest T_1 of the tissues, all tissues will be back to equilibrium before the next 90° and the signal in the transverse plane will depend only on the proton density. However, if TR is shorter, M_z will not have had sufficient time to grow back to M_0 and a smaller signal will be flipped into the xy plane. (Provided TR is still longer than five times T_2 , there will be no transverse magnetization to confuse the issue. When TR is so short that there is still M_{xy} before the next pulse, there is a more complex situation which will be discussed in Chapter 13.) This loss of signal is known as *saturation*.

To help fix this new picture of relaxation in your mind, let us review the way TR affects T_1 contrast in spin-echo images (first discussed in Section 3.5), illustrated in Figure 9.15. Assuming we start from full relaxation, the initial 90° pulse rotates all the longitudinal magnetization into the transverse plane. After the spin echo has been formed, T_2 decay continues while M_z grows in the z direction – the red vector has a longer T_1 than the blue one, so it recovers more slowly. When the second 90° pulse is applied, provided $TR > 5 \times T_2$, M_{xy} is zero, but T_1 recovery is not complete. Only the z magnetization will be flipped into the transverse plane to create signal for the next echo. Both M_z go back to zero and begin to relax back to equilibrium again. After a further TR, both vectors have recovered to exactly the same amount, so the third and all subsequent excitations create a steady signal height which is T_1 -weighted.

Strictly speaking, a dummy excitation is needed for a spin-echo sequence to reach the *steady state*. However, the normal linear phase encoding scheme means that the first echo does not affect contrast in the final image, so it is rarely done in practice. Gradient-echo sequences are another matter: the number of pulses needed to reach a steady state depends on TR and the flip angle, as well as the relaxation times of the tissues (see Section 13.1 and Figure 13.1).

In this section we will consider the interactions between protons and their environment which cause

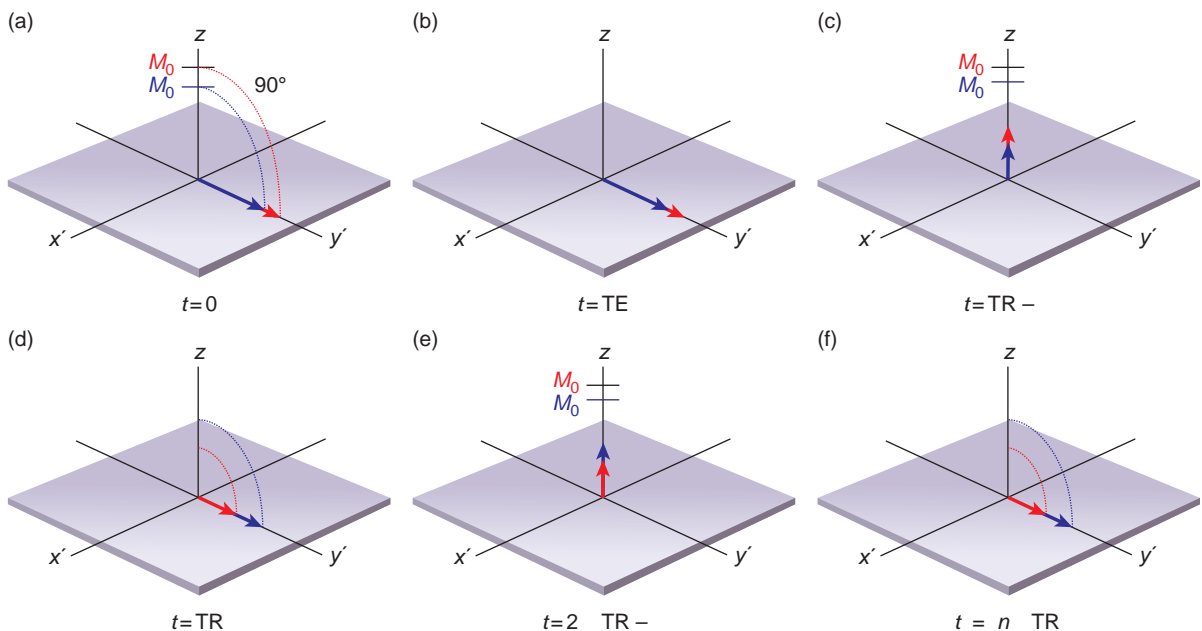


Figure 9.15 (a) During the first 90° pulse, both M_0 are rotated into the transverse plane, producing M_{xy} (b). (c) After $5 \times T_2$, M_{xy} has decayed to zero while M_z recovers from zero with T_1 relaxation. When the second 90° pulse is applied after time TR , (d) reduced signals are rotated into the transverse plane. (e) After another TR , both M_z have recovered to the same height as before, so the third 90° pulse creates the same T_1 -weighted signal in the transverse plane (f).

spin–spin and spin–lattice relaxation. Much of our understanding of relaxation is based on work published in 1948 by Bloembergen, Purcell and Pound, which is usually known as the BPP theory of relaxation. To understand this you must be familiar with the concept of molecular motions: every atom or molecule is rotating, vibrating and translating (i.e. moving from one position to another) in random directions. Not only that, molecules change their motion rapidly, so they will be vibrating one second and rotating the next, because they collide with each other. Actually a molecule spends only a tiny fraction of a second in a particular state of motion, as little as 10^{-12} s, before suffering a collision which changes its motion to something different. This is known as the correlation time τ_c of the molecule, and if you use the standard idea of gases, liquids and solids you will be able to imagine that solids tend to have very long correlation times (molecules are closely packed together and move slowly), while gases at the other extreme have shorter τ_c (molecules are further apart and move quicker). τ_c is also affected by temperature, with higher temperatures giving shorter correlation times.

The Bloch Equations

Bloch derived a set of differential equations which describe the changes in the magnetization during excitation and relaxation. They are sometimes called ‘phenomenological’ because they describe the phenomenon that we detect in the receive coil, rather than being derived from fundamental principles. Note that they are based entirely on classical mechanics. We start with

$$\frac{d\mathbf{M}}{dt} = \gamma \mathbf{M} \times \mathbf{B} = \gamma \begin{bmatrix} (M_y B_z - M_z B_y) \mathbf{i} \\ (M_z B_x - M_x B_z) \mathbf{j} \\ (M_x B_y - M_y B_x) \mathbf{k} \end{bmatrix}$$

We use a general expression for B which includes a static field along z and a second field rotating in the transverse plane

$$\begin{aligned} B_x &= B_1 \cos \omega t \\ B_y &= -B_1 \sin \omega t \\ B_z &= B_0 \end{aligned}$$

and add terms which account for the observed relaxations T_1 and T_2 , giving

$$\begin{aligned}\frac{dM_x}{dt} &= \gamma(M_yB_0 + M_zB_1 \sin \omega t) - \frac{M_x}{T_2} \\ \frac{dM_y}{dt} &= \gamma(M_xB_1 \cos \omega t - M_yB_0) - \frac{M_y}{T_2} \\ \frac{dM_z}{dt} &= -\gamma(M_xB_1 \sin \omega t + M_yB_1 \cos \omega t) - \frac{M_z - M_0}{T_1}\end{aligned}$$

These can then be solved with appropriate limiting conditions; for example, immediately after the RF pulse is switched off, $B_1 = 0$ and the solutions are

$$\begin{aligned}M_x(t) &= [M_x(0) \cos \omega_0 t + M_y(0) \sin \omega_0 t] \cdot \exp\left(-\frac{t}{T_2}\right) \\ M_y(t) &= [M_y(0) \cos \omega_0 t - M_x(0) \sin \omega_0 t] \cdot \exp\left(-\frac{t}{T_2}\right) \\ M_z(t) &= M_z(0) \exp\left(-\frac{t}{T_1}\right) + M_0 \left[1 - \exp\left(-\frac{t}{T_1}\right)\right]\end{aligned}$$

If the system was initially in equilibrium and the RF pulse was a 90° pulse applied along the $+x'$ axis, $M_x(0) = M_z(0) = 0$ and $M_y(0) = M_0$, giving the results

$$\begin{aligned}M_x(t) &= M_0 \sin \omega_0 t \cdot \exp\left(-\frac{t}{T_2}\right) \\ M_y(t) &= M_0 \cos \omega_0 t \cdot \exp\left(-\frac{t}{T_2}\right) \\ M_z(t) &= M_0 \left[1 - \exp\left(-\frac{t}{T_1}\right)\right]\end{aligned}$$

In complex notation this is

$$\begin{aligned}M_{xy}(t) &= M_0 \exp(i\omega_0 t) \cdot \exp\left(-\frac{t}{T_2}\right) \\ M_z(t) &= M_0 \left[1 - \exp\left(-\frac{t}{T_1}\right)\right]\end{aligned}$$

This tells us that the x and y magnetizations oscillate at the Larmor frequency while decaying with time constant T_2 , while the z magnetization simply grows from zero back to M_0 .

The Spectral Density Function and Water Binding

Statistical methods can be used to show that a collection of molecules with an average correlation time τ_c will have a range of motional frequencies described by something called the spectral density function $J(\omega)$. This simply shows the number of nuclei that tumble at each frequency. Figure 9.16 shows $J(\omega)$ for three materials with long, medium and short

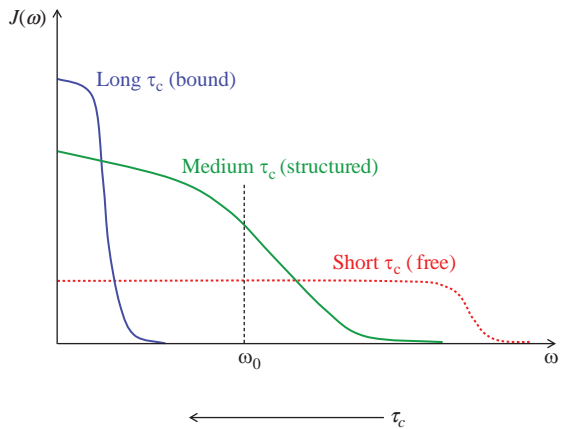


Figure 9.16 Spectral density functions $J(\omega)$ for three substances with varying correlation times τ_c .

τ_c . Long τ_c s mean that molecules spend a relatively long time in a particular motional state before suffering a collision, and we can see that most of the motional frequencies are very low. With shorter τ_c s, molecules are highly mobile and are changing their motional states with high frequencies. Notice that the Larmor frequency of most clinical MR systems, tens of MHz, is in the middle of the frequency range. We will come back to spectral density functions in the next two sections.

In biological systems, water is rarely a free liquid except in CSF, blood or cysts. Large molecules such as polysaccharides and proteins form hydration layers, layers of water molecules which are closely bound to the surface of the larger molecule. There is a continuous variation of 'binding', from the tightly bound protons close to the surface to the 'free' protons furthest away from large molecules. In addition, protons do not stay in one place but can be exchanged between different molecules. As they swap places, their bound properties change, and this changes the signal that they produce. This is known as free exchange of protons, and it means that the measured signal is a mixture of all the different signals, ranging from fully bound to completely free.

9.6.1 Spin–Lattice Relaxation

We know that an RF pulse on average promotes protons from the low-energy state to the high-energy state, causing a net absorption of energy. T_1 relaxation is the loss of the extra energy from the spin

system to the surrounding environment, or ‘lattice’ (hence ‘spin–lattice’ relaxation time). However, the high-energy state is a stable position for the proton and it does not return to the lower state spontaneously but requires an external stimulating field. Since the external B_1 field has been switched off, where does this field come from? As we have hinted in the previous section, it comes from neighbouring protons or other nuclei or molecules, which have magnetic moments. In water the nearest adjacent nucleus will be the other hydrogen atom on the same molecule. Therefore, relaxation will primarily arise through the magnetic moment that one hydrogen nucleus ‘sees’ as it tumbles relative to the moment of the other hydrogen nucleus. This is often called an intra-molecular dipole–dipole interaction (a dipole is simply a magnetic field with two poles, north and south – another term for a magnetic moment).

We have already seen that molecules have a range of motional frequencies, described by the spectral density function (see Box ‘The Spectral Density Function and Water Binding’). So the magnetic moments of these molecules will also have a frequency distribution. In order to induce the transitions needed for T_1 relaxation, the fluctuations have to be at the Larmor frequency, in the same way that the external B_1 field has to oscillate at the Larmor frequency. So we can predict that the more protons that tumble near the Larmor frequency the more efficient the T_1 relaxation will be. For example, more protons with intermediate binding tumble at the Larmor frequency than protons in either free fluids or bound in hydration layers. Hence the T_{1s} of such protons are short while both bound and free protons have long T_{1s} . The spectral density function also predicts that T_1 is frequency dependent, since a decrease in the strength of the static magnetic field will decrease the Larmor frequency. There will be more protons tumbling at the new lower Larmor frequency so the T_1 will be shorter.

9.6.2 Spin–Spin Relaxation

We know that T_2 relaxation arises from the exchange of energy between spins, hence the term ‘spin–spin relaxation’. No energy is actually lost from the spin system but the decay of transverse magnetization arises from the loss of phase coherence between spins, which arises from magnetic field inhomogeneities. These inhomogeneities may be either intrinsic or

extrinsic, i.e. internal to the proton system or external in the scanner. Only the intrinsic inhomogeneities contribute to T_2 .

Our description of molecular motions can also be used to describe the mechanism of T_2 relaxation. When molecules are tumbling very rapidly (i.e. free protons with short τ_c) then a particular dipole will see the local magnetic field as fluctuating very rapidly and effectively averaging out over a few milliseconds. This results in a relatively homogeneous local field and little dephasing, and is sometimes termed ‘motional averaging’. Conversely, a slowly tumbling molecule (bound protons close to large molecules) will see a relatively static magnetic field inhomogeneity and will be more effectively dephased with respect to other protons.

In terms of the spectral density function, we see that T_2 is affected by low-frequency motions as well as those at the Larmor frequency (for comparison, T_1 is only affected by Larmor frequency fluctuations). Bound protons have very short T_2 values, so short that even at the shortest echo times we can use in MRI their signals are completely decayed to zero. Free protons in bulk fluids have the longest T_2 s while those with intermediate binding have medium T_2 relaxation times.

A Magic Moment with Magic Angles

In highly ordered collagen-rich tissues such as tendon and ligament, water molecules bound to the collagen relax rapidly due to dipole–dipole interactions. Normally this results in a very short T_2 of less than 1 ms and the usual MR appearance of these structures is dark. However, the strength of the relaxation mechanism depends upon the angle of the collagen fibres with the B_0 field. At an angle approximately 55° or 125° to B_0 the interactions are very much reduced, resulting in an increase in T_2 and a hyperintense signal intensity on T_1w or PDw images. At the so-called magic angle, the T_2 of these tissues can be of the order of 20 ms. When the hyperintensity is unwanted this is known as the *magic angle artefact*, which is well recognized by musculoskeletal radiologists. Alternatively, scanning at the magic angle offers the opportunity to investigate tendon and ligament function and pathology, although in a conventional closed bore scanner it is extremely hard to arrange for the appropriate geometry. Studies on tendon and ligament properties have been carried out ex vivo (Figure 9.17).

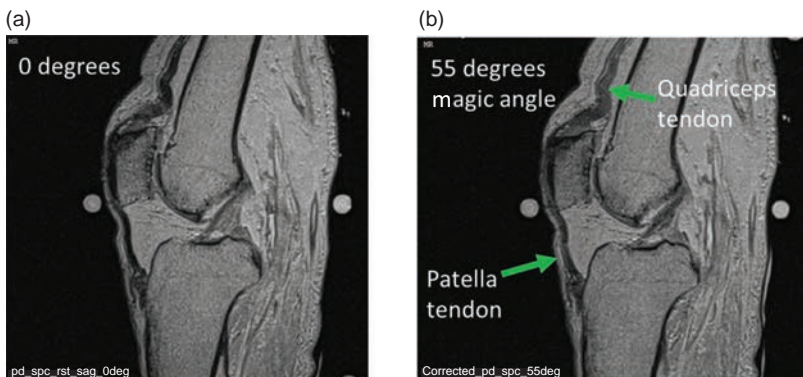


Figure 9.17 Cadaveric knee at 0° and the magic angle (55°) showing intensity increases (arrowed) in collagen-rich structures such as the quadriceps tendon and patellar tendon. Courtesy of K. Chappell, Imperial College, London.

9.6.3 BPP Theory for Body Tissues

We can summarize the BPP relaxation theory in terms of three tissue types. Let us start with water molecules that are essentially ‘free’ in solution, e.g. CSF, in which there is a reasonably uniform number of protons tumbling over a wide range of frequencies. There is only a small number tumbling at the Larmor frequency so T_1 relaxation is relatively inefficient, i.e. T_1 relaxation times are long. Similarly there is only a small number tumbling at very low frequencies; therefore, T_2 relaxation is also inefficient, i.e. T_2 relaxation times are long.

If we now consider water molecules that are ‘bound’ to larger macromolecules through the formation of a hydration layer, e.g. myelin, then there are a large number of protons tumbling at very low frequencies because their motion is restricted by the binding. In this case T_2 relaxation is very efficient (very short T_{2s}) and T_1 relaxation very inefficient (long T_{1s}). In fact, the T_2 relaxation times are so short that these molecules are ‘invisible’ with conventional MR imaging equipment, because by the time we collect echoes at even the shortest echo times their signals have fully decayed.

The third case to consider is when a proton is in the intermediate situation between bound and free; this is sometimes termed ‘structured’. Now there are a large number of protons tumbling at the Larmor frequency and T_1 relaxation will be the most efficient. T_2 relaxation will be intermediate between bound (short T_2) and free (long T_2). Most body tissues are in the structured water category. Lipids are a special case: due to the much larger size of unbound lipid molecules, their protons intrinsically tumble at lower frequencies, i.e. more tumble at the Larmor frequency and they therefore have short T_1 relaxation times.

Exchanging Protons

In describing relaxation mechanisms in this way we have ignored the fact that in reality water molecules are in fast exchange between the three states, i.e. over the time scale of an MRI scan a water proton will wander between bound, structured and free tissues. The proportion of time spent in each state will, in effect, be the same as the proportion of water in each state. The observed relaxation time is therefore a weighted-mean of the relaxation time of each fraction

$$\frac{1}{T_1^{\text{obs}}} = \frac{F^{\text{bound}}}{T_1^{\text{bound}}} + \frac{F^{\text{struct}}}{T_1^{\text{struct}}} + \frac{F^{\text{free}}}{T_1^{\text{free}}}$$

T_1^{bound} is very long, so only a small fraction of tissue water needs to be in the bound compartment to reduce the observed T_1 . A similar equation can be written for observed T_{2s} . While the bound compartment cannot be directly observed, it may however be investigated using magnetization transfer techniques (see Section 9.6.4). Water binding is not the only mechanism to affect relaxation in tissues. The presence of paramagnetic material, either intrinsic (blood breakdown products) or extrinsic (exogenous contrast agents such as gadolinium), can have a profound effect on observed relaxation times, as we will see in Section 9.6.4.

9.6.4 Magnetization Transfer and J-Coupling

Magnetization Transfer (MT) provides an additional source of contrast for certain tissues. A physical explanation is given in Box ‘Getting Bound Up: MT Explained’. MT can be exploited in imaging to reduce

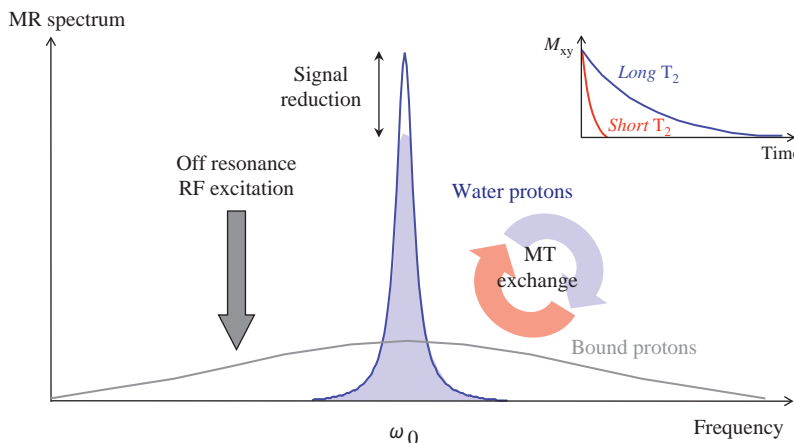


Figure 9.18 Magnetization transfer between bound and free protons. The free protons have long T_2 and the bound protons have a short T_2 , as shown in the inset. The bound protons are not normally ‘visible’ in the image.

the intensity of certain tissues and improve the contrast in images. Fluids, including CSF and flowing blood, fat and bone marrow are unaffected. A major application for MT Contrast (MTC) is for background suppression in time-of-flight angiography (see Chapter 15).

Getting Bound Up: MT Explained

MT contrast occurs where there is fast exchange between bound and free protons. The bound or restricted protons are those associated with macromolecules or hydration layers. This restricted pool has a very short T_2 and is invisible to direct imaging.

However, it can influence the observed MR signal through the exchange of energy (magnetization) between the two ‘pools’ (see Figure 9.18). The bound pool has a broad resonance and therefore can be excited by an RF pulse at a frequency several kilohertz away from the free water frequency, which therefore has no effect on the free protons. Exchange of protons between the bound and free pools means that saturated magnetization from the (invisible) bound pool will move into the free pool, thus reducing the total MR signal that can be observed.

APT and CEST

A new class of imaging techniques has been developed, based on the concept of magnetization transfer. These are known as **Chemical Exchange Saturation Transfer** (CEST) imaging. CEST methods use exogenous or endogenous agents with protons which easily exchange with targeted tissues *in vivo*.

For example, **Amide Proton Transfer** (APT) is a subclass of CEST that targets the proton part of the amide group (-NH-), which is available for exchange with other protons.

All these techniques use saturation at offset frequencies $\pm\Delta\omega$ on both sides of the water peak, and detect the slight drop in the water signal S_{sat} when the proton exchange occurs at one particular frequency (Figure 9.19). The saturation is achieved using a long pseudo-continuous RF train of pulses, typically lasting several seconds. The saturation train is followed by an image acquisition, for example EPI, multi-slice TSE, or 3D gradient echo. This is known as *z-spectrum imaging*, and typically generates 7–9 images at a few ppm either side of water. The saturation effect is very small, so it is common to process the images and generate an asymmetry map pixel-by-pixel:

$$MTR_{\text{asym}} = 1 - \frac{S_{\text{sat}}(\Delta\omega)}{S_{\text{sat}}(-\Delta\omega)}$$

CEST methods are very sensitive to both B_1 and B_0 inhomogeneities, and additionally take several minutes to acquire because it is necessary to sample several offset frequencies. Several CEST agents, including APT, show promise for good sensitivity in detecting malignant tumours. APT is also sensitive to changes in pH, which is potentially useful in acute stroke since lactic acid accumulates in the infarct core.

J-coupling is an interaction between the hydrogen nuclei on neighbouring atoms, which causes a splitting of the resonance peak. It is particularly important

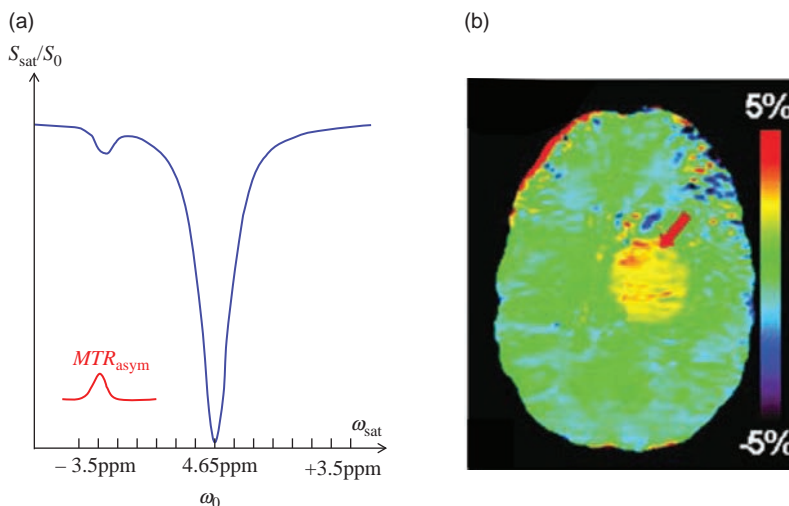


Figure 9.19 CEST imaging exploits the chemical exchange of protons between endogenous agents (in this case the amide group) and other tissues. (a) The amide proton resonates at 8.25 ppm , so $\Delta\omega$ is varied between $\pm 4 \text{ ppm}$ to capture the saturation transfer. (b) The MTR_{asym} image shows high signal in active tumour.

in fat molecules that contain long chains of carbon atoms. If the protons are saturated, usually by repeated RF pulses at relatively short TRs, they become decoupled and the split peak collapses to a single peak. The single peak has a higher amplitude and is narrower than the split peak, corresponding to a longer T_2 . The difference between J -coupled and J -decoupled signals can be seen by comparing turbo spin echo (TSE) T_2 -weighted images to conventional spin-echo (SE) T_2 -weighted images. The TSE images have brighter fat signals than they should because the protons are decoupled and their T_2 is apparently lengthened. In the conventional SE images, J -coupling in the lipids reduces their T_2 and they have a darker appearance.

9.7 Gadolinium-based Contrast Agents

Now that you have a good idea of the relaxation mechanisms in MR, it is time to look more closely at the effect of gadolinium-containing contrast agents. In Chapter 3 we mentioned that there are other contrast agents for MRI, based on super-paramagnetic iron oxides or manganese; however, many of these have been withdrawn by manufacturers so we will not waste our time discussing the SPIOs or manganese.

By now you already know that gadolinium is a paramagnetic element. It has seven unpaired electrons in its electronic structure and becomes quite strongly magnetized when placed in a magnetic field, whereas most body tissues are diamagnetic and only become weakly magnetized. Gadolinium is toxic in its elemental state, so for MRI use it is always chelated to a

ligand (a large inert molecule). You can think of these complexes as safe chemical ‘wrappers’ around the gadolinium atom which eliminate toxicity but preserve its paramagnetic properties.

When a gadolinium contrast agent is injected into the body, it is distributed via the vasculature to all perfused tissues. Although it is too large a molecule to cross the blood–brain barrier quickly, it does slowly leak out into the brain tissues, but rapidly accumulates in lesions where the blood–brain barrier is disrupted. In most other organs it passes from the vasculature into the interstitial space relatively quickly. After the initial redistribution into the extracellular fluid space with a half-life of about 11 min, gadolinium is gradually excreted via the kidneys with a biological half-life of approximately 90 min, so in most patients it is not detectable in tissues after about 6 h although it may linger in the urine and bladder for a day.

The effect of the strongly paramagnetic gadolinium is to decrease T_2 and T_1 relaxation times of protons in the immediate vicinity of the molecule. In this respect gadolinium behaves just like any magnetic field inhomogeneity but acting over a very small distance not much larger than the complex itself. As these protons exchange with other protons (see Section 9.6) further away from the gadolinium complex there is an overall reduction of T_1 and T_2 . At low concentrations such as those used in normal clinical practice, the major effect is the T_1 shortening (see Figure 9.20), and tissues which take up the agent have enhanced signal intensity on T_1 -weighted images.

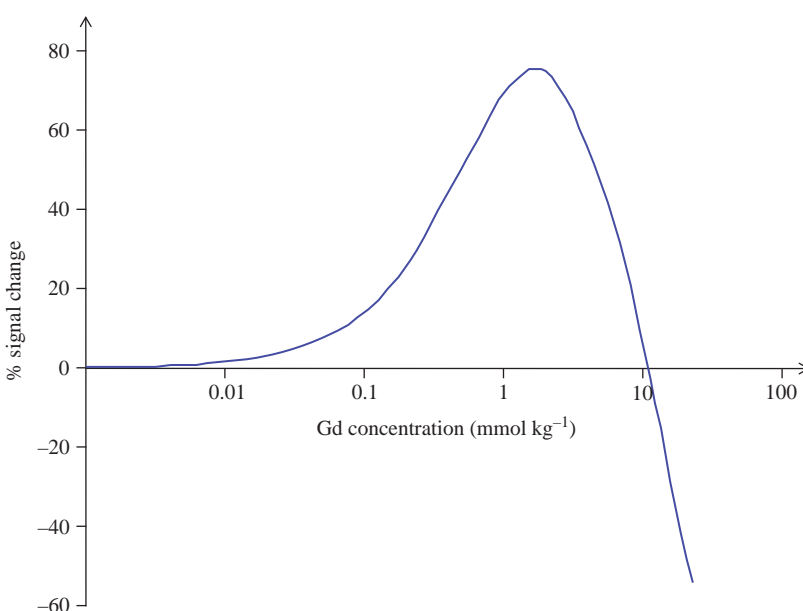


Figure 9.20 Signal intensity versus concentration of gadolinium, calculated using a T_1 -weighted SE sequence ($TR = 400$ ms, $TE = 15$ ms) and a tissue with $T_1 = 800$ ms and $T_2 = 75$ ms.

Dosage varies depending on the particular formulation, and to some extent the body area being imaged, but in general a dose of 0.1 mmol Gd per kilogram of body weight is used. Doses for children should always be adjusted based on the child's weight. Double-dose injections may be used for MR angiography, viability and perfusion imaging and have been shown to improve the conspicuity of lesions in multiple sclerosis and metastatic disease. Recent awareness about the link between Gd and a disease called Nephrogenic Systemic Fibrosis (NSF) has made the MRI community more cautious about very high doses (see Section 20.7).

There are several different formulations available commercially with various osmolalities and safety profiles (see Table 20.7). In general, gadolinium is a safe drug well tolerated by subjects, and apart from NSF there are only a handful of serious adverse effects noted in the literature. The main contraindications are poor renal function (with glomerular filtration rate <30 ml min $^{-1}$), and pregnancy. The gadolinium complex crosses the placenta into the fetal circulation and there is insufficient safety data about fetal exposure to gadolinium. Gadolinium also crosses into breast milk, so lactating mothers should not breastfeed for 24 h following gadolinium administration. Full details of contraindications and clinical applications can be found on the information insert in any preparation of gadolinium.

Contrast Agent Relaxivity

The effect of contrast agents on tissue relaxation times is best described using relaxation rates rather than times. The relaxation rate is simply the inverse of the relaxation time, so we can define

$$R_1 = \frac{1}{T_1} \quad R_2 = \frac{1}{T_2} \quad R_2^* = \frac{1}{T_2^*}$$

Relaxation rates are additive, so for example we can redefine the effective transverse relaxation rate as

$$R_2^* = R_2 + \frac{1}{2} \gamma \Delta B_0$$

For contrast agents we can define a specific relaxivity r , which describes how much they change relaxation rates per molar concentration. Multiplying the specific relaxivity by the concentration in a particular tissue gives the increase in relaxation rate caused by the contrast agent, so the new relaxation rate will be

$$R' = R + rC$$

The relaxivity r may be different for longitudinal and transverse relaxation rates (usually denoted r_1 and r_2 respectively), but in the case of gadolinium they are approximately the same, 4 and 5 mmol $^{-1}$ s $^{-1}$ respectively. Thus at a concentration of 0.1 mmol kg $^{-1}$ in a tissue with a T_1 of 700 ms and T_2 of 75 ms, we can calculate the new relaxation times

$$R_1' = R_1 + r_1 C = \frac{1}{0.700} + 4 \cdot 0.1 = 1.828 \Rightarrow T_1' \\ = \frac{1}{1.828} = 0.547 \text{ s}$$

$$R_2' = R_2 + r_2 C = \frac{1}{0.075} + 5 \cdot 0.1 = 13.833 \Rightarrow T_2' \\ = \frac{1}{13.833} = 0.072 \text{ s}$$

As you can see, at this concentration the biggest effect is the reduction of T_1 from 700 ms to 547 ms,

whereas T_2 only changes from 75 to 72 ms. We say that the relaxation rate due to the gadolinium dominates the effective T_1 relaxation, while for transverse relaxation the normal T_2 is the dominant relaxation rate.

See also:

- Image contrast: Chapter 3
- Quality control: Chapter 11
- In vivo spectroscopy: Chapter 17

Further Reading

- Abragam A (1983) *The Principles of Nuclear Magnetism*. Oxford: Clarendon Press, chapters I, II and III.
- Bernstein MA, King KF and Zhou XJ (2004) *Handbook of MRI Pulse Sequences*. London: Elsevier Academic Press, chapters 4 and 6.

- Brown RW, Cheng YCN, Haacke EM, Thompson MR and Venkatesan R (2014) *Magnetic Resonance Imaging: Physical Principles and Sequence Design*, 2nd edn. Hoboken, NJ: John Wiley & Sons, chapters 2–6 and 8.
- Elster AD and Burdette JH (2001) *Questions and Answers in Magnetic Resonance Imaging*, 2nd edn.

London: Mosby-Yearbook, chapter 2. Also on the web at <http://mri-q.com> [accessed 23 March 2015].

- Farrar TC and Becker ED (1971) *Pulse and Fourier Transform NMR: Introduction to Theory and Methods*. New York: Academic Press, chapters 1, 2 and 4.

Let's Talk Technical: MR Equipment

10.1 Introduction

At the start of this book we said that you don't need to understand the workings of the internal combustion engine to be able to drive a car. However, if you're curious, this chapter provides an opportunity to get down and dirty with the innards of the equipment. Most people will not need to build or service their own system, but you are likely to be involved in the exciting decision of which scanner to purchase. During this process you need to understand the technical specifications so that's what we will focus on. The basic components of an MRI scanner were introduced in Chapter 2. In this chapter we provide more technical information. A lot of the engineering detail is in the advanced boxes, leaving the most important information in the main text. You will see that:

- there are three types of magnets available for clinical MRI, capable of a range of field strengths, and each magnet type has its own advantages and disadvantages;
- magnetic field gradients are generated by a set of gradient coils and amplifiers, which are characterized by their maximum strength and slew rate, and often use active shielding to minimize eddy current artefacts;
- the radiofrequency (RF) transmit system is designed to produce a uniform excitation within the patient, using a large volume coil which may be embedded in the gradient set, and a powerful RF amplifier;
- to receive the MR signals, dedicated receive coils are used that fit closely to the patient's body, in order to maximize sensitivity and signal-to-noise ratio;
- several parts of the system require cooling systems, which may be managed with forced air or chilled water;

- the MR signal is digitized as soon as possible to minimize noise contamination in the cabling, and several computers within the MRI system are needed to synchronize scanning operations.

Figure 10.1 shows the basic architecture of a typical MR system.

10.2 Magnets

The magnet is the most expensive component of the MR system. All magnets produce a static magnetic field which is non-uniform and the homogeneity over the imaging volume needs to be optimized by a process known as shimming, whereby pieces of steel and/or electrical coils are incorporated into the system. Static shimming is performed at system installation; however, putting the patient into the system also introduces a relatively large inhomogeneity, and all systems can perform additional shimming on a per-patient or even per-scan basis (this is known as a pre-scan). A magnet will also generate a magnetic field outside of the patient aperture. Although the extent of this 'fringe field' is minimized by design, it can be necessary to use additional magnetic field shielding either for safety reasons or to avoid interference with nearby sensitive electronics. Magnets have three important properties which should be considered when purchasing a system: field strength, homogeneity over the imaging volume, and installation footprint.

10.2.1 Field Strength

Magnetic field strength (or flux density) is measured in tesla (T). The majority of clinical MR systems operate in the range of 1.5–3 T. Lower field strengths offer cost benefits, and there are several vendors offering low-cost systems in the range 0.2–0.6 T. The advantages of higher field strengths are a better SNR (see Chapter 11) and increased chemical shift, which can improve

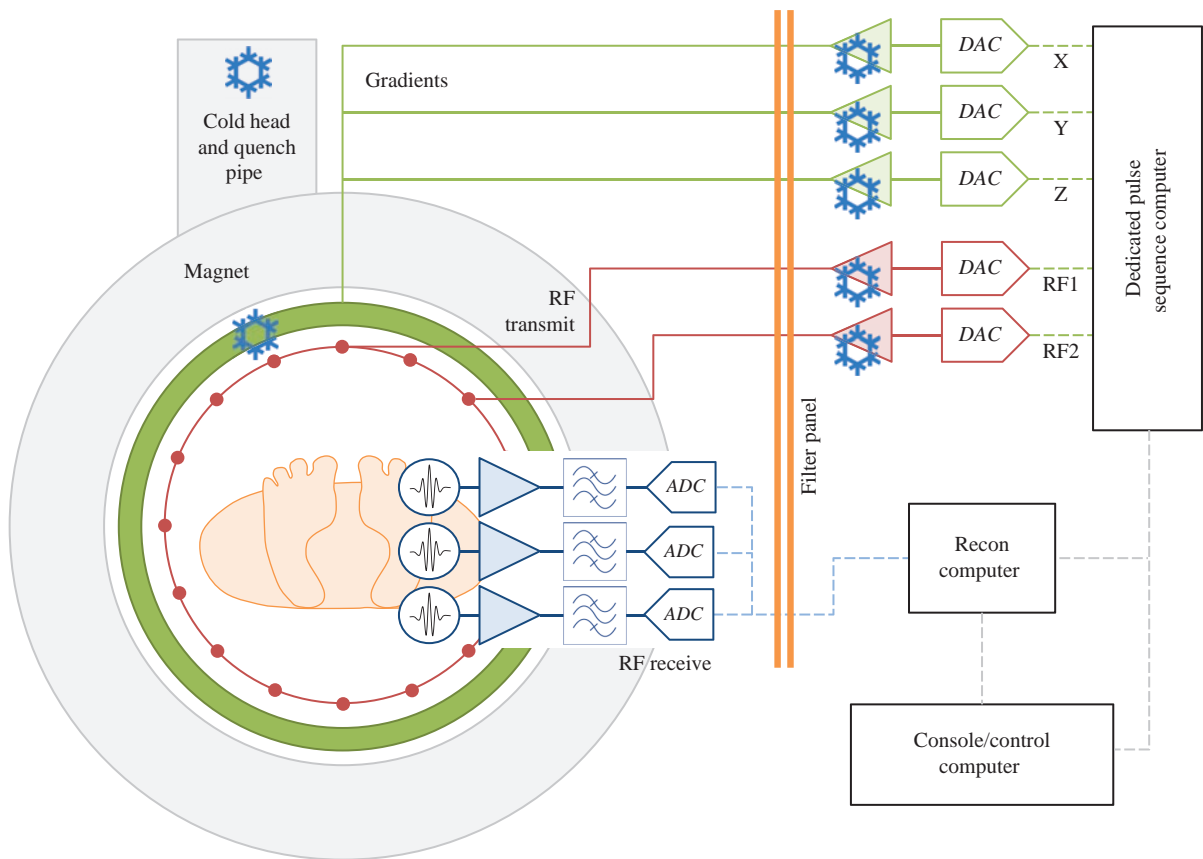


Figure 10.1 Basic components and architecture of an MR system. Solid lines indicate analogue signals, dotted lines are digital. The snowflake symbol indicates components which require specialist cooling (either by chilled water or forced air cooling).

spectral fat suppression and spectroscopy. The improvement in SNR with increasing field strength may be traded for increased spatial resolution, or decreased imaging time. The field strength available is strongly dependent on the type of magnet: superconducting, electromagnets, or permanent.

Superconducting magnets are by far the most common, having the typical ‘tunnel’ shape and allowing field strengths of 1.5–3 T. These magnets are made from special metal alloys, which have zero electrical resistance at temperatures close to absolute zero (-273.16°C , 0 K). The magnet construction includes a large volume of liquid helium (4 K) to keep the wires at their superconducting temperature. Once an electric current is running in a loop of superconducting wire, it will continue to circulate indefinitely without resistive losses, provided the coils remain below their critical temperature. As well as the highest field strengths, superconducting magnets also offer the best homogeneity and stability over time.

Super Cool Magnets

Since you are most likely to meet a superconducting magnet in your local MRI unit, let’s look at some of the design details. The superconducting wire is a niobium-titanium (NbTi) alloy, and is made up of many NbTi filaments embedded in a copper matrix, coated with an insulator. The copper matrix makes it easier to handle the delicate superconducting windings, and protects the superconducting windings against a quench. The NbTi filaments have a superconducting transition temperature of 7.7 K and become superconducting when immersed in liquid helium (He), which has a boiling point of 4.2 K. A typical superconducting magnet consists of a cryostat, i.e. a large chamber of liquid helium, in which the magnet coils are immersed, surrounded by a cold shield and a vacuum chamber (Figure 10.3a).

The helium continuously evaporates, and the helium gas is cycled through a refrigerating system to keep it below 20 K. So-called ‘zero boil off’

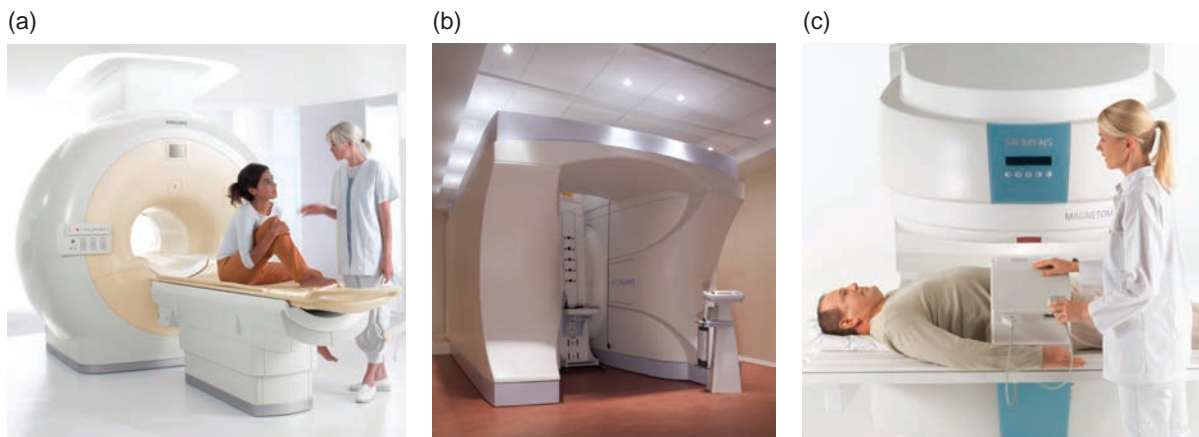


Figure 10.2 Commercial examples of different magnet types in MR systems. (a) 1.5 T Philips Ingenia, superconducting with horizontal main field B_0 ; (b) 0.6 T Fonar upright positional system, electromagnet with horizontal B_0 (courtesy of Medserena Upright MRI Centre, London); (c) 0.23 T Siemens Magnetom C, permanent magnet with vertical B_0 .

magnets also use cryogenic coolers to convert the gas back to liquid helium. A heater within the helium vessel is used to maintain a certain pressure in the gas space above the liquid surface – this limits the amount of evaporation. When heat is generated, e.g. by the gradients, the pressure increases and helps to limit the amount of evaporation. A pressure control circuit is used to maintain the pressure level within limits known as the ‘thermal margin’, and to allow escape of He gas in case of malfunction. The cryo-cooler or ‘cold head’ uses controlled gas expansion to keep the heat shield at 40 K within the magnet cryostat.

An external power supply is used when the magnet is first energized or ‘ramped’ up to the required field strength. A superconducting switch is used to short-circuit the magnet once the desired magnetic field has been established. Superconducting magnets have evolved significantly since MRI was introduced. The first generation of systems had two cryogenic baths, the outer one containing liquid nitrogen (Figure 10.3b) which, although very cheap, made the system cumbersome to refill. The second generation (Figure 10.3c), from the early 1990s until the early 2000s, used more efficient cold-head refrigeration and allowed for only the helium cryostat. These systems still consumed a lot of helium, which is expensive. The current state of the art is known as ‘zero boil off’ (Figure 10.3d), which actually means extremely low boil off: a well-maintained system will not need a refill during its lifetime. Systems in the future may use cryogen-free magnets (Figure 10.3e), which contain helium gas at around

40 K instead of liquid. Those magnets rely on extremely efficient cold-head units and have the disadvantage that if the cold-head malfunctions, the pressure and temperature can quickly rise until the magnet windings go ‘normal’. However, there are also significant advantages, the obvious one being that there is no need for thousands of litres of expensive liquid helium, and there is no risk of a catastrophic quench.

Quench

If any part of the superconducting windings gets too hot, above the critical temperature of around 7 K, the wire becomes resistive and the stored electrical energy will be dissipated as heat. This rapidly warms up neighbouring parts of the windings, which will in turn dissipate more heat and propagate the effect throughout the magnet. This is known as a ‘quench’ and results in the collapse of the magnetic field together with very rapid boiling off of the helium. The MR cryostat typically holds around 2000 litres of liquid helium, which expands 750 times when it becomes a gas. This very large volume of He gas needs to escape from the cryostat, so magnet designers incorporate bursting-disks that blow out under high pressure. Exhaust or quench pipes then vent the gas outside the imaging room to prevent asphyxia and cold burns. Oxygen-level monitors are sometimes installed in the magnet room to alert the users to a dangerous depletion of oxygen should any He gas leak from the quench pipe. Spontaneous

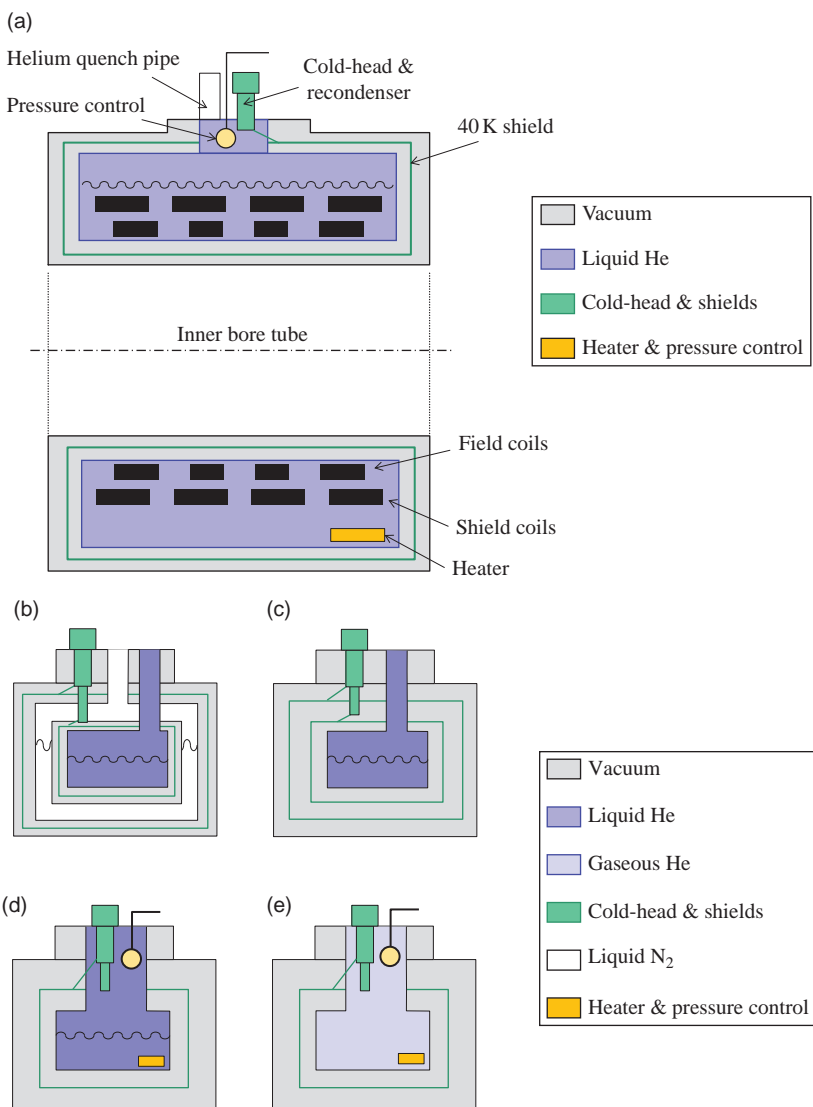


Figure 10.3 (a) Cross-section through a 'zero boil off' superconducting magnet. (b-e) Four generations of superconducting magnet designs (see Box 'Super cool magnets' for details). Adapted with permission from an original by Paul Harvey, Philips Healthcare.

quenches are rare occurrences, but there may be occasions when it is necessary to 'ramp down' the magnet through a controlled quench. In this situation the electrical energy is deposited in a dummy load to avoid damaging the magnet. In either case re-energizing the magnet can be a costly procedure.

Electromagnets use regular resistive coils wound around iron pole pieces. When an electric current flows through the coils the iron becomes a magnet. Magnetic fields of around 0.6 T can be achieved, putting these systems in the low-field range. MR

systems based on electromagnets tend to be heavier than superconducting systems, but have lower cost since they don't need the special wire or the expensive helium necessary to maintain the low temperature.

Permanent magnets can support fields up to 0.3 T and offer the advantage of very low running costs, since they need neither helium nor electrical power to maintain the field. They are heavier than other magnets and may require extra floor strength. The field is often orientated vertically, and it should be remembered that these systems can never be 'switched off'.

10.2.2 Homogeneity

The homogeneity of a magnetic field is usually expressed in parts per million within a given spherical volume. The size of this volume is often given as the Diameter of a Spherical Volume (DSV). For example, a 1.5 T magnet with a maximum variation of 7.5 μT (0.0000075 T) over a 40 cm DSV has an inhomogeneity given by

$$\Delta B_0 \text{ (ppm)} = \frac{\Delta B_0}{B_0} = \left(\frac{0.0000075}{1.5} \right) \times 10^6 = 5 \text{ ppm}$$

Modern superconducting scanners have excellent homogeneity, typically much less than 1 ppm over a 40 cm DSV. There is not much point trying to improve this in the fixed shim, since the human body causes inhomogeneity of 1–5 ppm, depending on which part of the body is in the centre of the system. Manufacturers' technical sheets often quote inhomogeneity over a range of different DSVs. Care is required in their interpretation, as these figures may represent only the mean or average inhomogeneity, typically called the Root Mean Square (RMS) value, and not the maximum (peak-to-peak) value, which may be considerably more.

Fixed shimming, performed at installation, improves the magnet homogeneity and corrects for any distortions caused by any nearby ferromagnetic structures. Shimming can be done passively or actively. Passive shimming involves adding small iron plates into special rails in the magnet bore, while active shimming is done with up to 18 in-built superconducting coils in addition to the main magnet coils.

10.2.3 B_0 Mapping

Mapping of the static magnetic field (B_0) is important for certain shimming applications, known as image-based shimming, and can be used in EPI imaging for removing distortion. The simplest method of spatially mapping the native system homogeneity is to use a phase difference technique in a large, ideally spherical, non-conducting uniform phantom. Two images are acquired with different echo times (TE), most efficiently as a dual-echo gradient-echo scan. Due to the B_0 non-uniformity there will be a spatial variation in the Larmor frequency. The phase accumulation between the two different TEs is proportional to the local frequency (see Figure 10.4). Keeping the images in complex form, the phase difference can be calculated from

$$\Delta\phi(x, y) = \angle[S_1(x, y) \cdot S_2^*(x, y)]$$

where S_1 and S_2 are the images at TE_1 and TE_2 respectively, the superscript * denotes the complex conjugate, and \angle represents taking the angle of the complex data. The difference in echo times $\Delta\text{TE} = \text{TE}_2 - \text{TE}_1$, and so we can estimate the local resonant frequency $\Delta\omega$, meaning the frequency difference from the nominal Larmor frequency, as follows:

$$\Delta\omega(x, y) = \frac{\Delta\phi(x, y)}{\Delta\text{TE}}$$

giving $\Delta\omega(x, y)$ in radians/second. Of course, this phase difference can exceed $\pm\pi$, in which case it is necessary to apply some form of phase unwrapping algorithm to the phase difference image. To minimize this, the ΔTE should be kept short.

Practical Considerations: Phase Images

Although most scanners allow you to generate phase images, they are not always directly usable for calculating a phase difference. If you have difficulty, it is generally easier to calculate the phase from the real (R) and imaginary (I) images, using the relationship

$$\phi_n(x, y) = \tan^{-1}\left(\frac{I_n(x, y)}{R_n(x, y)}\right)$$

Care should also be taken when using phased array receive coils for B_0 mapping, as the complex data may lose phase information during the coil combination reconstruction.

10.2.4 Installation Footprint

The amount of space needed to site the system has a direct influence on the cost of an installation. The magnet room is the largest of the spaces, and most hospitals choose to make it large enough to completely contain the magnetic fringe field, to the 0.5 mT (5 G) line. It is important to realize that the fringe field extends in all three directions, so ceiling height is also a consideration, as is the space under the floor of the magnet room.

Magnetic field shielding reduces the extent of the fringe field. Most modern magnets are actively shielded. This involves continuing the superconducting coil windings, carrying current in the opposite direction and positioned outside the inner main

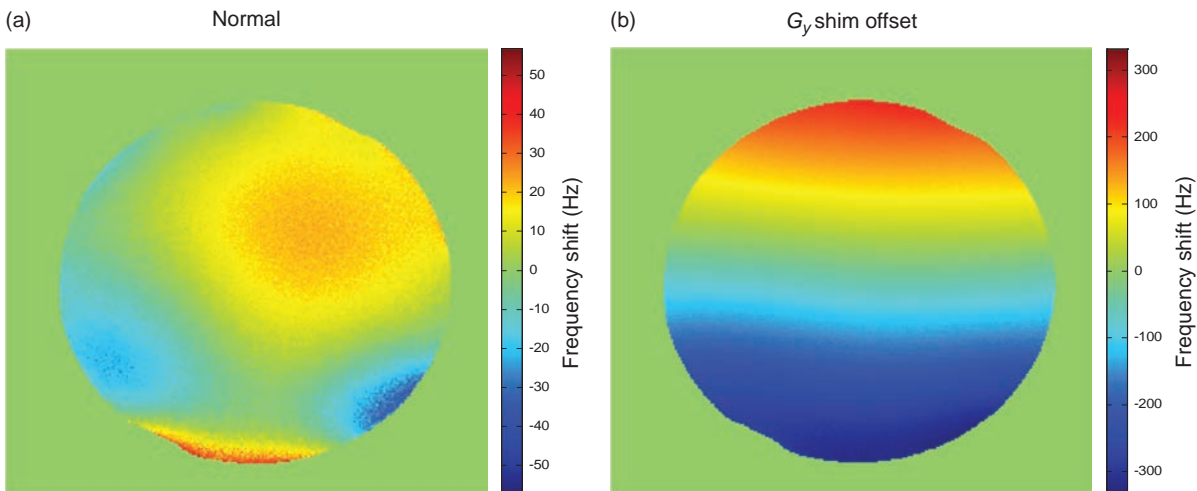


Figure 10.4 B_0 map in a 3 T system (a) using the default shim values and (b) with a large offset deliberately imposed on the y shim (up-down).

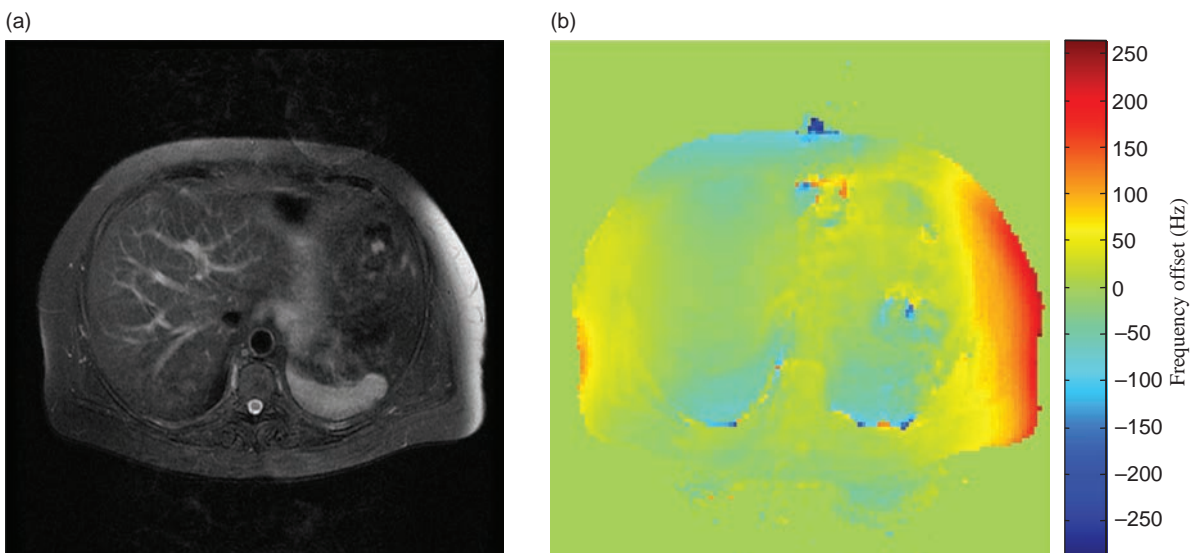


Figure 10.5 (a) T_2 -weighted FSE scan with poor fat suppression on the right. (b) The B_0 map at the same slice location shows a large frequency shift in this region explaining the failure of the fat suppression. This was the result of a poor shimming prescan.

magnet winding. This partially cancels the field outside the main magnet coils, thereby reducing the stray field strength. For all magnet types, shielding can also be ‘passive’, achieved by positioning iron or high-permeability steel plates close to the magnet. Active shielding makes the magnet more expensive; however, passive shielding can also be expensive, depending on how much steel is needed, and may require additional architectural reinforcement.

10.3 Gradient Subsystem

As we saw in Chapter 8, spatial localization of the MR signal requires the use of three orthogonal linear magnetic field gradients ('gradients' for short). The gradient subsystem comprises the set of gradient coils, inside the bore of the magnet, and the gradient amplifiers which drive electrical current through them. In the standard cylindrical clinical systems,

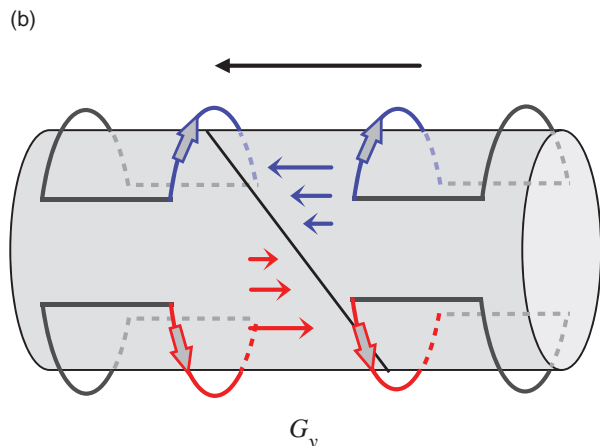
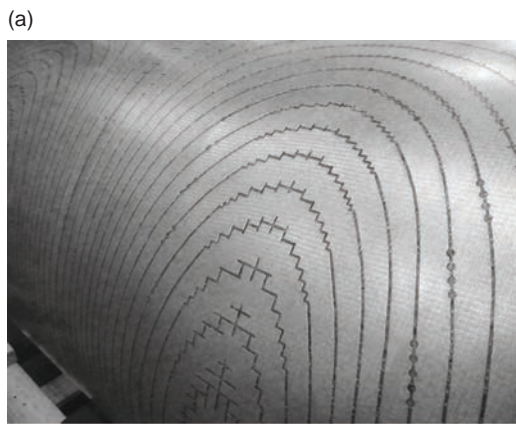


Figure 10.6 (a) Commercial gradient coil set, showing the outermost copper shield ‘coil’. (b) Schematic diagram of current path to generate the y gradient.

the direction along the bore is termed the z axis, the left-right direction is termed the x axis and the top-bottom direction is termed the y axis. The null point at the centre of the gradient coils, and also the centre of the magnet, is called the isocentre.

Each gradient coil is designed to produce a field which points along the z axis, with its magnitude changing along the gradient direction. Mathematically, this is written as e.g. $\partial B_z / \partial x$ for the x gradient. The ‘coils’ don’t look much like conventional solenoids though: they are more likely to be a sheet-like copper panel with cut-outs to create the current paths (Figure 10.6). This is known as distributed winding, or fingerprint winding, which optimizes the shielding and allows for the inductance to be minimized. If you follow the path of the current, it forms two opposing loops (Figure 10.6) which is essential to produce the desired magnetic field gradients. The coils heat up rapidly due to the large currents, and almost all commercial MR systems have a cooling system, tubes carrying chilled water through the gradient coils and amplifiers.

When considering the gradient subsystem, there are some key properties which affect performance. These include the maximum gradient strength and slew rate, the duty cycle, gradient linearity, and the capacity of the cooling system.

10.3.1 Gradient Strength and Slew Rate

Gradient pulses in conventional pulse sequences are trapezoidal in shape, with a sloping rise, followed by a flat plateau and a sloping fall (Figure 10.7). The

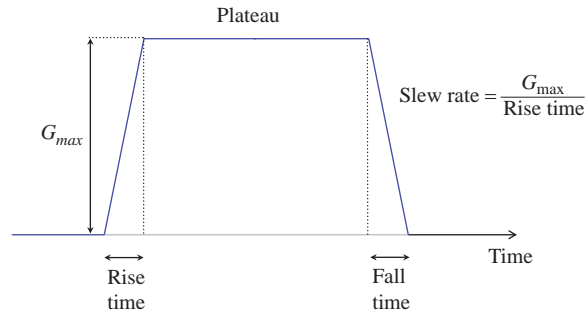


Figure 10.7 Trapezoidal gradient pulse showing definitions for G_{\max} and slew rate.

strength of the gradient, or how rapidly the field changes over distance, is expressed in milli-tesla per metre (mT m^{-1}), in the range of $1\text{--}50 \text{ mT m}^{-1}$, depending on the purpose of the gradient pulse. If the gradient set allows very high gradient amplitudes, images can be acquired with smaller fields of view and/or thinner slice thicknesses, while maintaining short echo times or echo spacings. Large peak gradient amplitudes are also required for some specialist scanning techniques, e.g. diffusion imaging. So the maximum gradient possible, G_{\max} , is an important property of the MR system.

The gradient rise time, or how rapidly the field changes with time from zero to the peak amplitude, is usually expressed in microseconds (μs), with typical values from $1000 \mu\text{s}$ down to $200 \mu\text{s}$. The gradient slew rate is calculated by dividing the peak gradient amplitude by the rise time. Typical slew rates are in the range $20\text{--}200 \text{ T m}^{-1} \text{ s}^{-1}$. High slew rates are

necessary for acquiring high-quality EPI images or for very short TE and TR, e.g. for cardiac imaging, and to achieve short echo spacing in TSE. Systems with very high slew rates may require software limits to prevent peripheral nerve stimulation (see Chapter 20).

10.3.2 Gradient Duty Cycle

There are at least three definitions of duty cycle in common use. It is not easy to find out how manufacturers define their measurement of gradient duty cycle, which obviously makes it difficult to compare systems. In addition, when you look at manufacturers' data sheets, you will find that almost all of them show a gradient duty cycle of 100%. So it's a rather useless property when it comes to making a purchase decision.

Reporting for Duty: Ways to Measure Gradient Duty Cycle

The first definition is quite easy to describe: a gradient which oscillates continuously from maximum positive to maximum negative strength at the maximum slew rate has a duty cycle of 100%. Since both the gradient coils and the gradient amplifiers experience large temperature changes, the duty cycle may

be limited in order to control thermal behaviour. This might reduce the slew rate, or the maximum strength, but in either case, the duty cycle would be reduced.

The second definition of duty cycle is the percentage of time for which the gradients can be run at maximum strength (without switching). Since this is a high-current situation, it is primarily limited by the temperature control of the system. Note that without a definition of the time for the measurement, the duty cycle figure is rather meaningless.

The last definition of duty cycle is also known as the RMS power, and is calculated using the formula:

$$\text{Duty cycle} = \frac{\int_{t_1}^{t_2} G^2 dt}{G_{\max}^2} \times 100\%$$

where G is a function of time, and G_{\max} is the maximum gradient reached between times t_1 and t_2 . When the time-integral is over the TR period, the duty cycle reaches a steady state. However, this definition of duty cycle is obviously dependent on the pulse sequence for measuring, as well as the gradient subsystem itself. So in order to compare different systems, you need to make sure they all use the same pulse sequence.

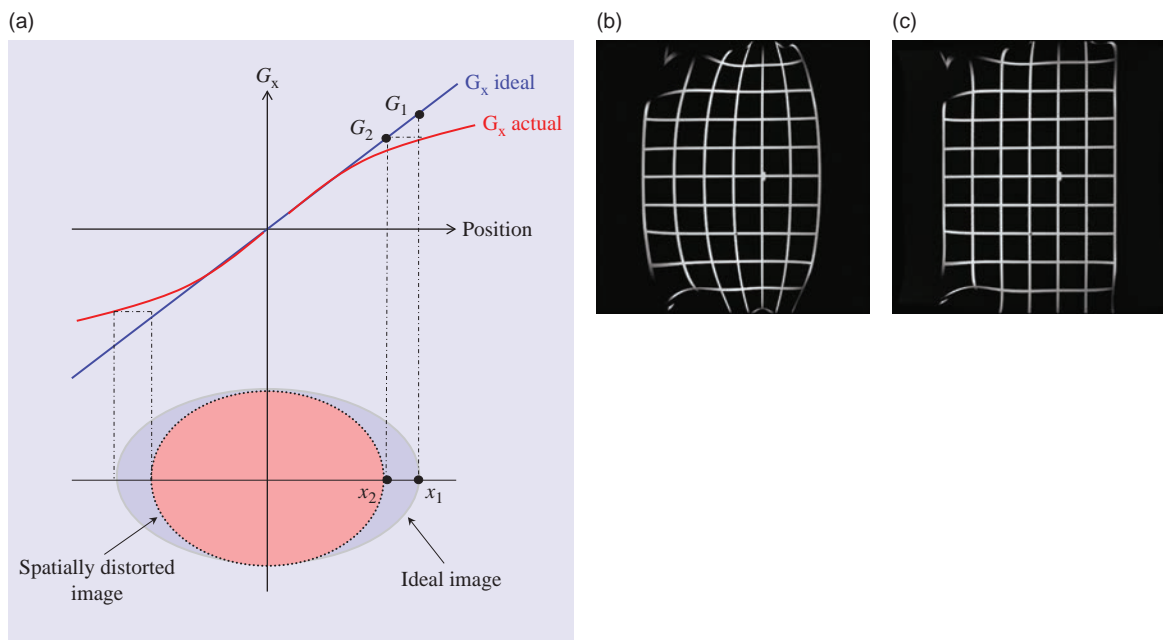


Figure 10.8 (a) Gradient field non-linearity; (b) a grid phantom scanned without correction for non-linearities; and (c) the same phantom with correction applied.

10.3.3 Gradient Linearity

Linear variation in the gradient field is required for accurate spatial encoding; however, the gradient coils have a finite length and diameter and so they produce non-linear fields close to their edges. Linearity usually decreases fairly rapidly towards the edge of the imaging volume. The consequence of non-linearity on an image is misplaced signal and geometric distortion (Figure 10.8a). Most manufacturers make use of computer algorithms that warp the images after reconstruction to compensate for the gradient non-linearities (Figure 10.8b).

Meet Eddy, the Current Guy

Whenever a changing voltage (or current) is experienced in a conductor, according to Lenz's law, a *back-emf* is generated (*emf* = electro-motive force, a nineteenth-century term for voltage). The back-emf is caused by eddy currents, which are localized currents running in the conductor. Eddy currents, in their turn, are induced by the changing magnetic field generated by the changing forward current, and they can be induced in nearby conductors too. Eddy currents generally cause energy losses in the form of heat, and since they are also changing with time, they generate time-varying magnetic fields of their own. The back-emf always acts to oppose the changing current, i.e. it slows down the rate of switching,

meaning that you don't get the gradient you asked for, at least not exactly at the right time. So, all the rapid switching of the gradients causes an avalanche of electromagnetic effects in the gradients themselves and in the surrounding magnet, which can result in image artefacts and signal loss. There are several engineering ways to reduce these problems: active shielded gradient coils, pre-emphasis on the driving waveforms, and careful design of the gradient to minimize its inductance.

All modern MR systems use active shielding on the gradients, very similar technology to the active shielding of the magnet coil itself. Additional 'secondary' or 'shield' coils surround the primary gradient coils and are driven with the opposite gradient waveform. This aims to cancel the gradient field outside the shield coils, magnetically isolating the gradients from the cryostat so that eddy currents cannot be induced. The shield coils make the entire gradient assembly larger, reducing the free space available inside the bore, and also require more power to generate a given gradient amplitude.

Although active-shielded gradients induce fewer eddy currents, they do not prevent the back-emf in the coil. This effect can be minimized by *pre-emphasizing* the gradient waveforms so that, when combined with the eddy current field, the resultant is close to the ideal gradient waveform (Figure 10.9). Pre-emphasis uses extra electronic circuits that add additional voltages, with adjustable amplitudes and

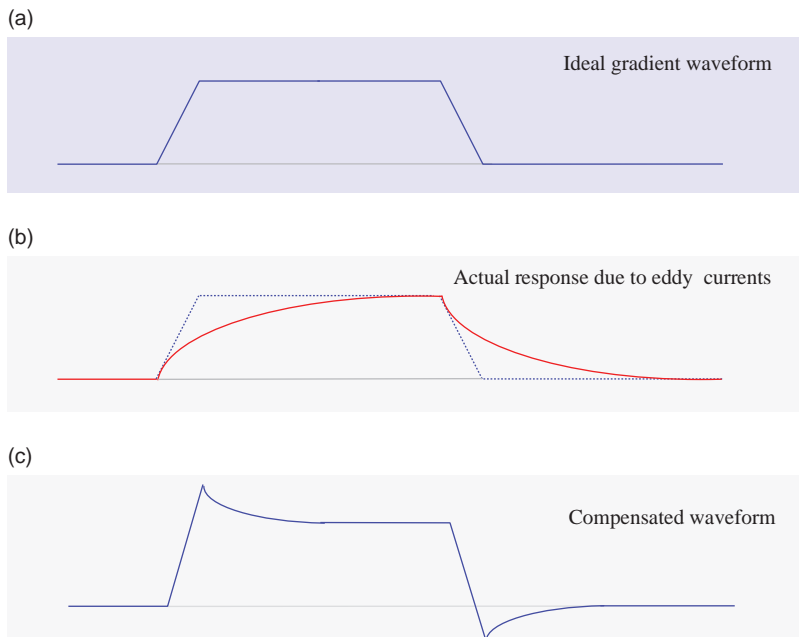


Figure 10.9 Gradient pulses. (a) Ideal gradient waveform; (b) actual response due to eddy currents; and (c) compensated waveform.

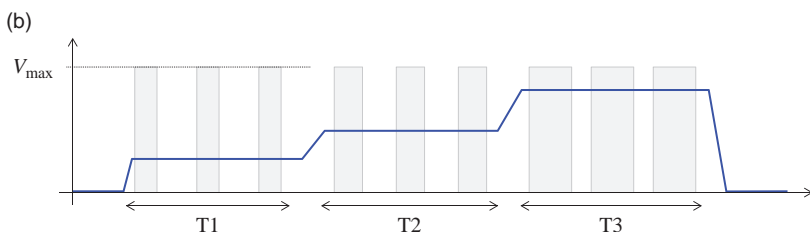
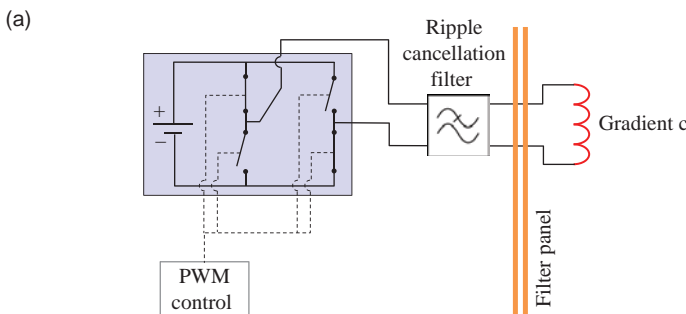


Figure 10.10 (a) Simplified diagram of a PWM amplifier. When the switches are closed, the full output power of the amplifier is driven through the gradient coil. The switches are implemented using transistors and controlled digitally by the PWM circuit. (b) Example of PWM waveform (grey line) switching on and off the amplifier voltage at different frequencies. In period T1 the on:off ratio is approximately 25%, giving an average output voltage of $0.25 \times V_{\max}$. In period T2 the ratio is 50%, while in T3 it is 80%. The output voltage waveform is shown in blue.

time constants, to the gradient driving waveform. Using electromagnetic simulations, pre-emphasis can also help to compensate for concomitant gradient fields, i.e. field variations induced on the other axes.

Finally, the back-emf depends on the rate of change of the current, and on the inductance L of the gradient coil:

$$\text{emf} = L \frac{di}{dt}$$

So to minimize eddy currents and reduce the back-emf, gradient coils are always designed to have minimal inductance. Specially designed software is used to calculate the optimal path for the primary and secondary gradient windings, so that L is minimized and the fields outside of the gradient assembly are close to zero, while maintaining the required current density to generate the gradient fields within the magnet field of view.

10.3.4 Gradient Amplifiers

Gradient amplifiers operate at audio frequencies and could also be used to hold your very own rock concert – one of the authors has been known to connect his guitar to the MR system, using the gradient coils as a loudspeaker! (Don't try this yourself, it's dangerous: he had help from professional service engineers.) The requirement for high gradient amplitudes means that the amplifier must be capable of producing large electrical currents through the coils. Furthermore, the requirement for short switching times means that this

current must be rapidly increased from zero to the maximum and then back down. The amplifier therefore needs to generate a sufficient driving voltage to meet this and of course to overcome the back-emf.

Analogue amplifiers similar to high-precision music amplifiers were widely used in the early years of MRI. Duty cycles achievable with this amplifier type are limited due to losses in the semiconductors. Pulse-Width Modulated (PWM) amplifiers overcome this drawback and have become the standard for MRI gradient drivers in the meantime. The basic idea behind PWM amplifiers is that the amplifier always produces its maximum voltage, and its output is modulated by a binary switching pattern at frequencies ranging from 20 to 200 kHz or even higher (Figure 10.10). When the switching frequency is high enough, the gradient coil reacts to the time-averaged output of the amplifier. Filters are needed to smooth out the modulated output. PWM amplifiers are capable of delivering very high voltages (or currents) with only modest heat dissipation.

10.3.5 Acoustic Noise

The switching of gradient currents is the source of acoustic noise, which is irritating at best and, at worst, can reach levels which may damage hearing. When a gradient is on (i.e. non-zero current in the coil), it interacts magnetically with the main field due to Lorentz forces. Typically the forces act radially to compress or expand the gradient set. As the gradient

currents change during the pulse sequence, the gradient set creates complex oscillatory patterns which in turn generate acoustic noise within the system bore. The noise level depends on the gradient strength, the switching time, and the mechanical properties of the gradient set. The noise in the bore can easily be higher than 85 dB (A), a noise level which is high enough to cause temporary hearing damage. That's why you should always encourage patients to use hearing protection.

There are various ways to limit the noise generation, and many manufacturers now offer special 'quiet' pulse sequences. The technology uses a mixture of limiting slew rates, avoiding gradient resonant frequencies, and so-called 'bridging' gradients. The noise reduction can bring it down to as low as 70 dB(A), which is experienced by the patient as a far nicer scan experience.

10.4 Radiofrequency Transmit Subsystem

The radiofrequency (RF) system comprises a transmitter and amplifier at the right frequency, and a transmit coil. We will first look at the transmit side in this section, and consider the receive side of the RF chain in the next section. The purpose of the RF transmit system is to generate homogeneous B_1 fields over the imaging volume, at the Larmor frequency.

10.4.1 Transmitter and RF Amplifier

The transmitter has to generate RF pulses with appropriate centre frequencies, bandwidths, amplitudes and phases in order to excite nuclei within the desired slices or slabs. The slice position and the strength of the slice-select gradient at that location determine the centre frequency of the pulse. The bandwidth, or the range of frequencies within the pulse, controls the thickness of the excited slice. The shape and duration of the RF pulse envelope determines the bandwidth. The amplitude of the RF pulse controls how much the magnetization is flipped by the pulse, while the phase controls along which axis the magnetization is flipped (in the rotating frame of reference). In modern MRI systems the RF pulse envelope is generated digitally (see Box 'On the Air: Transmitter Theory').

On the Air: Transmitter Theory

As we saw in Chapter 8, the slice-selective RF pulse is amplitude modulated by a function $S(t)$ to create a

slice. It has a frequency slightly offset from Larmor in order to select the required slice position, and may also have a phase angle. The required output is

$$S(t) \cos(\omega_{ss}t + \phi)$$

where

$$\omega_{ss} = \omega_0 \pm \Delta\omega$$

To avoid the possibility of stray RF reaching the receive coil from the transmitter (and completely bypassing the patient!), its internal frequency source does not operate at the Larmor frequency but at a fixed frequency ω_{fix} . For that reason ω_{ss} is only generated when the RF pulse is about to be applied, by combining a variable offset frequency ω_{off} with the fixed frequency ω_{fix} :

$$\begin{aligned}\omega_{ss} &= \omega_{fix} - \omega_{off} \\ \omega_{off} &= \omega_{fix} - \omega_0 - \Delta\omega\end{aligned}$$

This combination is performed in an electronic 'mixer' that multiplies the two frequencies and generates the sum and difference frequencies, known as side-bands, using the trigonometric identity

$$\begin{aligned}2 \cos(\omega_{fix}t) \cos(\omega_{off}t) &= \cos((\omega_{fix} + \omega_{off})t) \\ &\quad + \cos((\omega_{fix} - \omega_{off})t)\end{aligned}$$

We want the lower side-band at $(\omega_{fix} - \omega_{off})$, and the unwanted side-band at the higher frequency $(\omega_{fix} + \omega_{off})$ is filtered out.

To generate the RF pulse, the transmitter (Figure 10.11) takes the digitally generated amplitude-modulation function $S(t)$ and mixes it with the offset frequency ω_{off} and phase ϕ . This waveform is then passed to a digital-to-analogue converter (DAC). The power of this analogue RF pulse coming from the transmitter will only be about 0.1 mW. In order to perturb the spins in a patient this is amplified using an RF power amplifier.

Radiofrequency amplifiers are characterized by the frequency bandwidth, power range, and linearity of response. However, designing an amplifier for good linearity typically makes it inefficient for power, and vice versa. Phase and amplitude stability must be maintained during the whole pulse sequence, i.e. linearity is more important than power. To convince yourself of this, imagine that the amplifier's output amplitude is unstable, and generates different RF powers in each TR. This would mean different flip angles, and therefore time-varying behaviour of the MR signal. After Fourier transformation, that becomes a series of ghost images, interfering with

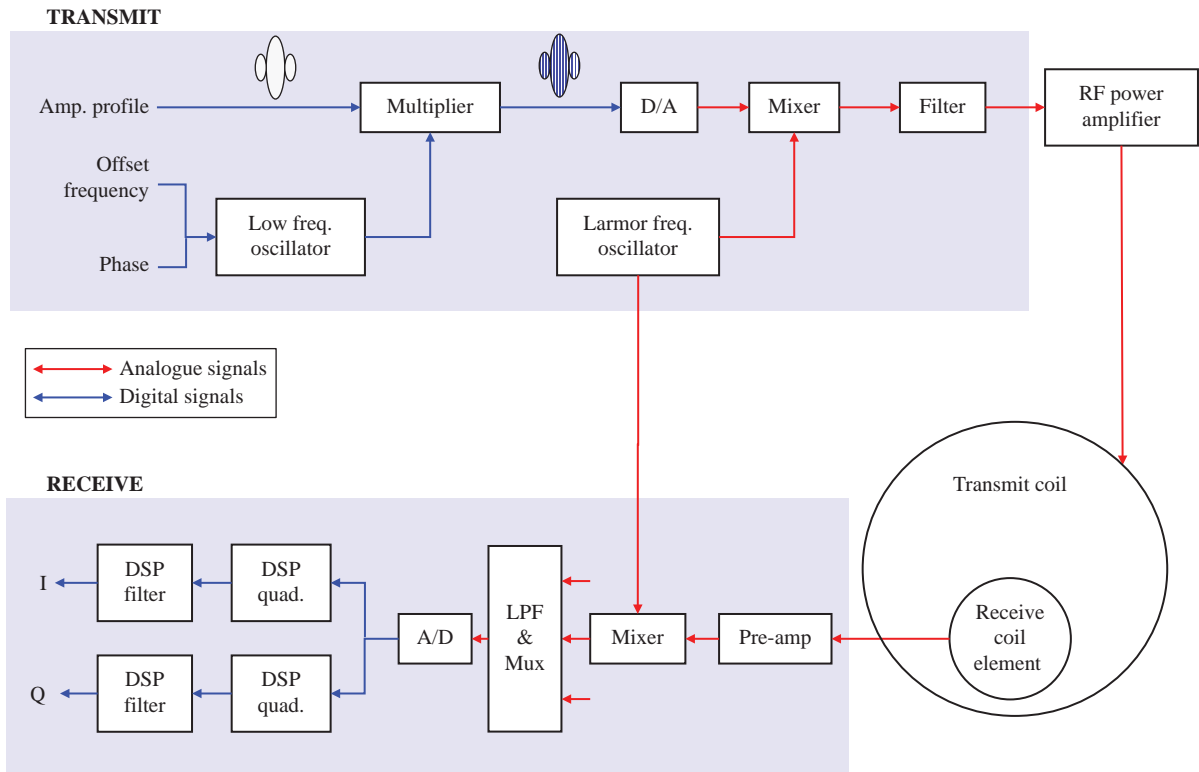


Figure 10.11 Digital radiofrequency transceiver. D/A denotes digital-to-analogue converter; A/D, analogue-to-digital converter; LPF, low-pass filter; Mux, multiplexer. See text for details on the theory of operation.

the diagnostic quality of the final image. Similarly, if the output phase is unstable, the MR response will vary per TR, leading to ghosting, loss of SNR and changes in image contrast. Modern solid state amplifiers use MOSFET transistors which can provide up to 1 kW power with a flat frequency response up to 500 MHz. Several transistor pairs are combined together to give a total output of up to 30 kW. These transistors generate a lot of heat, and the RF amplifier often has a cooling system using chilled water (like the gradient subsystem) or forced air.

The latest MR systems use parallel transmit technology to improve B_1 homogeneity, which is a particular problem at 3 T. The RF wavelength at 3 T is approximately 25–30 cm, which leads to more standing waves within the body. This leads to flip angle variations across the field of view and ‘shading’ effects, particularly noticeable in the liver, breast (Figure 10.12a) and in the thoracic spine. Conventional systems drive the transmit coil in quadrature, by splitting the output from a single RF amplifier and applying a 90° phase difference between two ports on the coil, which are also 90° apart (Figure 10.12b). Parallel

transmission works by driving the two ports on the coil by two separate amplifier chains (Figure 10.12c). This allows for fully independent control of amplitude and phase on each channel, and the B_1 field can be optimized to suit the anatomy of the patient in the bore, producing more uniform signal intensity (Figure 10.12d). Multi-transmit systems have two RF amplifiers, which must also be synchronized with each other with sub-nanosecond accuracy. In principle, parallel transmit systems can be designed with more than two channels; however, the benefits are limited at 3 T. In research systems at e.g. 7 T and higher, multiple channels may be necessary to achieve a uniform flip angle excitation in the body.

10.4.2 B_1 Mapping

On systems with full multi-transmit capabilities, it is important to map the spatial distribution of the transmit field B_1^+ in vivo as a calibration scan. This allows the system to adjust the output amplitudes and phases of the RF chain so that the optimum B_1 field can be generated for each patient and each anatomy.

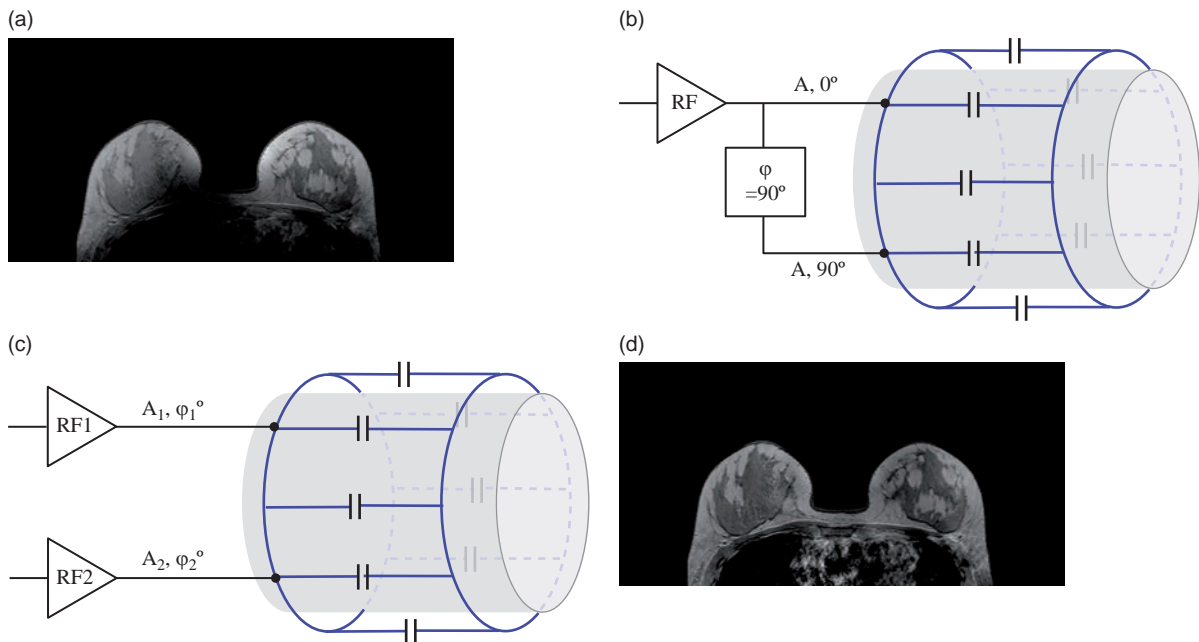


Figure 10.12 (a) Dark shading in breast image caused by B_1 inhomogeneity at 3 T. (b) Conventional transmit subsystem. (c) Modification of amplitude and phase in two independent transmit channels creates a more homogeneous B_1 field resulting in (d) a more uniform breast image.

Alternatively, specially shaped B_1 fields can be created to selectively excite a sub-volume within the patient's body. Many quantitative imaging procedures also rely on accurate flip angles, so B_1^+ -mapping is sometimes used in those techniques too (Chapter 19). There are two main ways to map B_1^+ : a dual-TR method (see Box 'Dual-TR Method for B_1 Mapping'), and a double angle method which is easier to try for yourself since it can be performed using standard pulse sequences. The double angle method, as the name suggests, involves the acquisition of two gradient-echo images with flip angles of α and 2α . This produces two images S_α and $S_{2\alpha}$ with signal intensities depending on $\sin\alpha$ and $\sin 2\alpha$ respectively. To produce the B_1^+ map, we find the flip angle α by first taking the ratio $S_{2\alpha}/S_\alpha$, and then using the relationship $\sin 2\alpha = 2 \sin\alpha \cos\alpha$:

$$\frac{S_{2\alpha}(x, y)}{S_\alpha(x, y)} = \frac{2 \sin\alpha \cos\alpha}{\sin\alpha}$$

$$\alpha(x, y) = \cos^{-1} \left[\frac{S_{2\alpha}(x, y)}{2 \cdot S_\alpha(x, y)} \right]$$

A limitation of this method is that the longitudinal magnetization must recover nearly to equilibrium to prevent different T_1 weightings in the two images, so the TR must be rather long. Also the technique is rather inaccurate for $80^\circ < \alpha < 100^\circ$ as $\sin\alpha$ hardly varies over

this range; also at low flip angles $<20^\circ$, the SNR is rather low and noise bias will reduce the accuracy. Specialized pulse sequences can remove these limitations, but they are not always commercially accessible.

Dual-TR Method for B_1 Mapping

The dual-TR method, proposed by Yarnykh in 2004, uses two interleaved scans with different TRs (Figure 10.13). Using the Bloch equations to describe the steady state signals, we again use a ratio of the two images:

$$\frac{S_2}{S_1} = \frac{1 - E_1 + (1 - E_1)E_2 \cos\alpha}{1 - E_2 + (1 - E_2)E_1 \cos\alpha}$$

where $E_1 = \exp(-\text{TR}_1/T_1)$ and $E_2 = \exp(-\text{TR}_2/T_1)$. Using a Taylor expansion for the exponentials, and assuming that both TR_1 and TR_2 are very short compared with T_1 , this ratio r reduces to

$$r = \frac{S_2}{S_1} = \frac{1 + \eta \cos\alpha}{\eta + \cos\alpha}$$

$$\alpha = \cos^{-1} \frac{\eta \cdot r - 1}{\eta - r}$$

where $\eta = \text{TR}_2/\text{TR}_1$. Provided $\text{TR}_1 < \text{TR}_2 < T_1$ of the tissue, the accuracy of the flip angle calculation is independent of T_1 , so the dual TR method is particularly useful *in vivo*.

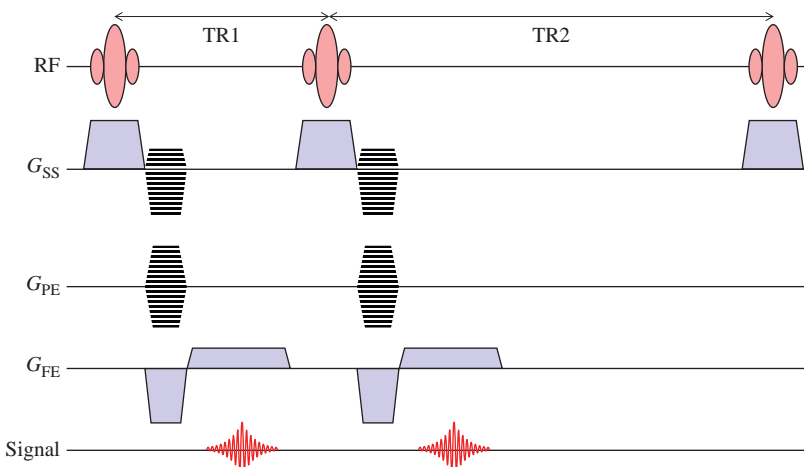


Figure 10.13 Pulse sequence diagram for dual-TR B_1 -mapping technique.

10.4.3 Transmit Coils

The coils used to excite the MR signal must produce a uniform field B_1 at right angles to the static magnetic field. Transmit coils are usually large to optimize their uniformity, and encompass a significant volume of tissue. A transmit coil may also be used to receive the MR signals, provided an appropriate Transmit/Receive (T/R) switch is used, but this is relatively uncommon (because it has lower SNR than using local receive coils). The T/R switch protects the receive circuitry from the very high voltages applied during transmit and also prevents the small MR signal from being lost in the electronic noise generated by the transmitter even in its off state.

The main transmitting coil is usually the body coil, which surrounds the entire patient. This is usually built into the scanner bore and is not generally visible. Since this coil is large it has a very uniform transmission field, but this also means that it is not particularly sensitive if used as a receive coil. In some systems other coils, e.g. head or knee, may also be used for transmission, in which case less power is required to flip the magnetization, but excitation uniformity may be sacrificed.

In typical cylindrical MR systems, the body coil usually has a birdcage design (Figure 10.14a). The number of elements is optimized so that the current distribution over the surface of the coil varies sinusoidally. Birdcage coils are always driven in quadrature, meaning that the output from the RF amplifier is connected to the coil at two ports, not just one.

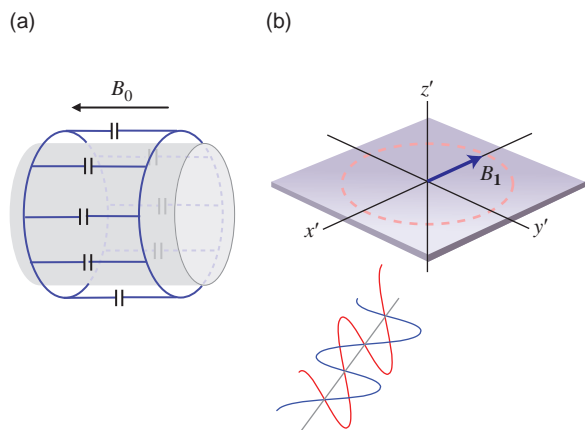


Figure 10.14 (a) Low-pass birdcage coil. (b) Quadrature transmission creates a circularly polarized B_1 field.

The two currents are 90° out of phase, and this combination generates just one rotating B_1 field, rotating in the same sense as the protons (Figure 10.14b).

Birdcage Coils

The birdcage coil physically consists of two circular end rings connected by N equally spaced straight conductors. The straight conductors and segments of end rings connecting adjacent conductors can be treated as inductors. In a birdcage coil the necessary sinusoidal variation in current is generated by the components acting to delay the current around the conductors. In the low-pass configuration each of the straight conductors includes a capacitance C , while in the high-pass configuration the capacitance

is placed on the end rings. Breaking the two end rings and unrolling the coil results in an equivalent circuit of N elements, each introducing a phase shift of $\Delta\phi(\omega)$. The requirement for a sinusoidal current distribution is that the total phase shift around the coil must equal a multiple of 2π

$$N\Delta\phi(\omega) = 2\pi M$$

where M is the resonant mode number and $1 \leq M \leq N/2$. A standing wave in the $M = 1$ mode produces the most homogeneous B_1 field.

10.5 RF Receiver Subsystem

It can be helpful to consider the RF receiver subsystem separately from the transmit chain, since in modern MR systems they are effectively independent. The receive chain is responsible for detecting the tiny MR signal, amplifying and digitizing it without introducing unnecessary noise, and then sending it to the reconstructor for image calculation. The receiver subsystem consists of receive coils, preamplifiers, digitizers, and digital signal processing to prepare the signal for reconstruction (Figure 10.11).

10.5.1 Receive Coils

The function of a receive coil is to maximize signal detection, while minimizing the noise. Usually the

major source of noise is from the patient's tissue (from the Brownian motion of electrolytes). To minimize the noise, and maximize the SNR, it is necessary to minimize the coil dimensions, i.e. the coil's volume should be filled as much as possible by the sample. A compromise needs to be made between adequate RF homogeneity and high SNR.

Play that Tune

An RF coil is essentially a tuned electrical circuit that comprises an inductor (the actual coil wires) and a capacitor connected in parallel (Figure 10.15a). The inductor has an electrical reactance $X_L = i\omega L$, where $i = \sqrt{-1}$ and L is the inductance in henrys. The capacitor has a reactance $X_C = -i/\omega C$, where C is the capacitance in farads. The parallel tuned circuit gives a sharp frequency response (Figure 10.15b), peaking when the reactances cancel, at a resonant frequency of

$$f_0 = \frac{1}{2\pi\sqrt{LC}}$$

At this frequency the impedance of the tuned circuit is a pure resistance

$$Z_p = \frac{LR}{C}$$

RF signals are usually piped around circuits using transmission lines, a typical example being coaxial

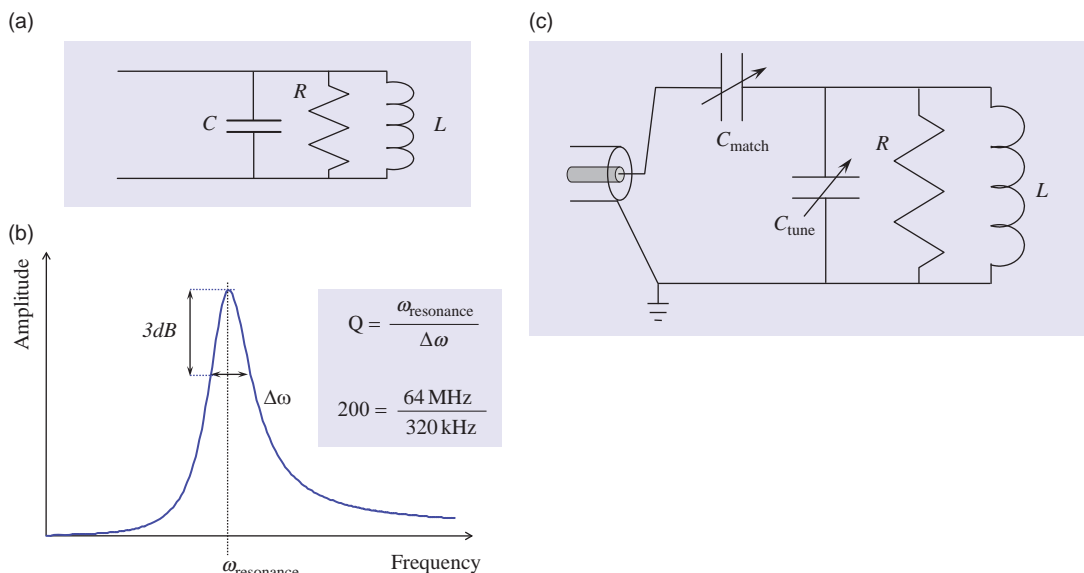


Figure 10.15 (a) Tuned circuit and (b) typical frequency response. (c) Tune-and-match circuit. A matching capacitor is added to cancel the inductive reactance at ω_0 and make the impedance of the circuit appear as a pure 50Ω resistance.

cable. The transmission line will have a characteristic impedance of typically $50\ \Omega$; therefore, for efficient power transfer the RF circuits should also have an input and output impedance of $50\ \Omega$. In order to match the tuned circuit to the $50\ \Omega$ output of the power amplifier, the impedance of the coil needs to be matched to $50\ \Omega$. At some frequency off-resonance the coil will have a resistance of $50\ \Omega$ in series with an inductive reactance. The addition of a series (matching) capacitor will cancel this inductive reactance, resulting in a pure $50\ \Omega$ resistance at this frequency (Figure 10.15c). The parallel tuning capacitor may then be adjusted to make this frequency the desired Larmor frequency. A measure of the tuned circuit (coil) performance is the Q or quality factor, which is the ratio of stored energy to dissipated energy. It may also be written as

$$Q = \frac{\omega L}{R}$$

Q is also a measure of the current or voltage magnification achieved by the tuned circuit. Q can be measured by dividing the centre frequency by the frequency difference at the half power points, or the -3 dB bandwidth (for voltage).

Coils should have reasonably high Q s, typically 200 when empty, but not too high since the circuit will continue to oscillate after the RF pulse. A good Q means that the frequency response is quite narrow and the coil is behaving like a band-pass filter, eliminating noise from outside the bandwidth of interest.

When a conducting sample, such as a human body, is placed inside the coil the Q (the loaded Q) decreases. The coil inductance also changes due to mutual inductance between the coil and the conducting tissues, changing its resonant frequency and impedance. In some systems the unloaded Q is deliberately decreased so that the coil has a fixed tuning for more operational convenience.

Birdcage coils used for transmit can also receive in quadrature. During reception the signals from the two-quadrature modes add constructively, while the noise from each is uncorrelated, i.e. it ‘averages out’, resulting in a $\sqrt{2}$ improvement in SNR over a comparable linear coil. Further consideration of SNR is given in Chapter 11. Note that both transmitter and receive coils require tuning and matching during manufacture, described in Box ‘Play that Tune’.

Some receive coils are single loops or figure-of-eight coils which are placed directly over the

anatomical region of interest. The signal response of a surface coil is non-linear with depth, resulting in an intensity fall-off into the patient. Surface coils are therefore only useful for imaging structures that lie relatively close to the surface of the patient. Flexible surface coils are very useful since they can be wrapped around the region of interest. Care must be taken to ensure that the surface coil is orientated perpendicular to B_0 otherwise no signal will be detected.

10.5.2 Phased Array Coils

The majority of receive coils in modern systems consist of multiple elements, each acting independently. These coils are formally known as ‘phased array’ coils, but since they are now so common, we often just use the word ‘coil’.

These coils need to be designed very carefully so that the individual elements do not interact with each other, a phenomenon known as coupling which reduces SNR in the images. One way of effectively ‘decoupling’ one element from its neighbours is to geometrically overlap the coils in a particular way. Ideally, each element is connected to an entirely separate preamplifier and receiver (see Sections 10.5.3 and 10.5.4) which has the advantage that the noise in each receiver is completely different, i.e. uncorrelated, resulting in a higher SNR in the final image (Figure 10.16).

Phased array coil imaging generates more raw data than imaging with a simple single receive coil, and needs extra reconstruction memory in order to keep reconstruction times reasonable. A key advantage of multi-element coils is the possibility of using parallel imaging techniques such as SMASH or SENSE (see Chapter 14 for full details). Parallel imaging is extremely useful for many techniques, particularly 3D CE-MRA, steady state imaging and for high-field (3 T) imaging since it offers another way to reduce SAR.

It is useful to be able to connect two or more array coils simultaneously, particularly for whole-body screening where the patient is imaged from head to toe using several stations. With this technique, a particular FOV is scanned (e.g. the head and neck), then the patient is automatically moved into the magnet by a fixed distance and the next station is scanned (e.g. the upper thorax). This is repeated up to six times to provide complete coverage without having to change coils. It is worthwhile to take extra care when

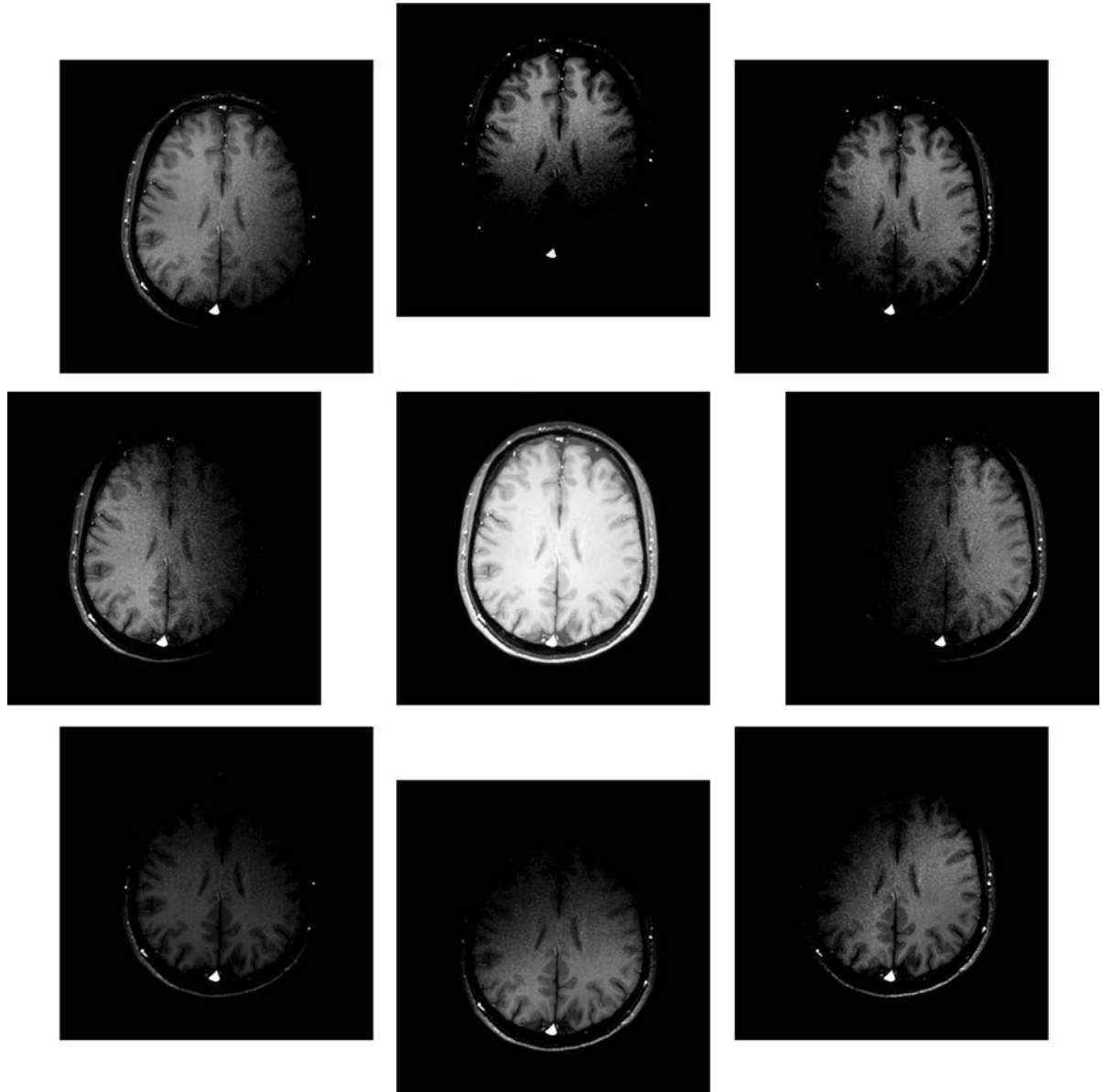


Figure 10.16 Separate images from each of the eight channels of a head phased array coil. The final combined image is also shown.

comparing receive systems: manufacturers' brochures often specify the maximum number of coil elements which can be connected at one time. But can you actually use them all at the same time, or is this just useful for reducing patient set-up time? Also be careful to check how many actual receivers (A/D channels) are provided. It is possible to combine two or three coil elements through a single receiver, but you should be aware that this reduces SNR and limits the

receiver bandwidth. Buying a system with a limited number of channels may be cheaper initially, but it may have significant financial impact in the future if you need to buy more channels to support new phased array coils with many more elements.

10.5.3 Preamplifier

The small MR signal detected by the coil needs to be boosted by an extremely low-noise preamplifier

before being fed to the receiver. Preamplifiers are often mounted on the coil assembly to avoid degradation of the signal by the leads. The quality of an amplifier is given by its noise figure, which is measured in decibels (dB, see Appendix). The noise figure is defined as

$$NF = \frac{\text{SNR at output}}{\text{SNR at input}}$$

and should be less than 1 dB typically.

10.5.4 Receiver (Digitizer)

The MR signal is within a narrow frequency range of interest $\Delta\omega$, embedded in or carried by the Larmor frequency ω_0 (with an offset due to the frequency encoding). In many MR systems, it is not possible to digitize directly at the Larmor frequency, so the MR signal has to be demodulated down to a lower frequency (e.g. 125 kHz). The signal is then low-pass filtered before being converted to a digital signal (Figure 10.11). The signal is then separated into the

two quadrature channels using digital signal processing – see Box ‘Digital Dexterity: Receiver Theory’ for details. In these systems, the A/D converter is the limiting factor in the receiver chain. To achieve maximum SNR, each element of the receive coil should be connected to a separate A/D converter. However, it is practical to use a multiplexer (‘Mux’ in Figure 10.11) to share a single receive channel (A/D) between two or three coil elements. This limits the minimum receive bandwidth and also sacrifices SNR.

Analogue-to-digital converters can be much faster, operating at very high frequencies (tens of MHz), and still allow at least 16-bit digitization. This allows for direct digitization at the Larmor frequency, avoiding the first analogue demodulation step. With further advances in miniaturization of electronics, these powerful receivers can be mounted close to the scanner or even within the coil itself, avoiding the need for lossy copper cables carrying the MR signal into the technical room. This also has the advantage of minimizing image artefacts caused by drift in the older analogue receiver circuitry (Figure 10.17).

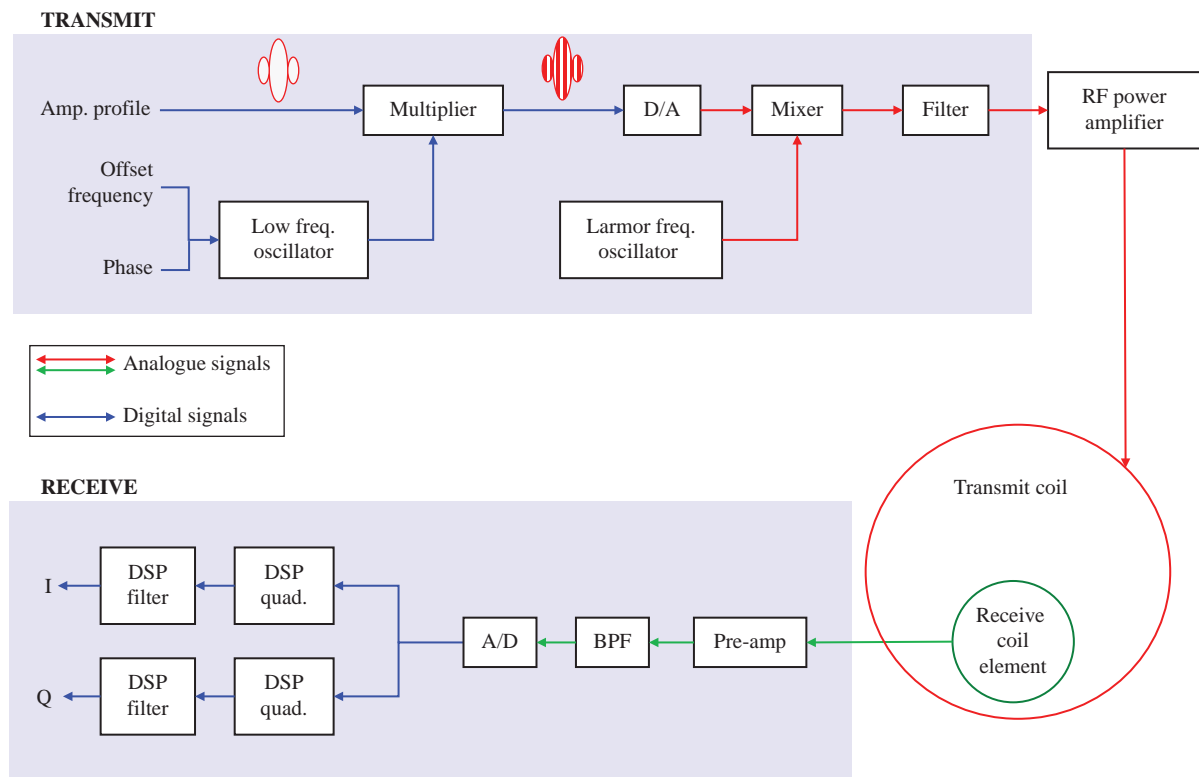


Figure 10.17 Broadband digital radiofrequency transceiver. D/A denotes digital-to-analogue converter; A/D, analogue-to-digital converter; BPF, band-pass filter. See text for details on the theory of operation.

The latest ‘broadband digital’ MR systems use digitization as close as possible to the coil, and carry the signal via fibre-optic cables back to the data acquisition system or reconstruction. With this receive architecture, the coil designer has complete freedom to optimize the element layout for the anatomy and can guarantee maximum SNR from the coil by including a dedicated receiver on each element. Eliminating all the analogue circuitry has made a huge improvement in the SNR available from modern scanners and allows you to buy new coils without the hassle (and expense!) of upgrading the whole receiver system.

Digital Dexterity: Receiver Theory

Although the analogue-to-digital converters are working at very high frequencies, they are typically lower than the Larmor frequency, which means they measure a series of alias frequencies ω_A of the true signal,

$$\omega_A = (\omega_0 + \omega_{FE} \pm \Delta\omega) - n \cdot \omega_s$$

where ω_s is the sample frequency of the ADC, and n is an integer. Provided that ω_s and n are chosen such that the bandwidth of the received MR signal is well within the sampled bandwidth, i.e. $\Delta\omega \ll \omega_s$, the MR signal is accurately measured.

Back in the technical room, the digital signal is processed to remove the Larmor frequency, and to separate the real and imaginary channels. The latter process is known as ‘quadrature detection’ and involves splitting the incoming signal and creating a 90° phase shift between the two components. In traditional MR systems this is done with analogue components, combining the signal with sine and cosine waves at the Larmor frequency, and this is still a good way to understand what is happening. Mathematically we describe the MR signal as

$$\cos(\omega_0 + \omega_{FE} \pm \Delta\omega)$$

using the cosine because it is symmetrical about the mid-point of the readout window. This signal is split and then combined with sine and cosine waves at the Larmor frequency:

$$\begin{aligned} & \cos(\omega_0 + \omega_{FE} \pm \Delta\omega) \cdot \sin(\omega_0) \\ &= \frac{1}{2} \sin(\omega_0 + \omega_{FE} \pm \Delta\omega + \omega_0) \\ &\quad + \frac{1}{2} \sin(\omega_0 + \omega_{FE} \pm \Delta\omega - \omega_0) \\ &= \frac{1}{2} \sin(2\omega_0 + \omega_{FE} \pm \Delta\omega) + \frac{1}{2} \sin(\omega_{FE} \pm \Delta\omega) \end{aligned}$$

$$\begin{aligned} & \cos(\omega_0 + \omega_{FE} \pm \Delta\omega) \cdot \cos(\omega_0) \\ &= \frac{1}{2} \cos(\omega_0 + \omega_{FE} \pm \Delta\omega + \omega_0) \\ &\quad + \frac{1}{2} \cos(\omega_0 + \omega_{FE} \pm \Delta\omega - \omega_0) \\ &= \frac{1}{2} \cos(2\omega_0 + \omega_{FE} \pm \Delta\omega) + \frac{1}{2} \cos(\omega_{FE} \pm \Delta\omega) \end{aligned}$$

Looking at both terms, you can see that one is at a very high frequency $> 2\omega_0$, while the other term is just slightly offset from zero (by ω_{FE}). The high-frequency terms are discarded, leaving the real and imaginary components of the signal:

$$\begin{aligned} & \cos(\omega_0 + \omega_{FE} \pm \Delta\omega) \cdot \sin(\omega_0) \\ &= \underbrace{\frac{1}{2} \sin(2\omega_0 + \omega_{FE} \pm \Delta\omega)}_{\text{high frequency side-band}} + \underbrace{\frac{1}{2} \sin(\omega_{FE} \pm \Delta\omega)}_{\text{real component}} \end{aligned}$$

$$\begin{aligned} & \cos(\omega_0 + \omega_{FE} \pm \Delta\omega) \cdot \cos(\omega_0) \\ &= \underbrace{\frac{1}{2} \cos(2\omega_0 + \omega_{FE} \pm \Delta\omega)}_{\text{high frequency side-band}} + \underbrace{\frac{1}{2} \cos(\omega_{FE} \pm \Delta\omega)}_{\text{imaginary component}} \end{aligned}$$

Analogue quadrature detection relies on having a perfect 90° phase difference between the sine and cosine waves – controlled by another piece of electronics, which is susceptible to temperature changes and other interference. In today’s scanners, quadrature detection is done digitally: alternate digital samples are sent to the real and imaginary channels, and then every other point on each side is inverted. In effect the real channel is the input signal multiplied by {0, 1, 0, -1}, the imaginary by {1, 0, -1, 0}, which corresponds to a sine and cosine respectively at the intermediate frequency, with perfect 90° phase difference between them. With digital receivers, artefacts such as quadrature ghosts or DC offset artefacts belong in the past; you will see them described in online artefact galleries, but you will never see them on your own scanner.

10.6 Computer Systems

The multi-tasking nature of MR means that it is impractical to control the many processes requiring accurate timing directly from the main or host computer, so many subsystems will have their own microprocessors whose commands can be downloaded from the host (refer back to Figure 10.1). A typical MRI system will have a host computer on which the operator will prescribe the scan in terms of the pulse sequence, its timing and various geometry

factors, etc. These parameters will then be converted into commands that are transferred to another microprocessor system, known as the Pulse Programmer (PP) or Data Acquisition System (DAS) that controls the hardware. The PP or DAS ensures that the RF, gradients and data acquisition are all properly synchronized. Once the data have been acquired, the image reconstruction may also be performed on a separate computer, or on a specialist array processor or GPU (just like the graphics card in your favourite games console). The finished images are sent back to the database on the host computer, which also manages the image display, processing, filming, archiving and networking.

In a purchasing decision, the most important factors to know are the image database capacity, and the reconstruction speed and capacity. You should look for enough database capacity for 4–5 days of patient data (this obviously will depend on how busy your unit is). Reconstruction capacity should be as big as possible – the larger the better – especially if you will regularly use coils with 20 elements or more. Reconstruction speed is not easy to measure; look for the reconstruction ‘latency’, which is the time between the end of the scan acquisition and the last image being available to view.

10.7 Siting and Installation

When purchasing an MRI system there are a number of considerations with respect to the siting and installation of the system that need to be addressed. Obviously you need to allow enough space in the magnet room to contain the system and, ideally, the fringe fields up to the 0.5 T (5 G) line. The technical room must be next to the magnet room and will contain air conditioning and the magnet compressor unit, as well as a dedicated mains electrical supply. It may be possible to contain some of the fringe field in the technical room, but you should take advice from the manufacturer’s siting specialists. Finally you need space for the operator’s console; don’t make it too small, as there will often be visitors who need to view the images (referring clinicians, radiologists, trainee radiographers, etc.). When choosing a location, take into account the safety zones described in Chapter 2, and make sure you will be able to control access adequately. Remember that the fringe field extends in three dimensions, so consider the floors above and below if necessary.

10.7.1 Radiofrequency Shielding

To avoid any extraneous sources of RF from interfering with the MR signals, all whole-body scanners are placed in an RF-shielded enclosure, also known as a Faraday cage. Typically this consists of a room lined on all six sides with copper sheeting. All electrical connections between the magnet system and the system’s electronics cabinets are connected via electrical filters through a ‘penetration panel’ or ‘filter panel’ in the RF shield. Special wire-embedded glass is used for windows, and any doors need to make a proper electromagnetic seal with their frame. It is possible to allow tubes or fibre-optic cable through the screen via the use of waveguides (metal pipes of a specific length and diameter through which unwanted RF signals below a certain frequency cannot pass). However, conducting wires, including power cables, should not be passed through waveguides since they will act as aerials, picking up unwanted RF interference outside the room and radiating it inside. This can create zipper artefacts on the MR images.

10.7.2 Technical Environment

Every iron or steel object in the stray field of the magnet will have a temporary magnetization induced into it. The stray fields from these items will in turn affect the homogeneity of the magnet. Providing they are static then the effect can be counteracted, up to a limit, by shimming of the magnet. Proximity to moving objects such as elevators or trucks can make siting even more complex. You should not allow architects to make structural changes around the proposed MRI unit, unless it is done in consultation with the manufacturer’s installation specialists.

MRI systems also have quite significant environmental requirements, particularly with respect to adequate cooling of the equipment racks and reliable electric power. Adequate air conditioning must be installed to maintain temperature and humidity within the equipment room. The air-conditioning unit should also provide the chilled water required by the compressor and other cooling units. A good-quality electrical supply is required since the sensitive electronic components do not react well to sudden losses of power, particularly if one phase of the three-phase supply fails. If necessary, additional transient suppression devices, line conditioners or even uninterruptible power supplies (UPS) may be required. In the event of power failure, the cold head

will switch off and this will result in increased helium boil-off; however, the magnet will still be at field. It is worthwhile to install a control panel in the operator room to show the status of the chilled water supplies, air-conditioning and compressor function if possible, since these services may not automatically switch back on when the power is restored.

Fluorescent lights should not be used in the magnet room since they produce RF interference. Low-voltage halogen or LED lighting is far better to avoid artefacts and also improve longevity of the bulbs.

10.8 Other Types of MRI Systems

In this book we mainly talk about cylindrical MR systems based on superconducting magnets. However, there are others, and in this section we will briefly review the main differences.

10.8.1 Open MRI Systems

Open systems are much more patient-friendly than the ‘tunnels’ of superconducting systems, and this is their main advantage. Such systems also offer the possibility of MRI-guided interventional procedures, for example image-guided breast or liver biopsy. Open systems are often based on permanent magnets or iron-cored electromagnets, designed to operate primarily between 0.1 T and 0.3 T. There are some open superconducting systems available in the range 0.5–1.0 T, but they are becoming rarer.

Many open systems have vertically orientated magnetic fields and have specially designed flat planar gradient coils. The RF transmit coil can have a solenoid design, which is 30–40% more efficient than a birdcage coil with the same dimensions. This can produce higher SNR, but do not expect it to behave like a 1.5 T system. There are one or two open systems that allow for imaging during weight bearing, i.e. the patient stands or sits in the imaging volume instead of lying supine.

Since open systems tend to have lower field strengths, their fringe fields are smaller and they can be located in a smaller footprint. It is not helpful to make direct comparisons between an open system and a cylindrical one; the conventional system will almost always have better gradients and a wider range of receive coils. The main reason to choose an open system is the greatly improved patient experience; during the purchase process you should pay extra attention to these details, while still ensuring that the

system is able to produce the right image quality for the proposed referrals.

10.8.2 Interventional (Therapy) Systems

There is continuing interest in the use of MRI for image-guided interventional procedures. Applications have included brain biopsy and neurosurgery, catheter-guided cardiac interventions, and vascular applications. Although there have been attempts to develop dedicated interventional systems they haven’t generally developed into mainstream products. Therefore most interventional procedures are now carried out using conventional or open systems. It is extremely expensive to install an MR system dedicated to only surgical interventions; many centres try to use the MR system for diagnostic imaging as well, in order to make a better business case. However, this inevitably leads to compromise for both the radiology and surgical departments, and the purchase process for an interventional MRI suite is often long-winded and complex.

10.8.3 Niche Systems

In addition to conventional whole-body systems there is also ongoing interest in niche systems for particular applications. For example, special systems are commercially available for imaging the arms or legs (joint imaging), head, breast or neonatal imaging. New prototypes appear fairly regularly at trade shows like the Radiological Society of North America (RSNA) or European Congress of Radiology (ECR); however, some of them never make it to a commercial product. Since one of their main advantages is reduced size (and therefore significantly reduced cost and installation requirements), many systems are based on low-field permanent or electromagnets. Such systems often use a more open magnet design. As with open whole-body systems, the purchasing decision is usually based on a business case for imaging only a certain type of referral in a certain location, e.g. where it is impossible to site a whole-body system. Once again, there is little point making direct comparisons between niche systems and conventional whole-body systems, since they are designed for very different purposes.

See also:

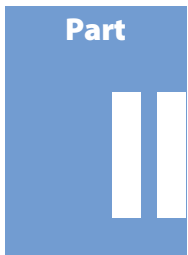
- Early daze: your first week in MR: Chapter 2
- But is it safe? Bio-effects: Chapter 20

Further Reading

Brown RW, Cheng YCN, Haacke EM, Thompson MR and Venkatesan R (2014) *Magnetic Resonance Imaging: Physical Principles and Sequence Design*, 2nd edn. Hoboken, NJ: John Wiley & Sons, chapter 27.

- Jianming J (1998) *Electromagnetic Analysis and Design in Magnetic Resonance Imaging*. London: CRC Press.
- Vlaardingerbroek MT and den Boer JA (2003) *Magnetic Resonance Imaging: Theory and Practice* 3rd edn. Berlin: Springer-Verlag.

ISMRM members should also browse the 'MR Systems Engineering' educational sessions for past annual meetings: for example www.ismrm.org/13/WK09.htm [accessed 28 March 2016].



The Specialist Stuff

Ghosts in the Machine: Quality Control

11.1 Introduction

Quality control (QC) or assurance (QA) often raises many questions. How do you do it? Who should do it and how often? (*Do I have to do it? Can't someone else?*) Quality has become more and more a part of service provision and professional practice in radiology. QA has long been established in the imaging modalities that utilize ionizing radiation, in response to regulatory requirements. No such requirement exists for MR; nevertheless, 'best practice' dictates that quality programmes should be implemented. With all QA activity, the importance is to achieve a balance between spending too much time and resources checking everything, and getting on with clinical work. This chapter will look at the aspects best covered by a QA programme, with other elements covered in the boxes.

MR QA is largely concerned with image quality. This is normally quantified through the measurement of particular image quality parameters using specially designed phantoms or test objects (Figure 11.1). Most MR manufacturers produce their own phantoms and use them in installation and routine preventative maintenance. In this chapter we will see that:

- signal-to-noise ratio (SNR) is the most useful (and fundamental) image quality parameter and should be measured and monitored both regularly and frequently;
- at field strengths above 0.5 T SNR is fundamentally related linearly to B_0 ;
- geometric parameters, e.g. spatial resolution and distortion, including slice-related quantities, are essential measurements for the initial commissioning of a system or after a re-shim, and more routinely for geometry-critical clinical applications such as radiotherapy treatment planning and stereotactic surgery;
- spatial resolution is normally determined by the size of the pixels (pixel-limited), except for highly

segmented sequences or where strong signal filtering is applied;

- relaxation parameters, particularly contrast and contrast-to-noise ratio (CNR) are important for protocol development and sequence evaluation;
- ghost artefacts and problems with fat saturation or water selection may give an indication of underlying technical problems with the scanner;
- national and international QA standards (AAPM, ACR, IEC, IPEM, NEMA) have been developed;
- specialized QA procedures are required for specific applications such as spectroscopy, fMRI and in clinical trials.

We will underpin this chapter with physics theory relating to SNR and resolution.

11.2 The Quality Cycle

The quality cycle for an item of radiological equipment begins with the drawing up of specifications, i.e. before purchase. On installation of a new or upgraded MR system, acceptance procedures should be carried out by an appropriately qualified MR physicist or engineer with any non-compliance receiving corrective action from the manufacturer. The acceptance report can then form the baseline for routine QA. At each point in the cycle reference to local, manufacturer or national/international standards can be made. Further details are in Box 'National and International Standards'.

National and International Standards

The National Electrical Manufacturers Association (NEMA) has published a series of standards for the methodology of image quality parameter measurement and phantom design principles. NEMA has stopped short of defining specific performance expectations or 'action criteria'. A similar approach

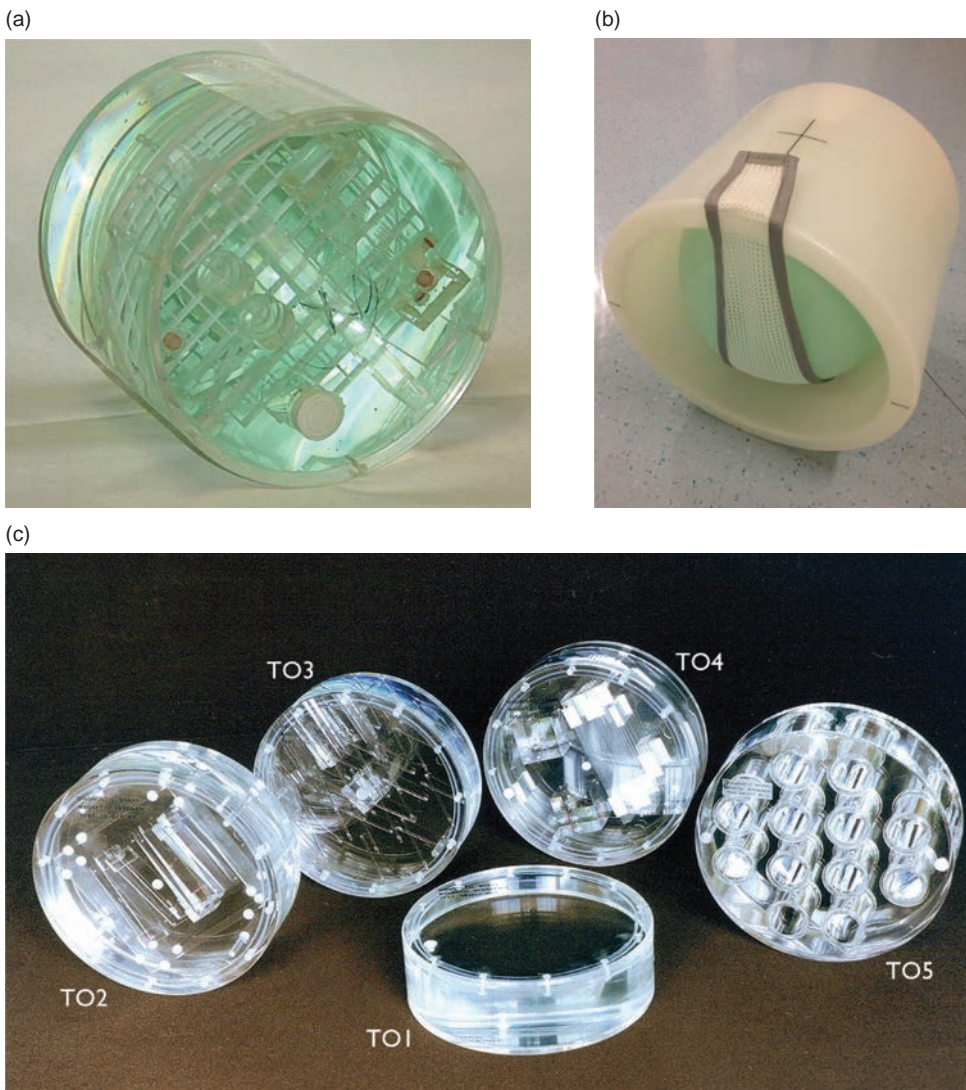


Figure 11.1 Phantoms for quality assurance (QA). (a) ACR multipurpose phantom, courtesy of the American College of Radiology. (b) Loading ring, courtesy of GE Healthcare. (c) Eurospin test object set, courtesy of Diagnostic Sonar Ltd, Livingston, UK.

has been taken by the American Association of Physicists in Medicine (AAPM) and includes action criteria. By contrast, the Eurospin Test System developed by a European Community Concerted Action programme in the 1980s is a set of five test objects for image quality evaluation, with a particular emphasis on the measurement and characterization of relaxation times (Figure 11.1c). The same group has published protocols, phantom designs and results of a multi-centre trial for spectroscopic QA. The Institute of Physics and Engineering in Medicine (IPEM) has

published generic and specialist (by clinical application) methodologies for quality control.

The American College of Radiology (ACR) has developed a standard for performance monitoring of MRI equipment, and its accreditation and quality control scheme uses a custom-designed phantom (Figure 11.1a) and protocol. The ACR also has defined clinical standards for performing and interpreting MRI. ACR standards include a summary of techniques, indications and contraindications, education, training and experience of personnel, staff responsibilities,

examination specifications, documentation, equipment specifications, safety guidelines, quality control and patient education. The ACR states that its standards 'are not rules but are guidelines that attempt to define principles of practice which should generally produce high-quality radiological care'.

The International Electrotechnical Commission (IEC) also has a standard for test methodologies and reporting of results in a uniform format. These standards can be found in the following publications:

American Association of Physicists in Medicine

Jackson EF, Bronskill MJ, Drost DJ, et al. (2010) AAPM Report 100: Acceptance Testing and Quality Assurance Procedures for Magnetic Resonance Imaging Facilities. College Park, MD: American Association of Physicists in Medicine.

The American College of Radiology

The ACR accreditation documents are available to download or purchase from www.acr.org/Quality-Safety/Accreditation/MRI [accessed 12 December 2014].

Of particular interest are the ACR phantoms:

www.acraccREDITATION.org/~media/ACRAccREDITATION/Documents/MRI/LargePhantomGuidance.pdf

www.acraccREDITATION.org/~media/ACRAccREDITATION/Documents/MRI/SmallPhantomInstructions.pdf

European Concerted Action Research Project

European Communities Research Project (COMAC BME II 2.3) (1988) 'Protocols and test objects for the assessment of MRI equipment'. *Magn Reson Imaging* 6:195–199.

European Communities Research Project (1995) 'Quality assessment in in-vivo NMR spectroscopy: results of a concerted research project for the European Economic Community I–IV'. *Magn Reson Imaging* 13: 117–158.

Institute of Physics and Engineering in Medicine (IPEM), UK

McRobbie D and Semple S (eds) (in preparation) 'Quality control and artefacts in MRI'.

International Electrotechnical Commission

International Electrotechnical Commission (2016) *Magnetic Resonance Equipment for Medical*

Imaging – Part 1: Determination of Essential Image Quality Parameters. Geneva: Commission Electrotechnique Internationale.

National Electrical Manufacturers Association

The following documents can be downloaded free or purchased (all accessed 13 January 2015).

NEMA Standards, 'Determination of signal-to-noise ratio (SNR) in diagnostic magnetic resonance imaging'. Publication MS 1-2008. www.nema.org/Standards/Pages/Determination-of-Signal-to-Noise-Ratio-in-Diagnostic-Magnetic-Resonance-Imaging.aspx

NEMA Standards, 'Determination of two-dimensional geometric distortion in diagnostic magnetic resonance images'. Publication MS 2-2008. www.nema.org/Standards/Pages/Determination-of-Two-Dimensional-Geometric-Distortion-in-Diagnostic-Magnetic-Resonance-Images.aspx

NEMA Standards, 'Determination of image uniformity in diagnostic magnetic resonance images'. Publication MS 3-2008. www.nema.org/Standards/Pages/Determination-of-Image-Uniformity-in-Diagnostic-Magnetic-Resonance-Images.aspx

NEMA Standards, 'Determination of slice thickness in magnetic resonance imaging'. Publication MS5-2003. www.nema.org/Standards/Pages/Determination-of-Slice-Thickness-in-Diagnostic-Magnetic-Resonance-Imaging.aspx

NEMA Standards, 'Determination of signal-to-noise ratio and image uniformity for single-channel non-volume coils in diagnostic MR imaging'. Publication MS 6-2008. www.nema.org/Standards/Pages/Determination-of-Signal-to-Noise-Ratio-and-Image-Uniformity-for-Single-Channel-Non-Volume-Coils-in-Diagnostic-Magnetic.aspx

NEMA Standards, 'Characterisation of phased array coils for diagnostic magnetic resonance images'. Publication MS 9-2008. www.nema.org/Standards/Pages/Characterisation-of-Phased-Array-Coils-for-Diagnostic-Magnetic-Resonance-Images.aspx

NEMA Standards, 'Quantification and mapping of geometric distortion for special applications'. Publication MS 12-2006. www.nema.org/Standards/Pages/Quantification-and-Mapping-of-Geometric-Distortion-for-Special-Applications.aspx

See also 'Further reading' at the end of the chapter.

This sort of QA is concerned with equipment aspects of the scanner. Human aspects (working

practice, safety procedures, training, skill, etc.), which are much more likely to be problematical, are best addressed through clinical audit or quality management systems such as ISO 9001 or equivalent. One such scheme, organized by the American College of Radiology (ACR), consists of an initial accreditation and the development of a QA programme for all MRI facilities including the evaluation of clinical images (see Box ‘National and International Standards’). All QA should be subject to audit, review and corrective action.

11.3 Signal Parameters

Signal parameters include SNR, image uniformity and centre frequency and RF transmitter gain. SNR is without doubt a key parameter. Equipment-related factors that affect SNR include field strength, choice of coil, coil loading (see Box ‘Theoretical Field Dependence of SNR’) and receiver bandwidth. Sequence-related factors include voxel size, sequence choice and timings. For SNR measurement it is important to use standard set-up arrangements and sequence parameters. Saving these into a user-defined QA protocol is highly recommended.

Signal parameters are normally measured using a uniform or ‘flood field’ phantom filled with a material with appropriate relaxation times (see Box ‘Filling Factors’). A crucial issue is whether to load the coil or not. Loading means using a slightly conductive solution (i.e. saline) to mimic the reduction of the coil quality factor (see Section 10.4) and to generate realistic image noise from tissue. For head and body transmit coils a loading ring is sometimes used (see Figure 11.1b). For other coils saline can be added to the paramagnetic solution to obtain the desired effect. At 3 T, however, water-based salt solutions become problematical (see Box ‘Phantom Problems’).

Measurement of the centre (Larmor) frequency may also be carried out using the uniform phantom. This value is normally available through the manufacturer’s prescanning software and is stored in the image series’ DICOM header (see Box ‘DICOM: A Common Language Leading to Misunderstanding?’ in Chapter 5).

11.3.1 SNR

SNR measurements should be carried out daily or weekly. Two methods are common for measuring SNR. In the signal-background method, the signal is given by the mean pixel value from a region of

interest (ROI) within the phantom. For head and body coils it is recommended that the ROI should include at least 75% of the phantom area (see Figure 11.2). The noise is measured from the standard deviation of the pixel values from small ROIs (between one and four) placed within ghost-free regions of background outside the phantom. You must take care to avoid using areas which may have atypical standard deviations, e.g. at the extreme edges of the field of view. The average of the standard deviations from these noise regions is used in the calculation of SNR

$$\text{SNR} = \frac{0.66 \times \text{mean signal}}{\text{average of noise region standard deviations}}$$

The factor of 0.66 is the Rayleigh distribution correction factor and applies for a single channel coil, e.g. a birdcage coil.

The second (NEMA) method involves acquiring two identical images consecutively and subtracting them, allowing negative values in the resultant image. An ROI covering 75% of the phantom area is used to measure the signal as before. Noise is measured from the standard deviation of pixel values within this ROI placed in the subtraction image. The SNR is

$$\text{SNR} = \sqrt{2} \cdot \frac{\text{mean signal in image ROI}}{\text{standard deviation in subtraction image ROI}}$$

The factor of $\sqrt{2}$ is required to compensate for the greater standard deviation from the subtraction of images. The Rayleigh correction factor is not required. Ideally, both SNR methods should yield the same result. Performance criteria are not normally quoted, being dependent upon fundamental and equipment-related factors (see Box ‘Theoretical Field Dependence of SNR’). For a practical approach refer to Box ‘Absolutely Fabulous SNR’. SNR is usually measured on a daily or weekly basis for either head or body coils. Other coils can be investigated less frequently on a rolling programme. This method also works for multi-element coils and when parallel imaging is used.

Filling Factors

Aqueous paramagnetic solutions such as chlorides and sulphates of nickel, copper or manganese are often used in phantoms. Alternatively, one can simply dilute leftover gadolinium contrast for a home-made phantom. It is important to understand

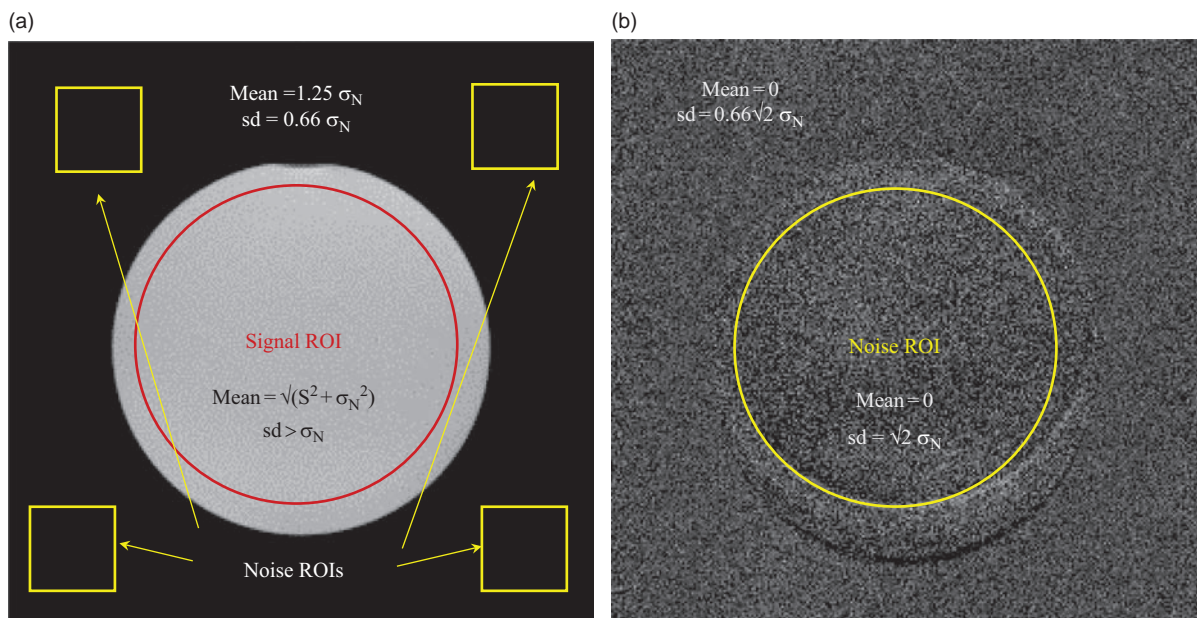


Figure 11.2 Signal-background and National Electrical Manufacturers Association (NEMA) SNR methods. (a) Magnitude image. (b) Subtraction of two consecutive magnitude images. In this example the subtraction was affected by scan-to-scan inconsistencies. σ_N is the standard deviation of the normal (Gaussian) noise distribution. S is the mean MR signal intensity of a region of interest (ROI).

the MR properties of the solution. These include the ratio of T_1 and T_2 , field dependence, magnetic susceptibility and temperature coefficient, and are summarized in Table 11.1. The AAPM recommends having T_1 between 200 and 500 ms and T_2 between 150 and 300 ms. NEMA recommends only an upper limit of 1200 ms for T_1 with T_2 greater than 50 ms. We favour keeping both T_1 and T_2 quite short, e.g. both about 200 ms, as this means that the QA can be completed more quickly by using a shorter TR, and that transverse coherence artefacts can be avoided.

The relaxation time is calculated as follows:

$$\frac{1}{T_1} = \frac{1}{T_{1,0}} + R_1 C$$

where $T_{1,0}$ is the T_1 of pure water (distilled and deionized – about 3000 ms for all B_0) and C is the molar concentration of ions. For example, a 7 mM solution of NiCl_2 gives T_1 and T_2 approximately equal to 200 ms. The ACR phantom uses 10 mM nickel chloride plus 75 mM sodium chloride for loading, giving it a T_1 and

Table 11.1 MR properties of paramagnetic ions

Ion	T_1/T_2 ratio	Relaxivity $r_1(\text{s}^{-1}\text{mmol}^{-1})$		Temperature coefficient dr/dT	Comments
		3 MHz (0.07T)	60 MHz (1.4T)		
Cu^{2+}	1.1	1.7	0.5	0.038	Varies with B_0 and temperature
Gd^{3+}	1.1	22.1	10	0.28	Varies with B_0 and temperature
Mn^{2+}	2–10*	13	7		* T_1/T_2 ratio varies with B_0 but can get more ‘tissue-like’ T_2
Ni^{2+}	1.1	0.6	0.65	-0.006	B_0 -independent up to 1.5 T; fairly independent of temperature

T_2 of approximately 150 ms at 1.5 T, but with a shorter T_2 at 3 T. However, beware of significant T_2 shortening for 3 T systems if using nickel-based solutions.

Theoretical Field Dependence of SNR

In a uniform static magnetic field of strength B_0 the equilibrium magnetization M_0 is given by the Langevin equation

$$M_0 = \frac{\gamma^2 h^2 B_0 \rho}{4k_B T}$$

where k_B is the Boltzmann constant, T is the absolute temperature in kelvin (K), ρ is the number of nuclei per unit volume and γ is equal to 42 MHz T⁻¹ for proton imaging.

The signal induced in the receive coil is proportional to the rate of change of the magnetization, i.e. the Larmor frequency ω_0 , the coil sensitivity (field per unit current) B_1 and M_0 which is proportional to B_0 , thus

$$S \propto \omega_0 \cdot B_1 \cdot B_0$$

Since both the Larmor frequency and M_0 are proportional to B_0 , the signal (S) can be written as

$$S \propto B_1 \cdot B_0^2$$

Random noise arises from the Brownian motion of electrons within a conductor. This thermally induced random noise, sometimes called Johnson noise, is given by

$$V_{\text{noise(rms)}} = \sqrt{4 \cdot k_B \cdot T \cdot R \cdot BW}$$

where R is the effective resistance and BW is the bandwidth of the measuring equipment.

The overall noise variance is the sum of the noise variances due to the patient, receive coil and receiver electronics. Effectively the resistance R is the sum of the coil resistance R_c and the resistance induced by the conductive losses in the patient R_p . Therefore $R = R_c + R_p$. In high-field imaging the dominant source of noise is the patient, whereas at low field the coil can be the dominant noise source.

If we consider the coil noise first, then we need to take account of the fact that at radiofrequencies the resistance of the coil increases with the square-root of the frequency due to the phenomenon of the skin effect. Therefore

$$V_{\text{noise(rms)}} \propto \omega_0^{1/4} \propto B_0^{1/4}$$

and for low-field systems

$$\text{SNR} \propto \frac{B_1 \cdot B_0^2}{B_0^{1/4}} \propto B_1 \cdot B_0^{7/4}$$

At low B_0 then SNR depends upon B_0 to the power of 7/4 and the coil sensitivity is crucial.

However, at high-field strengths (≥ 0.5 T) the effective patient resistance should dominate over the coil resistance. For the simplified case of a saline sphere of radius r with conductivity σ , for a uniform B_1 field (i.e. a coil with a perfectly uniform sensitivity), R_p is given by

$$R_p = \frac{2\pi\sigma\omega_0^2 B_1^2 r^5}{15}$$

Therefore,

$$V_{\text{noise(rms)}} \propto \sqrt{B_1^2 \cdot \omega_0^2} \propto B_1 \cdot B_0$$

and

$$\text{SNR} \propto \frac{B_1 \cdot B_0^2}{B_1 \cdot B_0} \propto B_0$$

So at high-field strengths the theoretical SNR is only proportional to B_0 . In practice, other factors, e.g. greater signal bandwidth and relaxation effects may reduce this dependence further. Notice that although SNR is independent of the coil sensitivity, noise and SNR are highly dependent upon the amount of tissue the coil 'sees' (proportional to the fifth power of the radius). This is the underlying reason for the greater SNR of surface and array coils.

Absolutely Fabulous SNR

The absolute SNR provides a calculation of the fundamental signal-to-noise performance of the system when measured under appropriate loading conditions and with minimal signal saturation and T_2 decay, i.e. a long enough TR and short enough TE. Absolute SNR (ASNR) can be directly related to the magnetic field strength. It is defined for conventional 2D images as

$$\text{ASNR} = \text{SNR} \frac{\sqrt{\text{pixel bandwidth}}}{\Delta x \cdot \Delta y \cdot \Delta z \sqrt{\text{NSA} \cdot N_{\text{PE}}}}$$

where the pixel bandwidth is measured in hertz and SNR is measured by any suitable method. As before, NSA is the number of signal acquisitions and N_{PE} is the phase-encode matrix size. ASNR has units of Hz^{1/2} mm⁻³. As a rule of thumb we expect ASNR to

be at least $10 \text{ Hz}^{1/2} \text{ mm}^{-3}$ per tesla for an appropriately loaded head coil. So for a 1.5 T scanner with pixel dimensions of 1 mm by 1 mm and a 5 mm slice with a pixel bandwidth of 100 Hz and 256^2 matrix, expect an image SNR of $10 \times 5 \times \sqrt{256}/\sqrt{100} = 80 \text{ Hz}^{1/2} \text{ mm}^{-3}$, assuming minimal T_1 saturation and minimal T_2 decay.

These methods can be applied to surface and special-purpose coils only with a great deal of care on the exact positioning and choice of ROI. NEMA has attempted to define a standard method for such coils. The ACR recommends measuring the ‘maximum SNR’ for surface coils using small ROIs for both signal and background noise.

11.3.2 Uniformity

Uniformity is particularly important for RF coils which transmit and receive, as any RF inhomogeneity will affect the flip angles and hence the contrast. Non-uniformity in receive-only surface coils is a feature of their design and is usually quite well tolerated by the observer. Homogenizing (image intensity correction) filters may be provided in the system. For this reason

uniformity is usually only measured for head and body transmit coils using a uniform phantom.

Integral uniformity I is defined as

$$I = 1 - \frac{M - m}{M + m} \cdot 100\%$$

where M is the maximum pixel value and m is the minimum pixel value within an ROI of 75% of the phantom area. A value of 100% represents perfect uniformity. (NEMA uses a non-uniformity parameter $U = (1 - I)$ with a value of zero representing perfect uniformity.) To overcome inaccuracies arising from a low SNR, NEMA recommends an image smoothing stage. In practice we have found this achieves little, and for systems with low SNR it is better to increase the number of acquisitions, NSA. Performance criteria have been defined for transmit/receive head coils, and these are shown in Table 11.2. Uniformity measurements are important for accepting new coils. They can usually be incorporated with scans performed for SNR measurements. At higher field strengths (3 T and above) there is a possibility of non-uniformity arising through standing wave effects caused by the dielectric properties of water. In this

Table 11.2 Action criteria and expected performance for head coil

Parameter	ACR ^a	AAPM
SNR	Not specified	Not specified
Uniformity	$\geq 87.5\%$ for $B_0 < 3 \text{ T}$ $\geq 82\%$ for $B_0 = 3 \text{ T}$	$\geq 90\%$ for head coil up to 2 T
Linearity/distortion	$\pm 2 \text{ mm}$ in 190 mm on diameter of phantom	$\leq 2\%$ over head FOV
Spatial resolution	$\pm 1 \text{ mm}$ using ACR specified sequence	Pixel size resolved, e.g. 1 mm for 256×256 , 256 mm FOV
Slice thickness	$\pm 0.7 \text{ mm}$ for 5 mm slice	$\pm 10\%$ for $\geq 5 \text{ mm}$ and SE
Slice position accuracy	Bar length difference should be $\leq 5 \text{ mm}$ ^b (see Figure 11.3)	$\pm 10\%$
Slice separation	Not defined	$\pm 10\%$
Low contrast object detectability	Specific to phantom Minimum ≥ 9 spokes for $B_0 < 3 \text{ T}$; ≥ 37 spokes for $B_0 = 3 \text{ T}$	Specific to phantom (minimum ≥ 9 spokes)
Ghosting	$\leq 2.5\%$	$\leq 1\%$
Centre frequency drift	Not specified	$\leq \pm 1 \text{ ppm}$ per day but expect $\leq \pm 0.25 \text{ ppm}$ per day

^a American College of Radiology (ACR) action criteria are dependent upon using the ACR phantom and test guidance and are somewhat stricter than those used by the ACR for accreditation, but in all cases are indicative of a minimum level of performance one can reasonably expect from a well-functioning MRI system. On the other hand, being minimum levels of performance, these criteria are not to be construed as indicators of typical or normal levels of performance.

^b This is equivalent to an error of $\pm 2.5 \text{ mm}$.

case an oil-based filling substance may be used. See Box 'Phantom Problems'.

Phantom Problems

Care has to be taken with phantom measurements to avoid obtaining misleading results. Phantoms generally contain higher signals than humans and have a different distribution of spatial frequencies, often with many high-contrast edges. The phantom geometry and materials may result in spurious susceptibility effects and the automatic shim may have trouble obtaining convergence. The filling materials may have atypical relaxation times with various consequences: greater occurrence of coherence and stimulated echoes due to long T_2 , and greater high spatial frequency signals in segmented sequences. There are simple practical considerations to remember:

- allow the phantom fluid to settle;
- let the phantom fluid reach thermal equilibrium with the environment, if temperature-dependent, and check the temperature before scanning;
- avoid bubble formation;
- minimize mechanical vibration.

It's also important to remember that patients breathe, pulsate and fidget (the usual cause of image quality problems) but that phantoms do not.

For higher-field systems (e.g. 3 T) relaxation times of the test materials need to be considered. The electrical conductivity of the test object may result in non-uniform RF deposition: always use an oil phantom for uniformity measurements. Expect

increased susceptibility problems: these may be related to the phantom design and construction rather than to the scanner's performance.

11.4 Geometric Parameters

Geometric parameters are mainly concerned with the accuracy of the spatial encoding, and reflect various technical factors, e.g. field uniformity, gradient linearity and eddy current compensation. Examples of specific action criteria are contained in Table 11.2. Appropriate phantoms may afford the measurement of different parameters in particular slice positions or throughout an extended volume. These are illustrated in Figure 11.3.

11.4.1 Linearity and Distortion

Linearity refers to the accuracy of distances within the image, and is usually associated with gradient amplitude calibration. Non-linearity indices L_{FE} and L_{PE} can be defined with respect to the frequency and phase axes as

$$L_{FE} = \frac{x - l}{l} \cdot 100\%$$

$$L_{PE} = \frac{y - l}{l} \cdot 100\%$$

where x is the measured distance in the frequency-encode direction, y is the measured distance in the phase direction and l is the true length in the test object. Good linearity is indicated by values close to 0%. NEMA and

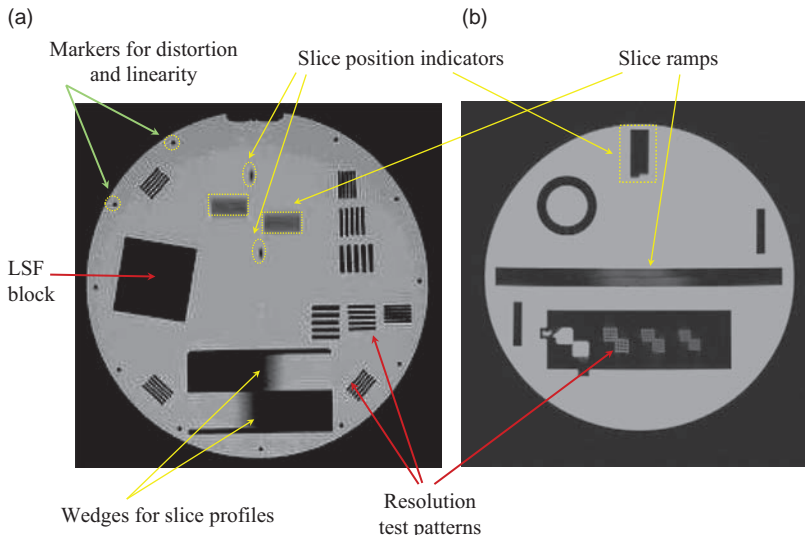


Figure 11.3 General-purpose geometric phantoms. (a) Volume phantom for which all parameters are measurable on every slice, courtesy of Charing Cross Hospital, London. (b) Slice from ACR phantom showing insert for measuring spatial resolution, slice width and slice position accuracy. LSF denotes line spread function. Courtesy of the American College of Radiology.

the AAPM do not distinguish between linearity and distortion, using similar definitions to those above (AAPM actually use the opposite, so values close to 100% mean good linearity). The ACR uses the term ‘geometric accuracy’. In Europe, distortion is calculated as the standard deviation from several distance measurements, usually between an array of points spaced regularly throughout the phantom. Indices for distortion include the maximum deviation of a location from its true position or the standard deviation of the measured distances. These tests are essential at commissioning and after a field ramp or re-shim. The measurement of linearity can indicate gradient amplifier problems and is useful in routine QA. Some distortion phantom images are shown in Figure 11.4.

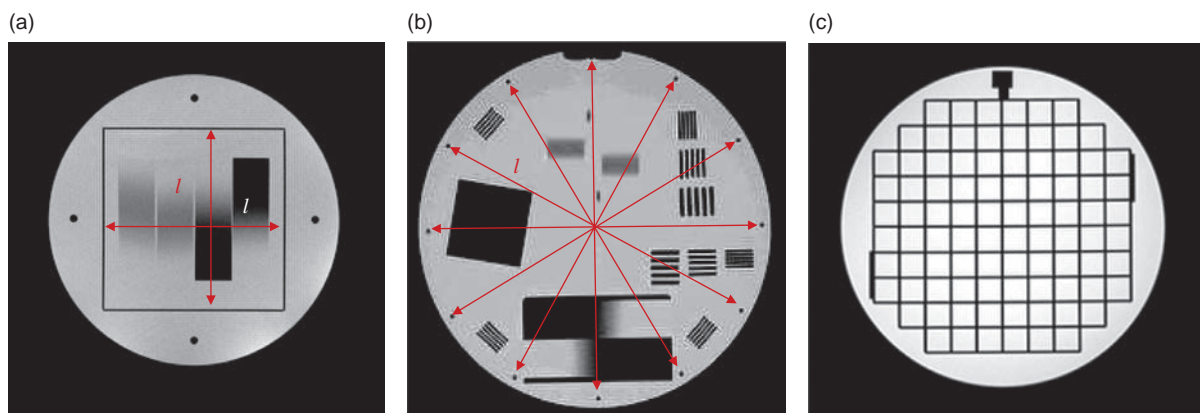


Figure 11.4 Distortion measurement phantom images. (a) Eurospin TO2, courtesy of Diagnostic Sonar Ltd, Livingston, UK. (b) Charing Cross TO2A, courtesy of Charing Cross Hospital, London. (c) ACR geometric accuracy insert, courtesy of the American College of Radiologists. / is the true length in the test object.

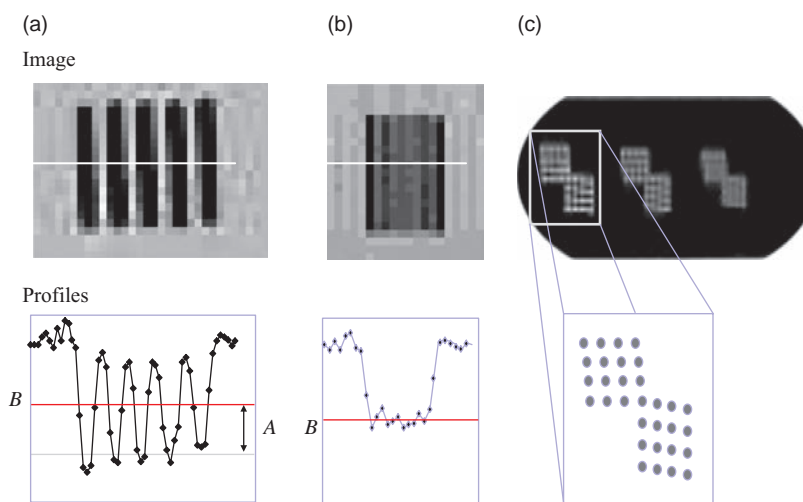


Figure 11.5 Measurement of spatial resolution from signal modulation across line pair patterns, showing (a) well-resolved and (b) poorly resolved features. A denotes the amplitude of modulation; B, the mean signal value along the profile. (c) Spatial resolution measurements from the ACR phantom using hole array pairs. Note the angular offsets of the hole array with respect to the pixel matrix. Courtesy of the American College of Radiology.

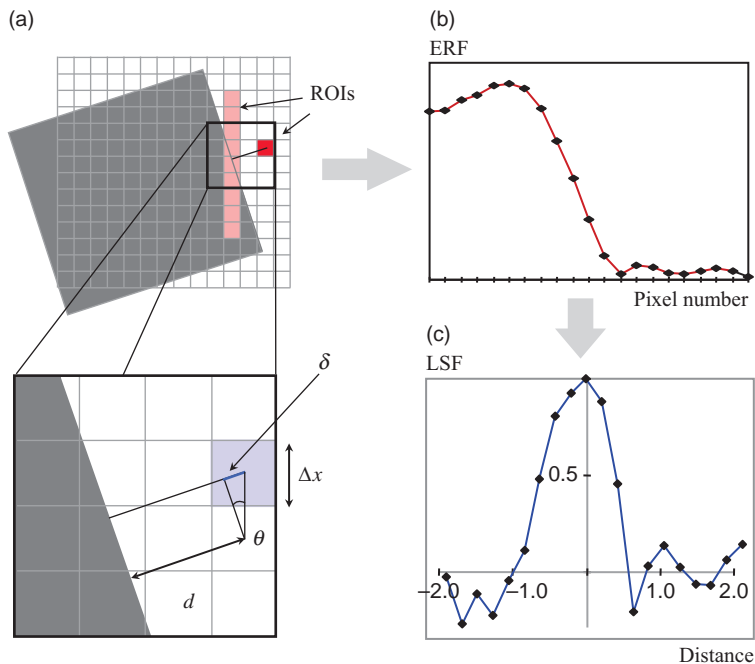


Figure 11.6 Derivation of the line spread function from an angled edge. (a) The edge response function (ERF) can be obtained from either a square region of interest (ROI) or a linear profile. In the latter case, the resolution measured is that perpendicular to the profile. (b) Example of an ERF. (c) The line spread function (LSF) is the normalized derivative of the ERF.

Care is required with alignment of the patterns with the pixel matrix. Aliasing of the patterns can occur and excessive Gibbs' ringing may also render the measurement void. Both effects are apparent in Figure 11.3a. More sophisticated measurements of spatial resolution are explained in Box 'Modulation Transfer Function and Line Spread Function'.

Modulation Transfer Function and Line Spread Function

In X-ray CT we would measure the modulation transfer function (MTF) of the scanner. This is not commonplace in MRI because an accurate method of MTF measurement is difficult; however, a line spread function (LSF) can be readily obtained using Judy's method. In this technique a high-contrast edge at a slight angle θ (e.g. 10°) to the pixel matrix (Figure 11.6) is scanned. For a square ROI centred on the edge, the centre of each pixel will be at a slightly different distance (as the crow flies) from the edge. The difference in distance of neighbouring pixels to the edge will be less than the pixel dimension (Δx). Hence from this ROI a magnified or over-sampled edge response function (ERF) may be reconstituted. In a simpler variant of the Judy method, a line profile obliquely crossing the edge yields a similar result.

In either method the effective sampling interval is given by

$$\delta = \Delta x \times \sin \theta$$

Differentiation of the ERF produces an LSF. A measurement of the full width at half maximum (FWHM) of the LSF will give a good indication of the spatial resolution. It is vital to remember that the axis in which you are measuring the resolution is the one nearly perpendicular to the edge, i.e. the horizontal axis in Figure 11.6.

If a real-valued inversion recovery sequence (with positive and negative values) is used then it is possible to calculate the MTF as the normalized Fourier transform of the LSF. This should not be attempted for other sequences as the outer lobes of the LSF will be distorted and asymmetric and do not yield a true MTF.

An alternative method uses arrays of small holes of varying diameters. The ACR phantom (Figure 11.5c) has hole diameters of 0.9, 1.0 and 1.1 mm to allow visual assessment of spatial resolution for a nominal pixel size of 1 mm. These are slightly offset with regard to the main gradient axes to avoid aliasing problems with the pixel matrix.

Resolution Limits

The spatial resolution of an imaging method is defined as the smallest resolvable distance between two different objects. In MRI it is easy to think of the pixel size as the intrinsic spatial resolution of the image; however, this is not necessarily the case.

The pixel-limited resolution was given in Section 8.5.6. For the frequency-encode (FE) axis this was

$$\Delta x = \frac{1}{\gamma G_x M \Delta t} = \frac{1}{\gamma G_x T_{\text{acq}}}$$

where T_{acq} is the data acquisition time = $M \cdot \Delta t$. We could in principle increase G_x , M or Δt to achieve any desired resolution, although in practice both gradient strength and acquisition time are subject to physical limits.

The frequency spread across a pixel from the spatial-encoding gradient is

$$\Delta f = \gamma G_x \Delta x$$

However, if the signal from a point source decays over the readout period with time constant T_2^* then, following Fourier transformation, this results in the point spreading out to give a characteristic linewidth of $\Delta \omega = 2/T_2^*$, i.e. the point would be blurred by this amount. The linewidth broadened frequency Δf^* is therefore given by

$$\Delta f^* = \frac{1}{\pi T_2^*}$$

To avoid T_2^* blurring we require that

$$\Delta f \gg \Delta f^*$$

i.e.

$$G_x \gg \frac{2}{\gamma \Delta x T_2^*}$$

This also implies an ultimate limit on the spatial resolution determined by T_2^* of $2/(\gamma G_x T_2^*)$.

11.4.3 Slice Parameters

Slice parameters include slice position, slice width and slice profile (see Box 'In Profile'). Slice position can be measured from a phantom containing a pair of crossed rods or ramps inclined at θ to the slice plane (Figure 11.7). The slice position p from isocentre is then given by

$$p = \frac{d}{2 \tan \theta}$$

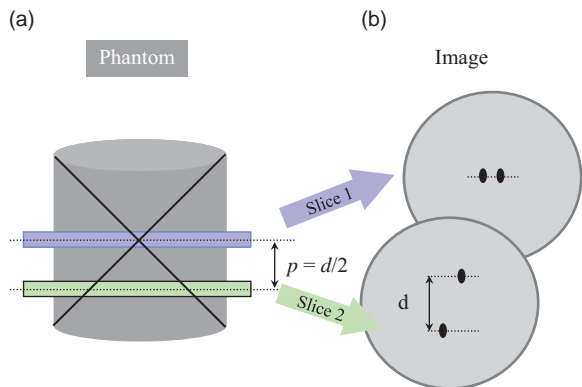


Figure 11.7 Slice position measurements from a pair of rods crossed at 45°. (a) View of phantom perpendicular to the slice-select axis showing slice positions. (b) Schematic of images produced from (a).

where d is the measured distance in the image plane. In Figure 11.7 θ is 45°. Slice separation is then the distance between adjacent slice positions.

Slice width measurements can be obtained by two methods: ramps and wedges (Figure 11.3 and Figure 11.8). Ramps may be either 'hot' or 'cold' depending upon whether they produce signal or lack of signal, e.g. a glass plate immersed in water would constitute a cold ramp. Figure 11.3 shows examples of both hot and cold ramps. The effect of the ramp is to project a magnified image or shadow of the signal in the z axis (the slice profile) onto one of the in-plane axes. A line profile drawn across this is related to the slice shape. If the ramp makes an angle θ with the slice plane the slice thickness can be determined, defined as the full width half maximum (FWHM) as

$$\text{Slice width} = \text{in-plane FWHM} \cdot \tan \theta$$

Using a different angle for the ramp or wedge changes the 'stretch factor' or degree of magnification, e.g. 26.6° gives a magnification of two while 11.3° magnifies by five. This method is adequate for slice widths down to about one-third of the ramp thickness. Below this you get an overestimation of slice thickness caused by the convolution of the ramp thickness with the slice profile (and also the in-plane pixel dimension).

Wedges can be used to measure very thin slices. An edge response function (ERF) is obtained from a line profile drawn along the wedge. The derivative of this represents the scaled slice profile, again according to the stretch factor above. This method requires a high SNR.

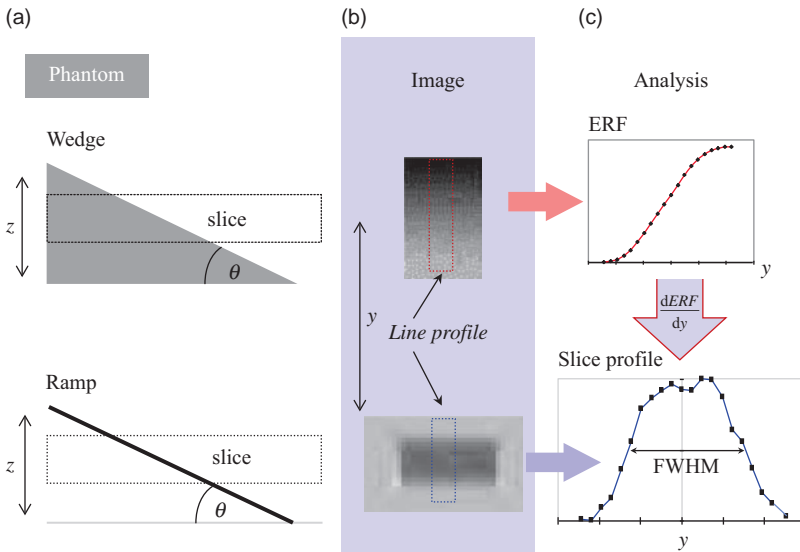


Figure 11.8 Slice width and profile measurement from a wedge and cold ramp. (a) View of phantom perpendicular to the slice-select axis showing slice position. (b) Images resulting from (a). (c) Line profiles from (b). ERF denotes edge response function and FWHM full width at half maximum.

In Profile

The slice profile P is a plot of the transverse magnetization (or signal) in the slice-select axis and is related to flip angle α by

$$P(z) = \rho(z) \sin \alpha(z)$$

Slice profiles are sensitive to relaxation effects, particularly T_1 when using gradient-echo sequences with short TRs. When TR/T_1 becomes less than 1, significant broadening and other distortions to the slice profile can occur in the regions where the flip angle is varying most, i.e. at the edges of the slice. These can be minimized by the use of a suitably low flip angle. For a perfectly rectangular profile, these would not occur. The need for short-duration RF pulses means that, in practice, slice profiles are never perfect. Once again, it's a case of the Fourier 'less-is-more' principle. Slice profile distortions can lead to changes in image contrast and unexpected partial volume effects (see Section 8.4).

In both methods, using pairs of opposed ramps or wedges allows one to correct for geometric misalignment with respect to the slice plane. While an exact correction is possible, it is usually sufficient to take the geometric mean of measurements across both features.

True slice width = $\sqrt{\text{slice width 1} \cdot \text{slice width 2}}$
Manufacturers often specify a tolerance of 10% of the slice width. These tests are important at acceptance

and for sequence evaluation, especially where selective inversion pulses are used, but may not be useful in routine QA. Ramps or wedges may also be used for slice position measurements as in the ACR phantom.

11.5 Relaxation Parameters

Relaxation parameters include contrast, contrast-to-noise ratio (CNR) and T_1 and T_2 measurement accuracy and precision. Contrast is probably the most important feature of MRI; however, because it is so sequence dependent, standard QA methodologies are not common. Nevertheless contrast can be measured for pairs of samples with differing relaxation times from the mean pixel values S_1 and S_2 in ROIs placed in each sample as

$$\text{Contrast} = \frac{S_1 - S_2}{|S_1| + |S_2|}$$

where $S_1 > S_2$. The moduli on the denominator are required for inversion recovery sequences where negative signals may be encountered. This gives a contrast range of 0–1 for all sequences.

CNR may be defined as

$$\text{CNR} = \frac{S_1 - S_2}{\text{Noise}}$$

for a suitable measurement of noise (e.g. standard deviation of background).

These tests would not commonly form part of a routine QA programme, but may be very helpful in protocol optimization and for evaluating new sequences.

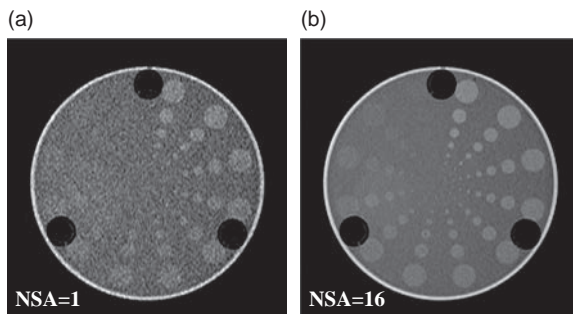


Figure 11.9 Examples of contrast-detail detectability phantom with a different number of signal acquisitions. (a) NSA = 1. (b) NSA = 16. Phantom by Philips Healthcare.

To be useful, one needs to know the appropriate relaxation times for the tissues of interest and have a suitable material that mimics them. Physical properties of tissue, such as proton density, heterogeneity, T_1/T_2 ratio, magnetization transfer and partial volumes, may not be adequately modelled by simple test materials. The Eurospin TO5 (Figure 11.1c) contains a set of doped polysaccharide gels with a range of T_1 and T_2 .

Contrast-Detail Detectability

A test that is very important in X-ray-based imaging methodologies is low-contrast-detail detectability. This is a test of the resolving power of the system for low values of contrast. A typical low contrast MRI phantom is shown in Figure 11.9, where differing diameters of disk details have a different signal contrast. The image is evaluated subjectively by counting the number of disks clearly seen for each diameter group. A constructional difficulty with contrast phantoms limits this test to proton density contrast evaluation. It can also provide a subjective assessment of SNR.

11.6 Artefacts

Artefacts tend to occur sporadically and would not be subject to a routine QA test, except for ghosting.

11.6.1 Ghosting

Ghosting is best measured using a small phantom offset diagonally in the field of view (FOV). Phase ghosts will then be apparent in the phase-encode (PE) direction. Additionally, ‘quadrature ghosts’ (which are eliminated in modern digital receiver systems) appear as a reflection of the primary image through the origin. The fourth quadrant (Figure 11.10) should

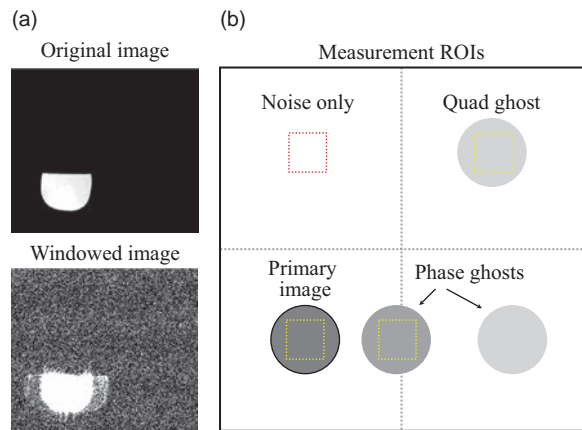


Figure 11.10 Ghosting. (a) Extreme windowing is usually required to see the ghosts. (b) Schematic diagram of ROI positions for signal-ghost ratio measurement.

contain only random noise. A Ghost-to-Signal Ratio (GSR) can be defined as

GSR

$$= \frac{\text{mean SI of ghost ROI} - \text{mean SI of background ROI}}{\text{mean SI of primary image (ROI)}}$$

where SI is signal intensity. You may have to manipulate the display window and level to extreme values to visualize the ghosts, but they will always be there somewhere. The AAPM action level is set at 1%, although we would recommend a more lenient 2% for most sequences (except EPI). Owing to the sensitivity of 2D FT to ghosting, this is a very useful test, although care needs to be taken to ensure that ghosts are not induced by mechanical vibration caused by the gradients. The presence of ghosting should be routinely investigated on a daily or weekly basis.

11.6.2 Chemical Shift and Fat Suppression

Chemical shift, as an artefact, is not worth measuring as we can determine the pixel shift if we know the receiver bandwidth (Section 7.3.1). However, it is very worthwhile to measure the effectiveness of fat suppression or water-only excitation methods as these critically depend upon the shimming of the magnet and can have a major effect upon the diagnostic value of certain examinations, especially musculoskeletal and any use of echo planar imaging (EPI).

This can be done simply using a water-based and a fat-based phantom (e.g. cooking oil) and taking the ratio of mean pixel values in images acquired with and without fat suppression enabled. The effect of

frequency-selective fat suppression on the water signal should also be tested to ensure that unwanted water signal saturation is not occurring. Care needs to be taken over shimming and the shape and positioning of the phantoms (see Box ‘Phantom Problems’).

11.7 Spectroscopic QA

Centres which depend heavily on spectroscopy should also perform QA regularly with an appropriate MR spectroscopy phantom which will be provided by the manufacturer. At the very least, phantom spectra should be acquired weekly using the clinical protocols (PRESS and/or STEAM at appropriate echo times; see Section 17.3). The SNR of the main peaks (creatinine, N-acetyl-aspartate and choline) and ideally linewidths should be measured and recorded.

If quantification of metabolite ratios is being used regularly, a weekly check is essential. For this purpose it may be better to use a single-metabolite phantom such as N-acetyl-aspartate at a known concentration in de-ionized water. When such a phantom is made up, it must include a buffer to regulate the pH to approximately 7, and 0.1% sodium azide as a fungicide and bactericide. Peak area (i.e. absolute metabolite concentration) is extremely sensitive to RF coil characteristics, so care must be taken to ensure that the phantom can be placed in exactly the same location each time to produce the same coil loading. It is also sensitive to temperature, and if the ambient room temperature fluctuates by more than 2 °C it will be necessary to store the phantom in a fridge. In this way, although the phantom begins to warm up as soon as it is placed in the scanner, it will be at the same temperature when the MRS scan is done provided the QA is performed in the same way each time – which of course is the whole point!

11.8 Temporal Stability

In fMRI, we depend on finding very small signal changes due to neurological activity, sometimes only a 0.5% change from the resting condition. So it’s extremely important that the scanner produces a stable signal from the brain tissue, over a period of at least 5 min. To be more precise, the background signal should not contain high-frequency variations; low-frequency drifts of signal intensity (SI) can be compensated during the fMRI processing steps (see Section 18.5.3).

Acquiring data to measure temporal stability is simple: just put a phantom into the head coil, and

acquire using a standard fMRI protocol for at least 5 min. For a simple analysis, you can measure SI in a region of interest (ROI) on a central slice, on every volume (also known as a dynamic or a time-point). Most scanners provide ROI tools which can display SI vs time, and a quick inspection will tell you if the temporal stability is satisfactory.

For more detailed analysis, the data should be taken offline. The Biomedical Informatics Research Network (BIRN), a group of universities who collaborate on multi-centre studies, have defined a number of stability metrics to support their own work. Known as fBIRN (Functional BIRN), these metrics have become the de facto standard in the fMRI community and processing tools can be downloaded from the internet. Some vendors have incorporated these metrics into their scanner software for users. They are explained in Box ‘fBIRN Processing’.

fBIRN Processing

Start by creating some new ‘summary’ images, using pixel-by-pixel operations on the dynamic data:

$$\begin{aligned} I_{\text{diff}} &= \sum_{N=1,3,5\dots} (I_{N+1} - I_N) \\ I_{\text{mean}} &= \frac{1}{N} \sum_N I_N \\ I_{\text{std}} &= \sqrt{\frac{1}{N} \sum_N (I_N - I_{\text{mean}})} \\ I_{\text{SFNR}} &= \frac{I_{\text{mean}}}{I_{\text{std}}} \end{aligned}$$

Using an ROI of at least 15×15 voxels, measure the mean μ and standard deviation σ to generate summary statistics:

$$\begin{aligned} (T)\text{SNR} &= \sqrt{N} \cdot \frac{\mu_{I_{\text{diff}}}}{\sigma_{I_{\text{diff}}}} \\ \text{SFNR} &= \mu_{I_{\text{SFNR}}} \end{aligned}$$

For any ROI of size $n \times n$ voxels, we can define the fluctuation as

$$\text{Fluct}_n = \frac{(\sigma_{I_{\text{diff}}})_n}{(\mu_{I_{\text{diff}}})_n}$$

and finally by taking the fluctuation at the largest ROI size and the smallest (1×1), we can define a measure called the ‘radius of de-correlation’ (RDC).

$$\text{RDC} = \frac{\text{Fluct}_n}{\text{Fluct}_1}$$

You can also measure the intensity (and temporal stability) of the EPI ghost, which is present in all images. For this, you need to make sure that the FOV of the image is at least double the size of the phantom, so that the ghost does not overlap with the main image. Measure the ghost intensity by placing an ROI around the main image, and then offset it by half the FOV in the phase-encode direction. Repeat with the offset in the opposite PE direction, so that you have two ghost ROI's at the edges of the image (Figure 11.12). Calculate the ghost level:

$$\text{Ghost\%} = \frac{SI_{\text{ghost}}}{SI_{\text{main}}} \times 100\%$$

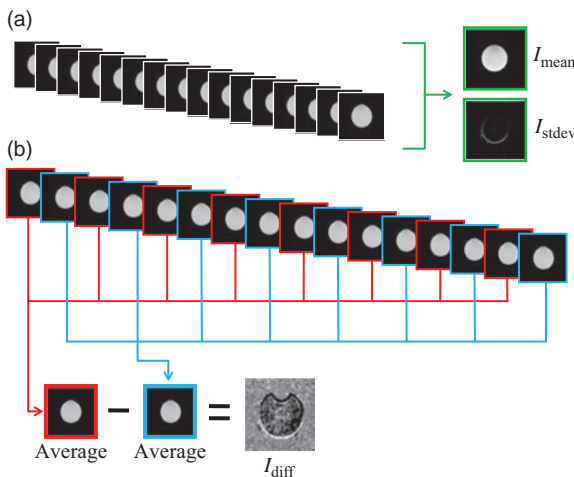


Figure 11.11 Creating summary images from fBIRN phantom scans. (a) Pixel-by-pixel, calculate the mean and standard deviation of the signal intensity (I_{mean} and I_{stddev}). (b) Calculate the mean signal intensity for all the odd-numbered time-points and even-numbered time-points, separately. Subtract the two averaged images to create the difference image, I_{diff} .

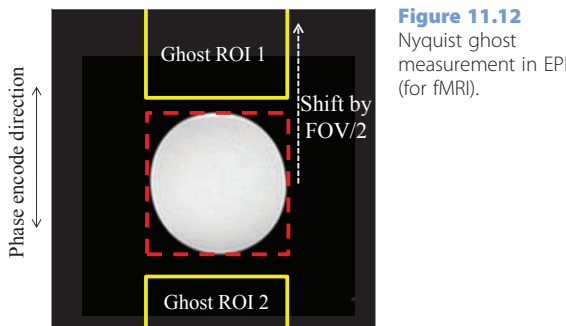


Figure 11.12
Nyquist ghost measurement in EPI (for fMRI).

Now that you have the summary metrics for your fMRI QA, how do you interpret them? Like any QA measure, they are most useful when you collect them regularly, produce a set of baseline values for your particular scanner, and then monitor for deviations. In the example shown in Figure 11.13, tracking SNR and SFNR metrics from the fBIRN analysis over a number of weeks, it is possible to detect a potential system problem. By inspecting the SI-vs-time curve for one of the later scans, sharp deviations can be seen, and it turned out that spike noise was responsible for the changes.

Some people claim that the radius of decorrelation (RDC) (see Box 'fBIRN Processing') is a measure of system 'quality' for fMRI. However, this is too simplistic. The RDC depends strongly on the basic SNR of the images. If you derive the RDC using two different head coils on the same scanner you will find that the RDC for the higher-channel coil is worse than with the simpler coil. So if you are comparing the fMRI results for two scanners, you will see that the scanner with worse SNR shows a higher RDC. That's not a good way to select the right scanner for fMRI!

Finally, there is another source of signal fluctuation in fMRI: physiological variation in the brain of the subject. Natural changes in oxygenation, caused by the respiratory and cardiac cycles, introduce changes in the fMRI signal-time curves even when the subject is not performing any task. This variation is so important that there are now many algorithms to try to remove these effects from fMRI data.

11.9 Other Specialist QA

Specialist QA may be required on a regular or per patient basis for particular quantitative, clinical investigations. Long-term stability is important for serial tumour response measurements for individual patients or in clinical trials in oncology. Geometric accuracy is paramount if MR is used for treatment planning in radiotherapy, radio-surgery or high-intensity focused ultrasound (HIFU) ablation treatment planning. It is also essential for multi-modality registration, for example with PET-CT (and hence the emergence of MR-PET – see Chapter 21). Quantitative studies of relaxation times, for example the

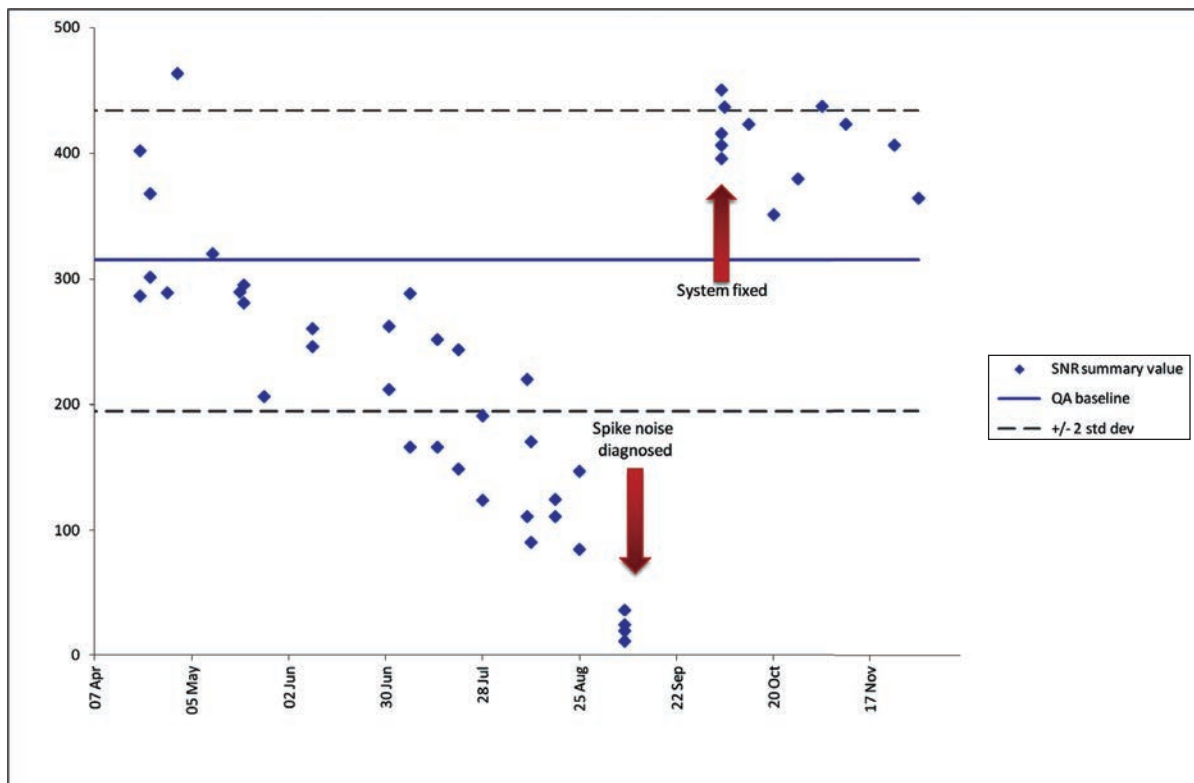


Figure 11.13 SNR tracked over several weeks using fBIRN QA procedure. During this period, the system developed a spike noise issue. By establishing the QA baseline, it is possible to distinguish between a couple of 'outliers' and the trend of decreasing performance.

assessment of organ iron overload using T_2 or T_2^* (Chapter 19), or apparent diffusion coefficient require a level of scanner and parameter precision and accuracy over and above that required for conventional diagnostic scanning.

Further Reading

ACR. www.acr.org/~/media/ACR/Documents/Accreditation/MRI/ClinicalGuide.pdf [accessed 22 March 2015].

Bodurka J, Ye F, Petridou N, Murphy K and Bandettini PA (2007) 'Mapping the MRI voxel volume in which thermal noise matches physiological noise: implications for fMRI'. *Neuroimage* 34: 542–549.

Edelstein WA, Bottomley PA and Pfeifer LM (1984) 'A signal to

noise calibration procedure for NMR imaging systems'. *Med Phys* 11:180–185.

fBIRN tools: www.nitrc.org/projects/bxh_xcede_tools [accessed 2 November 2014].

Judy PF (1976) 'The line spread function and modulation transfer function of a computed tomography scanner'. *Med Phys* 3:233–236.

Lerski RA, McRobbie DW, Straughan K, et al. (1988) 'Multi-centre trial with protocols and prototype test objects for the assessment of MRI

See also:

- Image optimization: Chapter 6
- MR safety standards: Chapter 20
- Equipment-related artefacts: Chapter 7

equipment'. *Magn Reson Imaging* 6:201–214.

McRobbie DW (1996) 'The absolute signal-to-noise ratio in MRI acceptance testing'. *Br J Radiol* 69:1045–1048.

McRobbie D and Semple S (eds) (in preparation) *Quality Control and Artefacts in MRI*. York: Institute of Physics and Engineering in Medicine. www.ipem.ac.uk.

Box 'National and International Standards' for details of ACR, IPEM and NEMA standards.

Acronyms Anonymous I: Spin Echo

12.1 Introduction

By now you will be familiar with the uses of the spin-echo (SE) sequence and its derivatives: TSE, STIR, FLAIR, 3D TSE, etc. In this chapter we delve a little deeper into the pulse sequence jungle, looking at the sequences from a more detailed and technical point of view, in particular how they are constructed to deliver the correct spatial and clinical information, and the limitations or compromises encountered in their use.

You will see that:

- segmented k-space acquisition schemes speed up SE-based acquisitions while retaining SE-like contrast;
- the effective echo time determines T_2 contrast in TSE;
- compromises are necessary: limited number of slices, increased spatial blurring and higher specific absorption rate (SAR);
- different types of RF pulses affect the image quality;
- single-shot turbo spin echo (TSE) and echo planar imaging (EPI) offer the ultimate speed for T_2 -weighted imaging but with image quality compromises;
- radial TSE reduces movement artefacts.

To understand this chapter you need to be familiar with the material from Chapters 4, 8 and 9 and have some grasp of the concept of k-space. For each sequence examined we will answer the following questions: How fast is it? How does it localize signal? What contrast does it produce? How does it avoid artefacts? And are there any performance compromises required? An overview of the pulse sequence jungle was given in Chapter 4, now let's get in among the trees!

12.2 Conventional Spin Echo

Refer back to Chapters 3, 4 and 9 for details on echo formation, contrast appearance and clinical use of

spin echo. The imaging gradients for a conventional SE sequence are shown in the right-hand side of Figure 12.1. These are similar to those illustrated in Chapter 8 for a GE sequence, but with a few differences: the 180° refocusing pulse and extra 'crusher' gradient lobes on its slice select (these prevent the 180° pulse from creating unwanted transverse magnetization), and the dephase lobe of the FE gradient now has the same sign as the readout portion. This is because the 180° pulse now forms the echo and spins must experience the same gradient moment before and after its formation to avoid phase errors.

We have seen that a clinical sequence also incorporates other features, e.g. fat saturation pulses and spatial saturation bands. These must be repeated within each TR period prior to the excitation of the imaging slice, and they take up time. These are shown in the left-hand side of Figure 12.1.

12.2.1 Limitations of Spin Echo

The basic reason for the slowness of conventional spin echo arises from the need to acquire each phase-encode line of the k-space raw data matrix from separate MR excitations, and the need to allow time for the magnetization to recover sufficiently between successive excitations. Addressing both of these problems, fundamental ways of speeding up an SE acquisition, other than the k-space tricks introduced in Chapters 6 and 8, are therefore:

- to acquire more than one line of data at once – this is called segmentation, used in fast or turbo spin echo (sometimes called RARE) – basically almost any sequence with the word 'fast' or 'turbo' in it;
- to 'cheat' the relaxation problem, by using restoration RF pulses;
- to use parallel imaging (Chapter 14).

Despite its slowness, spin echo has advantages that are worth keeping: its ability to generate T_1 , T_2 and PD

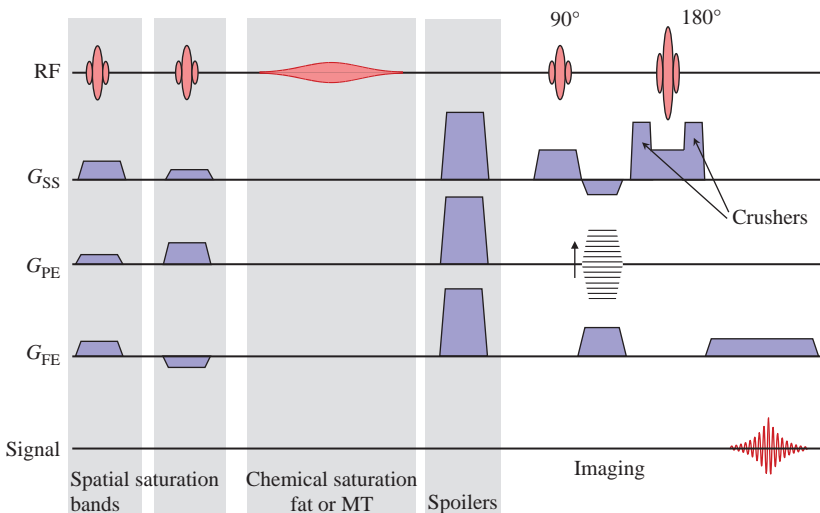


Figure 12.1 Imaging gradients for a simple SE sequence, including spatial saturation slabs and fat saturation pulses.

contrast, and its immunity from field inhomogeneity and susceptibility effects.

12.2.2 Multi-Echo Spin Echo

A precursor to the RARE segmented approach (TSE) is multiple spin echo, or ‘multi-echo’. This is a conventional SE sequence but with multiple RF refocusing pulses applied to form a train of spin echoes (Figure 12.2). This process can be repeated for as long as sufficient transverse magnetization remains to form an echo, i.e. as long as T_2 relaxation permits. Each echo has the same phase encoding and thus a series of images of the same spatial location, but each with different T_2 weighting, is acquired. Since a long TR is required for good T_2 contrast, the additional TE images are acquired for ‘free’ in terms of scan time. For example, the use of a double echo acquisition with a short and a long TE enables one scan to produce a good anatomical (PD-weighted) image and a pathology (T_2 -weighted) image. More details are given in Box ‘Getting Focused on Spin Echo’.

Getting Focused on Spin Echo

In Section 9.4 we saw that multiple spin echoes were susceptible to accumulated RF flip angle errors and diffusion effects. For longer echo trains the Carr-Purcell-Meiboom-Gill sequence (CPMG) reduces these errors by changing the phase of the refocusing pulses with respect to the 90° pulse.

CPMG corrects every even echo for B_1 errors and produces echo amplitudes of the same algebraic sign. CPMG also reduces diffusion effects. An alternative scheme is a modified or phase-alternated Carr-Purcell (CP) scheme, where the RF phase angle is kept the same for both the 90° and the 180° pulses, but the algebraic sign of consecutive 180° pulses is alternated. This flips the transverse magnetization forwards (clockwise) and back (anti-clockwise) about the same axis and also assures that every second echo will lie properly in the xy plane in spite of B_1 errors. The sign of the echoes will alternate.

It is not entirely obvious that both CP and CPMG can also produce multiple unevenly spaced spin echoes. For example, in the dual echo sequence shown in Figure 12.2, the ‘excitation’ for the second echo is considered to occur at the time the first echo is formed. In this case

$$\begin{aligned} \text{TE}_1 &= 2 \times T_A \\ \text{TE}_2 &= 2 \times T_B; \text{ provided } T_B \geq T_A \end{aligned}$$

Note that phase encoding is only applied once after the 90° pulse and that the first frequency-encode gradient readout lobe acts as a dephase lobe for the second echo.

12.3 RARING to Go: Fast Spin-Echo Techniques

Images with SE-type contrast can be acquired with dramatic time saving by collecting more than one

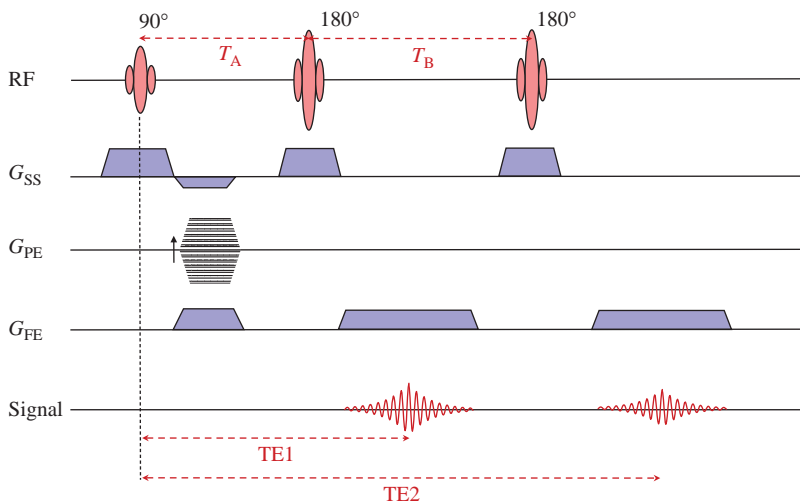


Figure 12.2 Dual echo imaging sequence. This produces two images with different TE but the same geometry.

line of data from a train of echoes formed by multiple refocusing RF pulses. This is known as segmentation. It can be achieved over several excitations and TR periods (multi-shots) or ultimately from a single shot. The T_2 contrast depends upon the ordering of the PE gradient steps or the filling pattern for k-space.

T_1 weighting can be achieved by using a short or intermediate TR as for conventional SE, or by using magnetization preparation, usually in the form of an inversion pulse. With TSE some resolution loss, in the form of blurring, may occur. Additionally, fat can appear very bright and some slice-to-slice variations in contrast may occur.

12.3.1 Turbo Spin Echo in Detail

Turbo Spin Echo (TSE), also known as Fast Spin Echo (FSE), is a commercial version of RARE (Rapid Acquisition with Relaxation Enhancement) with evenly spaced multiple refocusing pulses (commonly, but not always, 180°) forming an echo train. These extra echoes are not used to acquire free images with different TE but are used to acquire multiple lines of data, i.e. different phase encoding applies for each echo (Figure 12.3). The Inter Echo Spacing (IES or ESP, Echo SPacing) is the time between successive echoes. This is always a fixed value as the RF pulses are all evenly spaced in time to avoid problems with coherence pathways (see Chapter 13). The echo train length (ETL) or turbo factor (TF) is the number of echoes in the spin-echo train.

The total scan time is

$$\text{Scan time} = \frac{\text{TR} \times N_{\text{PE}} \times \text{NSA}}{\text{ETL}}$$

A TSE sequence with, for example, 16 echoes (turbo factor of 16) will run 16 times faster than the equivalent spin echo. If TR is chosen to be 3 s, this means an acquisition requiring 12 min as a conventional spin echo will run in just 40 s. Sometimes TSE has an unusual number of phase-encode steps, as the latter has to be a multiple of the turbo factor. For example, if there are five echoes, the matrix could be 256 × 255 and a total of (255 ÷ 5) TR periods or excitations would be required.

In TSE, lines of k-space are acquired from different echoes and this affects the image contrast. The effective echo time (TE_{eff}) is the one that dominates the image contrast. We saw in Chapter 8 that the overall image brightness is primarily determined by the low spatial frequencies, those acquired with low step values of the phase-encode gradient. The centre of k-space dominates the image contrast. This is exploited in TSE, where TE_{eff} is arranged to coincide with the central segment of k-space (Figure 12.4). The order in which the phase encoding is applied affects the contrast, and various options are contained in Box ‘Getting Wound Up: The Details of TSE’.

TSE can be PD-, T_1 - or T_2 -weighted in the same way as conventional spin echo. For T_1 weighting, where TR has to be relatively short, a smaller ETL may be required in order to achieve sufficient slice coverage. Dual-echo TSE is possible where the echoes

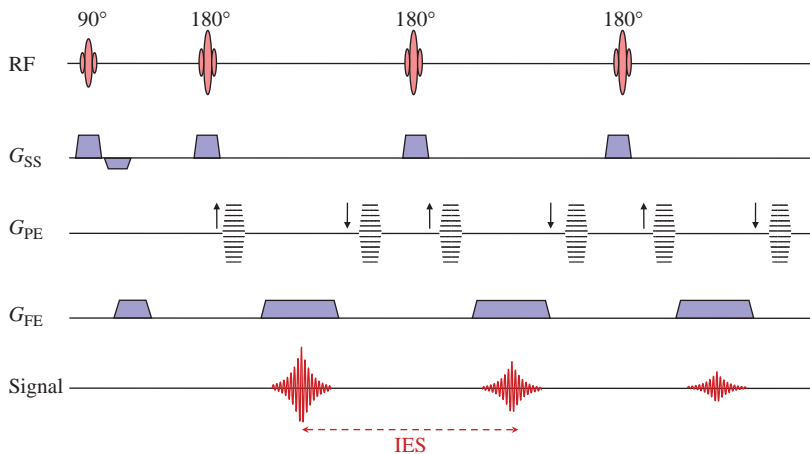


Figure 12.3 Turbo spin-echo sequence with an echo train length (turbo factor) of 3. IES denotes inter-echo spacing, i.e. the time between successive echoes.

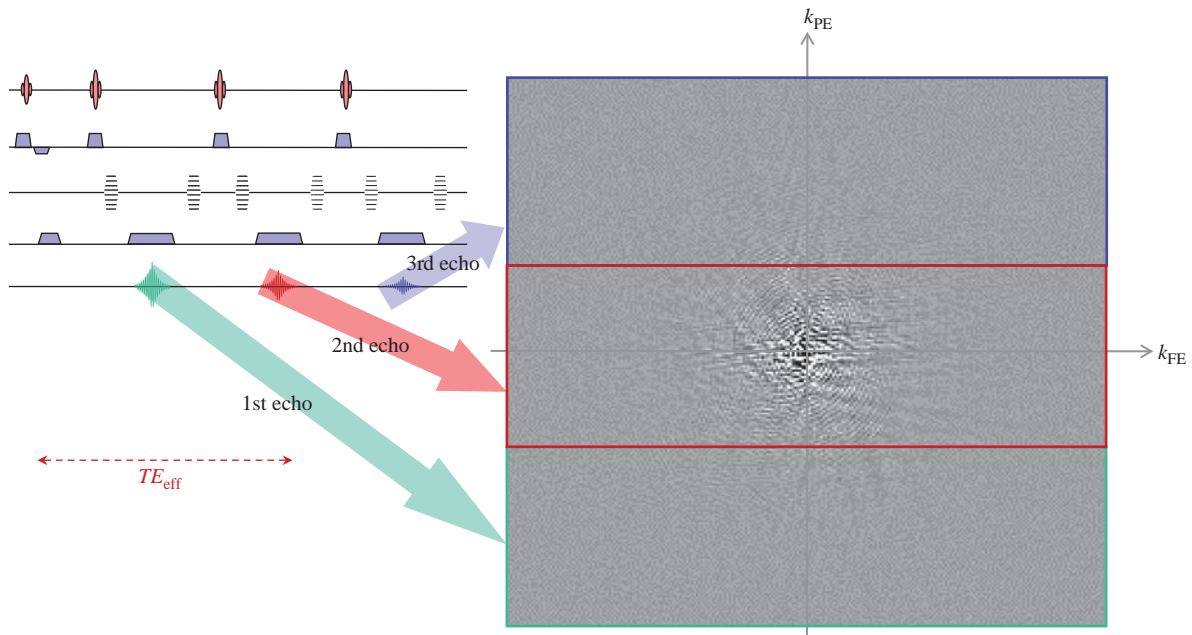


Figure 12.4 Data acquisition (k-space) filling for a three-echo TSE. The effective TE (TE_{eff}) is given by the time from the initial excitation to the second echo. Each point k_{FE} and k_{PE} represents a spatial frequency in the image

are divided between the different images with different TE_{eff} . This can be done by assigning the earlier echoes in the train to one image with a shorter TE and the later echoes to form a longer TE image. A more efficient way of achieving dual-echo TSE is by echo sharing, whereby some of the high spatial frequency data are shared between both images and only the low k-space data are encoded for more than one echo. Figure 12.5 shows spin-echo and TSE T_2 -weighted images.

Getting Wound Up: The Details of TSE

In the sequence illustrated in Figure 12.3 the formation of the first spin echo is entirely conventional. In TSE the CPMG form of spin echo is used to avoid the accumulation of flip angle errors over the echo train (see Section 9.4). However, before we can acquire the second echo, we have to ‘rewind’ the phase encoding to undo the dephasing of the spins. To do this a phase-encoding step of equal strength but opposite

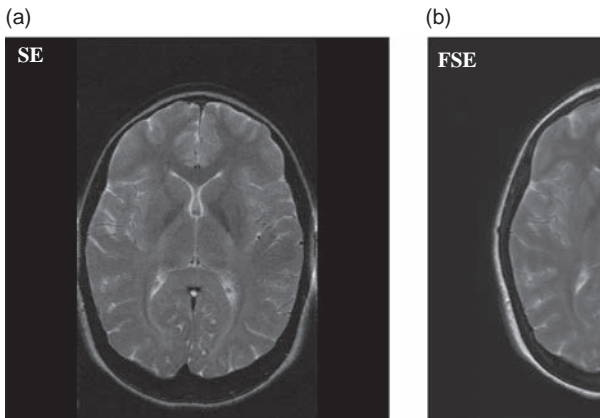


Figure 12.5 Representative images for spin echo (SE) and turbo spin echo (TSE) with similar TE. (a) SE: TR = 1500 ms, TE = 120 ms, scan time 4 min. (b) TSE: TR = 2735 ms, TE = 102 ms, ETL = 5, scan time 1 min 46 s. Note the appearance of fat, and the scan times.

in sign is applied after the completion of the data acquisition. In addition to rewinding, a form of phase correction of the data is required.

Each echo is responsible for a portion or segment of k-space. So different lines of k-space will have different T_2 weighting. The echo that contributes the central segment determines the effective echo time. By mixing the functions of contrast generation and localization, we have blurred the distinction between contrast and detail. Sequences with high values of ETL/turbo factor may display reduced spatial resolution. Additionally the echo train reduces the number of slices that can be acquired within the selected TR, approximately to

$$N_{\text{slices}} = \frac{\text{TR}}{\text{ETL} \times \text{IES}}$$

Also we can see from Figure 12.4 that we could assign any of the echoes to acquire the centre of k-space, thus changing the effective TE, sometimes known as asymmetric echoes, to achieve PD or T_1 -weighting.

When a refocusing pulse of less than 180° is used, the signal will include contributions from stimulated echoes (see Box 'Echoes and coherences: Hahn and stimulated echoes' in Chapter 13), affecting contrast. For this reason, the rewinding scheme for phase encoding is applied in preference to 'blipping' (the accumulation of phase encoding from smaller, non-rewound phase-encoding steps) as used in EPI and GRASE (see Section 12.5).

The slice number restrictions will be apparent to anyone who has sat at the MR console planning a TSE scan. We saw in Section 8.4.3 how slice interleaving within the TR is used to deliver multiple slices within the same overall acquisition time. As the time occupied by the longer echo train in TSE is greater, it reduces the possibility of acquiring a large number of interleaved slices within the TR. To compensate for this, a longer TR can be used with an increased scan time for T_2 - or PD-weighted images, but not for T_1 -weighted images.

However, even if the required number of slices can be reconciled with the ETL and TR required, you often find your plans thwarted by the scanner on account of SAR limits. The SAR (explained further in Section 20.2) is a measure of the patient's RF exposure and is subject to national and international limits. TSE techniques with their many large RF pulses can very easily exceed the SAR limit, particularly at higher field strengths. To reduce the SAR to an acceptable level you need to reduce the number of slices, increase the TR, reduce the ETL or reduce the flip angle of the refocusing pulses (see Box 'Turning Down the Heat: Reducing SAR'). This latter is possible on some scanners and usually solves the SAR limitation problem, but at the cost of some reduction in SNR. In a properly constructed sequence it does not cause artefacts.

12.3.2 A Compromising Situation

So is TSE 'the best thing since sliced bread'? Not quite; there are compromises involved, including reduced slice numbers, higher RF exposure, complicated contrast behaviour and possibly reduced resolution.

We Still Use Conventional T_1 -Weighted SE. Why?

T_{1w} imaging, particularly of the brain and spine, requires TR in the range 400–600 ms for a 1.5 T scanner. If we are acquiring 3 mm slices we will need more than 30 to fully cover the cerebrum,

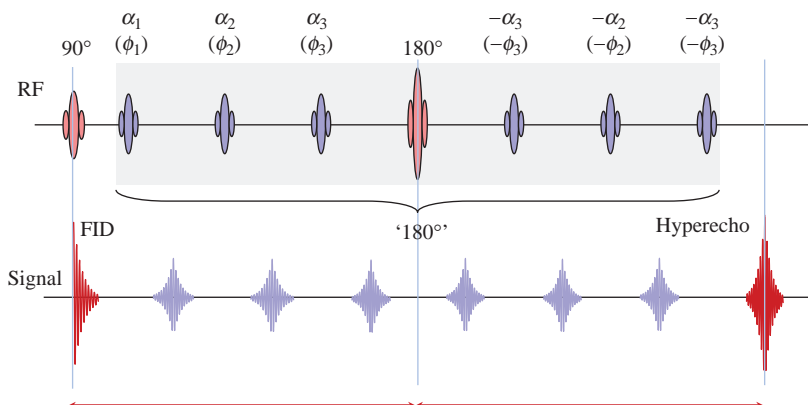


Figure 12.6 TSE echo train showing reduced refocusing angles and the hyperecho formed by making the fourth refocusing pulse a full 180° pulse.

giving us less than 20 ms per slice. If we further divide k-space into three (the minimum) segments, we have less than 7 ms to acquire each echo. This is not long enough. It is simply better to use 'old-fashioned' SE for this acquisition. It has further advantages of lower SAR and less T_2 blurring, insensitivity to flow artefact and responds in a predictable manner to Gd contrast.

Turning Down the Heat: Reducing SAR

The TSE pulse sequence has a high SAR per unit time, particularly on high-field scanners since the SAR is proportional to B_0^2 . One way of reducing this effect is to use smaller flip angles during the refocusing echo train. You would think that the expected signal amplitude would be reduced with this scheme. However, a number of extra coherence pathways (see Box 'Coherence Pathways' in Chapter 13) are formed, including stimulated echoes, and these can combine to produce spin echoes with larger signals. Of course, the contribution from stimulated echoes means that the contrast is a function of both T_2 and T_1 .

It can be shown that the signal forms a 'pseudo-steady-state' (ignoring relaxation effects) proportional to $\sin(\theta/2)$. Furthermore, the signal can be 'catalysed' into the steady state by choosing the first few refocusing pulses to have specific flip angles. For example, if the first refocusing pulse is a $(90 + \theta/2)^\circ$ pulse, and θ is the flip angle of the rest of the refocusing train, the echo amplitude is close to the maximum theoretical amplitude.

The reduced SNR can be further recovered by using 'hyperechoes'. A hyperecho is produced by using a 180° refocusing pulse in a train of reduced θ refocusing pulses. By arranging the timing so that

the hyperecho occurs when the centre of k-space is acquired, the overall image SNR will be increased. Figure 12.6 shows a train of seven refocusing pulses, with the fourth pulse a full 180° and the others reduced. The hyperecho occurs after the seventh refocusing pulse, and has an amplitude almost equal to that achieved by a conventional train of 180° pulses.

If the low values of phase encoding in the centre of k-space determine the overall image contrast, what do the higher k-space data contribute? They determine the high-frequency or detailed content of the image and their relative strength may be emphasized or reduced, depending on the k-space ordering scheme employed. If the high frequencies are acquired for longer actual TE then they will be attenuated by T_2 relaxation and some spatial resolution will be lost. If they are acquired at a shorter TE than the effective TE they will be emphasized, which may lead to excessive ringing or Gibbs' artefact. For this reason additional filtering may be applied for TSE sequences.

A major consequence is that the spatial resolution will depend on the T_2 of the tissues. In practice, an arbitrarily large echo train length cannot be used without impairing the spatial resolution (Figure 12.7). This is most apparent in single-shot techniques such as HASTE (see Section 12.4.3). However, while it is true that sequences with large turbo factors may lead to blurring or resolution loss compared with a non-segmented sequence such as spin echo, TSE offers the opportunity to acquire large matrices (512×512 or even 1024×1024) and therefore produce very high-resolution images within a reasonable scan time.

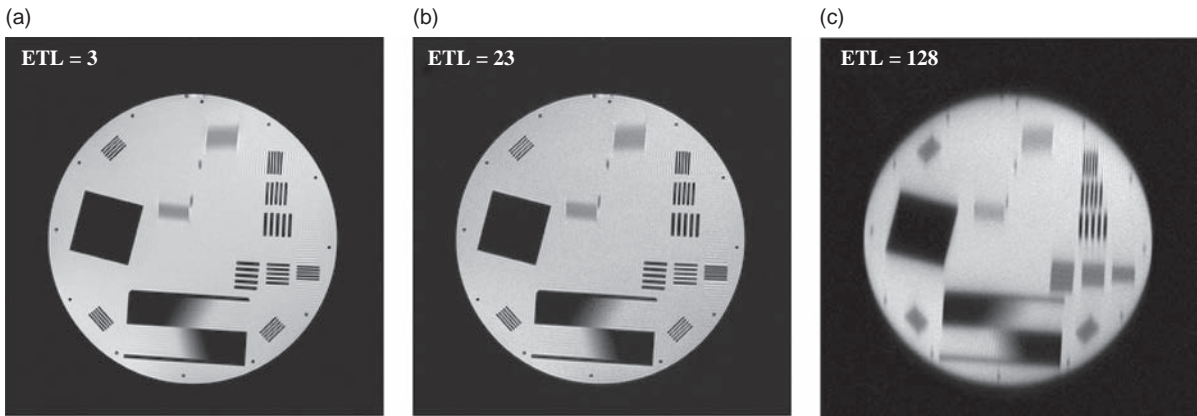


Figure 12.7 Resolution in segmented sequences showing resolution loss in the phase-encode (PE) direction. (a) TSE with three echoes (ETL = 3), TR = 600 ms, TE = 12 ms, scan time 52 s. (b) TSE with 23 echoes, TR = 600 ms, TE = 128 ms, scan time = 6 s. (c) HASTE (ETL = 128), single shot ('TR' = ∞), TE = 87 ms, scan time = 1 s. Phase encode is vertical. Note the subtle resolution loss for ETL = 23, and the major resolution loss for HASTE. The phantom fluid had a T_2 of 200 ms.

A final issue of compromise relates to the appearance of fat in the images. In TSE fat is bright, as shown in Figure 12.5. Bright fat may be useful, particularly in the abdomen where it outlines all of the organs and bowel. However, it may also reduce the dynamic range available in the image and therefore obscure subtle contrast changes (e.g. in the knee), or sometimes it may result in a high level of motion artefact (e.g. from the highly mobile suborbital fat) or conceal pathology. This can be addressed by applying further pre-pulses in the form of fat suppression by a number of techniques (see Chapter 7). Further details are given in Box 'Is TSE the Same as SE?'.

Is TSE the Same as SE?

The image contrast in TSE is not the same as for SE. The multiple RF pulses result in the generation of stimulated echoes in TSE which add to the spin-echo component of the signal.

In particular, fat appears very bright in TSE. Actually, it is conventional spin echo that depicts fat less bright than expected for a tissue with its combination of short T_1 and relatively long T_2 . The reason lies with J -coupling, which is an interaction between different nuclei within the fat molecule and results in a shortening of T_2 . In TSE the rapid train of refocusing pulses breaks this coupling and thus fat signals have effectively a longer T_2 and appear brighter in the image.

A TSE sequence designed to conserve the J -coupling effect and look more like spin echo is DIET

(Delayed Interval Echo Train), which has a longer IES for the first pair of refocusing pulses. At the time of writing this is only commercially available on Toshiba systems.

The application of various fat suppression techniques is common for TSE imaging. Additionally, there may be slice-to-slice variations in image contrast. This may be due to unwanted magnetization transfer interactions caused by off-resonance RF from adjacent slices.

In GRASE imaging (Section 12.5) the use of intermediate gradient echoes between each spin echo means that a longer IES (for the 180° pulses) can be employed. This may conserve the J -coupling and produce images that are more spin-echo-like.

12.4 The Extended Family of TSE

12.4.1 Inversion Recovery TSE

The use of turbo spin echo to obtain T_1 weighting with shorter TR is limited by compromises between the number of slices achievable and the echo train length (ETL). It is possible, however, to achieve T_1 weighting by the addition of a preparation pre-pulse in the form of an inversion combined with a high ETL, i.e. as inversion recovery TSE (or IR-TSE or turbo-IR). One of the downsides of conventional inversion recovery is the long scan time involved because of the need for a TR of at least three (and preferably five) times the T_1 of tissue. Combining IR

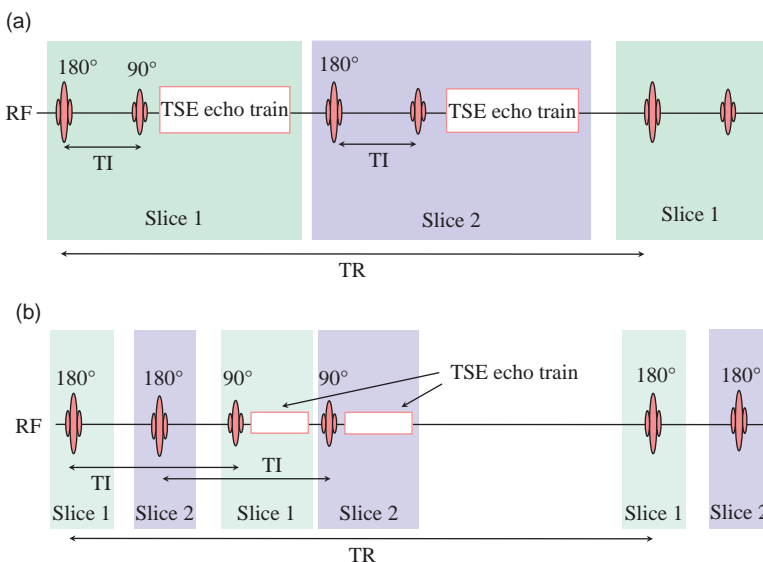


Figure 12.8 Interleaving schemes for inversion recovery TSE: (a) sequential where each TI is completed before incrementing the slice; (b) interleaved where more than one slice is inverted within each TI.

with TSE enables the use of the long TR required but with a clinically acceptable scan time. The T_1 contrast is conventional and is primarily determined by the inversion time (TI).

Clinical applications of this include Short TI Inversion Recovery (STIR), in which a short TI is used to null the fat signal and something akin to T_2 -weighted appearance is achieved in the image (Section 3.7), and FLAIR imaging (Section 3.4) where a long TI (e.g. 2000 ms) combined with a long TR (up to 10 s) is used to null the cerebrospinal fluid (CSF) signal in neuro-imaging. The use of k-space segmentation makes the scan time for FLAIR clinically acceptable. Another application is real-reconstruction (or true) inversion recovery, useful for examining the degree of myelination in the immature brain, where the inversion pulse is used to improve contrast.

The combination of IR with TSE involves certain complications over how slice interleaving is achieved. There are compromises regarding turbo factors (ETLs), TI and TR, which are examined in Box 'Interleaved IR-TSE'. The scan time is given by the same expression as for TSE; however, there may be limitations on the number of slices achievable. With IR-based techniques there are also limitations in the spatial quality of the inversion pulses (see Box 'More on RF Pulses'). It is common in IR-TSE to have a significant gap between slices and to use an interleaved slice order to avoid crosstalk.

An improvement in the quality of the inversion can be achieved by using adiabatic pulses (see Box

'Adiabatic RF Pulses'). This is particularly important when the uniformity of the B_1 transmission field is poor, as may occur at 3 T. Adiabatic inversion methods are known as Spectrally Adiabatic Inversion Recovery (SPAIR) by Siemens; SPectral Attenuated Inversion Recovery (SPAIR) by Philips; or Adiabatic Spectral Inversion Recovery (ASPIR) by GE Healthcare.

Interleaved IR-TSE

The potential for slice interleaving in TSE sequences is reduced because the data-acquisition time is longer to encompass the whole echo train. This presents special problems for inversion recovery, where each slice has to undergo inversion at a time TI before the signal readout/spatial encoding part of the sequence. We have two options for arranging the slices shown in Figure 12.8:

- Interleave within the TR, i.e. invert and readout one slice before inverting the next one. In this case the maximum number of slices is

$$N_{\text{slices}} = \frac{\text{TR}}{\text{TI} + (\text{IES} \times \text{ETL})}$$

For very long TI such as those used in FLAIR this restricts the number of slices obtainable for a given TR and the number is dependent upon the TI you chose. It works best for short TI, such as in STIR. This scheme is sometimes referred to as 'sequential'.

- Interleave within TI, i.e. we invert all the slices first within the time TI and then read them all out. The

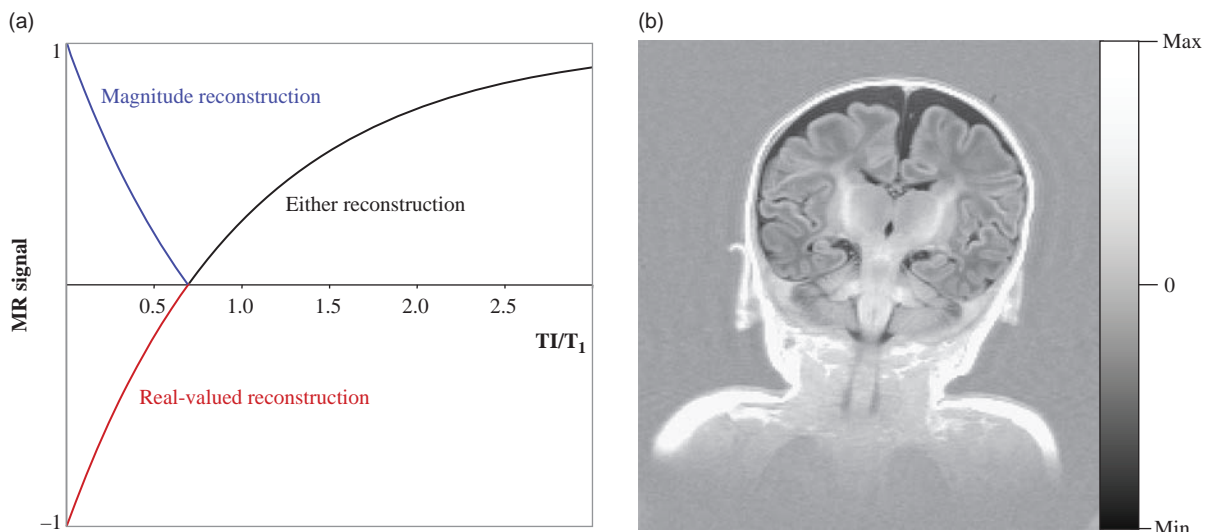


Figure 12.9 (a) Signal dependence of real-valued IR. (b) Example of true inversion recovery sequence of an infant brain. The image background is mid-grey, allowing the display of both positive and negative MR signals

number of slices is now independent of TR but depends upon TI:

$$N_{\text{slices}} = \frac{TI}{(IES \times ETL)}$$

Obviously for very high turbo factors, the number of slices is going to be restricted. A compromise between number of slices and speed of acquisition is usually required. This arrangement works best for long TI, e.g. for FLAIR, and is sometimes called 'interleaved'.

Inversion recovery offers the possibility of the MR signal being positive or negative. Usually MR images are presented in magnitude form, i.e. with no negative values, the sign of the signal being ignored in the final image (this is to overcome artefact problems arising from phase changes due to susceptibility variations and magnet inhomogeneity). With real-valued inversion recovery, the image is reconstructed in real rather than magnitude mode, i.e. with positive and negative voxel values (Figure 12.9a). This means that the background is mid-grey and the image values range from black to white. Exceptionally good contrast, particularly in brain tissues, is achievable with true inversion recovery. Figure 12.9b gives an example for a neonatal brain.

More on RF Pulses

Selective pulses, as seen in Section 8.4, utilize a shaped RF pulse in conjunction with a gradient. If

the pulse generates transverse magnetization, i.e. if it is anything but a refocusing pulse, it is usually necessary to have a rephase gradient to ensure that the transverse magnetization points in the same direction. The rephase portion has half the gradient moment of the selective part and the opposite sign. For a 180° pulse, rephasing is not required. In the case of a refocusing pulse (i.e. in spin echo), the gradient is self-rephasing. For an inversion pulse, there is no transverse magnetization (ideally) and the selective gradient ideally produces no phase changes.

Selective slices are not uniform in the selection direction, but have a variation in flip angle perpendicular to the image plane they define, known as the slice profile. A consequence is that for a 180° pulse there will be regions where magnetization is partially tipped into the transverse plane (at some point the flip angle will pass through 90°).

For a refocusing pulse a pair of 'crusher' gradients, as shown in Figure 12.10, can overcome this problem. These are equal gradients applied either side of the refocusing pulse. Refocused magnetization that goes on to form an echo will have seen both gradients and, because of refocusing, will be unaffected. However, fresh free induction decay (FID) created by the refocusing pulse only experiences one gradient lobe and will be dephased.

In practice it is quite difficult to achieve good inversion, e.g. in inversion recovery sequences. Particularly at higher field strength, 'adiabatic' pulses

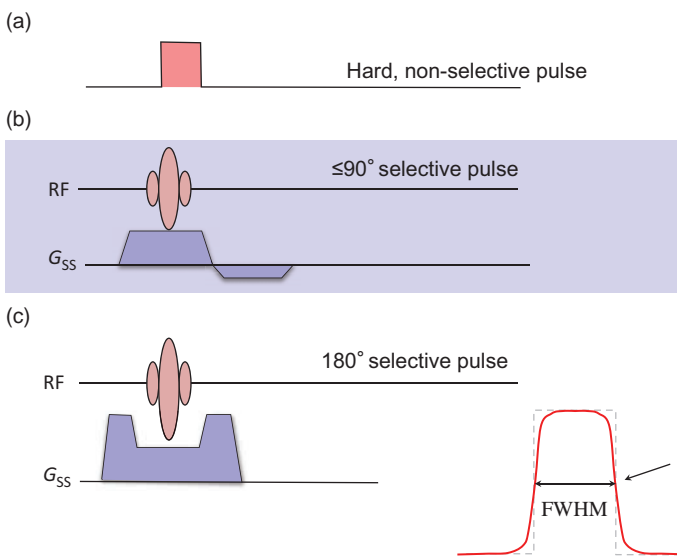


Figure 12.10 Types of RF pulse. (a) Hard, non-selective pulse. The RF is applied as a short, broad bandwidth pulse. (b) Selective excitation pulse. The spectrally shaped RF pulse is applied simultaneously with a slice-select gradient. A rephase gradient lobe is required to correct phase shifts. (c) Selective 180° pulse. No rephasing is necessary, but crusher gradient lobes are required. The slice profile shows that at some point along the selection axis the flip angle will be 90°.

provide more uniform inversion (see Box 'Adiabatic RF Pulses') since they are less sensitive to B_1 inhomogeneities. For single-shot sequences with an inversion pre-pulse, the inversion pulse may be non-selective. A non-selective pulse is applied without a gradient, so it has no spatial localization. Subject to the RF coil's homogeneity and tissue RF absorption, it will have the same effect at all points of space. A non-selective pulse can have any temporal waveform, and it is advantageous to keep the pulse short, a rectangular waveform being common. Such pulses are often called hard pulses.

Composite RF pulses, or 'binomial' pulses, are often used for spectral excitation, i.e. to obtain a signal from either water or fat. These pulses are made up of a series of either selective or hard pulses and are always followed by spoiler gradients to 'mop up' any residual fat signal (see Box 'Water-Only Excitation').

Adiabatic RF Pulses

Adiabatic pulses behave quite differently to normal RF pulses. They use both amplitude and frequency modulation to pull the magnetization away from the z axis. If this sounds weird, it's because adiabatic pulses are weird! To explain them, we have to go back to the rotating frame and consider how the protons precess around an RF magnetic field.

Previously we have assumed that B_1 is applied at the Larmor frequency along x' or y' in the rotating frame. However, if the frequency of the RF is slightly off resonance there is also a component of B_1 in the z'

direction. In this situation, the transverse and longitudinal components of B_1 combine to give an effective field B_{eff} at an angle ψ to the z' axis. When the amplitude of B_1 is small or the RF frequency is a long way off resonance, B_{eff} is very close to the z' axis; as the amplitude is increased and the frequency is exactly on resonance, B_{eff} is exactly in the transverse plane.

The magnetization obeys the Larmor equation and precesses (in the rotating frame) about B_{eff} (Figure 12.11a). If we create an RF pulse such that B_{eff} is initially in the z' direction, then gradually change the amplitude and frequency so that B_{eff} slowly rotates towards the transverse plane, the magnetization will continue to precess about B_{eff} until it is also precessing in the transverse plane. If the pulse is now switched off, lo and behold, the magnetization is in the transverse plane and can give us an MR signal. The only constraint is that the changing angle of B_{eff} is much less than the precessional frequency about B_{eff} , described mathematically by

$$\frac{d\psi}{dt} \ll \gamma B_{\text{eff}}$$

This can be achieved by choosing a strong effective field (high B_1) or a slow frequency modulation. The term 'adiabatic' comes from Greek, meaning 'impassable to heat', and is used in thermodynamics to describe processes where no external energy is used. Returning to the idea that protons absorb energy from a normal RF pulse during excitation, we can think of adiabatic pulses as forcing the protons to use their own internal energy to change

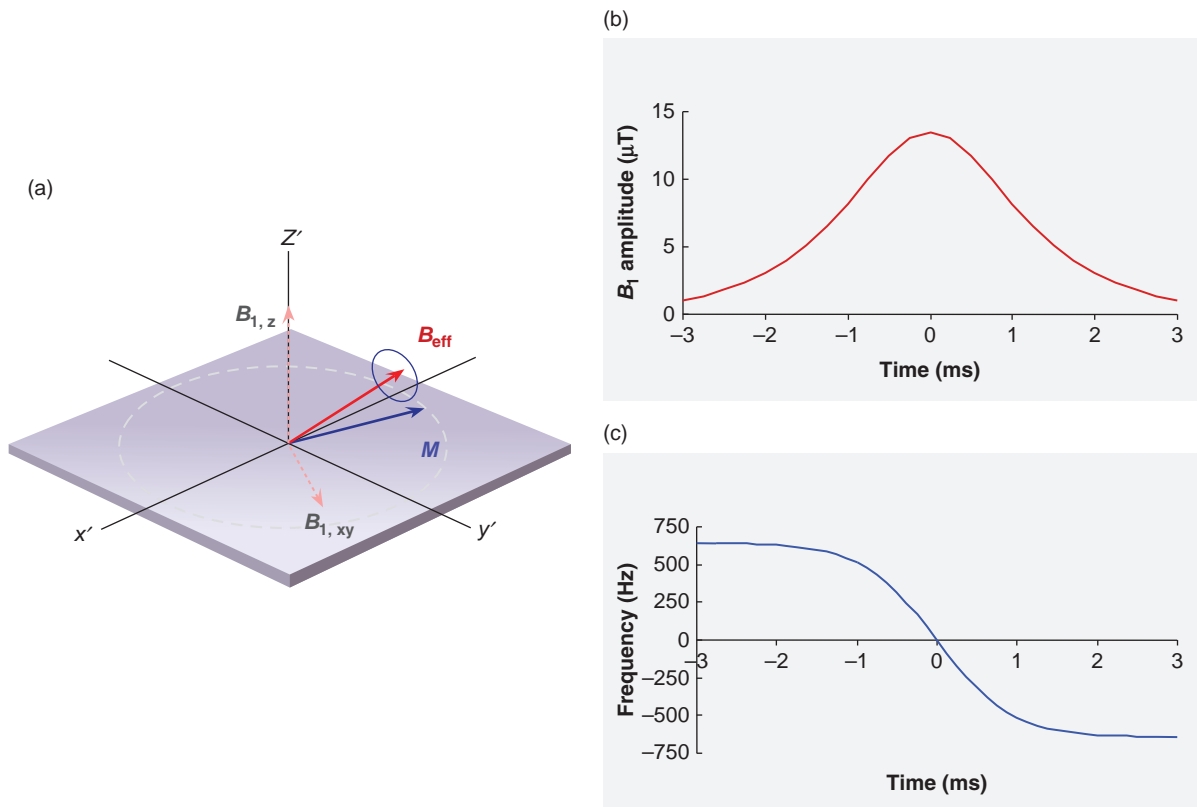


Figure 12.11 Adiabatic pulses. (a) When the RF is slightly off resonance, B_{eff} is at an angle between z' and the transverse plane and protons precess about B_{eff} . (b) Amplitude and (c) frequency modulation for a hyperbolic secant (sech) adiabatic inversion pulse. Note that the amplitude starts low, increases to a maximum and then returns to zero, and that the frequency is swept from several hundred hertz below ω_0 to several hundred hertz above.

their orientation. No energy is absorbed from the RF pulse, so the spin temperature does not change. We warned you that these are weird pulses!

Different types of amplitude and frequency modulation can be used to create adiabatic pulses for excitation, inversion or refocusing. For example, the hyperbolic secant pulse is popular for inversion; Figure 12.11b,c shows the amplitude and frequency modulation of the pulse. All adiabatic pulses have the major advantage of being insensitive to B_1 inhomogeneities, making them particularly useful at higher field strengths.

Water-Only Excitation

Instead of saturating the signal from fat, an alternative approach is to excite only the water signal. Binomial pulses are one such way to achieve water-only

excitation. Binomial pulses consist of a series of RF pulses with flip angles following a binomial series such as 1:1. The interval between the pulses τ equals the time for fat and water to become 180° out of phase, i.e., $\tau = 2.3$ ms at 1.5 T. The simplest example is a 1- τ -1 pulse shown in Figure 12.12. First a 45° pulse is applied along the $+x'$ axis, then the fat and water protons are allowed to dephase. When they are exactly out of phase, a second 45° pulse is applied, taking the water protons into the transverse plane and returning the fat protons to the longitudinal direction. Other binomial pulse schemes use a 1:2:1, and 1:3:3:1 sequence, i.e. 22.5° - τ - 45° - τ - 22.5° or 11.25° - τ - 33.75° - τ - 33.75° - τ - 11.25° . The use of a 1:1 pulse essentially provides a sinusoidal modulation with a very narrow-band saturation of fat, whereas increasing the number of pulses results in a broader fat suppression (Figure 12.12) at the cost of an increase in duration of the excitation.

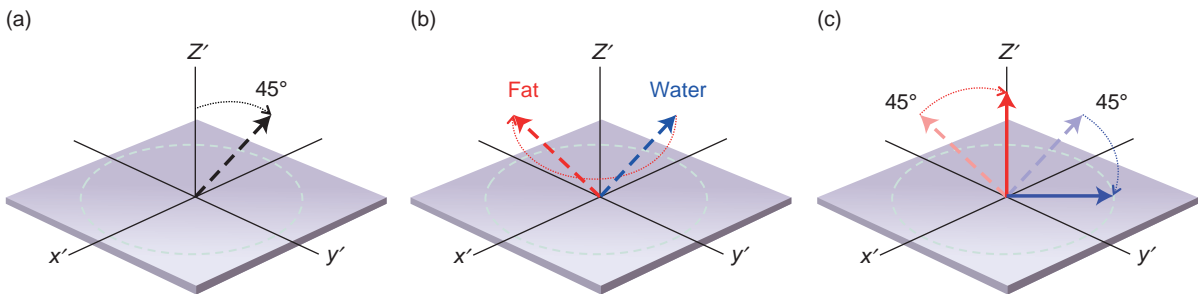


Figure 12.12 A 1:1 binomial pulse suppresses fat by (a) exciting both water and fat, (b) allowing time for the fat to dephase by 180°, then (c) applying a second 45° pulse to leave the water protons in the transverse plane and the fat protons returned to the z axis.

Binomial pulses are more robust against B_0 homogeneity; however, they are usually achieved with hard (rectangular) pulses which means they are most suitable for 3D imaging, not multi-slice 2D. If the hard pulses are replaced by slice-selective pulses, then they become B_0 -sensitive. If the binomial pulses are slice selective then the pulse train is known as a spectral-spatial excitation. Different manufacturers will have slightly different implementations of spectral-spatial pulses. The Philips binomial implementation, for example, is called PROSET (**P**Rinciple **O**f Selective Excitation **T**echnique).

12.4.2 Drive Time: Driven Equilibrium

Driven Equilibrium (DE) is a technique to drive the magnetization back to the positive z axis (towards equilibrium) by using an additional RF pulse rather than through longitudinal relaxation, which is a much slower process. Transverse magnetization can be driven back towards equilibrium by a 90° pulse on the $-x'$ axis (-90°), as in Figure 12.13a. This enables a shorter TR to be used in TSE sequences. DE works best for tissues with longer T_1 and T_2 , where the residual magnetization lies mainly in the transverse plane and has a relatively low amount of dephasing. It is therefore good for imaging fluids.

12.4.3 Single-Shot TSE and HASTE

The ultimate turbo sequence is single-shot TSE, where there is only one initial RF excitation (90°) pulse followed by a very long echo train over which all the phase-encode steps are acquired. This type of sequence is applied sequentially for multiple slice acquisitions, i.e. a whole slice is acquired at a time before moving on to the next slice. Usually an inter-slice delay (time delay

or TD) is required between successive slices. The scan time will therefore be

$$\text{Scan time} = N_{\text{slices}} \times (\text{scan time for slice} + \text{TD})$$

With this type of sequence there will necessarily be significant T_2 signal decay over the course of the acquisition and hence its clinical use is limited to the study of predominantly fluid structures, such as the biliary system, as a technique for MRCP (see Box ‘MR Cholangiopancreatography’) and Figure 12.14.

HASTE (Half Fourier Single Shot TSE) is a form of single-shot TSE available on Siemens scanners, which uses a phase-alternated CP echo train combined with half Fourier acquisition (Section 8.7.1). HASTE produces a moderate spatial resolution (256 × 128 or 240) with a moderate to long TE (60–120 ms) giving T_2 -weighted images. It can also be combined with an inversion recovery pre-pulse to give a single-shot variant of STIR or FLAIR. Often non-selective inversion pulses will be used (see Box ‘More on RF Pulses’). In this case a sufficient inter-slice delay is required to ensure full recovery to equilibrium of the inverted magnetization.

So why don’t we use single-shot sequences all the time? The answer lies in the compromises involved with all segmented spin-echo techniques, of which single-shot-TSE and HASTE are the most extreme examples, and therefore the most extremely compromised. The single-shot image in Figure 12.14a (HASTE) clearly results in impaired spatial resolution. However, this limitation must be weighed up against the benefit of taking only 1 s to acquire, which effectively eliminates bowel and respiratory motion.

MR Cholangiopancreatography

The MRCP is a common examination which investigates the biliary and ductal system of the liver and

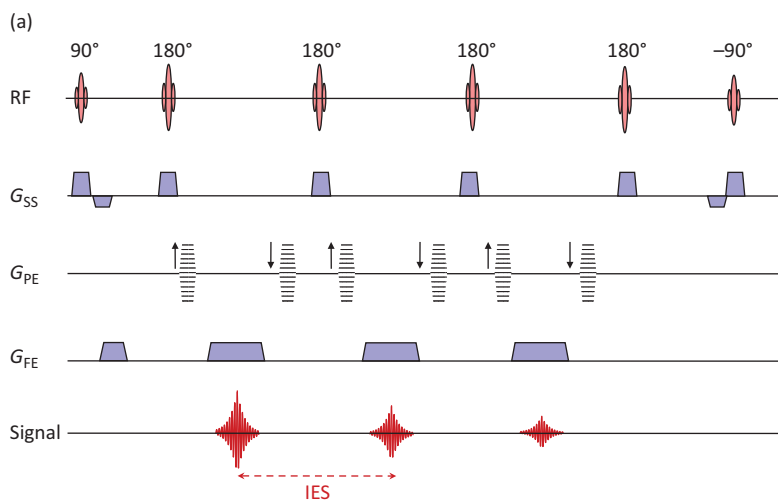


Figure 12.13 (a) Pulse sequence diagram for TSE with driven equilibrium. (b) TSE MRCP images without (left) and with (right) driven equilibrium. TR = 1146 ms, TE = 446 ms.

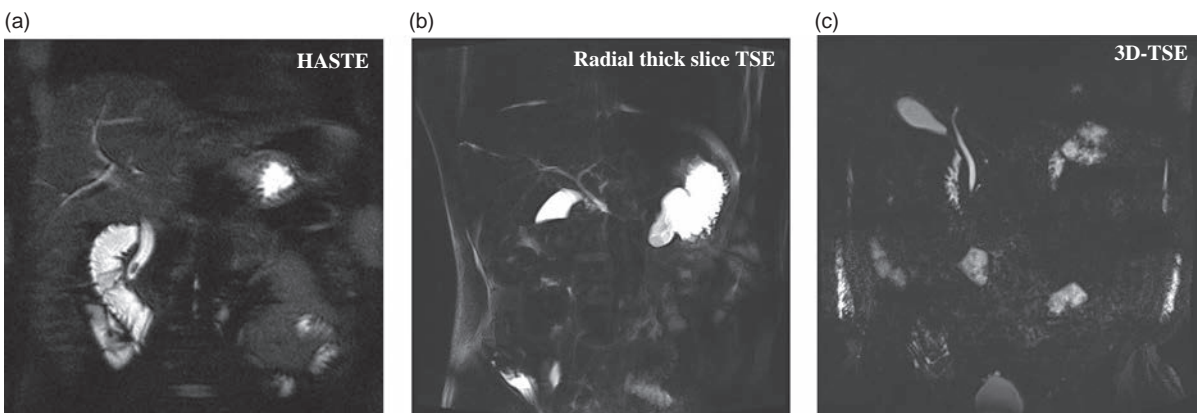
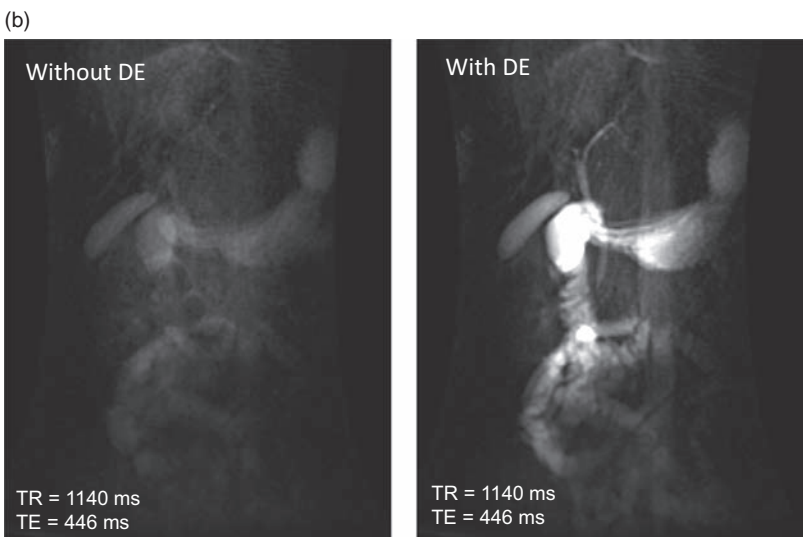


Figure 12.14 Half Fourier single-shot TSE (HASTE) and single-shot TSE images (MRCP). (a) HASTE, slice thickness 5 mm. (b) Radial SS-TSE, thick slab (50 mm). (c) 3D TSE, 1 mm slice.

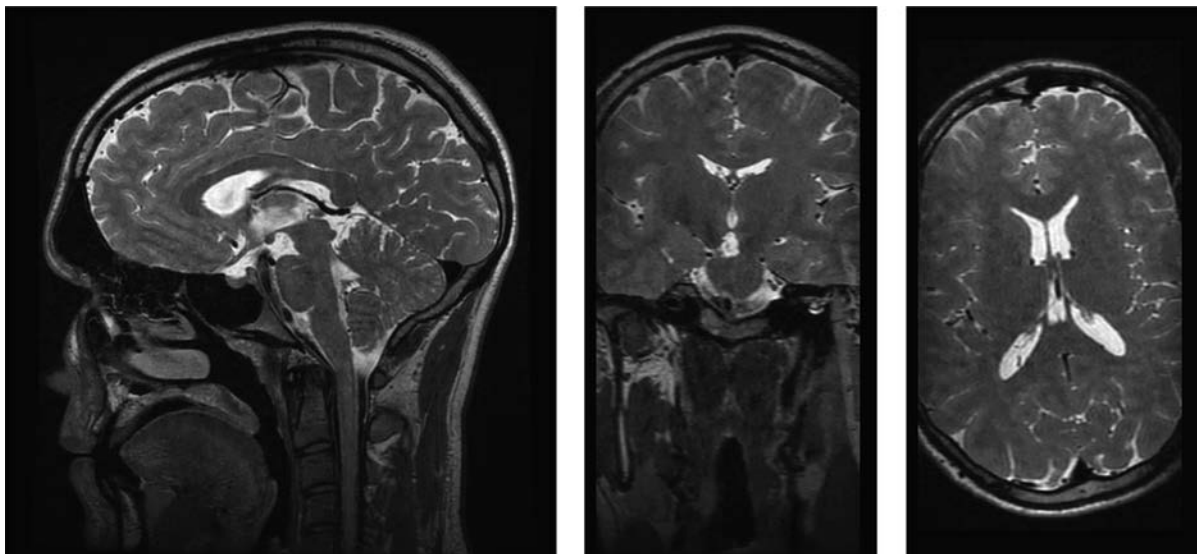


Figure 12.15 3D TSE SPACE images and reformats of the brain.

pancreas. The ducts and gall bladder can be visualized using a very long TE – of at least 500 ms. This ensures that all other signals have decayed, leaving just the bile fluid. Single shot TSE methods are ideal for this as they enable entire slices to be acquired in a breath-hold. Three imaging strategies are common:

- 1 Multi-slice SS-TSE or HASTE, with slice width 5–10 mm (Figure 12.14a).
- 2 Radially arranged SS-TSE/HASTE thick slices of typically 50 mm, which resemble MIPs without the post-processing. Only a small number of angled coronal slices are required (Figure 12.14b).
- 3 A third strategy is to acquire a 3D RF-modified TSE (SPACE, CUBE, 3DVIEW, etc.). This can supply the same information, but with high resolution, e.g. 1 mm isotropic, from which MIPs and MPRs can be calculated (Figure 12.14c).

12.4.4 3D TSE

As we saw in Section 8.8, by adding an extra phase-encode gradient series, acquisitions can be made three-dimensionally. 3D FT offers the prospect of very thin ‘slices’ or even isotropic voxels which makes the acquisitions suitable for multi-planar reformatting. Conventional spin echo is not practical as a clinical 3D sequence because of its long scan time. However 3D TSE offers scan times of just a few minutes. The scan time is

$$\text{Scan time} = \frac{\text{NSA} \times N_{\text{PE1}} \times N_{\text{PE2}} \times \text{TR}}{\text{ETL}}$$

and is kept short by using a high ETL or turbo factor and possibly partial Fourier and parallel imaging. The sequence gives the geometric and SNR advantages inherent in a 3D acquisition, while retaining the TSE features of long TE (T_2 weighting) and long TR.

In order to avoid artefacts and to keep within SAR limits, some tricks have to be done with the RF pulses (see Box ‘3D-views by Spacey Cubists: 3D TSE’). Figure 12.15 shows an MPR from an RF-modified 3D TSE image. These sequences produce T_1 , T_2 , PD and FLAIR contrast and are good for inner ear, joints and MRCP examinations. Vendor acronyms are given in Table 4.1.

3D-Views by Spacey Cubists: 3D TSE

With a conventional train of spin echoes, the echo height decays with the time from the initial excitation, so for the n th echo in TSE

$$E(n) \propto M_0 \exp\left(-\frac{n \cdot \text{IES}}{T_2}\right)$$

where IES is the inter-echo spacing. For very long ETL of the order of 100–200, the signal decay from most tissues will be unacceptably large.

In 3D TSE (SPACE, CUBE, 3DVIEW, etc.) the IES is minimized by using non-selective refocusing pulses.

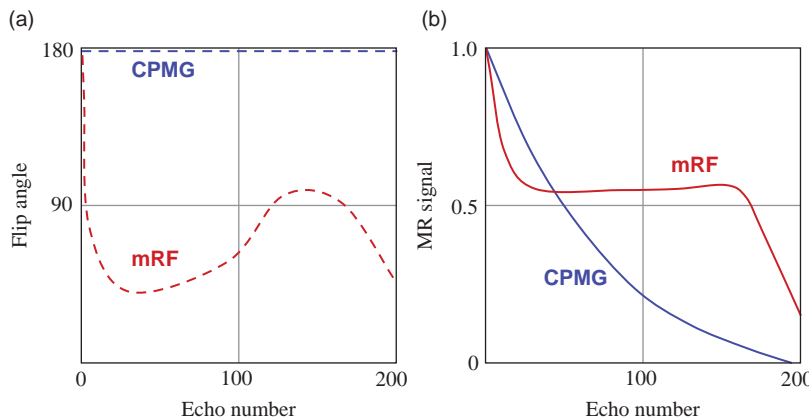


Figure 12.16 Example of RF flip angle and signal evolution for conventional TSE (CPMG) shown in blue and RF-modified 3D TSE shown in red.

Additionally, the flip angle is modulated throughout the echo train, starting large and decreasing to a smaller value of typically 30–60°. The use of smaller flip angles results in some of the transverse magnetization being temporarily ‘stored’ as longitudinal magnetization. As T_1 is generally longer than T_2 , this means that the signal intensity from the echo train is maintained for longer than in a conventional CPMG echo train. In 3D TSE the echoes are formed as a combination of spin echoes and stimulated echoes (see Box ‘Echoes and coherences: Hahn and stimulated echoes’, in Chapter 13). Figure 12.16 shows a schematic of the RF pulse modulation and echo height for a conventional CPMG and a 3D TSE acquisition. The use of lower flip angle refocusing pulses also minimizes SAR.

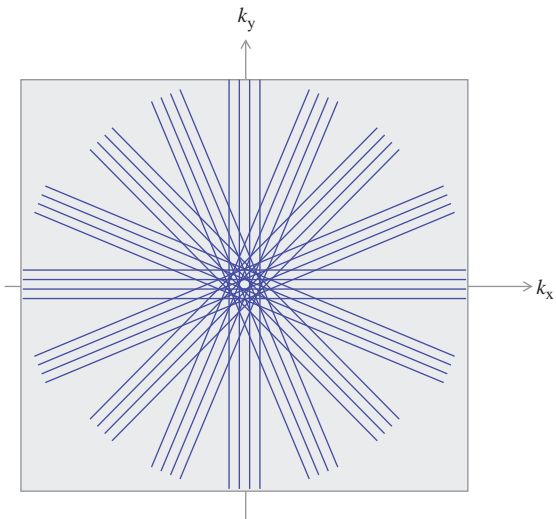


Figure 12.17 k-space trajectories for radial TSE acquisition (PROPELLER) with four echoes per blade and eight blades.

12.4.5 Radially Acquired TSE

One of the downsides of TSE is its sensitivity to motion artefact. Radial k-space acquisition is a way to overcome this problem. Originally called PROPELLER (Periodically Rotated Overlapping Parallel Lines with Enhanced Reconstruction) it acquires a number of parallel lines, each rotated about its centre through a series of angles in order to fully sample k-space (Figure 12.17). The k-space path then resembles an aircraft propeller, the ‘blades’ being the rotating block of parallel lines, each acquired during a single echo train. Radial TSE takes $\pi/2$ times longer than a conventional Cartesian TSE acquisition, e.g. in order to match a conventional acquisition with an N_{PE} of 480 lines, using a radial acquisition with an ETL of 28, would require $(480 \div 28) \times \pi/2 \approx 27$ blades. The scan time would therefore be $TR \times 27$.

The advantage of using radial TSE is that the centre of k-space is heavily oversampled, reducing any artefacts due to patient motion. Furthermore, since each blade samples the centre of k-space any rotational or translational motion between blades during the reconstruction can be identified by any inconsistencies between each blade. Depending upon the similarity between blades, data can either be corrected to account for the motion or individual blades may even be discarded.

Radial TSE can produce good-quality images even in the presence of quite severe motion. Figure 12.18 shows two T_2 -weighted TSE acquisitions in a normal volunteer who was asked to rotate their head from side to side during a conventional TSE acquisition

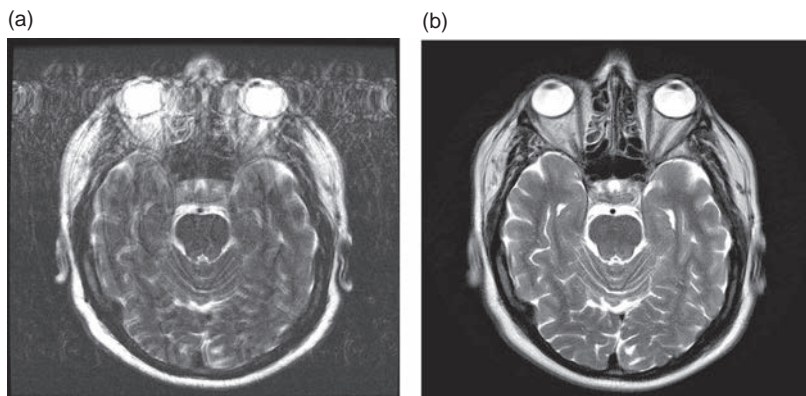


Figure 12.18 Effect of head motion on (a) conventional TSE (scan time 2 min 41 s) and (b) PROPELLER (scan time 3 min 12 s).

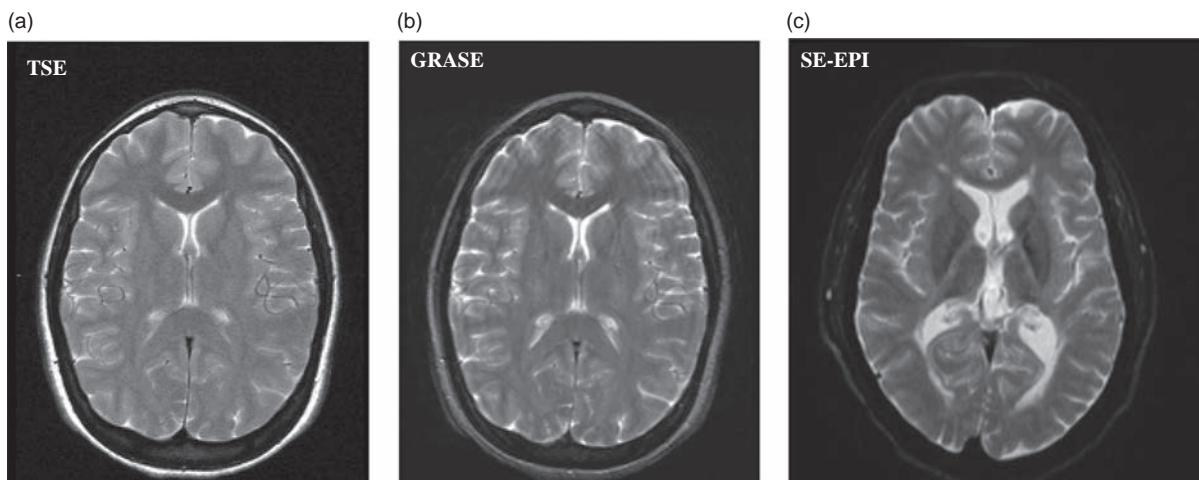


Figure 12.19 TSE, GRASE and SE-EPI images. (a) TSE, ETL = 5, TR = 2735 ms, TE = 102 ms, NSA = 2, scan time 3 min 32 s. (b) GRASE, turbo factor = 7, EPI factor = 3, TR = 3735 ms, TE = 132 ms, scan time 34 s. (c) SE-EPI, single shot, TE = 109 ms, scan time = 0.2 s per slice. Note the different appearance of the scalp fat between the sequences. The EPI uses fat suppression and exhibits significant distortion. Ringing artefacts are evident for GRASE

and a radial acquisition. It can also be used with diffusion weighting and, although significantly slower than EPI, the use of a TSE readout means that susceptibility issues are significantly reduced and that the overall image SNR is much higher. The issue of patient motion during the extended acquisition time is addressed by the inherent motion correction. Chapter 14 contains more detail about radial acquisitions.

12.5 Combining Gradient and Spin Echoes

A branch of the SE family tree involves sequences that utilize both spin and gradient echoes: GRASE and SE-EPI. As their contrast behaviour is more akin to conventional SE they are considered in this

chapter. 2D GRASE is not often used, although 3D GRASE is recommended for readout in Arterial Spin Labelling (ASL – see Chapter 18). GRASE is a logical precursor to EPI, while SE-EPI is most commonly encountered in diffusion-weighted imaging (DWI) and diffusion tensor imaging (DTI). Representative images are shown in Figure 12.19.

12.5.1 GRASE

GRadient And Spin Echo (GRASE) or Turbo Gradient Spin Echo (TGSE) is a fast segmented sequence that combines a multiple spin-echo train and intermediate gradient echoes, each with distinct values of phase encoding (Figure 12.20). Although it is a hybrid sequence, we class it in the spin-echo section as its

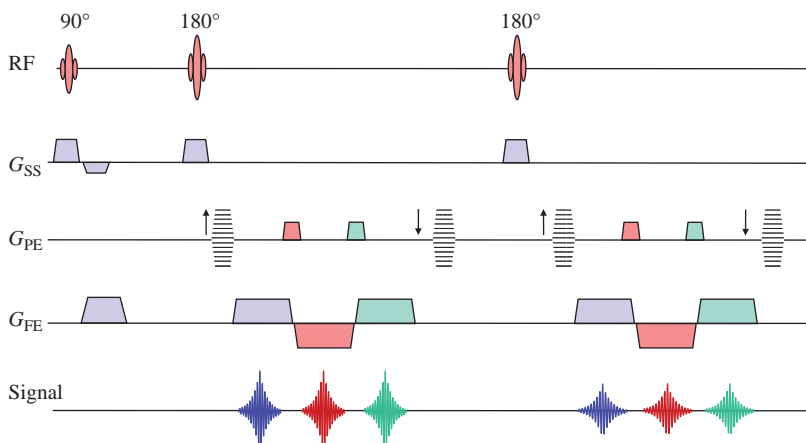


Figure 12.20 GRASE sequence diagram with three gradient and two spin echoes giving six lines of k-space per TR period.

behaviour and use are along the lines of spin echo. The scan time for GRASE is

$$\text{Scan time} = \frac{\text{TR} \times N_{\text{PE}}}{N_{\text{spin echoes}} \times N_{\text{gradient echoes}}}$$

Some systems call the number of spin echoes the ‘turbo factor’ and the number of gradient echoes the ‘EPI factor’. Typically three gradient echoes will be used for each spin echo. The advantages of this are that much less RF power is used and that higher ‘turbo factors’ can be achieved. It is sometimes claimed that GRASE contrast is more like T_2 -weighted spin echo than TSE (see Box ‘Is TSE the Same as SE?’), although its current clinical use is not yet widespread. The complicated k-space scheme (see Box ‘Grace Notes: k-Space Schemes for GRASE’) can lead to substantial ringing artefacts in the phase-encode direction.

Grace Notes: k-Space Schemes for GRASE

Figure 12.21 shows the k-space scheme for the GRASE sequence of Figure 12.20 with a turbo factor of 2 and an EPI factor of 3. The 180° pulse is followed by a conventional phase-encode gradient, determined by a phase-encode table. However, fixed phase-encode gradients are used for the gradient-echo portion of the acquisition. These cause big fixed-length jumps in k-space, with phase changes being additive from the previous echoes for the current refocusing cycle. The phase encoding is rewound before the next RF and the phase-encode table will increment for the next spin echo. Thus successive lines of k-space will be subject to a T_2

decay envelope, with this pattern repeated periodically over k-space in the phase-encode axis. This results in the ringing or ghosting artefacts seen in the image in Figure 12.19b. As for TSE the contrast is dominated by the echo time used to acquire the centre of k-space.

12.5.2 Echo Planar Imaging

Spin-Echo-based Echo Planar Imaging (SE-EPI) can be regarded as an extreme case of GRASE, where a single excitation is given and the whole of k-space is sampled with gradient echoes under a single spin echo (Figure 12.22). It produces sequential slices in less than 100 ms with low spatial resolution, but is prone to artefacts. It is primarily used in dynamic or diffusion-weighted imaging. When using EPI, what immediately strikes you is that it sounds very different from other sequences, giving a single very loud, moderately high-pitched beep. Within this beep the whole of one slice is acquired, the sound being generated by a rapidly oscillating read gradient. EPI can be single or multi-shot, spin- or gradient-echo based. Here we consider the spin-echo version, SE-EPI. EPI contrast can be amazing. In single-shot EPI, TR is effectively infinite. Thus one can obtain very highly T_2 -weighted contrast with no T_1 contribution at all.

In EPI the series of phase-encode gradients are replaced by small ‘blips’ placed at each readout gradient reversal. Each blip is of constant size and adds further phase encoding to the previous blips, resulting in a regular path through k-space (Figure 12.23), leading to a conventional 2D FT reconstruction. Large

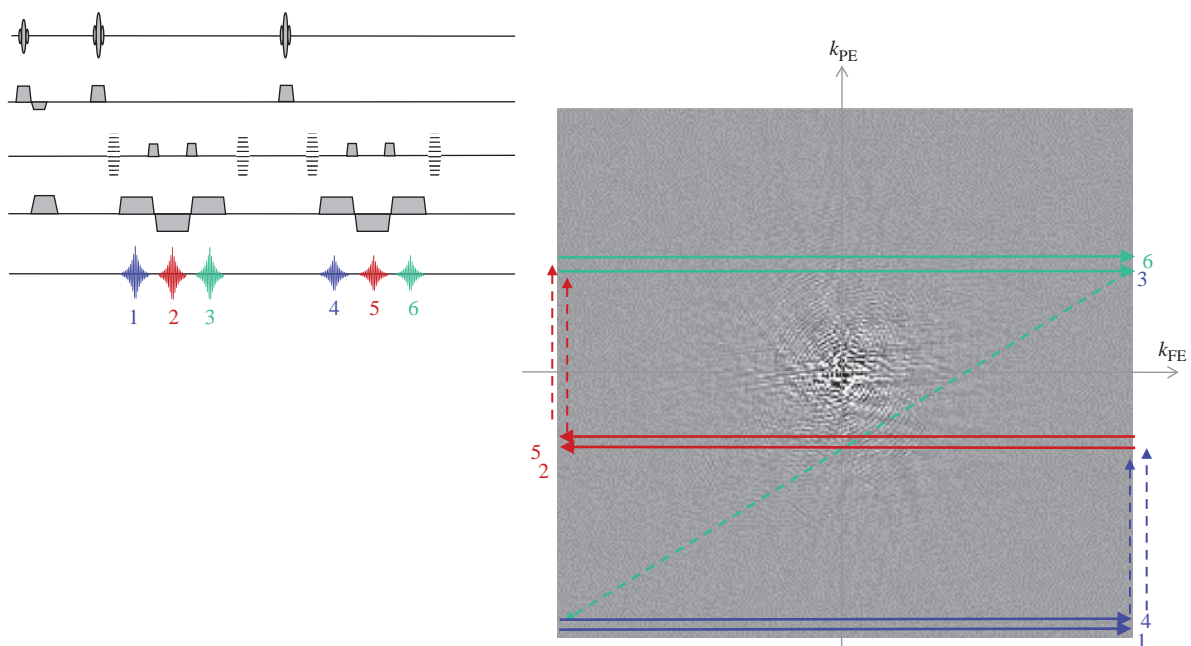


Figure 12.21 k-space acquisition for GRASE with two spin echoes and three gradient echoes. The k-space path corresponding to each echo is numbered.

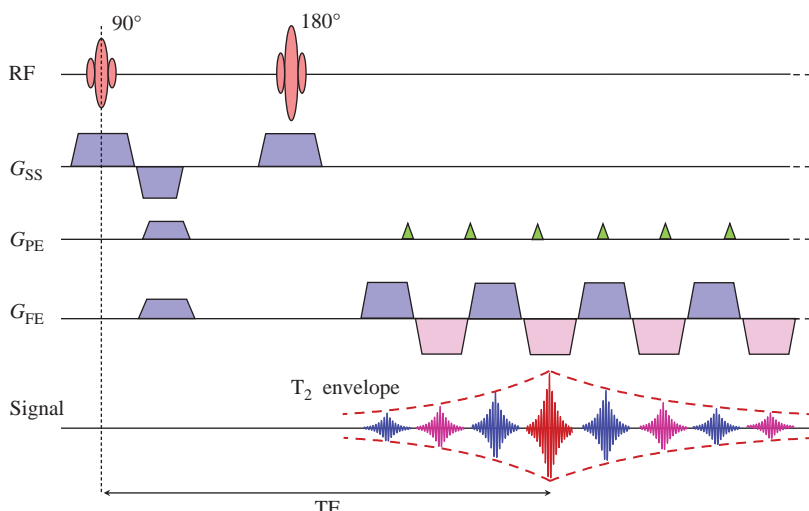


Figure 12.22 SE-EPI sequence diagram. Only eight echoes are shown. In practice 64 or 128 may be used.

read gradient amplitudes are required so that the appropriate values of k_{FE} can be sampled quickly, and the whole set of k_{PE} collected within a single spin echo envelope. This limits single-shot EPI acquisitions to the order of 100 ms, resulting in a typical resolution of 64×64 or 128×128 . The time limitation imposed by the duration of the echo means that

in EPI data are usually acquired during the gradient ramp-up times.

As for other segmented sequences, an effective echo time, where the centre of k-space is acquired, applies. Because the phase encoding is accrued monotonically, line-by-line, TE is generally of moderate length (e.g. 30–60 ms).

12.5.3 Image Quality in EPI

EPI is notorious for a high level of artefact. The classic EPI artefact is the $N/2$ (or ‘Nyquist’) ghost (Figure 12.24a), a phase ghost separated by exactly one-half the field of view. This arises because of imperfections in the rephasing-dephasing cycle of the rapidly switching bipolar frequency-encode gradient caused by eddy currents, resulting in alternate lines of k-space being misaligned (see Box ‘Exorcism!’). In practice, a ghost level of a small percentage is almost always present.

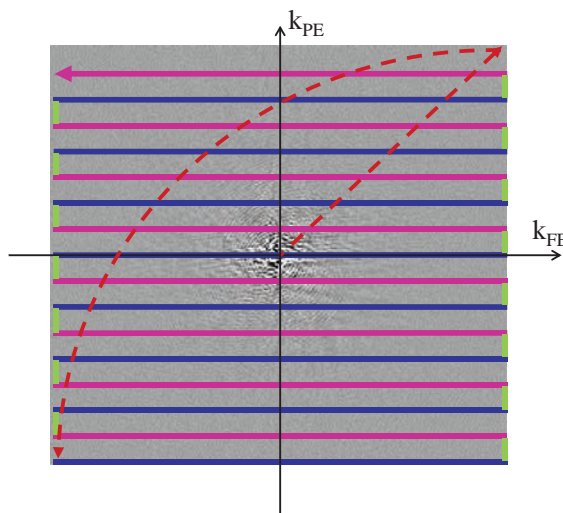


Figure 12.23 EPI k-space. The colours of the trajectory correspond to the similarly coloured gradient components in Figure 12.22.

The other artefacts are consequences of bandwidth. Each frequency-encode lobe is sampled rapidly with a very high gradient amplitude resulting in a very large signal bandwidth. The phase encode is sampled 64 or 128 times over the whole gradient-echo train. This rather slow sampling rate means that the signal bandwidth in the phase-encode direction may be as little as 10 Hz per pixel. This has two major consequences.

First, chemically shifted signals from fat will be displaced by many pixels, a significant fraction of the entire field of view in the phase-encode direction (Figure 12.24b). For this reason effective fat suppression is mandatory in EPI.

Second, small magnetic field differences (of the order of 1 ppm) will result in much greater spatial distortion. In particular, air-tissue boundaries will result in large image distortions. Additionally, signal drop-out may occur for locally shortened T_2^* . The orientation of tissue-air boundaries within the magnet can dramatically influence the extent and nature of these effects. Regions of brain close to the nasal sinuses, auditory meatus, frontal and temporal lobes are particularly affected (Figure 12.24c).

Exorcism!

The origin of the $N/2$ ghost is a slight mispositioning of every alternate refocusing of the FID, resulting from gradient imperfections (Figure 12.25), which result in a misregistration of alternate lines of k-space. Phase correction can be derived from a

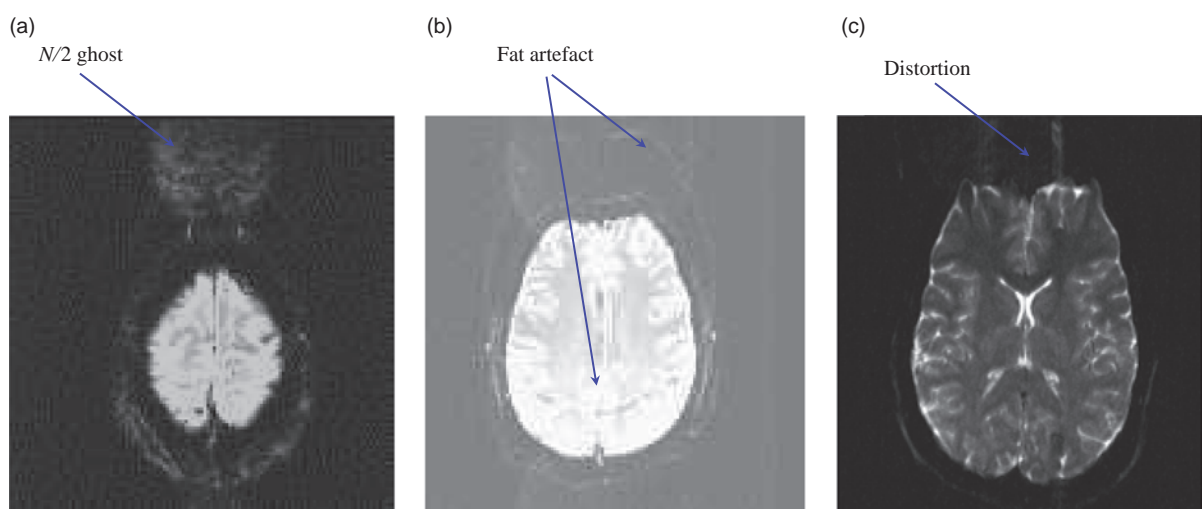


Figure 12.24 EPI artefacts: (a) $N/2$ (Nyquist) ghosts in the PE direction; (b) chemical shift – scalp fat is displaced by several pixels in the PE direction; (c) distortion in the frontal lobe.

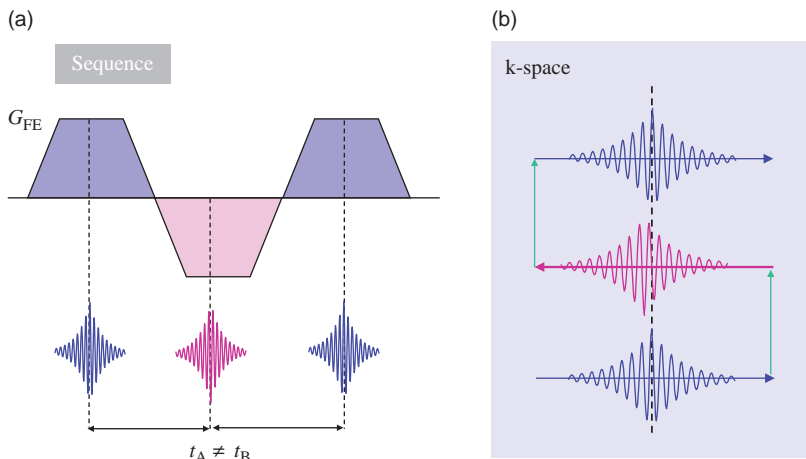


Figure 12.25 Origin of the Nyquist ghost in EPI. Timing errors result in misplacement of the centre of the consecutive echoes.

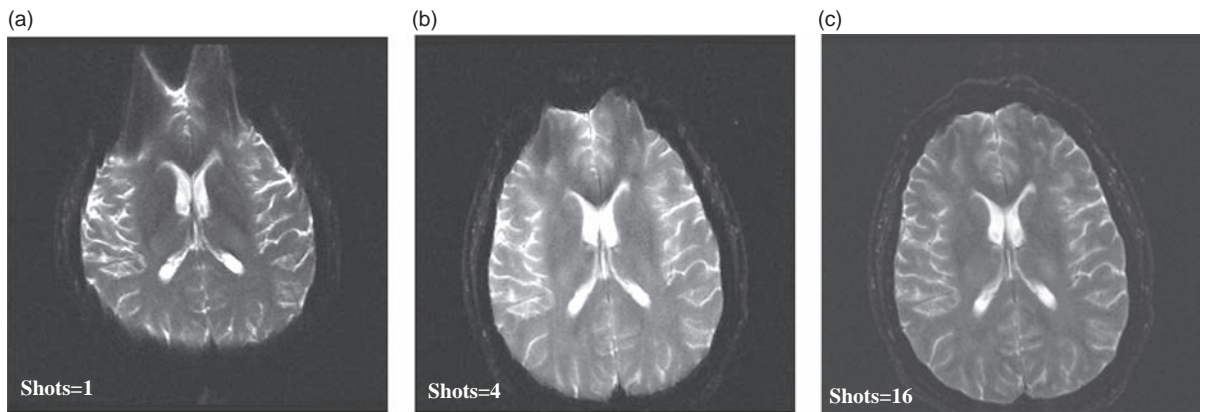


Figure 12.26 (a) Examples of extreme spatial distortion in single-shot EPI and improvements for multi-shot EPI; (b) 4 shots; (c) 16 shots.

reference scan which is identical to a full scan but without phase encoding. From the 1D FT of these data lines, phase correction filters can be produced which will then be applied to every line of image data. Phase correction is also used in RARE imaging techniques. Additionally, the position of the sampling points (the ADC raster) may be shifted to ensure the echoes are all centred. This requires a substantial pre-scan calibration procedure. To reduce artefacts, shimming using the gradients is required before an EPI acquisition. Even so, $N/2$ ghosts are almost always a small percentage of the main image signal.

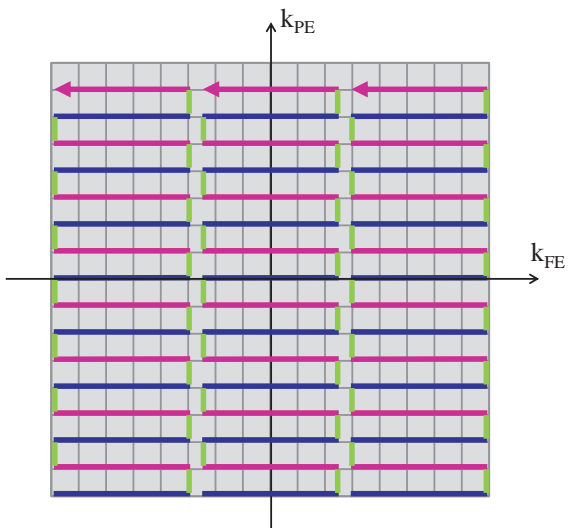


Figure 12.27 k-space trajectories for multi-shot EPI segmented in frequency encode. The entire k-space is covered in three shots.

12.5.4 Multi-Shot EPI

In multi-shot EPI, k-space is divided into two, four or eight segments, each of which is acquired by separate EPI trains. The advantages are that

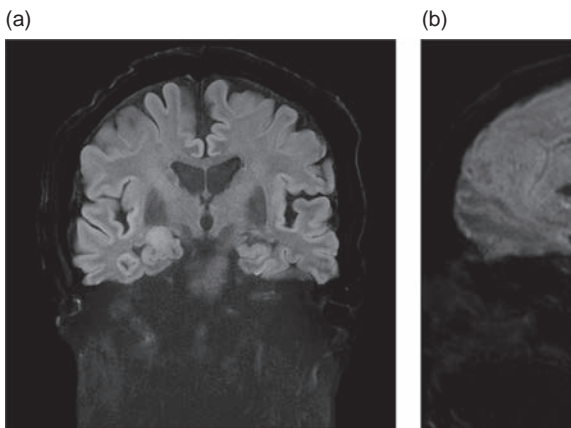


Figure 12.28 Multi-shot EPI using RESOLVE: (a) coronal, (b) sagittal. Note the lack of spatial distortion. Courtesy of Siemens Healthcare.

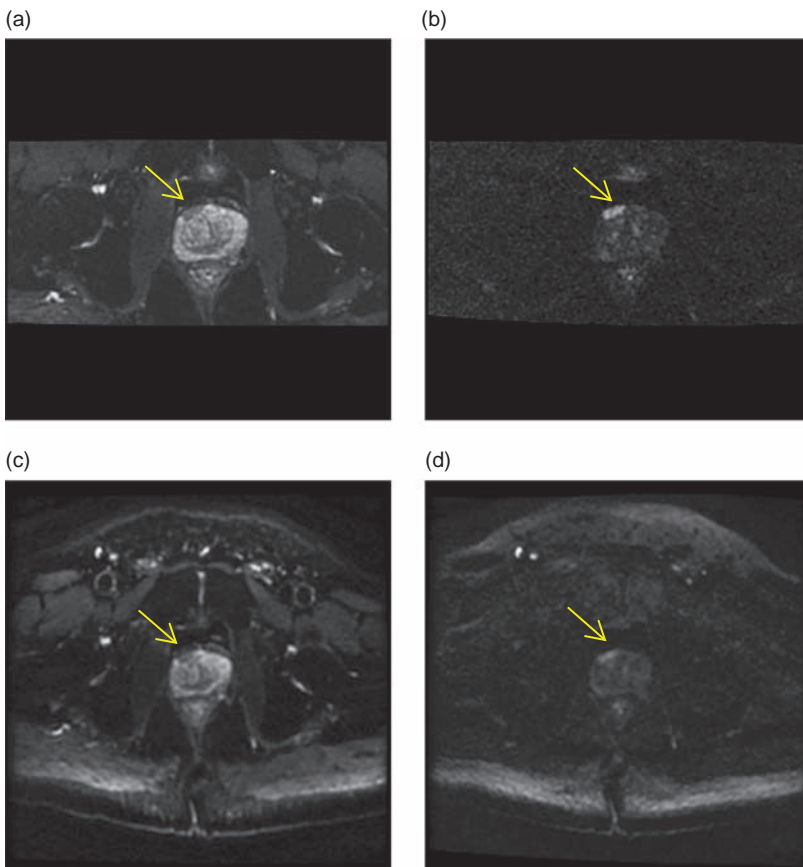


Figure 12.29 Standard DWI-EPI compared with reduced field-of-view (RFOV) DW-EPI using 2D RF excitation in the prostate. (a) and (b) RFOV DW-EPI with (a) $b = 100 \text{ s mm}^{-2}$ and (b) $b = 1400 \text{ s mm}^{-2}$. Standard DW-EPI sequence with (c) $b = 100 \text{ s mm}^{-2}$ and (d) $b = 1400 \text{ s mm}^{-2}$. Note the improved image quality with the RFOV acquisition.

susceptibility effects can be reduced as the PE bandwidth is effectively higher than for an equivalent single shot (Figure 12.26). Scan time is obviously increased and there is a need for a finite TR as in conventional scanning. Multiple-slice interleaving is possible, thereby helping to keep overall acquisition

times short. The acquisition of 20 slices in 30 s, for example, is quite reasonable; however, the snapshot ability to freeze physiological motion is compromised.

A variation on multi-shot EPI is to acquire the segmentation in the frequency-encode direction

(Figure 12.27). This allows for better motion correction in addition to improving the level of distortion. This sequence is useful for body or spine diffusion imaging and is called RESOLVE on Siemens scanners. Another EPI development is to have multi-dimensional RF selective excitation. This can be used to produce small FOV EPI scans. FOCUS by GE Healthcare is one example. Images using RESOLVE

and FOCUS are shown in Figure 12.28 and Figure 12.29 respectively.

See also:

- How frequency and phase-encoding gradients work: Chapter 7
- Basic image contrast: Chapter 3
- Introduction to pulse sequences: Chapter 4
- MRI Glossary

Further Reading

- Bernstein MA, King KF and Zhou XJ (2004) *Handbook of MRI Pulse Sequences*. London: Elsevier Academic Press.
- Brown MA and Semelka RC (1999) 'MR imaging abbreviations, definitions and descriptions: a review'. *Radiology* 213:647–662.
- Brown RW, Cheng YCN, Haacke EM, Thompson MR and Venkatesan R (2014) *Magnetic Resonance Imaging: Physical Principles and Sequence*

- Design*, 2nd edn. Hoboken, NJ: John Wiley & Sons, chapters 18 and 26.
- Elster AD and Burdette JH (2001) *Questions and Answers in Magnetic Resonance Imaging*, 2nd edn. London: Mosby-Yearbook, chapters 5 and 12. Also on the web at <http://mri-q.com> [accessed 23 March 2015].
- Haacke EM and Tkach JA (1990) 'Fast MR imaging: techniques and clinical applications'. *Am J Roentgen* 155:951–964.
- Liney G (2011) *MRI from A to Z*, 2nd edn. London: Springer-Verlag.
- Mansfield P and Maudsley AA (1977) 'Medical imaging by NMR'. *Br J Radiol* 50:188–194.
- ReviseMRI.com (n.d.) 'MRI abbreviations'. www.revisemri.com/questions/misc/mri_abbrev [accessed 24 October 2013].
- Twieg DB (1983) 'The k-trajectory formulation of the NMR imaging process with applications in analysis and synthesis of imaging methods'. *Med Phys* 10:610–623.

Acronyms Anonymous II: Gradient Echo

13.1 Introduction

The other major branch of the pulse sequence family tree is Gradient Echo (GE), also known as Gradient Recalled Echo (GRE), Field Echo (FE) or Fast Field Echo (FFE). We'll use the acronym GE. Gradient echo was originally conceived as a means of speeding up the MR acquisition, by reducing the amount of longitudinal (M_z) recovery required between successive RF excitations. Gradient-echo sequences are commonly encountered as localizer or scout planning scans, or in dynamic (with contrast) studies in the body, or for angiographic or bright blood imaging, often as three-dimensional acquisitions.

In this chapter you will learn that

- speed enhancement in GE is achieved by a combination of low flip angle and short TR, which minimizes the T_1 recovery required between successive TR periods;
- spoiled GE produces T_1 , proton density (PD) or T_2^* contrast;
- water and fat images can be produced using in-phase and out-of-phase TEs;
- rewound GE gives mixed contrast depending upon the ratio of T_2 and T_1 but higher SNR than spoiled GE, and is also subject to T_2^* decay;
- time-reversed GE shows 'spin-echo' type properties giving T_2 weighting;
- k-space segmentation applied to GE results in ultra-fast acquisitions such as turbo-FLASH and GE-EPI.

To understand this chapter you need to be familiar with the material from Chapters 4, 8 and 9 and have some grasp of the concept of k-space. For each sequence examined we will answer the following questions: How fast is it? How does it localize signal? What contrast does it produce? And how does it avoid artefacts?

13.2 Image Formation in Gradient Echo

The image-formation principles of a basic GE sequence were considered in Chapter 8. The echo is formed by the dephasing and rephasing of the FID signal by the frequency-encoding gradient (refer back to Figure 8.4 for a reminder). In GE, speed is enhanced by using a small flip angle so that TR can be reduced dramatically without saturating or driving the signal to zero. After a few RF pulses the magnetization gets into a steady-state where the recovery in each TR period exactly matches the effect of the excitation as considered briefly in Chapters 3 and 4 and shown in Figure 13.1

A key point for GE is that the dephasing effects of magnet inhomogeneities and local susceptibility variations are not corrected. The MR decay signal is therefore determined by T_2^* rather than T_2 , so shorter values of TE are used, generally less than 10 ms. Additionally there are interesting cancellation effects relating to water and fat signals which are peculiar to GE. We shall see that there are three main branches in the gradient-echo family tree: spoiled GE, rewound GE and time-reversed GE. Example images are shown in Figure 13.2.

The extension of spoiled and rewound GE sequences to 3D is relatively straight forward by the addition of a second ('slab direction') phase-encode gradient as we saw in Section 8.8. The scan time becomes

$$\text{Scan time} = \text{NSA} \times N_{\text{PE1}} \times N_{\text{PE2}} \times \text{TR}$$

where NSA is the number of signal acquisitions and $N_{\text{PE1,2}}$ the dimensions of the phase-encode matrices.

13.3 One Tree, Many Branches: FIDs, Echoes and Coherences

If we have a train of RF pulses with TR significantly greater than T_2 as in conventional spin echo, then the

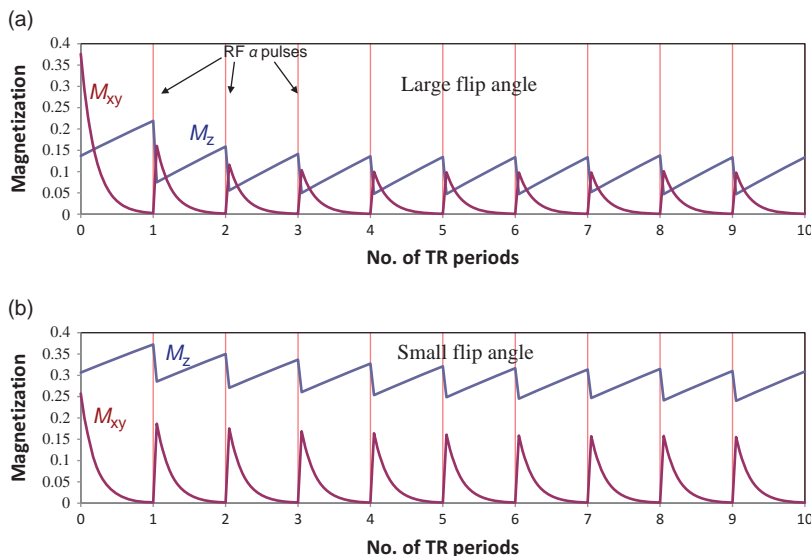


Figure 13.1 Steady-state magnetization in spoiled gradient echo. After a number of TR, a constant signal (M_{xy}) is obtained. (a) Large flip angle (70°), (b) small flip angle (40°). $TR/T_1 = 0.1$, $T_2^* = 0.02 \times T_1$.

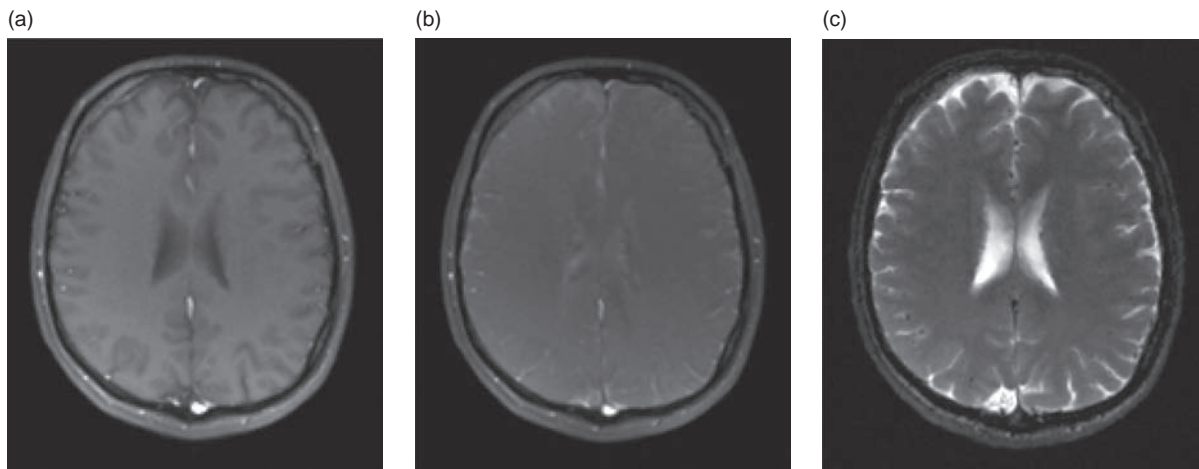


Figure 13.2 Gradient-echo images. (a) spoiled GE, (b) rewound GE, (c) time-reversed GE. All with $TR = 20$ ms, $TE = 5.8$ ms, flip angle $\alpha = 25^\circ$.

transverse component of magnetization always fully decays before the onset of the next RF pulse. Each RF pulse will always act solely on longitudinal magnetization and the strength of the FID signal will depend mainly upon T_1 . However, if TR is less than T_2 then a remnant of transverse magnetization will remain as the next RF pulse is applied. This results in 'Hahn' or partial echo formation in addition to the FID. The origin of these signals is considered in Box 'Echoes and Coherences: Hahn and Stimulated Echoes'.

Echoes and Coherences: Hahn and Stimulated Echoes

We have seen that a $90-180^\circ$ pulse pair can generate a spin echo. However, any pair of RF pulses, of any flip angle (except true 180°), can form a Hahn or partial spin echo, and each echo can be further refocused by a subsequent RF pulse. The Hahn echoes are smaller in magnitude than spin echoes and have a T_2 dependence.

The formation of a Hahn echo for a pair of 90° pulses is shown in Figure 13.3. We see that it is not a fully refocused echo but that at time TE all the spin

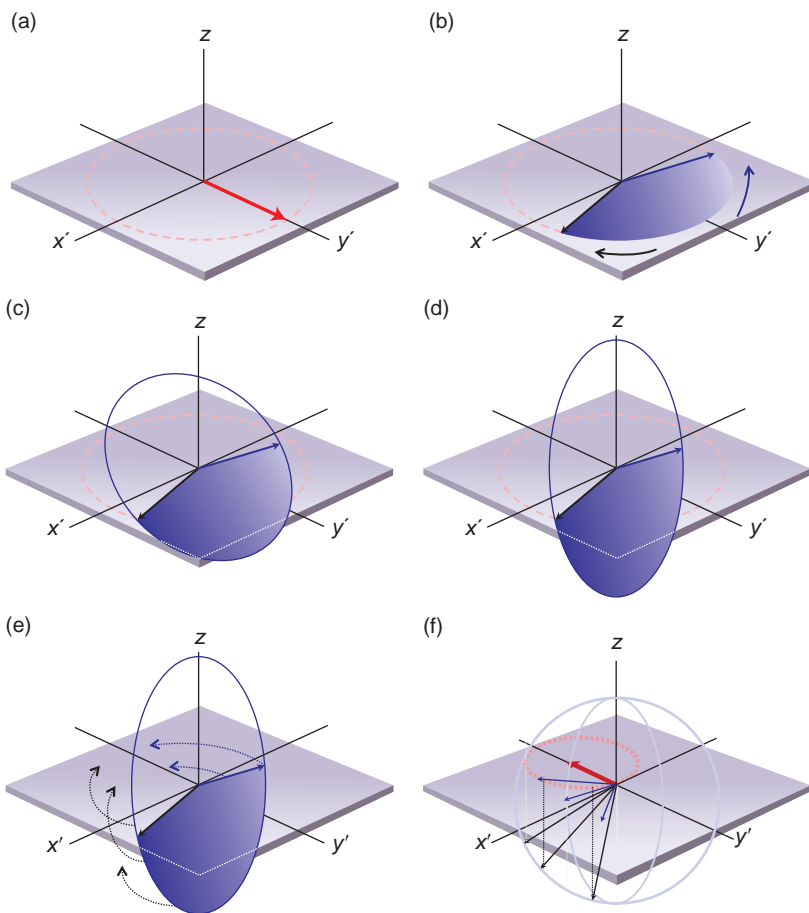


Figure 13.3 Formation of Hahn 'partial' echoes. (a) Transverse magnetization after first RF pulse; (b) immediately before the second RF pulse; (c) during and (d) immediately after this pulse; (e) continued transverse dephasing before the echo (f). The partially refocused Hahn echo occurs when all the transverse components (shadows) of the magnetization lie in a circular arrangement after a time twice the echo spacing.

vectors are of the same sign and lie in a circle, giving an echo magnitude of half of a full spin echo. For angles smaller than 90°, visualizing how the echo is formed is less intuitive. Instead of forming a circle of vectors they lie in an ellipse which refocuses less fully in the $-x'y'$ quadrant.

Stimulated echoes arise when you have three RF pulses. The first pulse generates transverse magnetization, which is 'converted' to and stored as longitudinal (T_1) magnetization by the second, and finally refocused by the third. In Figure 13.4 we see that three RF pulses will produce five echoes, three Hahn echoes from each pair of pulses, an echo created by refocusing the first echo by the third pulse and the stimulated echo. The stimulated echo has T_1 and T_2 behaviour. Its echo time with respect to the first RF pulse is

$$TE_{STE} = 2 \cdot t_a + t_b$$

In a long RF pulse train, it is not just successive RF pulses that give rise to echoes, but each pair of

pulses may do so as well. If the TR is constant, which is normal, these echoes will coincide with the wanted FID signal but, since they arose from earlier excitations, they may have different spatial encoding and contrast – and if left unintended may cause artefacts.

GE sequences cope with this by either 'spoiling' the residual transverse magnetization after data acquisition and before the next RF pulse (sometimes called incoherent sequences), or by rewinding the gradients, so that the transverse magnetization at the end of each TR period has no spatial encoding. This results in a rewind (sometimes called coherent) steady-state sequence.

In a regularly spaced train of RF pulses, the echo signals will coincide with the following RF pulses and therefore add to the FID signal. How these so-called transverse coherences are dealt with determines the contrast behaviour of the sequence. 'Spoiling'

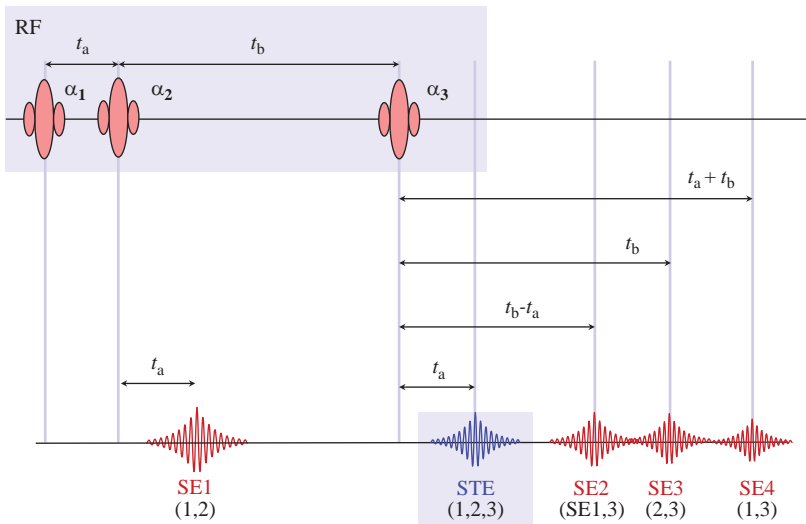


Figure 13.4 Three RF pulses may give rise to four Hahn echoes from each pair of RF pulses SE1, SE3, SE4 and the refocusing of the first echo by the third RF pulse. The stimulated echo STE is generated by all three RF pulses. The times of echo formation are given in terms of t_a and t_b , the time intervals between the RF pulses.

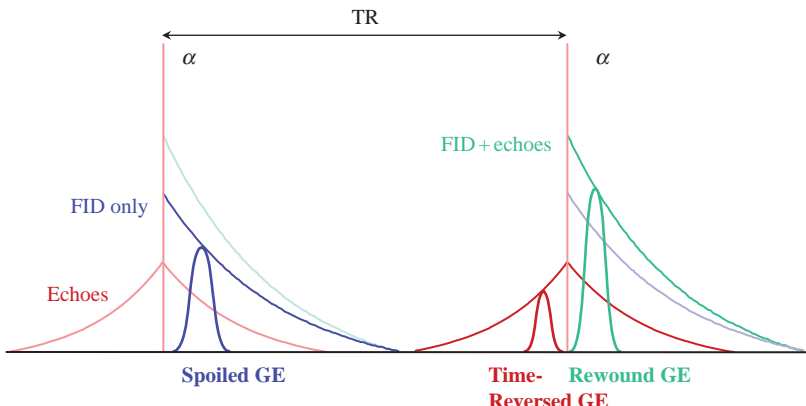


Figure 13.5 Gradient echo: coherent and incoherent signal formation in the steady state from a regular train of RF excitation pulses α .

removes the transverse coherences. ‘Rewinding’ utilizes them as signal. In time-reversed GE the echoes alone, excluding the fresh FID signal, are used in image formation. This gives us three main ways to obtain the images in Figure 13.2, illustrated in Figure 13.5, each with distinctive appearance. The relative size of the different signal components is explored further in Box ‘Echo Amplitudes’.

Echo Amplitudes

A further way of understanding coherence is to think of an RF pulse of arbitrary flip angle as acting in three separate ways, as follows.

- 1 Part of it acts like a 0° pulse. This means it has no effect upon either transverse or longitudinal

magnetization. The relative amplitude of magnetization affected by this component is

$$M_{0^\circ\text{-like}} \propto \cos^2(\alpha/2)$$

- 2 Part acts like a 90° pulse, converting longitudinal magnetization into transverse, and transverse into longitudinal magnetization. The amplitude of this component is

$$M_{90^\circ\text{-like}} \propto \sin \alpha$$

- 3 Part of it acts like a 180° pulse, inverting pre-existing longitudinal magnetization and refocusing transverse magnetization by means of a partial or Hahn echo with amplitude

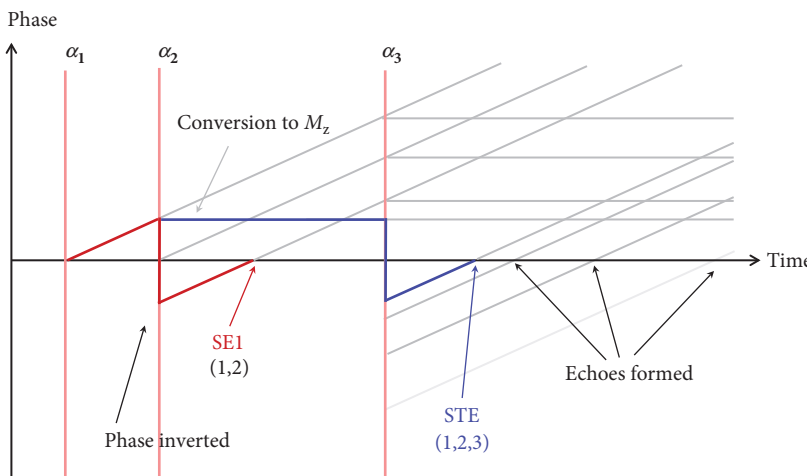


Figure 13.6 Coherence pathway diagram showing the formation of the first spin echo (red line), the stimulated echo (blue) and all the other echoes (grey).

$$M_{180^\circ\text{-like}} \propto \sin^2(\alpha/2)$$

From this, one can predict that the Hahn echo from two 90° pulses will have half the amplitude of a spin echo. Similarly, a true 180° pulse will only invert or refocus, and not cause partial or stimulated echoes, but we can predict that an imperfect 180° pulse will cause unwanted components of magnetization. The nature of the slice profile means that such imperfections will almost always exist for a selective refocusing pulse. This was a source of potential artefact in TSE but is avoided by using phase rewinder gradients before each 180° pulse so that any partial or stimulated echo components are properly spatially encoded.

Rewound GE sequences contain components from transverse coherences and FID and give mixed contrast depending upon the ratio of T_2 and T_1 . They are also subject to T_2^* decay. Time-reversed GE sequences use just the transverse coherence signals to give T_2 weighting. All GE sequences must be constructed to avoid the formation of artefacts from coherence pathways (see Box 'Coherence Pathways').

Coherence Pathways

The analysis of coherence pathways is of prime importance to the sequence developer, but an understanding of coherence helps to know what the images are about and how the sequences perform. Every time an RF pulse occurs, magnetization will be flipped to both longitudinal and transverse

planes resulting in a fresh FID, the possibility of echo formation and the storing of magnetization for later RF pulses to refocus. Figure 13.6 shows a so-called coherence pathway diagram which can be used to predict the echo-formation properties of trains of RF pulses. In the diagram, phase is represented vertically and time horizontally. For simplicity we only consider one component (sometimes called an 'isochromat') of the transverse magnetization rather than multiple vectors fanning out. The rules are simple. Every time there is an RF pulse the magnetization divides into three parts:

- 1 A part continues to dephase as if nothing had happened.
- 2 A part is converted to longitudinal magnetization which then does not further dephase and runs parallel to the time axis at constant phase.
- 3 Another part of transverse magnetization receives the opposite phase, and then continues to dephase (or 'rephase' if it's heading back towards the zero phase axis). Whenever one of the lines crosses the zero-phase axis you get an echo.

Figure 13.6 also shows how a stimulated echo is formed, first by converting the transverse magnetization to longitudinal by α_2 , then inverting the phase with α_3 which converts it back to transverse magnetization. You can see that the diagram correctly predicts the existence and timing of the stimulated echo. When the pulse train is regular (i.e. $t_a = t_b$), the stimulated echoes will coincide with the spin echoes. The coherence diagram in Figure 13.6 does not show the effect of the imaging gradients, although these can also be included.

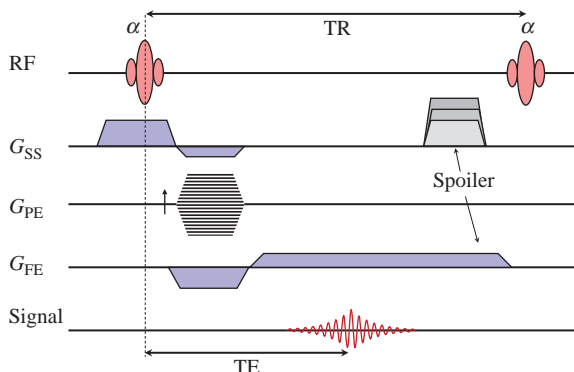


Figure 13.7 Spoiled gradient echo sequence utilizing gradient spoiling as a table on the slice-select gradient and a constant value on the frequency-encode axis and/or RF spoiling by varying the RF phase angle.

13.3.1 Spoiled Gradient Echo

In spoiled gradient echo only the FID signal, generated by the action of the current RF pulse on longitudinal magnetization, is utilized. The residual transverse magnetization remaining after the data-acquisition period (Figure 13.7) is removed by gradient spoiling, RF spoiling or both (see Box ‘Spoil Sport’). In all other respects, the image-formation mechanism is conventional, with one line of k-space acquired per TR period.

The image contrast, mainly T₁W or PDW, is determined by TR and α , as was shown in Section 3.9. For each value of T₁ occurring in the image there is an optimum flip angle, known as the Ernst angle, that gives the most signal for a given TR. At flip angles greater than the Ernst angle you tend to get T₁ weighting. At less than the Ernst angle the contrast is flatter, more PD-like (Figure 13.8). With very low flip angles you can get pure PD weighting and also T₂* weighting by increasing TE. A mathematical expression for the signal is given in Box ‘Flash in the Pan: Signal Strength and the Ernst Angle’.

Flash in the Pan: Signal Strength and the Ernst Angle

The signal obtained from a spoiled GE sequence is

$$\text{Signal} = \rho \frac{\sin \alpha \cdot (1 - \exp(-\text{TR}/T_1)) \cdot \exp(-\text{TE}/T_2^*)}{1 - \cos \alpha \exp(-\text{TR}/T_1)}$$

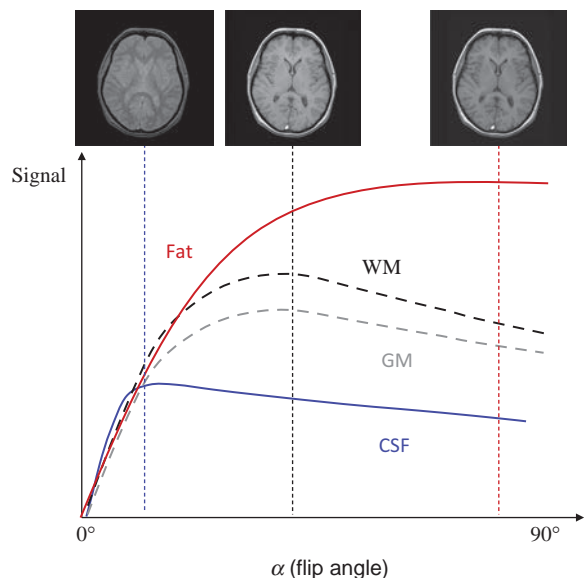


Figure 13.8 Signal intensity flip angle in spoiled GE, and image contrast below the Ernst angle, at the Ernst angle, for WM of above the Ernst angle.

and you can see that flip angle α is an important parameter in determining the image contrast as illustrated in Figure 13.8.

The Ernst angle for the maximum signal is given by

$$\alpha_{\text{Ernst}} = \cos^{-1}[\exp(-\text{TR}/T_1)]$$

Of course the Ernst angle can only be met for one value of T₁ in an image.

Spoil Sport

Failure to spoil the transverse magnetization can result in two problems: the formation of image artefacts and wrong contrast. Image banding artefacts may also arise from incomplete spoiling, due to interference between differently phase-encoded signals from different excitations. A constant spoiling gradient will dephase only non-echo-forming parts of the signal. More thorough spoiling can be achieved by using a pseudo-randomly varying (i.e. the value isn't actually random, but the effect is) spoiler gradient table. Spoiler gradients can be applied on any axis, but the slice-select axis is commonly chosen as this represents the largest dimension of the voxel.

In RF spoiling we apply each α excitation pulse with a random or pseudo-random phase angle (direction in the rotating frame), as in Figure 13.9. The effect of this is to accentuate the natural dephasing of the spins, thus giving an apparent reduction in T_2 for the remnant of transverse magnetization from previous excitations.

Gradient spoiling (Figure 13.10a) must be sufficient to cause dephasing within a voxel, illustrated by the three lines. This effectively dephases any transverse magnetization that does not lead to a Hahn echo. However, it does not prevent echo formation. To avoid this, RF spoiling must be used (Figure 13.10b). Each RF pulse causes a vertical

(phase) offset and if properly randomized the iso-chromats never add up constructively. The current FID signal is not affected. When RF spoiling is utilized the phase-encode gradients are usually rewound, otherwise unwanted spatial inhomogeneities in the signal can occur.

Gradient echo does not compensate for magnetic field differences. This includes dephasing from water and fat, which have slightly different resonant frequencies. Immediately after excitation, water and fat signals are in phase but precessing at different rates, seen as a dephasing over time in the rotating frame of reference. Once the two components get 180° out of phase with each other, the signals will subtract from one another. This does not affect the image, unless a voxel contains a mixture of water and fat, in which case a partial cancellation will occur. See Section 7.3.2 for a full discussion of this artefact and how to avoid it.

Alternatively, this feature can be utilized to provide information about the relative amounts of water and fat in tissues using in-phase/out-of-phase (IP/OP) GE. In the OP images, any voxels that contain both water and fat will have lower signal intensity than in the IP images. This is particularly noticeable at fat-water interfaces where partial volume means that voxels at the interface experience signal cancellation, giving a black line outlining the structure. IP/OP imaging is often used clinically to identify fat containing lesions such as adrenal adenomas. The IP/OP images can be acquired in a dual-echo GE sequence with breath-holding for abdominal imaging. These

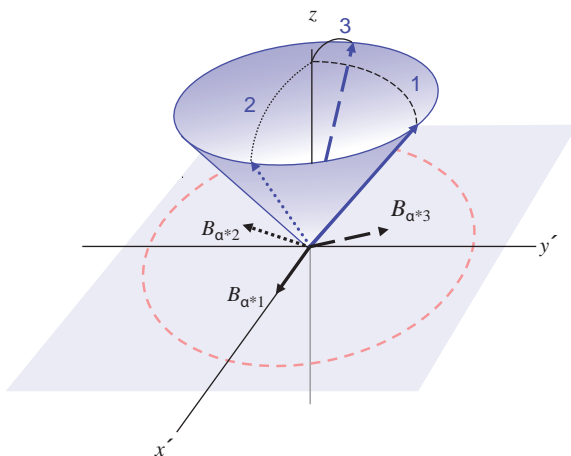


Figure 13.9 Principle of RF spoiling. Changing the RF phase changes the direction of the B_1 field in the rotating frame of reference. RF spoiling is denoted by the asterisks.

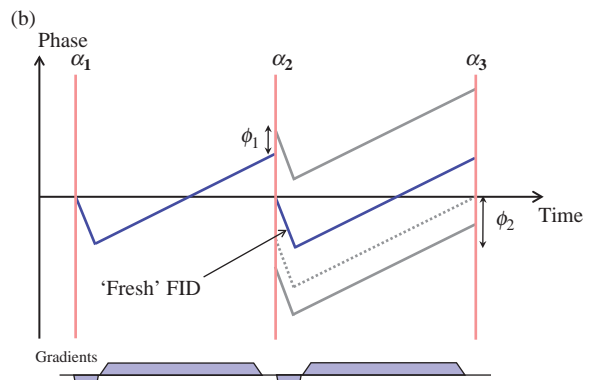
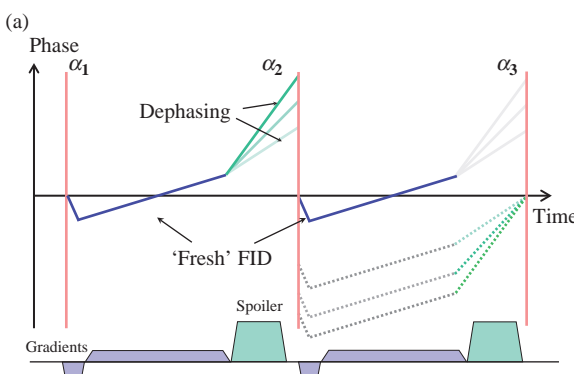


Figure 13.10 (a) Coherence diagram showing that gradient spoiling with a constant gradient amplitude dephases the non-echo-forming part of the FID, but that the echo-forming parts (dotted lines) are repassed. (b) Coherence diagram for RF spoiling showing that echo-forming and non-echo-forming parts of transverse magnetization do not form coherences. The dotted line shows the coherence pathway without RF spoiling. Fresh FID is considered to be 'in-phase'.

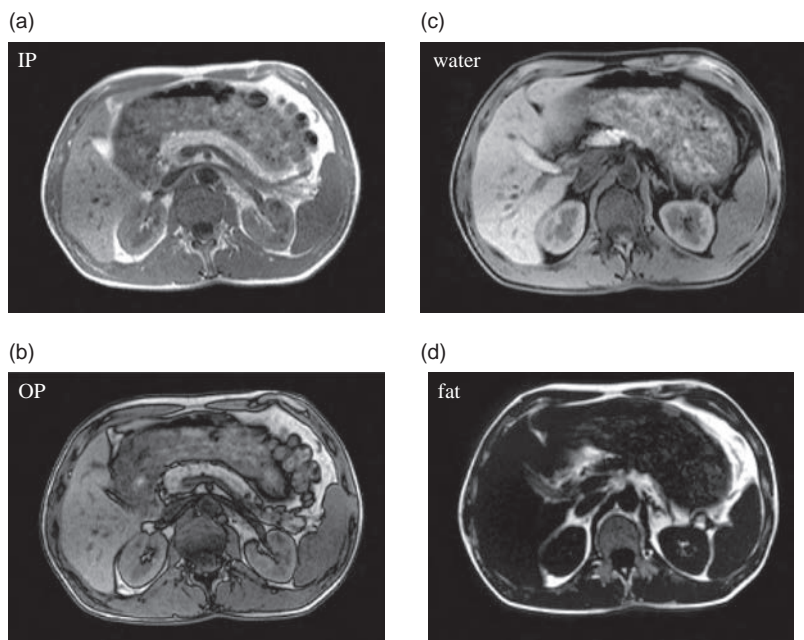


Figure 13.11 Dual in-phase (a) and out-of-phase (b) images together with calculated water (c) and fat (d) images using the two-point Dixon technique.

are often called two-point Dixon (2PD) methods and they can also be used to obtain images of water and fat as shown in Figure 13.11 and Box 'Two-Point Dixon Reconstruction'.

Two-Point Dixon Reconstruction

The IP/OP method described above is the basis of 'simple spectroscopic imaging' proposed by W. Thomas Dixon in 1984. Dixon's original method used two spin-echo acquisitions (and forms the basis of TSE-Dixon sequences), but here we apply it to GE.

The signal in the first echo OP image will be

$$S_{\text{OP}} = S_w - S_f$$

where S_w and S_f are the water and fat signals in a voxel. The second echo IP voxel signal will be

$$S_{\text{IP}} = S_w + S_f$$

From these we can calculate the water image from

$$S_w = 0.5(S_{\text{OP}} + S_{\text{IP}})$$

and the fat image as

$$S_f = 0.5(S_{\text{OP}} - S_{\text{IP}})$$

These are illustrated in Figure 13.11 and are good enough to give a subjective (i.e. radiological) assessment of the water and fat content of tissues. For fat quantification a more rigorous approach using a third echo to compensate for phase errors is required (see Chapter 19).

13.3.2 Rewound Gradient Echo

In coherent steady-state sequences, the transverse magnetization remaining after the signal-acquisition period is rewound, i.e. reset to zero by reversing the sign of the gradient pulses. In Fast Imaging with Steady Precession (FISP) only the phase-encode gradient is rewound (Figure 13.12). Thus the signal contains FID enhanced with echo and coherent transverse components. This gives more signal than spoiled gradient echo but more complicated weighting. At longer TR values (>100 ms) and small flip angles there is little difference between spoiled and rewound gradient sequences. Also, if T_2 is short then there is little opportunity for enhanced contrast to develop from the coherent component. The ideal contrast behaviour depends only upon the flip angle and the ratio of T_2 to T_1 , shown in Box 'On the Rewound'. As for spoiled sequences, the image-formation principles are completely conventional and the extension to 3D FT is standard, with the same equations for scan time applying.

Rewound GE produces good myelographic effect images. Figure 13.2b shows an example of rewound GE in the brain with bright CSF and little grey/white matter contrast. Since the signal is relatively independent of TR, rewound sequences are excellent for high contrast between fluid and solid structures in rapid imaging. However, because of the combination of

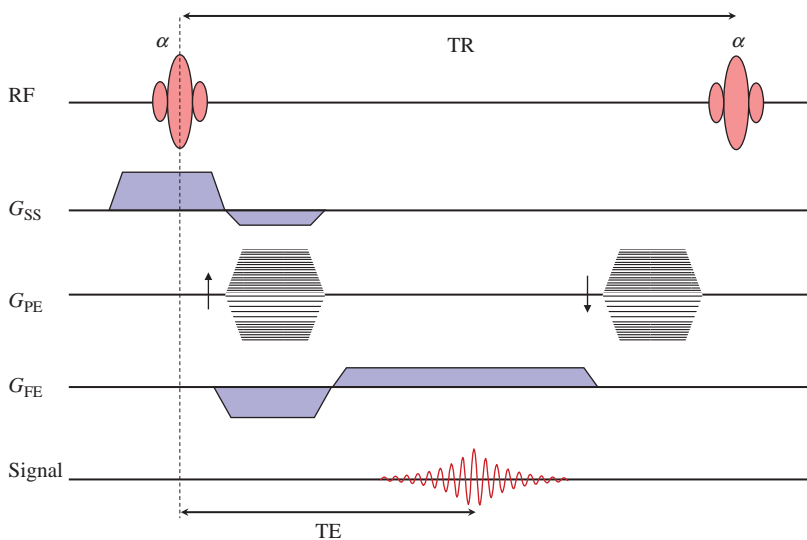


Figure 13.12 Rewound gradient-echo sequence. Only G_{PE} is rewound to avoid producing 'resonant offset' artefacts

refocused and fresh transverse magnetization, rewound GE sequences are sensitive to motion and flow, which can destroy the steady-state transverse coherence.

sometimes quoted as the 'signal from true FISP'. Unlike spoiled GE sequences, however, the flip angle dependence is only moderate for most practical applications, e.g. imaging of fluids.

On the Rewound

A general solution for gradient-echo signal strength is

$$\text{Signal} = \rho \frac{\sin \alpha \cdot (1 - \exp(-\text{TR}/T_1)) \cdot \exp(-\text{TE}/T_2)}{1 - \cos \alpha \exp(-\text{TR}/T_1) - \exp(-\text{TR}/T_2) \cdot [\exp(-\text{TR}/T_1) - \cos \alpha]}$$

Rewound gradient-echo sequences (FISP, GRE, FFE, FAST) are used with very short TR, much less than T_1 and T_2 . In this case the exponential terms can be approximated by Taylor expansions [e.g. $\exp(-\text{TR}/T_2) \approx 1 - \text{TR}/T_2$], and the above equation simplifies to

$$\text{Signal} = \rho \frac{\sin \alpha \cdot \exp(-\text{TE}/T_2^*)}{1 + T_1/T_2 - \cos \alpha(T_1/T_2 - 1)}$$

so the signal is ideally independent of TR, dependent only on flip angle and the ratio T_1/T_2 . If $\alpha = 90^\circ$ we get

$$\begin{aligned} \text{Signal} &= \frac{\rho}{1 + T_1/T_2} \\ &\approx \frac{\rho T_2}{T_1} \end{aligned}$$

if T_1 is much greater than T_2 . As with spoiled gradient echo, there is a flip angle which gives an optimum SNR

$$\text{Signal}_{\text{opt}} \propto \sqrt{\frac{T_2}{T_1}}$$

True FISP or balanced fast field echo (bFFE) is a sequence which has balanced, rewinding gradients in all three directions, as shown in Figure 13.13. An extension to 3D FT can be made by adding phase encoding and rewinding on the slice-select axis in place of the rephasing lobes. True FISP requires high-performance gradient technology to obtain a very short TR and good shimming. If this is not achieved the images become degraded with banding artefacts, which have spacing inversely proportional to the field inhomogeneity (see Box 'A Right ROASTing: Resonant Offsets'). Phase alternation of the RF pulse also helps to achieve a rapid steady-state magnetization and shifts these artefacts. True FISP has found clinical applications in cardiac imaging, where it provides excellent SNR and contrast between blood and the myocardium. Examples are shown in Chapter 16.

A Right ROASTing: Resonant Offsets

The main technical difficulty in true FISP arises from 'resonant offsets' (Figure 13.14). The number of RF excitations required to achieve a steady-state magnetization is dependent upon the amount of dephasing during TR. For spins that are not exactly on

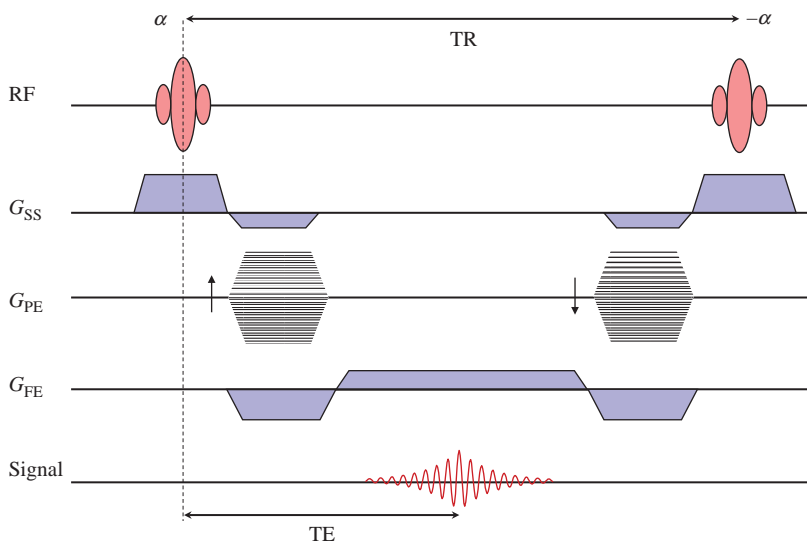


Figure 13.13 True FISP sequence. All gradients are balanced over one TR period.

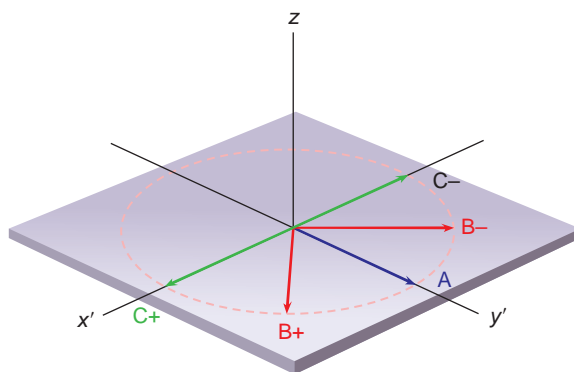


Figure 13.14 Resonance offsets. B_1 has maximum effect upon spins in orientation A, and no effect upon C. Only A is on resonance. In a fully balanced sequence, the spin orientations A, B and C would occur at different positions within the field of view, resulting in artefactual banding. In an unbalanced sequence the residual spread of phase angles from the imaging gradients will mask differences arising from field homogeneity.

resonance, e.g. due to main field inhomogeneities, the MR signal will oscillate from excitation to excitation, resulting in banding in the image related to the field inhomogeneity. A simple way of visualizing this is that progressive systematic errors are introduced to the flip angle. Phase-alternating the RF pulse can help to alleviate the problem, as does reducing TR. This problem only arises when all the gradients are balanced, e.g. in true FISP. In rewound sequences that are not fully balanced, the degree of residual dephasing is chosen to ensure that each voxel

contains a full range of resonant offset angles and the problem is averaged out, i.e. each RF pulse will have the same effect. The term ROAST (Resonant Offset Averaging STeady State) is sometimes used to describe this technique

13.3.3 Echoes Only: Time-Reversed Gradient Echo

Gradient echo sequences that only utilize the echo component are known as time-reversed GE. An example is the oddly named PSIF sequence (try saying it after a few gins), an acronym that stands for nothing – but is FISP backwards both in spelling and in function! It is shown in Figure 13.15. Strictly speaking it is not a gradient-echo sequence as its signal is of Hahn echo origin. This is how it works: you start with the data acquisition, then you do the phase encoding and finally excite the signal! See Box ‘If I Could Turn Back Time: How Time-reversed GE Works’ for details. The images (Figure 13.2c) give a T_2 -weighted appearance but with the advantage of a faster acquisition than spin echo. Time-reversed GE has the slightly odd property that the effective TE is approximately twice TR and that the degree of T_2 weighting is controlled mainly by adjusting TR. Its disadvantages are sensitivity to motion and relatively low signal-to-noise ratio (we are not using the majority of the signal at all). Time-reversed GE images are acquired in sequential mode (slice by slice) or 3D mode. Clinical

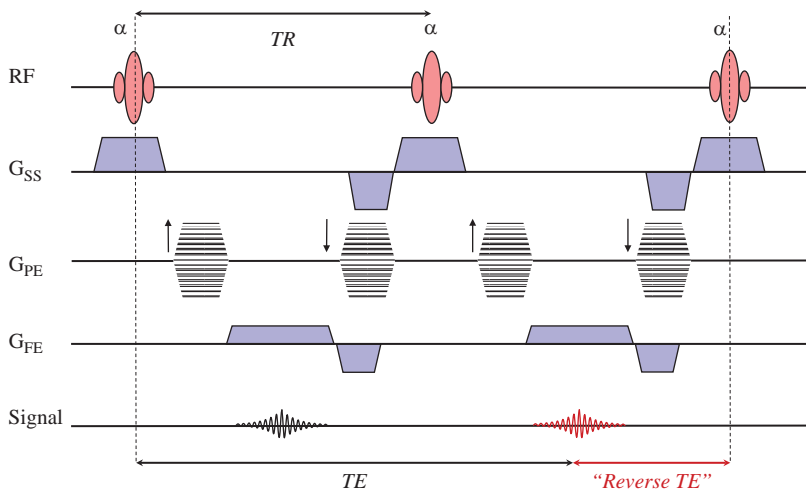


Figure 13.15 Time-reversed GE sequence. The first echo (shown in grey) occurs from an earlier TR period.

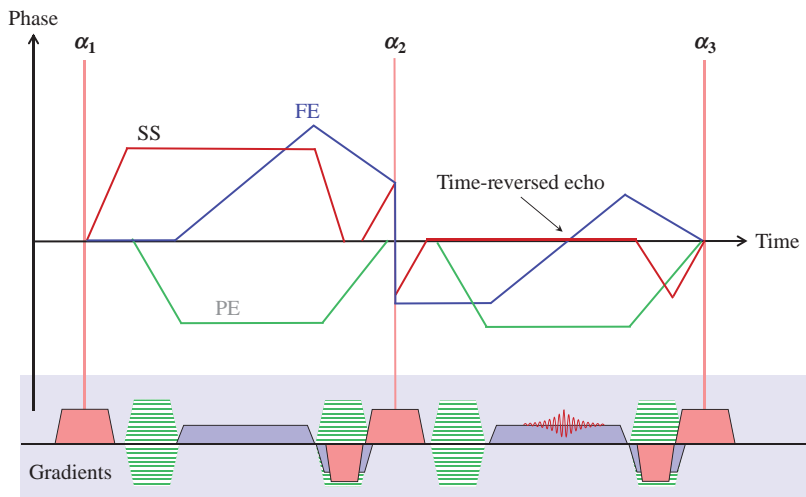


Figure 13.16 Coherence pathway diagram showing echo formation for time-reversed GE. The dephasing effect of each gradient is shown separately.

applications of time-reversed GE are few, but one is as an alternative to echo planar imaging for diffusion-weighted imaging.

If I Could Turn Back Time: How Time-Reversed GE Works

Figure 13.16 shows a coherence diagram for time-reversed GE. If we plot out the phase evolution for time-reversed GE we see that the first RF pulse causes the initial excitation of transverse magnetization, and this is dephased by the readout gradient and then partially rephased.

The second RF pulse flips the phase of part of this and the next readout gradient rephases this midway

between the TR period to give the echo. Because two RF pulses are involved the behaviour is that of a Hahn echo, and hence T_2 weighted in nature. As in other coherent sequences, the phase encode requires rewinding. Slice selection is also rewound. As this is a time-reversed sequence, we often consider a ‘reverse TE’ (Figure 13.15) in which case the signal strength approximates to the following:

$$\text{Signal} \propto \exp\left(-\frac{2 \cdot \text{TR} - \text{TE}_{\text{reverse}}}{T_2}\right)$$

So the T_2 weighting is related to twice TR. For a short reverse TE we can say that the effective TE is approximately twice TR.

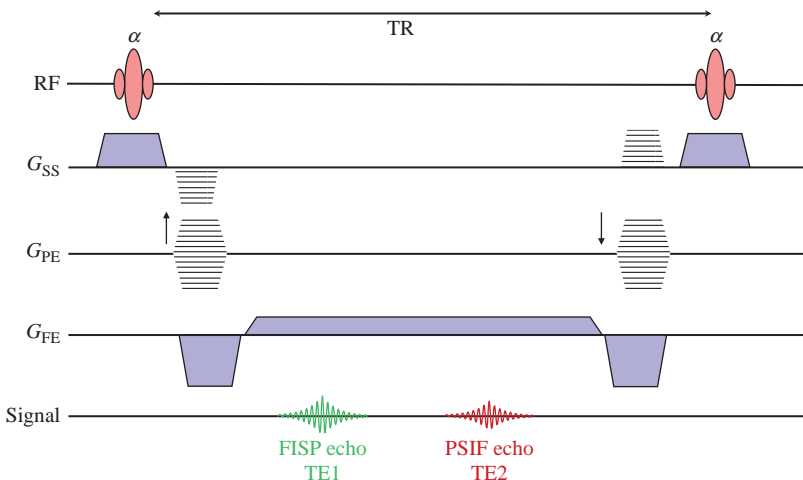


Figure 13.17 DESS sequence. The ‘FISP’ echo is the rewound gradient echo arising from the most recent RF pulse. The ‘PSIF’ echo is refocused from the previous excitation.

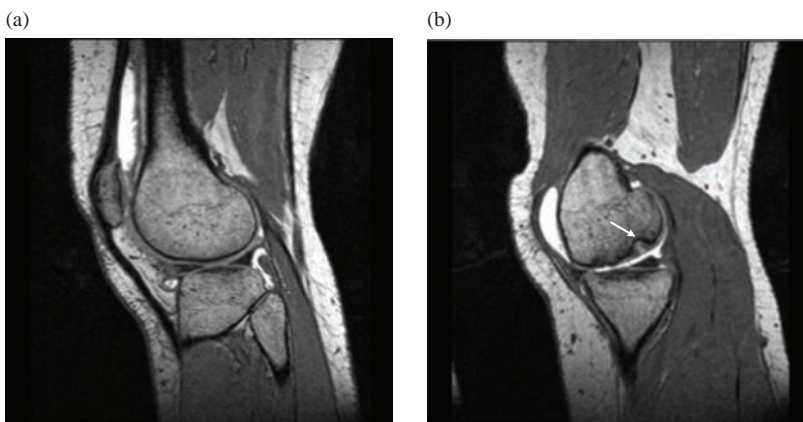


Figure 13.18 (a) DESS image of the sagittal knee showing bright fluid. (b) Cartilage defect and bone erosion (arrowed) shown by DESS. TR = 26.8 ms, TE = 9 ms, $\alpha = 40^\circ$.

13.3.4 Double Trouble: DESS and CISS

DESS (Double Echo Steady State) is a Siemens sequence in which two echoes are acquired, one a FISP gradient echo, the other a time-reversed (or PSIF Hahn) echo. The heart of the DESS sequence is shown in Figure 13.17. As this is primarily a 3D technique, phase encoding is applied on two axes after prior slab selection. The dephase and rephase portions are arranged such that the FISP echo occurs ahead of the PSIF echo. In the resultant image these two components are combined to give high-resolution images (the FISP part), with strong T_2 weighting (the PSIF part) giving strong fluid signals. DESS is quite sensitive to motion artefacts, but is well suited to high-resolution 3D orthopaedic scanning with spatial resolution at sub-millimetre dimensions, as shown in Figure 13.18.

CISS (Constructive Interference in Steady State), another Siemens sequence, is a combination of two true FISP images, one acquired with and one without alternating the sign of the RF pulses. The purpose of the sequence is to avoid banding artefacts that arise in true FISP when the TR is too long. It allows for very high-resolution GE images. State-of-the art gradient technology renders this sequence obsolete since we can now use 3D TSE instead.

13.4 Ultra-Fast GE Imaging

The GE sequences we have examined so far have utilized conventional spatial localization methods. In this section we look at sequences that use segmentation of k-space and non-steady-state methods in their image formation. This, combined with low flip angle techniques, enables them to run ‘ultra-fast’. How fast

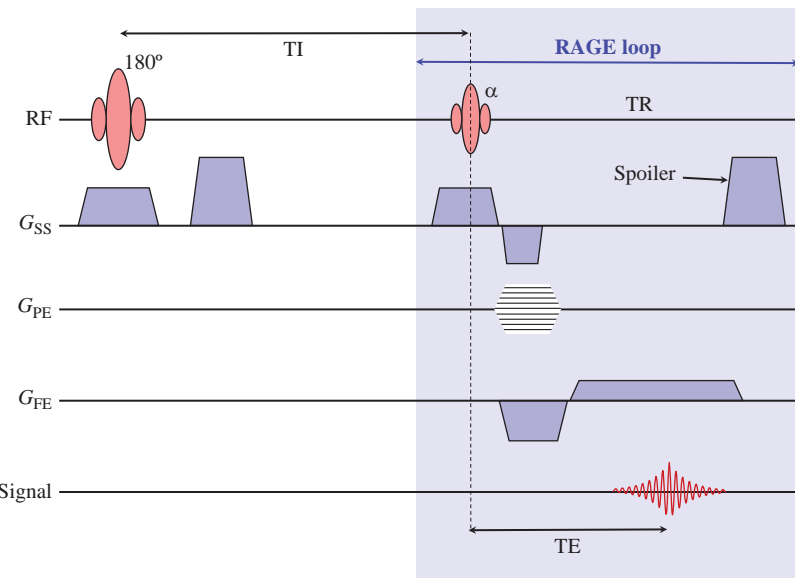


Figure 13.19 Turbo-FLASH sequence. An inverting prepulse and spoiler gradient precede the rapid acquired gradient echo (RAGE) loop for image formation.

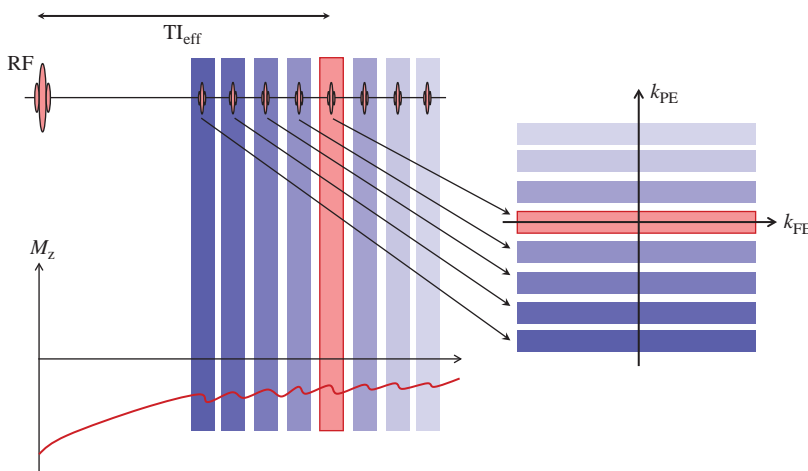


Figure 13.20 k-space acquisition for turbo-FLASH showing how the effective TI (T_{eff}) occurs.

is ultrafast? How short is a piece of string? Generally scan times of a few seconds or less per whole slice used for dynamic studies.

13.4.1 Turbo-FLASH

Turbo-FLASH is a spoiled GE technique applied ultra-quickly with extremely short TR and very low flip angle. One of the consequences of a very short TR and low flip angle is that the T_1 contrast is very poor. To get round this problem, turbo-FLASH uses an inversion pre-pulse followed by a delay to generate T_1 weighting as shown in Figure 13.19. As for TSE, the order of phase encoding affects the contrast, with

an effective inversion time TI from the centre of the inversion RF pre-pulse to the centre of k-space shown in Figure 13.20. For a linear-ordered phase encoding this is

$$T_{\text{eff}} = TI + \frac{N_{\text{PE}}}{2} \cdot TR$$

Therefore with this sequence changing the matrix size (in the phase-encode direction) changes the contrast.

On most scanners the definition of TI has been changed to be the time from the initial inversion to the middle of k-space (Figure 13.20). This makes much more sense as now you don't change the contrast if you change the matrix size; instead the scanner

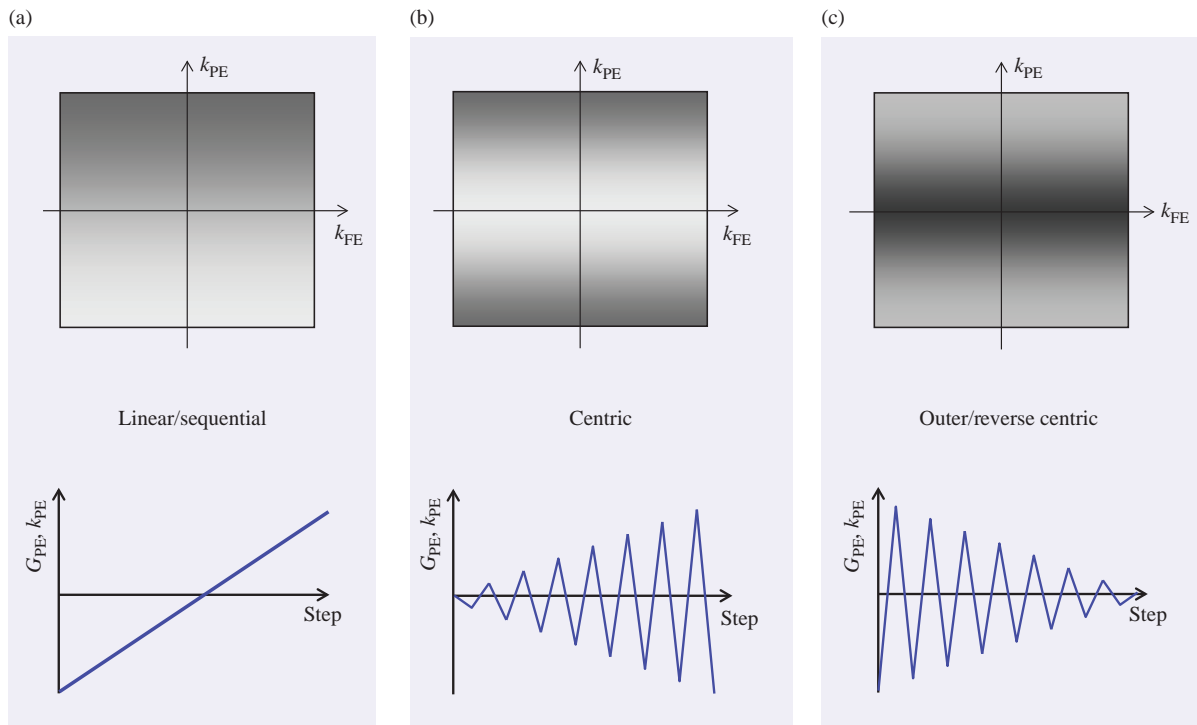


Figure 13.21 k-space ordering schemes: (a) linear or sequential, (b) centric, (c) reverse centric. In centric the image contrast is determined by the beginning of the acquisition, in reverse centric by the end.

adjusts the delay between the inversion pulse and the start of the RAGE loop to give the desired TI.

Turbo-FLASH can run very fast, acquiring a whole slice in 1 or 2 s. When used in a multiple-slice mode, it is applied sequentially. That is, the whole of one slice is acquired before the next. A delay, TD, between slice acquisitions must be applied if a non-selective inversion pulse is used. The scan time is therefore proportional to the number of slices:

$$\text{Scan time} = N_{\text{slices}} \times (\text{TI} + N_{\text{PE}} \cdot \text{TR} + \text{TD})$$

Turbo-FLASH can be applied in both single-shot and segmented mode. In single-shot mode the whole of k-space is acquired by the train of RF pulses. This imposes practical limits on the spatial resolution achievable but makes for very rapid (1 s per slice) acquisitions. In segmented turbo-FLASH k-space is divided into segments and the whole sequence repeated a number of times. Typically up to 32 lines of k-space may be acquired per shot. In order to avoid jumps in signal intensity from one segment to the next, interleaving schemes may be employed.

Furthermore, the ordering of phase-encode steps affects the contrast as shown in Box 'k-space Ordering Scheme'.

k-Space Ordering Scheme

In standard spin-echo imaging the order in which the lines of k-space are acquired is generally from maximum negative to maximum positive (or vice versa). This is called linear or sequential ordering. In spin echo the actual order does not matter, as the underlying signal does not change from line to line. The order does matter for segmented k-space and single-shot sequences.

Another commonly used order is centric, where the lowest k_{PE} values are measured first with positive and negative values alternating, i.e. 0, -1, 1, -2, 2, ..., $-N_{\text{PE}}/2, N_{\text{PE}}/2$. This will result in contrast dominated by the beginning of the acquisition period.

Reverse or outer centric is similar but starts from the large values and works backwards. Image contrast will be dominated by the end of the acquisition. These are illustrated in Figure 13.21.

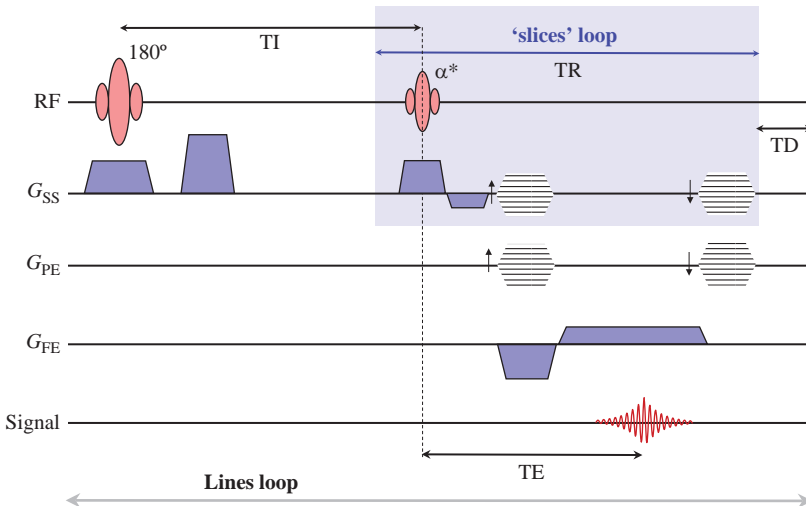


Figure 13.22 3D MP-RAGE sequence. Note that when RF spoiling (denoted by asterisk) is deployed the phase-encode gradients are rewound.

The turbo-FLASH sequence involves RF spoiling to avoid contamination of T_1 -weighted contrast by T_2 effects. It is, however, different from spoiled gradient echo in that a steady state is not achieved during data acquisition. The magnetization exists in a transient state, undergoing repetitive very small flip angles while the longitudinal relaxation is recovering from its initial inversion. By appropriately varying the flip angle during the readout portion of the sequence, oscillations of magnetization and, subsequently, inconsistencies of k-space data can be avoided.

Turbo-FLASH is also known as IR-FSPGR (on GE Healthcare scanners) or sometimes T_1 -Turbo-FLASH. It is also possible to have T_2 -Turbo-FLASH (DEFSPGR on GE Healthcare systems), which as the name suggests gives T_2 -weighted images. This is achieved by replacing the inversion pulse with a 90° – 180° – 90° set of preparation pulses. The 90° – 180° pair produces a T_2 -weighted spin echo, which is returned to the z axis by the second 90° . The turbo-FLASH loop immediately follows to produce the image, so ‘TI’ now defines the amount of T_2 weighting.

13.4.2 MP-RAGE

MP-RAGE or Magnetization Prepared Rapid Acquisition by Gradient Echo is the same in principle as turbo-FLASH. However, the name has tended to apply to a particular 3D implementation of turbo-FLASH shown in Figure 13.22. As a 3D technique there are too many combinations of the two phase-encode gradients to acquire the whole of 3D k-space from a single preparation. The solution is to acquire

all the ‘slice’ encoding lines of data from each prep, then introduce a recovery delay (as in segmented turbo-FLASH) before moving on to the next in-plane line of k-space. As a result the in-plane resolution is not compromised, the data being all acquired with the same degree of relaxation. MP-RAGE can produce very high-resolution, T_1 -weighted images showing very good anatomical detail, particularly of the brain (Figure 13.23). The introduction of this delay means that MP-RAGE is not ultra-fast in its scan time (although it uses ultra-fast methods). The scan time is

$$\text{Scan time} = \text{NSA} \times N_{\text{PE}} \times (N_{\text{slices}} \cdot \text{TR} + \text{TI} + \text{TD})$$

13.4.3 Other Ultrafast GE Sequence Variations

It has become commonplace for MR manufacturers to offer anatomy- or application-specific optimized GE protocols. For example, VIBE, LAVA or THRIVE are 3D gradient-echo sequences with optimized k-space coverage and interpolation, all intended for imaging of liver in a breath-hold. The contrast behaviour follows that of a T_1 -weighted spoiled gradient echo (Figure 13.24).

An extension of the 3D-optimized k-space GE approach is to combine 3D imaging with radial acquisition in a stack of 2D planes, the so-called ‘stack of stars’ (Figure 13.25). Two-dimensional radial scanning utilizes two simultaneous gradients for the frequency encoding with amplitudes varying to produce a range of angles in k-space. One advantage is immunity from

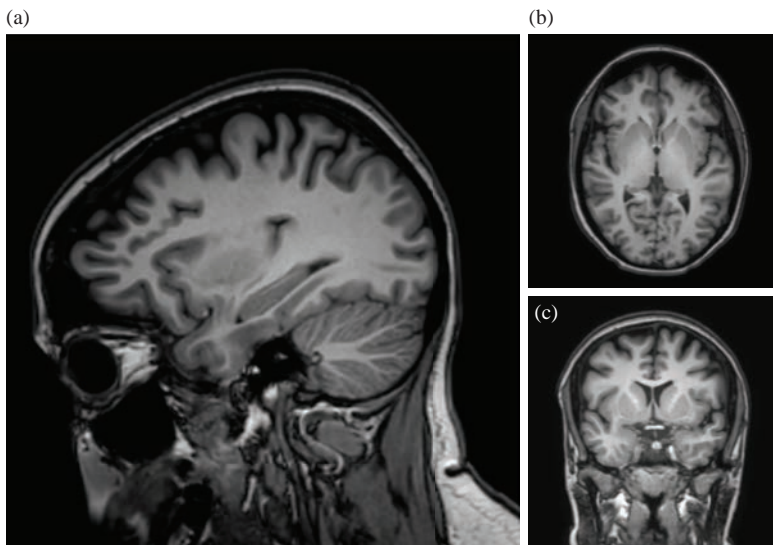


Figure 13.23 Multi-planar reformatted high-resolution 3D T₁-weighted MP-RAGE images: (a) transverse, (b) sagittal, (c) coronal.

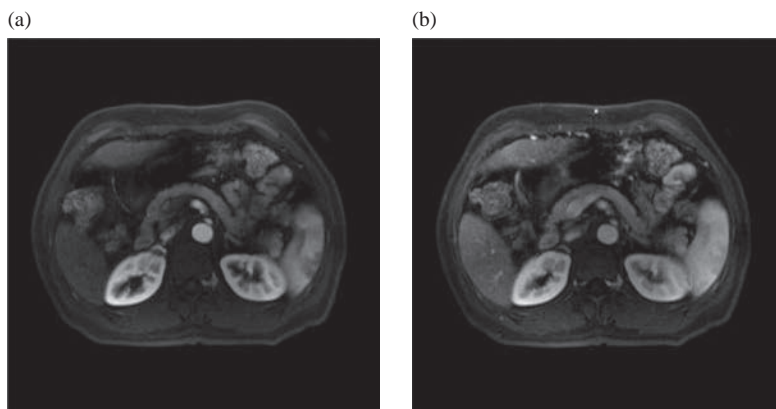


Figure 13.24 VIBE images: (a) arterial phase, (b) venous phase.

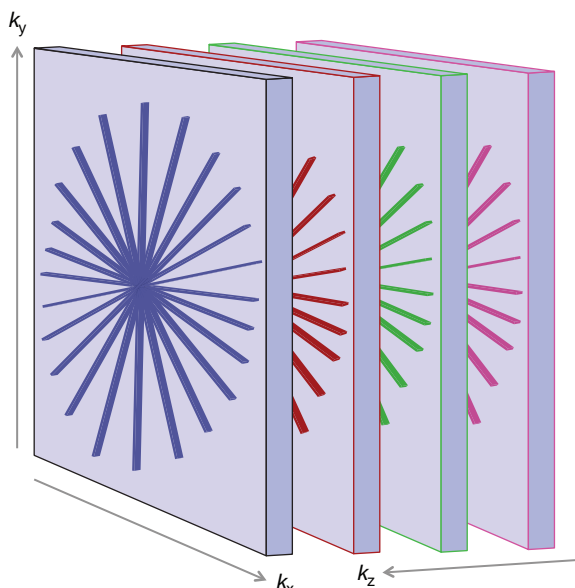


Figure 13.25 k-space for 'stack of stars'.

phase-wrap since the only phase encoding occurs in the slice-selective direction. Small FOVs can easily be acquired. A second advantage is that the continual sampling of the centre of k-space allows for motion correction (as was the case for PROPELLER). It also allows for a finer sampling of the centre of k-space than the edges, good for interpolation and for keeping the scan time down. Further details on radial and other non-Cartesian acquisitions are contained in Section 14.8. The stack of stars sequence has been implemented as Star-VIBE on Siemens scanners.

13.4.4 GE Echo Planar Imaging

Echo planar imaging (EPI) is the fastest pulse sequence, capable of producing a whole slice in under 100 ms. In single-shot GE-EPI the whole train of gradient echoes are acquired following a single RF excitation pulse (Figure 13.27). In this instance, the phase encoding of each line is acquired by adding a

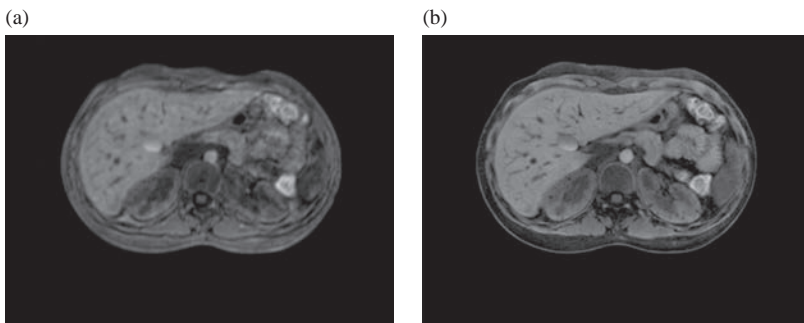


Figure 13.26 (a) conventional VIBE image, (b) Star-VIBE image. Courtesy of Siemens Healthcare.

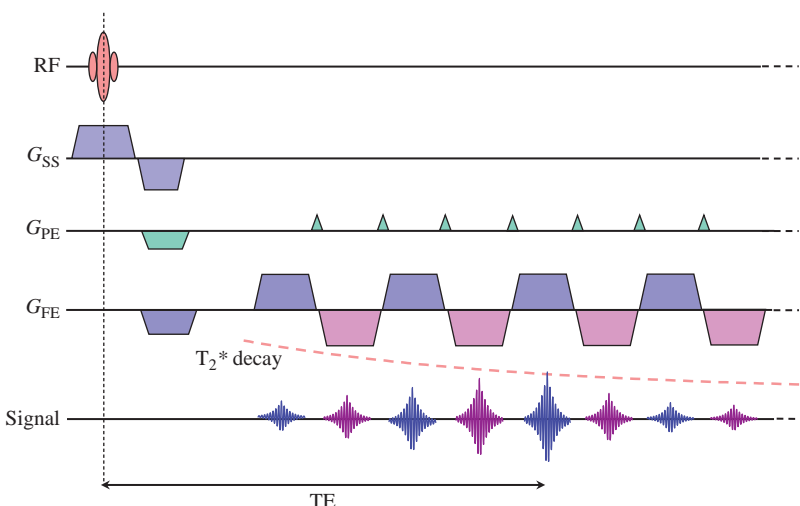


Figure 13.27 ‘Blipped’ single-shot GE-EPI sequence. In practice 64–128 echoes would be used.

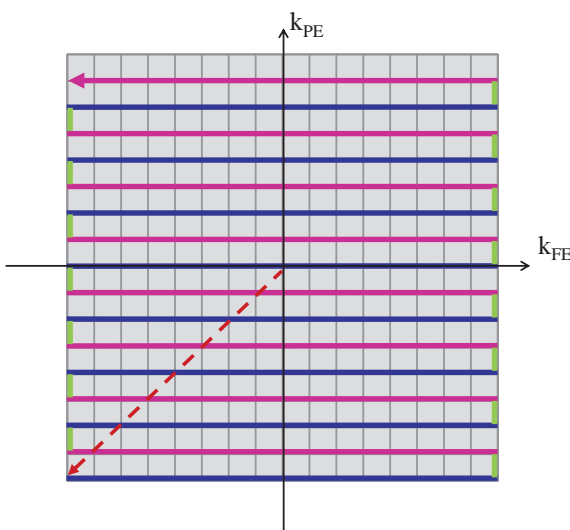


Figure 13.28 k-space trajectory for gradient echo EPI.

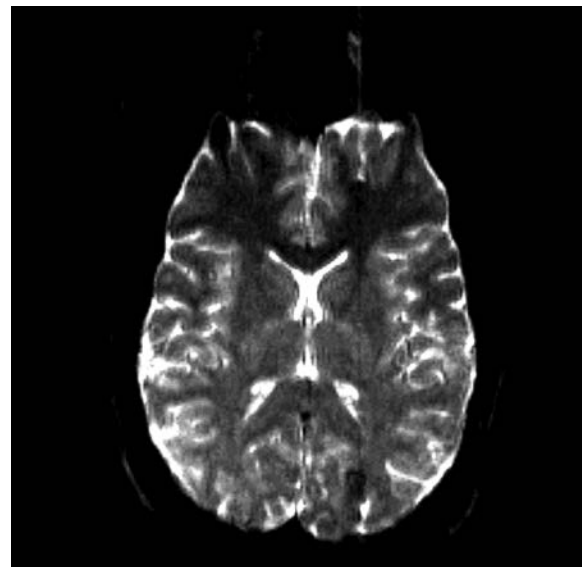


Figure 13.29 Gradient echo EPI image used for BOLD ‘brain activation’ imaging.

constant-amplitude gradient lobe, or ‘blip’, after each frequency-encode gradient reversal. Figure 13.28 shows the corresponding k-space trajectory.

GE-EPI consists of a lengthy series of gradient echoes, symmetrical about the centre of k-space. This results in a relatively long (effective) TE and the image contrast of GE-EPI is consequently T₂^{*}-weighted and exhibits a strong sensitivity to susceptibility variations (Figure 13.29). This, together with its speed, makes it the sequence of choice for BOLD (Blood Oxygenation Level Dependent) fMRI studies, considered in Chapter 18.

To run successfully, EPI requires high-performance gradients. EPI suffers from a number of inherent limitations in image quality, including relatively low spatial resolution and spatial distortions.

GE-EPI artefacts are similar in nature to those from the spin-echo variant, considered in Section 12.5.3.

An alternative approach to imaging tissue susceptibility differences is SWI (Susceptibility-Weighted Imaging). This yields high-resolution 3D images that are sensitive to small vessels and micro-bleeds in the brain. See Chapter 15 for details and clinical usage of SWI.

See also:

- How frequency- and phase-encoding gradients work: Chapter 8
- Basic image contrast: Chapter 3
- Pulse sequences for angiography and cardiac imaging: Chapters 15 and 16.

Further Reading

- Bernstein MA, King KF and Zhou XJ (2004) *Handbook of MRI Pulse Sequences*. London: Elsevier Academic Press.
- Brown MA and Semelka RC (1999) ‘MR imaging abbreviations, definitions and descriptions: a review’. *Radiology* 213:647–662.
- Brown RW, Cheng YCN, Haacke EM, Thompson MR and Venkatesan R (2014) *Magnetic Resonance Imaging*:

Physical Principles and Sequence Design, 2nd edn. Hoboken, NJ: John Wiley & Sons, chapters 18 and 26.

Elster AD and Burdette JH (2001) *Questions and Answers in Magnetic Resonance Imaging*, 2nd edn. London: Mosby-Yearbook, chapters 5 and 12. Also on the web at <http://mri-q.com> [accessed 23 March 2015].

Haacke EM and Tkach JA (1990) ‘Fast MR imaging: techniques and

clinical applications’. *Am J Roentgen* 155:951–964.

Liney G (2011) *MRI from A to Z*, 2nd edn. London: Springer-Verlag.

Mansfield P and Maudsley AA (1977) ‘Medical imaging by NMR’. *Br J Radiol* 50:188–194.

Twieg DB (1983) ‘The k-trajectory formulation of the NMR imaging process with applications in analysis and synthesis of imaging methods’. *Med Phys* 10:610–623.

The Parallel Universe: Parallel Imaging and Novel Acquisition Techniques

14.1 Introduction

As Figure 14.1 shows, in order to halve the scan time, the gradient slew rate must be quadrupled. Producing higher and higher gradient slew rates presents significant engineering challenges. However, we will also see in Chapter 20 that rapidly switched fields can lead to peripheral nerve stimulation, so physiology rather than physics may ultimately limit scanner speed. So does this mean fast imaging development has ground to a standstill? Surprisingly not, as even this fundamental limitation can be overcome, (or rather, circumvented) by using parallel imaging and reconstruction techniques together with phased array technology for even faster scanning. It must be stressed that parallel imaging methods are not sequences, but entirely new ways of acquiring and reconstructing images. The two classic formulations of parallel imaging are SMASH and SENSE, working in k-space and image space respectively. This chapter will explain the various types of parallel imaging and other novel reconstruction and acquisition

techniques, how they work, what advantages they provide and the image quality trade-offs involved.

In this chapter we will see that parallel imaging

- makes MR acquisitions faster by a factor known as the reduction factor R , by reducing the number of phase-encode steps you need to actually acquire an image;
- can be applied to any existing MR sequence, including EPI;
- is enabled by phased array technology and may be performed in k-space or in image space;
- involves an image quality trade-off.

Additionally

- non-Cartesian acquisition methods can offer some advantages such as very short echo times, self-navigation and increased SNR;
- compressed sensing is the next speed-up revolution in MRI;
- you will also learn lots of lovely new acronyms!

14.2 Groundwork

To understand parallel imaging we need to revisit two concepts considered earlier in the book, namely: array coils (Chapter 10) and phase encoding (Chapter 8). If you are confident you understand both of these you can skip forward to Section 14.2.3.

14.2.1 Simple Conceptual Explanation of k-Space and Phase Encoding

Phase encoding was explained in detail in Chapter 8. For the present purpose we need to see that each phase-encode gradient step adds a further 2π of phase change across the image field of view (Figure 14.2). Alternatively, we can say that each line of k-space is separated by $2\pi/\text{FOV}$. Each phase-encoding step sensitizes the MR acquisition to specific patterns of signal distribution, or in other words, picks out a particular

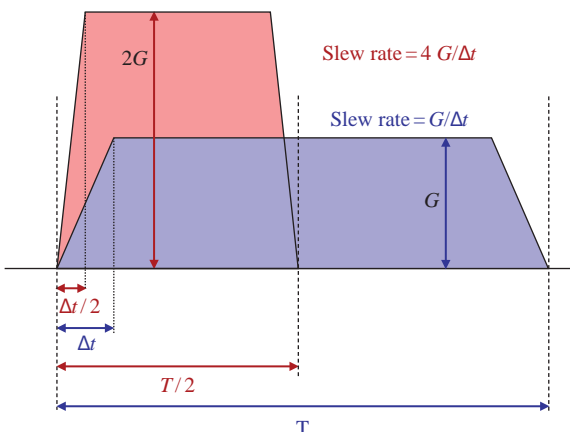


Figure 14.1 In order to halve the acquisition time while maintaining the same resolution and field of view, the gradient strength must be doubled and the gradient slew rate quadrupled.

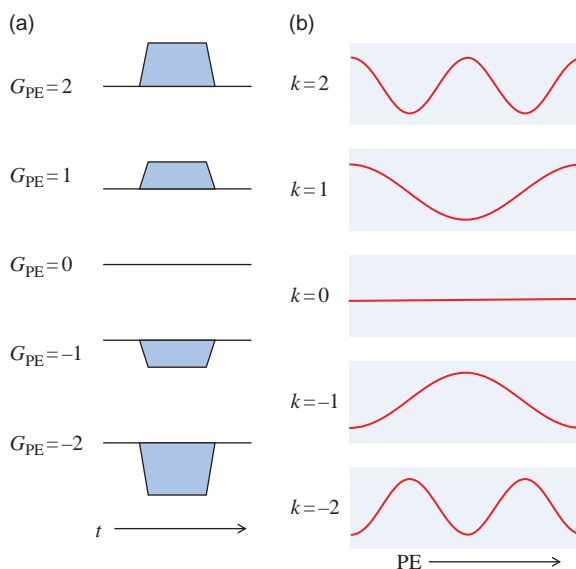


Figure 14.2 The effect of phase encoding on a uniform region of signal-producing material: (a) phase-encode gradient waveforms, (b) signal phase variation across the field of view.

spatial frequency of the image. The steps of phase encoding and signal acquisition need to be repeated until k -space is filled, prior to Fourier transformation to generate the final image. If we double the separation between the lines of k -space by skipping lines of k -space we halve the image field of view and if the imaged object exceeds this, aliasing or foldover will occur.

14.2.2 Basic Principles of Phased Arrays

The conventional use of phased array coils is to achieve superior SNR. Each array element is sensitive to a smaller volume of tissue than an equivalent larger coil. Inductively coupled noise, which usually dominates the noise formation process, has a theoretical strong dependence on the volume of tissue to which the coil is sensitive. The smaller array elements thus 'see' less noise than larger coils (Figure 14.3). Each array element has a separate receiver channel, with up to 32 channels being common. Additionally, arrays benefit from the combination of uncorrelated noise sources offering the same sort of advantage that quadrature coils have over linear coils (see Section 10.4.3). Separate reconstructions are carried out for each array element, with the final image being a combination of these. The increased SNR can be used to

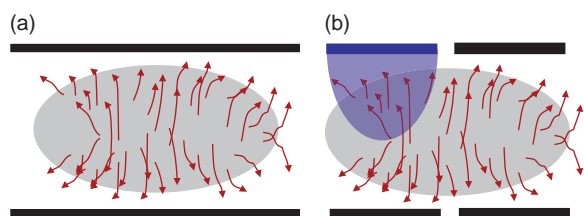


Figure 14.3 The inductive noise-reduction principle of phased array coils. (a) A larger single coil 'sees' more noise from the greater volume of tissue it surrounds. (b) Smaller coil elements are less sensitive to inductive noise while adequate signal coverage is achieved by combining images from the separate elements.

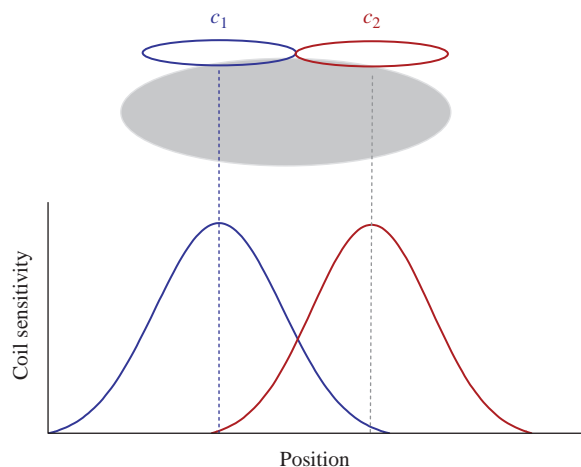


Figure 14.4 Coil sensitivity profiles: two loop surface coils.

achieve higher resolution, shorter scan times, greater anatomical coverage or a combination of all three. Many clinical applications would be impossible without array coils. In parallel imaging we are going to trade part of the superior SNR to give us shorter acquisition times.

14.2.3 Coil Sensitivity Profiles

In the conventional use of phased arrays, the images produced from each element are combined to form the resultant image. The spatial variations inherent to the individual coil responses, or the coil sensitivities, have been combined. This is illustrated in Figure 14.4, where individual sensitivity profiles are shown for two coils. The determination of array element sensitivity profiles or maps and the linear combination of signals from array elements are both crucial aspects of parallel imaging.

14.3 Making SENSE: Parallel Imaging in Image Space

In parallel imaging we are going to speed up scanning by acquiring fewer lines of k-space and using our knowledge of the array coils used to unravel the aliased images or to generate the missing lines of k-space. The former technique employs parallel imaging reconstruction in image space, the latter in k-space. In both methods the scan time is reduced by a reduction factor R :

$$\text{Scan time}_{2D} = \frac{\text{NSA} \times \text{TR} \times N_{PE}}{R \times \text{ETL}}$$

where N_{PE} is the full (unreduced) PE matrix size and ETL the echo train length or turbo factor (where appropriate) for 2D scans. For 3D scans

$$\text{Scan time}_{3D} = \frac{\text{NSA} \times \text{TR} \times N_{PE} \times N_{SS}}{R_{PE} \times R_{SS} \times \text{ETL}}$$

where R_{PE} and R_{SS} are reduction factors for each phase-encode direction.

14.3.1 SENSE

SENSE (SENSitivity Encoding) was the first parallel imaging technique to be realized commercially (by Philips). ASSET on GE Healthcare scanners and SPEEDER (Toshiba) are broadly similar. In SENSE, a reduced k-space is acquired by using fewer phase-encode gradient steps in conjunction with phased

array coil acquisition. A mathematical description is given in Box 'Making SENSE with Maths'.

SENSE reconstruction works post-Fourier transformation on the images. In a conventional acquisition if we omit every second phase-encode step we will halve the scan time, but will get an aliased image. In parts of the image aliased signal is superimposed upon unaliased signal. However, the position in the resultant image of the aliased signal contribution is entirely predictable from knowledge of the field of view. What is unknown is the intensity of the aliased component. The trick in SENSE is to apply knowledge of the sensitivities of the coil elements to calculate the aliased signal component at each point.

An example with a reduction factor of 2 and two coil elements is shown in Figure 14.5, where the point P in the aliased image can be seen to be composed of signal originating from two different locations: $S(y)$ from the true location y and $S(y + \Delta Y)$ from the aliased position. Provided we know the coil sensitivities we can calculate the true and the displaced signal components. Having computed the aliased signal component $S(y + \Delta Y)$, it can be reassigned to its proper location.

Figure 14.6 illustrates the acquisition and reconstruction with clinical images. First, sensitivity maps are generated for each coil element from a short, low-resolution calibration scan, then an aliased image is reconstructed for each element before being fed into the SENSE reconstructor to produce the final image.

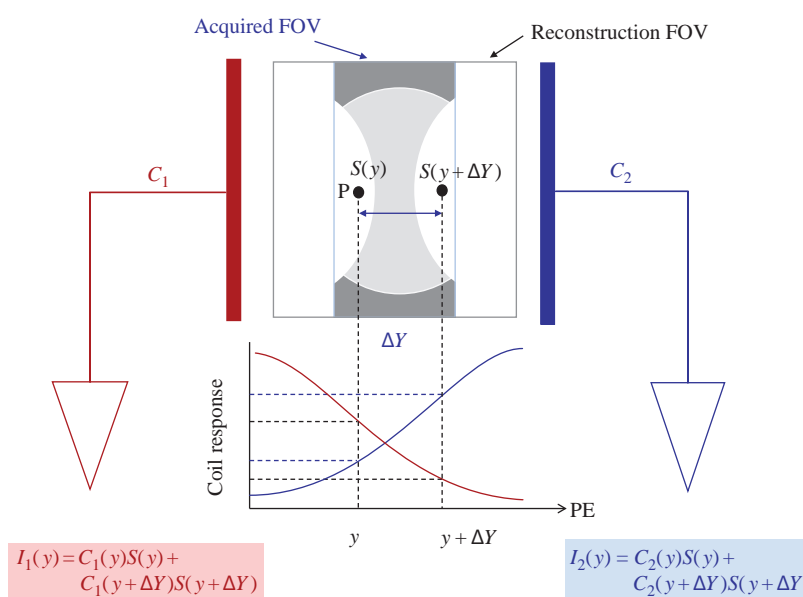


Figure 14.5 Image reconstruction in SENSE. Prior knowledge of the coil sensitivity profiles permits the unfolding of the image.

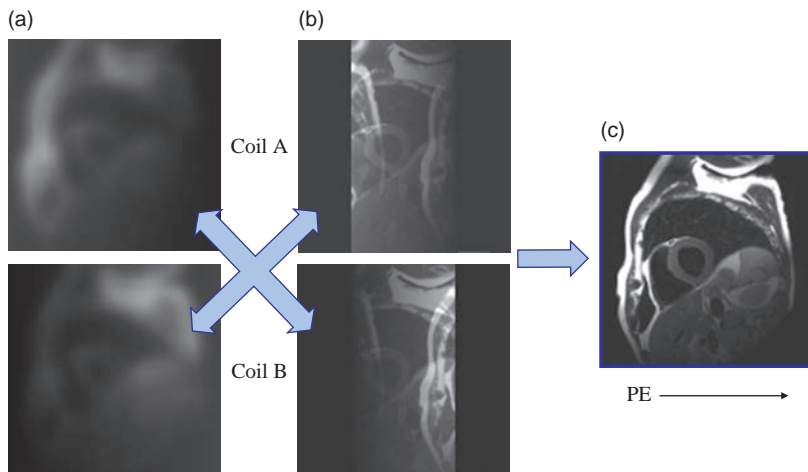


Figure 14.6 Example of SENSE reconstruction steps: (a) reference scans, (b) folded images from each element, (c) reconstructed SENSE image.

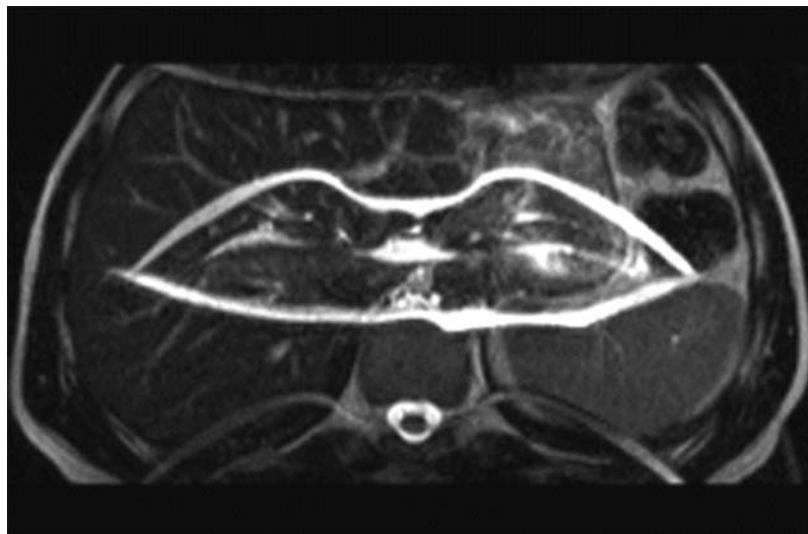


Figure 14.7 SENSE reconstruction 'hot lips' artefact resulting from attempting to use SENSE when the unfolded field of view does not contain all of the anatomical region of interest.

The principle can be applied for a higher reduction factor R as shown in Box 'Making SENSE with Maths'. For SENSE to work at all, there must be a coil sensitivity variation along the phase-encode direction. For array coils with appropriate geometry and in 3D FT acquisitions SENSE can be applied in both phase-encode directions, thereby increasing the overall reduction factor.

Another feature of SENSE is that the reduction factor can be any value between 1 and the number of coil elements. It is not restricted to integer values. In prescribing a SENSE scan the operator chooses the reconstructed FOV. This must encompass all the signal-producing material, otherwise serious artefacts will occur (Figure 14.7). In other words, SENSE cannot

tolerate any inherent aliasing. The calibration procedure is explained further in Box 'To Auto-Calibrate or Not'.

Making SENSE with Maths

In the two-coil example of Figure 14.5, the signal at point y is made up of the correct signal for this position and one aliased signal. We can write

$$\begin{aligned} I_1(y) &= C_1(y)S(y) + C_1(y + \Delta Y)S(y + \Delta Y) \\ I_2(y) &= C_2(y)S(y) + C_2(y + \Delta Y)S(y + \Delta Y) \end{aligned}$$

where I_1 and I_2 are the image intensities measured for each coil which have sensitivities C_1 and C_2 . Hence we have two simultaneous equations and

two unknowns which can be solved exactly by algebra. The aliasing distance ΔY is

$$\Delta Y = \frac{\text{FOV}_{\text{rec}}}{R}$$

where FOV_{rec} is the reconstruction field of view for PE and R is the SENSE reduction factor. With higher R , we may have two or more aliased signals at point y as well as the correct signal, and we can write

$$\begin{aligned} tI_1(y) &= C_1(y)S(y) + C_1(y + \Delta Y)S(y + \Delta Y) \\ &\quad + \cdots + C_1(y + n_A\Delta Y)S(y + n_A\Delta Y) \\ I_2(y) &= C_2(y)S(y) + C_2(y + \Delta Y)S(y + \Delta Y) \\ &\quad + \cdots + C_2(y + n_A\Delta Y)S(y + n_A\Delta Y) \end{aligned}$$

where n_A is the number of aliased signals which is spatially variant and depends on the size of the object being imaged. If the object exactly fills the reconstructed FOV, then $n_A = R$ at all points; in all other cases $n_A \leq R$. We can formalize this in terms of image intensities $I_j(x, y)$ for each of J coil elements:

$$I_j(x, y) = \sum_{n=0}^{n_A} C_j(x, y + n\Delta Y)S(x, y + n\Delta Y)$$

If there are L coil elements, we can write L simultaneous equations as above, most conveniently represented in a matrix equation as

$$\begin{aligned} &\begin{bmatrix} I_1(x, y) \\ I_2(x, y) \\ \vdots \\ I_L(x, y) \end{bmatrix} \\ &= \begin{bmatrix} C_1(x, y) & C_1(x, y + \Delta Y) & \cdots & C_1(x, y + n_A\Delta Y) \\ C_2(x, y) & C_2(x, y + \Delta Y) & \cdots & C_2(x, y + n_A\Delta Y) \\ \vdots & \vdots & \ddots & \vdots \\ C_L(x, y) & C_L(x, y + \Delta Y) & \cdots & C_L(x, y + n_A\Delta Y) \end{bmatrix} \cdot \begin{bmatrix} S(x, y) \\ S(x, y + \Delta Y) \\ \vdots \\ S(x, y + n_A\Delta Y) \end{bmatrix} \end{aligned}$$

which is more economically expressed as

$$\mathbf{I} = \mathbf{CS}$$

and the solution arises from inverting the $L \times n_A$ element matrix C to obtain the true image signal $S(x, y)$ for every pixel. This is always possible if there are at least as many coil elements as the maximum number of aliased signals and if the coil sensitivities are sufficiently unique. Notice that since $R > n_A$ for the majority of images, it is possible for R to be greater than the number of elements in the coil.

Prescan calibration data, or as in the case of mSENSE, reference lines, are required to obtain the coil sensitivities.

14.3.2 mSENSE

Modified SENSE (mSENSE) is a version of SENSE which does not require a separate calibration scan. Instead, additional lines are acquired at the centre of k-space during the diagnostic scan (Figure 14.8). These central lines are extracted for each coil element and used on their own to reconstruct low-resolution, unaliased images from each coil element which may then be used to provide sensitivity maps. A SENSE reconstruction algorithm can then be used to unfold the images from the sparse k-space data (the red arrows in Figure 14.8). The full-time saving by the reduction factor R is not achieved because of the additional lines required for calibration.

To Auto-Calibrate or Not

In the calibration method used by SENSE, low-resolution images are acquired from each array element and also from the body coil. The array element images are divided by the body coil image (to remove sensitivity variations due to anatomy rather than coil response). Then various image processing steps (thresholding, filtering, extrapolation, smoothing) are performed to produce the sensitivity map for each coil. Note that due to the thresholding step, the background noise is suppressed in SENSE images.

The calibration scan takes about 20 s and once acquired can be used on all subsequent parallel image acquisitions provided the geometry or the patient's position does not change. ASSET (GE) and SPEEDER (Toshiba) also require calibration scans. ASSET does not employ the body coil division step.

In mSENSE, GRAPPA and ARC (see Section 14.4.3) the calibration data are inherent to the main scan acquisition. No body coil image is required and there is no image division. This means that the background noise is not suppressed. Having the calibration (ACS) lines integral to the acquisition also means there will be no misregistration problem if the patient moves between scans. However, the scan time will be increased by the number of ACS lines used, thus the full reduction factor will not be realized. In GRAPPA, the ACS lines may also be included in the reconstruction, giving a slight increase in SNR.

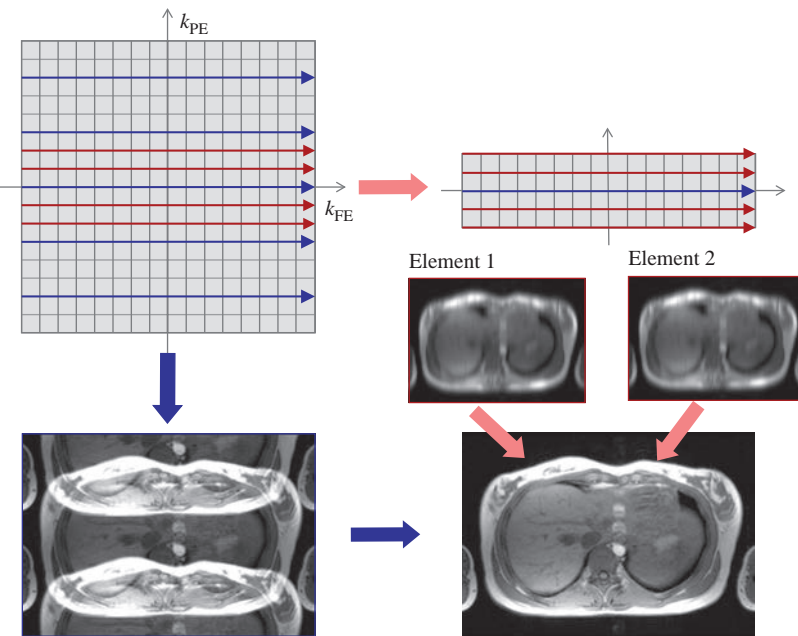


Figure 14.8 Modified SENSE (mSENSE). The centre of k-space is fully sampled and extracted for each coil to form a low-resolution image which can be used as a sensitivity map in a SENSE reconstruction. Images courtesy of Siemens Healthcare.

14.4 SMASH Hits: Parallel Imaging in k-Space

Historically SMASH (SiMultaneous Acquisition of Spatial Harmonics) was the first parallel imaging technique. The term spatial harmonics refers to the spatial frequencies: SMASH works in k-space. It uses combinations of array coil element sensitivities to create virtual phase encoding. In principle it can be applied to any sequence. Just like SENSE, it reduces the number of phase-encode gradient steps you need, giving a scan time reduction by factor R .

14.4.1 SMASH

Looking back at Figure 14.2 we see the signal distributions in the phase-encode direction for various values of k . The principle of SMASH is simply to generate a similar pseudo k-space phase encoding by using the spatial response of the RF reception. In practice this means using arrays of coils and combining the various elements to obtain the required sinusoidal variations in response across space.

Figure 14.9 shows how two simple linear coils could be combined to produce either a uniform response by adding the signals together, or a non-uniform response which resembles a sinusoidal variation by subtraction of the coil sensitivities. In other words, by the appropriate combination of signals from

different coil elements we can obtain a spatial signal distribution which can be made to match either zero spatial frequency (uniform response, $k = 0$) or the lowest non-zero spatial frequency ($k = 1$). In practice weighted combinations of the coil sensitivities are used. Figure 14.10 shows the coil weights necessary to produce $k = 0$ and $k = 2$ spatial harmonics for a notional eight-element array coil. Further details are given in Box 'More about spatial harmonics'.

This use of RF reception properties to achieve spatial encoding opens the intriguing prospect of an MR acquisition without the use of any phase-encode gradients. The RF engineering required to produce a sufficiently complex phased array coil is just too demanding at the moment – the coil would need at least 128 elements spread out along the phase-encode direction! Consequently, in SMASH a combination of phase encoding with gradients, and virtual phase encoding (with array coils) is applied. This is illustrated in Figure 14.11, showing the phase change over the FOV for the $k = 2$ PE gradient from the uniform coil combination ($\Delta k = 0$). By combining the coils differently a modified response ($\Delta k = 1$) is obtained and when added to the effect of the gradient produces a line of virtual phase encoding with $k = 3$. Figure 14.12 shows combinations of gradient and array coil phase encoding to generate six lines of k-space from only three actual acquisitions. In this

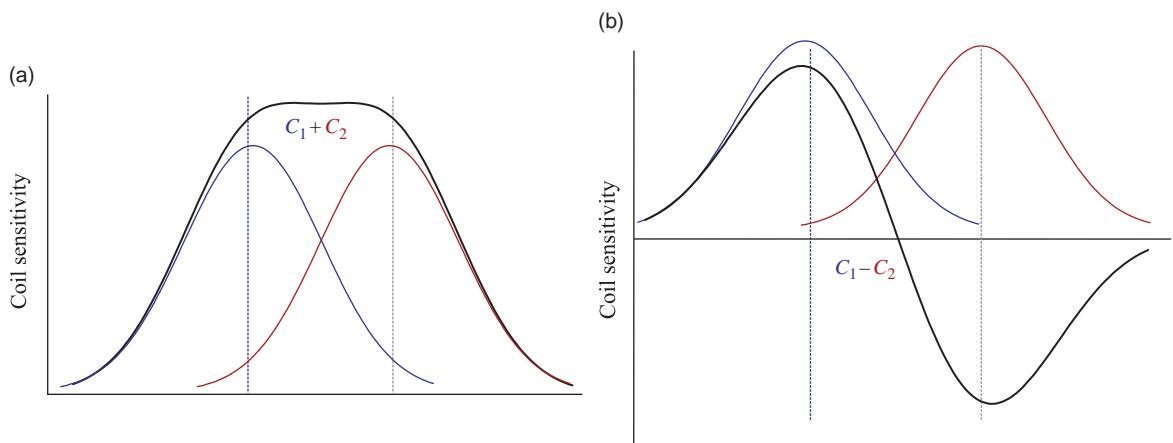


Figure 14.9 Coil sensitivity profile combinations for two loop surface coils: (a) coil combination (addition) to achieve uniform spatial response, (b) coil combination (subtraction) to produce non-uniform spatial response.

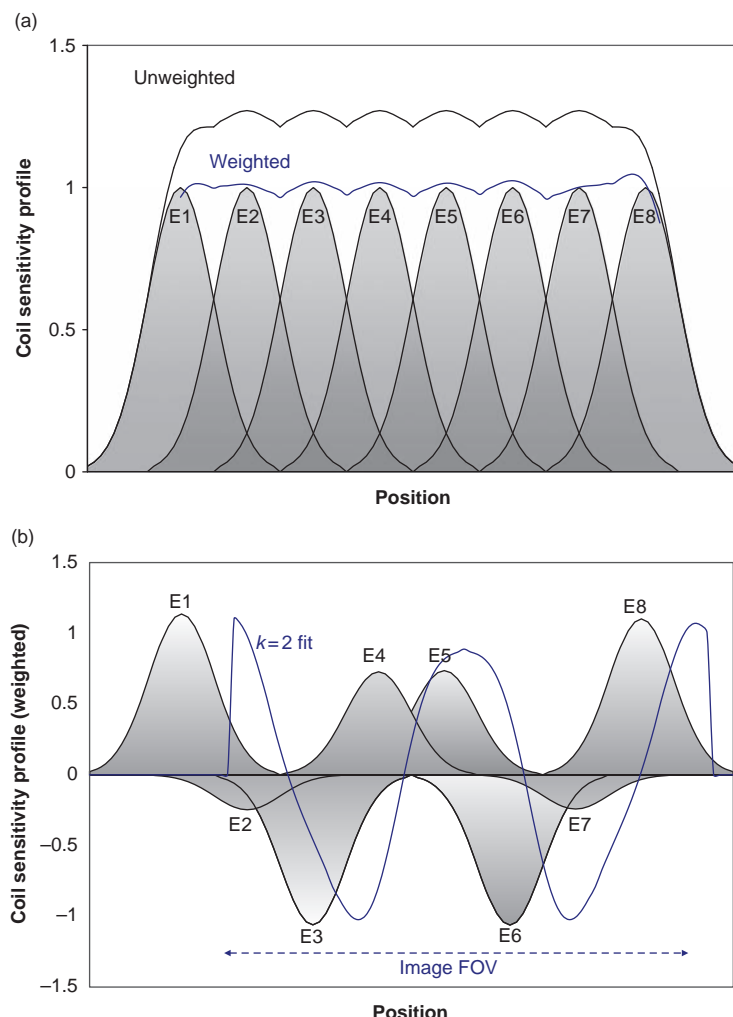


Figure 14.10 (a) Unweighted and optimally weighted coil combinations to produce a uniform ($k = 0$) response for an eight-element array coil. (b) Weighted coil sensitivity functions to produce the second harmonic ($k = 2$). Shaded areas represent the coil sensitivity profiles multiplied by their respective weight.

example, then, we can halve the number of phase-encode gradient steps required, and therefore halve the number of excitations required and halve the scan time. The reduction factor R is therefore equal to 2.

The acquisition in k-space is illustrated in Figure 14.13a, where we see that k-space is filled completely using a sparser set of phase-encode gradient steps (represented by the blue arrows) and the synthesizing of virtual phase-encode lines (the dotted lines) from the combinations of the coils.

More About Spatial Harmonics

The purpose of phase encoding is to produce a linearly varying phase change to the MR signal along the phase-encode axis, as illustrated in the clockface

diagram in Figure 14.11. In order to generate the rotational nature of phase encoding, we need to add sine and cosine functions (see appendices A.2 and A.5). Mathematically this is:

$$\exp(i2\pi yk_{PE}) = \cos(2\pi yk_{PE}) + i\sin(2\pi yk_{PE})$$

remembering that k-space uses complex maths. The first harmonics are shown in Figure 14.14 for the example of an eight-element coil, along with the $\Delta k = 1$ combination. The figure shows both the calculated harmonics and the ideal ones.

Figure 14.14 also shows the higher harmonic, $\Delta k = 3$, for the same eight-element coil, showing that significant deviations exist between the ideal and the fitted harmonics. Errors in the generation of the coefficients will result in image artefacts (see Figure 14.19).

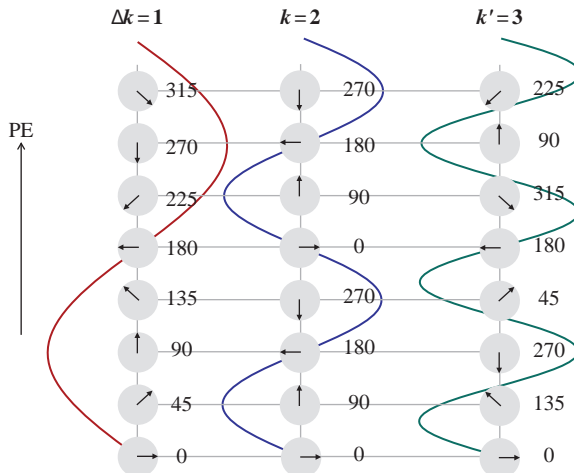


Figure 14.11 Virtual phase encoding from combinations of coil sensitivities ($\Delta k = 1$) combined with an actual phase encoding line ($k = 2$) produces an additional line of phase-encoded signal $k' = 3$.

14.4.2 Auto-Calibrating SMASH

The constraints of coil design make true SMASH very hard to realize on a clinical scanner. In order to make SMASH techniques more applicable to real phased array coils a change of strategy was needed. Instead of making coils to give a ‘spatial frequency-type’ signal response, why not accept whatever spatial sensitivity response the coils actually give and then work out how to combine their signals to get the desired lines of k-space? The first technique to do this was Auto-SMASH. The principle is shown in Figure 14.13b, where a reduced k-space is acquired by skipping lines (e.g. every third line to give a reduction factor $R = 3$). However, we also acquire additional ‘auto-calibrating signal’ (ACS) lines near the centre of k-space. The scanner then

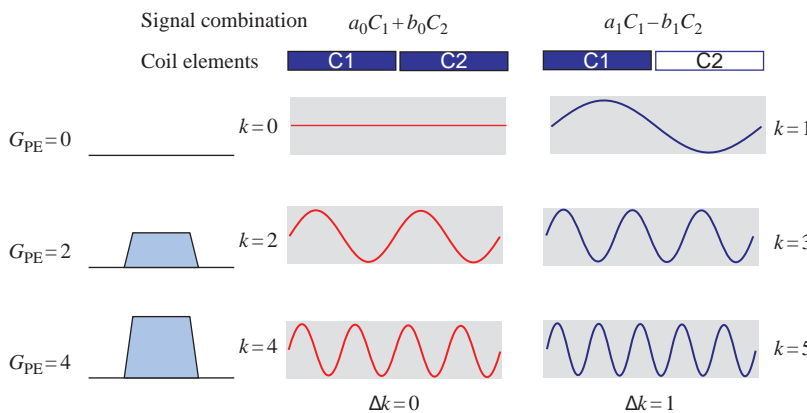


Figure 14.12 The addition of gradient phase-encoding and RF coil combinations produces additional virtual lines of k-space. In this example two lines of k-space can be acquired per gradient, the original with $\Delta k = 0$ and one additional with $\Delta k = 1$.

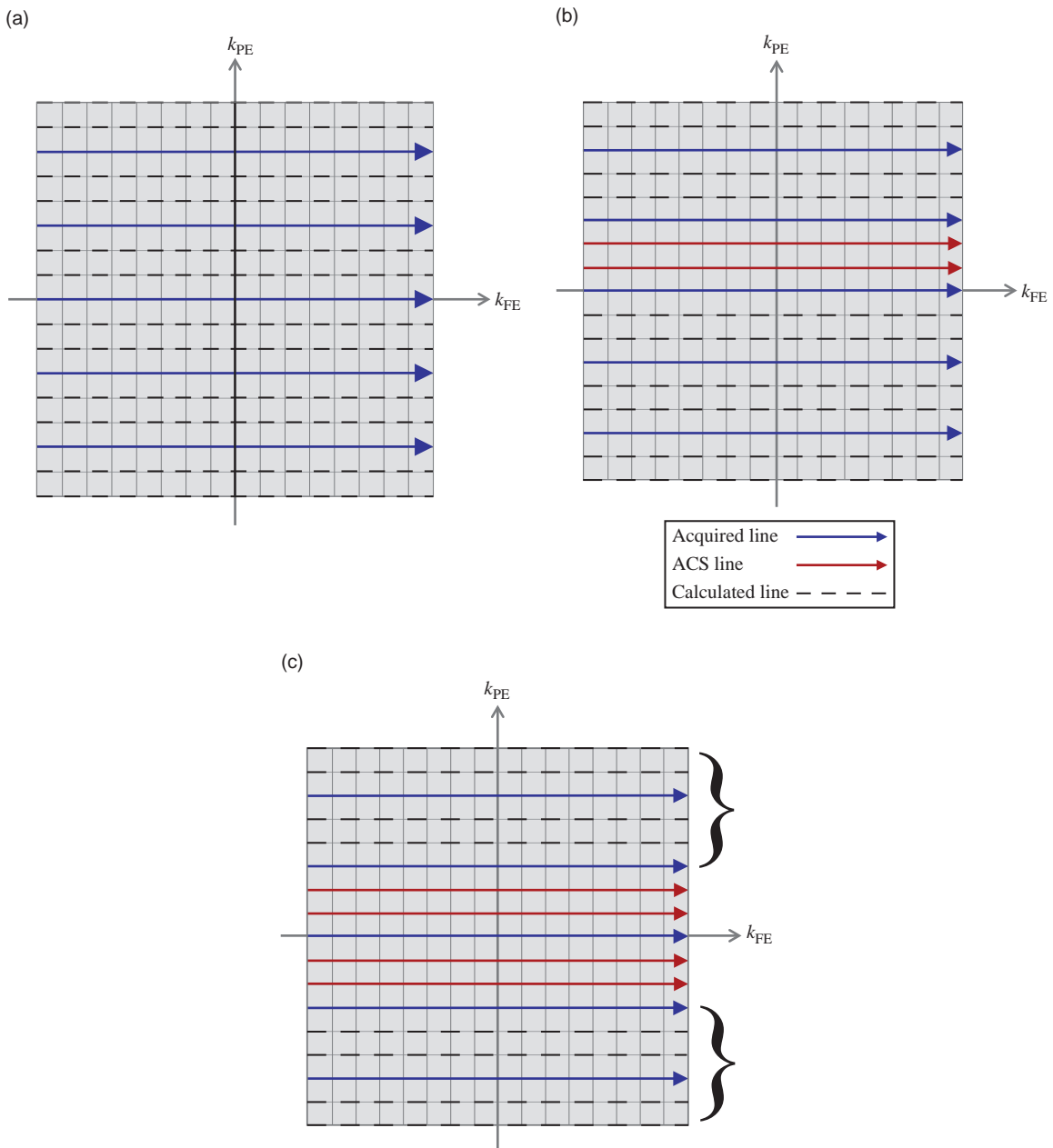


Figure 14.13 k-space scheme for (a) SMASH, (b) Auto-SMASH with two ACS lines and (c) VD-Auto-SMASH where an outer reduction factor (ORF) applies away from the centre of k-space. In each example $R = 3$. Arrowed lines are acquired with gradients, the interspersed (non-arrowed) lines are computed from combinations of the coil element signals. The fully filled k-space is Fourier transformed to generate the image.

computes from the signals acquired from the array coil elements the nearest linear combination of these signals to match the actual acquired ACS line. The coefficients calculated can then be applied throughout the remainder of k-space to fill in the unacquired lines, before standard reconstruction by

Fourier transformation. In practice a minimum of $R-1$ ACS lines are required.

Variable density Auto-SMASH (VD-Auto-SMASH) extends the above principle, but adds additional ACS lines, illustrated in Figure 14.13c. This makes it more robust from artefacts and

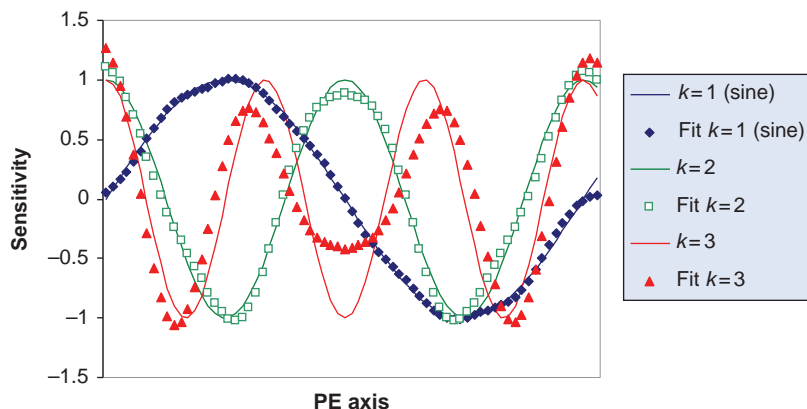


Figure 14.14 Fitted (calculated) and ideal sensitivity profiles for $\Delta k = 1$ (sine) and cosine profiles for $\Delta k = 2$ and 3. Solid lines show the ideal response, points show the weighted fits for an eight-element array.

reconstruction errors. The centre of k-space is more highly sampled and we can talk of an inner and an outer reduction factor. The scan time compared with Auto-SMASH will be longer because of the additional ACS lines. As in Auto-SMASH, a composite k-space (i.e. just one for all the array elements) is acquired and estimated.

SMASH and k-Space Methods

As usual in MRI, those of a mathematical nature get it easy as the whole thing can be reduced to one equation:

$$S(k_x, k_y) = \iint \rho(x, y) \cdot C(x, y) \cdot \exp\left(\frac{-t}{T_2^*}\right) \cdot \exp(i2\pi x k_{FE}) \cdot \exp(i2\pi y k_{PE}) \cdot dx dy$$

This is similar to the equation for 2D FT given way back in Chapter 7, but with one additional term: $C(x, y)$ which represents the coil sensitivities. For an array of coils with sensitivities $C_j(x, y)$

$$S(k_x, k_y) = \iint \rho(x, y) \cdot \left[\sum_j n_j C_j(x, y) \right] \cdot \exp\left(\frac{-t}{T_2^*}\right) \cdot \exp(i2\pi x k_{FE}) \cdot \exp(i2\pi y k_{PE}) \cdot dx dy = \sum_j n_j \cdot S_j(k_{FE}, k_{PE})$$

where n_j are weighting factors for a superposition of coil and signal sensitivities. By judicious choice of weights we can obtain the combinations

$$\sum_j n_j C_j(x, y) = 1 \quad \text{or} \quad \sum_j n'_j C_j(x, y) = \exp(i2\pi \cdot y \Delta k_{PE})$$

where Δk is a step in spatial frequency. Using the first of these yields the standard 2D FT equation for a uniform coil. Using the second gives

$$S' = \iint \rho(x, y) \cdot \exp\left(\frac{-t}{T_2^*}\right) \cdot \exp(i2\pi x k_{FE}) \cdot \exp(i2\pi y [k_{PE} + \Delta k_{PE}]) \cdot dx dy = S(k_{FE}, k_{PE} + \Delta k_{PE})$$

which is the acquired line of k-space offset by Δk . With the appropriate linear combination of coil signals we can therefore acquire purely gradient-phase-encoded signals or we can calculate additional virtual lines of k-space without having to acquire them.

In SMASH the sensitivities are computed from a calibration scan. In Auto-SMASH and GRAPPA additional auto-calibration signal (ACS) lines are acquired and the coil weights calculated from a fit of the ACS data with the known (acquired) neighbouring line or lines:

$$S(k_{FE}, k'_{PE}) = \sum_j n_j S_j(k_{FE}, k_{PE})$$

thus the coefficients n_j can be calculated to give a particular k-space offset. ARC extends this to three dimensions.

14.4.3 GRAPPA and ARC

GRAPPA (GeneRalized Auto-calibrating Partially Parallel Acquisitions) is a further extension of the Auto-SMASH principle. GRAPPA is illustrated in Figure 14.15. It deploys multiple ACS lines and uses data from every coil for the fitting of the appropriate weights for each ACS line. A separate sub-k-space

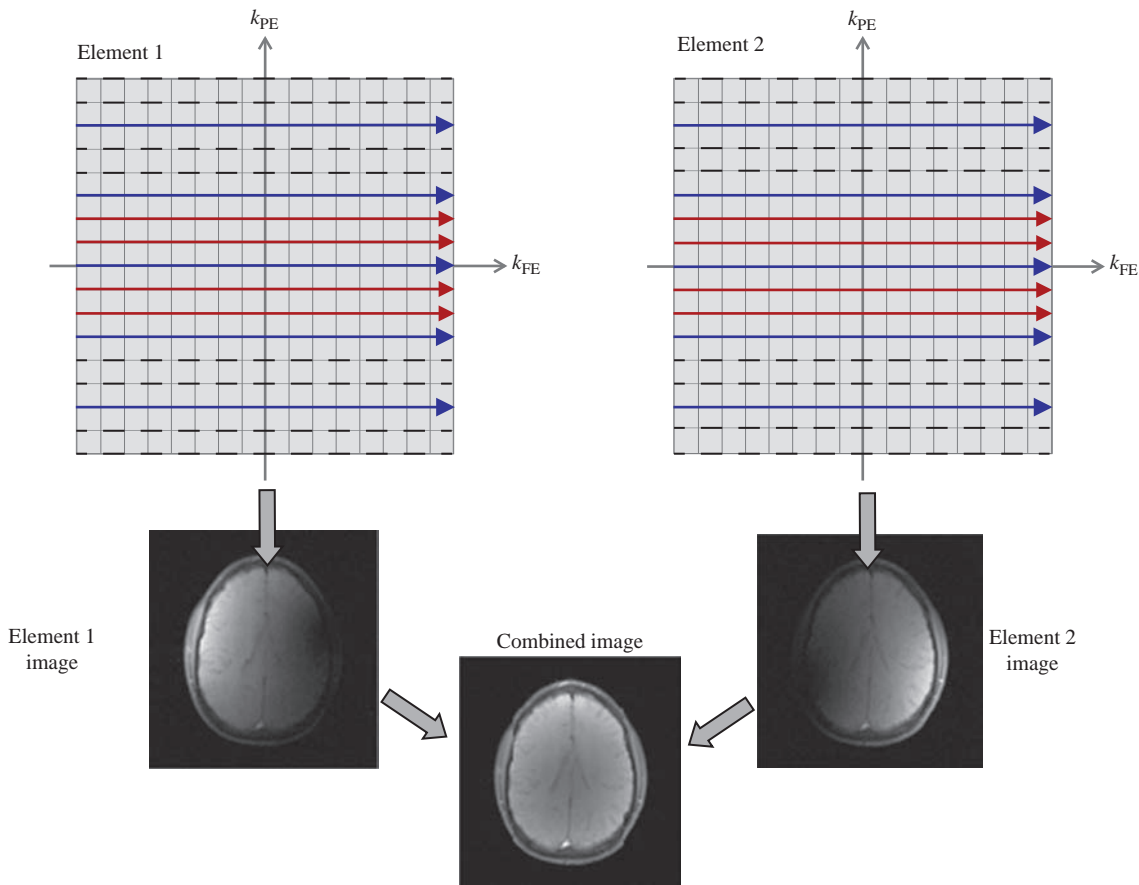


Figure 14.15 GRAPPA acquisition and reconstruction with $R = 2$. A separate k -space for each coil element is generated using multiple ACS lines and signal combinations from all the coil elements. Each element's k -space is Fourier transformed to generate images from each element which are then combined as in conventional phased array reconstruction.

is filled for each array element, which is then reconstructed, giving an image for each element. These separate images are then combined by the usual ‘sum-of-squares’ algorithm used in conventional array coil reconstructions. GRAPPA has been implemented commercially in Siemens scanners where the reduction factor is known as the iPAT factor and parallel imaging (both mSENSE and GRAPPA) goes under the generic name iPAT (where PAT stands for Parallel Acquisition Technique and the ‘i’ stands for ‘integrated’ – but we suspect is really just to appear trendy). ARC (Auto-calibrating Reconstruction for Cartesian imaging) is a 3D variant of this technique implemented on GE Healthcare scanners.

14.4.4 Air on a g-Factor: CAIPIRINHA

The principles of undersampling of k -space used in parallel imaging for 3D scans can be extended to more

exotic acquisition patterns. For a given R factor, the g-factor (see Section 14.6) can be improved by increasing the distance between k -space points, particularly by introducing some asymmetry. In SENSE and GRAPPA and their equivalents we skip lines in both k_y and k_z , producing a regularly undersampled 3D k -space. Looking at Figure 14.16a we see a regularly undersampled k -space, looking at the k_y-k_z plane. However, other patterns are possible with the same undersampling factor, as shown in Figure 14.16b; we can characterize them by their diagonal shift Δ . As with simple ($\Delta = 0$) undersampled acquisitions, these patterns result in aliasing. However, the location of the aliasing can be better controlled and shifted to the edges of the FOV. This can result in a superior g-factor (see Figure 14.19), resulting in reduced artefacts, less dependence upon the coil array geometry and ultimately allowing the potential for higher acceleration

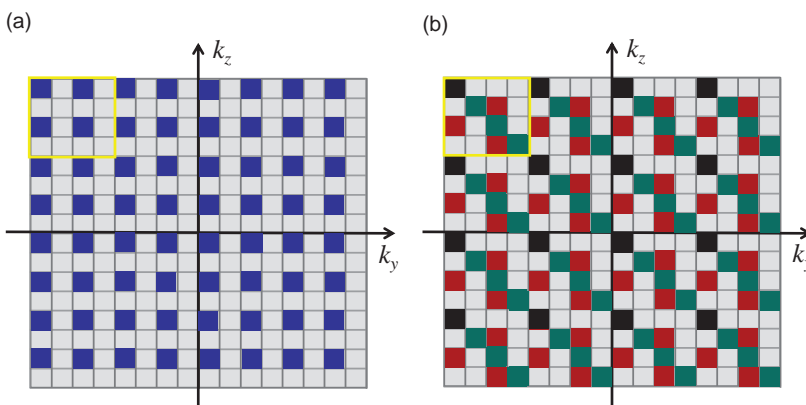


Figure 14.16 (a) Conventional parallel imaging k-space acquisition scheme in two PE directions with combined $R = 4$. (b) Two CAIPIRINHA k-space acquisition schemes, both with $R = 4$ and $\Delta = 1$, shown in green and red. The black points are acquired for both.

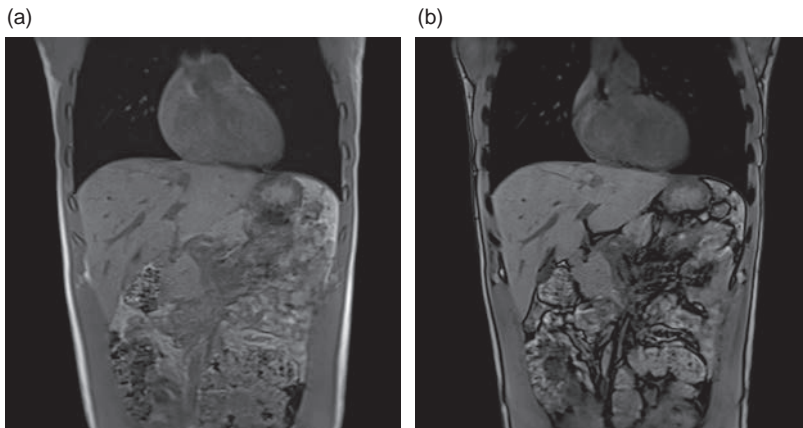


Figure 14.17 CAIPIRINHA images: (a) 3D-VIBE in-phase, (b) 3D-VIBE out-of-phase, reduction factor $2 \times 3 = 6$, 128 slices acquired in 20 s. Courtesy of Siemens Healthcare.

factors. This type of acquisition is commercially available on Siemens systems, under the name of CAIPIRINHA (Controlled Aliasing In Parallel Imaging Results IN Higher Acceleration). CAIPIRINHA uses a GRAPPA-style reconstruction, but SENSE can also be used (with the name ‘diamond SENSE’). Figure 14.17 shows some representative CAIPIRINHA images.

14.5 Undersampling by Simultaneous Multi-Slice Excitation

Undersampling in the slice direction works easily for 3D acquisitions, but it is less obvious to see how to undersample a 2D multi-slice acquisition. We can’t skip phase-encoding steps in the slice direction, because it isn’t part of the pulse sequence. However, we can use so-called multi-band RF pulses to generate simultaneously excited slices, two or more at a time.

Multi-band excitation has been around for a long time: it is used (on some systems) whenever you plan two parallel saturation bands (see Box ‘Seeing Double: Exciting More than One Slice’), and for a few years in the early 1990s it was a feature on GE Healthcare systems, called Phase Offset Multi-Planar (POMP). By modulating the phase of the RF excitation pulse, it is possible to produce slices with distinctly assigned phases, e.g. four slices can be excited at 0° , 90° , 180° and 270° . For (turbo) spin-echo scans, each of the 180° refocusing RF pulses also has to be phase-modulated.

Phase modulation of the different slices can be done in different ways. For example, in multi-slice GE imaging, phase modulation of the RF pulse can be used along with the cosine amplitude modulation. In EPI, a series of ‘blip’ gradients is added on the slice-select axis, coinciding with the normal phase-encode

Two slices excited simultaneously Overlapping images with FOV offset

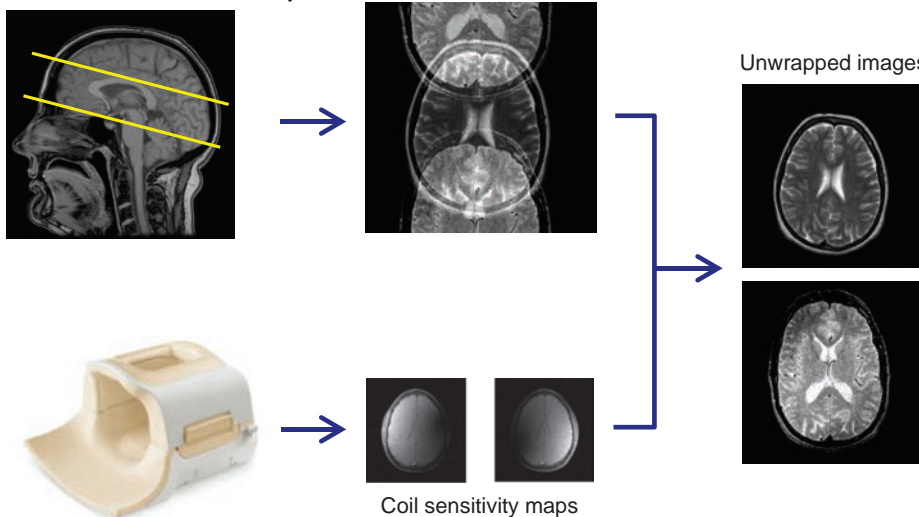


Figure 14.18 Principle of using controlled aliasing to separate simultaneously acquired slices.

blips. Fourier transformation of the signal from multi-band excitation in combination with phase-offsets will result in all the slices being aliased into a single image, with each slice offset in a controlled manner (by the Fourier transform shift theorem) within the field of view. If the coil sensitivities are known, it is possible to use a modified version of parallel reconstruction (i.e. the SENSE or GRAPPA algorithm) to separate the slices and generate the unaliased images (Figure 14.18). There must be sufficient separation of the receive coil elements along the slice direction, or separation of the excited slices, to preserve a low g-factor. At the time of writing, this technique is not commercially available, but it is known on Siemens systems as MS (Multi-Slice) CAIPIRINHA (even though there's really no relationship to the other CAIPIRINHA) and on other systems as Multi-Band (MB) SENSE.

In theory, simultaneous multi-slice excitation has no SNR disadvantage, unlike other parallel imaging methods. This is because the reduction factor R is compensated by the higher signal from N_{slices} being simultaneously excited (see Box 'SNR in Parallel Imaging'). However, in practice the g-factor will be slightly compromised by the geometry of the coil. Multi-band excitation can also be combined with in-plane GRAPPA or SENSE, provided the total g-factor is not increased too much.

Seeing Double: Exciting More than One Slice

Converting an excitation RF pulse to select two physical locations is achieved by multiplying it by a cosine function:

$$\text{FT}\{\cos(2\pi f_{\text{sep}}t)\} = \frac{\delta(f - f_{\text{sep}}) + \delta(f + f_{\text{sep}})}{2}$$

where f_{sep} is related to the required separation of the two slices, and δ represents a delta function. The frequency of the cosine can be calculated from the bandwidth of the RF pulse, and the gradients being used. This is also known as Hadamard excitation or double-sideband excitation. To preserve the original flip angle in the slices, it is necessary to double the peak B_1 and therefore double the SAR. For spatial sat bands, the advantage of multi-band excitation is that the time taken is halved.

14.6 Image Quality in Parallel Imaging

We saw in Chapter 6 that the image SNR was dependent upon the number of phase-encode lines acquired. This is also true in parallel imaging. So if we use a reduction factor R , then the SNR will be reduced theoretically by at least \sqrt{R} . In practice it will also be reduced by a geometric efficiency factor g , which is dependent upon the geometrical arrangement of the array elements and their sensitivities. Figure 14.19 shows the dramatic

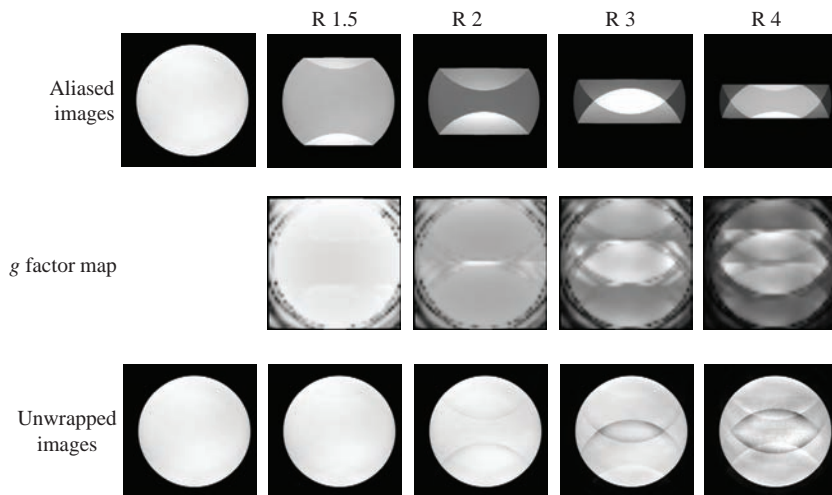


Figure 14.19 Image noise and reconstruction artefacts in SENSE at various reduction factors. Image courtesy of Philips Healthcare.

change of image quality with increasing R resulting from deterioration of the g-factor. Of course, the extent to which this occurs is dependent upon the number and arrangement of the array coil elements as well as the overall R-factor. More information is contained in Box 'SNR in Parallel Imaging'.

SNR in Parallel Imaging

The SNR in SENSE can be expressed as

$$\text{SNR}_{\text{SENSE}} = \frac{\text{SNR}_{\text{full}}}{g\sqrt{R}}$$

where g is a geometry factor which is always greater than or equal to 1, and is not spatially uniform across the image. An additional feature of SNR in SENSE is that the noise is not uniformly distributed across the image as in conventional acquisitions. This can be seen in Figure 14.19 for different R with the level of noise and artefact increasing with R .

The SNR in mSENSE and GRAPPA does not have such a simple relationship with R , as ACS lines can be used in the reconstruction to boost the SNR. Like SENSE, the noise varies spatially across the image in SMASH-type techniques.

In simultaneous multi-slice imaging, e.g. the so-called MS-CAPIRINHA, the loss of SNR due to the reduction factor R is balanced by the number of simultaneously acquired slices:

$$\text{SNR} = \sqrt{N_{\text{slices}}} \frac{\text{SNR}_{\text{full}}}{g\sqrt{R}}$$

This means that the only SNR loss (compared to the regular multi-slice acquisition) is due to the g factor.

If too high a reduction factor is used then artefacts will appear in the image. These are shown for mSENSE and GRAPPA in Figure 14.20. Artefacts also appear if too few ACS lines are used in the auto-calibrating techniques. Typical parallel imaging artefacts are increased noise in the centre of the image (or wherever the coil sensitivities are weakest), and residual foldover ghosts, particularly if there is a very strong signal (like fat on T₁-weighted images).

We have already noted that for a SENSE acquisition, the field of view must be sufficiently large to encompass all the signal-producing regions. If it is not, then the images cannot be unfolded properly (Figure 14.7). However, SENSE can now be combined with no-phase-wrap in a flexible way which allows the user to achieve a scan time reduction overall.

In single-shot techniques like SS-TSE and EPI, parallel imaging can actually improve image quality by reducing T₂ blur and geometric distortion by shortening the echo trains (Figures 14.21 and 14.22). More details are given in Box 'Parallel EPI'.

Parallel EPI

Figure 14.23a shows that with parallel imaging the length of the echo train is reduced. The shorter echo train results in a higher PE bandwidth and hence less susceptibility distortion artefacts and reduces the minimum TE. Figure 14.23b shows the resulting k-space trajectory.

The single-shot nature of EPI, however, has implications for the reference images and calibration

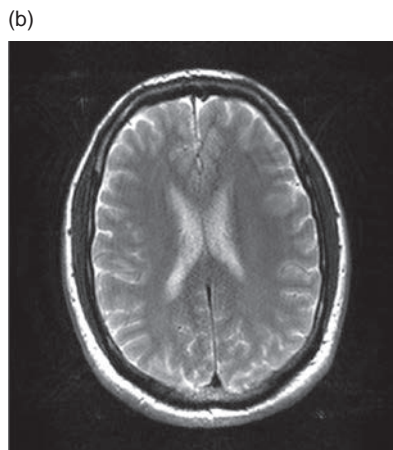
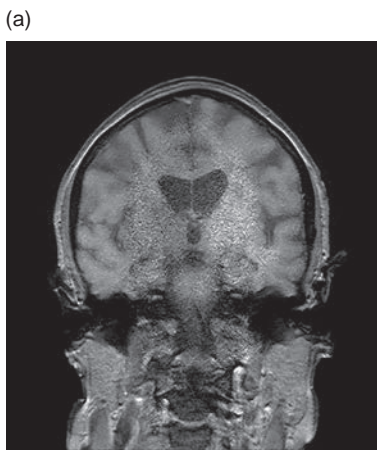


Figure 14.20 Parallel imaging artefacts from using too high a reduction factor: (a) SENSE, (b) GRAPPA.

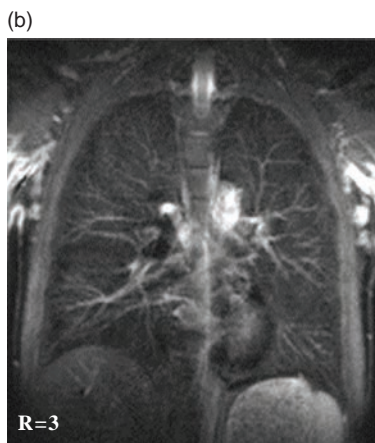
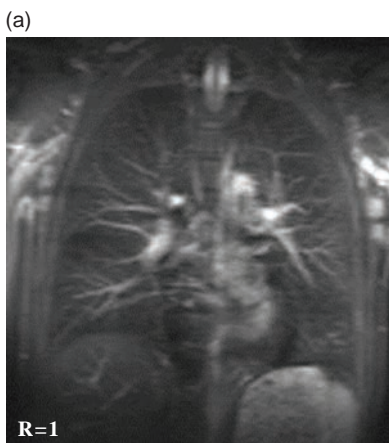


Figure 14.21 Reduction of T₂ blurring in HASTE imaging of the lungs. (a) Conventional 128 × 256 (207 ms), echo spacing 2.88 ms; (b) 256 × 256 (149 ms), effective echo spacing 0.96 ms. Images courtesy of Siemens Healthcare.

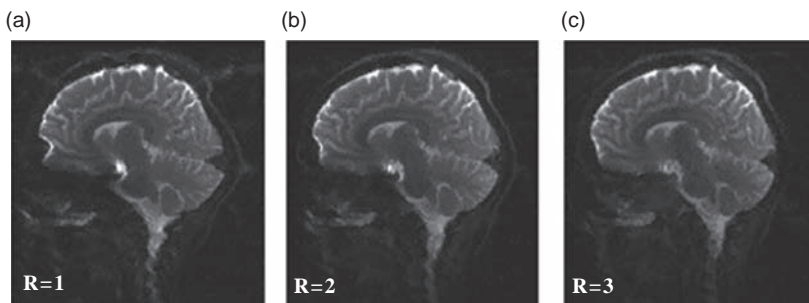


Figure 14.22 Parallel imaging reduces T₂ distortion in EPI, by shortening the echo train length (increasing the PE bandwidth): (a) conventional, (b) R = 2, (c) R = 3. Images courtesy of Siemens Healthcare.

procedure. For SENSE and similar techniques, a standard calibration is run prior to the EPI acquisition(s), as for other sequences. For GRAPPA, the auto-calibration traversal of the centre of k-space takes place before the reduced acquisition. In a repeated series of acquisitions as required for fMRI, this results in one additional 'TR' period. Another odd thing

about EPI-GRAPPA is that, because the ACS data are real data and can be used in the reconstruction, the SNR for a reduction factor of 2 is higher than without parallel imaging, even if we control for the change of TE. For $R = 3$ and above SNR and image quality are degraded as the fitting to the ACS lines becomes more approximate.

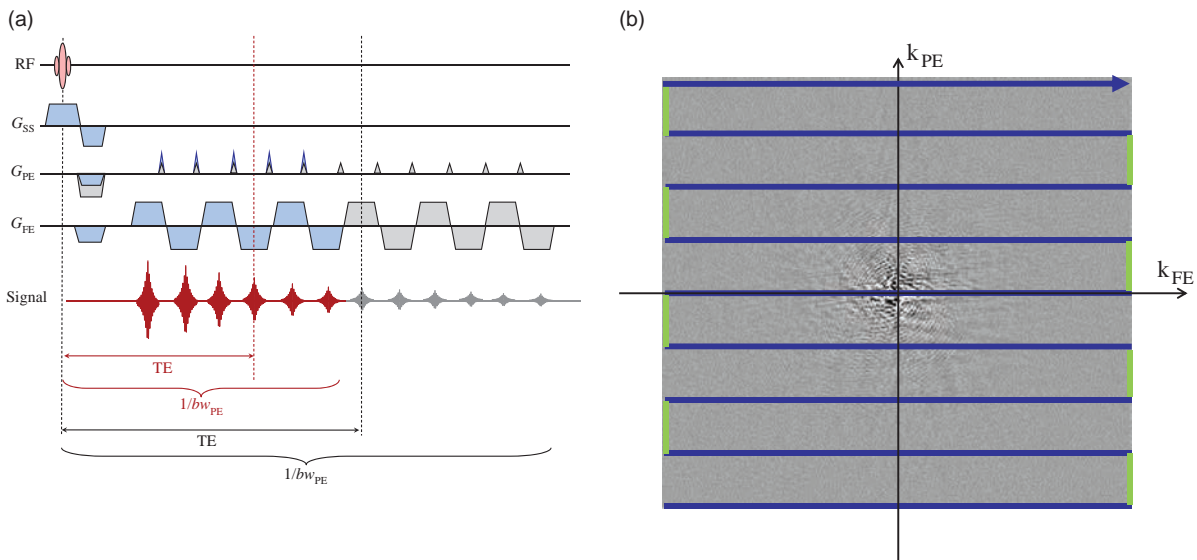


Figure 14.23 Parallel imaging and EPI. (a) EPI sequence corresponding to k-space in (a) with (blue) and without (blue) a reduction factor of 2. The use of parallel imaging reduces TE and increases the PE bandwidth, resulting in less susceptibility distortion. (b) k-space path of EPI with $R = 2$.

Clinical Benefits of Parallel Imaging

The benefits to parallel imaging can be summed up by the ‘five Fs’: faster, further, finer, (more) faithful and fainter (meaning quieter).

Figure 14.24 illustrates how shorter scan times can be achieved with very little discernible loss of image quality, but remember SNR is always reduced by at least $1/\sqrt{R}$, so use sparingly and only when you have to. Faster scanning also means shorter breath-holds with the potential for reduced respiratory motion artefact or the second ‘F’, further, or more slices per breath-hold. The application of even a modest reduction factor can enable successful breath-hold acquisition (Figure 14.25).

The reduction in the number of phase-encode steps acquired means that higher matrices, and hence better resolution, finer images, may be acquired within a reasonable scan time (but with a massively reduced SNR). Thus a 1024 matrix image using $R = 2$ can be acquired in the same time as a convention 512 matrix image (Figure 14.26).

Parallel imaging should be used whenever possible for echo planar acquisitions (EPI) to reduce the effect of susceptibility artefacts. It also enables a shortening of TE, very useful in DWI and DTI. For high-field systems, the susceptibility distortions in EPI can be particularly bad. Parallel imaging helps

reduce this. Also, particularly for EPI, parallel imaging can help to reduce the acoustic noise.

There is an additional ‘F’ which is particularly relevant to high-field MR systems: fry. We don’t want to overheat our patients! As the SAR increases with the square of field strength (or frequency), high-field systems (e.g. 3 T and above) are potentially limited by the permissible SAR. Of course these limits prevent us from frying our patients, but they do result in a need to lengthen TR, or reduce the number of slices or the echo train length. Parallel imaging helps by reducing the number of RF pulses required to form an image, and indeed, without it, even the simplest head scan can prove problematical at 3 T.

14.7 k-t BLAST

This technique is only available on some systems, but it is very promising for dynamic techniques such as cardiac imaging and dynamic contrast enhancement. k-t BLAST (Broad-use Linear Acquisition Speed-up Technique) takes advantage of the fact that most of the image does not change at all during these acquisitions. For example, in a typical short-axis cine of the heart, the chest wall, lungs, spine and muscles do not

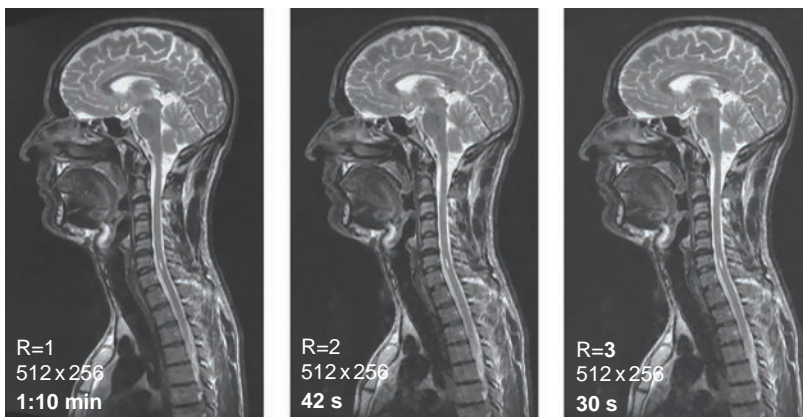


Figure 14.24 Use of parallel imaging (GRAPPA) to speed up T₂-weighted TSE scans. Images courtesy of Siemens Healthcare.

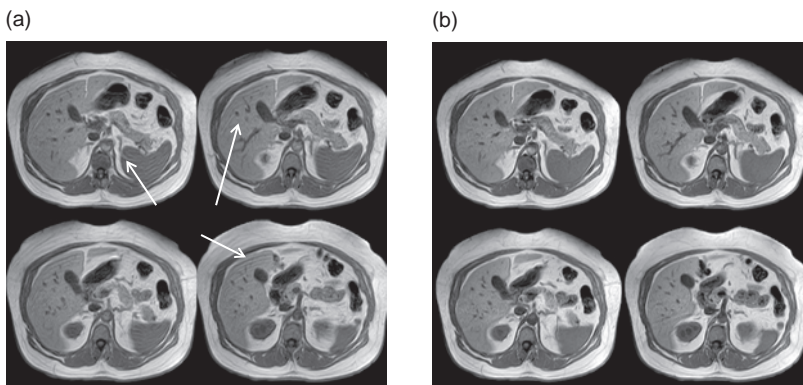


Figure 14.25 Use of SENSE to obtain better slice coverage within a breath-hold, resulting in reduced motion artefact (arrowed), (a) without SENSE, 22 s, (b) with SENSE, 13.5 s. Images courtesy of Philips Healthcare.

vary (much) from one frame to another. Once we have the first frame, these voxels do not need to be re-sampled during the rest of the cine. The remaining voxels can therefore be sampled quicker and provide better temporal and/or spatial resolution.

Figure 14.27 illustrates the principle for a single line through the cardiac frame. If we take the Fourier transform of this line through time, we find ourselves in x-f space, which shows the spectrum of motional frequencies. In the middle are all the voxels which do not change through the frames of the cine acquisition: out to the edges are the faster moving voxels which represent the ventricle walls and moving blood. It is obvious that most of this space is empty!

In normal imaging, every point in k-space is sampled at each of t time-points. By skipping some of the k-space points for some of the time-points, k-t space is undersampled. In x-f space, the periodic nature of the signal means they are folded in. Reconstruction of these signals will give foldover in real

space and undersampling of the temporal frames, just like real-space signals are folded in during parallel imaging. To unfold the signal intensities, k-t BLAST uses a set of training data, usually a low-resolution cine with relatively few frames (Figure 14.28). The training data give an estimation of the signal distribution in x-f space. Combining the training data with the undersampled dynamic data allows the reconstructor to produce the final cine images.

k-t SENSE is k-t BLAST plus sensitivity encoding. By using the coil sensitivities of a multi-element receive coil, k-t space is undersampled even more, allowing speed-up factors up to 8. The reduced scan time can be traded for more slices (better coverage), higher spatial resolution, better temporal resolution or a combination of all three. For example, velocity mapping through the aorta can be achieved in a 10 s breath-hold instead of a 3 min scan time, or six slices may be acquired instead of only one in the same 3 min scan time.

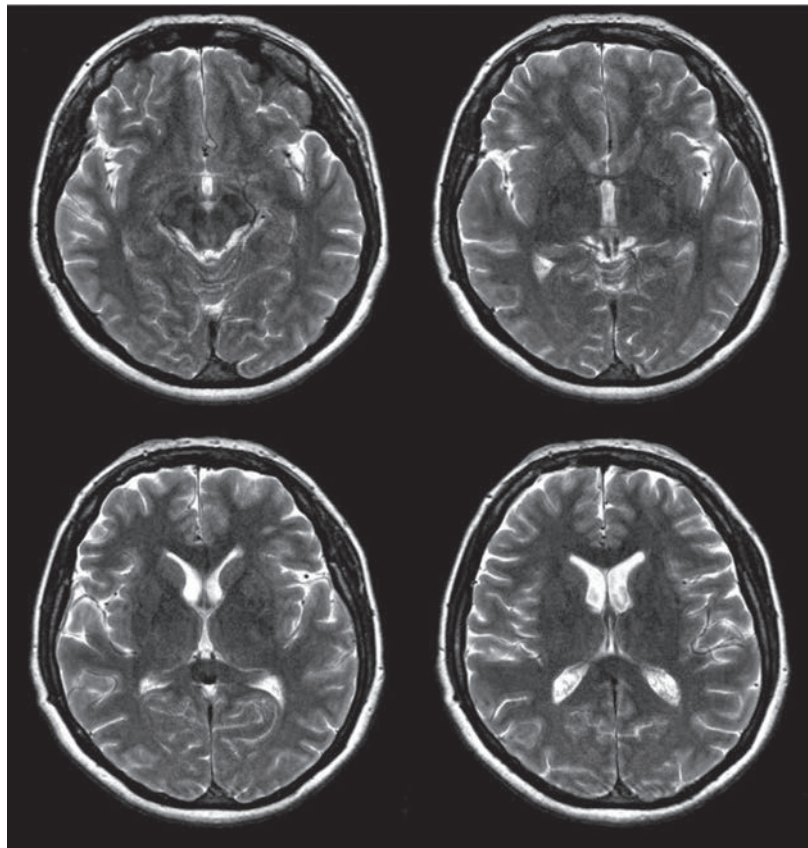


Figure 14.26 Use of parallel imaging (ASSET) to reduce acquisition time for 512×512 matrix acquisitions.

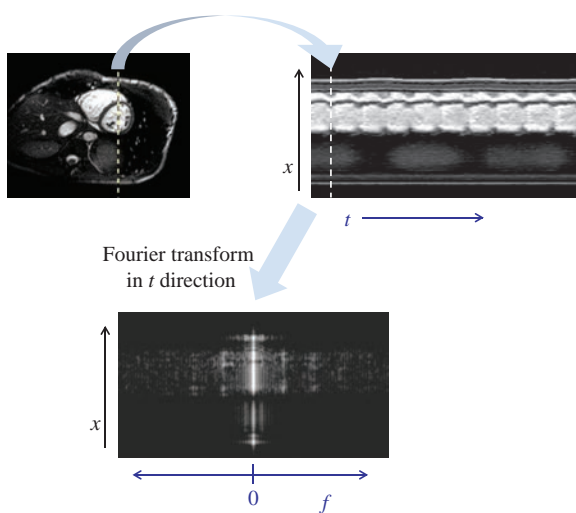


Figure 14.27 In a cine cardiac scan, most of the voxels do not change between frames. By Fourier transforming a line of pixels in the time direction, we can see the frequency distribution of voxel 'motion' (actually it is signal intensity which is changing).

In dynamic contrast enhanced imaging, the anatomy is not changing position but certain voxels will show higher intensity during the injection of gadolinium. In this situation one could acquire a training data set using a small test bolus, but it is preferable to acquire small bits of training data throughout the main bolus injection. k-t BLAST has great potential for applications in dynamic liver imaging, where we need to acquire a large number of slices at a temporal resolution of at least one frame per second.

14.8 Non-Cartesian Acquisition Schemes

Projection Reconstruction (PR) was the first MR k-space trajectory and was used by Lauterbur to produce the first MR image of two tubes of water. This method is similar to the reconstruction of

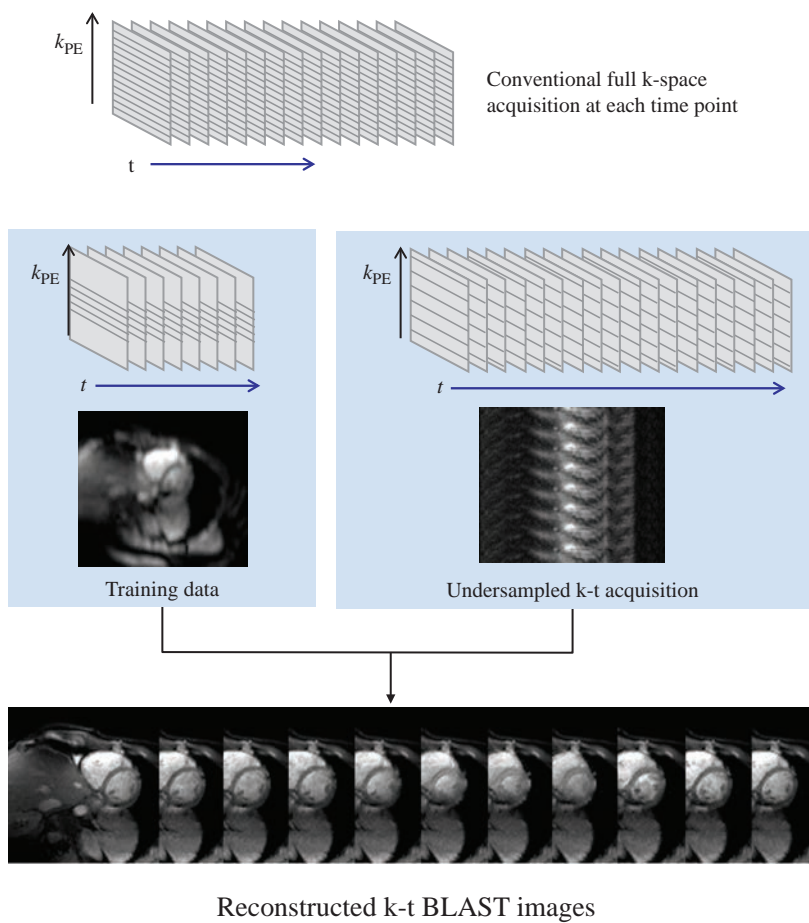


Figure 14.28 A conventional cine scan acquires the whole of k-space at every time-point. In k-t BLAST, a set of training data is acquired with low spatial and temporal resolution. This is followed by a rapid acquisition which undersamples in both k-space and time in a well-defined pattern. The training data can then be used to unwrap the aliased signals.

computerized tomography (CT) images. In CT, projections of the object are acquired at a number of angles around the object. The images are then reconstructed by ‘back-projecting’ the individual projections. Since simple back projection results in blurred images the projection data are usually filtered before reconstruction. In the earliest MR scanners magnetic field inhomogeneity and gradient non-linearities resulted in excessive image blurring (see Figure 1.3) and PR was subsequently replaced by the ‘spin-warp’ (2D FT) technique, which was much more forgiving (see Chapter 8). However with technical improvements in scanner performance PR has been reborn with a new name: radial imaging.

14.8.1 2D and 3D Radial Imaging

In radial imaging we acquire a number of projections through the object at different angles, ϕ . To produce the radial projection pattern, frequency

encoding is applied simultaneously on two physical axes (e.g. x and y for transverse slices) with varying amplitudes to produce the rotational pattern. The pulse sequence simply involves slice selection and frequency encoding; there is no concept of a phase-encoding direction. Figure 14.29a shows a 2D gradient-echo radial sequence and 12 radial projections overlaid on a Cartesian k-space. In Figure 14.29b the sequence is shown for the projection at $\phi = 45^\circ$ i.e. the G_x and G_y gradients have the same amplitude. The radial approach can also be extended into 3D by acquiring radial projections with components along x , y and z . This has sometimes been termed a Koosh ball trajectory due to its similarity with the child’s toy and adult stress-buster!

In radial imaging the data are not reconstructed using filtered back projection but are ‘re-gridded’ onto a conventional Cartesian (x,y) k-space and then reconstructed via direct Fourier transformation (see Box ‘Re: Gridding’).

(a)

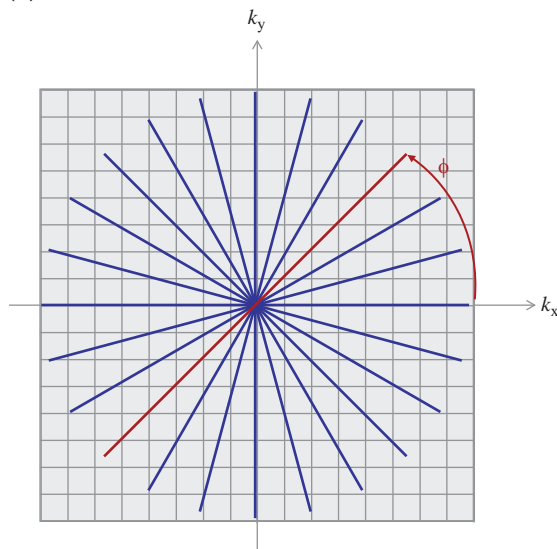
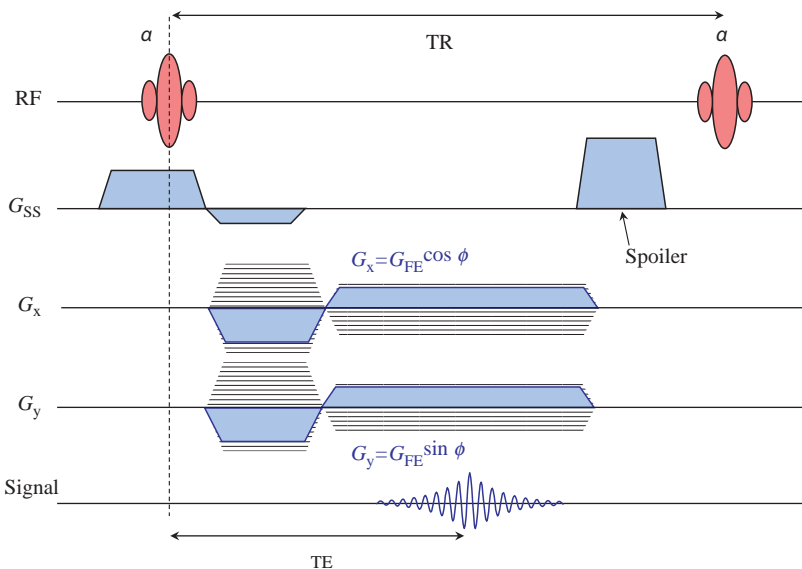


Figure 14.29 Radial scanning: (a) k-space for radial acquisition, the projection for $\phi = 45^\circ$ shown in red. Re-gridding to the underlying Cartesian k-space is required prior to reconstruction. (b) Pulse sequence for radial acquisition for $\phi = 45^\circ$. There is no phase encoding and the amplitude of G_x and G_y vary to produce the radii.

(b)



Re: Gridding

In conventional MRI raw data are acquired along a uniformly sampled rectilinear k-space trajectory and the image reconstructed by direct Fourier transformation. In radial and spiral imaging the k-space trajectories are non-uniform. While any non-uniform data can be reconstructed using extensions of the standard discrete Fourier transform (DFT) algorithm the methods are generally far too slow to be

clinically useable. Instead, in a process called 're-gridding', the data are re-sampled or interpolated onto a uniform rectilinear grid prior to a standard FFT. Figure 14.30 shows the principle of gridding in a very simple way, where each acquired data point contributes to the signal in four nearest neighbours on the Cartesian grid. An important part of gridding is that the data also need to be corrected for the non-uniform sampling density, i.e. some sequences

like radial and spiral imaging heavily oversample the centre of k-space. Each data acquisition point therefore needs to be multiplied by an appropriate 'weighting' factor to compensate for this effect, usually based on a Bessel function.

Clinical Applications of Radial Imaging: Ultra-Short TE

Radial imaging has a number of advantages. First, because no phase-encoding gradient is used the minimum TE for gradient-echo based radial imaging can be made very short if the acquisition starts at the centre of k-space. Using non-selective or half-pulse excitation together with half-Fourier readout and ramped sampling TE can be as short as a few hundred microseconds. Furthermore, if hardware changes are made to the system such that system delays and switching times are substantially reduced then echo times as short as 8 μ s can be achieved. This makes it possible to image previously unobservable tissues such as cortical bone, tendons, ligaments and menisci, which have very short T_2 (Figure 14.31). The term ultra-short TE is used to describe these applications and it gives us another new acronym, UTE. The UTE images themselves are heavily PD-weighted, so it is common to acquire a second echo at a later time (e.g. 4 ms) and subtract it from the UTE image. The subtracted image highlights the short T_2 tissues as bright structures against a darker background.

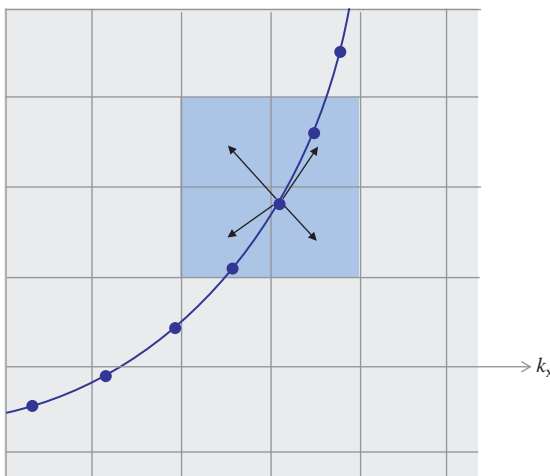


Figure 14.30 Re-gridding: each point affects the four nearest neighbours. The blue line and points represent actual k-space trajectory and sampled points.

Stealth Mode: Silent Scanning

The use of a 2D or 3D centre-out k-space trajectory means that the gradient amplitudes only need to change very slightly between TRs. Since the majority of the acoustic noise is associated with gradient switching this makes the sequences considerably quieter. Figure 14.32 shows the x and y gradient waveforms for a simulated 2D radial sequence with 36 spokes. The reduced amplitude of the gradient transitions between TRs can be clearly seen. Of course in this case we have ignored the conventional slice-selection gradient which would still create noise. Implementing this sequence as a 3D volume acquisition with very short, non-selective RF pulses can produce an almost totally silent acquisition, and the magnet cold head then becomes the noisiest component in the magnet room. While there are many advantages to silent scanning, particularly for babies, it is a weird experience for those of us who are scanned regularly and like to count the gradient pulses!

Sampling in Radial Imaging

The oversampling of the centre of k-space means that radial acquisitions take $\pi/2$ times longer than conventional Cartesian acquisitions for the same matrix. The scan time can be reduced by undersampling the radial data, i.e. decreasing the number of spokes. In conventional Cartesian imaging this results in image aliasing. In radial imaging it results in radially positioned streak artefacts (Figure 14.33). In the same way as for undersampled Cartesian imaging, reducing the number of radial spokes does not compromise spatial resolution but reduces SNR and leads to increased streaking artefacts. However, with a high enough degree of undersampling the artefacts become a nearly uniform background haze instead of discrete streaks. With an appropriate trade-off between acquisition time and artefact, undersampled PR offers a means of rapidly acquiring high-resolution images.

14.8.2 Spiral

In spiral imaging the k-space trajectory samples data along an Archimedean spiral (see Box 'k-Space Spirograph'). Spiral acquisitions can achieve greater scan efficiency than conventional Cartesian acquisitions, i.e. a spiral acquisition can cover a greater portion of k-space with each RF excitation. As the spiral readout starts at the centre of k-space, spiral sequences can have very short echo times. Spiral acquisitions may be

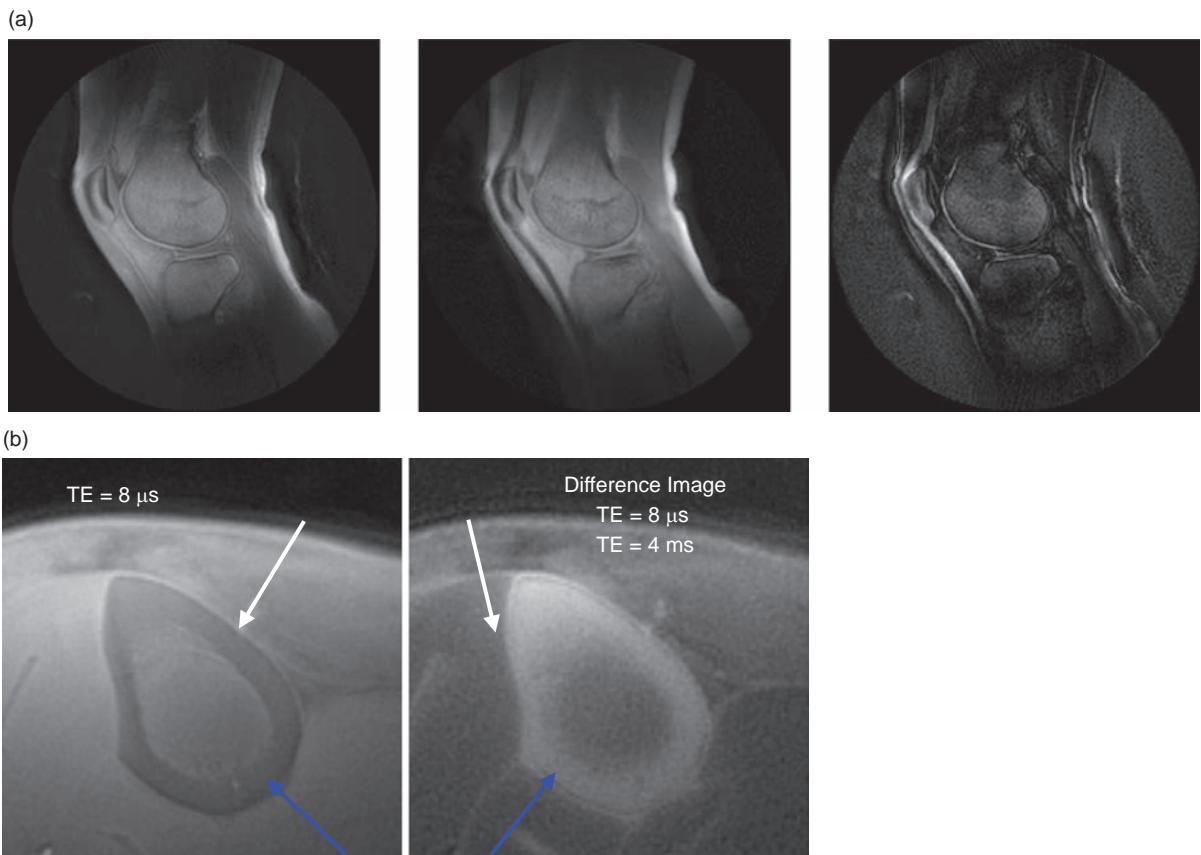


Figure 14.31 (a) Ultra-short TE images of normal knee: FID, gradient echo and subtracted image which highlights the short T_2 components such as the femoro-patellar tendon. Images courtesy of Philips Healthcare. (b) Normal tibia: FID and subtracted image, showing high signal in cortical bone ($T_2 = 500 \mu\text{s}$, blue arrows) and periosteum ($T_2 = 5-11 \text{ ms}$, white arrows). Images courtesy of Jean Brittain, GE Healthcare.

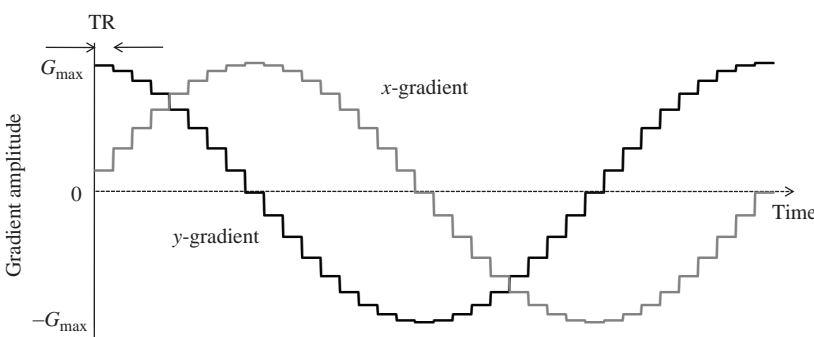


Figure 14.32 In-plane (x and y) gradient activity for a simulated 2D centre-out radial acquisition. Note the reduced amplitude transitions, i.e. switching, between TRs. The reduced gradient switching results in a considerable reduction in acoustic noise.

either single-shot or multi-shot. In a single-shot acquisition all of the k-space data are acquired following a single RF excitation. Figure 14.34 shows the k-space trajectory for a single-shot acquisition and the in-plane gradient waveforms required to generate

this trajectory. Like radial imaging, there is no longer any concept of phase or frequency encoding and data are constantly acquired during the spiral readout.

For multi-shot acquisitions, a number (N_{shot}) of spiral interleaves are performed, each shot being

rotated by an angle of $\pm 2\pi/N_{\text{shot}}$ (Figure 14.35). Figure 14.36 shows a phantom image acquired with a single-shot spiral comprising 16 384 complex data points, and a multi-shot acquisition with 16 interleaves each of 4096 data points.

Since spirals are a method of in-plane data readout then they can be combined with any other pulse

sequences, for example spin echo. The spirals can also be acquired in a reverse fashion so that the centre of k-space is acquired last. This is one way of acquiring a T_2^* -weighted spiral acquisition suitable for fMRI studies. Spirals can also be extended to 3D, the simplest method being to incorporate a conventional slice-select phase encoding; the resultant data are often called a stack of spirals.



Figure 14.33 Radial artefacts: streak artefacts (very similar to CT) can be seen in the background.

k-Space Spirograph

Spiral trajectories use an Archimedean spiral which is defined by

$$r = a\theta$$

where r is the radius, a is a constant and θ the angle. The k-space path for a simple constant spacing spiral is given by

$$k_x = \frac{N_{\text{shot}}}{2\pi \cdot \text{FOV}} \theta \sin \theta$$

$$k_y = \frac{N_{\text{shot}}}{2\pi \cdot \text{FOV}} \theta \cos \theta$$

where N_{shot} is the number of interleaved spirals or shots. The gradient waveforms necessary to produce a spiral k-space trajectory come from the derivative of k with respect to time:

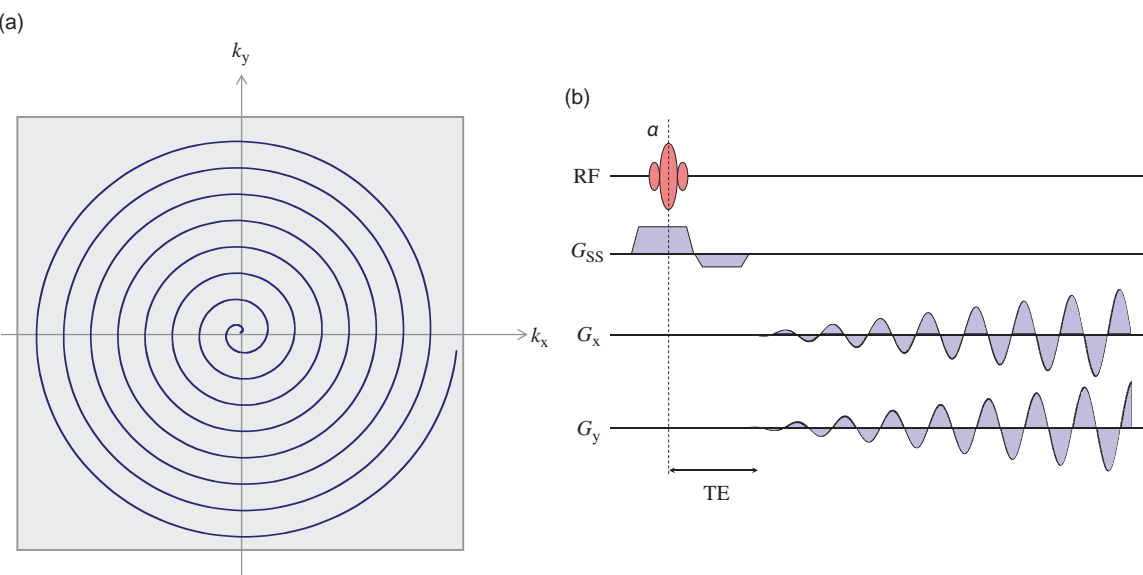


Figure 14.34 (a) k-space for single-shot spiral acquisition, (b) spiral pulse sequence to generate the k-space trajectory in (a).

$$G_x = \frac{N_{\text{shot}}}{\gamma \cdot \text{FOV} \cdot dt} \frac{d\theta}{dt} (\sin\theta + \theta \cos\theta)$$

$$G_y = \frac{N_{\text{shot}}}{\gamma \cdot \text{FOV} \cdot dt} \frac{d\theta}{dt} (\cos\theta - \theta \sin\theta)$$

These are shown in Figure 14.34a. In practice, slew rate constraints need to be considered and the rotation velocity $d\theta/dt$ may not be constant.

Problems with Spirals

The major problem with spiral acquisitions is the blurring due to off-resonant spins. These frequency offsets can come from B_0 field inhomogeneity, local susceptibility effects and chemical shifts. In conventional Cartesian imaging these frequency offsets result in a simple shift in the frequency-encoding

direction – e.g. chemical shift artefact – while in spiral imaging, since the trajectory is changing simultaneously in both in-plane directions the effect is a 2D blurring (Figure 14.36c). To reduce this blurring spiral imaging sequences are usually performed with a water-only excitation (spatial-spectral) (Chapter 12). To correct for the effects due to B_0 inhomogeneity, it is usual for the system to rapidly acquire a field map to determine the frequency offset as a function of spatial location. This can easily be done during the prescan period by acquiring two single-shot spiral images with slightly different TEs and constructing a phase map by complex subtraction. The calculated frequency shifts can then be incorporated into the spiral gridding algorithm to correct for the off-resonance spins.

14.9 Compressed Sensing

Compressed Sensing (CS) is a new method of accelerating image acquisition that is based upon the concepts used in image compression. We are all familiar with the concept of compressing images or movies to reduce the space required for storage. The Joint Photographic Experts Group (JPEG) standard is a typical example of a compressed image format that is extensively used to reduce the size of image files, while the Motion Picture Encoding Group (MPEG) standard is used to compress video. Both can be performed with little or no reduction in image information. JPEG, for example, exploits redundancies in the data and can typically achieve 10:1 compression without any perceptible loss of image quality.

CS essentially involves this process in reverse. We sample a reduced number of data points and then iteratively reconstruct the image by estimating the missing data points. There are, however, a number of requirements for CS to work in the context of MRI.

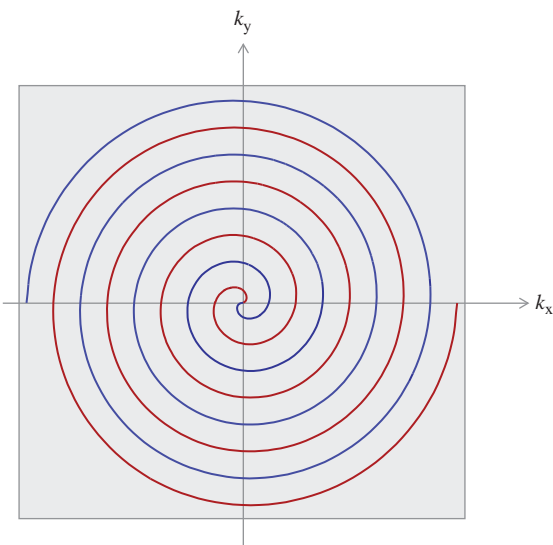


Figure 14.35 Multi-shot spiral k-space with two interleaved shots.

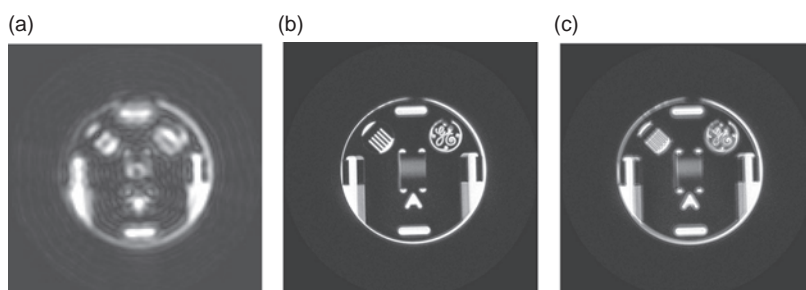


Figure 14.36 (a) Single-shot spiral image; (b) 16-shot interleaved spiral image; (c) 16-shot interleaved spiral but with 50 Hz offset.

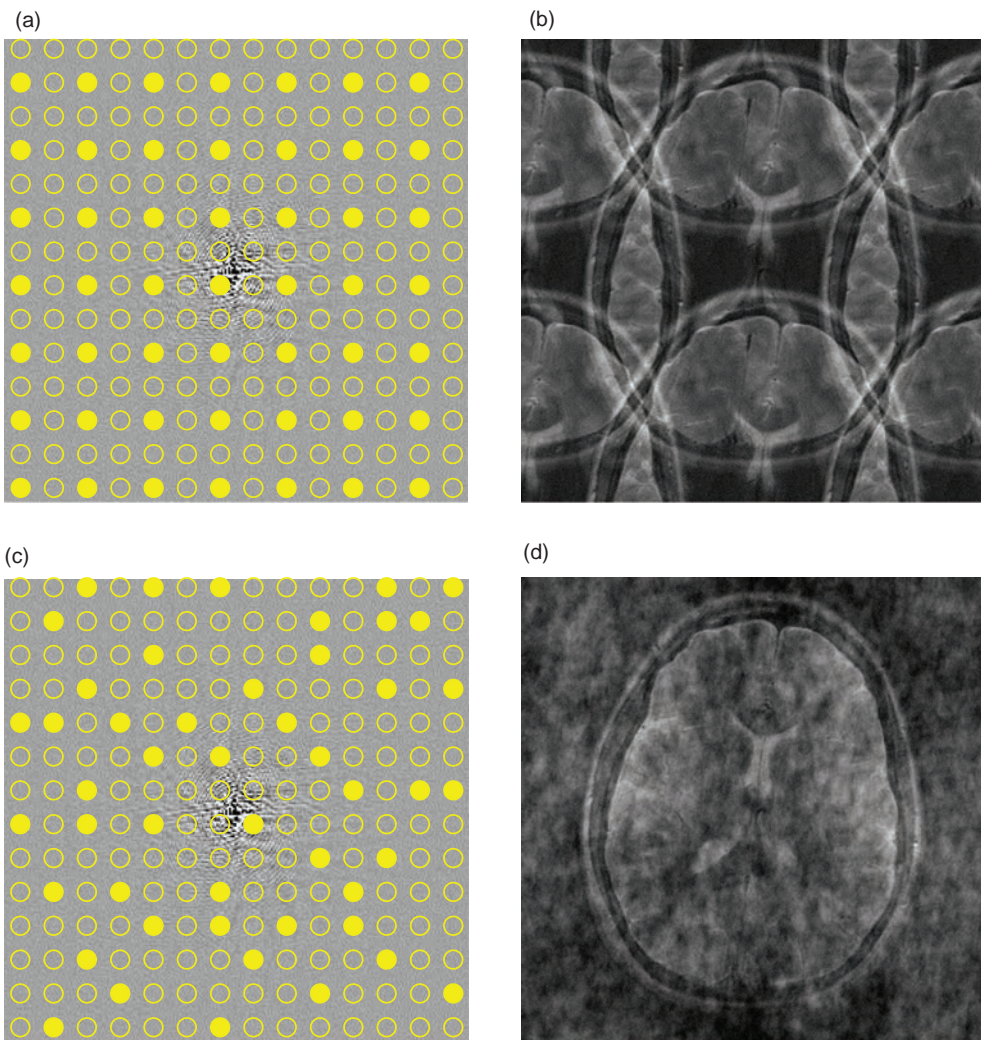


Figure 14.37 Principles of compressed sensing. (a) Regularly undersampled (25% of the original data), k-space. (b) The image obtained following standard 2D Fourier transformation – note the coherent image aliasing. (c) A random 2D undersampling pattern (33% of the original data). (d) The image reconstructed using a standard Fourier transform – note the incoherent artefacts now appear as an increase in background ‘noise’.

First, the data must be sparse, or be transformed into a sparse representation. Sparsity in this context means that the data contain very little information. An MR angiogram is a good example of sparse data in the image domain. There are only a few voxels containing signal of interest, while the rest of the image is essentially blank. Other images may require some form of transformation to make them sparse – for example, the voxels in a standard brain image are relatively smooth-changing with location, i.e., two adjacent voxels are likely to be very similar. Therefore a suitable sparsifying transform could be to

simply take the difference between adjacent voxels. In practice more sophisticated sparsifying transformations are used, such as the discrete cosine transformation (DCT) used in JPEG compression or the wavelet transformation used in JPEG-2000 compression. In a dynamic MRI acquisition there is very little change between adjacent temporal frames, so temporal differences can also be used to sparsify dynamic data. Second, the aliasing artefacts caused by the sub-sampling of k-space must be incoherent (noise-like). We know that regular sub-sampling of k-space results in foldover artefacts (Figure 14.37a,b).

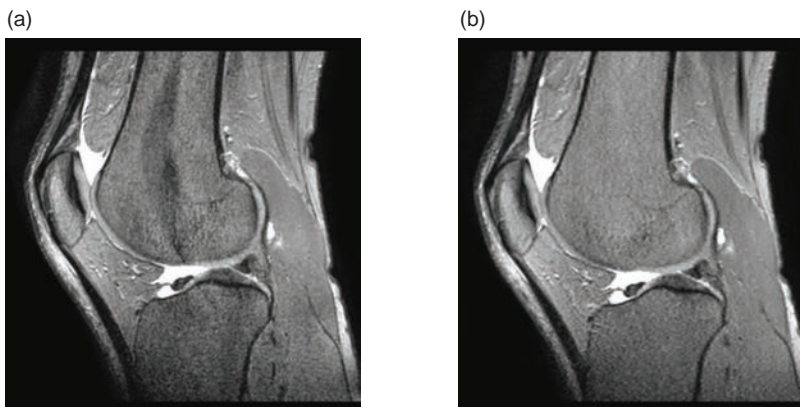


Figure 14.38 Image of the knee using (a) conventional parallel imaging (SENSE) with reduction factor of 4; (b) compressed sensing with undersampling factor of 4.

These are coherent artefacts, whereas if we randomly sample k_y space then the resulting incoherent artefacts appear much more like background ‘noise’ (Figure 14.37c,d).

The quality of a CS reconstruction is very dependent upon the sparse sampling pattern. As we already know, the bulk of the contrast in an image is at the centre of k-space, so a CS sampling pattern usually fully samples the centre of k-space and then more randomly samples the periphery.

CS reconstructions are best used with 3D acquisitions where it is relatively straightforward to sub-sample in k_y-k_z space. Since 3D imaging is inherently time-consuming, any acceleration technique can have a significant impact on overall acquisition

times. Non-Cartesian sampling schemes, such as radial or spiral, are also attractive from a CS perspective since undersampling artefacts are incoherent. CS can be combined with parallel imaging, but the requirement for random sampling required by CS conflicts with the requirement for large sampling gaps, therefore careful choices need to be made in terms of the random sampling distribution. Figure 14.38 shows how the randomized undersampling schemes used in CS produce fewer artefacts than conventional regularly undersampled acquisitions.

See also:

- Totally phased: phase encoding; Section 8.5.2
- Phased array coils: Section 10.5.2

Further Reading

Bernstein MA, King KF and Zhou XJ (2004) *Handbook of MRI Pulse Sequences*. London: Elsevier Academic Press, chapters 13 and 17.

Brown RW, Cheng YCN, Haacke EM, Thompson MR and Venkatesan R (2014) *Magnetic Resonance Imaging: Physical Principles and Sequence Design*, 2nd edn. Hoboken, NJ: John Wiley & Sons, chapters 14 and 19.

Griswold MA, Jakob PM, Heidemann RM, et al. (2002) ‘Generalised

autocalibrating partially parallel acquisitions (GRAPPA)’. *Magn Reson Med* 47:1202–1210.

Lustig M, Donoho D and Pauly JM (2007) ‘Sparse MRI: the application of compressed sensing for rapid MR imaging’. *Magn Reson Med* 58:1182–1195.

Pruessmann KP, Weiger M, Scheidegger MB and Boesiger P (1999) ‘SENSE: sensitivity encoding for fast MRI’. *Magn Reson Med* 42:952–962.

Sodickson DK and Manning WJ (1997) ‘Simultaneous acquisition of spatial harmonics (SMASH): fast imaging with radiofrequency coil arrays’. *Magn Reson Med* 38:591–603.

Tsao J, Boesiger P and Pruessman KP (2003) ‘k-t BLAST and k-t SENSE: dynamic MRI with high frame rate exploiting spatiotemporal correlations’. *Magn Reson Med* 50:1031–1042.

Go with the Flow: MR Angiography

15.1 Introduction

Magnetic Resonance Angiography (MRA) uses a variety of methods to visualize the blood flow within arteries and veins. There are two main classes of MRA technique that can create angiographic-type images: those that exploit the intrinsic contrast created by moving spins and those that rely on the use of an injected contrast agent. The former endogenous contrast methods are now typically classified by the term ‘Non-Contrast’ MRA (NC-MRA) to separate them from techniques that require administration of an external (or exogenous) contrast agent, typically referred to as ‘Contrast-Enhanced’ MRA (CE-MRA). NC-MRA techniques use a variety of pulse sequences to create the desired contrast between blood moving within vessels, and the stationary background tissue.

In this chapter we will see that:

- flowing blood has different appearances on spin-echo and gradient-echo pulse sequences, compared to static tissues;
- NC-MRA sequences utilize in-flow, phase effects, or the inherent vessel pulsatility to produce angiographic images;
- CE-MRA sequences can be acquired as 3D and 4D, meaning that we can observe the temporal changes in blood flow;
- intracranial venography is possible using susceptibility-weighted imaging methods.

15.2 Effect of Flow in Conventional Imaging

The effect of moving spins on the magnetic resonance signal has been known since the earliest days of NMR and was rapidly exploited in the development of the first commercial imaging systems in the mid to late 1980s to produce angiographic images. The main effect of moving spins can be classified according to

their influence on the longitudinal (time-of-flight) or transverse (phase shift) magnetization. In this chapter we will refer to these effects on blood, as shorthand for the effect on the actual moving spins.

15.2.1 Time-of-Flight Effects

The Time-Of-Flight (TOF) effect in MRI arises due to the blood flow between the RF pulses. In a spin-echo sequence all blood within the imaging slice of thickness Δz will experience the 90° excitation pulse. During the time between the 90° excitation pulse and the 180° refocusing pulse (TE/2), the excited blood will have flowed, either partially or completely, out of the slice and fresh, i.e. unexcited, blood will flow into the slice. We know that only blood that experiences both a 90° and a 180° pulse will create a spin echo at the echo time. The spin-echo signal within the vessel will therefore depend upon the fraction of spins that experience the excitation pulse and are still present within the slice at the time of the 180° refocusing pulse. If the blood completely washes out of the slice between the two pulses then the lumen appears dark or hypointense. However, in the case of very slow flow, the wash-in of unsaturated spins with a large longitudinal magnetization between TRs, together with the lack of wash-out, may lead to a bright signal. Figure 15.1 shows the TOF effect in spin-echo imaging.

TOF effects in gradient-echo imaging generally appear as a signal hyperintensity due to the in-flow of fresh blood, that has not experienced any prior RF pulses, into the imaging slice between TRs (Figure 15.2). The degree of enhancement will depend upon the velocity (v), slice thickness (Δz) and TR. When v is equal to or greater than $\Delta z/TR$, the blood is completely replaced with fresh, i.e. unsaturated, blood during TR, resulting in a maximum signal. When v is less than $\Delta z/TR$ there is only partial replacement of spins resulting in reduced signal

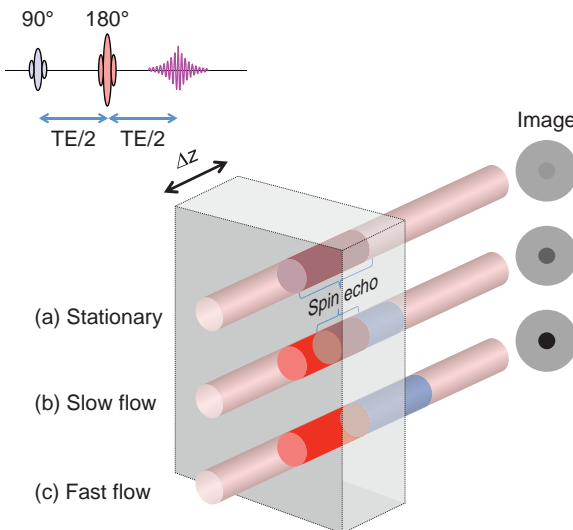


Figure 15.1 Time-of-flight effect in spin-echo imaging. The 90° pulse (blue) excites all the spins in the slice of thickness Δz . (a) Stationary blood will experience both a 90° and a 180° (red) pulse yielding a spin-echo signal (purple). (b) Slow-flowing blood may not completely leave the slice between the 90° and 180° pulses, resulting in a spin-echo signal only from the blood experiencing both (purple). (c) Fast-flowing blood will only experience the 90° pulse and no spin echo will occur resulting in zero signal. This is known as wash-out.

intensity. Figure 15.2 shows the TOF effect in gradient-echo imaging.

15.2.2 Flow Artefacts

As you should hopefully know by now, spins in the presence of a magnetic field gradient will accumulate phase. Whereas stationary spins accumulate phase in proportion to time (T), moving spins accumulate phase in proportion to time-squared (T^2) (see Box ‘Velocity-Induced Phase Shift’). Since different phase-encoding steps will occur at different points in the cardiac cycle, unless the sequence is ECG gated, the temporal changes in flow velocity will result in temporal changes in phase. Following Fourier transformation these phase modulations will result in discrete ‘sidebands’ or ghosts in the images along the phase-encoding direction.

One way to reduce these artefacts for bright blood imaging is to eliminate the phase shift for moving spins. We are already used to the idea of eliminating stationary tissue phase shifts in a pulse sequence by using an equal area, but opposite sign (polarity), gradient pulse. For example, the slice-selection

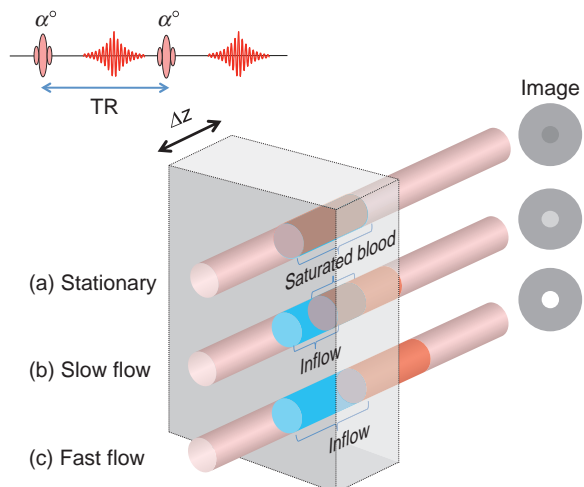


Figure 15.2 Time-of-flight effect in gradient-echo imaging. The α° pulse (red) excites all the spins in the slice of thickness Δz . (a) Stationary blood will experience both α° pulses yielding a partially saturated signal (purple). (b) Slow-flowing blood may not completely leave the slice during TR and only a proportion of the blood will experience both pulses (purple). However, unsaturated blood (blue) that has not experienced any prior RF pulses will enter the slice during TR. The signal will be a combination of the unsaturated (blue) and saturated (purple) blood. (c) Fast-flowing blood will be completely replaced during the TR period, resulting in maximal signal in the second echo.

gradient is followed by a negative rephasing gradient to compensate for the phase shift induced across the slice thickness by the slice-select gradient. For stationary spins the phase shift is given by the product of the gradient amplitude G and its duration T , known as the zeroth-order moment $M_0 = G \cdot T$. However, for spins moving with a constant velocity the phase shift is proportional to the first moment $M_1 = G \cdot T^2$. In this case a three-lobed gradient can be used to eliminate the phase shift for both stationary spins and those moving with a constant velocity. The three-lobed gradient can be considered as the sum of two back-to-back bipolar gradients with opposite polarities where the second bipolar pair compensates for the velocity-induced phase shift caused by the first pair.

Since these gradient pulses compensate for both the zeroth (stationary) and first-order (velocity) induced phase shifts their application in a pulse sequence is often referred to as Gradient Moment Nulling (GMN). Alternative names include velocity compensation or flow compensation (although it is strictly velocity, not flow, that is compensated). Figure 15.3 shows zeroth and first-order gradient

moment nulled waveforms and the effect of first-order nulling on pulsatile flow ghosting. Phase shifts induced by higher orders of motion, e.g. acceleration (a second-order effect), would require a four-lobed gradient waveform to compensate for zeroth, first- and second-order motion. The first three orders of GMN can be represented by binomial gradient amplitudes, e.g., 1:-1, 1:-2:1, and 1:-3:3:-1. The time required to play out these GMN waveforms invariably increases the minimum TE. Often, as a compromise, only first-order motion is compensated. Alternatively the use of pulse sequences with very short TEs reduces the time available for dephasing and may be preferable to the use of a longer TE associated with GMN. Figure 15.3 also shows a 2D gradient-echo pulse

sequence with and without velocity compensation, and the effect of velocity compensation on reducing flow ghosting.

If all the blood within a vessel is moving at the same velocity (known as ‘plug flow’) then the phase shift across the vessel will be constant. However, usually there is a range of blood velocities across a vessel. In long, straight vessels the flow profile is parabolic, where the velocity is almost zero at the vessel walls and maximum in the centre. This is often called ‘laminar flow’ since adjacent layers of fluid flow past each other without mixing. Since a blood vessel is typically only a few voxels across, each voxel will contain a range of velocities, particularly those near the vessel wall where the range of velocities can be

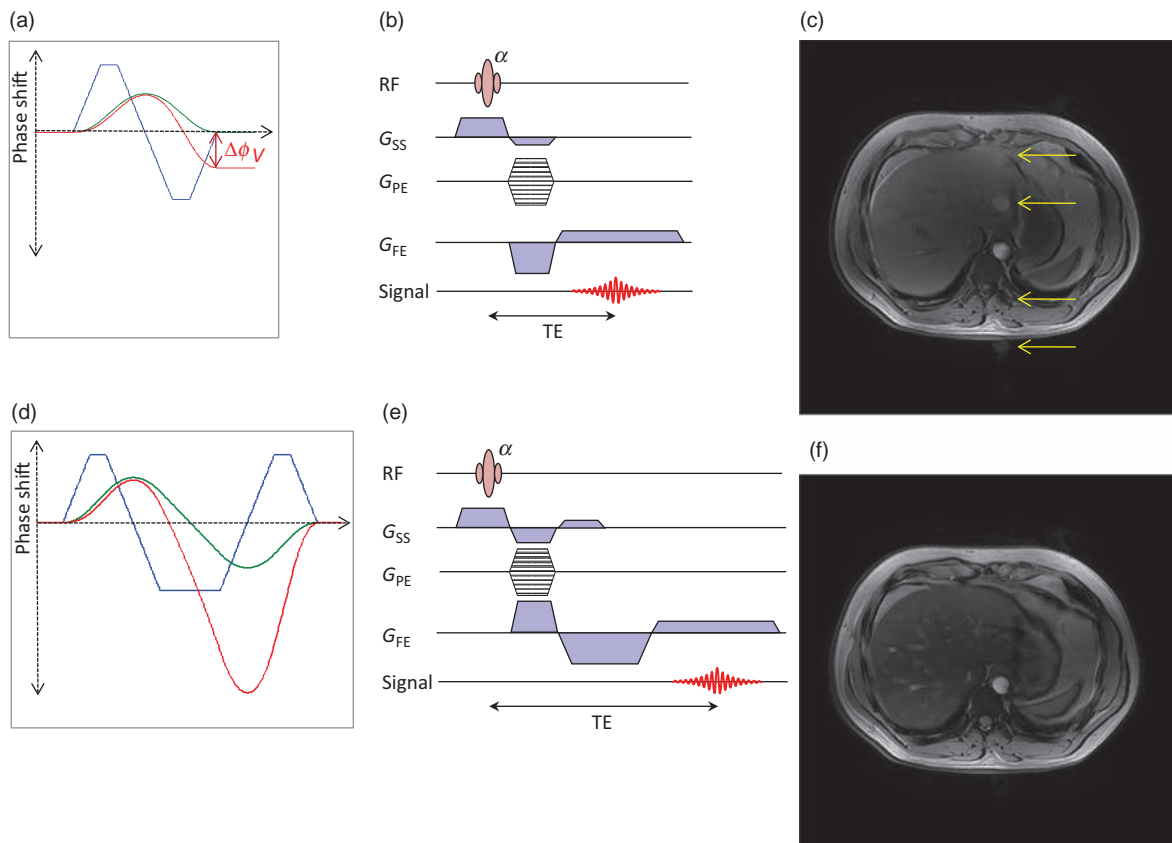


Figure 15.3 Gradient moment nulling. (a) Zeroth-order (M_0) nulling uses a bipolar gradient (blue) with equal areas but different signs (1:-1). There is zero phase shift for stationary spins (green) but a net phase shift $\Delta\phi$ for spins moving with a constant velocity (red). (b) A standard 2D gradient-echo pulse sequence without velocity compensation results in (c) ghosts of the aorta (arrows) due to the phase shifts induced by the pulsatile blood flow. (d) First-order (M_1) nulling uses a three-lobed gradient with areas in the ratio 1:-2:1. There is now zero phase shift for both stationary spins and those moving with constant velocity. (e) A 2D gradient-echo sequence with velocity compensated G_{SS} and G_{FE} results in (f) an image where the ghosting is effectively eliminated by the velocity compensation. Note that G_{PE} is not usually velocity-compensated since the amplitude and hence the phase shift is very small when sampling the centre of k-space.

quite large. Individual voxels will therefore contain a range of velocities and hence phase shifts. If the range of intravoxel phase shifts is large enough then signal cancellation can occur and the edges of vessels may appear with reduced signal and the apparent width of the vessel may appear smaller. This effect may also be seen distal to pathologies such as a vascular stenosis, where turbulent flow can potentially overestimate the degree of stenosis.

GMN can also be used in combination with T_2^* TSE imaging. Flow in the cerebrospinal fluid can often cause signal dephasing in the spinal cord. The use of velocity compensation gradients can reduce the appearance of these artefacts.

GMN is an effective method for reducing ghosting artefacts and ensuring that the vascular signal is bright. If bright flow is not a requirement then ghosting artefacts can be most effectively dealt with by eliminating the signal from flowing blood before it enters the imaging slice, using adjacent spatial pre-saturation bands (see Section 7.2.5). Spins within the pre-saturation slabs are flipped into the transverse plane and have their magnetization dephased by spoiler gradients. These saturated spins then flow into the imaging slice, where they have zero signal. A consistently low intra-luminal signal means that artefacts are not produced. The disadvantage is that the TR must be slightly increased because of the additional RF and gradient pulses required for the pre-saturation bands.

Velocity-Induced Phase Shift

Nuclei precess at the Larmor frequency

$$\omega = \gamma B_0$$

Phase (ϕ) is the time integral of frequency (ω), i.e.

$$\phi = \int \omega \, dt$$

In a magnetic field gradient along the x axis, for example, G_x , this phase shift becomes

$$\phi = \gamma \int (B_0 + G_x \cdot x) \, dt$$

For spins moving at a constant velocity v along the x direction, the phase shift is

$$\phi = \gamma \int (B_0 + G_x \cdot (x + vt)) \, dt$$

If we consider a single gradient pulse of amplitude G and duration T then the phase shift due to velocity alone will be

$$\phi = \gamma \int_0^T v G t \, dt = \left[\frac{1}{2} \gamma v G t^2 \right]_0^T = \frac{1}{2} \gamma v G T^2$$

The product GT^2 is usually called the 'first moment' of the gradient, M_1 , so we can write

$$\phi = \frac{1}{2} \gamma v M_1$$

If a second gradient of the same duration (T) but opposite amplitude ($-G$) immediately follows the first then we have a bipolar gradient pulse with a total phase shift of

$$\phi = -\gamma v M_1$$

If we repeat the acquisition with the polarity of the bipolar pulse reversed and subtract the phases, then we have the phase difference $\Delta\phi$, which can be expressed as the difference in the two moments of the bipolar pulses ΔM_1

$$\Delta\phi = \gamma v \Delta M_1$$

The velocity encoding or 'venc' parameter is defined as the velocity that produces a phase shift of π radians or 180°

$$\pi = \gamma \cdot venc \cdot \Delta M_1$$

therefore,

$$venc = \frac{\pi}{\gamma \cdot \Delta M_1}$$

15.2.3 The MR Angio Pulse Sequence Jungle

Since angiography is a very popular application for MR, there is a whole new set of acronyms available from the different manufacturers. MR angiography sequences can be divided into three main types: non-contrast (NC) MRA, contrast-enhanced (CE) MRA and susceptibility MRA. There are four types of NC-MRA: the very common time-of-flight effect, phase-contrast scans, sequences based on 3D TSE and finally those based on fully rewound gradient echo. CE-MRA techniques use a bolus injection of gadolinium contrast agent, and can be classified as either time-resolved (also known as 4D) or fluoro-triggered.

Table 15.1 is a guide to the different names used by the main manufacturers for MRA sequences.

Table 15.1 Acronyms for MR angio sequences; see Glossary for more details

Generic name	GE Healthcare	Hitachi	Philips	Siemens	Toshiba
NC-MRA using time-of-flight effect	TOF, MOTSA	TOF	TOF, Multi-chunk MRA	TOF	TOF
NC-MRA using phase-contrast effect	PC	PC	PC, Q-Flow	PC	PS
NC-MRA using 3D TSE	Inhance 3D Deltaflow	VASC FSE	TRANCE	NATIVE-SPACE	FBI, CIA
NC-MRA using fully rewound GE	IFIR	VASC ASL	b-TRANCE	NATIVE-TrueFISP	Time-SLIP
Time-resolved (4D) CE MRA	TRICKS	TRAQ	4D-TRAK	TWIST	LDRKS
Fluoro-triggered CE MRA	Smart-Prep, Fluoro Triggered	FLUTE	BolusTRAK	CARE Bolus	Visual Prep
Susceptibility-weighted imaging	SWAN	BSI	SWIp	SWI	FSBB

15.3 Non-Contrast MR Angiography

NC-MRA refers to techniques used to create angiograms without the use of an exogenous contrast agent, e.g. gadolinium. The original NC-MRA techniques are based on TOF and PC. However, in recent years, other techniques have been developed, partly to address concerns associated with Nephrogenic Systemic Fibrosis (NSF) (see Section 20.7) and partly to address imaging in areas for which TOF and PC are less successful, such as the abdomen and peripheral vasculature.

15.3.1 Time-of-Flight Angiography

Time-of-flight MRA was developed in the mid to late 1980s and utilizes the fact that flowing blood appears bright on gradient-echo imaging due to the TOF effect discussed above, particularly if steps are taken to reduce the signal from the stationary background tissue. Typically, first-order GMN is used to reduce signal dephasing. Images are acquired either as multiple 2D slices or as 3D volume acquisitions, with 3D angiographic images produced by stacking the slices and performing a Maximum Intensity Projection (MIP) algorithm in which parallel rays are cast through the 3D volume and a 2D projection image is created using the maximum pixel intensity traversed by the ray, as shown in Figure 15.4.

In a 2D TOF technique multiple sequential thin (approximately 1.5 mm) slice gradient-echo images are acquired perpendicular to the direction of flow. Usually a relatively large flip angle, e.g. 60°, is used to saturate the stationary tissue, resulting in good vascular contrast. Figure 15.5 shows example images from a 2D TOF study of the extracranial circulation.

Applications of 2D TOF

2D TOF is often used for fast vascular localizers, particularly in the carotid arteries where the slices are perpendicular to the vessel. Superior saturation bands are applied to provide directional flow selectivity. Since the slice thickness is relatively thick compared to the in-plane pixel size, the reformatted images can show a 'stair-casing' artefact following MIP. The relatively long TE associated with exciting a thin slice and the use of GMN also means that complex flow dephasing secondary to a stenosis can result in an apparent overestimation of the length and diameter of the stenosis, as shown in Figure 15.6.

In 3D TOF technique a relatively thick slab of tissue is excited and then sub-divided into thin slices or partitions by a second phase-encoding process along the slice-selection direction, followed by a 3D

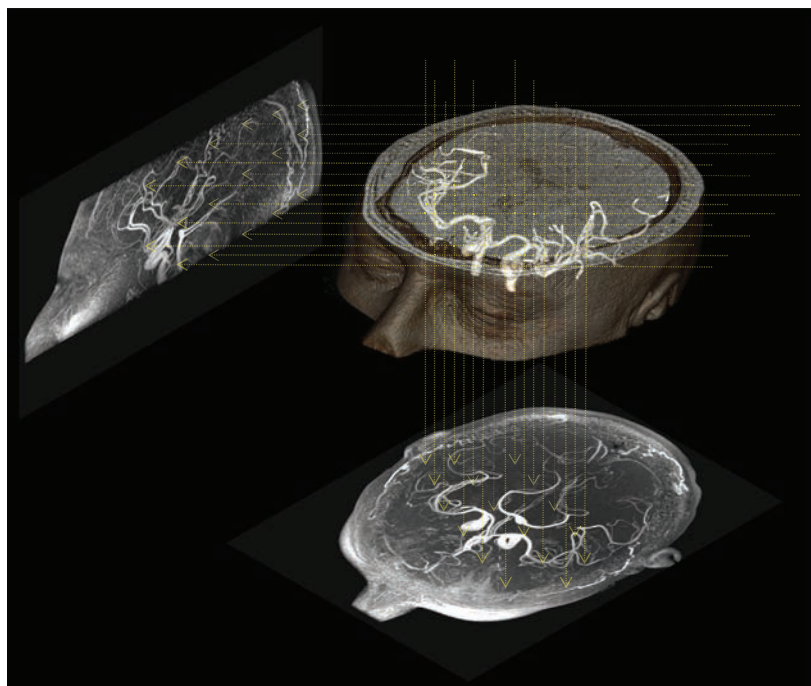


Figure 15.4 Maximum intensity projection (MIP) algorithm. Parallel rays (dotted lines) are projected through the data volume. The maximum pixel brightness is then displayed on the projection images. This has the effect of collapsing all the data along the ray into a single image. The data volume may be rotated a few degrees and the MIP repeated. If the projection images are then displayed in a movie loop, they provide all the necessary visual cues to allow '3D' perception of the data.

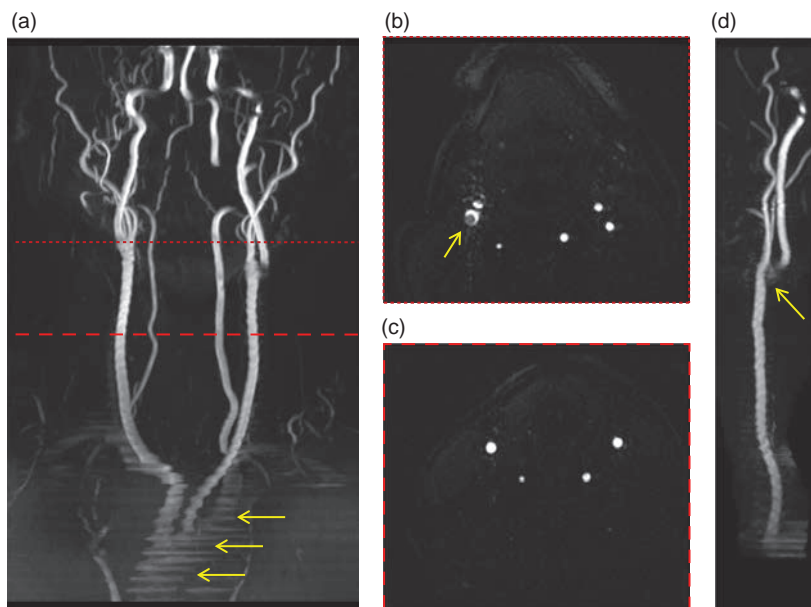


Figure 15.5 2D time-of-flight (TOF) MRA. (a) Coronal MIP from a stack of 240 slices through the extracranial circulation. The alternating signal intensity around the aortic arch (arrows) is due to pulsatile flow. (b) An axial slice at the location of the dashed red line, through the right carotid bifurcation. Note that complex flow around the carotid bulb causes signal loss (arrow). (c) A single 2 mm slice at the location of the dashed red line. The use of a superior sat band means that only the blood flowing inferior to superior, i.e. in the common carotid and vertebral arteries, is visible. (d) A MIP around just the left carotid bifurcation. Note the loss of signal (arrow) where the blood flows in-plane.

FT to reconstruct the images. The advantage of 3D encoding is that much thinner slices can be reconstructed (typically as little as 0.7 mm), which improves the resolution and hence vessel conspicuity by reducing the partial volume effects. Since Δz is

now the slab thickness, from our equation $v = \Delta z/TR$, the threshold velocity is quite high. Therefore 3D TOF methods are best applied intracranially where there is very fast-flowing blood. Since venous blood in the intracranial circulation flows much slower, 3D

TOF methods cause an intrinsic saturation of slow flow without the need for saturation bands. Figure 15.7 shows example images from a 3D TOF study of the intracranial circulation.

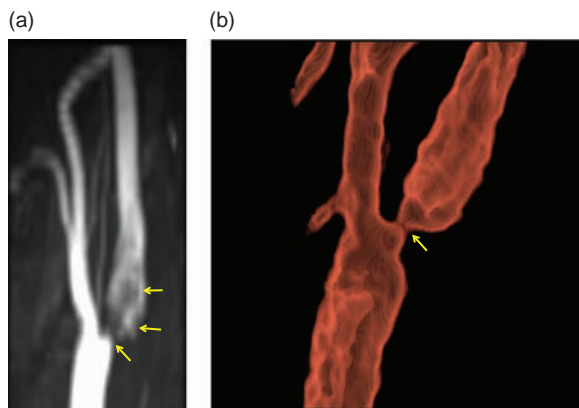


Figure 15.6 2D TOF overestimation of stenosis. (a) MIPed 2D TOF in a patient with a short 70% stenosis of the internal carotid artery. Note the signal loss and hence overestimation of the stenosis (arrows). (b) The true extent of the stenosis is shown in this rendering from a 3D contrast-enhanced MRA with a very short TE that minimizes the signal dephasing.

Applications of 3D TOF

In 3D TOF we try to avoid saturating the signal from spins as they flow deeper into the volume, hence we use a lower flip angle compared to 2D TOF, e.g. 30°. 3D acquisitions also means that the SNR in individual images is also significantly improved compared to 2D methods. However, this improvement in SNR also applies to the background tissue which limits the contrast and visibility of some small distal vessels. Magnetization transfer techniques can also be used to reduce background tissue signal since blood does not demonstrate a significant MT effect, but brain parenchymal signal is reduced. A low flip angle may not be enough to avoid spin saturation with depth so special RF pulses known as ramped excitation or **Tilted Optimized Non-saturating Excitation (TONE)** can be used. These pulses effectively increase the flip angle with distance into the volume. Alternatively multiple 3D slabs can be used; these should be slightly overlapped to eliminate the artefacts that can occur at the edges of 3D slabs, as shown in Figure 15.8.

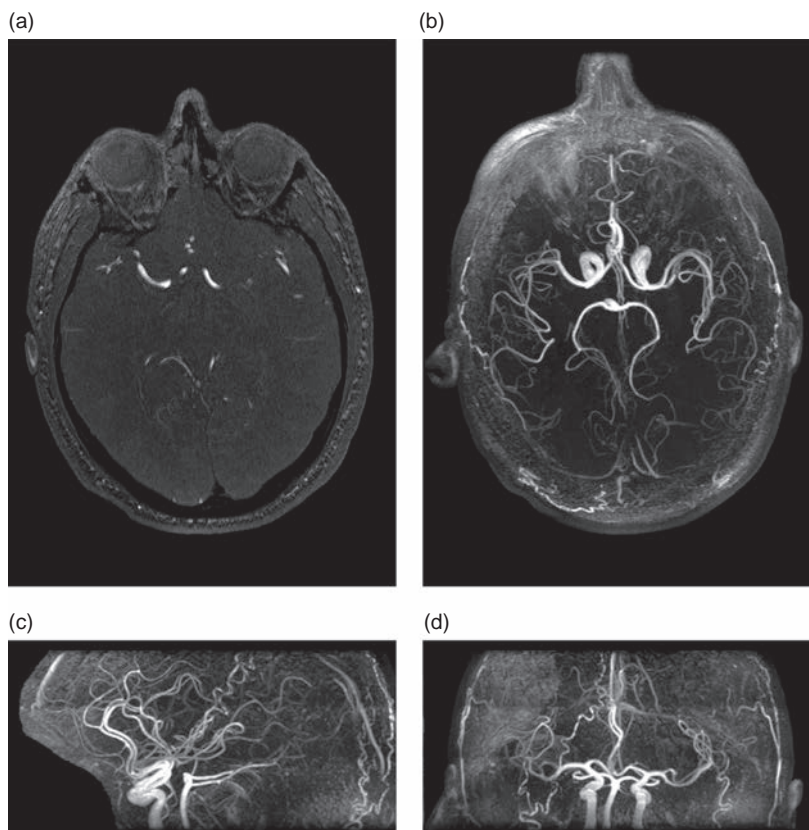


Figure 15.7 3D TOF MRA. (a) A single 1 mm slice from a 3D TOF acquisition through the main intracranial vessels. (b) The top-down MIP from all 172 slices, (c) sagittal projection and (d) coronal projection. Note the relatively high signal in the stationary background tissue compared to 2D TOF.

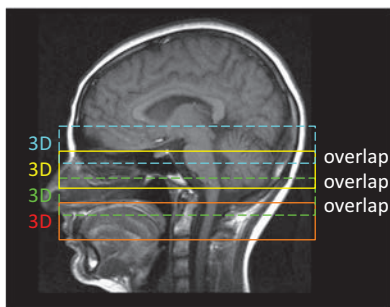


Figure 15.8 Multiple Overlapping Thin Slab Acquisition (MOTSA). Multiple thin 3D slabs are acquired to try to reduce the progressive signal saturation associated with thick 3D slabs. The slabs are overlapped to avoid artefacts at the slab boundary. Even so there is often some residual artefact at the slab boundaries (arrows), known as Venetian blind artefact.

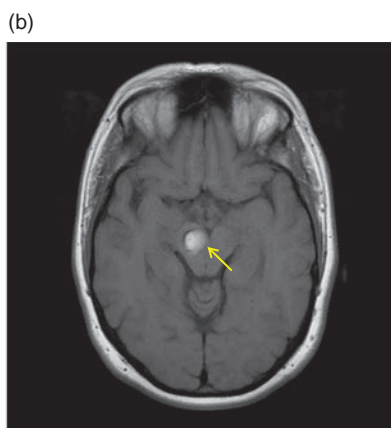


Figure 15.9 Cavernous angioma. (a) MIP from a 3D TOF study showing a cavernous angioma (arrow) that appears hyperintense. This could be mistaken for flowing blood within an aneurysm. (b) T₁w spin echo where the angioma also appears hyperintense, indicating the presence of short T₁ blood breakdown products.

Since TOF MRA exploits the changes in the longitudinal magnetization of flowing blood to create contrast, any tissue with a short T₁ can also appear bright in a TOF angiogram. This can be particularly problematic in certain pathologies that result in tissues with very short T₁s, such as methaemoglobin in haemorrhage. These tissues appear hyperintense in TOF and may be mistaken for flowing blood. Figure 15.9 shows a flow-mimicking artefact in a patient with a cavernous angioma.

15.3.2 Phase Contrast Angiography

Phase Contrast (PC) MRA exploits the changes in the phase of blood's transverse magnetization as it moves along a magnetic field gradient. We have already seen how a bipolar imaging gradient gives zero phase shift for stationary spins, but a non-zero phase shift for moving spins. In a PC pulse sequence additional bipolar velocity-encoding gradients are applied along each of the three gradient directions to create a linear relationship between the velocity of the blood and the phase of the MR signal. This relationship is scaled by

setting a user-controlled velocity encoding value (*venc*). Since we have 360° of unique phase available, flow in one direction, relative to the gradient, is allocated 0° to +180°, while flow in the opposite direction is allocated 0° to -180°. The *venc* is the maximum velocity, along each direction, that will result in a 180° phase shift. Since the MRI signal is acquired in quadrature, it is possible to create images of this phase shift and hence velocity.

Gradient-echo sequences, due to their short TR, are most commonly used for PC-MRA acquisitions. However, variations in the static magnetic field uniformity produce phase shifts in the background stationary tissue. To eliminate these phase shifts, two acquisitions are performed along each gradient direction, with the bipolar velocity-encoding gradients reversed in polarity for the second acquisition. The phase images for both acquisitions are then calculated and subtracted, cancelling the stationary background phase and leaving only positive and negative phase shifts depending upon the direction of blood flow. Finally, to suppress background pixels, e.g. air, where the phase is random, the phase subtraction image is

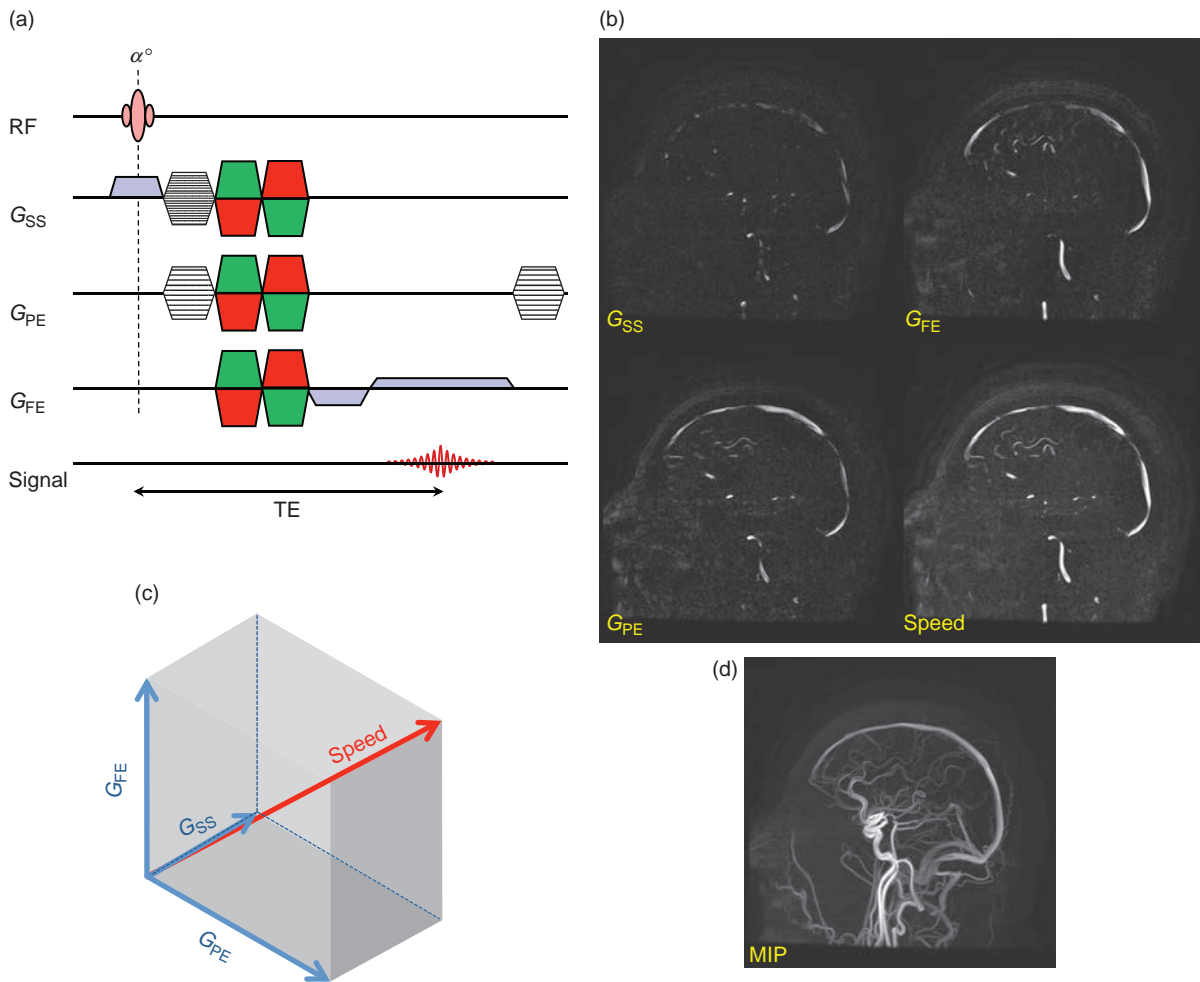


Figure 15.10 Principles of 3D phase contrast (PC) MRA. (a) Bipolar flow encoding gradients (green and red) are applied separately in subsequent TRs and then along each direction. The phase images for each encoding along a particular direction are then subtracted. (b) Images from a mid-line sagittal slice from a 3D PC acquisition. The three velocity components are shown as well as the combination as a speed image. (c) The three velocity vectors are combined into a single speed value. (d) MIP of the full 3D speed images. Since the phase shift is proportional to the velocity the faster-flowing blood appears brighter.

multiplied, pixel-by-pixel, with the conventional magnitude image.

PC MRA is directionally sensitive, since only blood moving in the same direction as the bipolar flow-encoding gradient results in a phase shift. Blood vessels follow a fairly tortuous path throughout the body so it is generally necessary to encode along all three gradient directions. This means that a pair of alternate polarity velocity-sensitizing gradients must be applied along each gradient axis in turn, as shown in Figure 15.10, i.e. six acquisitions are required. However, in practice this can be reduced to four: one velocity sensitive acquisition along each direction

followed by one acquisition with zero velocity sensitization (first-order GMN) along all axes. This requires subtracting each of the velocity-sensitive phase images from the same reference image, which is suboptimal from an SNR perspective. In practice more efficient methods, such as Hadamard encoding schemes that sensitize in two directions simultaneously, address this issue. Even so, a PC MRA study with velocity sensitization in all three directions will take at least four times as long as an equivalent TOF study.

The individual phase images are usually combined to produce a single 3D angiogram by calculating the

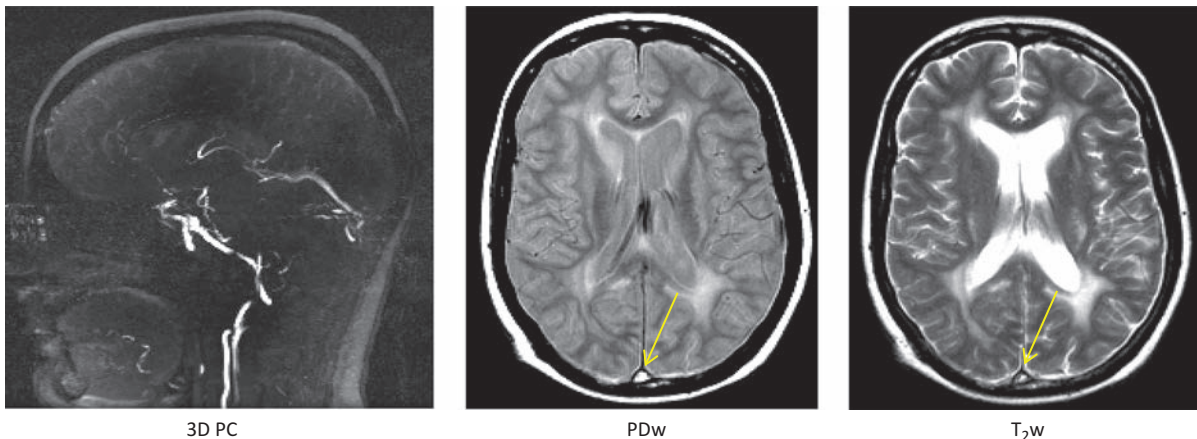


Figure 15.11 Superior sagittal sinus thrombosis. MIP from a 3D PC MRA acquisition. Note the absence of signal due to sinus thrombosis. High signal, i.e. no flow wash-out, is also seen in the sagittal sinus (arrow) on PDw and T₂w images.

resultant flow magnitude image $|v|$ from the x , y and z , i.e. slice-select, phase-encoding and frequency-encoding directions for each pixel using

$$|v| = \sqrt{v_x^2 + v_y^2 + v_z^2}$$

The resultant magnitude image has no directional information and is often termed a ‘speed’ image. Also, since each velocity value is squared in the calculation, all the positive and negative velocity information is eliminated and so any directional information is lost, although the greyscale is still proportional to the speed.

Applications of 3D PC

In 3D PC MRA you excite a slab of tissue, with each slice encoding having velocity sensitization applied along each of the required directions, usually all three. This makes 3D PC studies quite time-consuming and you may have to sacrifice some resolution in the phase-encoding direction or employ parallel imaging techniques to achieve an acceptable acquisition time. Like TOF MRA the speed images from each 3D slice are processed by the MIP algorithm to produce the standard angiographic display.

With PC MRA you have to set a *venc*. If you know the velocities in the vessels of interest then you should set your *venc* to be about half the peak velocity. It is possible to use a 2D PC MRA method whereby you prescribe just a single slice which is thick enough to cover the vessels of interest. This produces a projection angiogram of the blood flow within that thick slice. Since the method is quick, i.e.

only a single slice, you can acquire images with different *vencs* to find the most suitable value for your time-consuming 3D PC acquisition. These 2D projection images are sometimes called *venc* localizers. Finally, since only moving spins give signals on PC MRA images, they do not have the same problem with short-T₁ blood-breakdown products as TOF MRA images. PC MRA is therefore the technique of choice in conditions such as sinus thrombosis, as shown in Figure 15.11

15.3.3 3D ECG-Triggered TSE-Based NC-MRA

Both TOF and PC MRA methods do not work particularly well outside the head and neck. The use of Gd-based contrast-enhanced MRA has been the method of choice for body and peripheral MRA for a number of years. However, concerns over the safety of Gd-based contrast agents, particularly related to NSF, have sparked an interest in the development of NC-MRA methods in the rest of the body. ECG-triggered 3D TSE methods, originally called Fresh Blood Imaging (FBI) by Toshiba, have been used to obtain large FOV angiograms in a variety of regions, although most commonly in the periphery. The method uses two interleaved 3D TSE readouts. The first TSE echo train is gated to systole and the second to diastole. In the systolic images, fast arterial flow dephases the MRI signal and blood appears dark. In the diastolic image the arterial flow is slower, hence the dephasing is less and so blood appears with a high signal. Venous flow is

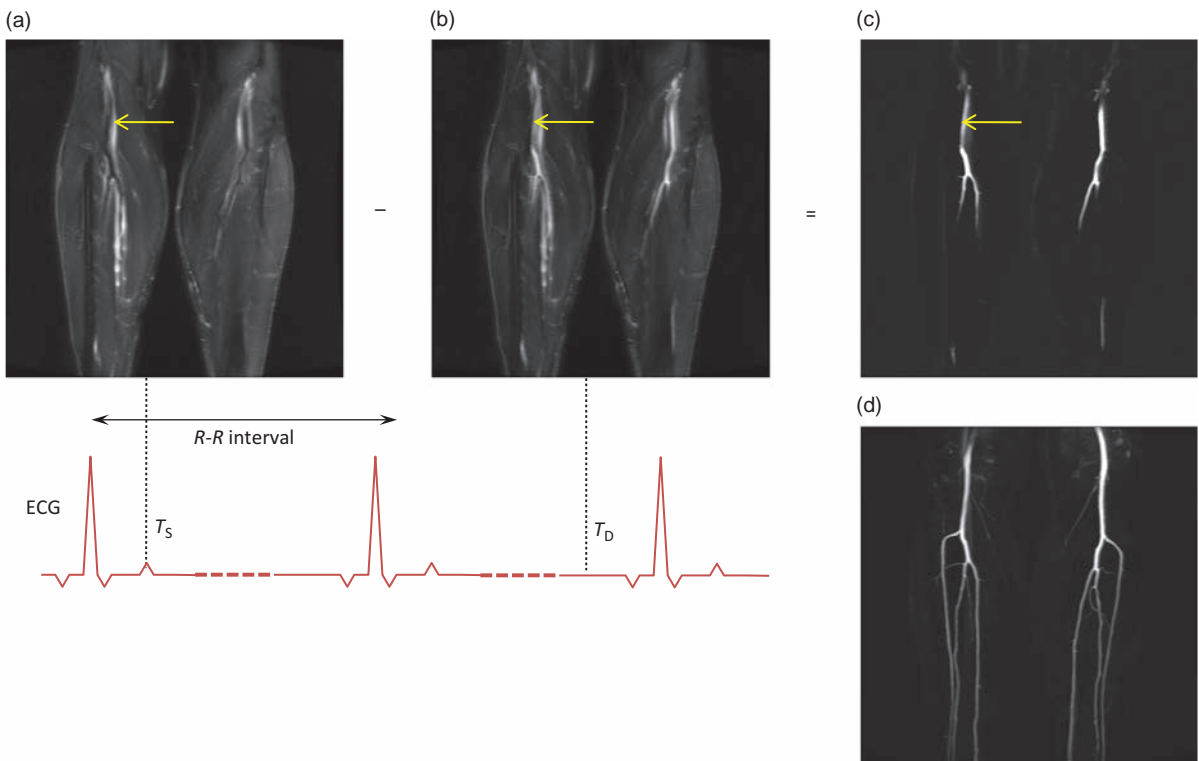


Figure 15.12 Fresh blood imaging. This method uses two 3D multi-shot TSE acquisitions. (a) The first echo train is timed to systole, where fast-moving systolic blood is dephased (arrow). (b) The second echo train is acquired 1 to 3 R-R intervals later and is timed to diastole, where blood velocities are reduced and there is less dephasing. (c) Since venous blood and stationary tissue are identical in both acquisitions, subtraction of the images results in only signal from the arteries. (d) Coronal MIP of subtracted data.

relatively slow and constant throughout the cardiac cycle and appears bright in both acquisitions. Likewise, stationary background tissue appears similar in both acquisitions. A simple magnitude subtraction of the systolic images from the diastolic images results in suppression of the background and venous signals, leaving only the arterial signal as shown in Figure 15.12. An additional STIR preparation helps to reduce the background signal from fat. Non-contrast MR of ArTerIes and VEins (NATIVE) by Siemens, TRiggered Angiography Non-Contrast Enhanced (TRANCE) by Philips and Inhance 3D Deltaflow by GE Healthcare are similar techniques.

Limitations of these techniques include spatial misregistration between the two acquisitions, as only part of the 3D acquisition can be performed in each heartbeat, and image blurring due to T_2 relaxation during the TSE readout. This can be reduced by the use of parallel imaging to shorten the echo train. It is also important to identify the optimal systolic and diastolic trigger delays required for each body area.

An ‘ECG-Prep’ scan such as a single-slice, multiphase, single-shot TSE (SS-TSE) with progressive ECG trigger delays can be used to visually identify the optimal systolic (darkest intravascular signal) and diastolic (brightest intravascular signal) trigger delays.

The scan time for these methods is approximately four minutes for a single 3D location. Multiple vascular territories can be covered by moving the patient and repeating the acquisition. Given the differences in flow profiles, it is often necessary to repeat the ECG-Prep in order to optimize the timings for each location. Since this technique primarily relies on having a good differential flow between systole and diastole, its primary application is in peripheral angiography.

15.3.4 Balanced Steady-State-Free-Precession

Balanced Steady-State-Free-Precession (bSSFP) is a term widely used in the MR angiography literature as a generic term for fully rewound gradient-echo sequences used in MRA. In this chapter, instead of

using our normal term (fully rewound gradient echo) we will use the abbreviation bSSFP. This sequence has an inherently high signal from blood which is relatively independent of flow. ECG and/or respiratory-triggered 3D bSSFP has been used in a number of body areas including imaging the coronaries and thoracic aorta. In bSSFP both arteries and veins appear bright as well as background tissue. An inversion pulse applied prior to the bSSFP readout can null the background signal. Commercial implementations include NATIVE-TrueFISP by Siemens, b-TRANCE by Philips, Inhance inFlow Inversion Recovery (IFIR) by GE Healthcare and time-Spatial Labelling Inversion Pulse (time-SLIP) by Toshiba.

Applications of NC-MRA: Renal Arteries

Balanced SSFP methods are used for renal MRA, particularly in patients with impaired renal function in whom Gd-based agents are contraindicated. In this application, the 180° inversion pulse is used to invert the signal from a large region encompassing the kidneys, inferior vena cava and other tissues. Following the inversion pulse the longitudinal magnetization of the tissue and the blood in the inferior vena cava will recover due to T₁ relaxation and, after a TI of around 1 s, will become zero. In addition, during this TI period arterial blood that originates outside of the inverted region will flow into the imaging region. A spectral inversion pulse is applied

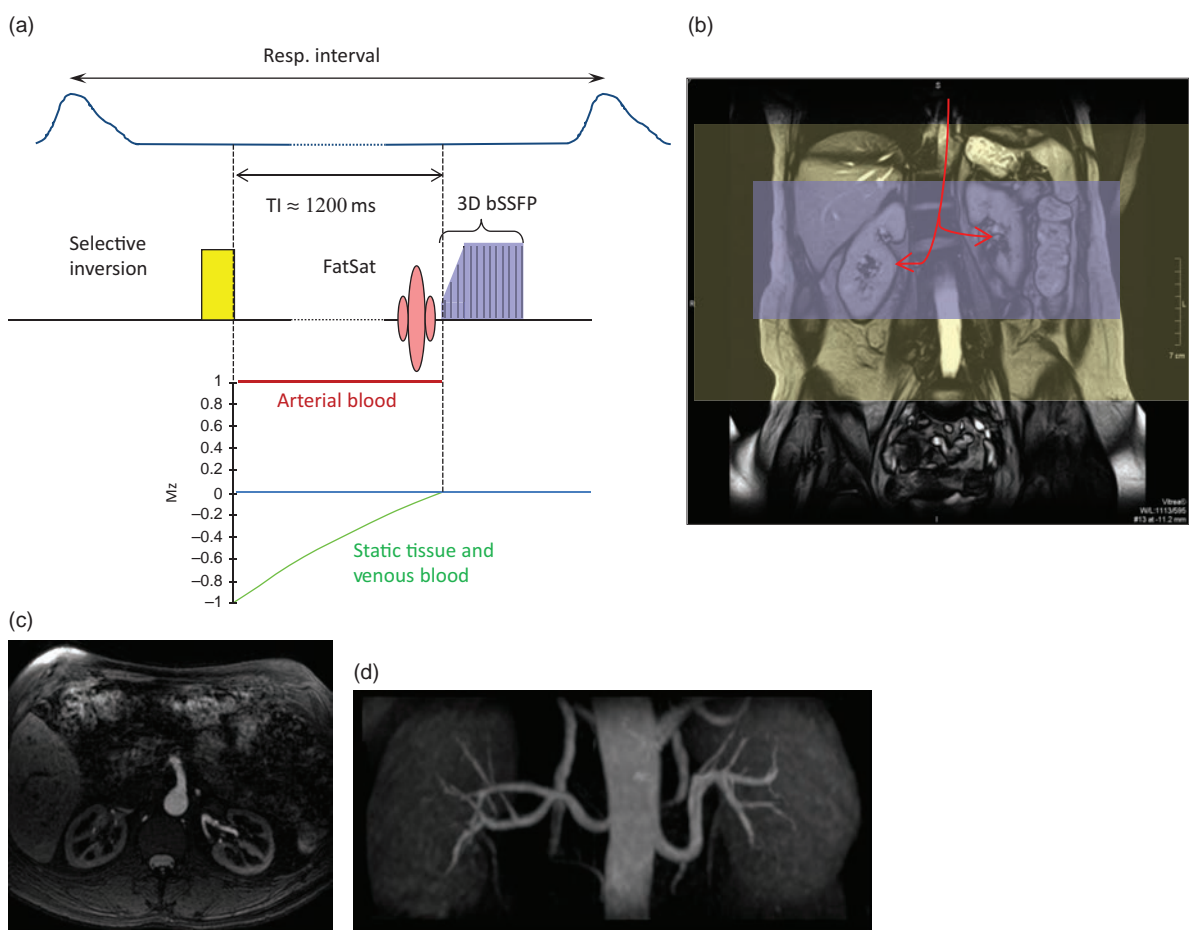
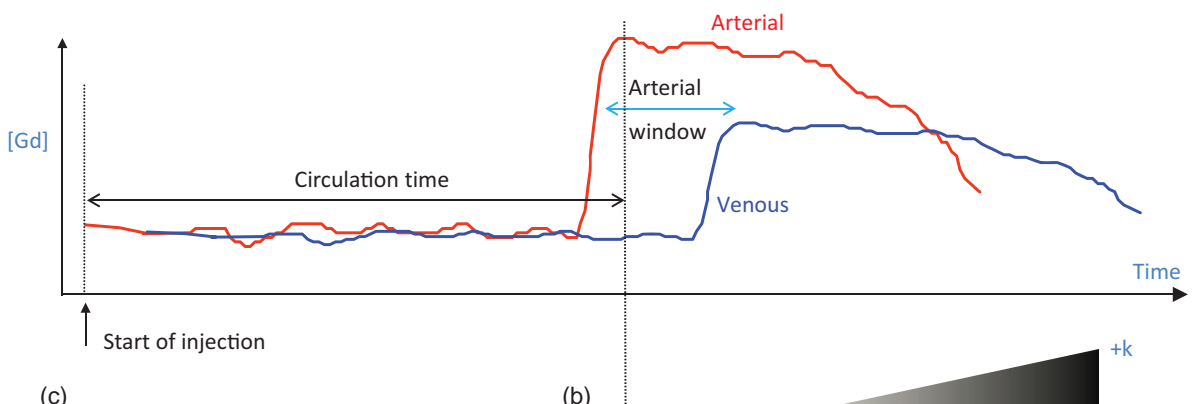


Figure 15.13 NC-MRA of the renal arteries. (a) The pulse sequence has a thick slab selective inversion pulse (yellow) which inverts a region covering both the kidneys and the inferior vena cava. (b) During the inversion time (TI) non-inverted blood from the heart (red arrows) flows into the kidneys. At the same time the inverted magnetization recovers due to T₁. After the TI period the static tissue and venous blood should be approximately zero. A segmented 3D bSSFP readout, which yields a high signal from blood, is then performed. The 3D bSSFP slab (blue) is positioned directly over the kidneys and renal arteries. A spectral inversion recovery pulse is applied just prior to the bSSFP readout to further suppress the signal from fat. (c) A single axial slice from the 3D bSSFP slab. Note the high signal from the blood. (d) Coronal MIP demonstrating the renal arteries.

(a)



(c)



(b)

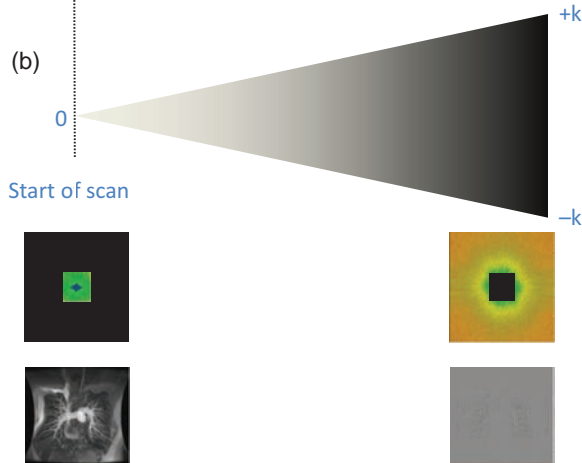


Figure 15.14 Basic principles of contrast-enhanced MRA. (a) Following injection of the contrast agent there will be a delay, known as the circulation time, before the agent reaches the area of interest. There will then be a short period of time, the arterial window, when the contrast is mainly in the arterial circulation and has not reached the venous circulation. (b) Since this arterial window is generally shorter than the full image acquisition, it is usual to start data acquisition from the centre of k-space outwards. This ensures that most of the image contrast is acquired during the arterial window and the periphery of k-space, i.e., the edge information, is acquired later when venous contamination is less of an issue. (c) With the correct timing good-quality arterial-phase angiograms can be obtained, often in a breath-hold.

just prior to the bSSFP readout to reduce the high signal from fat. The bSSFP readout slab is positioned just covering the kidneys and renal arteries. The whole sequence is triggered by the respiratory waveform, with part of the 3D bSSFP acquisition acquired in each respiratory cycle, to minimize misregistration artefact. The overall scan time is around two to four minutes depending upon patient cooperation and the desired spatial resolution. Since the venous and background signals are naturally suppressed, there is no requirement for subtraction of data. The inversion and imaging regions are usually independently positioned to allow targeting of the desired vessels. As with other techniques, the final projection angiogram is produced using a MIP. Figure 15.13 shows the principle of the method for renal NC-MRA.

15.4 Contrast-Enhanced MRA

In CE-MRA a Gd-based contrast agent, injected as a rapid bolus, is used to produce an angiogram. We can think of this as a variant of the 3D TOF techniques since we are exploiting differences in the longitudinal magnetization to yield vascular contrast. But, unlike TOF methods, we are using Gd to shorten blood's T_1 relaxation time, rather than relying on the TOF effect, to cause enhancement of the blood signal. CE-MRA is usually used to acquire large field-of-view 3D angiograms in the coronal or sagittal plane without suffering from spin saturation. A fast 3D T_1W gradient-echo sequence, with very short TE and TR, is used to capture the first-pass transit of the contrast agent bolus through the anatomy of interest. The TE is kept as

short as possible by not using flow-compensation and by employing fractional echo data collection.

15.4.1 Timing Matters

The basic premise of CE-MRA is that a bolus administration of a Gd-based contrast agent will transiently reduce the T_1 of blood during its first pass through the anatomy of interest (see Box 'Reducing the T_1 of Blood'). This will have the effect of substantially increasing the vascular signal. Image acquisition has to be timed to coincide with when the contrast agent concentration is maximal in the area of interest and before the contrast agent reaches the venous circulation and the images become contaminated by the venous return. Because the acquisition time will typically be much longer than this arterial-only time window, we arrange the acquisition so that the centre of k-space, which primarily contributes to the contrast in an image, is acquired when the arterial contrast agent concentration is at its peak. This typically involves acquiring the centre of k-space first. Figure 15.14 shows the relationship between circulation time, arterial contrast agent concentration and data acquisition for a centrically encoded 3D acquisition. Acquiring data too early with respect to the injection can result in poor arterial enhancement and edge enhancement artefacts, while acquiring data too late not only gives poor arterial enhancement but also increases unwanted venous signal. Various methods have been proposed over the years to optimize the timing, ranging from the administration of a small separate test bolus, to administration of the full

bolus with triggering performed either automatically using a 1D 'tracker' region placed inside a vessel or using a 'real-time' fluoroscopic triggering system. Some manufacturers offer a 'real-time' fluoroscopic triggering system in which the operator sees the contrast agent arrival in the desired area and then manually activates the 3D acquisition.

Reducing the T_1 of Blood

The reduction in T_1 achievable with a paramagnetic contrast agent is given by

$$\frac{1}{T_{1,post}} = \frac{1}{T_{1,pre}} + r_1 \cdot [C_A]$$

where $T_{1,pre}$ is the T_1 of blood prior to administration of the agent (typically 1200 ms), $T_{1,post}$ is the T_1 of blood following administration, r_1 is the longitudinal relaxivity of the contrast agent and $[C_A]$ is the concentration of the agent in the blood. Standard Gd-DTPA

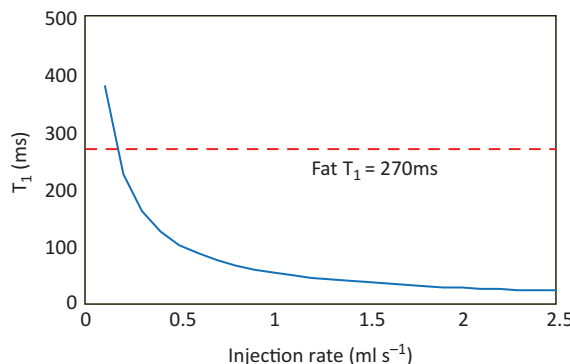


Figure 15.15 Contrast agent T_1 shortening. The curve shows the reduction in blood T_1 as a function of 0.5 M Gd-DTPA injection rate (in ml s^{-1}) for a cardiac output of 5 l min^{-1} . Since fat is usually the brightest tissue in T_1w imaging, the T_1 of fat at 1.5 T (approx. 270 ms) is also shown.

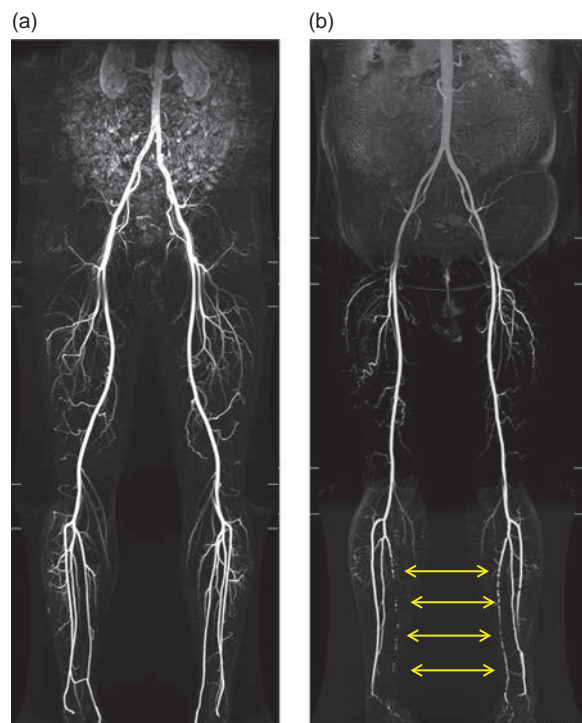


Figure 15.16 Multiple-station peripheral CE-MRA. (a) Three-station moving table subtraction peripheral MRA using a single bolus of contrast at 3 T (patient with no vascular abnormalities). (b) A similar acquisition in a patient with run-off disease in the calf (arrows). Images courtesy of Dr Paul Malcolm, Norwich, UK.

(see Section 3.10) has a concentration of 0.5 mol l^{-1} and an r_1 of approximately $4.5 \text{ s}^{-1} \text{ mM}^{-1}$ at 1.5 T.

For first-pass studies the dynamic contrast agent concentration [C_A] is given by

$$[C_A] = \frac{\text{injection rate } (\text{ml s}^{-1})}{\text{cardiac output } (\text{l s}^{-1})}$$

Figure 15.15 shows the reduction in the T_1 of blood for standard 0.5 M Gd-based contrast agent.

Applications of Moving Table MRA

Contrast-enhanced MRA is ideally suited to large field of view (FOV) coverage since data can be acquired in the coronal or sagittal planes without spin saturation. However, some regions of the body, e.g. the peripheral vasculature, are much larger than the maximum FOV of most MRI scanners. To overcome this FOV limitation we can use so-called 'moving table' or 'bolus chase' techniques, where the patient is automatically moved through the scanner by a fixed distance and a further MRA

acquisition performed. The process is then repeated until the total desired coverage is obtained. The entire peripheral vasculature can be covered in typically three or four slightly overlapping 'stations', as shown in Figure 15.16.

CNR is maximized by first performing a mask run without contrast to use for background subtraction. SNR is high on moving table peripheral MRA because a single, large contrast bolus is imaged multiple times as it travels down the torso and legs. However, timing can be complicated because it is important for the rate at which the table is moving to roughly match the rate at which contrast flows down the legs. In practice, it is virtually impossible for MRA data acquisition and table movement to keep up with the contrast agent flow. The time for table movement between stations should be as short as possible, typically less than 3 s.

15.4.2 4D (Dynamic) CE-MRA

Four-dimensional (4D) MRA are methods to acquire dynamic 3D CE-MRA data. This eliminates the

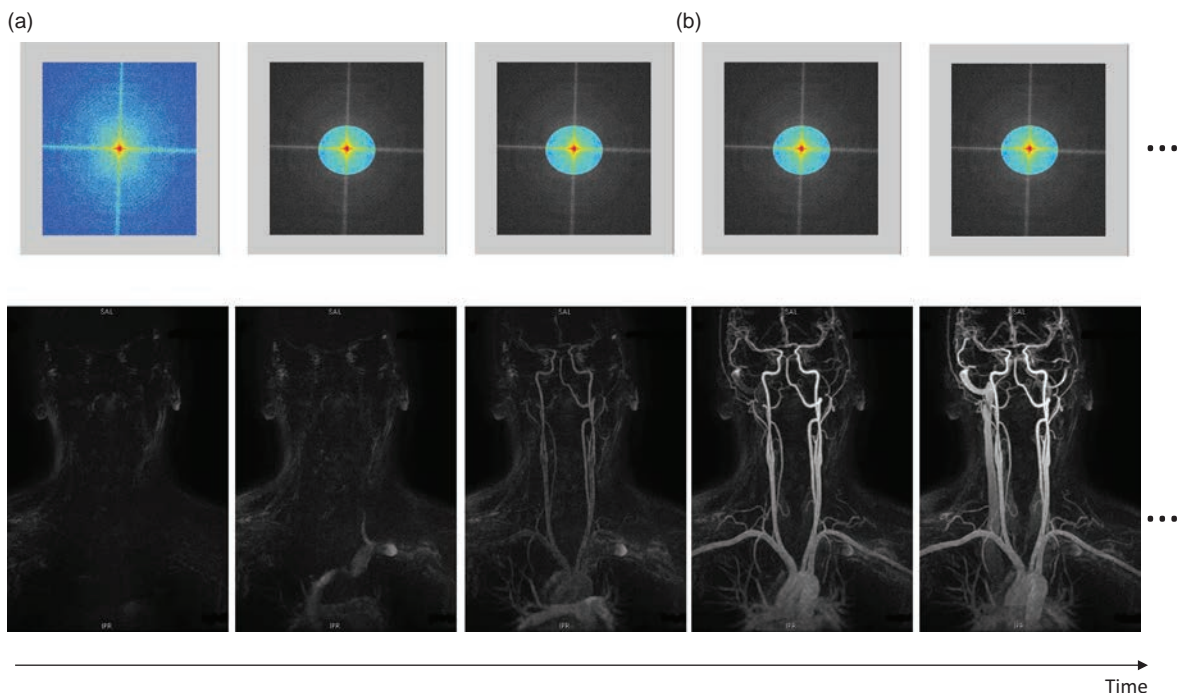


Figure 15.17 Principle of view-sharing or 'keyhole' imaging. (a) Full k-space (colour image) is acquired at the start of the acquisition before the contrast is injected. (b) The contrast is injected but only the centre of k-space (colour region) is acquired to keep the acquisition time short. Once the acquisition is completed the peripheral k-space data are copied to produce a full k-space acquisition. Each temporal phase is then reconstructed. Each of the images is a MIP of the full 3D acquisition for that temporal phase.

necessity of accurate timing since data can be acquired continuously before, during and after the contrast agent injection in order to demonstrate temporal changes in the circulation of the contrast agent through the vasculature. Since, as discussed above, the time to acquire complete 3D data is generally much longer than the contrast agent circulation time it is necessary to use methods of k-space data sharing in order to reduce the effective temporal sampling time. The simplest method of k-space data sharing is to acquire fully sampled 3D k-space at either the start or end of the dynamic acquisition, but to only acquire data from the centre of k-space during the

dynamic acquisition. This is sometimes referred to as 'key-hole imaging'. Full 3D k-space data for each temporal phase are then created by using the same peripheral data from the full k-space acquisition, as shown in Figure 15.17. Clearly in such a situation only the centre of k-space, i.e. the low spatial frequency information, is updated in each temporal phase.

Slightly more sophisticated data-sharing algorithms also update the periphery of k-space during the dynamic acquisition but at a slower rate than the centre. For example, in the Temporally Resolved Imaging of Contrast KineticS (TRICKS) technique

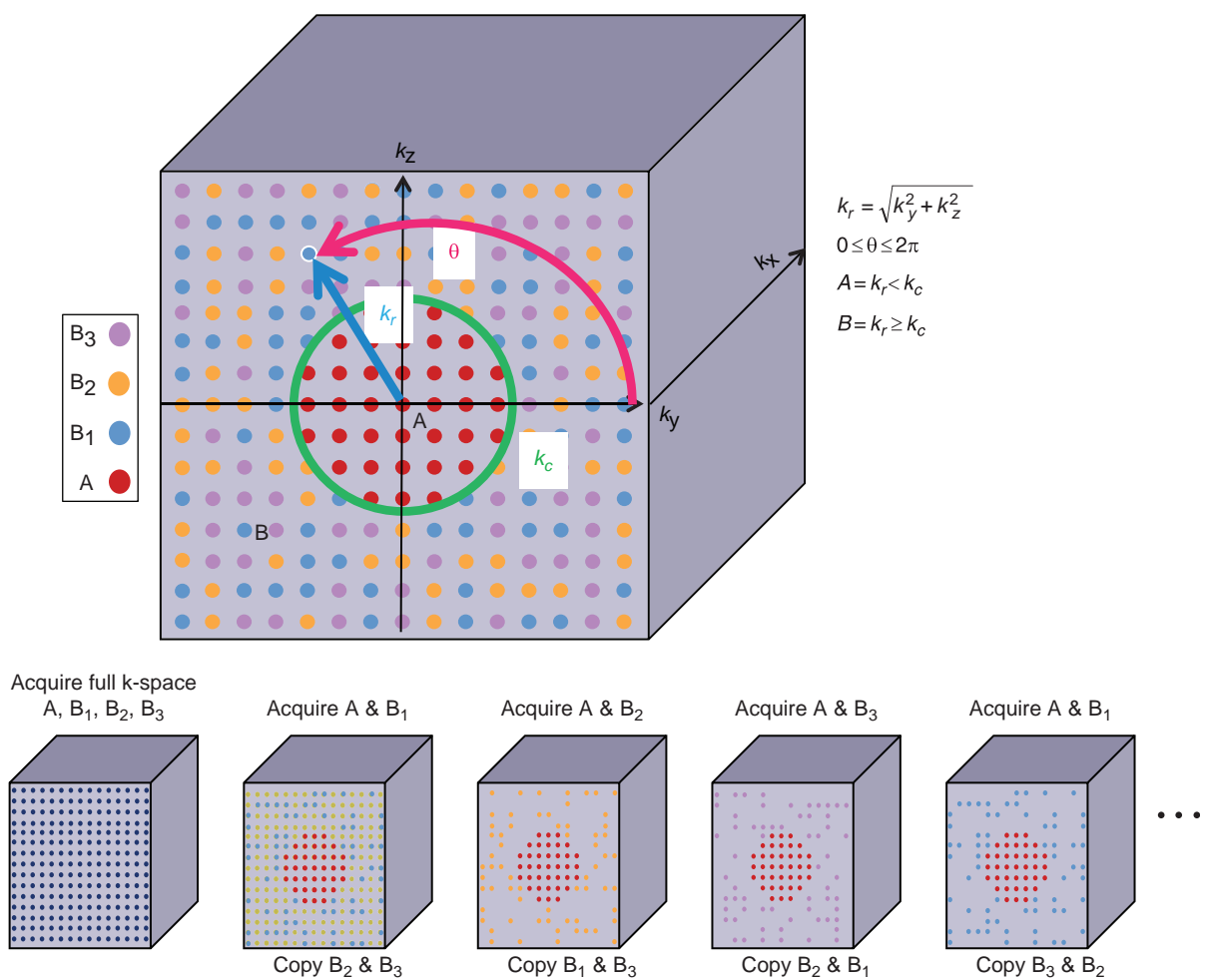


Figure 15.18 TWIST k-space scheme. The k_y-k_z space is divided into two regions A and B, by a circle with radius k_c . The points in the B region are randomly allocated to one of three equally sized groups: B₁, B₂ and B₃. The acquisition starts by fully acquiring k-space, then acquires the k-space regions in the pattern A-B₁-A-B₂-A-B₃. Regions A and B₁ are combined with B₂ and B₃ from the initial acquisition to create a full k-space; this represents the first phase. Phase 2 is created from the newly acquired regions A and B₂, B₁ is copied from the previous k-space and B₃ from the initial k-space. The third phase uses newly acquired regions A and B₃, B₂ copied from phase 2 and B₁ from phase 1.

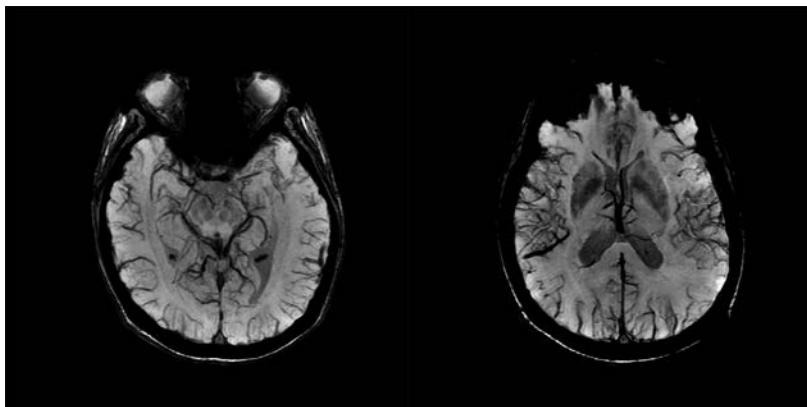


Figure 15.19 Susceptibility-weighted images emphasizing the venous circulation.

available on GE Healthcare systems, k-space, i.e. each k_z-k_y view, is divided into a central region (A) and three concentric outer rings (B, C and D). Initially all three regions are acquired A_1, B_1, C_1 and D_1 and then the central region is acquired every time one of the peripheral rings is acquired, i.e. $A_2, B_2, A_3, C_2, A_4, D_2, A_5, B_3, \dots$ etc. Full k-space data for each temporal phase (ϕ_n) is then reconstructed by sharing the data, i.e. $\phi_1 = [A_2 \ B_1 \ C_1 \ D_1], \phi_2 = [A_3 \ B_2 \ C_1 \ D_1], \phi_3 = [A_4 \ B_2 \ C_2 \ D_1], \dots$ etc. Similarly, the Time-resolved angiography With Interleaved Stochastic Trajectories (TWIST) method (Siemens systems) also has a central region A but then the whole of the peripheral k-space is randomly assigned to one of three groups B₁, B₂ and B₃. The A region is then sampled more frequently than the B region and the data shared to create full k-space, as shown in Figure 15.18. Note that the order of sampling in any particular B group is smoothly varying based on the angle θ and radial distance k_r of an individual sampling point, with every odd point acquired on the way out towards the maximum k_r and every even point on the way back in towards k_c . The full range of parallel imaging techniques can also be applied with these methods to further reduce the apparent temporal resolution.

15.4.3 Contrast Agents

The majority of commercially available contrast agents are based upon particular chelates of gadolinium. Different ligands result in different contrast agents having different relaxivities (r_1). The majority of ligands have r_1 values in the range 4.3 to $6.7 \text{ mM}^{-1} \text{ s}^{-1}$. Gadobenate dimeglumine is an example of an agent that

weakly and reversibly binds to human serum albumin (HSA), increasing the r_1 value to around $11 \text{ mM}^{-1} \text{ s}^{-1}$, while gadofosveset binds strongly to HSA and has an r_1 value of around $30 \text{ mM}^{-1} \text{ s}^{-1}$ and acts as an intravascular/blood-pool contrast agent. It should be noted that r_1 values are dependent upon the media in which they are placed – blood is different to saline – as well as the Larmor frequency at which r_1 is measured. Ultra-small paramagnetic iron oxide (USPIO) nanoparticles were evaluated as blood-pool agents for MRA but these have not become commercially available.

15.5 Susceptibility-Weighted Imaging

Susceptibility-Weighted Imaging (SWI) is a method of enhancing susceptibility differences in tissues. The basic SWI acquisition is a long-TE 3D gradient-echo acquisition, flow-compensated in all three directions, in which both the magnitude and phase data are collected. The phase data is high-pass-filtered to remove the low-spatial frequency phase variations that occur across the field-of-view due to poor magnetic field shimming or air–tissue interfaces. The resulting phase mask is then used in combination with the magnitude image to emphasize either positive or negative, or both, phase shifts. Susceptibility-weighted imaging, like the BOLD techniques, is sensitive to deoxyhaemoglobin in the venous circulation. In SWI the negative phase mask is used to enhance the contrast for veins and is hence sometimes referred to as Susceptibility-Weighted Angiography (SWA). The processed SWA images can then be displayed by the use of a minimum Intensity Projection (mIP)

to demonstrate the venous vasculature. Alternative methods of acquiring SWA include the acquisition of multi-echo gradient-echo images followed by a

weighted sum of the images obtained at different echo times without the use of the phase data. Figure 15.19 shows an example of susceptibility-weighted images.

Further Reading

- Carr JC and Carroll TJ (eds) (2012) *Magnetic Resonance Angiography: Principles and Applications*. New York: Springer.
- Haacke EM, Mittal S, Wu Z, Neelavalli J and Chenga Y-CN (2009) 'Susceptibility-weighted imaging: technical aspects and clinical

- applications, part 1'. *Am J Neuroradiol* 30:19–30
- Hartung MP, Grist TM and Francois CJ (2011) 'Magnetic resonance angiography: current status and future directions'. *J Cardiovasc Magn Reson* 13:19. Available online at www.jcmr-online.com/content/13/1/19 [accessed 8 May 2015].
- Hashemi RH and Bradley WG Jr (2010) *MRI The Basics*, 3rd edition. Baltimore, MD: Lippincott, Williams & Wilkins.
- Wheaton AJ and Miyazaki M (2012) 'Non-contrast enhanced MR angiography: physical principles'. *J Magn Reson Imaging* 36:286–304.

16.1 Introduction

Cardiac MRI has always been one of the most challenging clinical applications. Imaging in the presence of cardiac and respiratory motion as well as blood flow has required the development of robust methods to obtain good-quality images in patients who, by definition, have irregular ECGs, and often present with difficulties in holding their breath. Fortunately continued developments in system hardware, pulse sequences and reconstruction algorithms have improved the reliability of standard imaging methods and have also introduced new techniques for myocardial tissue characterization. Given these technical advancements, challenges remain for the user in understanding and optimizing the sequences and methods.

In this chapter we will explain that:

- good patient preparation is important for obtaining high-quality cardiac studies;
- ‘dark-blood’ imaging techniques provide morphological scans of the heart;
- ‘bright-blood’ cine imaging methods are used to assess global and regional ventricular cardiac function;
- contrast-enhanced MRI can be used to evaluate myocardial ischaemia and viability.

16.2 Patient Set-up

Historically, cardiac MRI has often been considered as ‘difficult’. However, modern scanners have removed much of the mystique and complexity of performing cardiac imaging. The major technical challenges arise from motion: of the heart itself, pulsatile blood flow and respiratory motion. Many artefacts arise because of changes in signal intensity or phase with time and commonly result in ghosting artefacts.

The most effective method to reduce motion is to trigger or gate the acquisition to the patient’s physiology. Triggering is usually used to describe a sequence that is started by a particular event, such as the scanner hardware detecting an ECG ‘trigger’, while gating is used to describe a method where data are only acquired during a particular time period, or ‘gate’, such as during a quiet period of the patient’s breathing. However, the terms gating and triggering are often used interchangeably.

ECG triggering is used so that data are always acquired in the same part of the cardiac cycle so ideally the position of the heart is the same. This requires a good-quality ECG waveform for the MRI system to detect the R-wave and trigger the acquisition (see Box ‘Perfect Gating Needs Good Preparation’). Obtaining a good ECG inside the bore of an MRI system is not easy, for two reasons: first, the electrodes need to be placed reasonably close together to avoid large differential voltages being induced in the cables by the gradients and RF; and second, the ECG waveform itself is distorted through the magneto-hydrodynamic effect: an additional voltage induced by blood (a conducting fluid) moving within a magnetic field. Since the fastest blood flow in the aorta occurs at the time of ventricular ejection, this additional voltage is superimposed on the T-wave of the ECG. The amplitude of the T-wave may then be greater than that of the R-wave, resulting in incorrect triggering.

Fortunately, ECG triggering has become significantly more reliable through the widespread use of Vector Cardiac Gating (VCG), as shown in Figure 16.1. Four electrodes are placed in a cross arrangement so that there is a left-right signal component (x) and a superior-inferior signal component (y). Simultaneously acquiring both components allows the direction of the R-wave to be tracked as it moves with the cardiac cycle. It has been shown that

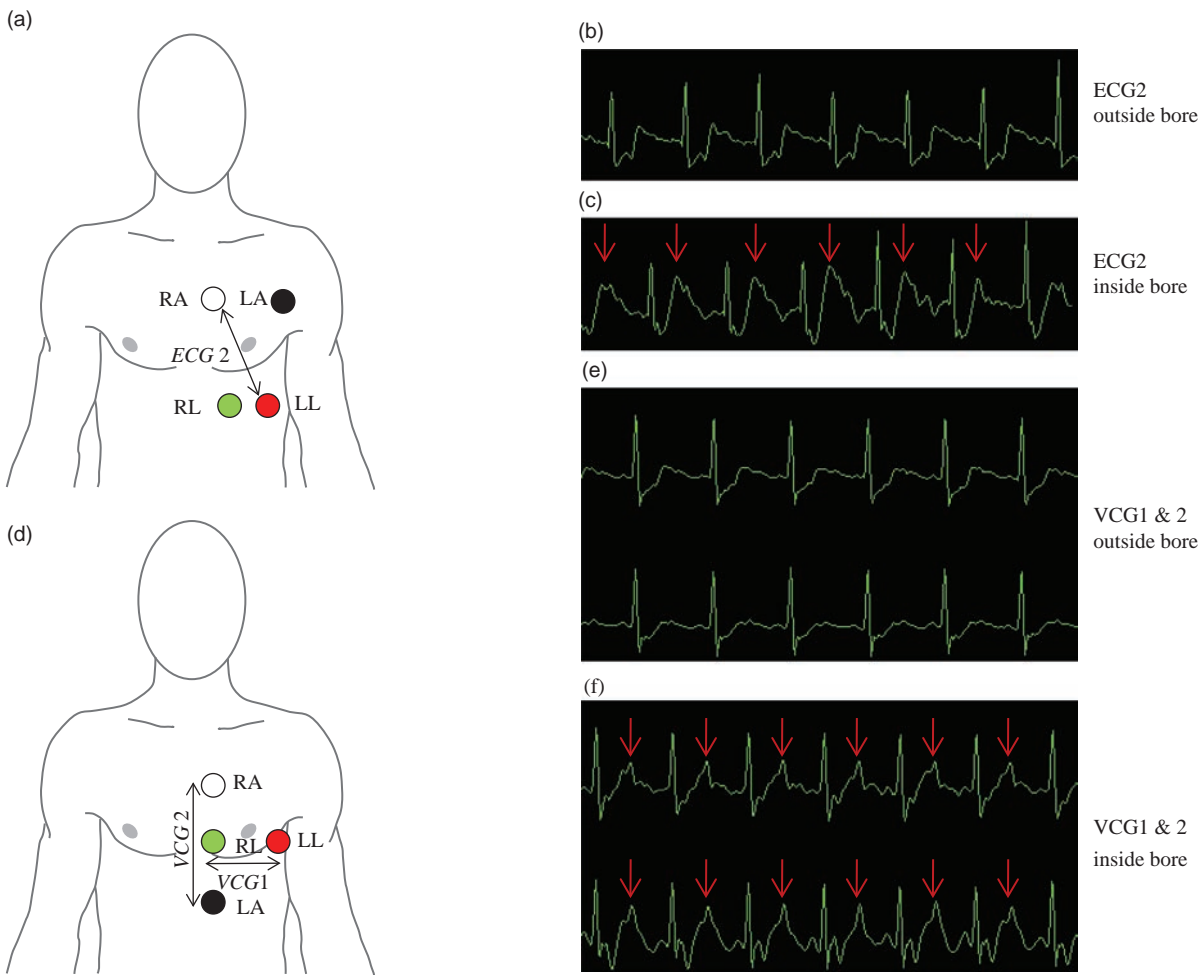


Figure 16.1 ECG gating. (a) Original ECG electrode placement to obtain a standard Lead II ECG (ECG2). (b) This arrangement can produce an acceptable waveform outside of the magnet. (c) Inside the bore of the magnet the magneto-hydrodynamic effect means that the T-wave can increase in amplitude (arrows). This may cause false triggering. (d) Electrode arrangements for vector electrocardiogram (VCG). The electrodes are positioned in a crossed arrangement so that there is a left-right signal component ($x - VCG1$) and a superior-inferior signal component ($y - VCG2$). (e) Outside of the magnet the waveforms are good. (f) Inside the bore of the magnet there is still a larger T-wave (arrows), but signal processing of both the VCG1 and VCG2 waveforms can reduce false triggering.

the electrical vector of the heart tracks a different path to that of the magneto-hydrodynamic artefact. Appropriate signal processing of both the spatial and temporal changes of these 2D vectors significantly improves the triggering reliability compared to just using a standard ECG.

To overcome respiratory motion, nowadays we usually make sure that the entire data collection is acquired in a single breath-hold. However sequences that cannot be made fast enough, e.g. some 3D acquisitions, may require respiratory triggering. This is typically achieved by the use of either a pneumatic

bellows positioned around the patient's chest, or by respiratory navigators. The respiratory signal from the bellows triggers the MRI acquisition when the patient's chest movement is relatively quiet, i.e. at end expiration. You typically select the desired trigger point of the acquisition as well as the repeat time in terms of the number of respiratory cycles. While the bellows are an indirect method of monitoring respiration, a navigator is an MR method for directly tracking the motion of the diaphragm.

A navigator is a mini pulse sequence that excites and receives the MR signal from a one-dimensional

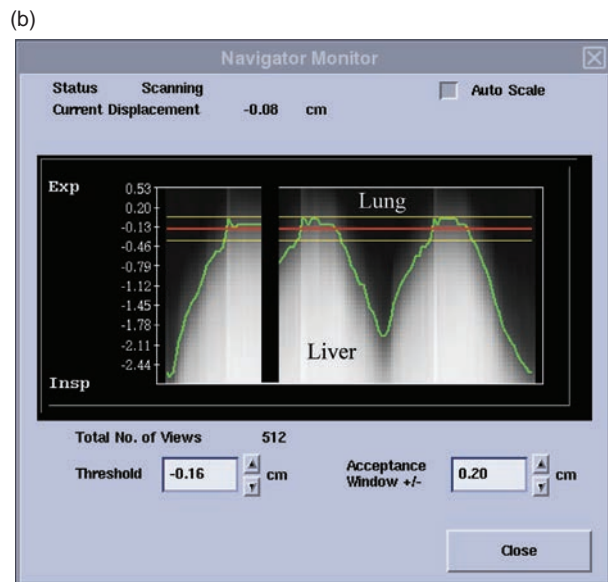
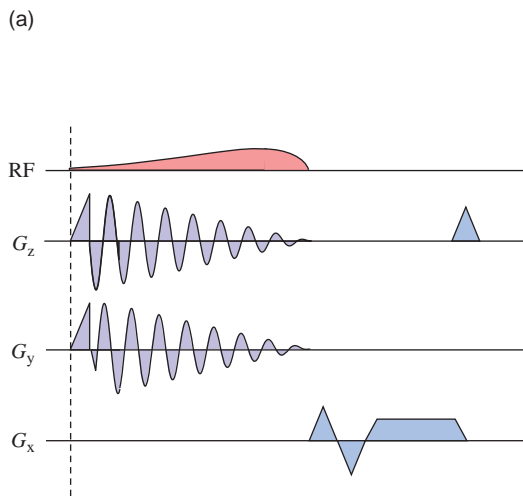


Figure 16.2 Navigator echoes. (a) 2D cylindrical navigator pulse sequence. The navigator is positioned on the dome of the left hemidiaphragm. (b) Typical navigator output. The bright signal below the green line is the liver, while the darker signal above is the lung. The two yellow parallel lines represent the acceptance window and the red line the threshold.

column of spins usually positioned on the right hemidiaphragm (see Box ‘Navigating the Pulse Sequence’). The signal is Fourier transformed and shows the contrast between the lung (dark) and the diaphragm/upper edge of the liver (bright). The navigator initially monitors the patient’s diaphragm motion and establishes a user-controllable acceptance window. Once the imaging sequence is started, the navigators are played out repeatedly until the diaphragm position falls into the acceptance window, at which point a proportion of the total data acquisition is performed. In more sophisticated applications the diaphragm position is monitored before and after the image acquisition, and data are rejected if the post-acquisition navigator indicates that the diaphragm has moved out of the acceptance window during the image acquisition. Figure 16.2 shows the sequence and data acquisition for a navigator.

The use of multiple channel coil arrays that can exploit parallel imaging techniques has made a particularly big impact on cardiac imaging. Parallel imaging can be used, for example, to reduce the overall acquisition time, or to improve the temporal resolution or coverage of a particular acquisition. All the methods described in this chapter can be accelerated and you should work with your system vendor to optimize their use on your particular system.

Perfect Gating Needs Good Preparation

The key to obtaining a good triggering waveform is to spend some time preparing the electrode sites. First, any chest hair should be removed with a razor; second, the skin should be gently abraded using an appropriate gel to strip away the top layer of skin and moisten the underlying layer. This reduces the skin impedance and improves the electrical conductivity. Appropriate MRI-safe ECG electrodes and leads should always be used. Poor VCG signal is the single largest cause of failed cardiac MR exams. Your manufacturer will often have special advice, and you should take some time to practice electrode positioning to make sure you do everything you can to get it right every time.

If it is not possible to obtain an adequate ECG trigger, then **Peripheral Gating (PG)** could be used for triggering, using a photoplethysmograph, often just called the ‘pleth’, positioned on a finger or toe. However, it should be noted that there is a significant delay (150–500 ms) between the R-wave of the ECG and the peak of the peripheral pulse. The PG signal simply reflects the change in blood volume through the vessels in the finger or toe and is therefore insensitive to magnetic field effects. Note that images acquired immediately after the PG trigger will fall in diastole and that systole may be lost in any arrhythmia rejection (AR) period at the end of the PG cycle.

Navigating the Pulse Sequence

Navigators involve some unusual methods for pulse sequence programming. The first question is how do you excite a column? The first possibility is a spin-echo sequence with orthogonal slice-selective gradients on the 90° and the 180° pulses, thus the spin-echo signal only arises from the column of spins where the two intersect. The column can be freely positioned and angled, but has the disadvantage of creating black bands where the navigator selection intersects with the main image – possibly right through the anatomy of interest.

The alternative is a 2D excitation, as shown in Figure 16.2. The alternating gradients during the RF pulse excite a circular column, often known as a pencil beam. Since it's a gradient echo, it can be used with a shorter TR and less SAR than the spin-echo technique.

16.3 Morphological Imaging

Most morphological imaging is done with ECG-triggered fast/turbo spin echo acquired in a breath-hold. Since the duration of a TSE echo train may be relatively long, data acquisition is usually performed in diastole when cardiac motion is minimized. Unfortunately blood within the cardiac chambers is also stationary in diastole, and this can result in undesirable high signal from stationary blood within the ventricles. To overcome this, we use a Double Inversion Recovery (DIR) scheme before the TSE acquisition, known as blood suppression, dark blood or black blood preparation. Figure 16.3 shows the principles of DIR blood suppression. The DIR preparation starts with a non-selective 180° pulse, which inverts spins in the entire imaging volume. This is immediately followed by a

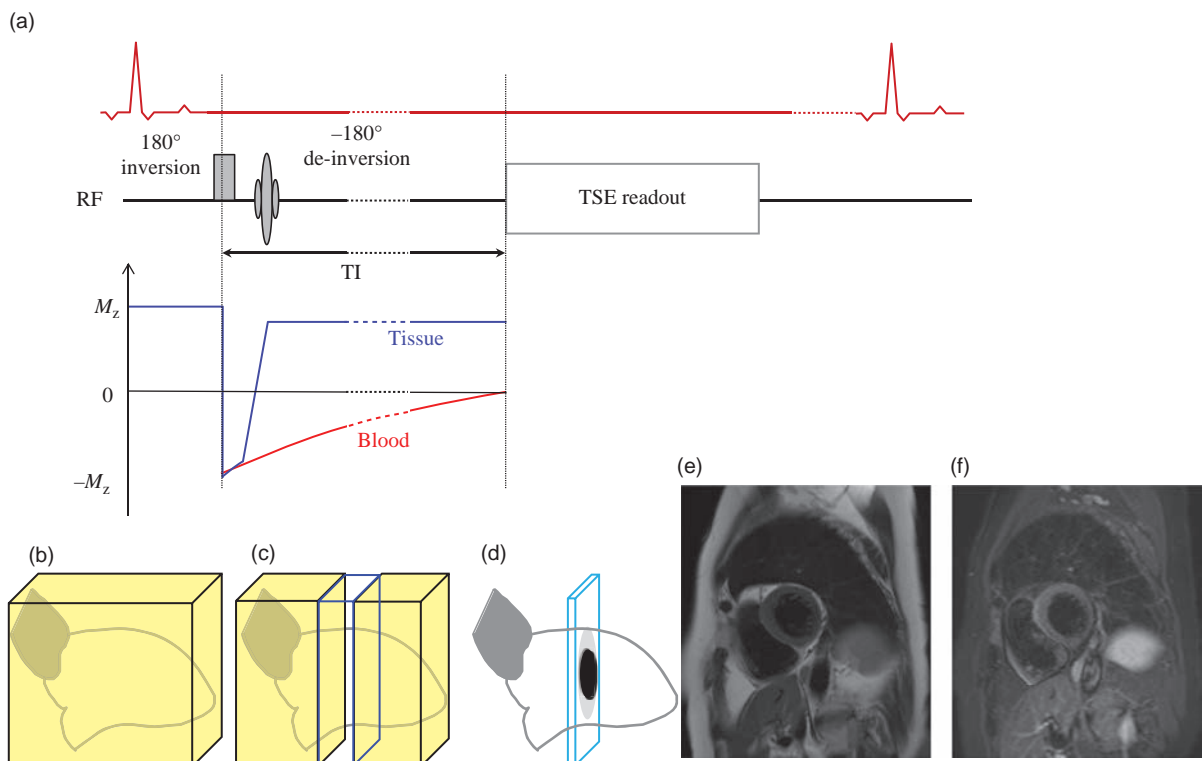


Figure 16.3 Principles of black-/dark-blood suppression. In (a) the first non-selective 180° inversion pulse inverts all the magnetization (b). This is immediately followed by a slice-selective 180° de-inversion that returns the tissue signal back to equilibrium (c). However, the blood outside the de-inversion slice remains inverted. During the TI time blood washes out of the de-inverted slice and inverted blood washes in. The TI is chosen so that the readout is applied when the M_z magnetization of blood crosses zero. The readout slice thickness (d) is thinner than the de-inversion slice thickness to account for myocardial motion during the TI time. The resultant image (e) demonstrates good blood suppression. A third inversion pulse can also be included, which can be used to suppress the signal from fat (f), to give a fat- and blood-suppressed image.

slice-selective 180° de-inversion. The goal is to invert all the spins outside of the imaging slice, while the static spins within the slice experience both the inversion and the de-inversion, i.e. they are effectively unchanged. There is a delay time T_1 before the start of the TSE sequence, which fulfils two requirements: first, blood within the imaging slice will wash out of the slice and be replaced by inverted blood; second, the inverted blood will recover due to T_1 relaxation. As you might expect, the T_1 is calculated so that at the image acquisition the blood is at the null point, giving no signal. If all the blood in the slice is replaced by in-flowing blood during T_1 , we will get a perfect ‘black blood’ appearance within the ventricles. Note that blood that is not replaced during the T_1 period, i.e. very slow-flowing blood, or blood flow that is mainly in-plane, may not be completely suppressed. The T_1 is normally calculated based on literature values for T_1 of blood (around 1400 ms at 1.5 T, and 1600 ms at 3 T), but it also depends on the duration of the echo train, and the TR (generally one or two R-to-R-wave intervals). Therefore black-blood preparation schemes are not easy to use post-Gd, since the T_1 of blood will be reduced to an unknown value.

DIR preparation can also be combined with single-shot turbo spin echo (SS-TSE) or HASTE. This allows a complete image to be acquired in a single heartbeat, and therefore multiple images can be acquired in a single breath-hold. These scans are typically used for cardiac localizers or scouts.

A third slice-selective 180° pulse can also be incorporated into the sequence preparation to give a STIR contrast mechanism. This permits fat-suppressed images to be obtained with the benefits of a blood-suppressed, breath-hold TSE acquisition. T_2 -STIR is widely used to assess the oedema associated with acute myocardial infarction, with the size of the T_2 abnormality correlating with the so-called area-at-risk (AAR), the region of the myocardium that may or may not go on to infarction.

16.4 Functional Imaging

Functional cardiac imaging is designed to visualize the heart motion throughout the cardiac cycle. We use gradient-echo sequences for this, triggered by the VCG. Gradient-echo sequences have very short repetition times (TR), so data from the same slice location can be acquired at different time-points through the

cardiac cycle. Each time-point is known as a ‘cardiac phase’ or ‘temporal phase’. Thanks to the flexibility of MR slice selection, it is possible to acquire multiphase ‘cine’ images in any plane. For example, a properly positioned four-chamber view demonstrates the function of the left and right ventricles and atria as well as the tricuspid and mitral valves in the same slice. From this plane a stack of Short Axis (SA) cine images encompassing the entire left ventricle can be obtained. The SA view is the preferred orientation for the study of global and regional ventricular function. Another commonly used orientation is the Left Ventricular Outflow Tract (LVOT) view which allows visualization of blood entering and leaving the left ventricle. There are some special MR techniques unique for cardiac cine imaging, explained in the following sections.

Finding Your Way with Cardiac Planes

Cardiac MRI does not typically use standard, axial, sagittal and coronal views. Most imaging planes are double oblique, orientated to the heart chambers and the valves. Obtaining these standard views requires a good knowledge of cardiac anatomy and lots of practice. Figure 16.4 shows the slice prescriptions in order to obtain the main cardiac planes. Each image is a single (end-diastolic) phase from a 20 temporal-phase cine acquisition.

16.4.1 Balanced Steady-State-Free-Precession

In the early days of cardiac MRI, cine imaging used spoiled gradient-echo sequences. These sequences relied on the in-flow of blood to provide the contrast between the bright blood-pool and the darker myocardium; hence image quality could be quite variable. Cardiac MRI was therefore substantially improved with the development of cine balanced steady-state-free-precession (bSSFP), a fully rewound GE sequence. As in the MRA world, ‘bSSFP’ is widely used as the generic term in the cardiac MR world, so in this chapter we will follow the same convention. Since the contrast in bSSFP depends mainly on the ratio T_2/T_1 , the contrast between blood (where the ratio is high) and myocardium (where it is less), is much better. You might know bSSFP as FIESTA, bFFE or True-FISP, depending upon your scanner.

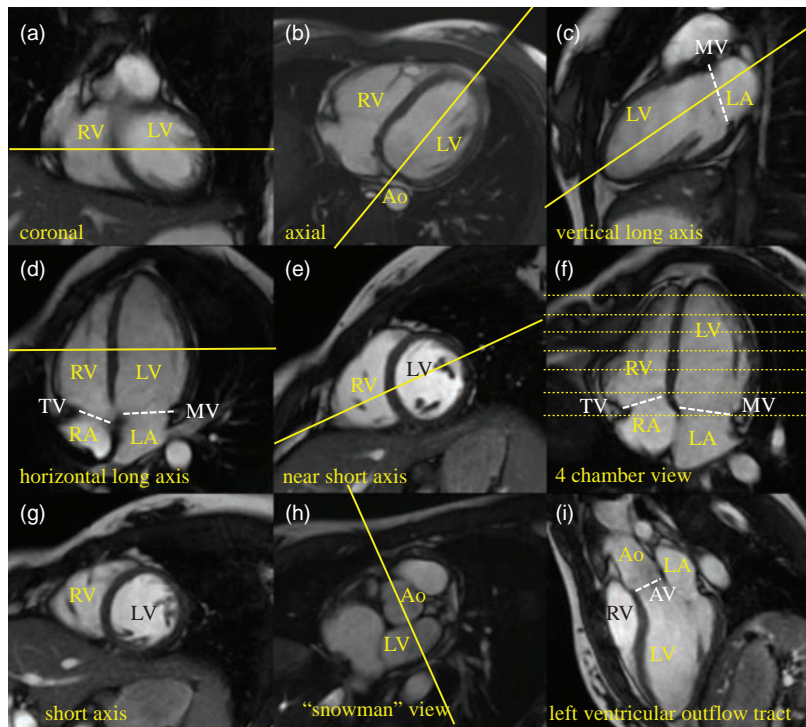


Figure 16.4 Cardiac planes prescription, starting from (a) a coronal view. From this an axial slice through the left ventricle (LV), right ventricle (RV) and aorta (Ao) is obtained (b). (c) An oblique slice through the centre of the LV parallel to the septum, to create a vertical long axis (VLA) view (c). (c) An oblique slice through the apex of the LV and the middle of the mitral valve (MV), which creates a horizontal long axis (HLA) view showing the right atrium (RA), left atrium (LA), MV and the tricuspid valve (TV) (d). (d) A slice perpendicular to the septum obtains a near short axis slice (e). An oblique slice through the centre of the LV and the inferior margin of the RV obtains the standard four-chamber view (4CH). The standard stack of short axis slices (dotted lines) is then prescribed on this 4CH view, perpendicular to the septum. A typical mid-ventricular short axis slice is shown in (g). (h) A more basal short axis slice demonstrating the ‘snowman’ view of the Ao and top of the LV. (i) An oblique slice through the middle of the snowman results in the view of the left ventricular outflow tract (LVOT) which shows the aortic valve (AV).

16.4.2 Segmented k-Space Acquisitions

Ideally we would like to acquire all the data for each multiphase cine slice in a single breath-hold. Each temporal phase involves the acquisition of a number of phase-encoding steps, similar to the echo-train length in turbo spin echo. Unfortunately different manufacturers use different terms to refer to this method, which has enormous potential to confuse both us (the authors) and you (the reader). We will therefore make our own definitions, as follows: an individual phase encoding is called a ‘view’ and the number of views that make up an individual temporal phase as the ‘echo train length’ (ETL). This technique of acquiring multiple views in a single R-R interval is called segmented k-space imaging. The basic principles of segmented k-space cine imaging are shown in Figure 16.5.

Let’s use an example to show how segmented k-space imaging works. We will acquire a multiphase cine acquisition with a frequency \times phase matrix of 256×128 , i.e. each cine phase comprises 128 views. If we acquire one view per temporal phase in each heartbeat then the total acquisition time would be 128 heartbeats. If the heart rate was 60 bpm, i.e. the

R-R interval was 1000 ms in duration, then the acquisition time would be over 2 min, which is certainly not a breath-hold. However, since the individual TR for each bSSFP view might only be 3.5 ms, we could theoretically acquire $1000/3.5 \approx 285$ temporal phases. That’s far more than we really need, so it would make sense to acquire more than one view per temporal phase in each R-R interval. Suppose that instead of collecting one view per temporal phase we collect 12, i.e. we make the ETL = 12. The overall acquisition time is now only $128/12 \approx 11$ heartbeats, which is a reasonable breath-hold time of 11 s. The data acquisition time for each ETL, i.e. the effective temporal resolution, would now be $3.5 \times 12 = 42$ ms, and the maximum number of temporal phases we could acquire would be $1000 \div 20 \approx 23$.

In keeping with our TSE analogy, some manufacturers, such as Siemens, refer to the 42 ms duration of each temporal phase as the ‘TR’ and the duration of each view (3.5 ms) as the echo-spacing (ESP), i.e. the $TR = ETL \times ESP$. The choice of ETL in practice will depend upon how long the patient can hold their breath and the amount of acceptable artefact, i.e. blurring and ghosting due to motion, which can occur during each temporal phase.

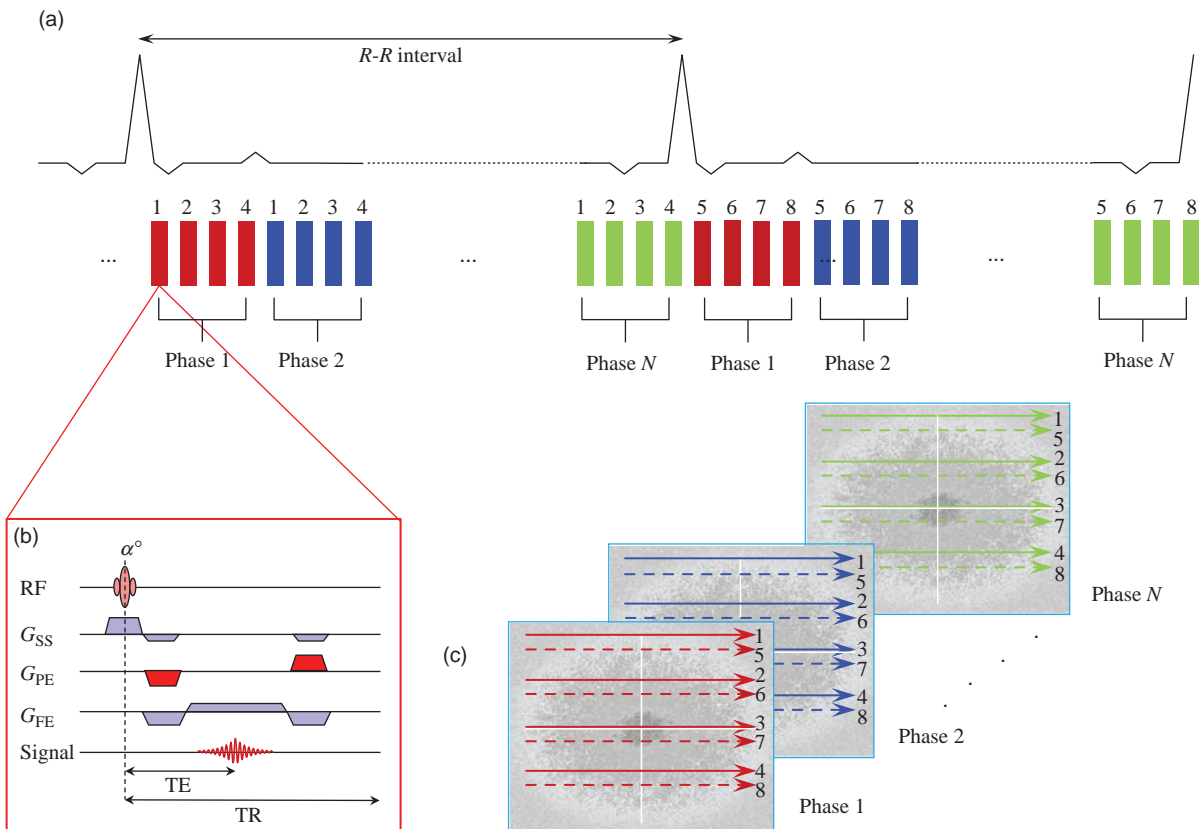


Figure 16.5 Segmented k-space cardiac imaging. In order to reduce the overall acquisition time a number of phase-encoding steps, or views, are acquired in the same heartbeat. Each line in (a) represents a single TR balanced steady-state-free-precession gradient-echo sequence (b) with a specific phase-encoding gradient amplitude. In this case four views are acquired for each raw data temporal phase (c) per R-R interval.

16.4.3 Prospective and Retrospective Cine Imaging

So far we have assumed that the heart rate does not change for the 11 heartbeats that are required to fully complete the cine scan. In reality many patients have arrhythmias which means that their heart rate may vary during the scan. Any heartbeat that is shorter than normal will result in incomplete data acquisition. A simple way to prevent this is to monitor the patient's heart rate for a few beats to establish its variability. The user can then set a period known as the Arrhythmia Rejection Period (ARP) shown in Figure 16.6, during which the data acquisition will be disabled. The ARP is typically 10–20% of the duration of the average R-R interval. This allows the R-R interval to vary within the ARP without the data from the arrhythmic heartbeat being rejected. In order to maintain the magnetization in a steady state

the pulse sequence continues to play out during the ARP; it is just data acquisition that is disabled. This method is known as prospective triggering since the system looks for the next R-wave trigger after the ARP to occur. Any data that are acquired when an R-R interval falls outside of the arrhythmia rejection window are discarded and reacquired. The disadvantage of prospective gating is that data are not acquired during the ARP and therefore we may miss important information about ventricular function during end-diastole.

The alternative to prospective triggering is retrospective gating, in which data are acquired throughout the cardiac cycle, including the ARP, and the duration of each heartbeat is recorded. The arrhythmia rejection window may be much larger, typically 50%, so fewer beats are discarded. Any variation in R-R interval length is addressed by the retrospective processing. After the scan is complete, each heartbeat

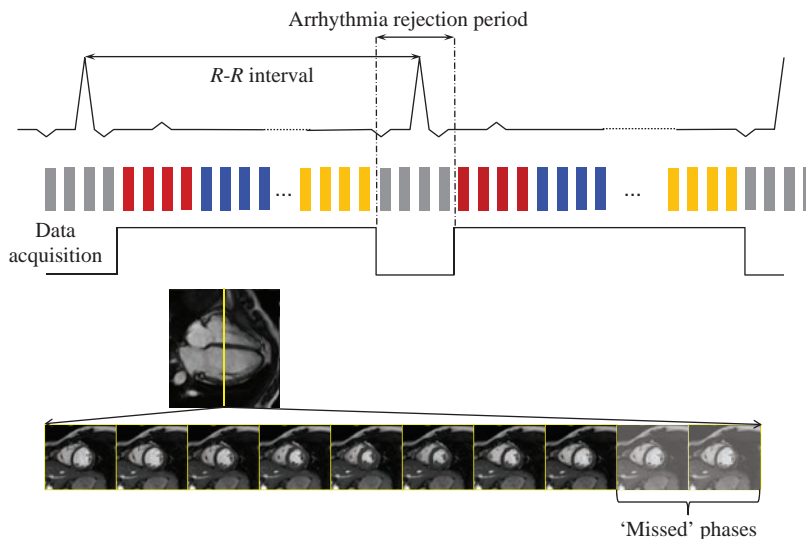


Figure 16.6 Prospective gating. Data acquisition is initiated or triggered by the ECG; however, data acquisition is turned off during the arrhythmia rejection period, typically 10–20% of the nominal *R-R* interval. Phases at the end of the cardiac cycle are therefore missed. The pulse sequence continues to play out during the arrhythmia rejection period (grey segments) to ensure that the magnetization remains in the steady state. Any data that are acquired when an *R-R* interval falls outside of the arrhythmia rejection window are discarded and reacquired.

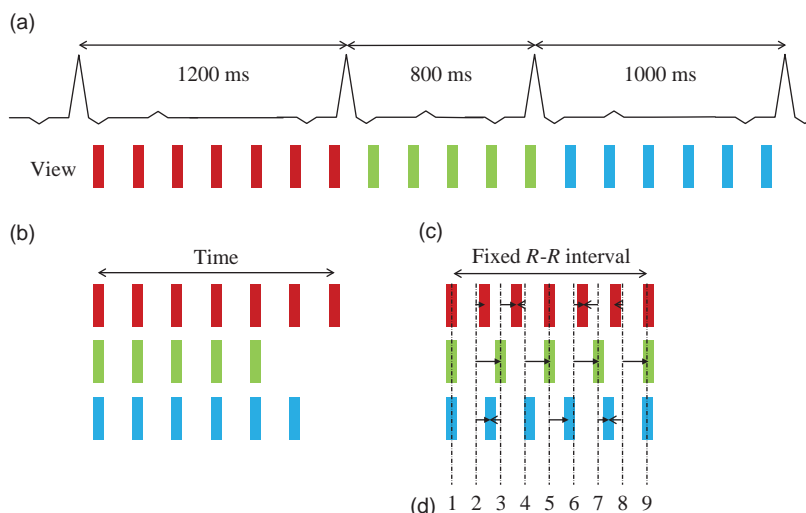


Figure 16.7 Retrospective processing. (a) Three consecutive heartbeats have different *R-R* intervals. Each line represents one phase encoding step or view, i.e. this example shows three different views (red, green and blue), each acquired in a different heartbeat. (b) This results in a different number of views for each heartbeat. (c) In retrospective processing, each *R-R* interval is made the same fixed length by either contracting or stretching the cardiac cycle. The user decides on an arbitrary number of reconstructed phases, in this case nine. (d) The nearest temporally acquired view for each of the reconstructed phases is then selected. Arrows are used to show the nearest-neighbour view where necessary. Note that some views are used for two adjacent reconstructed phases to ensure that each phase has three views.

is stretched or compressed to match the nominal *R-R* interval, and the time-point of each view (or ETL) is re-assigned as shown in Figure 16.7. The data are retrospectively allocated to a new, user-defined, number of temporal phases, independent of the number of actually acquired phases. A simple approach for allocating acquired temporal views to the new user-defined temporal phase is to use the nearest-neighbour algorithm. Since the relative time of acquisition of each acquired view may no longer be the same, it may be necessary for the same acquired temporal view to be used in adjacent user-defined phases, but the reconstruction ensures that the whole

cardiac cycle is fully sampled. Retrospective gating still uses an ARP, but it is typically much bigger, e.g. 50% of the average *R-R* interval, than the value used for prospective triggering. Therefore only very short or very long beats will be rejected.

16.4.4 View Sharing

Sometimes it is necessary to increase the ETL in order to keep the scan acquisition time short. When this happens the effective temporal resolution will be decreased, resulting in blurring in the images or jerkiness in cine movies. To maintain a good temporal

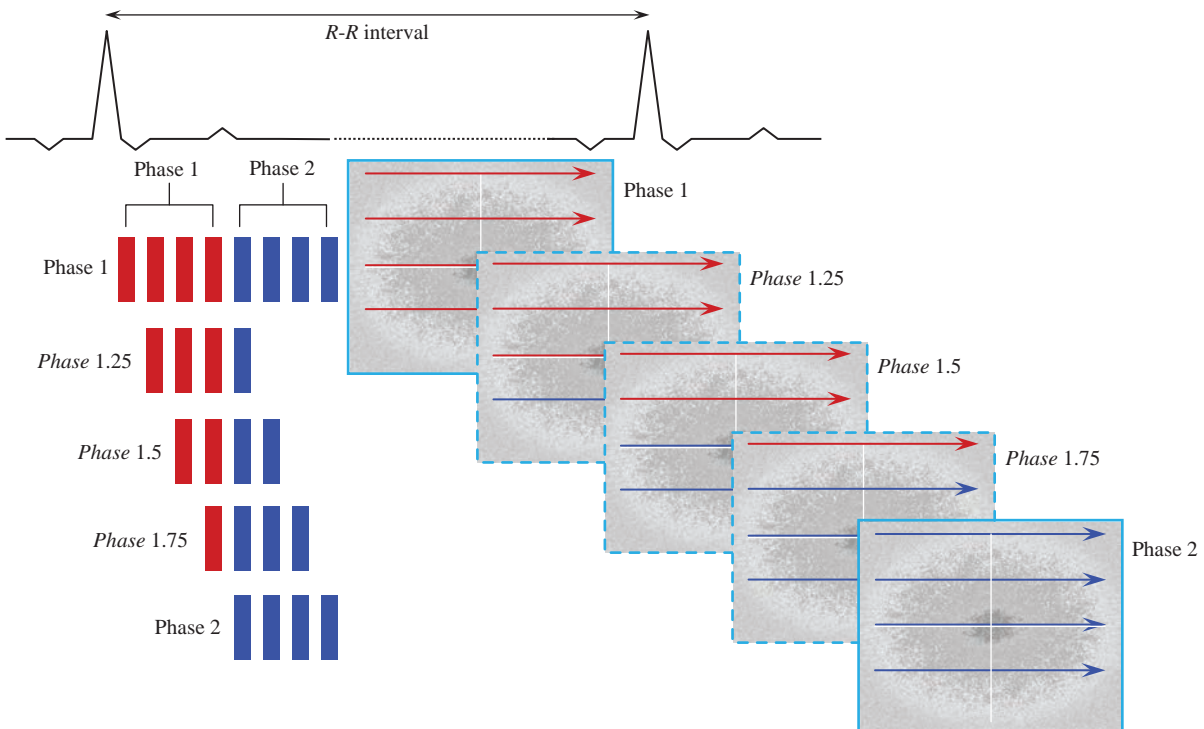


Figure 16.8 Variable view sharing. In this example there are four phase-encoding steps, or views, acquired for each temporal phase in the same R - R interval. The diagram shows that phase 1 is made up of the four red views and phase 2 is made up of the four blue views. Additional intermediate temporal phases can be synthesized by ‘sharing’ the views between phases 1 and 2. The diagram shows how varying numbers of views from phase 2 can be shared with phase 1 to create additional phases. Note that there is no additional data acquisition, only that the original data are shared.

resolution we can use a technique known as ‘view sharing’ (also known as ‘echo sharing’). With view sharing, the lines of raw data from adjacent temporal phases are combined to synthesize an intermediate temporal phase image. For example, if we now consider an ETL of 8, we can combine the last four views of phase n with the first four views of phase $n + 1$ to produce a new temporal phase with eight views. The time-point of this new phase will be positioned at $1/2(t_n + t_{n+1})$. Using this equal (or symmetric) view sharing, the total number of temporal phases can be increased from N to $2N - 1$. There is of course no reason why views could not be asymmetrically, or variably, shared; for example, the last two views from phase n with the first six views of phase $n + 1$ to generate a new temporal phase positioned at $3/4(t_n + t_{n+1})$. However, you should be aware that view sharing does not create new data, it is performing temporal interpolation between the real acquired phases to generate intermediate steps. View sharing definitely helps to produce smoother cine movies. Figure 16.8 illustrates how variable view sharing can

be used to create additional interpolated temporal phases. Variable view sharing is particularly useful in retrospectively gated acquisitions where there is a need to share the views appropriately to match the number of desired user-defined temporal phases.

Real-Time Cine Imaging

It is important to realize that although cine images show function over a single cardiac cycle, the raw data are actually acquired over a number of heartbeats, meaning that a reasonably stable heart rate is needed in order to obtain good-quality images. If this is not the case, e.g. with patients in atrial fibrillation, then it is possible to acquire images rapidly enough to demonstrate cardiac function without using ECG triggering or gating. These methods are often referred to as real-time cine imaging. If an entire image can be acquired rapidly enough then it is possible to acquire sequential images at around 8–12 frames per second. In order to acquire at a sufficiently good temporal resolution it is generally

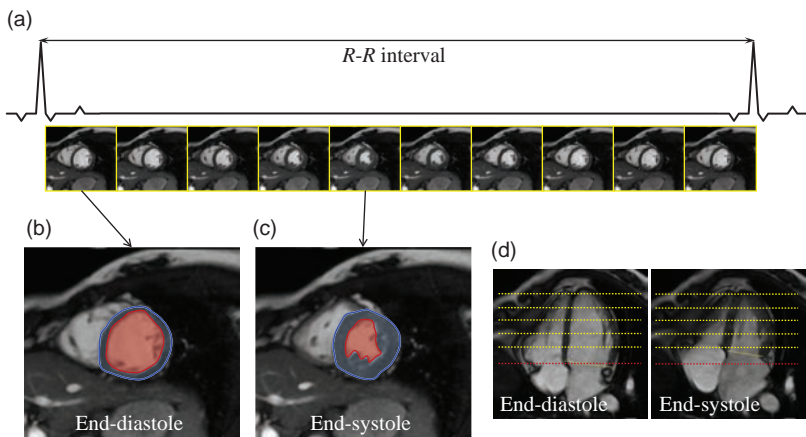


Figure 16.9 Functional cardiac analysis. (a) Ten phases from a single-slice cine acquisition in the short axis. (b) The largest ventricular volume is at end-diastole and (c) the smallest ventricular volume is at end-systole. The endocardial (red) and epicardial (blue) borders have been outlined on both phases. The left ventricular blood-pool is shaded red, while the ventricular muscle volume is shaded blue. Measurement of ventricular volume and mass requires outlining the borders on all the end-diastolic and end-systolic slices (dotted lines) in (d). Care should be taken when evaluating the most basal slice (dotted red line) since the longitudinal shortening of the heart during systole means that the most basal slice may not be in the ventricle.

necessary to sacrifice some spatial resolution. The development of both spatial and temporal parallel imaging techniques as discussed in Chapter 14 has also helped with the development of real-time cine imaging.

16.4.5 Functional Cardiac Analysis

If our short-axis stack of cine slices covers the entire left ventricle then we can measure the volume of the blood-pool at the end-systolic (smallest ventricular volume) and end-diastolic (largest ventricular volume) phases and calculate the percentage of blood ejected in each heartbeat. This is known as the ejection fraction (EF), and is an important measure of cardiac function. Specialized cardiac processing software can be used to either manually or (semi-)automatically define the endocardial border between the blood-pool and the myocardium, as shown in Figure 16.9. Summing the left ventricular blood-pool volume (blood-pool area \times slice thickness) across all slices acquired at the end-diastolic phase gives the end-diastolic volume (EDV). Similarly, summing all the volumes at the end-systolic phase gives the end-systolic volume (ESV). The stroke volume, the volume of blood ejected during each heartbeat, is then calculated as the difference between EDV and ESV.

$$SV = EDV - ESV$$

The ejection fraction (EF) as a percentage can then be calculated from

$$EF = \frac{SV}{EDV} \cdot 100\%$$

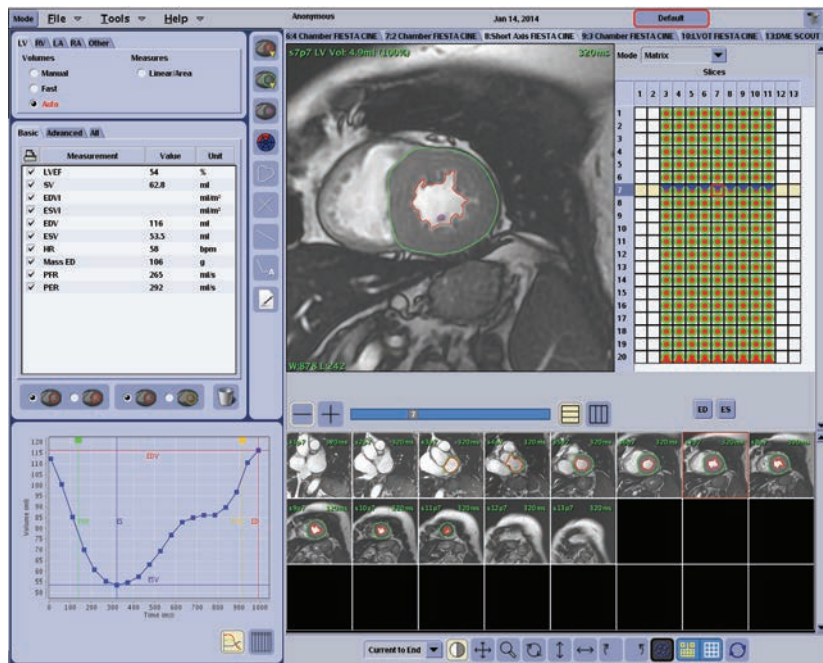
If we also define the outer contour of the myocardium, called the epicardial border, we can then measure the volume of the myocardium. Multiplying the myocardial volume by the density of tissue (1.06 g ml^{-1}) gives us an estimate of the myocardial mass. This is another quantitative metric that can be used to monitor patients who have thickened ventricular walls.

With both endocardial and epicardial borders defined in the software, we can go still further and estimate regional function of the heart. In order to calculate these measures, the software (semi-) automatically calculates the centre-line midway between the endo- and epicardial borders. Short lines known as 'chords' which are perpendicular to the mid-line are then defined. The length of these chords can be displayed graphically, showing either their length at a particular phase, i.e. 'systolic wall thickness' or the difference in thickness between systole and diastole, i.e. 'wall thickening'. When this type of analysis is performed on all of the multi-slice short axis data it is usually displayed as a 'bull's-eye plot', a set of concentric rings with the inner-most ring representing the apical slice and the outermost ring the most basal slice. The metric is then usually represented as a colour scale. Figure 16.10 shows a regional left ventricular analysis in a patient with a thickened, i.e. hypertrophic, left ventricle.

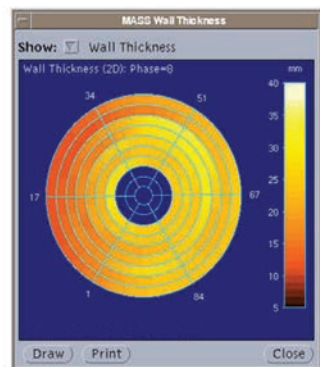
16.4.6 Quantitative Velocity and Flow Imaging

Functional cardiac imaging includes quantitative imaging of blood flow, a powerful technique for assessing cardiac pathologies such as valvular regurgitation, ventricular shunting and quantifying

(a)



(b)



(c)

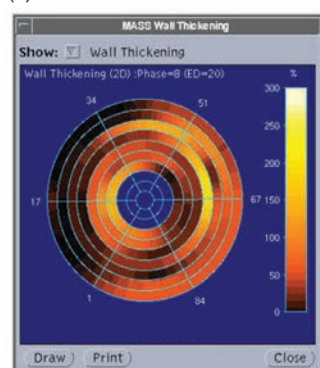


Figure 16.10 Regional left ventricular functional analysis. (a) The endo- and epicardial borders have been outlined on all the slices and phases from the short axis cine acquisition. The curve at the bottom left shows the ventricular volume time curve and the table above reports a stroke volume (SV) of 62.8 ml, ejection fraction (EF) of 54% and end-diastolic (ED) myocardial mass of 106 g. In a different patient with myocardial hypertrophy (b) shows a bull's-eye plot of the end-systolic wall thickness, demonstrating gross thickness of the entire left ventricle. (c) A bull's-eye plot can also show the change in wall thickness between end-systole and end-diastole. The plot shows general ventricular dysfunction with the septal region, in particular, showing poor contractility.

stenotic valves. In the last chapter we explained how it is possible to encode the velocity of moving spins using phase contrast imaging techniques. In quantitative velocity/flow imaging we usually perform a single-slice cine phase contrast (CPC) acquisition perpendicular to the direction of the vessel or valve in which we wish to quantify the velocity. The velocity-encoding gradients are usually applied along the slice-selection direction in order to quantify velocities through the slice, and the two encodings are usually interleaved within the same heartbeat to minimize spatial misregistration as shown in Figure 16.11. Like cine bSSFP functional imaging, CPC acquisitions can also be combined with segmented k-space acquisitions, retrospective gating and variable view-sharing techniques to reduce the overall acquisition time.

Figure 16.12 shows images from a typical CPC acquisition through the ascending aorta. If the instantaneous flow is plotted against time for all the temporal phases, then the area under the curve represents the blood flow in one heartbeat and is known as the stroke volume. Multiplying the stroke volume by the heart rate gives the volume of blood ejected in one minute, which is known as the cardiac output (ml min^{-1}). Figure 16.13 shows a CPC study in a patient with severe aortic regurgitation. The CPC slice was positioned perpendicular to the ascending aorta, just above the aortic valve. The area under the positive flow part of the curve (shaded green) represents the volume of blood ejected by the left ventricle in one heartbeat, while the area under the negative part of the curve (shaded red) represents the volume of blood that regurgitates back into the ventricle.

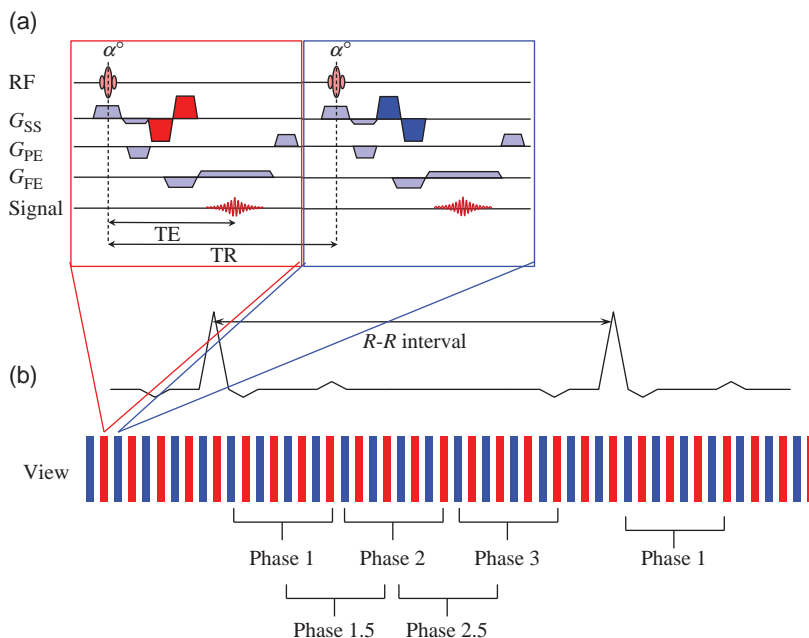


Figure 16.11 Cine phase contrast. The gradient-echo sequence (a) incorporates additional bipolar gradients to encode velocity into signal phase. The two encodings (red and blue) are usually performed in subsequent TRs. In this example the encodings are applied along the slice-select direction to encode velocity through the slice. In (b) the encodings are shown as part of a retrospectively gated segmented k-space acquisition. Multiple phase encoding steps or views are acquired in each R–R interval. In this case four views are acquired for each of the two encodings. Since the temporal resolution is $8 \times \text{TR}$ in this example, we can use symmetric view sharing to improve the apparent temporal resolution as shown.

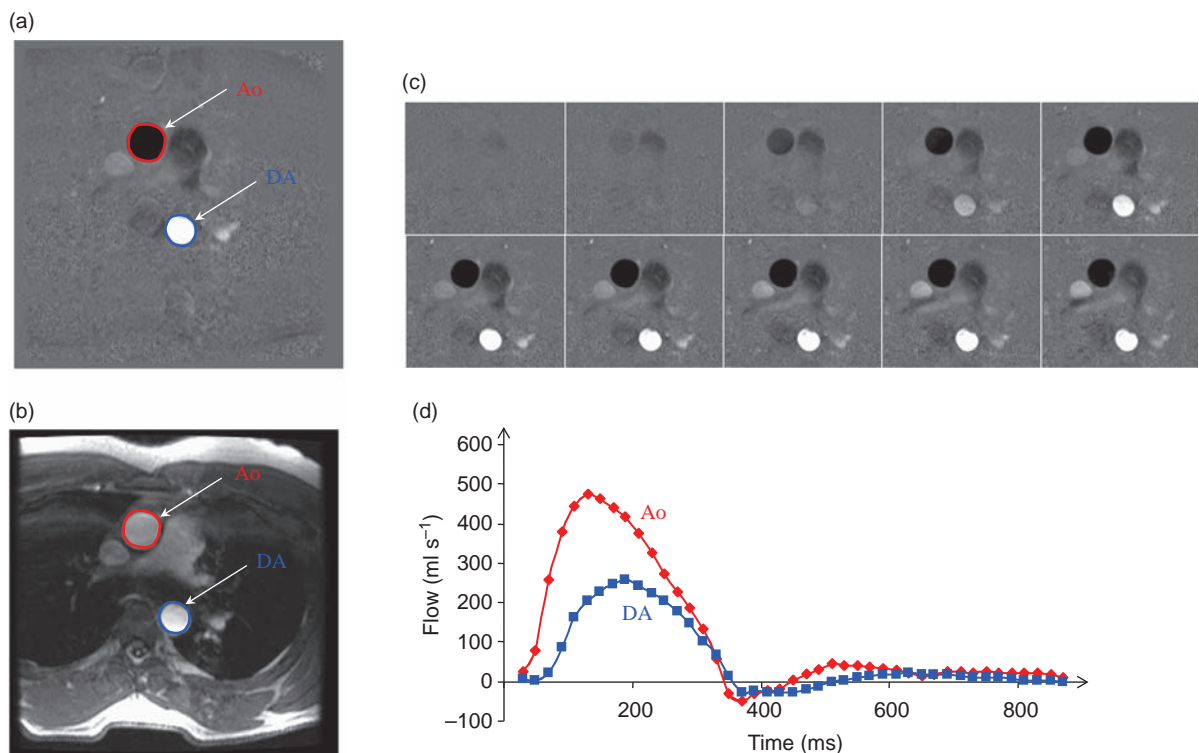


Figure 16.12 Cine phase contrast imaging through the ascending aorta (Ao). (a) The phase/velocity image and (b) the magnitude image from a single temporal phase. The velocity in the Ao is shown as shades of mid-grey to black, while velocity in the opposite direction in the descending aorta (DA) is shown as shades of mid-grey to white. Regions of interest (ROI) for both vessels have been outlined. (c) The first ten temporal phases of the phase/velocity images, giving (d) the flow vs time curve. The flow at each temporal phase is obtained by multiplying the average velocity in each ROI (mm s^{-1}) by the area of the ROI (mm^2) to give a flow in $\text{mm}^3 \text{s}^{-1}$ or ml s^{-1} .

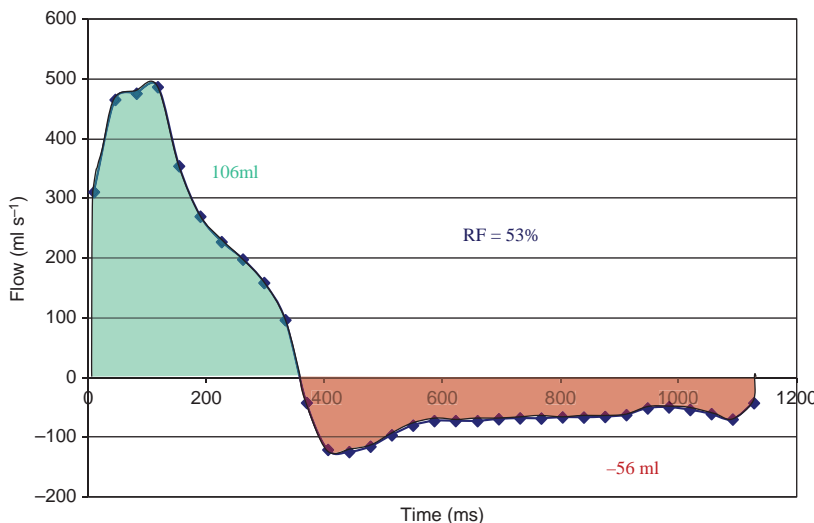


Figure 16.13 A flow-time curve obtained in the aorta of a patient with aortic regurgitation. There is a large forward flow during systole (green area under the curve) of 106 ml. During diastole approximately 56 ml of blood (red area under the curve) then flows back into the ventricle. This patient therefore has a regurgitant fraction (RF) of approximately 53%.

Remember from Chapter 15 that the user-defined velocity encoding (*venc*) parameter sets the velocity for which a 180° phase shift occurs. If the actual velocity exceeds the *venc* then aliasing will occur. This can be observed as a sharp transition from either black to white or white to black, as shown in Figure 16.14. If your analysis software supports the capability then it is possible to ‘unwrap’ this aliasing, otherwise it will be necessary to repeat the acquisition using a higher *venc*. You might think it’s more sensible to select a very high *venc* to avoid the possibility of aliasing, but velocity images have velocity-to-noise ratio (VNR), just like standard images have an SNR. Therefore, velocity images will appear noisier as the *venc* is increased.

Even though the phase images from positive and negative flow encoding are subtracted to eliminate background phase errors, there may be residual errors due to the different eddy currents produced by the different flow-encoding gradient polarities. These errors appear as offsets in the data, so typically the stationary background is no longer zero. Correction of the data using the background signal offset may therefore be required.

Velocity mapping can also be performed in-plane by applying the flow-encoding gradients on the appropriate axis. Furthermore, like 3D phase contrast angiography, it is possible to acquire velocity data along all three directions, which when combined as

part of an ECG-triggered 3D acquisition can provide 4D velocity quantification. These data can then be used to calculate temporally resolved 3D flow streamlines such as the example shown in Figure 16.15. These acquisitions are quite time consuming and require respiratory gating, typically using navigators.

Imaging Myocardial Strain

Qualitative review and quantitative analysis of cine cardiac images is widely used to demonstrate impaired myocardial wall contractility which is an important diagnostic and prognostic indicator of coronary heart disease. While it is easy to see the relative motion of the endo- and epicardial borders it is not possible, with standard cine imaging, to observe transmural myocardial motion, i.e. motion within the myocardium itself. However, there are a number of unique MRI techniques that can actually image myocardial strain, i.e. quantitatively measure the deformation within the myocardium. The most common method used for this application is ‘tissue tagging’. A binomial combination of RF pulses and gradients, e.g. 1:-2:1 are applied immediately after every R-wave, and are then followed by a cine imaging sequence. The combination of RF pulses and gradients, known as SPAMM (**SPAtial MODulation of Magnetization**), temporarily superimposes a regular signal modulation pattern on to the images. These tags are typically applied in the form of either a 1D

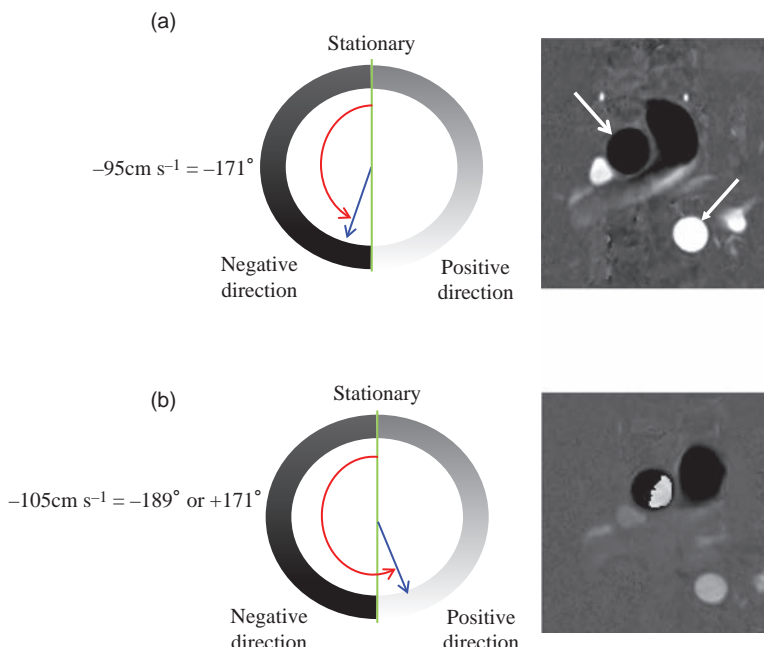


Figure 16.14 Phase contrast velocity aliasing. Velocities in one direction are allocated the range 0° to 180° and velocities in the opposite direction 0° to -180° . As a greyscale 0° is represented by mid-grey, while $+180^\circ$ is allocated white and -180° is allocated black. In (a) velocities in the ascending aorta (upper left arrow) are shown as shades of mid-grey to black, while velocities in the descending aorta (velocity is in the opposite direction) are shown as shades of mid-grey to white (lower right arrow). In (a) the v_{enc} is set to 100 cm s^{-1} so a velocity of -95 cm s^{-1} results in a phase shift of -171° . However, if the velocity exceeds the v_{enc} then the data will appear aliased (b). In this case with a v_{enc} of 100 cm s^{-1} a velocity of -105 cm s^{-1} results in a phase shift of -189° . Since this is greater than 180° the reconstruction makes it appear as $+171^\circ$. In this case the velocity in part of the ascending aorta exceeds 100 cm s^{-1} and part of the aortic signal appears aliased with a sudden transition from black to white.

(lines) or a 2D (grid) structure as shown in Figure 16.16. As the myocardium moves and deforms throughout the cardiac cycle, the tagging pattern also deforms to visually demonstrate regions of normal and impaired contractility. Various image processing techniques can then be used to track the tag displacements and calculate the strain as well as ventricular torsion – the twisting of the ventricle as it contracts. HARP (HARmonic Phase) is a particular method that can rapidly analyse tagged images and create parametric images demonstrating the motion of every material point within the myocardium. More recently methods such as DENSE (Displacement ENcoding with Stimulated Echoes) have been used to encode tissue displacement into signal phase from which the strain can then be calculated, while the SENC (Strain ENCoding) technique directly produces images of tissue strain. In addition, conventional cine phase contrast techniques can also be used to encode in-plane and through-plane myocardial wall velocity. The velocity information can then be integrated over time to determine tissue displacement and subsequently calculate the strain.

effects as well as an absence of ionizing radiation. Clinical myocardial perfusion MRI involves imaging the heart during the bolus administration of Gd-based contrast agent, during which we observe a transient T_1 -enhancement effect whereby the myocardial signal intensity increases during the passage of the contrast agent through the myocardium. Regions of ischaemia with poor perfusion will show a significantly reduced and/or delayed enhancement compared to the normally perfused regions. Note that at the time of writing, Gd-enhanced MRI of the heart is an off-label use for all FDA-approved gadolinium-based contrast agents.

Since the first pass of the contrast agent through the myocardium is very rapid, typically 10 s or less, the imaging requirements are extremely demanding. Ideally we would like to get whole-heart coverage with a temporal resolution of one heartbeat, however we can really only achieve 3–4 slices per heartbeat. The basic sequence is therefore a very short TR gradient-echo sequence with an acquisition time of less than 200 ms. A non-selective 90° saturation pulse is applied prior to the imaging sequence, which increases the sensitivity for changing T_1 s. The saturation pulse also provides a degree of arrhythmia insensitivity to allow for any differential signal recovery if the heart rate varies. Figure 16.17 shows one phase from a multi-slice imaging acquisition using an interleaved gradient-echo planar imaging sequence. This study shows a region of sub-endocardial ischaemia as an area of reduced

16.5 Myocardial Perfusion

MRI offers a number of advantages over the conventional nuclear medicine methods for the evaluation of myocardial perfusion, including improved spatial resolution, the absence of overlying tissue attenuation

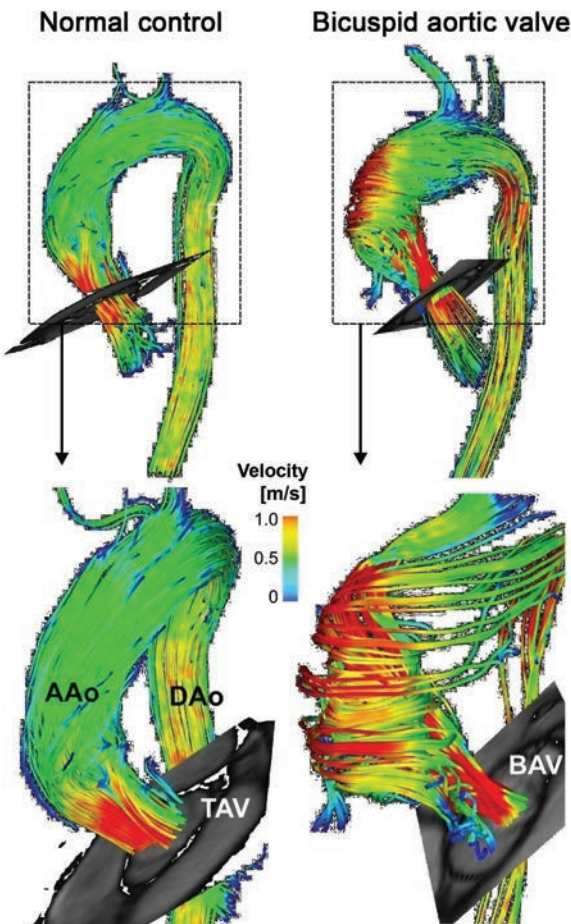


Figure 16.15 3D velocity streamlines calculated from 4D phase contrast data encoded in all three orthogonal directions. The individual lines represent traces along the instantaneous velocity vector field in a systolic phase. The colour scale represents the velocity in m s^{-1} . The figure shows the difference in flow patterns from two subjects; one with a normal tricuspid aortic valve (TAV) and one with a congenitally abnormal bicuspid aortic valve (BAV). Courtesy of Dr Michael Markl, Northwestern University, Chicago.

contrast agent uptake. Care must be taken in viewing these perfusion images to ensure that apparent perfusion ‘defects’, particularly those in the sub-endocardium, are not actually due to susceptibility effects from the high concentration of contrast agent in the left ventricle during the first pass, or motion artefacts due to the myocardium moving during the readout period.

Stress Testing

Patients usually feel the typical symptoms of ischaemic heart disease, such as chest pain, when they physically exert themselves. This is because in the

resting state the coronary arteries can deliver sufficient blood flow to the heart, but during exertion they may not be able to deliver the increased blood flow required by the myocardium, hence the pain. Similarly, if we perform a myocardial perfusion scan in the resting state there may not be any noticeable regional differences in blood flow. It is necessary therefore to ‘stress’ the patient by increasing the myocardial blood flow. While exercise is the best way to achieve this, it is not easy to do in an MRI scanner. Alternative methods include using drugs, like adenosine, that can transiently increase myocardial blood flow while the perfusion sequence is running. Some centres also like to perform a resting state perfusion scan as well. That way any apparent perfusion defects that appear on both stress and rest images can be identified as artefacts and real perfusion defects will only be seen on the stress images.

Quantitative Perfusion Imaging

Perfusion images are usually reviewed qualitatively, with true perfusion defects usually persisting for at least a few heartbeats while also following the boundaries of the feeding coronary artery territories. While qualitative analysis has demonstrated good sensitivity and specificity compared to conventional radionuclide techniques, there have been some studies of semi-quantitative indices that may offer improved sensitivity and specificity. A popular method is to compare the maximum upslope of the myocardial signal intensity curves at both stress and rest in order to calculate a myocardial perfusion reserve index (MPRI). However, since the patient’s general cardiac function may be very different between rest and stress, the data are usually normalized to the upslope of the signal in the left ventricular blood-pool. More sophisticated quantitative analysis methods have also been proposed, similar to those used for DCE-MRI.

A problem with all quantitative image analysis is the necessity to ensure that all the temporal phases are aligned. If the patient can hold their breath for at least the first 20–30 seconds then upslope analysis is fairly straightforward, otherwise each phase needs to be spatially co-registered. Analysis may be further confounded by ectopic beats that may occur in patients when undergoing pharmacological stress. Absolute quantification of myocardial perfusion in $\text{ml g}^{-1} \text{ min}^{-1}$ of tissue is complicated by the fact that using standard contrast doses, e.g. 1.0 mmol kg^{-1} , the signal intensity is not linearly related to the

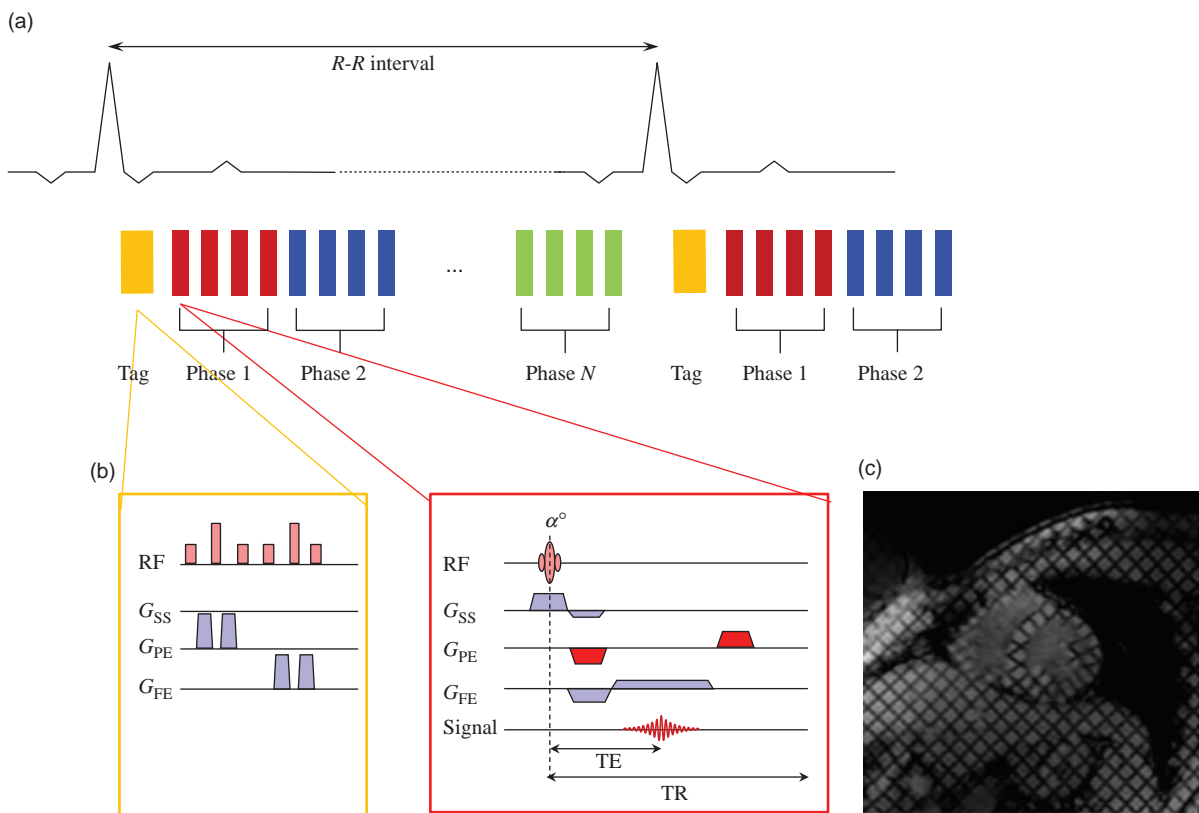


Figure 16.16 Myocardial tagging. (a) Prospectively triggered segmented k-space acquisition which is preceded by a myocardial tagging module (b). The 1:2:1 tagging module creates a spatial modulation of the signal, i.e. a regular grid pattern, at the start of the cardiac cycle. As the heart twists and deforms throughout the cardiac cycle, the tag lines will distort accordingly. (c) One frame from a tagging cine loop demonstrating transmural myocardial motion. Note that the tag lines fade through the cardiac cycle due to T_1 recovery.

contrast agent concentration. This has led some groups to use lower concentrations, e.g. in the range of 0.05–0.075 mmol kg⁻¹, where a linear relationship can be assumed. In addition, all clinically approved contrast agents distribute in both the vascular and extracellular space, affecting the amount of signal enhancement. Lack of knowledge about the relative volumes of these tissue spaces also contributes to the difficulties in absolute quantification.

16.6 Myocardial Viability

A myocardial infarction, or ‘heart-attack’, occurs when there is insufficient blood flow to a part of the myocardium resulting in tissue damage due to insufficient oxygen. The damage may be either permanent, i.e. a myocardial infarction, or reversible, in which case the tissue is still viable and function may be restored with suitable revascularization. It is therefore

very important to be able to determine whether a region of dysfunctional myocardium is either viable or infarcted.

One way to identify viable myocardium is to perform cine imaging while increasing the dose of a pharmacological agent such as dobutamine which increases myocardial contractility. Any myocardial tissue with a wall motion abnormality at rest and which subsequently improves with low-dose dobutamine is regarded as viable. Further increases in the dobutamine dose results in the myocardium becoming ischaemic and ceasing to contract.

An alternative and extremely powerful approach is the direct imaging of non-viable myocardial regions using Late Gadolinium Enhancement (LGE). Recent evidence shows that LGE is exclusively related to irreversible injury, irrespective of contractile function or age of injury. After either an acute ischaemic injury or a chronic infarction there is an increase in the

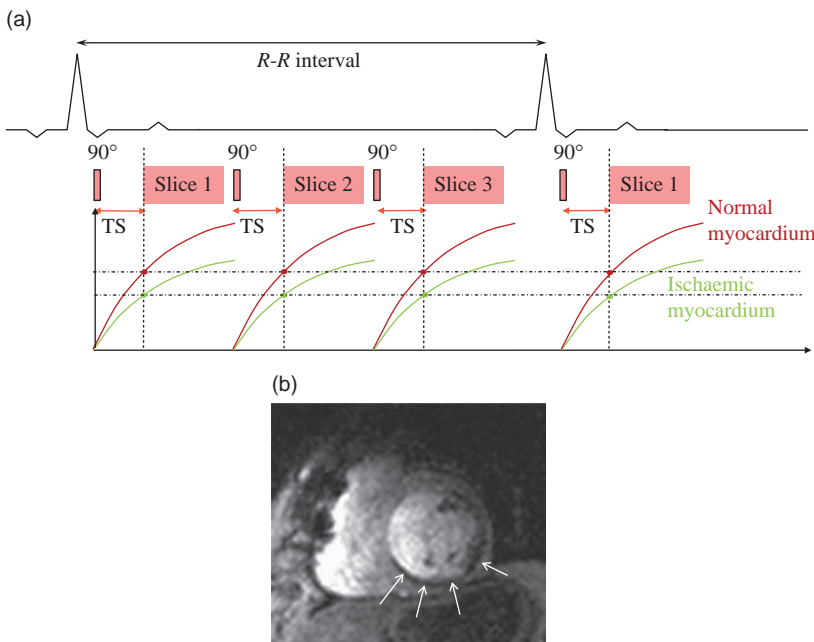


Figure 16.17 Myocardial perfusion imaging. (a) Each slice acquisition comprises a very fast ECG-triggered T₁w sequence. A small number of slices are repeatedly acquired during each R-R interval. Prior to each acquisition a non-selective 90° saturation pulse is applied. During the saturation recovery time (TS) the magnetization recovers due to T₁ recovery. The contrast agent, which was injected at the start of the acquisition, will flow into the normally perfused myocardium, causing the signal to recover more rapidly (red curves showing enhanced myocardium). Ischaemic myocardium will show a diminished uptake of the contrast agent (green curves). (b) One slice from a myocardial perfusion study showing a sub-endocardial perfusion defect (arrows) compared to normally enhancing myocardium. The 90° pulse ensures that all the longitudinal magnetization recovery starts from zero. This makes the sequence robust to cardiac arrhythmias where the R-R intervals may vary in length, resulting in variable signal intensity.

extracellular volume which results in retention of a standard extracellular gadolinium contrast agent. In acute infarcts the loss of cell membrane activity allows the contrast agent to accumulate in the extracellular space, while in chronic infarcts the cardiomyocytes are replaced by fibrotic tissue that has a smaller intracellular space compared to the extracellular space. If T₁w imaging is performed 10–20 min following administration of the contrast agent there is maximal signal difference between infarcted and normal myocardium.

To maximize visualization of the infarct the imaging sequence of choice is an inversion-recovery prepared gradient-echo acquisition in which the inversion time (TI) is optimized to null the signal from normal myocardium as shown in Figure 16.18. The choice of TI can be somewhat tricky and various approaches have been developed over the years. First, rapid, low spatial resolution, LGE images can be obtained at different TIs to visually assess which yields the minimal signal in normal myocardium.

Second, TI ‘scout’ sequences have been developed which employ a single inversion pulse followed by multiple low spatial resolution gradient-echo read-outs, each effectively acquired at an increasing TI. Finally, sequences that retain the sign of the inverted magnetization, so-called Phase Sensitive Inversion Recovery (PSIR), have been developed. PSIR images maintain good normal/infarcted tissue contrast over a wider range of TIs than the magnitude-reconstructed standard IR sequences.

Infarct Imaging

If a cine study shows a region of wall motion abnormality that is ‘bright’ and transmural on LGE imaging, then the myocardium will not recover function following revascularization. Conversely, if the wall motion abnormality does not demonstrate hyper-enhancement on LGE then this most probably represents viable tissue that is likely to recover function after revascularization. The technique is sometimes

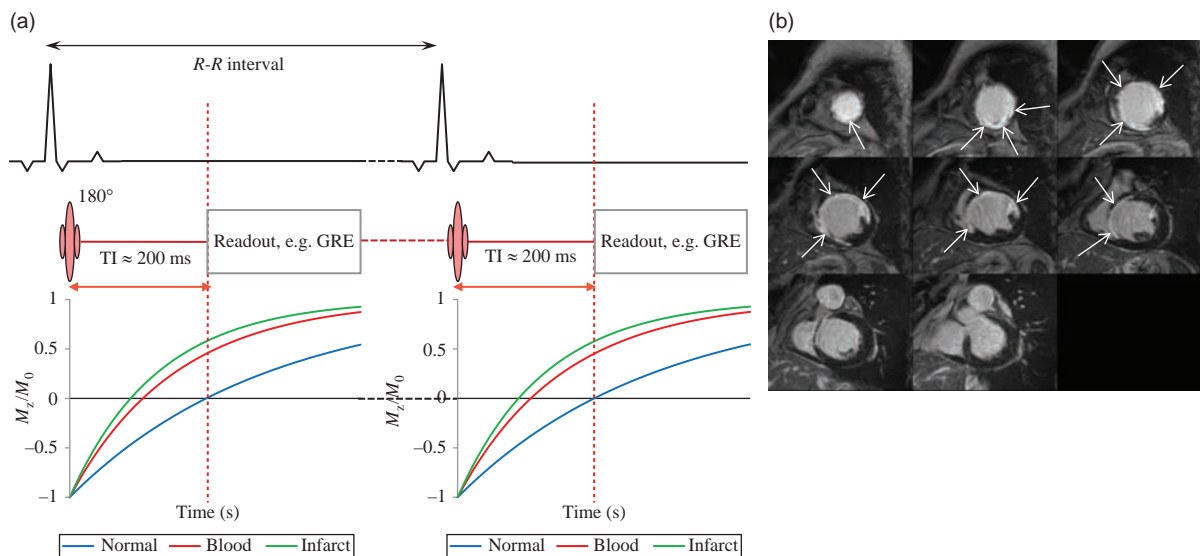


Figure 16.18 Late gadolinium enhancement imaging. (a) A 180° pulse inverts the magnetization which then recovers. If the correct TI is chosen, then when the centrically ordered segmented GRE sequence is played out the signal from the normal myocardium should be zero while the signal within the infarcted tissue is hyperintense, as shown by the arrows in (b).

called 'infarct sizing', since the region of hyper-enhancement correlates with the region of infarction. The transmural extent of myocardial enhancement has been shown to predict the probability of functional recovery. Figure 16.18 shows a set of myocardial delayed enhancement images with a very large region of hyper-enhancement.

While LGE works well for identifying chronic infarcts, early gadolinium enhancement (EGE), with imaging around two minutes after contrast injection, can be used to detect acute myocardial infarction. In this situation the hyper-enhancement represents regions of dead myocardial cells due to compromised myocardial blood flow at the capillary level, despite having a patent coronary artery. This is termed microvascular obstruction (MVO) or 'no-reflow' and is an important prognostic indicator for future cardiac events.

It should be noted that fibrosis, and hence LGE, can also occur in a number of other non-ischaemic cardiac muscle diseases (cardiomyopathies).

and the measurement of T_1 pre- and post-contrast can be used to measure diffuse myocardial fibrosis. Quantitative T_2 imaging has the potential to improve the accuracy and reliability of oedema imaging compared to T_2 -STIR imaging. Myocardial iron overload is a common finding in iron storage diseases like β -thalassaemia. The response to chelation therapy may be monitored using quantitative MRI techniques, most notably T_2^* mapping, since this method can assess tissue iron concentrations over a wide range. These methods, and their advantages and disadvantages, are explained fully in Chapter 19.

16.8 Coronary Artery Imaging

The visualization of the coronary arteries using MRI presents numerous technical challenges. Coronary vessels have small lumens, follow tortuous paths within the epicardial fat and move significant distances during the cardiac and respiratory cycles. The simplest approach to coronary MRA is to use breath-hold (segmented k-space) gradient-echo imaging with a short acquisition window in diastole. Multiple 2D slices with fat saturation are prescribed parallel to the coronary vessel. While this method can produce good results, complete coverage generally requires multiple breath-holds, and the slice thickness limits the spatial resolution achievable.

16.7 Myocardial Tissue Characterization

Relaxation times of the myocardium are altered in various disease states due to changes in water content as well as the local molecular environment. Elevated T_1 has been reported in a number of cardiac diseases

Better results can be obtained using ECG-gated 3D-bSSFP sequences that produce a high signal from blood. T_2 preparation schemes and fat suppression are often used to reduce myocardial muscle and fat signal respectively. The extended imaging time generally makes breath-holding impractical and thus respiratory gating is required. This is usually performed using navigators. The navigator

signal may be used to gate the data either prospectively, i.e. before data acquisition, or retrospectively, i.e. after data acquisition but before image reconstruction.

While MR coronary angiography can be used for looking at the proximal coronary arteries, CT angiography is far quicker and more robust for assessing the whole of the coronaries.

Further Reading

- Biglands JD, Radjenovic A and Ridgway JP (2012) 'Cardiovascular magnetic resonance physics for clinicians: part II'. *J Cardiovasc Magn Reson* 14:66. Available online at www.jcmr-online.com/content/14/1/66 [accessed 7 May 2015].
- Coelho-Filho OR, Rickers C, Kwong RY and Jerosch-Herold M (2013)

- 'MR myocardial perfusion imaging'. *Radiology* 266:701–715.
- Doltra A, Amundsen BH, Gebker R, Fleck E and Kelle S (2013) 'Emerging concepts for myocardial late gadolinium enhancement MRI'. *Current Cardiology Reviews* 9: 185–190.
- Kwong RY (ed.) (2008) *Cardiovascular Magnetic Resonance Imaging*. Totowa, NJ: Humana Press.
- Ridgway JP (2010) 'Cardiovascular magnetic resonance physics for clinicians: part I'. *J Cardiovasc Magn Reson* 12:71. Available online at www.jcmr-online.com/content/12/1/71 [accessed 7 May 2015].

It's Not Just Squiggles: In Vivo Spectroscopy

17.1 Introduction

By now you are familiar with the chemical shift between fat and water in the human body, which can cause artefacts. It occurs because protons in different environments experience shielding of the magnetic field by the electron clouds of neighbouring atoms. Chemists use magnetic resonance to investigate the structure of molecules by measuring very precisely the position of peaks in a spectrum (they still call it ‘nuclear magnetic resonance’). The area of each peak is a measure of the relative number of protons in that particular position. In the chemical soup of the human body, the number of water and fat protons is several thousand times higher than the number of protons on other molecules so we can’t usually distinguish other metabolites. In vivo spectroscopy uses gradients to selectively excite a volume of tissue, from which the Free Induction Decay (FID) is recorded and, after Fourier transformations, produces a spectrum from the nuclei within that voxel. For many years this technique was technically difficult and results were not diagnostically helpful, but it has become much more reliable and is now considered by many to be an essential part of a brain MR examination.

In this chapter we will explain the following:

- the main features of a proton spectrum for normal brain include metabolite peaks for N-acetyl aspartate, creatine and choline;
- either PRESS or STEAM sequences can be used for single-voxel spectroscopy – PRESS is more common in clinical practice;
- combining spectroscopy with phase-encoding gradients in two or three directions allows us to create chemical shift images or ‘maps’.

An MRS Dictionary

MR spectroscopy has its own language too, which will be unfamiliar to users who have only done MR

imaging. For a start, it is frequently abbreviated as MRS, distinct from MRI.

Peaks on the spectrum are also called *resonances*. Some metabolites do not have simple resonances, but may be split into two (called a *doublet*), three (*triplet*) or even more sub-peaks. Effective *water suppression* is essential to allow the metabolite peaks to be detected.

Shimming refers to the process of adjusting field gradients to optimize the magnetic field homogeneity over the voxel, and is usually performed automatically. The uniformity of the magnetic field over the voxel is usually expressed as the *linewidth* (the full-width at half-height) of the water resonance and may be quoted in Hz or ppm. Anything which reduces the homogeneity is described as causing *line broadening*, i.e. increasing the linewidth of the peaks.

The FID is detected in *quadrature* and produces a spectrum with both *real* and *imaginary* components. The phase-corrected real spectrum is known as the *absorption* spectrum and contains all the useful information; the imaginary part is called the *dispersion* spectrum and is not used in clinical MR spectroscopy. Processing of the FID usually includes *zero-filling* to improve the spectral resolution and *apodization* to improve the signal-to-noise ratio. *Phase correction* is necessary to remove *baseline roll* from the spectrum, and the *residual water peak* can also be removed using specialist algorithms.

17.2 Some Basic Chemistry

A proton spectrum is shown in Figure 17.1a from a specialist spectroscopy phantom designed to mimic the in vivo brain metabolites. The water peak has been suppressed so that the lower-concentration metabolites can be seen. In all spectra the reference frequency (zero ppm) is set according to the chemical shift of a standard compound, tetramethylsilane $\text{Si}-(\text{CH}_3)_4$, which has a single proton resonance because it is a completely symmetrical molecule. When $\text{Si}-(\text{CH}_3)_4$ is

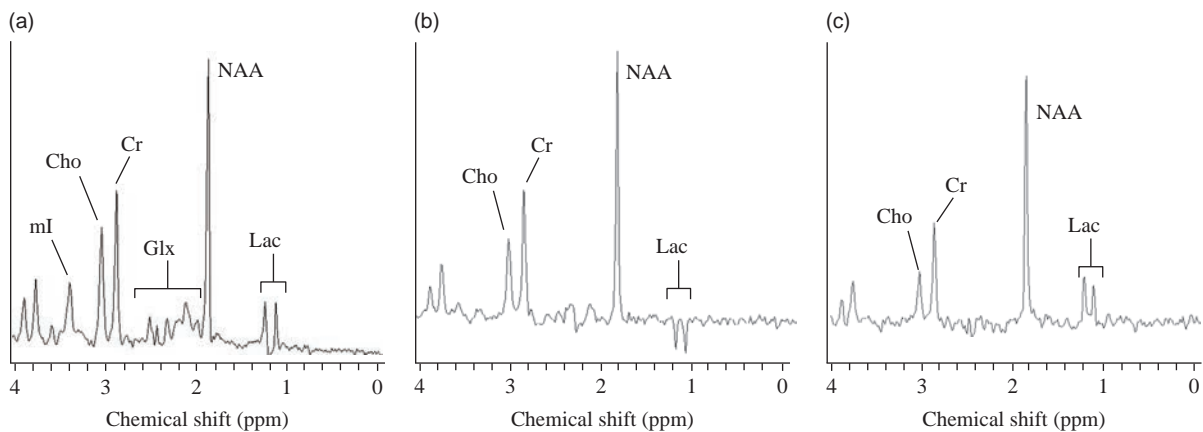


Figure 17.1 (a) A spectrum ($TE = 30\text{ ms}$) from an MR spectroscopy phantom containing the main brain metabolites in normal concentrations, plus lactate. Echo times of (b) 135 ms and (c) 270 ms produce spectra with different appearances. (All spectra are 0.1 ppm lower than in vivo spectra due to the temperature difference.) Cho denotes choline; Cr, creatine; Glx, glutamine and glutamate complex; Lac, lactate; mI, myo-inositol; NAA, N-acetyl aspartate.

at zero ppm, water at 37°C is at 4.65 ppm . Since we don't have $\text{Si}-(\text{CH}_3)_4$ in the human body, we can just set the water resonance to be 4.65 ppm , and everything else is relative to that. Notice that the zero frequency is on the right-hand side of the spectrum, and it is usual to 'read' a spectrum from right to left. All other metabolites have a unique pattern of peaks at specific chemical shifts, and the presence and concentration of these chemicals can be found by detecting peaks at the appropriate ppm. Above 4 ppm the spectrum becomes unreliable, since the suppression of the water peak at 4.65 ppm tends to corrupt the neighbouring portions of the spectrum too. (Note that the phantom temperature is considerably lower than human body temperature, which causes a shift in the spectrum of about -0.1 ppm , i.e. to the right.) The most important peaks are as follows:

- 1.3 ppm : Lactate (Lac) is a doublet and a very specific marker of cell death and tissue necrosis. If both peaks of the doublet can be seen, it is a good indication that the resonance is indeed lactate and not lipid contamination. Lipids have very broad resonances at 0.9 and 1.4 ppm (not seen in the phantom spectrum). On in vivo spectra it's often hard to distinguish lipid from lactate.
- 2.0 ppm : N-Acetyl Aspartate (NAA) is regarded as a marker of neuronal integrity and will be reduced if neurons are being destroyed by a disease process.
- $2.1\text{--}2.5\text{ ppm}$: Glutamine and Glutamate complex (Glx) is a mixture of peaks that may be elevated or decreased in conditions related to liver function.

- 3.0 ppm : Creatine (Cr) is the total peak from phosphocreatine and creatine and is often taken as a reference level, as it is relatively constant throughout the brain and it tends not to change significantly in disease processes. However, there is evidence that it can change particularly in malignant tumours.
- 3.2 ppm : Choline (Cho) is considered to be an indicator of membrane activity since phosphocholines are released during myelin breakdown, and it is often elevated if malignant processes are present.
- 3.6 ppm : myo-Inositol (mI) is a sugar alcohol which is thought to be a product of myelin breakdown and its peak is often higher in conditions such as Alzheimer's disease and malignant tumours.

Just as image contrast is highly dependent on the sequence chosen and the timing parameters, so the height of peaks depends on the MR spectroscopy sequence and on the TE and TR used. Each metabolite has T_1 and T_2 relaxation times which, for brain spectra, are reasonably independent of the tissue in which they are present. In spectroscopy we are only interested in maximizing the signal-to-noise ratio of the spectrum peaks, so we need to avoid signal loss due to T_1 relaxation and T_2 decay. Ideally TR should be at least 2000 ms and certainly no less than 1500 ms . TE should be short, usually 30 ms , but for historical reasons TEs of $135\text{--}144\text{ ms}$ and $270\text{--}288\text{ ms}$ are also used (see Section 17.3.2). Figures 17.1b,c show spectra

from the same phantom at these TEs; in both spectra the NAA, Cr and Cho peaks are still visible, and you can see that the signal-to-noise ratio is reduced (look at the baseline between 0 and 1 ppm). A spectrum at TE = 144 ms is particularly useful to separate lactate from lipid contamination: not only is the lipid signal lost because it has a short T₂, but the lactate peak is inverted, making it easily identifiable.

Currently the main clinical applications for in vivo spectroscopy are stroke, dementia, tumours and multiple sclerosis. Epilepsy shows marked changes in proton spectra, but consistently acquiring high-quality spectra is difficult because the epileptic focus is often in the temporal lobe (see Box ‘Technical Challenges of Proton Spectroscopy’). The MRS changes seen in pathology are rather generic, and MRS tends to be sensitive but not specific for a particular disease. This means that MRS results must be used together with MRI or other tests to reach a diagnosis for an individual patient. Clinical boxes in this chapter will describe the most common applications in use today.

Clinical Application: Stroke

Current clinical guidelines for acute stroke advise a very rapid imaging assessment to rule out haemorrhagic stroke, followed by ‘clot buster’ drugs or removal of the thrombus. CT is still much faster and more widely available than MR, so MR – imaging or spectroscopy – remains a research application for stroke. The ischaemic infarct rapidly shows signs of cell death and MRS in this area demonstrates the characteristic lactate peak, often with a broad lipid peak (Figure 17.2 shows lipids at 0.9 and 1.4 ppm, with the lactate doublet overlying the latter). Lactate may also be present in smaller concentrations in the ischaemic penumbra, the region around the core which, if reperfused sufficiently quickly, may recover its function. In sub-acute or late stages of stroke, reduced NAA and Cr peaks and elevated Cho are present (the latter feature is not shown in Figure 17.2). Chemical shift imaging (CSI, see below) is probably the best way of getting metabolite information about the penumbra, but due to the longer scan times CSI is even more challenging in the acute phase of stroke.

Technical Challenges of Proton Spectroscopy

The frequency separation of peaks in the spectrum depends on the field strength and on the magnetic

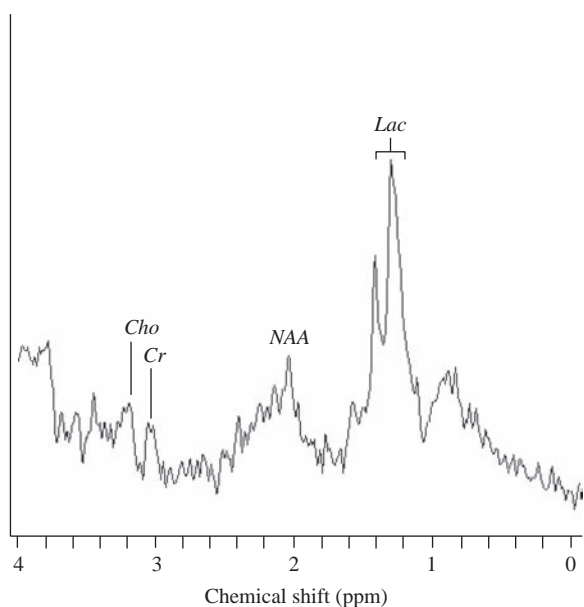


Figure 17.2 Typical spectrum from a patient with stroke.

field homogeneity. At low fields or with a poor shim the peaks tend to overlap and that causes difficulty in interpretation and in measuring peak heights. It is generally thought that a field strength of 1.5 T is the minimum necessary for in vivo spectroscopy. However, it is not obvious that the highest field strengths will give much better results, as at 3 T and above patient susceptibility becomes the dominant source of non-uniformity and thus spectral resolution may be degraded unless there is good local shimming, probably involving higher-order shim coils.

Regardless of the pulse sequence used for proton spectroscopy, effective water suppression and high magnetic field homogeneity are essential to produce a good spectrum. The water peak is at a much higher concentration than the peaks of all the other metabolites, and without suppression those peaks cannot be seen. Typically a very narrow bandwidth frequency-selective pulse, often called a CHEMical Shift Selective (CHESS) pulse, is applied at exactly the Larmor frequency of water using a low-power Gaussian pulse to give a 90° pulse, followed by gradient pulses to spoil any transverse magnetization. Optimization of the strength and central frequency of the water suppression is essential, as inaccurate CHESS pulses can leave too much water (Figure 17.3) and suppress neighbouring metabolite peaks.

To be clinically useful the automated shimming performed by the scanner must give reproducible

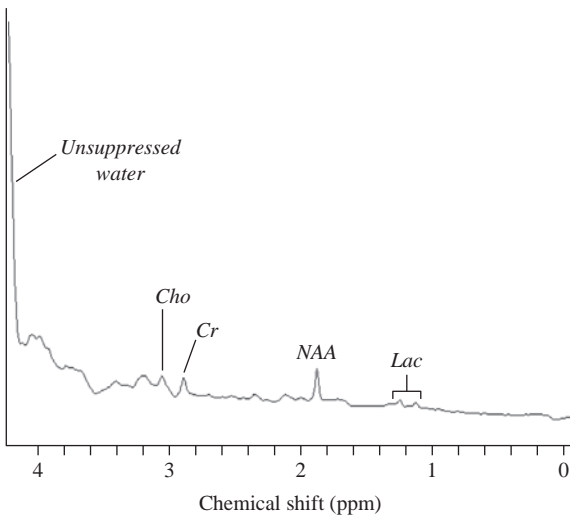


Figure 17.3 The effects of inaccurate water suppression. The large residual water peak at the left of the spectrum dominates the signal and none of the metabolite peaks can be reliably detected.

results. Manual shimming (where the operator adjusts the currents for the linear and higher-order shim coils while observing the FID or the water linewidth) is a tricky technique to perform well and adds a significant time penalty to the scan time. Research studies, however, may require skilled operators to check the automated shimming and adjust it manually if necessary.

17.3 Single-Voxel Spectroscopy

17.3.1 Steam

STEAM stands for STimulated Echo Acquisition Mode and uses three selective 90° pulses, applied in succession on orthogonal gradients to excite a single voxel (Figure 17.4). A total of four echoes is produced from this set of pulses (or five if the first two RF pulses are closer together than the second and third), one of which is a stimulated echo, and this is the signal that is acquired for spectroscopy. For many years STEAM was the only sequence capable of short echo times (down to 30 ms), which show the Glx and mI peaks, and so it has been used for many research studies. Because there is such a large body of literature about a range of conditions, it is still popular with many researchers, especially those with long-term studies. However, it has a lower signal-to-noise ratio than PRESS (Section 17.3.2) and does not show the useful Lac inversion at TE = 144 ms.

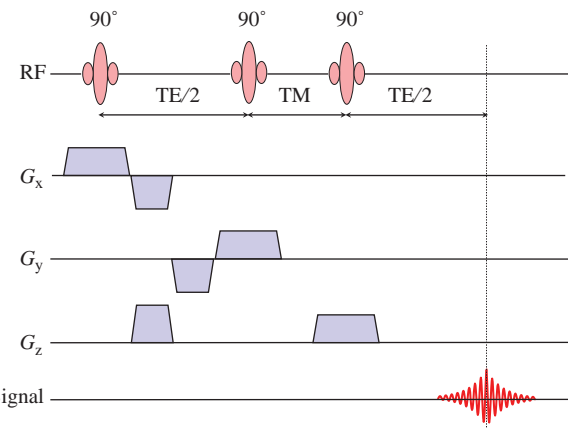


Figure 17.4 The STEAM pulse sequence. TM denotes the mixing time – see Box 'Stimulated Echoes'.

17.3.2 Press

PRESS stands for Point-RESolved Spectroscopy and is based on the spin-echo sequence. A 90° pulse is followed by two 180° pulses so that the primary spin echo is refocused again by the third pulse. Each pulse has a slice-selective gradient applied along one of the three principle axes (Figure 17.5a), so that protons within the voxel are the only ones to experience all three RF pulses.

The signal intensity depends on the pulse spacing and relaxation times, and is intrinsically twice as high as STEAM, so spectra can be acquired with good signal-to-noise ratio (SNR) in a relatively short time.

When PRESS was first developed on clinical scanners, its minimum TE was rather long and often only NAA, Cr and Cho could be reliably detected. At an echo time of 144 ms, lactate is completely out-of-phase with the rest of the spectrum and appears as an inverted peak (refer to Figure 17.1b). Since TE was long anyway with PRESS, it made sense to choose a TE of 144 ms for their studies. At 288 ms TE Lac is back in phase again (although SNR is even lower), and the acquisition of two spectra could be used to confirm the presence of Lac (Figure 17.1c). Modern scanners are able to produce short-echo-time PRESS with a 30 ms TE, and since the SNR is twice as high, PRESS is taking over from STEAM for almost all MRS studies (Figure 17.5b).

Stimulated Echoes

Stimulated echoes were first described in 1950 in an important paper by Hahn, which also contributed greatly to the understanding of spin echoes. To

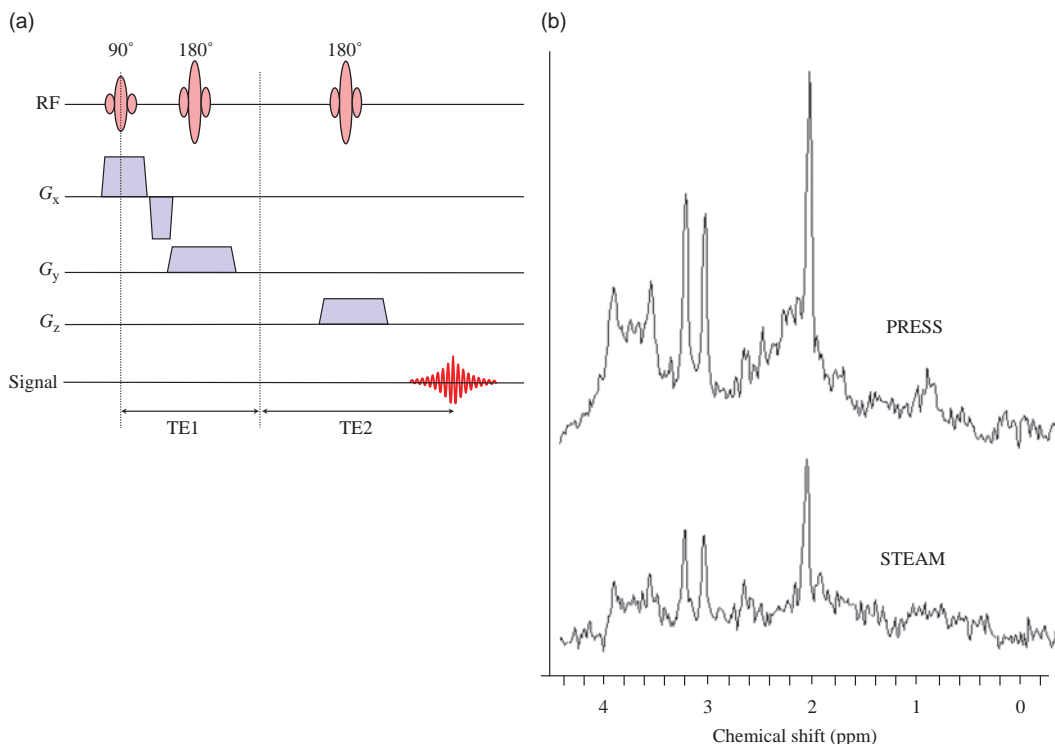


Figure 17.5 (a) The PRESS pulse sequence. (b) In vivo spectra acquired with PRESS and STEAM with the same timing parameters are only subtly different, mainly around the Glx complex.

understand how they are produced, consider a series of three 90° pulses with unequal spacing (Figure 17.6). Some dephasing occurs after the first pulse, and the fan of protons is turned through 90° by the second pulse, leaving some components in the transverse plane, which refocus to produce the first spin echo. Other components are put into the longitudinal direction, where they relax with T_1 only, until the third RF pulse is applied. These components are turned into the transverse plane again, where they refocus to produce a stimulated echo. The maximum height of the stimulated echo can be calculated from the expression

$$S \propto \frac{M_0}{2} \cdot \sin \alpha_1 \cdot \sin \alpha_2 \cdot \sin \alpha_3 \cdot \exp\left(\frac{-TE}{T_2}\right) \cdot \exp\left(\frac{-TM}{T_1}\right)$$

i.e. it is affected by both T_2 relaxation during the first inter-pulse period and T_1 relaxation between the second and third pulses (known as the mixing time, TM). If we assume that TE and TM are both short compared with the relaxation times and provided each pulse is a perfect 90°, the maximum possible signal is 50% of M_0 . To use stimulated echoes for

spectroscopy, it is only necessary to add slice-selective gradients to each axis so that only protons within the required voxel experience all three RF pulses.

In order to understand the formation of echoes with multiple RF pulses of an arbitrary flip angle it is helpful to use coherence pathway diagrams, as described in Chapter 13. Note that if $TE/2 > TM$, four echoes will be produced in total, whereas if $TE/2 < TM$ there will be five, the extra one being the second refocusing of the spin echo due to RF pulses 1 and 2.

17.3.3 Voxel Positioning

The choice of voxel position is critical to achieving a good-quality diagnostic spectrum. Obviously it is important to put the voxel in an appropriate place to detect the pathology under investigation. For example, within a focal brain lesion there may be necrosis, active tumour and oedema. Appropriate contrast images are needed for planning the voxel.

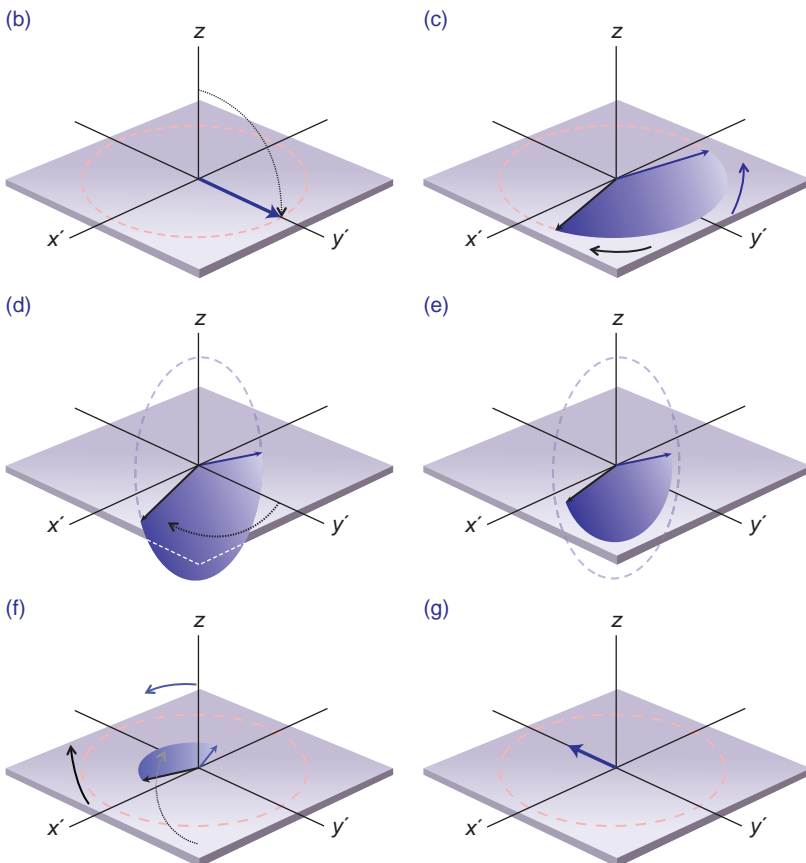
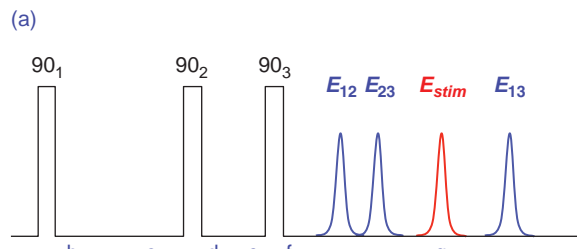


Figure 17.6 (a) Three RF pulses at uneven spacing produce three primary spin echoes and one stimulated echo. (b) The components which form the stimulated echo are flipped first into the transverse plane where they dephase with T_2 relaxation (c), then into the longitudinal plane (d) where dephasing stops and T_1 relaxation occurs (e), then finally flipped back into the transverse plane (f) where they rephase and form an echo (g).

In order to grade a tumour, the voxel should be in the active tissue, but it can be difficult to distinguish these regions on standard T_1 -weighted or T_2 -weighted scans. It has been shown that gadolinium has only a small effect (causing a small amount of line broadening), so post-contrast T_1w scans can be useful for positioning the voxel. However, this is only true if the concentration of gadolinium within the voxel is relatively low: at higher concentrations the T_1 and T_2 shortening effects must be considered. The question of whether to perform MR spectroscopy before or

after gadolinium administration is a controversial one and there are strong opinions both ways.

Clinical Application: Dementia

Diagnosis of dementia is primarily based on clinical signs, although both PET and MRI show promise in this area. MRI is mainly used to measure volumes of the hippocampus or temporal lobe. Spectroscopy has a role to distinguish Alzheimer's disease from other dementias. Proton spectra show decreased NAA and

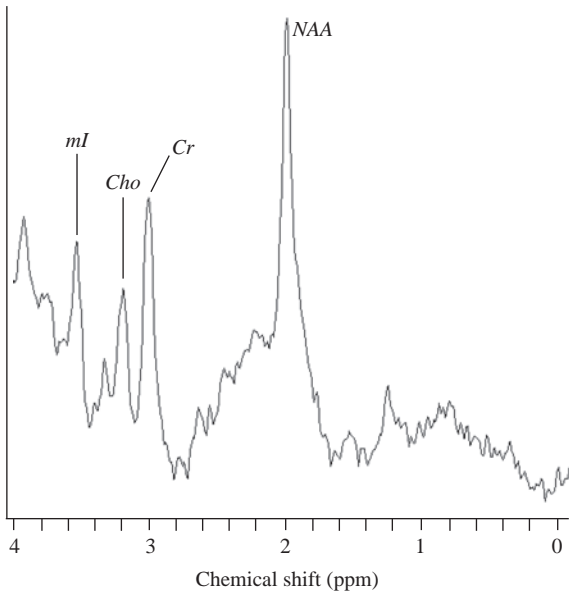


Figure 17.7 Typical spectrum from a patient with Alzheimer's disease.

elevated *ml* and *Cho*, although *Cho* also tends to increase with age so this must be interpreted with care. A short TE is needed to see the *ml* peak. Figure 17.7 shows an example from a patient in the early stages of disease, where the main diagnostic feature is the increased *ml*. There are metabolite variations between different parts of the brain, and in the future CSI is a promising technique for dementia.

A good shim over the voxel is absolutely essential to produce a readable spectrum, and a linewidth of less than 0.08 ppm (5 Hz at 1.5 T) is ideal. Voxels in inhomogeneous regions of the brain are always difficult to shim, in particular the temporal lobes, the base of the brain and the cortex near the skull. For non-focal diseases a good choice would be the occipital grey matter or white matter (Figure 17.8). Obviously lesions and stroke infarcts do not always place themselves in positions that are easy to shim, and we just have to live with that. If the prescan results in a higher linewidth, a repeat prescan can sometimes bring it down as the automated shimming technique improves on its starting point. Spectra with linewidths of 0.15 ppm (9 Hz at 1.5 T) or higher are probably not worth acquiring, as the resulting spectrum will be poor quality (Figure 17.9) and unlikely to help a diagnosis. In general smaller voxels are easier to shim

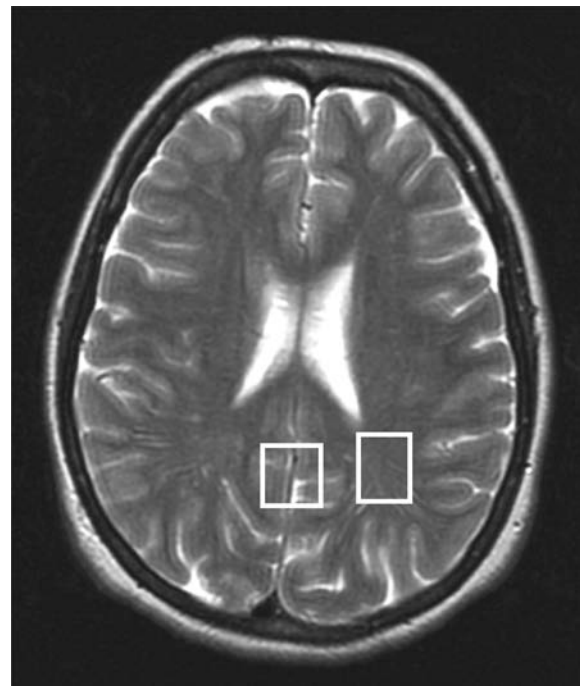


Figure 17.8 Axial image of the brain showing suggested voxel locations for grey matter (occipital mid-line) and white matter (parietal).

than larger ones, but the SNR also depends on volume, so a voxel with 1 cm sides is often considered the practical minimum size to achieve a reasonable SNR. If the volume of the voxel is further reduced in order to help the shim, then the number of signal averages recorded (also known as transients in MRS) should be increased.

Whatever criteria are chosen for positioning MR spectroscopy voxels, consistency is the key to obtaining reliable spectra. Don't be tempted to change the timing parameters, as the resulting spectrum will not be comparable with a normal reference spectrum. The only exception to this rule is the number of signal averages, which may be increased to improve SNR in small voxels. Short echo times are preferred because the improved SNR allows more peaks to be seen, and a second spectrum with long echo time (144 ms) may be used to confirm the presence of Lac if necessary. Alternatively a second short TE spectrum could be acquired from a contralateral site to provide a 'normal' reference, although this really only works if lesions are truly focal (even a stroke may cause changes on the contralateral side if the blood supply is altered).

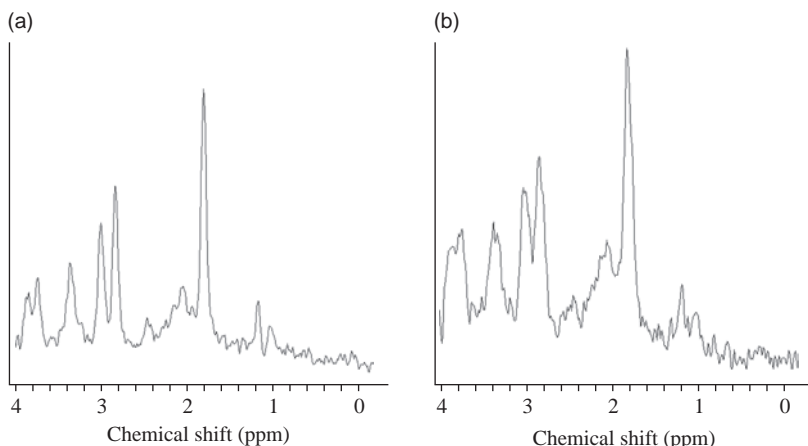


Figure 17.9 The effects of shimming on a phantom spectrum: (a) well shimmed and (b) badly shimmed.

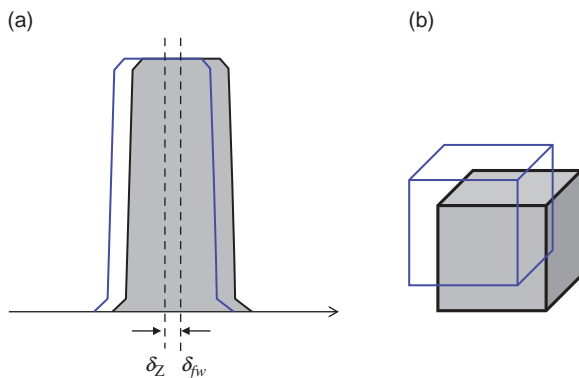


Figure 17.10 (a) The chemical shift effect causes fat and water to have slightly offset slice locations. (b) In three dimensions and with a small voxel size, the offset may be significant.

Chemical Shift Effect in Excitation

A significant problem in exciting the tissue within a MRS voxel is sharpness of the voxel edges. Taking water and fat as a simple example, a frequency-selective pulse (Figure 17.10a) will excite slices of water and fat at slightly different physical locations due to the chemical shift of 3.5 ppm. In three dimensions, the fat voxel will be offset with respect to the water voxel (Figure 17.10b). With the added complication of the excitation profile caused by imperfect selective pulses, you can see that the edges of the voxel become rather poorly defined. This is sometimes known as 'voxel bleed', and if the voxel is positioned close to the scalp it can lead to contamination of the spectrum with lipid signals. In this situation, it can help to rotate the voxel so that a corner is pointing towards the scalp, rather than having an edge parallel to the scalp. Adding spatial saturation bands on all six

sides (right, left, superior, inferior, anterior and posterior) can improve the voxel profiles.

A voxel which overlaps the ventricles will have reduced SNR because the cerebrospinal fluid (CSF) contains almost no metabolites, but contributes to the water peak. Partial volume effect is impossible to avoid with MRS, and it is really a matter of experience and careful positioning to get the best results.

Clinical Application: Brain Lesions

The most widespread use of MR spectroscopy currently is in the differential diagnosis between various brain lesions. Low-grade lesions and meningiomas show reduced NAA and elevated Cho (Figure 17.11a), features that progress in more malignant tumours (Figure 17.11b) where Lac may also be present. Many researchers have found a correlation between the levels of NAA and Cho with the tumour grading, and lipids are also found in necrotic tissue or cysts. Metastatic lesions may be distinguished from gliomas by taking a voxel just outside the enhancing rim of the lesion. Gliomas will show the typical pattern of lower NAA and higher Cho, while metastases show a normal brain spectrum. Alanine, a metabolite seen at ~1.5 ppm, is considered specific for meningiomas. Abscesses may also show alanine, but always show lactate and lipids at 1.1–1.4 ppm, and an absence of NAA.

17.4 Processing of Single-Voxel Spectra

Several specialized processing steps are performed on the acquired FID to produce a high-quality spectrum. Whether they are done in the time domain or the

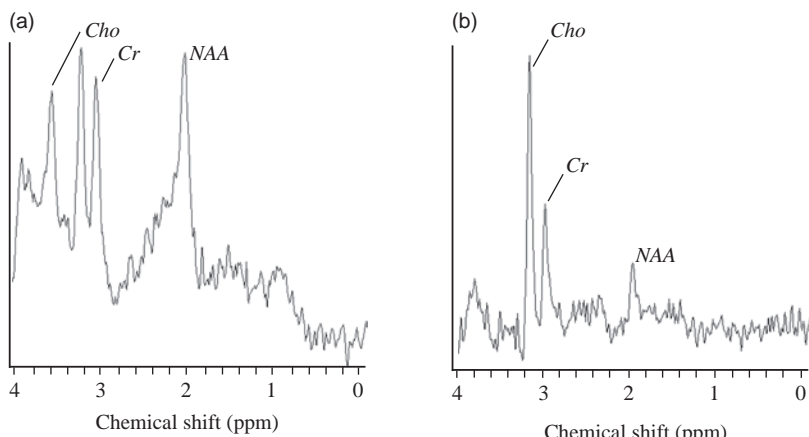


Figure 17.11 Typical spectra from a patient with (a) low-grade glioma and (b) grade III astrocytoma.

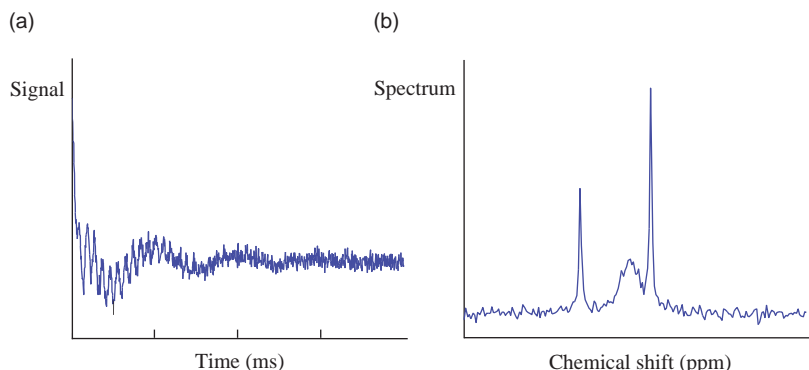


Figure 17.12 The raw FID (a) and spectrum (b) from simulated data (PRESS, 30 ms TE).

frequency domain, i.e. before or after the Fourier transform, depends on which is computationally easier. All the figures in this section are from a simulated acquisition of a spectrum with two narrow resonances and one broader peak: the raw ‘FID’ and its spectrum are shown in Figure 17.12.

The FID is usually digitized for only a few tens of milliseconds. Extending the digitization time would just increase the noise level in the spectrum, since the FID will have decayed away. It is common to zero-fill the data at this stage, i.e. extra data points all set to zero are added to the end of the acquired data (Figure 17.13). This corresponds to interpolating between data points in the frequency domain, giving a smoother-looking spectrum, and is much easier to do before the Fourier transform. Apodization is also applied before Fourier transform of the FID. This means multiplying the acquired FID by a smoothly varying function such as an exponential decay or a Gaussian function (Figure 17.13). Apodizing has the effect of suppressing the noisier tail-end of the FID,

which therefore improves the SNR. However, it also makes the peaks slightly broader in the frequency domain, and so is also often called line-broadening. It corresponds to convolving the frequency spectrum with a Lorentzian or Gaussian function, which is computationally far more difficult than apodization in the time domain.

After Fourier transformation, the spectrum needs to be phase-corrected. A zeroth-order phase correction compensates for any mismatch between the quadrature receive channels and the excitation channels (Figure 17.14) to produce the pure absorption spectrum. This is usually done using the residual water peak, which is still the largest peak in the spectrum. The need for localizing gradients means that there is always a delay between excitation and turning on the receivers. During this delay the nuclei will dephase by an angle that is proportional to their frequency, which then needs to be corrected by a first-order phase correction (i.e. a linear phase shift across the spectrum, Figure 17.14). Unfortunately the first-order phase

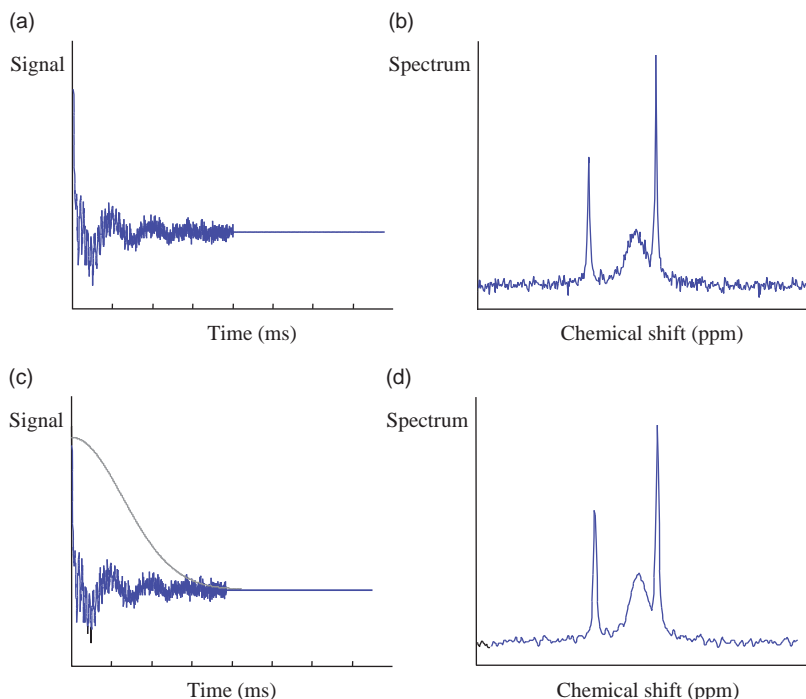


Figure 17.13 (a) Zero-filling the FID is equivalent to (b) interpolating between points in the frequency spectrum. (c) Apodization (multiplication of the FID by a special function) improves SNR (d) at the expense of a little line-broadening.

correction introduces another feature, a slowly varying baseline known as baseline roll. This can be corrected by fitting a spline or polynomial function to the spectrum between the metabolite peaks and then subtracting the resulting function (Figure 17.14).

At this stage the spectrum is presented to the user and is ready for qualitative interpretation. Quantitatively, simple ratios are calculated by finding the area under the spectrum between defined ppm limits for the main metabolites, and these are also presented on the screen. Further quantification is usually done by moving the raw data offline onto an independent workstation. For example, to measure absolute concentrations of the metabolites a model of their known resonances can be fitted to the data using a specialist software package. As with the other processing steps, fitting can be done either in the time domain or the frequency domain.

assess steatosis, MRS is an attractive non-invasive alternative. Fat and water suppression are not needed and a large voxel can be used, as the goal is simply to assess the ratio of fat to water. However, it is still difficult to obtain a high-SNR spectrum within one breath-hold, so the results are often contaminated by motion (Figure 17.15a). Recently, imaging methods, using Dixon techniques, have started to replace MRS for liver fat assessment.

In breast cancer there can be many suspicious bright spots in the MR scans, and MRS may be used to distinguish benign lesions from malignant cancers. Normal breast tissue or benign tumours have almost no Cho signal, while malignant tumours have elevated Cho (Figure 17.15b). Breast spectroscopy is made difficult by respiratory motion and by the presence of large lipid signals. Fat suppression can be achieved by increasing the echo time (the fat signal is lost due to the short T_2 of fat) or using a fat suppression pulse.

Clinical Application: Liver and Breast

The primary application of MRS in liver is to assess the fat content in diffuse liver disease. Steatosis is characteristic of non-alcoholic fatty liver disease which is linked with obesity and can lead to cirrhosis. Since liver biopsy is the gold standard method to

17.5 Chemical Shift Imaging

Chemical Shift Imaging (CSI) uses phase-encoding techniques to acquire spectra from a matrix of voxels. Each slice-selective gradient is replaced with a phase-encoding gradient, which works in the same way as

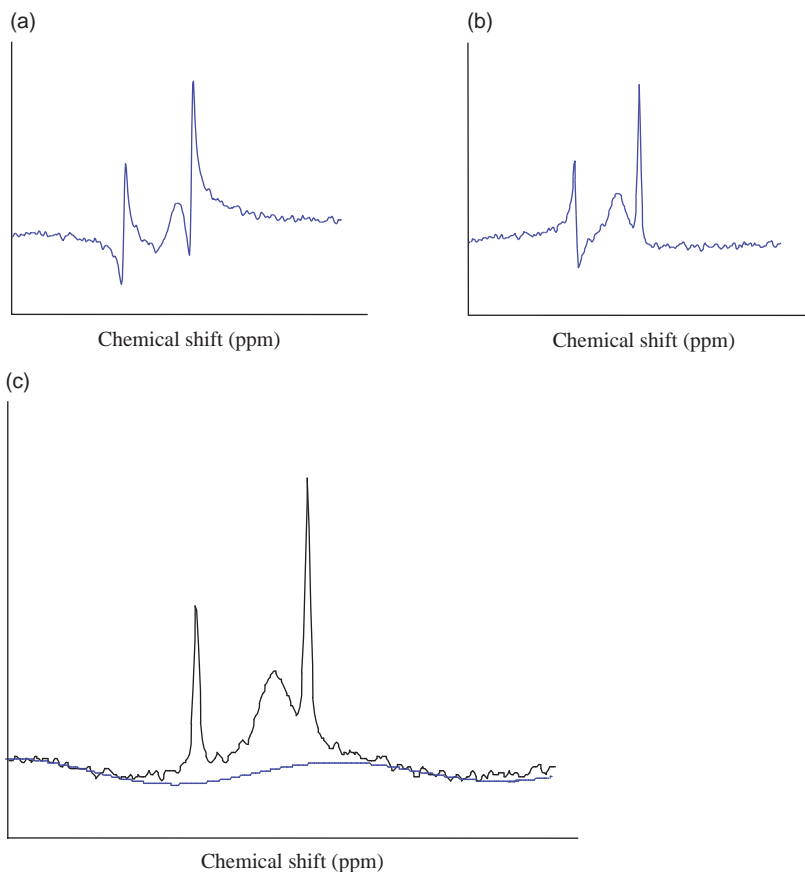


Figure 17.14 (a) A real spectrum may not be correctly phased immediately after Fourier transform (FT). (b) Zeroth-order phase correction has correctly phased the right-most peak, but first-order phase correction is now necessary to correct for hardware delays. (c) Baseline correction is achieved by fitting a spline function (a smoothly varying polynomial function) to the portions of the spectrum known to contain only noise, then subtracting that function.

the slab-select gradient in 3D imaging sequences (see Section 8.8). In principle this can be done for all three directions, but it is more usual to leave one direction as a straightforward slice select, i.e. to perform 2D single-slice CSI.

CSI is normally performed with PRESS. Instead of producing an echo from a small voxel, the ‘voxel’ is now a chunky slab. The phase-encoding gradients sub-divide the slab into a grid of voxels of the required size. The first phase-encoding gradient must step through all its values for each value of the second phase-encode gradient, so the acquisition time will be $\text{TR} \times N_{\text{PE1}} \times N_{\text{PE2}} \times \text{NSA}$. If $15 \times 15 \times 15 \text{ mm}^3$ voxels are required with a head-sized field of view (FOV) of 24 cm, the matrix required is 16×16 . Since TR should be at least 1500 ms to avoid T_1 effects in the spectra, the minimum scan time is thus 6 min 24 s. The good news is that although the voxel size is rather small, the SNR is similar to the equivalent single voxel acquisition thanks to the repeated excitations

(in this case $16 \times 16 = 256$). Multi-slice CSI can be done in an interleaved fashion by changing the frequency of the slice-select RF pulse (just as 2D multi-slice images can be produced). Alternatively Hadamard encoding can be used, which offers improved slice profiles and further improves the SNR of the whole acquisition. This is preferable to phase encoding in the third direction, which would push up the scan time to 25 min for just four slices.

Significant time savings in CSI can be made by using a few tricks from normal MR imaging. A simple example is to use a rectangular FOV and reduce the number of phase encodes accordingly. For a typical axial brain CSI, this can reduce the scan time by 20–25%. It is also possible to use a RARE-like echo train with different phase encoding for each echo, known as Turbo CSI. The acquisition time for a PRESS echo is a lot longer than for imaging, typically 200 ms, so the turbo factor is only 2–4 in order to avoid T_2 blurring. Even a small turbo factor allows

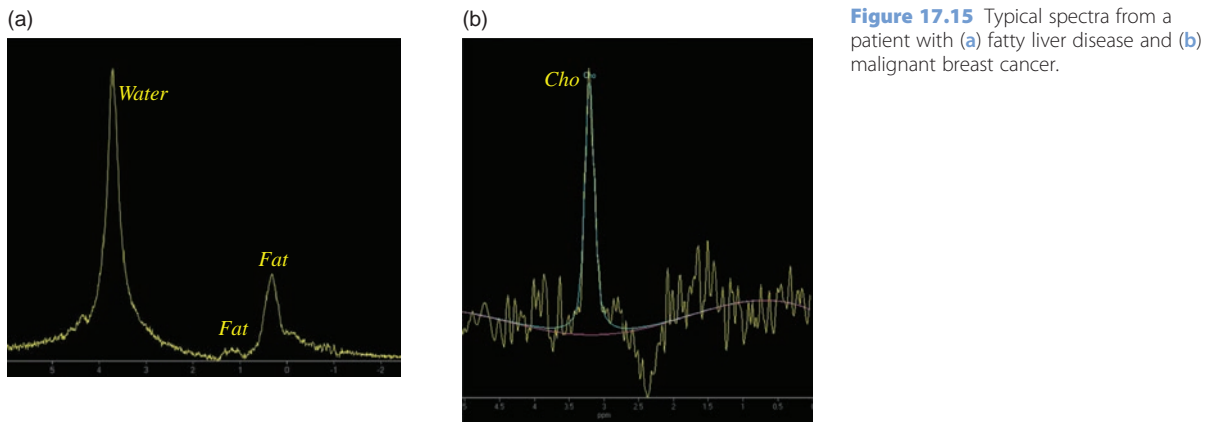


Figure 17.15 Typical spectra from a patient with (a) fatty liver disease and (b) malignant breast cancer.

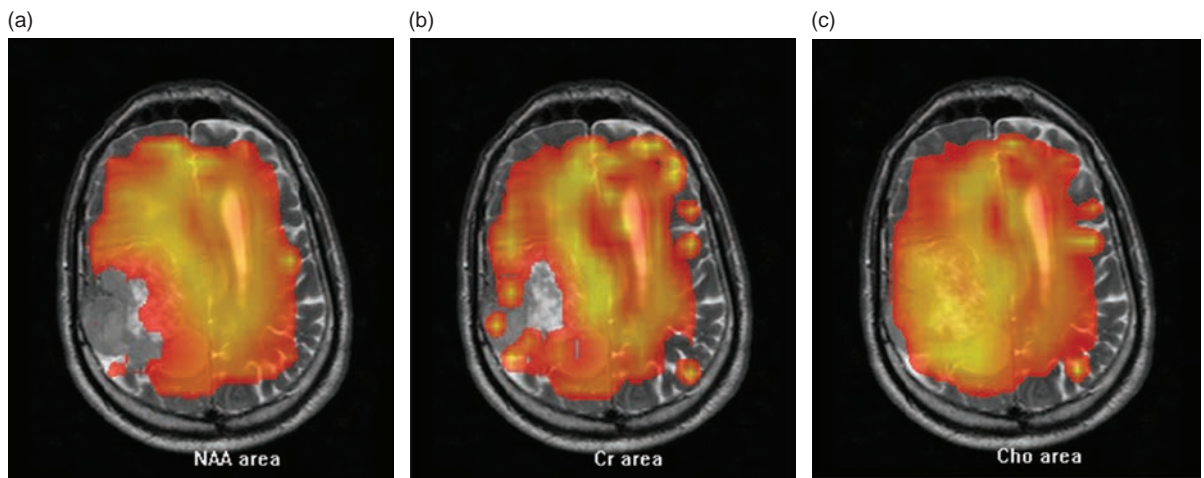


Figure 17.16 CSI metabolite maps from a patient with a brain tumour. (a) NAA, (b) Cho, (c) Cr.

significantly higher matrix sizes within a reasonable scan time, for example a 24×24 matrix with a turbo factor of 4 and TR of 2500 ms takes 6 m and offers significantly improved voxel resolution of $10 \text{ mm} \times 10 \text{ mm}$.

New parallel imaging techniques (such as SENSE and GRAPPA) offer further time savings with multi-element receive coils by using coil sensitivities to reduce the number of phase-encoding steps required. Both Turbo CSI and parallel imaging have disadvantages of course: they both involve a reduced spectral resolution because the echo has to be acquired more quickly, and parallel imaging reduces SNR in the final images.

Having produced a matrix of spectra, the usual way to display the data is as a series of maps, usually of the main metabolite peaks NAA, Cr and Cho, or

other important metabolites (Figure 17.16). In these maps the intensity of the voxel depends on the area of the relevant peak in that position's spectrum. Software is available which allows the user to define a chemical shift range from which to produce a map; for example, a 'lactate' map could be created from the range 1.2–1.4 ppm. As a colour scale is often used for these maps they need careful interpretation as even small changes in peak area can produce dramatic colour changes.

Clinical Application: Prostate

MR imaging is widely used to assess prostate cancer and chemical shift imaging is a useful part of this examination. A normal prostate spectrum contains Cr and Cho, with a high level of citrate (Cit). The Cit peak

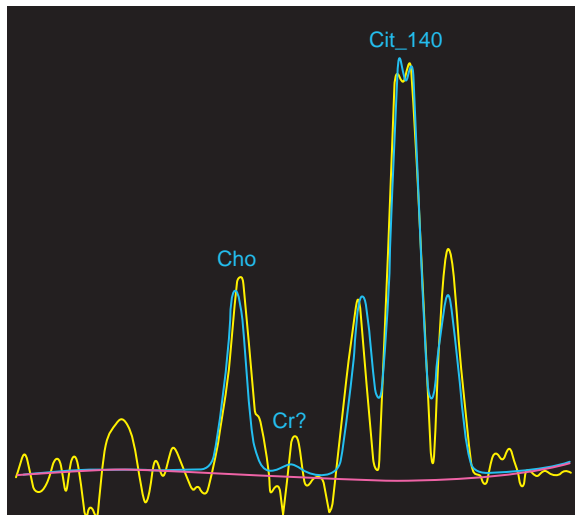


Figure 17.17 Typical spectrum from a patient with normal prostate.

has complex *J*-coupling and, like lactate, its appearance changes with echo time. It has been shown that an optimal echo time is 120 ms at 1.5 T, or 100 ms at 3 T. At this TE, the two outer peaks almost disappear and Cit appears as a doublet (Figure 17.17), upright at 1.5 T and inverted at 3 T. In cancer, Cho levels are elevated and Cit is reduced. It is therefore possible to measure the ratio of Cho to Cit, which should be <1 in normal tissue and increased in cancer. Lipids frequently interfere with the spectrum, so fat suppression is used as well as water suppression. Haemorrhagic breakdown products can linger for days or weeks after biopsy and can also make the spectrum unreadable, so it is recommended to avoid MRS during this period.

Technical Difficulties in CSI

CSI has all the technical problems of single-voxel spectroscopy and a few more of its own! A major problem is the difficulty of shimming an entire slice to the level necessary for good spectra from every voxel in the matrix. In fact this is so difficult that it is usual to define a sub-region within the brain which is used for shimming (Figure 17.18). Outside of this region the shim is allowed to remain poor and spectra in these voxels will be very low quality. When setting up a CSI scan, the edges of the region of interest should lie well within the skull to avoid the susceptibility changes associated with bone.

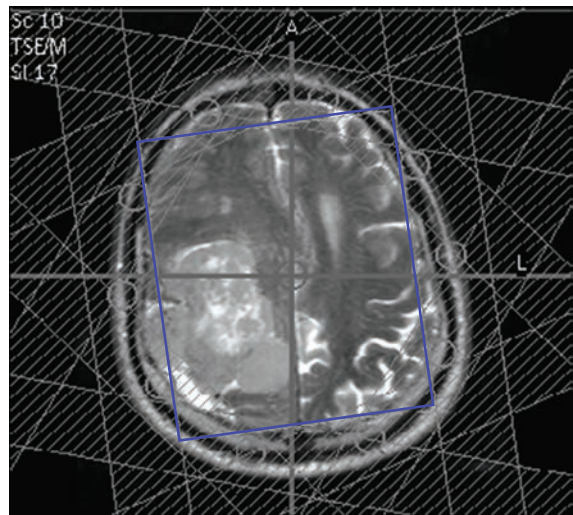


Figure 17.18 When planning CSI, a sub-volume is defined for shimming (blue box). Multiple saturation bands (hatched white bands) are placed over the scalp and skull bone marrow to reduce lipid contamination.

Since the ‘imaging’ matrix is so small (usually only 16×16), the Fourier transform produces large ringing (Gibbs) artefacts across the field of view and smoothing is usually applied in an effort to reduce this. However, the smoothing introduces smearing across the voxels, making the voxel bleed much worse than in single-voxel MRS. The resolution of CSI is therefore not just the size of the pixels as in normal MRI, but is always worse. It is now measured using the point-spread function (PSF), which can be calculated if you know the k-space sampling and post-processing filters. Absolute quantification of metabolite concentration is difficult and relative quantification is more useful, not least because there are so many voxels in a single CS image.

Residual field non-uniformities across the field of view may cause incorrect water suppression, as the suppression pulses are applied to the wrong part of the spectrum. Phase errors in the selective RF pulses are significant over the larger volume in CSI, and vary from voxel to voxel across the field of view. Baseline correction is often compromised and spectra will rarely be as high a quality as those obtained from single-voxel techniques. This makes it particularly difficult to produce reliable metabolite maps from short echo time CSI, where the baseline is also compromised by short- T_2 macromolecules. Interpretation of CSI maps should include inspection of the underlying spectra to decide whether or not a ‘deficit’ or ‘elevation’ is actually present.

Phosphorus Spectroscopy

After protons, phosphorus is the second most studied nucleus for in vivo spectroscopy. Phosphorus spectro packages are available commercially from the main vendors, typically on 3 T platforms. Phosphorus (^{31}P) has a lower Larmor frequency than hydrogen, which means that a higher field strength is necessary to achieve good spectral resolution. Phosphorus is also much less abundant than protons, with a whole-body concentration 1000 times smaller, and so SNR is relatively poor. Since phosphorus is a major component in adenosine triphosphate (ATP), consumed and renewed during the conversion of sugars to energy, ^{31}P spectra are typically used to study muscle metabolism.

In vivo ^{31}P has much shorter T_2 than protons and a rather long T_1 . Echo-based sequences such as PRESS, even at short echo times, are unsuitable; instead, sequences are used that acquire the FID immediately after excitation. ISIS (Image Selective In vivo Spectroscopy) is a subtractive technique that uses $\pm 180^\circ$ selective pulses in all possible combinations on the three axes, such that the final signal is only from the required voxel. Although it is a good voxel-selective technique, eight TRs are required for each signal acquisition. A normal ^{31}P spectrum from muscle is shown in Figure 17.19. Notice that the spectral width is nearly 20 ppm, in contrast with that of proton spectra, which is only about 5 ppm. Reading from right to left, ATP has three main

resonances at about -15 ppm, -8 ppm and -4 ppm labelled β -ATP, α -ATP and γ -ATP respectively, one for each phosphorus atom in the molecule. Phosphocreatine (PCr) is used as the reference chemical shift at 0 ppm. The other main peaks are phosphodiesters (PDE) at 3 ppm and inorganic phosphates (Pi) at 5 ppm.

During and after exercise, ^{31}P spectra show changes reflecting the initial decrease in ATP then its recovery during aerobic exercise. The main changes during aerobic exercise are a reduction in the PCr peak accompanied by an increase in the Pi peak, which returns to normal gradually when exercise ceases. In diseases such as muscular dystrophy ^{31}P spectra show a high Pi:PCr ratio at rest, and during exercise abnormal patterns are seen. ^{31}P spectroscopy is also used to investigate the liver, where the main difference in the appearance of the spectrum is that PCr is not present in the liver; a PCr peak in such a spectrum indicates contamination with overlying muscle. Repeated ^{31}P spectra can be acquired to study the metabolism of the liver, in the normal state and in hepatitis and cirrhosis, and to monitor the response of malignant lesions to therapies.

Other Nuclei

Other nuclei are used by research groups, but these have not yet made it to routine clinical applications.

Our bodies contain plenty of carbon, but unfortunately only the ^{13}C isotope is MR-visible and this isotope only comprises about 1% naturally. Most studies rely on adding ^{13}C to a compound which is either injected or ingested. For example, ^{13}C -glucose can be used to examine glucose metabolism in the brain, where studies of stroke patients have shown that lactate turnover is higher in the ischaemic penumbra compared with the infarct core.

Fluorine is another nucleus which is present in high concentrations in the bones and teeth, but is not MR-detectable because it has an extremely short T_2 . Like carbon spectro, pharmaceuticals can be labelled with ^{19}F (an MR-active isotope), and then used to investigate pharmacokinetics. For example, ^{19}F -CSI of the brain is possible using ^{19}F -tagged deoxyglucose ($[^{19}\text{F}]DG$), which is taken up by tissues from the blood supply in the same

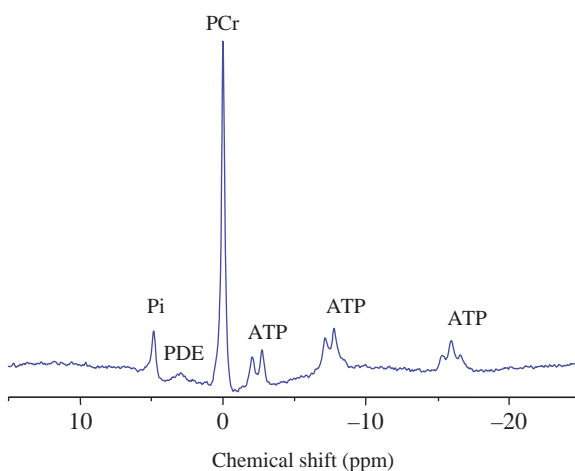


Figure 17.19 Phosphorus spectrum from normal muscle showing the main metabolite peaks. PDE denotes phosphodiesters; Pi inorganic phosphate and PCr phosphocreatine. Courtesy of Dr F. Howe, St George's Hospital Medical School, London.

way as glucose. The more common form of FDG using ^{18}F is regularly used in PET imaging to study brain perfusion. So MR studies of $[^{19}\text{F}]$ DG have the potential to provide the same information without the radiation dose associated with PET.

Finally, ^{23}Na is MR visible, but is present at very low concentrations *in vivo*. Like ^{19}F and ^{31}P , it has very short T_2 and requires an FID acquisition method.

There is interest in ^{23}Na imaging for stroke, where it is shown to be sensitive for changes in the intra- and extracellular concentration of sodium ions.

See also:

- Slice-selective RF pulses: Section 8.4.1
- 3D phase encoding: Section 8.8

Further Reading

Abragam A (1983) *The Principles of Nuclear Magnetism*. Oxford: Clarendon Press, chapters I, II and III.

Danielsen EB and Ross B (2010) *Magnetic Resonance Spectroscopy*

Diagnosis of Neurological Diseases, 2nd edn. New York: CRC Press.

Hahn EL (1950) ‘Spin echoes’. *Phys Rev* 80(4):580–594.

Salibi N and Brown MA (1998) *Clinical MR Spectroscopy First Principles*. New York: Wiley-Liss.

Van Hecke P and Van Huffel S (eds) (2001) ‘Special issue: NMR spectroscopy quantitation’. *NMR Biomed* 14(4):223–283.

To BOLDly Go: fMRI, Perfusion and Diffusion

18.1 Introduction

We turn now to some of the more advanced areas of MR straight from the cutting edge between research and clinical practice. The techniques in this chapter all relate to what is sometimes termed ‘micro-contrast’ mechanisms. This term is unfortunate because basic T₁ and T₂ relaxation depend upon the microscopic (at molecular level) interactions of spins. Nevertheless, these new techniques give specific information about aspects of tissue not readily available through conventional contrast mechanisms. In this chapter you will learn that:

- diffusion-weighted imaging relates to the mobility of water molecules, particularly when mobility is restricted to specific orientations, as in white-matter tracts;
- perfusion-weighted imaging relates to the delivery of blood to tissues, in terms of relative or absolute concentrations, or in terms of rates of delivery or mean transit times;
- perfusion-weighted imaging can use exogenous contrast (i.e. a bolus of contrast agent) or endogenous contrast, by the ‘spin labelling’ of arterial blood;
- dynamic contrast-enhanced MRI, also called permeability imaging, relates to the leakiness of blood vessels;
- BOLD (Blood Oxygenation Level Dependent) imaging, sometimes called fMRI (functional MRI – note the small ‘f’), is used to investigate regional brain activation; in lay terms, to observe the brain working.

Echo planar imaging (EPI), which was explained in Chapters 12 and 13, is the imaging sequence of choice for these applications on account of its extreme speed. The compromise for speed in EPI is extreme sensitivity to susceptibility-induced image distortion, low resolution and higher artefact levels.

18.2 Diffusion Imaging

The sensitivity of MR signals to random molecular motions, self-diffusion, has been known since the original pioneering work of Hahn, Carr and Purcell over half a century ago. More recently diffusion-weighted MRI (DW-MRI) has established itself as an important method in the assessment and diagnosis of acute stroke, revealing dramatic signal differences within an hour of onset.

18.2.1 A Trip to the Mall: Molecular Motion

Figure 18.1 shows the types of molecular motions that occur in tissues: bulk flow (e.g. along vessels), isotropic diffusion (which occurs in pure fluids) and restricted diffusion where cell membranes restrict the movement of molecules in one or more directions. It is important to understand that diffusion is different from flow. In bulk flow there is a net transport of molecules from one location to another, like cars driving down the highway from one city to another. In diffusion there is no overall shift in the average location of the molecules – just increased agitation or energy. Their movement is similar to that of the shoppers in a mall – no one is actually getting anywhere – but there’s loads of activity all in seemingly random directions! Figure 18.2 illustrates the ‘random walk’ of molecules under diffusion.

18.2.2 Pulsed Gradient Spin Echo

The most commonly applied method for producing diffusion-weighted contrast is the Pulsed Gradient Spin Echo (PGSE) method, sometimes called Stejskal and Tanner after its inventors. It consists of a 90°–180° pair of RF pulses with large and equal sized gradients placed on either side of the 180° pulse (Figure 18.3). By manipulating the gradients we can control the degree of diffusion weighting or *b*-factor. This involves the scanner changing the strength of the diffusion sensitizing gradients (G) and their timing as described in Box ‘To *b* or not to *b*’.

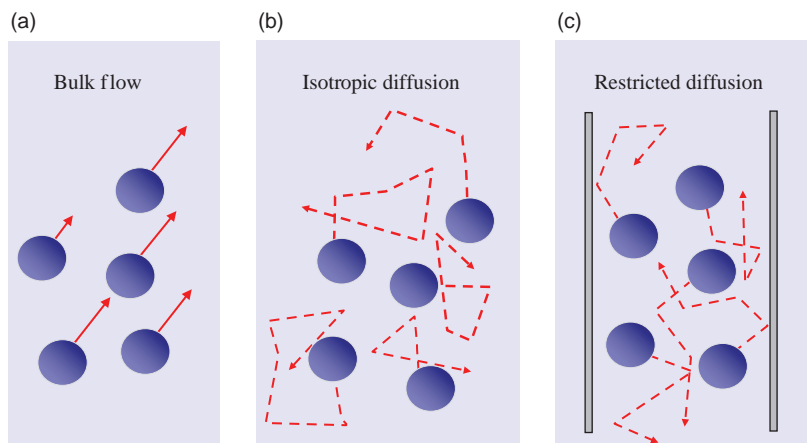


Figure 18.1 Three types of molecular motion (indicated by arrows) which may occur in tissue in (a) bulk flow, (b) isotropic diffusion where molecular motion is random and (c) restricted diffusion where random motion is constrained by physical barriers, e.g. by cell membranes.

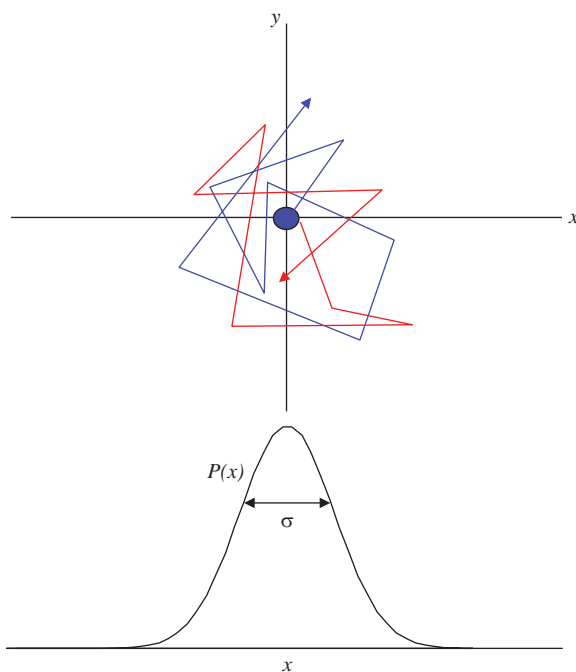


Figure 18.2 Random walk of molecules or ‘Brownian motion’. More diffusion results in a greater spread of the molecules, but the average location remains constant. The probability of a molecule’s location follows a Gaussian bell-shaped distribution with standard deviation σ .

DW contrast behaves rather like inverse T_2 weighting, in that watery tissues that have very mobile molecules give lower signal intensity, while more solid and static tissues give a stronger signal. The signal strength is described by the equation

$$S(b) = S_0 \exp(-bD)$$

where $S(b)$ is the signal for a particular b -value (see Box ‘To b or not to b ’) and D is the self-diffusion constant of the tissue. In MRI we use the term *apparent diffusion coefficient* (ADC) (see Box ‘The Diffusion Coefficient – Apparently’). This can be calculated from two or more images with different b -values and can be displayed as an ADC map. The diffusion coefficient D is measured in units of $\text{mm}^2 \text{ s}^{-1}$. At room temperature pure water has a value of D approximately $2.2 \times 10^{-3} \text{ mm}^2 \text{ s}^{-1}$. With a b of 1000, the water signal will be reduced to 11% of its unweighted value. In cancerous tissues there is often a proliferation of cellularity and a subsequent reduction in the intercellular space. This can result in a reduction in the free diffusion of extracellular water molecules and hence a reduction in ADC values. Thus the use of ADC values can help in the detection of cancer and in differentiating between benign and malignant lesions. Typical values are given in Table 18.1.

Another reason for calculating ADC maps is to deal with the issue of ‘ T_2 shine-through’. As DWI images necessarily involve a long TE, they are T_2 weighted in addition to being diffusion weighted. Areas which have an elevated T_2 may be indistinguishable on a DW-image from those with low diffusion (Figure 18.4). The ADC map removes this ambiguity.

To b or not to b

In the PGSE sequence the value of b is given by

$$b = \gamma^2 G^2 \delta^2 \left(\Delta - \frac{\delta}{3} \right)$$

and is determined by the gradient amplitude G and duration δ ('little delta') and trailing-to-leading edge separation ($\Delta - \delta$) where 'big delta' is the centre-to-centre separation. b has units of s mm^{-2} . We most often use a b -factor of 1000 s mm^{-2} to obtain good contrast. Large gradient amplitudes (of up to 50 mT m^{-1}) are very useful because they allow the timing parameters to be minimized, thus reducing the TE. Even so a DW acquisition will always have some T_2 weighting which can result in the so-called ' T_2 shine-through'.

The quantity $(\Delta - \delta/3)$ is known as the diffusion time τ and is related to molecular motion through the Einstein equation

$$\langle R^2 \rangle = 6D\tau$$

where $\langle R^2 \rangle$ is the mean square displacement of a collection (or ensemble) of molecules.

The PGSE gradient scheme works like the velocity-encoding gradients used in MR angiography.

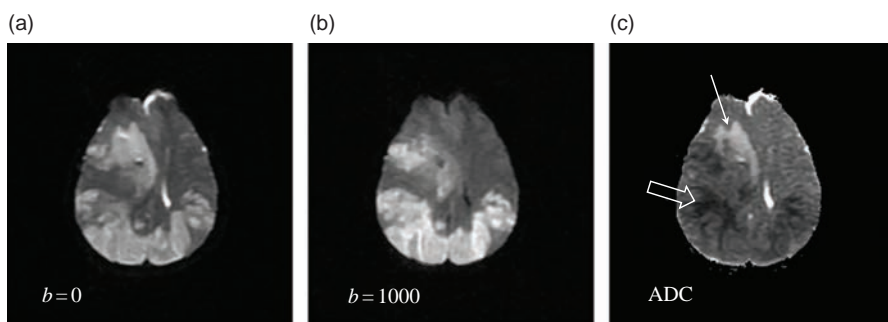
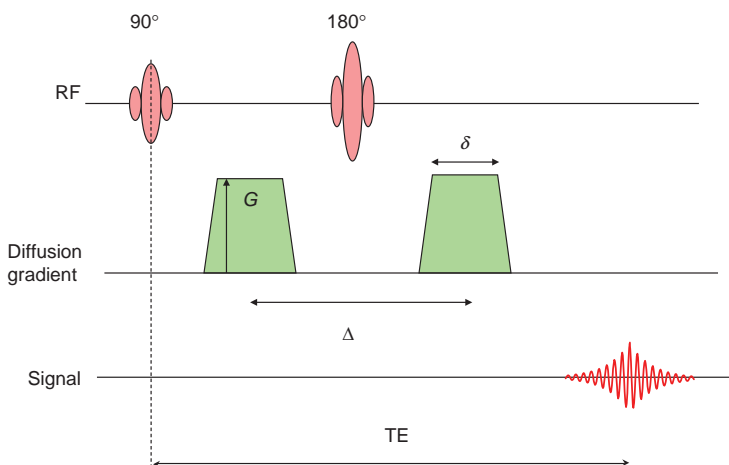


Figure 18.4 DW imaging of a stroke patient: (a) EPI image with $b = 0$, (b) $b = 1000$, (c) calculated ADC map. Acute infarcts have reduced ADC (open arrow) while chronic infarcts have elevated ADC (arrow). T_2 shine-through is evident where the DW image is bright, but the corresponding ADC is unchanged.

Table 18.1 Typical apparent diffusion coefficient (ADC) values for human tissues

	ADC ($\times 10^{-3} \text{ mm}^2 \text{ s}^{-1}$)	Relative signal (at $b = 1000$)
CSF	2.94	0.05
Grey matter	0.76	0.47
White matter	0.45	0.63
White matter parallel to fibres	0.95	0.39
Liver	1.8	0.17
Liver benign (cysts, haemangioma)	2.5	0.08
Liver (metastases, HCC)	1.1	0.33

Figure 18.3 Basic pulsed gradient spin echo (PGSE) sequence for diffusion weighting. For imaging this precedes a spin-echo EPI acquisition. δ denotes the pulse width and Δ the centre-to-centre spacing. G is the magnitude of the diffusion-weighting gradient.

Bulk flow will have its phase changed according to its velocity, but the phase angle will be many times 2π . With self-diffusion the molecules are moving about randomly, changing direction many times. DW imaging works because all the spins accrue random and unique phase changes as they move about within the gradient. This results in a net loss of signal within each voxel, provided sufficient DW is applied. Restricted diffusion applies where physical barriers, e.g. cell walls, prevent or limit this motion. A high value of D (the self-diffusion constant of the tissue) or ADC implies high motion and therefore low signal in DW-MRI. The corresponding ADC map will be bright.

The Diffusion Coefficient – Apparently

Diffusion weighting in an image is actually measured indirectly, via the relative dephasing of signals where diffusion occurs. However, dephasing can be caused by several other physiological motions, e.g. CSF or blood flow. In a simple diffusion scan we cannot distinguish between these effects, so we usually refer to the apparent diffusion coefficient or ADC, which can be calculated from

$$\text{ADC image} = -\frac{1}{b} \ln \left(\frac{\text{DW image}}{\text{T}_2\text{w image}} \right)$$

for cases where the same TE is used for both the weighted and unweighted images. Since SE-EPI has geometric distortions, it is normal to use SE-EPI for the T₂w image. All manufacturers provide this automatically in the pulse sequence, so that the scan contains a $b = 0$ image together with one or more b factors for diffusion weighting. b -values of 500 and 1000 s mm⁻² are common in DWI of the brain, while slightly lower values are common in body applications, e.g. prostate.

Instead of using just two b -values (0 and a higher value), a range of b -values can be applied and a ‘least-squares’ fit can be performed on a plot of $\ln(S_b)$ against b . The gradient of this line will give a more accurate value of ADC. See Chapter 19 for more sophisticated quantification methods.

Clinical Applications: Neuro

Neuro DWI is by far the most common clinical application. DWI is very sensitive for early changes in ischaemic stroke and in focal brain lesions. Ischaemic stroke, arising from thrombotic or embolic occlusion of a cerebral artery, leads to cell swelling or cytotoxic

oedema, which results in a depressed ADC. Acute stroke thus appears hyperintense (bright) on DW imaging (Figure 18.4). These changes are apparent in under an hour on DW imaging (compared with over 6 h on CT or 12 h on T₂-weighted MRI). It can also help to distinguish between acute stroke and other conditions with acute neurological deficits such as transient ischaemic attacks and atypical migraine, which show no abnormality in DW imaging. DWI can also help in differentiating solid tumours from cystic ones, and for trauma, haemorrhage and infections.

18.2.3 Anisotropy and Diffusion Tensor Imaging (DTI)

Pure water has isotropic diffusion properties, meaning that the molecules are equally likely to wander off in any direction. So the diffusion gradients can be applied in any physical direction and the effect on the MR signal should be the same. In many biological tissues (and especially white-matter tracts) diffusion is restricted by the presence of cell membranes and there may be a preferential direction, e.g. along nerve fibres.

This type of diffusion behaviour is called anisotropic. The measurement of diffusion anisotropy can yield useful biological information on the tissue’s microstructure, e.g. degree of myelination. To measure anisotropy it is necessary to apply diffusion weighting on a number of different directions, known as Diffusion Tensor Imaging (DTI). We define a new parameter, called ‘fractional anisotropy’ (FA) which has values from 0 to 1. For pure isotropic tissues FA = 0, while for tissues which have very strong anisotropy in one direction FA = 1. Figure 18.5a shows an FA map of the brain. There have been many clinical studies showing that reduced FA is a sensitive (but non-specific) indicator of a disease process. Colour maps (Figure 18.5b) for fractional anisotropy provide a way of displaying two types of information simultaneously: the hue represents the principal direction of the anisotropy and brightness represents how strongly anisotropic the diffusion is within that voxel.

For anisotropic tissues, the physical orientation of the tissue (e.g. fibre direction) in conjunction with the applied gradient direction will determine the signal intensity. If these two directions happen to be co-linear, we can accurately measure the diffusion

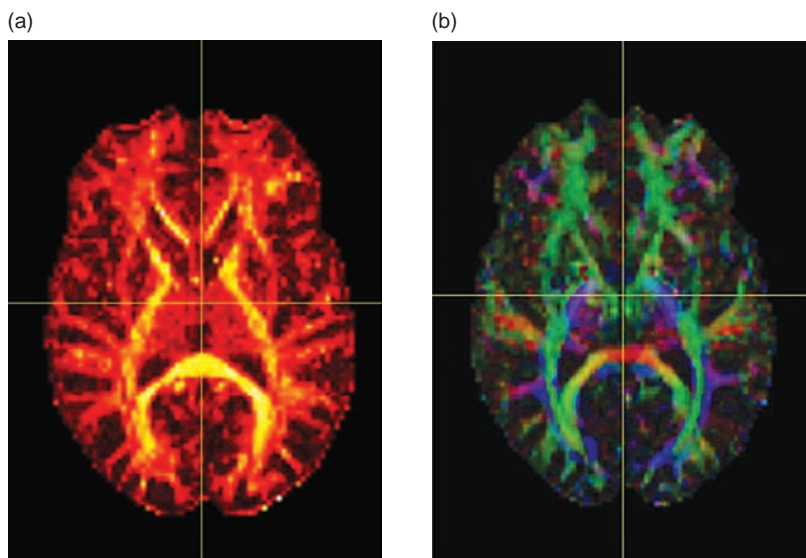


Figure 18.5 (a) FA map of the brain. Note how it resembles a strongly T₁-weighted image. (b) Colour FA map from the same subject. Green represents the principal eigenvector of diffusion in the AP direction, red is LR, blue is SI.

coefficient in that direction. However, that's not normally the case and we must generalize using a tensor. The diffusion tensor is a kind of two-dimensional vector and so has nine elements or values, each corresponding to a gradient orientation and a cell orientation as described further in Box 'Diffusion Tensor Maths'. In practice we don't know before the scan what the cell orientation values will be, so many diffusion gradient directions are applied, typically 30–60, or even more in research studies. Figure 18.6 shows the elements of the diffusion tensor.

Once the tensor terms have been found, we can define several new diffusion parameters: the 'trace-ADC' (see Box 'Diffusion Tensor Maths') always comes out as the same number no matter the direction – so is a very useful parameter in stroke or oncology. From this average ADC can be computed.

Once we have the diffusion tensor for every voxel in the image, we can also create a 'tractography' image, which shows the water diffusion pathways. Since white-matter bundles are the main biological cause of anisotropy, these pathways tend to follow the direction of the white-matter fibres. The resulting tractography images are remarkably similar to anatomical dissections showing WM bundles (Figure 18.7). Although there are many caveats to interpreting tractography (see Box 'Tractography Processing'), they are hugely popular with neuroradiologists and neurosurgeons, as they can reveal important relationships between brain lesions and surrounding normal tissue.

Diffusion Tensor Maths

The diffusion tensor is defined as:

$$DT = \begin{bmatrix} D_{xx} & D_{xy} & D_{xz} \\ D_{yx} & D_{yy} & D_{yz} \\ D_{zx} & D_{zy} & D_{zz} \end{bmatrix}$$

The first subscript (x, y, z) refers to the 'natural' orientation of the cells or tissue, and the second refers to the gradient orientation. The diagonal elements D_{xx} , D_{yy} and D_{zz} correspond to the simple three-direction measurements found in commercial scanners. To make a full measurement of ADC in an anisotropic tissue all these components plus a $b = 0$ unweighted image is required. In practice there is a degree of redundancy (because D_{xy} is the same as D_{yx} , etc.) and only seven measurements are required, six diffusion directions and an unweighted ($b = 0$) image as in Figure 18.6.

The trace diffusion constant, which is a so-called scalar invariant, can be computed as

$$\text{Trace}(D) = D_{xx} + D_{yy} + D_{zz}$$

from which an average ADC is obtained, equal to

$$D_{\text{ave}} = \frac{1}{3} \text{Trace}(D)$$

The fractional anisotropy FA is calculated from the principal eigenvalues λ of the tensor:

$$FA = \sqrt{\frac{3}{2}} \cdot \sqrt{\frac{(\lambda_1 - \bar{\lambda})^2 + (\lambda_2 - \bar{\lambda})^2 + (\lambda_3 - \bar{\lambda})^2}{\lambda_1^2 + \lambda_2^2 + \lambda_3^2}}$$

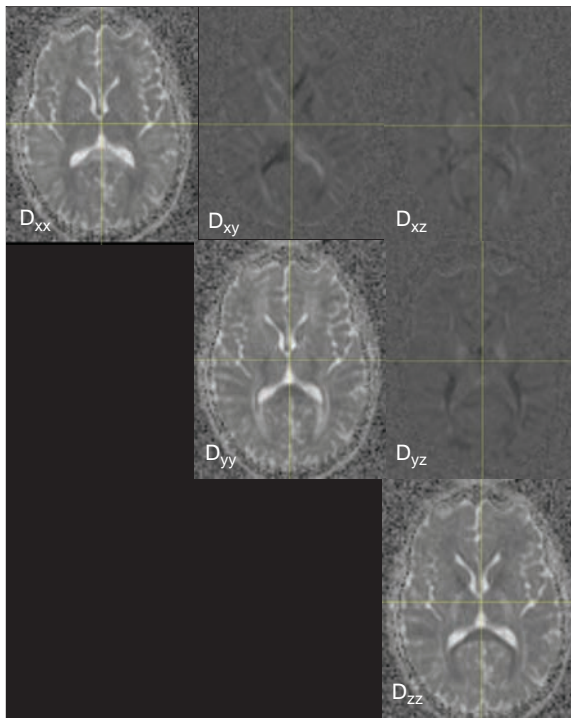


Figure 18.6 Elements of the diffusion tensor determined from a multi-direction DTI acquisition.

Tractography Processing

Conventional tractography requires the selection from a seed (or starting point from which to draw the tracts). It is essential that this seed point is chosen in an anatomically meaningful way and that a neurology or neuro-radiology specialist reviews the tractography images to ensure they do not contain artefactual information. One problem with DTI tractography is how to resolve fibres which cross paths within a voxel. Several approaches have been tried, including the use of very high b -values, 'Q-ball' and 'q-space' techniques.

Constrained Spherical Deconvolution (CSD) is a tractography method that can account for crossing fibres and does not require a user-defined seed point. CSD works by estimating a fibre response function. To do this a normal DTI acquisition is made using at least 30 directions. From these a tensor image is derived (Figure 18.6) and corresponding FA maps. From the FA maps voxels which only contain single direction fibres (e.g. from the corpus callosum) are selected (Figure 18.8a). From these a response function for a single fibre direction can be calculated (Figure 18.8b). Deconvolution of this with the tensor image results in

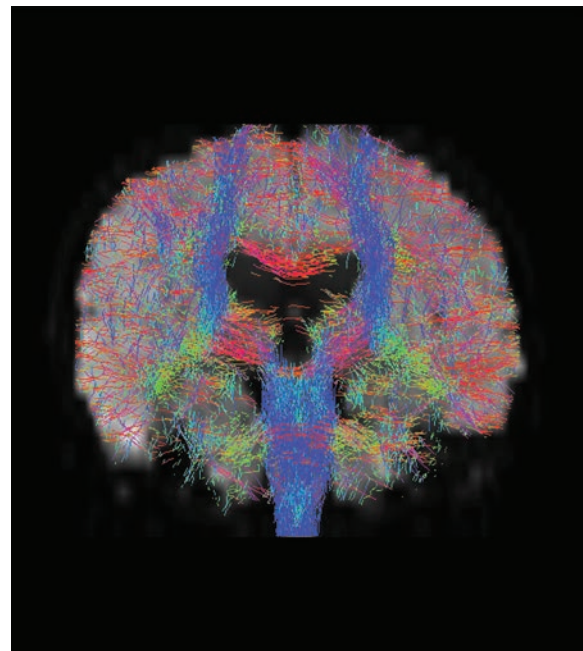


Figure 18.7 Tractography using constrained spherical deconvolution. Tract directions are blue – SI, green – AP, red – LR.

an orientation map, where crossing fibres are unambiguously depicted (Figure 18.8c). A tractography map can be computed by plotting the streamlines from the orientation plots (Figure 18.7).

18.2.4 Diffusion Sequences

Spin-echo EPI is the sequence of choice for DW imaging. Its very rapid acquisition time means that very little motion-induced artefact is encountered. The PGSE portion is appended to the front of the sequence as a preparation phase. Often sequences will be arranged to provide multiple images with a range of diffusion directions and b -values, and sometimes the scanner software will calculate an ADC map. Because of the need to have a reasonable diffusion time in the PGSE preparation, the TE value is normally quite high, greater than 100 ms. However, parallel imaging should be used to reduce the EPI echo train, which not only reduces the TE to a more suitable 60–70 ms, but also reduces the amount of geometric distortion in the images and reduces T_2 shine-through. Since SE-EPI is a multi-slice technique, DWI is typically performed with slice thicknesses of 5 mm. For DTI, it is desirable to have isotropic voxel resolution – typically 2–3 mm

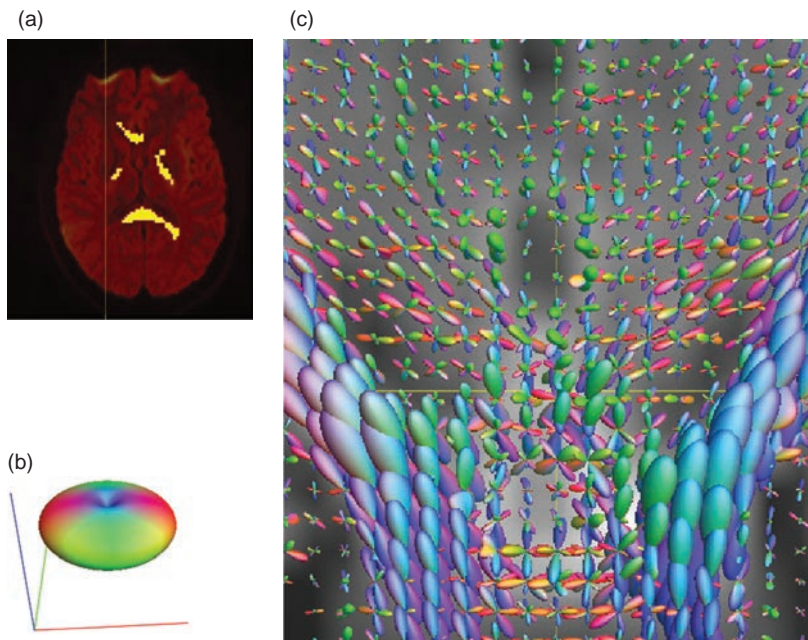


Figure 18.8 (a) Using an FA map, voxels containing single fibre orientations are selected. (b) A direction response function is generated. (c) Deconvolution of the tensor with the response functions resolves crossing fibres, displayed in an ellipsoid map, where the size of each ‘bubble’ represents the ADC value, with colours as before.

slice thickness is used, and so the number of slices to cover the brain is 80–100.

Conventional sequences such as (turbo) spin echo can also be used for DW imaging. However, their long scan times render the images very sensitive to bulk motion. DW-TSE is typically used for non-neuro diffusion imaging, e.g. the inner ear or head-neck region, where the long scan times are acceptable because the images have no EPI distortion. However, for the vast majority of DWI and DTI, spin-echo EPI is still the best choice.

Clinical Applications: Non-neuro

Outside of the brain, DWI is also very important, and is becoming a mandatory imaging sequence in many examinations. The main role is to localize tumours, e.g. in breast, prostate, liver and bone cancers. In all these areas, the lesion has a lower diffusion coefficient (more restricted diffusion), so it shows as a bright area on the DWI.

The key difficulty with non-neuro DWI is that SE-EPI is sensitive to B_0 inhomogeneity and the images can be very distorted. As well as making it difficult to recognize the anatomy, the distortion also leads to signal distortions, and especially signal pile-up which can be misinterpreted as a lesion. There are ways to avoid the distortion, e.g. using turbo spin echo instead of EPI, or using multi-shot EPI, but these all extend the scan time and are sensitive to patient motion.

When quantifying diffusion in non-neuro applications, it is important to separate perfusion (e.g. capillary flow) from diffusion. In order to do this, several b -values are acquired, and the signal curve is fitted using a bi-exponential model. The shorter exponential represents the perfusion fraction, while the longer one is the true diffusion coefficient.

Whole-Body Diffusion

The technique of whole-body diffusion, sometimes called DWIBS (Diffusion-weighted Whole-body Imaging with Background Suppression) can produce ‘PET-like’ images useful for evaluating metastases. DWIBS combines DW-EPI with a STIR-based fat suppression using a high b -value (typically 1000). The scans are acquired with free-breathing with multiple NSA used to attenuate any movement artefact. Images are acquired from multiple positions (stations) usually in the axial plane (Figure 18.10a) and are reformatted (Figure 18.10b) and stitched together to make a whole-body image. They are often viewed as Maximum Intensity Projections (MIPs) with a contrast reversal (Figure 18.10c). This renders them similar in appearance to PET images – although it must be remembered that DWIBS is measuring molecular motion while FDG-PET is sensitive to glucose metabolism.

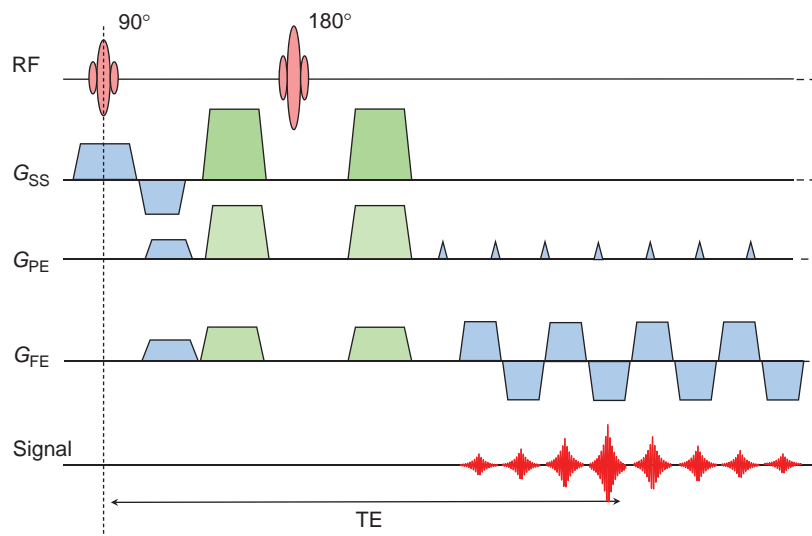


Figure 18.9 Diffusion-weighted EPI sequence. The diffusion gradients are shown in green and their relative amplitudes are varied to give the different directions.

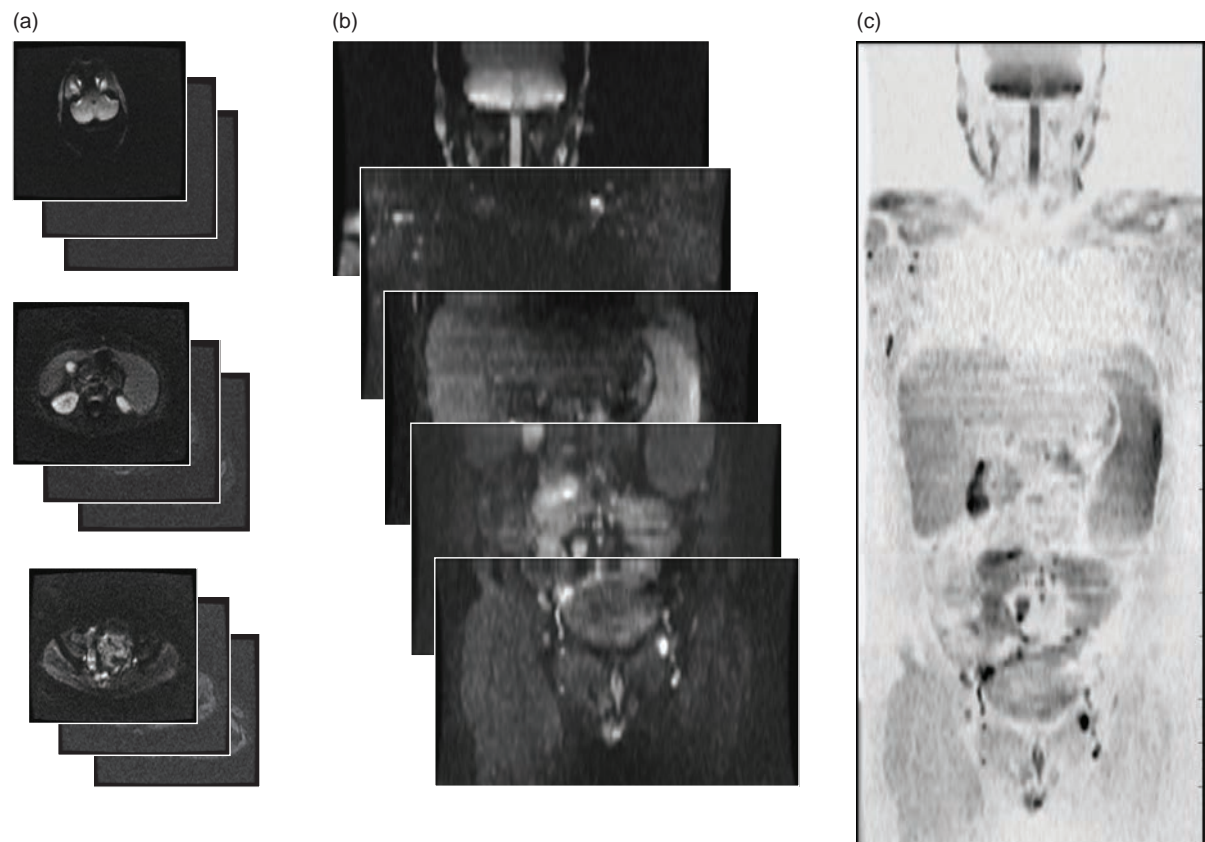


Figure 18.10 Whole-body diffusion – axial DWI images are acquired (a), then reformatted (b) and stitched together with contrast reversed (c).

18.3 Perfusion Imaging

Perfusion is a term that has different meanings to different professionals. Biotechnologists use it to mean the process of keeping tissues alive in a solution containing all the vital nutrients. In MRI it has a much more specific meaning, and refers to the capillary blood supply to a tissue, measured in $\text{ml min}^{-1} \text{ g}^{-1}$. In the brain this is usually called the cerebral blood flow (CBF) or simply f . Two other measures are commonly used in perfusion MRI, the cerebral blood volume (CBV) and mean transit time (MTT). Often these terms are prefixed with 'r' (rCBF, rCBV and rMTT) meaning 'relative', since it is difficult to quantify them absolutely and it is usually preferable to find a ratio between the ipsilateral and contralateral sides.

Two MRI techniques for imaging perfusion have been developed in the last few years to distinguish perfused tissue from unperfused, primarily for neurological applications (see Chapter 16 for cardiac perfusion). The quicker method is to image the required slices rapidly and repeatedly during the first pass of a gadolinium bolus, sometimes referred to as 'Dynamic Susceptibility Contrast MRI' (DSC-MRI). The other technique tags protons in the arterial blood supply with a magnetic 'label', then images the required slices with and without the labelling. Although a slower technique with poor signal-to-noise ratio (SNR), it is completely non-invasive and can be repeated as often as required (without having to wait for excretion of the gadolinium). It is known as 'arterial spin labelling' or 'arterial spin tagging', and there are several variations on this basic theme (which produce another rash of acronyms!). We will start by considering DSC-MRI, which to date has been more popular in clinical applications.

18.3.1 Dynamic Susceptibility Contrast MRI

In DSC-MRI a volume of tissue is imaged repeatedly using an EPI sequence. After a few images have been collected as a baseline, a bolus of gadolinium is injected as fast as possible. During the first pass through the intracranial circulation the gadolinium remains in the vasculature, causing a reduction of T_2 and T_2^* , which is seen as a dramatic drop in signal intensity on T_2 -weighted or T_2^* -weighted images (Figure 18.11). The second pass may also be detected as a slight drop in intensity, before the signal returns

to baseline. The whole imaging sequence takes no more than 2–3 min.

Originally gradient-echo EPI sequences were used for DSC-MRI since they are most sensitive to changes in T_2^* . However, it is preferable to use spin-echo EPI and measure changes in T_2 , which has been shown to be due only to the microcirculation, excluding the confounding signals from larger arteries and veins. A TE of 35–60 ms is used to detect the T_2 changes, with a TR of no more than 1500 ms in order to maintain reasonable temporal resolution. This rather short TR usually restricts the volume coverage even on a system with high-power gradients, or requires rather thick slices. The exception is on Philips scanners with a 3D perfusion sequence called PRESTO, which uses a time-reversed gradient-echo sequence to produce a Hahn echo collected by an EPI acquisition. There should be at least five images (time-points) in the baseline section for analysis purposes; since a bolus injection in the antecubital vein typically takes 8–10 s to reach the brain, the injection should be started soon after the start of the imaging sequence. Many groups regard a power injector as essential, as an injection rate of 3–5 ml s^{-1} is necessary to achieve a good bolus. (Compare this with the requirements for contrast-enhanced MRA, where the timing of the injection is more critical relative to the image acquisition and the bolus shape should be rather longer.) If the injection is performed by hand, large-gauge IV tubing with a minimum of connections and a mechanism for rapidly switching to saline flush should be used. It is also possible to make rapid hand injection easier by warming the gadolinium to body temperature, which reduces the viscosity by a factor of two. Repeated imaging of the volume should continue for a total of 2–3 min.

Analysis of all these images in the clinical setting is best done with proprietary software on a workstation, although for quantitative results or research work it may be better to use home-written software which can be well controlled. Most software produces pixel-by-pixel maps of the required parameters and often colour scales are used for display (Figure 18.12), giving a similar 'look' to nuclear medicine or PET scans. At a simple level, so-called summary parameters can be measured directly from the signal intensity curves; for example, the area under the curve (or 'negative enhancement integral'), the bolus arrival time (t_{arr}) and the time to peak (t_p), and the peak height (C_p). These are roughly related to rCBV, rMTT

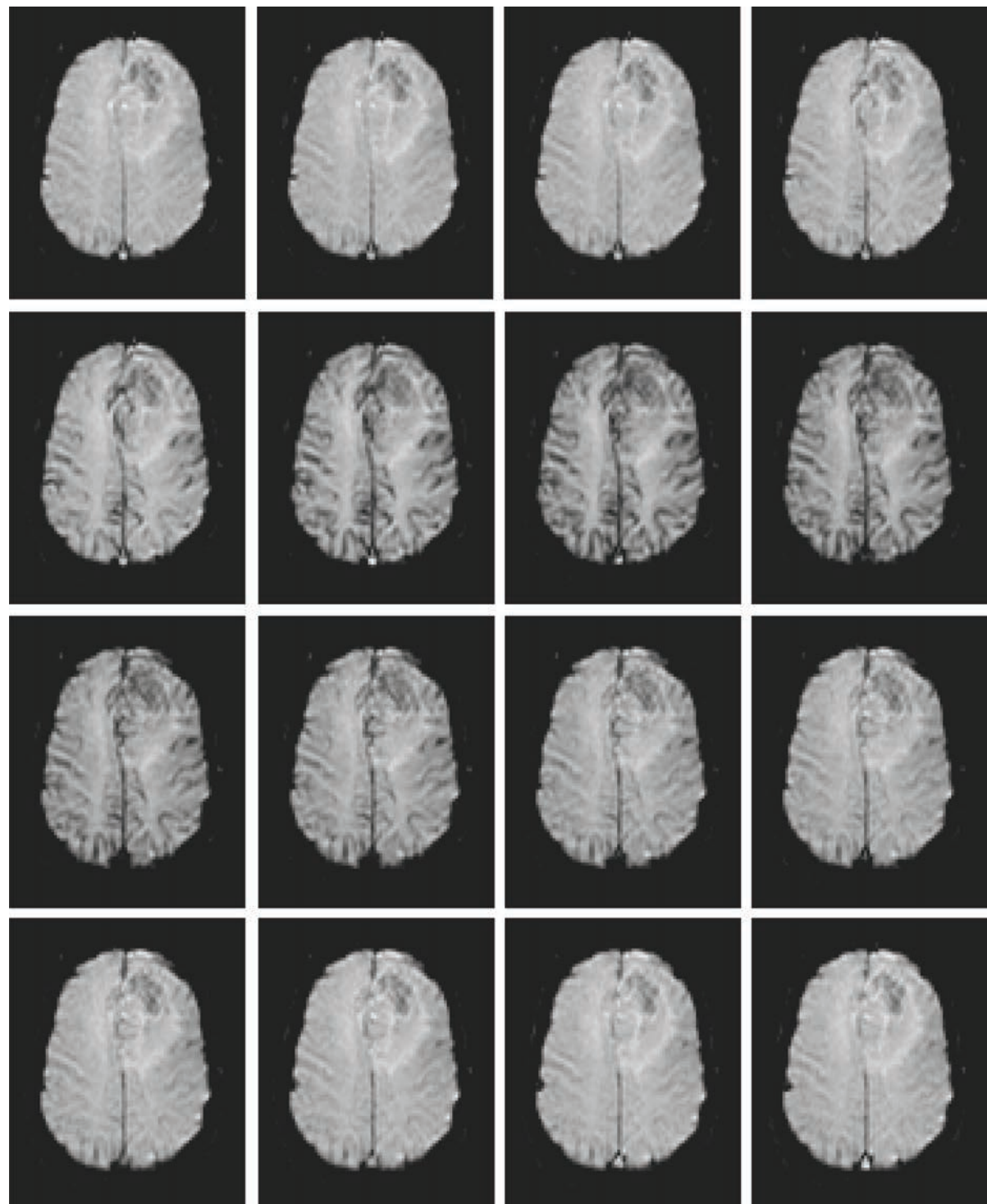


Figure 18.11 Sixteen images from a DSC-MRI examination of a low-grade glioma as the bolus of gadolinium passes through the vasculature. Time runs from left to right then down the rows, temporal resolution 1.2 s. As the bolus of gadolinium passes through the vasculature the signal intensities drop because of reductions in T_2^* .

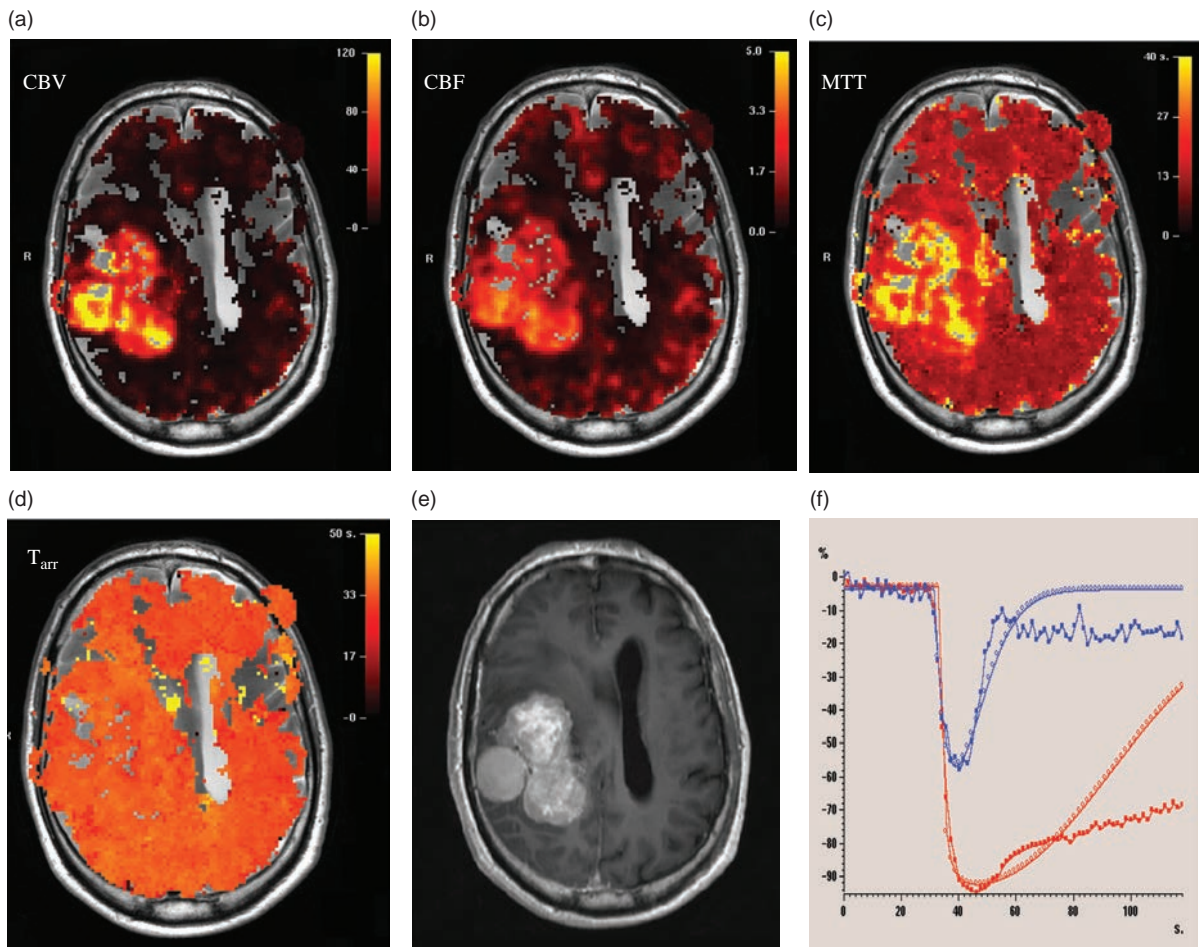


Figure 18.12 Perfusion parameter maps from DSC-MRI in a patient with a glioma. (a) CBV, (b) CBF, (c) MTT, (d) time of arrival (t_{arr}), (e) matching post-Gd T_1 -weighted image, (f) time-intensity curves for normal brain (blue) and tumour (red). Note how the fitted gamma-variate curve deviates from the real data due to rapid leakage of Gd into the tumour.

and rCBF respectively, but have the disadvantage that they depend strongly on the shape of the bolus.

Full analysis for quantification uses deconvolution of the shape of the injected bolus, known as the arterial input function (AIF). This can be measured in the middle cerebral artery or any other easily identifiable vessel, but caution should be exercised in patients with stroke who may not have a normal arterial supply. Good SNR is essential for the deconvolution to work successfully and it is common to use spatial filtering (smoothing) to reduce the noise level in the images.

Advanced Processing and Quantification

The starting point for perfusion quantification, or for generating parametric maps, is to find the Gd concentration as a function of time for each voxel, $C_{\text{tissue}}(t)$.

This can be done by assuming an inverse linear relationship between the T_2^* of the tissue and $C_{\text{tissue}}(t)$:

$$C_{\text{tissue}}(t) \propto \frac{1}{\Delta T_2^*} = -\frac{1}{TE} \cdot \ln \left[\frac{S_{\text{tissue}}(t)}{S_{\text{tissue}}(0)} \right]$$

where $S_{\text{tissue}}(t)$ is the tissue signal intensity at time t and $S_{\text{tissue}}(0)$ is the initial baseline signal intensity. From the concentration-time curve (Figure 18.13) we can measure some simple parameters such as the time of arrival (t_{arr}), time to peak (t_p) and maximum concentration C_p . Maps of these parameters are particularly useful in stroke studies, where a delayed t_{arr} is an indication of collateral blood supply. However, they are sensitive to differences in the bolus injection, which is a good reason for using a power injector in perfusion studies.

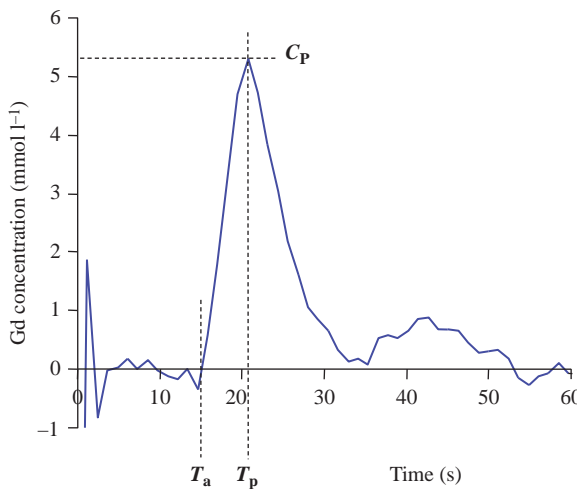


Figure 18.13 Concentration–time curve for white matter, showing the definition of various summary parameters. C_p denotes peak height; t bolus time arrival and t_p time to peak.

For more accurate quantification, we use indicator dilution theory (see Further reading for some useful references). This is a well-known model which describes how an indicator (gadolinium) is distributed (diluted) in the blood supply following an instantaneous bolus injection. In the ideal case of an intact blood–brain barrier, the concentration–time curve has a gamma-variate shape:

$$C_{\text{ideal}}(t) = C_p \cdot \left(\frac{e}{rs}\right)^r \cdot (t - t_{\text{arr}})^r \cdot \exp\left(-\frac{(t - t_{\text{arr}})}{s}\right)$$

where e is $\exp(1)$, $e \approx 2.718$; r and s are related to the rate of increase and rate of decrease respectively. Of course the bolus is certainly not ideal, and the tissue concentration curve is modified by the shape of the input concentration curve, known as the arterial input function, $AIF(t)$. Mathematically this is a convolution,

$$C_{\text{tissue}}(t) = C_{\text{ideal}}(t) \otimes AIF(t)$$

which means that if we measure the AIF , typically in a cerebral artery, we can find the ideal concentration–time curve by deconvolution. To do this, we divide the Fourier transform of $C_{\text{tissue}}(t)$ by the Fourier transform of $AIF(t)$ and take the inverse Fourier transform of the result:

$$C_{\text{ideal}}(t) = \text{FT}^{-1} \left\{ \frac{\text{FT}(C_{\text{tissue}}(t))}{\text{FT}(AIF(t))} \right\}$$

It is usual to fit a gamma-variate curve to the measured $C_{\text{ideal}}(t)$, using $r = s = \text{full-width-half-maximum}$

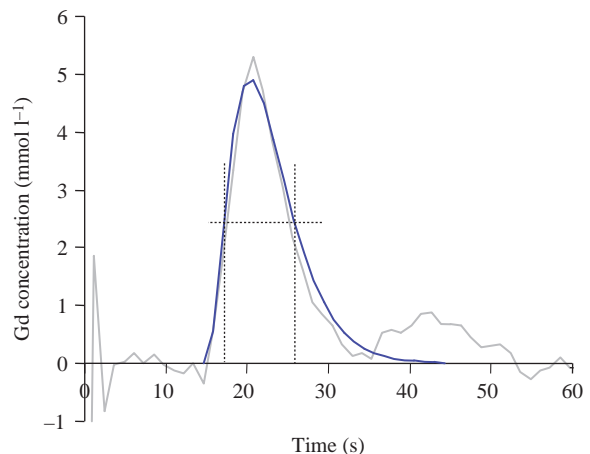


Figure 18.14 Gamma-variate fitting to the concentration–time curve. Starting points for the fitting parameters are found from the peak height and the times of the two half-heights.

as starting values for the fitting (Figure 18.14). The fitted curve $C_{\text{fit}}(t)$ can then be integrated to provide the cerebral blood volume (CBV), mean transit time (MTT) and cerebral blood flow (CBF):

$$\text{CBV} = \frac{\kappa}{\rho} \int C_{\text{fit}}(t) \cdot dt$$

$$\text{MTT} = \frac{\int t \cdot C_{\text{fit}}(t) \cdot dt}{\int C_{\text{fit}}(t) \cdot dt}$$

$$\text{CBF} = \frac{\text{CBV}}{\text{MTT}}$$

where ρ is the density of brain tissue and κ is a constant that accounts for the difference in haematocrit between large and small vessels. There are many problems associated with quantification of perfusion from Gd bolus studies, not least being the requirement for good SNR for both the deconvolution and the fitting process. However, with care it is possible to achieve reliable results.

18.3.2 Arterial Spin Labelling

Arterial Spin Labelling (ASL) imaging is based on magnetically labelling protons in the arterial blood supply, usually with an inversion pulse. When images are then acquired from slices in the brain, there will be a very small signal loss compared with unlabelled images. This is because there is an in-flow enhancement even in the capillaries. The label decays in only

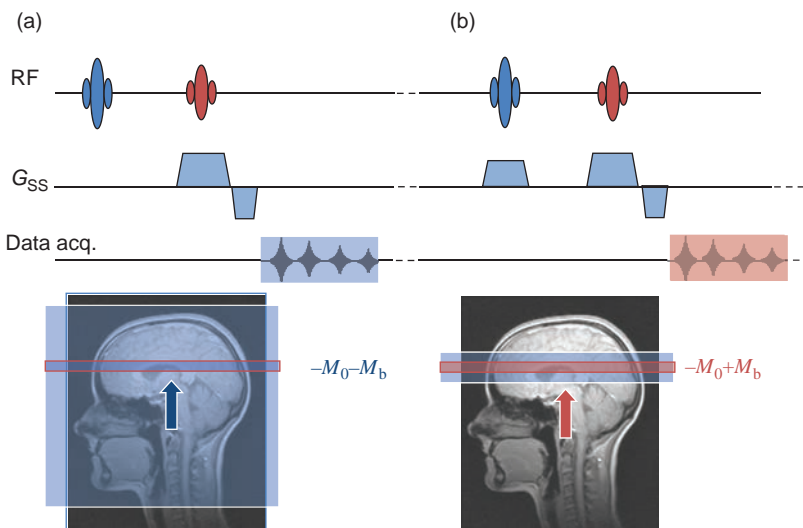


Figure 18.15 Schematic diagram for FAIR. (a) The labelled image is produced by applying a non-selective inversion pulse to the whole head while (b) the control image is produced with a slice-selective inversion pulse slightly wider than the image slice thickness.

4–5 s due to T_1 relaxation of the blood protons, so EPI is used for the image acquisition. There are several different ASL techniques, differing mainly in the way they apply the labelling and control pulses. We will only describe one, Flow-sensitive Alternating Inversion Recovery (FAIR), in order to illustrate the principles. You should check out the references at the end of this chapter for the other ASL techniques.

In the FAIR labelled images, an inversion pulse is applied to the whole brain before a single-slice EPI image is acquired (Figure 18.15). In the labelled image, inverted protons in the arterial supply are carried into the capillary bed of the imaged slice and exchange with protons in the tissues. Depending on the time delay between inversion and imaging, the signal intensity of protons in perfused tissue is reduced. For the control experiment the inversion pulse is applied only to the imaged slice. In the control experiment, arterial blood protons outside the slice, which are unlabelled, are carried into the image slice during the TI and the image will have a slightly higher SNR overall. Large bipolar crusher gradients (effectively diffusion weighting) are added to the pulse sequence to remove the signal in larger blood vessels, so one of the advantages of ASL over DSC-MRI is that it only measures capillary perfusion.

There are two main classes of ASL pre-pulse: pulsed and continuous. The pulsed ASL schemes include STAR, FAIR and PICORE, and can be easily understood; they simply apply a magnetization label to the up-stream arteries, which is then carried to the image volume. Pulsed ASL lends itself to time-resolved

techniques, which can track the magnetized bolus as it travels through the vasculature and into the brain. Continuous ASL uses a much longer RF pulse, most commonly as a train of smaller RF pulses, known as pseudo-continuous ASL (PCASL). The train of pulses continues until a steady state is reached in the perfused tissues, typically 1800 ms, and is followed by a delay to allow time for the tagged protons to reach the imaging volume, another 1800 ms. PCASL provides much higher SNR than pulsed techniques, and especially when combined with a 3D readout sequence, gives diagnostic image quality in a very acceptable 3–4 min scan time. This is becoming the ‘gold standard’ for ASL, both in clinical practice and in research studies.

Clinical Applications of ASL

In the last few years, PCASL has become widely available on commercial scanners. With a 2D SE-EPI readout, or a 3D GRASE readout, this sequence is relatively robust and offers good SNR with a scan time of around 4 min. Although this is easily within the scope of many clinical centres, ASL is still not routine practice everywhere. One reason is that ASL is very sensitive to patient motion, and special techniques are needed to correct the images in post-processing. Also, most commercial packages offer only the perfusion map as output; it is not possible to calculate the arrival times of the tagged protons in ASL. This puts ASL at a disadvantage compared with DSC-MRI, or with CT-perfusion techniques, which can produce bolus arrival-time maps.

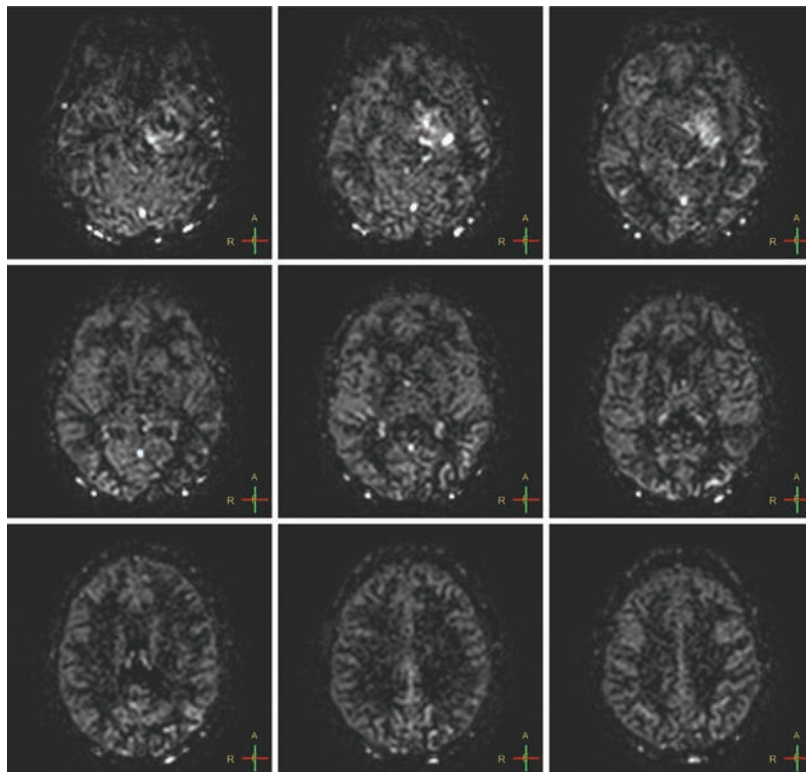


Figure 18.16 Arterial spin labelling perfusion images, showing higher perfusion as bright signal intensity. The focal lesion in the left basal ganglia has higher perfusion than normal grey matter and white matter.

In acute stroke, CT is still the preferred diagnostic method due to its speed and greater availability. In sub-acute stroke, and in other neurological diseases, ASL has good potential to add diagnostic value, particularly when the quantitative ASL methods are fully validated. For example, PET scanning shows a distinctive pattern of brain perfusion in dementia; in the future, this could be achieved using ASL at lower cost and without radioactive agents.

Outside of the brain, ASL is being used to image renal and liver perfusion. However, these methods are still in the research domain as they require sophisticated motion-compensation to correct for respiration. Non-neuro applications will continue to grow in the coming decade.

ASL Analysis

The difference in signal intensity can be shown to be related to M_0 , T_1 and perfusion of the tissue. The theory for ASL is not derived from the indicator dilution theory, since the tracer (labelled water) is freely diffusible whereas gadolinium is merely transported by the blood. Instead the theory is derived from the

Bloch equations using a two-compartment exchange model for water in the blood and tissues. For the FAIR technique

$$\Delta M = 2M_0 \frac{f}{\lambda} \left[\frac{\exp(-Tl \cdot R_{1a}) - \exp(-Tl \cdot R_1)}{R_1 - R_{1a}} \right]$$

where f is tissue perfusion, Tl is the inversion time, R_1 is the relaxation rate ($1/T_1$) of the tissue and R_{1a} is the relaxation rate of arterial blood. λ is a constant called the blood-brain water partition coefficient, which is usually assumed to be 0.9 (i.e. 90% of water is in the brain tissues and only 10% in the intracranial blood vessels). Although literature values for M_0 and T_1 could be used in theory, in practice it is usual to acquire images at a series of Tls , and to calculate M_0 and T_1 maps from the control images. With the M_0 and T_1 maps the signal differences can be fitted to the above equation to produce a perfusion map (Figure 18.16).

18.4 Dynamic Contrast Enhancement: Permeability Imaging

DCE is generally used to describe the process of dynamically acquiring MRI images during the

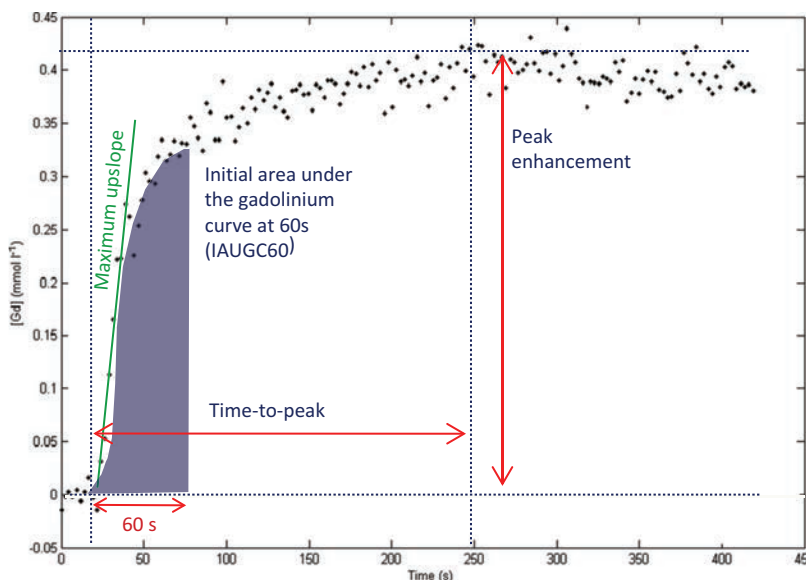


Figure 18.17 Four examples of non-model-based analysis metrics for DCE data (data points).

passage of an exogenous contrast agent, usually a standard chelate of gadolinium. In comparison to dynamic susceptibility contrast (DSC) techniques that exploit differences in T_2^* to create contrast in the images, DCE techniques rely on differences in T_1 . Depending upon the anatomy of interest, a T_1 -weighted acquisition may be performed either continuously during the wash-in and wash-out of the contrast agent or at specific time-points. In the liver, for example, it is common to acquire 3D T_1 -weighted data pre-contrast, at the peak of arterial enhancement (arterial phase) and at the peak of venous enhancement (portal venous phase). A subsequent (delayed) phase may also be acquired. Since different lesions exhibit differential enhancement it is a requirement to have these different temporal phase acquisitions. If the data are acquired with a sufficiently high temporal resolution, then it is possible to perform pharmacokinetic analysis of the contrast agent uptake and wash-out in order to provide quantitative or semi-quantitative indices of the tissue, or more commonly, the tumour vascularity. The blood supply to a tumour is typically made up of very chaotic and immature blood vessels which have a very 'leaky' endothelium. If a contrast agent is administered as a tight bolus then it will leak out of the vessels into the tumour, causing a transient signal intensity increase in the T_1 -weighted images. If images continue to be collected then the signal may start to decrease due to wash-out of the contrast agent.

There are various approaches to the quantification of contrast agent uptake. These can be divided into either model-based or non-model-based. The latter, non-model-based, methods use semi-quantitative indices that make no assumptions about the kinetics of the contrast agent uptake (Figure 18.17). For example, we can measure time-to-peak, maximum upslope, peak enhancement and the area under the signal-time curve for a fixed period after the start of contrast uptake. If the signal intensity is converted to $[Gd(t)]$ then the latter index is referred to as the Initial Area Under the Gadolinium Curve (IAUGC). This often has a subscript referring to the number of seconds for which the area is calculated, e.g. IAUGC₆₀ or IAUGC₉₀.

Model-based methods to quantify contrast enhancement use a mathematical equation with a number of unknown parameters. The best-fit of the experimental data to the model provides values for these parameters. One of the most common models in use for DCE-MRI data analysis is the Tofts' model. This model is a simplification of the *in vivo* situation and assumes two 'compartments'; the vasculature (or more correctly the blood plasma) and the tissue into which the contrast agent leaks, more correctly called the extravascular, extracellular space (EES), i.e. the interstitial space that contains neither blood vessels or cells. The Tofts' model is a fairly complex mathematical equation (see Box 'Mathematical Modelling: The MRI Catwalk') that yields a number of quantitative indices such as K^{trans} , k_{ep} and v_e (Figure 18.18).

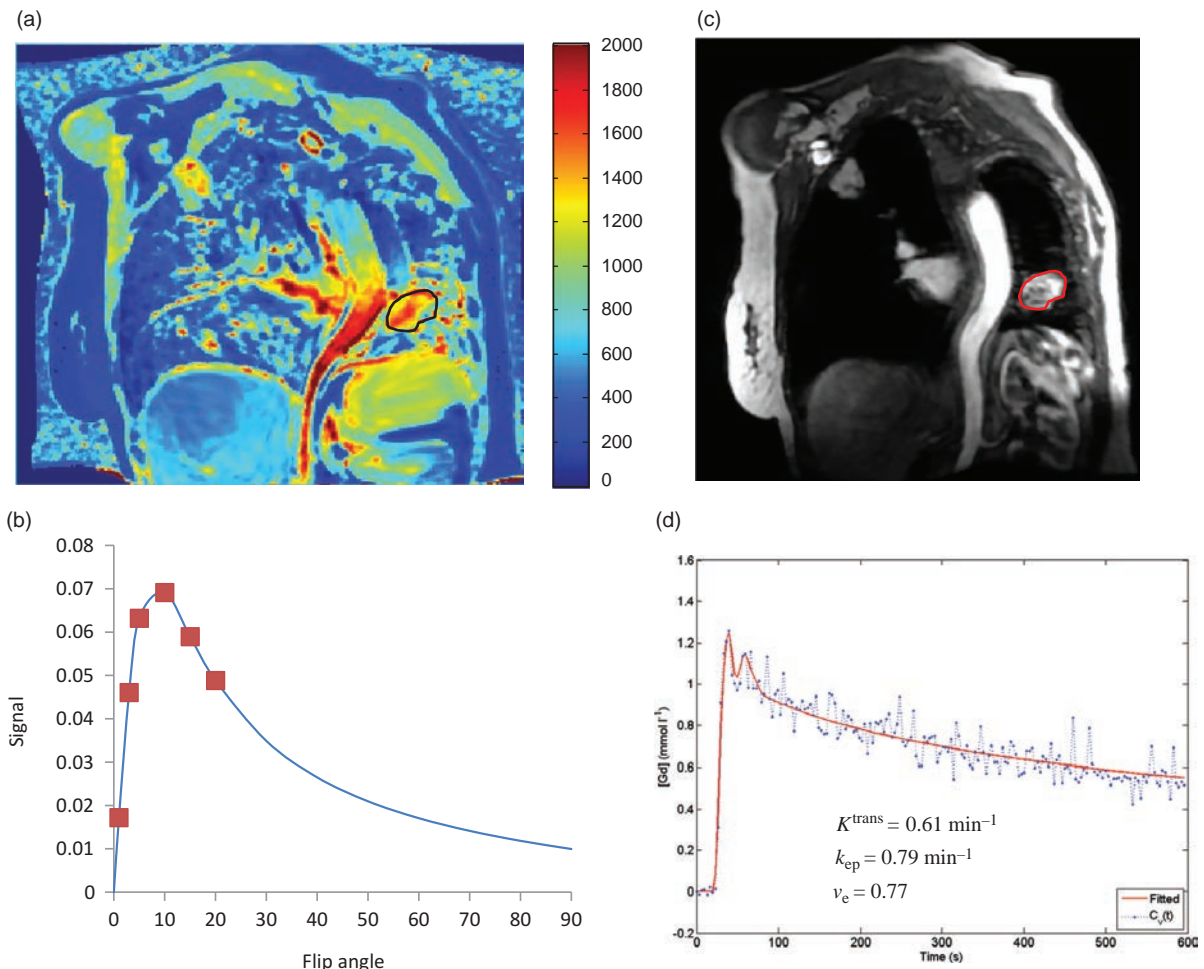


Figure 18.18 (a) shows a T_1 map calculated from six different flip angles using the signal equation for a T_1 w spoiled gradient-echo sequence. The tumour is outlined. (b) Shows the signal/flip angle curve for the tumour ROI that was used to calculate the T_1 . The six flip angles are marked. (c) Shows a single phase from the DCE acquisition at peak enhancement in the ROI. (d) Shows the Gd concentration time curve (blue data points) and the fitted Tofts' model (red line). Courtesy of Dr Andrew Gill, University of Cambridge, UK.

A large number of research studies have shown that these indices may be more sensitive biomarkers of tumour changes than standard measurements, e.g. the RECIST (Response Evaluation Criteria In Solid Tumours) method which involves simply measuring the largest diameter of the tumour.

Mathematical Modelling: The MRI Catwalk

Using the standard Tofts' model the uptake of the contrast agent in a region of interest (ROI) can be approximated using the following equation

$$C_{\text{tissue}}(t) = \frac{K^{\text{trans}}}{1 - Hct} \cdot C_{\text{art}}(t) \otimes \exp(-k_{\text{ep}}(t - \tau))$$

where $C_{\text{tissue}}(t)$ and $C_{\text{art}}(t)$ are the Gd concentration in tissue and arterial blood respectively, both measured as a function of time; Hct is the haematocrit; K^{trans} is the transfer constant from blood plasma to the EES; k_{ep} is the transfer constant from EES back to blood plasma; τ is the onset time of arterial Gd contrast uptake; and v_e is the total EES volume. \otimes is a convolution operator. K^{trans} , k_{ep} and v_e are related by the equation

$$v_e = \frac{K^{\text{trans}}}{k_{\text{ep}}}$$

So, although you might expect the two transfer constants to have the same units, they don't. K^{trans} is measured in $\text{ml g}^{-1} \text{s}^{-1}$, while k_{ep} is measured in s^{-1} , and the EES volume v_e is measured in ml g^{-1} .

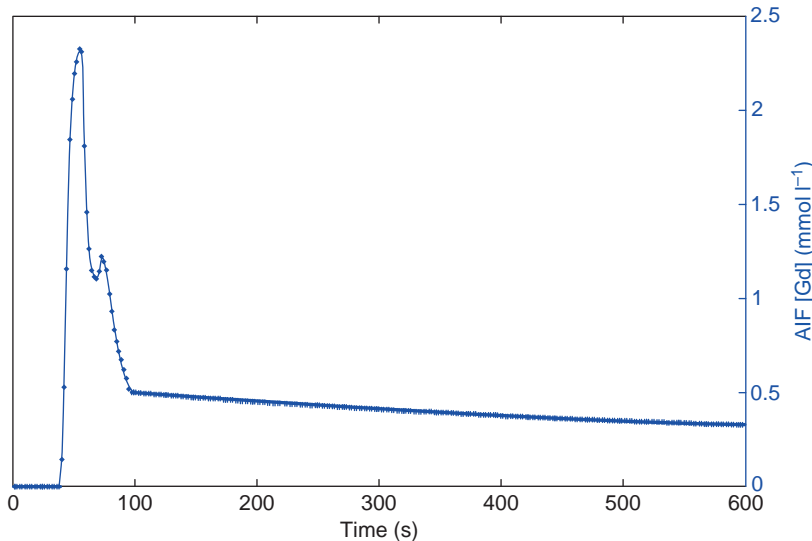


Figure 18.19 The model arterial input function (AIF) that was used in the Tofts' analysis for the data in Figure 18.18. Courtesy of Dr Andrew Gill, University of Cambridge, UK.

Since MRI only reports arbitrary signal intensities it is necessary to first determine the actual gadolinium concentration as a function of time $[Gd(t)]$. If we make the assumption that there is a linear relationship between signal intensity (S) and $[Gd]$ then

$$[Gd(t)] = \frac{S(t) - S(0)}{S(0) \cdot T_{1,0} \cdot r_1}$$

where $S(t)$ is the signal at each time-point t , $S(0)$ is the signal pre-contrast injection, i.e. $t = 0$, $T_{1,0}$ is the T_1 of the tissue prior to contrast agent injection and r_1 is the known T_1 relaxivity of the contrast agent. However, this linear relationship assumes that the TR of the sequence measuring $S(t)$ is approximately the same as $T_{1,0}$ and that T_1 is independent of time. Therefore a non-linear model based on the signal equation of a $T_{1,w}$ spoiled gradient-echo sequence with known TR and flip angle α° can be used

$$S = S_0 \frac{\sin \alpha (1 - E_1)}{1 - \cos \alpha E_1}$$

where $E_1 = \exp(-TR/T_1)$. This can be rearranged as follows

$$\frac{1}{T_1(t)} = \frac{1}{TR} \cdot \ln \left(\frac{S_0 \sin \alpha - S_0 \cos \alpha}{S_0 \sin \alpha - S(t)} \right)$$

Using this equation $[Gd(t)]$ can be calculated from

$$[Gd(t)] = \frac{1}{R_1} \left[\frac{1}{T_1(t)} - \frac{1}{T_{1,0}} \right]$$

It is therefore necessary to know the value of $T_{1,0}$ for every voxel. There are various methods of

determining $T_{1,0}$ (see Section 19.2), with the multiple flip angle method quite popular for DCE techniques since the same 2D or 3D spoiled gradient-echo imaging sequence can be used.

While it is reasonably straightforward to determine $C_{tissue}(t)$, it is rather more difficult to determine $C_{art}(t)$, which is often termed the arterial input function (AIF) or vascular/vessel input function (VIF). First, it may be difficult to localize the main vessel feeding the tumour; second, since $C_{art}(t)$ changes very rapidly, very high temporal resolution is required to accurately capture the AIF. For these reasons a number of 'model-based' AIFs have been described in the literature (Figure 18.19). These have typically been derived from either blood-sampling or by averaging a population of measured AIFs. The choice of AIF is still an area of contention and will depend upon the tissue being studied. Likewise, there are a number of other DCE models described in the literature and the Tofts' model may not be optimal in all applications.

18.5 Brain Activation Mapping Using the BOLD Effect

In recent years the term functional MRI or fMRI (note the small 'f') has become synonymous with brain activation imaging using the BOLD effect. This is in some ways related to ASL perfusion imaging, except that intrinsic T_2^* contrast rather than T_1 contrast is utilized. In BOLD fMRI we 'see the brain working'.

18.5.1 The BOLD Effect

The BOLD (Blood Oxygenation Level Dependent) effect was observed at the start of the 1990s in animal-based experiments. It was known that oxyhaemoglobin is diamagnetic (i.e. essentially non-magnetic) and that deoxyhaemoglobin is paramagnetic. This means that deoxygenated blood has a shorter T_2^* and hence lower MR signal than fully oxygenated blood. That the opposite was observed in visual cortex during sensory stimulation was initially surprising – the MR signal increasing or ‘lighting up’ at times when oxygen consumption was heightened due to neuronal activity as in Figure 18.20. The scientific consensus is now that the increased consumption of oxygen by neurons during activation is accompanied by a disproportionate increase in the supply of fully oxygenated blood, so that downstream from the site of activation the concentration of deoxyhaemoglobin decreases and so T_2^* is elevated and the MR signal increases. Gradient-echo EPI, with its strong T_2^* weighting, is the sequence of choice for many fMRI examinations.

Brain or Vein

In fMRI we detect blood oxygenation changes in the draining veins, i.e. downstream from the actual activation site (Figure 18.20). The difference in magnetic susceptibility between fully oxygenated and deoxygenated blood is about 9.5×10^{-7} . However, fully

oxygenated blood has a magnetic susceptibility χ similar to that of the extravascular space in grey matter and so differences in oxygenation will affect the local field homogeneity and therefore change T_2^* .

The BOLD effect during activation is illustrated in Figure 18.20, where following neuronal activity, although there is a greater number of deoxygenated red blood cells, the increase in fresh oxygenated blood delivery results in a reduction of the concentration of deoxyhaemoglobin and therefore T_2^* increases, as does the MR signal.

MR perfusion can also detect neuronal activation by its sensitivity to the blood flow changes in the capillaries. It is thought that perfusion fMRI may pinpoint the actual activation site more directly than BOLD fMRI, although the sensitivity of BOLD is higher. The localized blood flow changes in activation can also be detected using non-EPI sequences such as spoiled gradient echo, although the high sensitivity to flow may result in vessels on the cortical surface being mistaken for activation.

18.5.2 fMRI Acquisitions

To say that the ‘brain lights up’ during activation is a bit of an exaggeration as the actual signal intensity changes are no more than a few per cent. In fMRI we detect these by modulating the oxygenation level at the site of brain activity and look for correlated signal changes. Rapid scanning, usually with EPI, is carried out continuously while the subject performs various tasks (known as the paradigm). These are commonly arranged in a block design with periods of activity interspersed with periods of contrasting activity or rest. The periods of activity might involve motor tasks, stimulus presentation or cognitive activity (e.g. generating words, doing mental arithmetic, etc.). A block length or ‘epoch’ will typically be about 30 s, with perhaps three or four complete cycles of the two contrasting tasks. This is shown in Figure 18.21 for a simple on-off visual stimulus and in Box ‘Clinical fMRI’.

Block design paradigms are robust and simple to arrange. However, for some mental tasks it may be difficult to generate extended periods of activation to form an epoch. Some brain events, e.g. hallucinations resulting from psychosis, may be of a transient and unpredictable nature. One solution to this is to use so-called Event-Related (ER) fMRI. In ER-fMRI scanning is carried out continuously at a higher image acquisition rate (e.g. once per second) and we simply

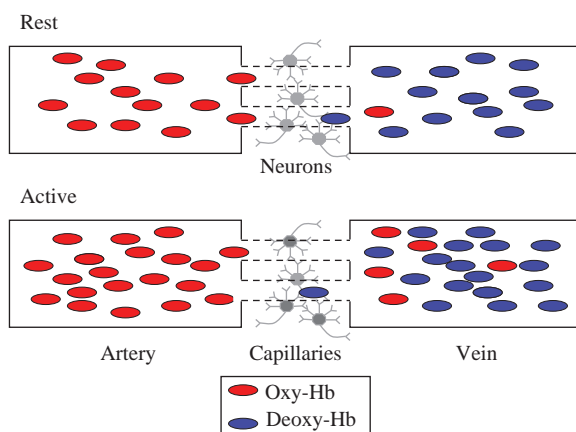
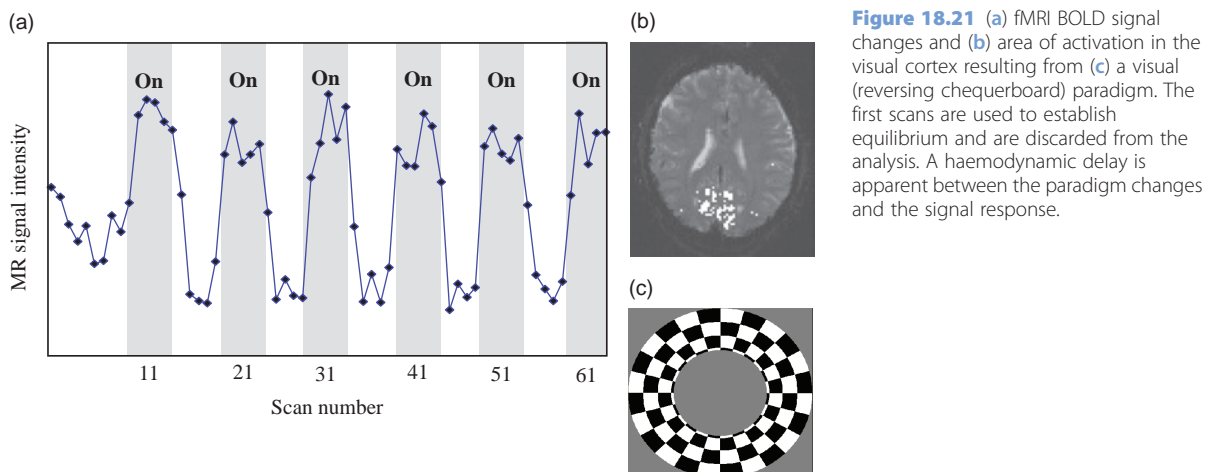


Figure 18.20 The origin of the BOLD effect. In activation (below) the over-provision of fully oxygenated blood leads to a reduction in deoxy-Hb and an increase in local T_2^* in the draining veins compared with the rest condition (above).



wait until the event occurs and look for corresponding changes in the MR signal that resemble the haemodynamic response of activation (see Box 'Haemodynamic Delay and Convolution').

Having acquired the time series of scans, there is much post-processing required. This is normally done offline on an independent computer. Finally, an image is produced that represents the statistical significance of signal changes correlated with the paradigm.

18.5.3 fMRI Processing

The common steps of fMRI processing are illustrated in Figure 18.22. First, the images are realigned or co-registered with themselves. This is necessary because even the smallest shift in the position of a voxel can generate significant signal changes. Stimulus-correlated motion would result in false-positive 'activations' unless removed in this way. Normally the first few volumes will be discarded to ensure that the magnetization is in a steady state, usually required for the realignment algorithm to be accurate. Post-acquisition realignment is required even if prospective slice positioning using navigator echoes has been used for the acquisition.

Data Meltdown

A typical fMRI scan may involve 24 slices of the brain, acquired with in-plane resolution of 128×128 . We may collect 100 volumes in a single run, performing several runs on each subject. By the time we have done all the processing the data volume will have been at least trebled or quadrupled.

$$\begin{aligned}\text{Total raw data per run} &= 24 \times 128 \times 128 \times 100 \\ &= 39\,321\,600 \text{ voxels} \\ &= 80 \text{ MB}\end{aligned}$$

and this represents 5 min scanning only. Generating several gigabytes (1 GB = 1000 MB) in one day is not hard.

A second step is to spatially normalize the images to a standard brain space, often to the Talairach Brain Atlas. This aids the neurological interpretation of the resultant activation maps and it also allows data to be averaged over groups of subjects. For individual patients with structural brain abnormalities or tumours this step is omitted.

The third step is to smooth the data. This helps to boost the SNR but has to be applied carefully to avoid excessive loss of spatial resolution. A fourth step may be to de-trend or normalize the data according to an overall or global mean or to apply a high-pass temporal filter. This step is designed to remove any bias resulting from scanner drift, for example, over the acquisition.

Next, statistics are calculated. Various levels of sophistication are involved here, but the simplest is to subtract the rest images from the active images and look for significant increases in signal, characterized by the Z-score defined as

$$Z = \frac{\text{mean signal difference}}{\text{standard deviation}}$$

In practice Z needs to be greater than 3 for any degree of confidence in the results. Z-scores are related to p-values commonly quoted with regard to the normal

distribution (*t*-test). The resulting brain activation map is made by displaying only those voxels that have the appropriate statistical parameter (e.g. Z-score, *p*-value) greater than a given statistical threshold. Sometimes spatial extent thresholding is carried out to exclude isolated voxels or small groups and only show clusters of activation. Sophisticated analyses can be applied to obtain better inferences of the statistical significance of clusters of activated voxels. A number of statistical approaches other than *t*-tests are possible, including correlation, Fourier, wavelet and independent component analyses. Software packages are available through the academic domain as well as those supplied by MR manufacturers. It is common for an fMRI statistics program to model the haemodynamic effect either by introducing a fixed or variable time delay, or by a more complex convolution of the paradigm waveform over the time series with a notional haemodynamic response curve.

Finally the resultant statistical maps are combined with underlying anatomical information. It should be

recognized that there may not be full geometric correspondence between the EPI BOLD images and the anatomical images (unless a similar EPI protocol is used for both). This is due to the inherent image quality limitations of EPI.

Haemodynamic Delay and Convolution

One of the complexities of BOLD imaging is that the effect we are detecting lags behind the actual firing of the neurons by as much as 6 s. This is known as the haemodynamic delay and can be allowed for in the data analysis. Similarly, the effect will outlast the neural activation to a similar degree. This makes the temporal resolution of fMRI rather limited. There is also a considerable undershoot post-activation. The effects of the delay and undershoot can be seen in the actual data of Figure 18.21 and schematically in Figure 18.22.

Mathematically the combination of haemodynamic delay with the stimulus waveform, a boxcar or series of impulses, can be described by a

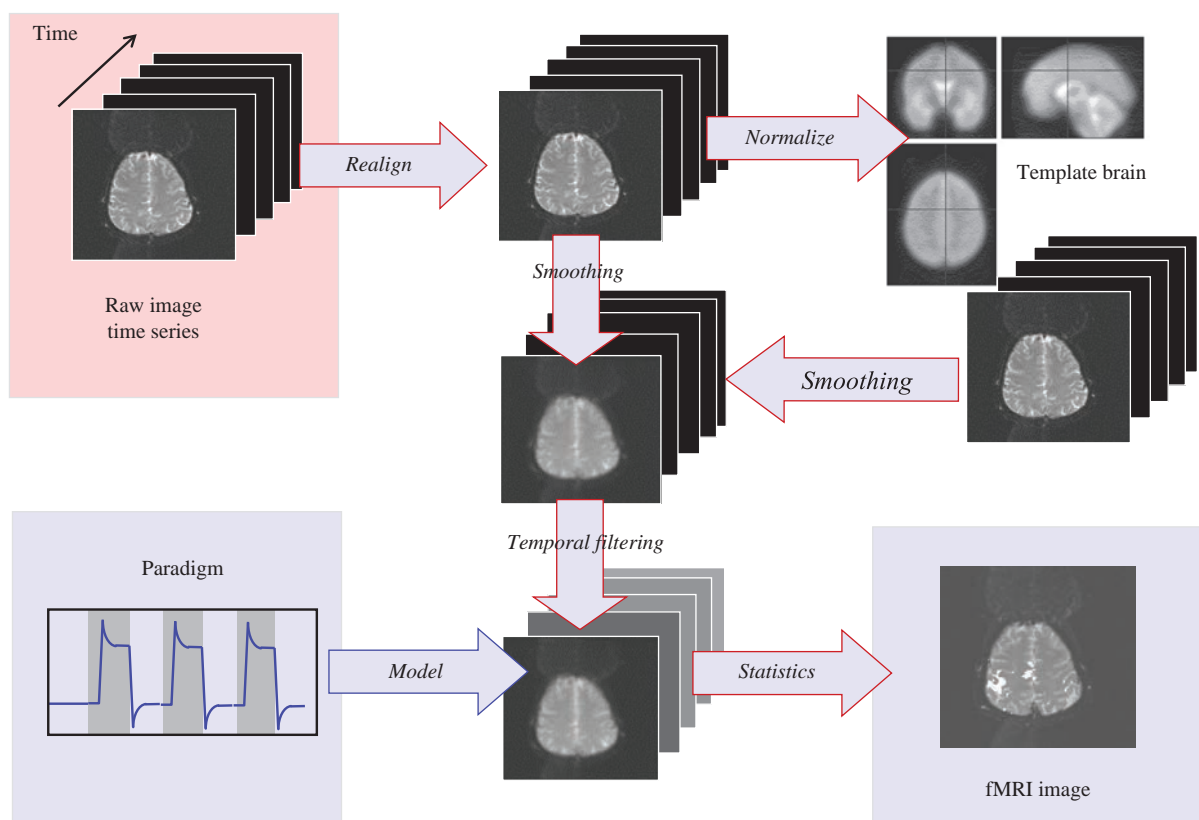


Figure 18.22 fMRI processing from the input of a time series of EPI data and a paradigm. The final image is a superposition of a statistical map on a raw image.

convolution process. By deconvolution of the actual response the haemodynamic response function (HRF) may be obtained. In the case of an impulse stimulus (because of the mathematical properties of the delta-function) the MR signal intensity changes can directly yield the HRF, although correction for the exact timing of the slices with respect to the stimulus timing is required.

One further feature of the HRF is an initial MR signal dip, thought to be due to the initial oxygen consumption increase, before the increase in blood delivery which causes the BOLD signal kicks in. This dip is usually too rapid to be observed with standard EPI sequences.

18.5.4 Interpreting fMRI: 'Blobology'

What are we looking at in a functional MR image? fMRI brain activation maps are normally presented as coloured 'blobs' superimposed on a greyscale anatomical background image, or as a colour overlay on a 3D

surface-rendered image of cortical grey matter, as in Figure 18.23.

It is important to understand that the coloured blobs do not themselves signify brain activation, but represent areas of statistically different MR signals. The intensity of the colour represents the degree of statistical confidence that a voxel value or a group of voxels has changed according to the 'paradigm'. Actual signal changes may only be a small percentage or less. For this and other reasons the clinical interpretation of individual fMRI examinations is fraught with difficulty. BOLD signals can go down as well as up, and this so-called deactivation may be artefactual, due to inhibitory brain processes, or simply the result of the subject's mental processes, e.g. shifts in attention.

Clinical fMRI

Clinical fMRI can be used for patient selection and pre-surgical planning for epilepsy surgery or resection of brain tumours, or in the clinical evaluation of

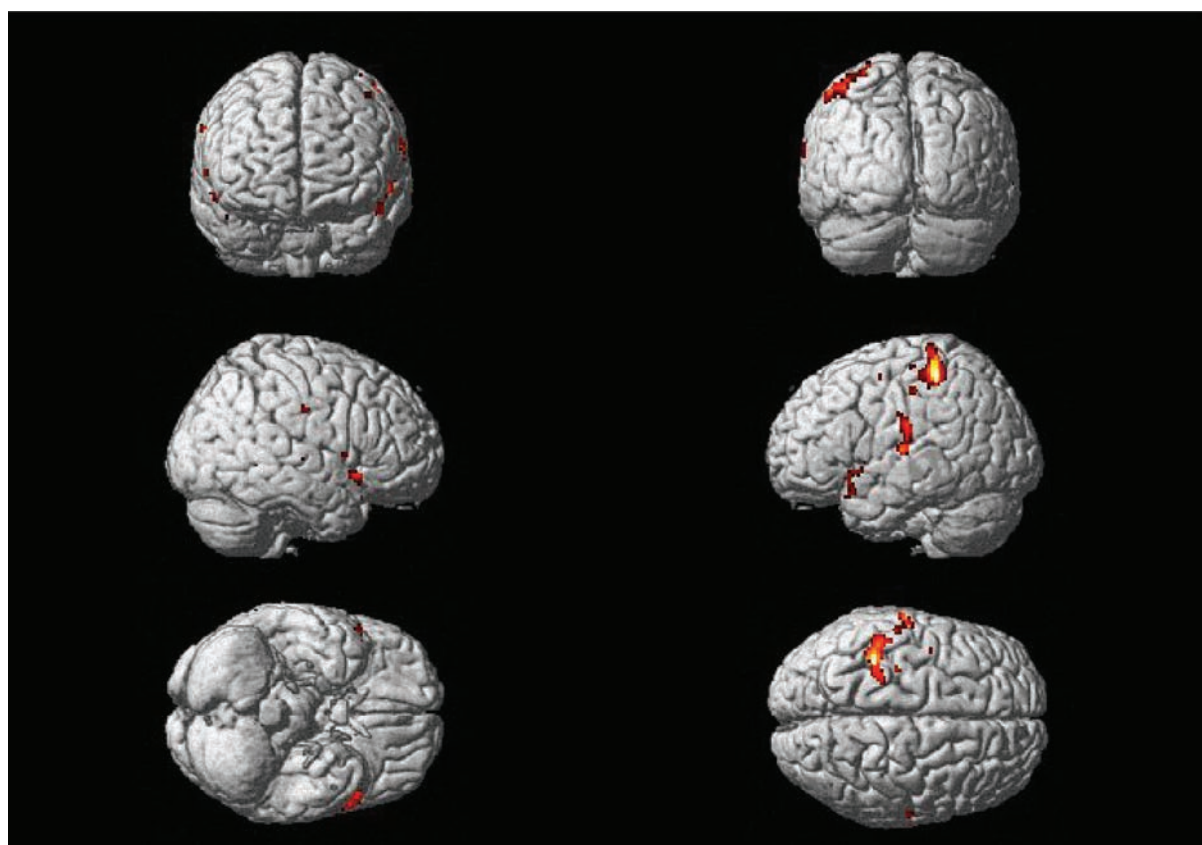


Figure 18.23 Colour fMRI rendered map. The statistical map is normalized to a standard brain atlas and rendered in 3D to show the activated areas.

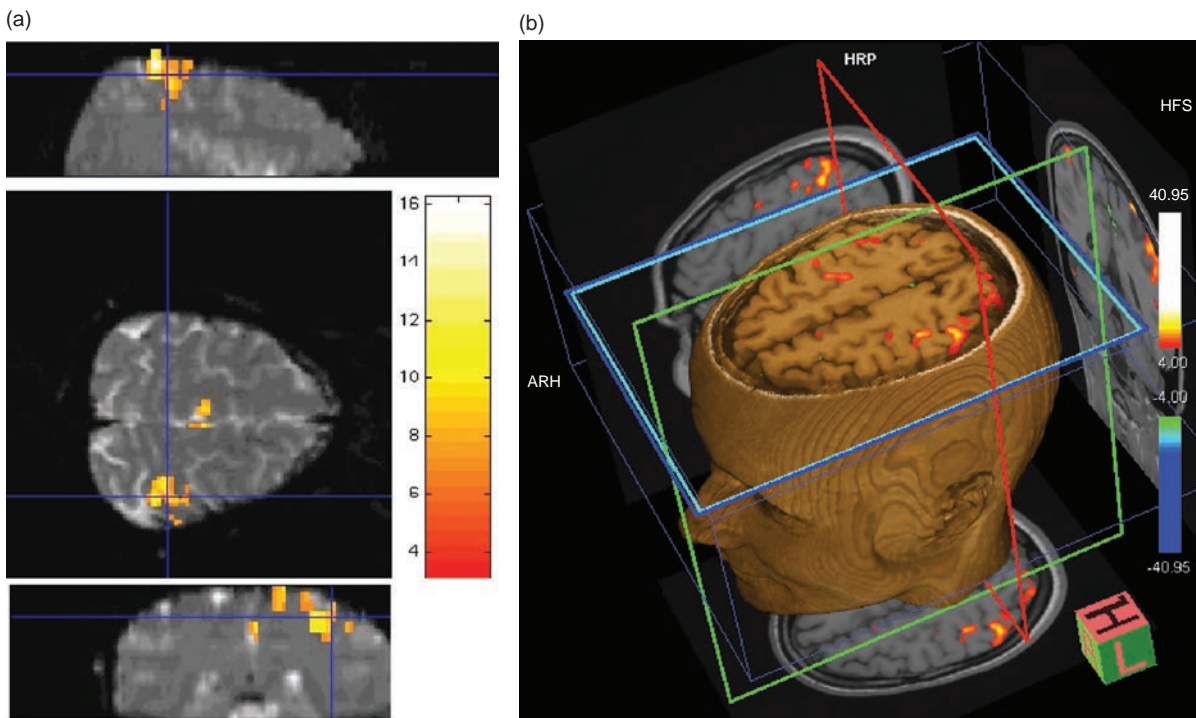


Figure 18.24 Clinical fMRI (a) orthogonal views with colour overlay showing the activation. (b) Real-time 3D display shown during the acquisition.

brain plasticity following injury. It can help with decision-making for patients with low-grade astrocytomas and arterio-venous malformations (AVMs) who have slight neurological impairments. It may be used in repeat studies for patients with slow-growing tumours or congenital lesions. Most clinical examinations are of the motor cortex for hand, foot and facial movement control (Figure 18.24a). One specialized but promising application is in the determination of the hemispheric dominance of language, as an alternative to the invasive Wada test.

Typically in clinical fMRI the question is, 'if we operate, how close will the surgeons have to go to particular key functional areas of the brain?' Getting a definitive answer to this is difficult for a number of reasons. Patients may have some brain abnormality, AVM, tumour, etc., which makes spatial normalization to a standard brain atlas impossible. They may have impaired ability to cooperate, e.g. patients with an impaired motor function, and may find it harder to keep still when exercising their affected side. There is much scope for error and misinterpretation arising from false-positive and false-negative responses. Pre-surgical fMRI findings can be

confirmed at the time of operation by direct electrical stimulation in the open-skull situation. Further research will determine the role for fMRI in psychiatric illness.

Clinical fMRI doesn't have to be a long-winded examination. A typical clinical fMRI protocol might consist of a scout scan (three orthogonal views), followed by a 3D structural scan, e.g. MP-RAGE with matrix $256 \times 256 \times 120$ and scan time 8 min. This would be followed by fMRI EPI scans for each functional area, each taking typically 5 min scan time. The EPI scans would have 24 transverse slices parallel to the anterior commissure–posterior commissure (AC–PC) line, 5 mm slice thickness, in-plane resolution 96×96 or 128×128 , 220 mm field of view, 35–50 volume acquisitions, interscan interval ('TR') 3–6 s, block paradigm with a repeating pattern of 30 s activity followed by 30 s rest. To establish the position of the motor cortex requires two paradigms: first with left-hand finger motion versus rest, and second with right-hand finger motion versus rest. The total scan time for this examination is approximately 20 min plus patient handling time.

18.5.5 Paradigm Shift

fMRI is extremely difficult to do well. Very good subject cooperation is required, even a small degree of patient head movement is intolerable and there are lots of data and much complicated analysis; but, more fundamentally, the paradigm itself may be flawed. Except for simple sensorimotor fMRI, it is quite hard to be certain that the subject is actually performing the task properly. Overt speech generally causes excessive head motion. Moreover, for subtle cognitive effects, the paradigm has to be psychologically effective, easily transferable to the inside of a scanner and capable of generating detectable BOLD responses. The scanner environment, with its excessive noise and claustrophobia-inducing space, presents a major limitation. Special stimulus delivery systems are required for the presentation of visual and audible stimuli. Despite these technical difficulties, fMRI opens up new avenues of research into cognitive neuroscience, psychiatric illness and neuropathology that are not possible with positron emission tomography (PET) due to its limited availability and the radiation dose involved.

T_2^* (Star) Wars: The Field Strength Question

As the BOLD effect is related to MR susceptibility, it should increase with field strength. Add to this the increase in SNR with B_0 and we would therefore expect the sensitivity of BOLD experiments to increase dramatically with the field strength. Reports in the literature suggest an increase in BOLD contrast of 30–40% for simple sensory-motor activations for 3 T compared with 1.5 T and greater again at 7 T. However, the overall picture is more complex as T_2^* is reduced at higher field strengths (T_2^* depends upon the field inhomogeneity in absolute units, i.e. microtesla). Moreover, in areas of particular neurological significance, e.g. the frontal or temporal lobes, the distortion and signal drop-out due to susceptibility differences may be excessive. Improving upon this is a particular focus of high- B_0 MRI research.

See also:

- Combining gradient and spin echoes: Section 12.5
- GE echo planar imaging: Section 13.4.4

Further Reading

Alsop DC, Detre JA, Golay X, *et al.* (2015) 'Recommended implementation of arterial spin-labelled perfusion MRI for clinical applications: a consensus of the ISMRM perfusion study group and the European consortium for ASL in dementia'. *Mag Res Med* 73:102–115.

Buxton RB (2009) *Introduction to Functional Magnetic Resonance Imaging: Principles and Technique*, 2nd edn. Cambridge: Cambridge University Press.

Calamante F, Thomas DL, Pell GS, Wiersma J and Turner R (1999) 'Measuring cerebral blood flow using magnetic resonance imaging

techniques'. *J Cereb Blood Flow Metab* 19:701–735.

Jefferd P, Matthews PM, and Smith SM (eds) (2002) *Functional MRI: An Introduction to Methods*. Oxford: Oxford University Press.

Koh D-M and Collins DJ (2007) 'Diffusion-weighted MRI in the body: applications and challenges in oncology'. *Am J Roentgenol* 188:1622–1635.

Moonen CTW and Bandettini PA (eds) (2000) *Functional MRI*. Berlin: Springer-Verlag.

Schmitt R, Stehling MK and Turner R (2012) *Echo-Planar Imaging: Theory, Technique and Application*. Berlin: Springer-Verlag.

Takahara T, Imai Y, Yamashita T, Yasuda S, Nasu S and Van Cauteren M (2004) 'Diffusion weighted whole body imaging with background suppression (DWIBS): technical improvement using free breathing, STIR and high resolution 3D display'. *Radiat Med* 22:275–282.

Tofts PS (ed.) (2003) *Quantitative MRI of the brain: Measuring Changes Caused by Disease*. Chichester: John Wiley.

Tournier JD, Calamante F and Connelly A (2007) 'Robust determination of the fibre orientation distribution in diffusion MRI: non-negativity constrained super-resolved spherical deconvolution'. *NeuroImage* 35:1459–1472.

Making it Count: Quantitative MRI

19.1 Introduction

Ever since the earliest days of NMR and MRI the possibility of using quantitative measurements of NMR parameters has been proposed as a way of characterizing tissues and distinguishing pathologies. Apart from the obvious ones (T_1 and T_2 relaxation times), researchers have invested huge efforts to quantify blood velocity and flow, apparent diffusion coefficient (ADC), brain perfusion, fat content and tumour permeability. In addition MR is used to quantify some parameters indirectly, e.g. iron concentration (via T_2 or T_2^*), and cardiac functional parameters such as ejection fraction (via volumetric measurements). Unfortunately many of these techniques have not made the transition from research to daily clinical use, mainly because results for pathological tissue are not sufficiently different from those for normal tissue, or specific to a particular pathology. In this chapter we will show that:

- relaxation times can be measured *in vivo* with fairly good accuracy (if you pick the right technique);
- ADC can be measured but we need a more sophisticated model to achieve good accuracy;
- brain perfusion can be quantified in two ways, one of which may be accurate enough for clinical use;
- fat content of the liver is emerging as an important quantitative application;
- all quantitative methods suffer from systematic errors due to the imaging process;
- it is not enough to find a significant difference between healthy and disease groups; you have to pay attention to the statistics to know if a new technique will really change the MRI world.

19.2 Relaxation Times

19.2.1 T_1 Relaxation Time

A gold-standard T_1 measurement is a rather time-consuming process if you want to avoid compromises.

A series of inversion recovery sequences is used with varying TI. After the initial inversion pulse, there is T_1 recovery during the time TI. When the 90° is applied some of the tissue signals may still be negative (Figure 19.1c). In conventional MR imaging we usually generate the magnitude images, converting all negative signals to positive, which gives the IR curves shown in Figure 3.11. However, for T_1 measurement it is better to use a ‘real’ reconstruction to make the post-processing easier. The signal at each TI is given by

$$S(TI) = M_0 \left[1 - 2\exp\left(-\frac{TI}{T_1}\right) + \exp\left(-\frac{TR - TI}{T_1}\right) \right]$$

Provided $(TR - TI) > 5 \times T_1$, we can ignore the second exponential term, and by plotting $\ln(S_\infty - S(TI))$ against TI, we get a straight line with a slope equal to T_1 . As a quick-and-dirty method, just plot $S(TI)$ against TI and look for the crossing point where $S(TI) = 0$, and then estimate $T_1 = \ln 2 \times TI$.

The time-consuming part is that the delay between the 90° pulse and the next inversion pulse must always be at least five times the longest T_1 present to relax (Figure 19.1d) (which presents a chicken-and-egg problem: you don’t know what the T_1 is until you’ve measured it, and if TR is too short you won’t measure it correctly!). For *in vivo* scanning, these TRs prove very impractical. There are two alternative methods which are commonly used in clinical applications: the Look-Locker (LL) method, and Driven Equilibrium Single Pulse Observation of T_1 (DESPOT $_1$), which uses two gradient-echo scans with different flip angles to compute T_1 .

The Look-Locker (LL) technique uses an initial inversion pulse followed by a series of low flip angle α° pulses (Figure 19.2). Each α pulse tips M_z very slightly away from the z axis, giving a signal of $M_z \sin \alpha$ in the transverse plane. As M_z relaxes from $-M_0$ back to equilibrium, the α° pulses give a series of images

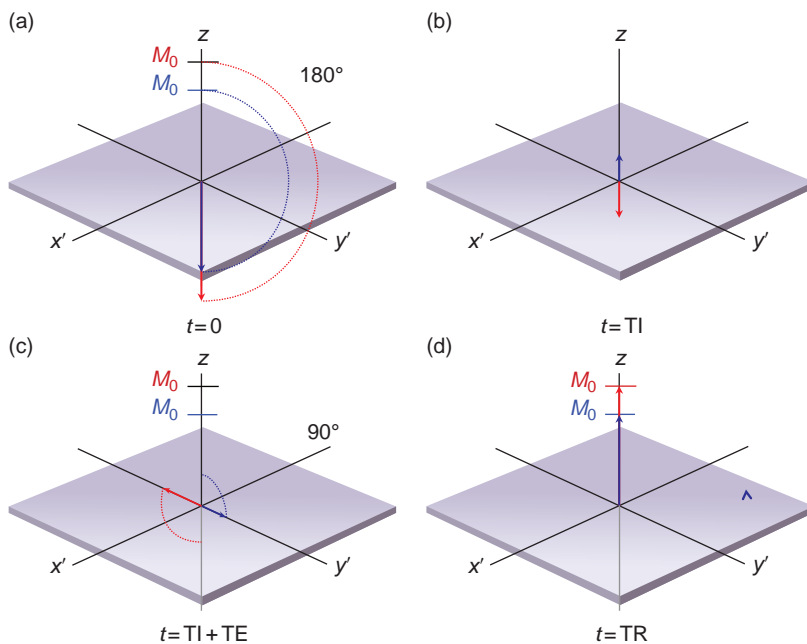


Figure 19.1 (a) The initial 180° pulse inverts the magnetization, which then starts to recover. (b) When the 90° is applied some of the tissue signals may still be negative, so (c) a mixture of positive and negative echoes will be formed. The TR must always be at least five times the longest T_1 present to allow full relaxation (d).

showing the changing magnetization. The main compromise with LL imaging is in the choice of the α° flip angle. If it is too small, the noise floor will dominate and SNR will be too low for reliable measurements. However if α° is too large, it will interfere with the true relaxation curve, accelerating the recovery towards $+M_0$ and leading to underestimation of the true T_1 . LL relaxometry lends itself to low-resolution fast imaging, in particular breath-hold cardiac T_1 mapping (see Box ‘A Light Heart? Cardiac T_1 Relaxometry’).

When high resolution is more important than speed, the DESPOT₁ method is a better choice. DESPOT₁ uses two (or more) spoiled gradient echo 3D sequences with different flip angles, keeping the same TR and TE for all the scans. From the signal equation for spoiled gradient echo, we can derive a linear relationship so that when we fit the data to a straight line, we can calculate T_1 from the gradient of the fitted line (see Box ‘Drawing the Line: Plotting Graphs for T_1 Relaxometry’). In practice, the choice of flip angles is critical and depends upon the TR chosen. In commercial versions of this method, it is common to be asked to enter a ‘target’ T_1 . DESPOT₁ is commonly used for quantitative dynamic contrast enhancement (DCE) imaging (see Section 19.4).

As with all imaging techniques, there are unavoidable errors which mean that T_1 mapping can never be

perfect. For example, slice profiles are not perfect, giving a range of flip angles across the slice; B_1 or B_0 non-uniformities may have an impact on the signal; partial volume effects make it difficult to isolate single tissues. In spite of these problems – or rather by being aware of them and taking steps to minimize them – T_1 relaxometry can achieve fairly good accuracy and precision.

Drawing the Line: Plotting Graphs for T_1 Relaxometry

In the LL technique, the apparent T_1 (denoted T_1^*) is found as usual by fitting the data to an exponential recovery curve. We can then use the following relationship to correct T_1^* and find the true T_1 :

$$T_1 = T_1^* \left/ \left[\frac{T_1}{T_1^*} + \ln(\cos \alpha) \right] \right.$$

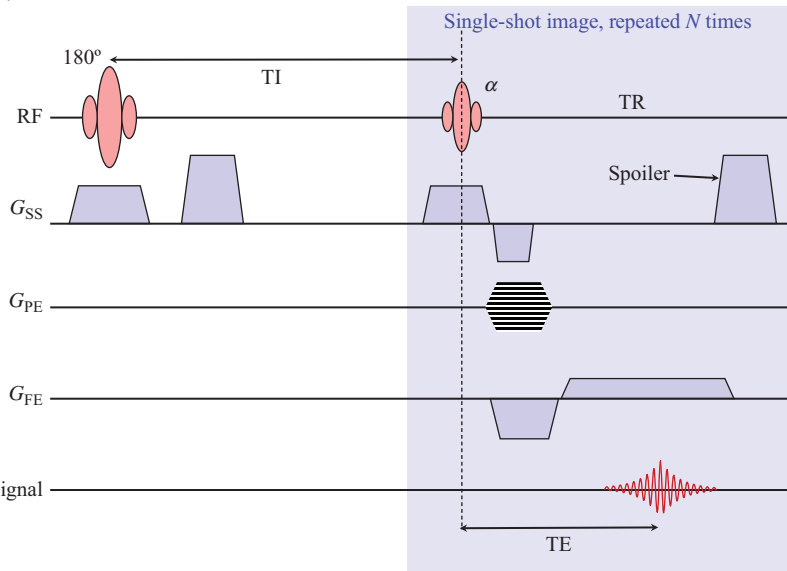
The DESPOT₁ method requires a bit more maths to see the linear relationship. We start with the signal equation for spoiled gradient echo, which can be written as

$$S(\alpha) = \frac{M_0(1 - E_1) \sin \alpha}{1 - E_1 \cos \alpha}$$

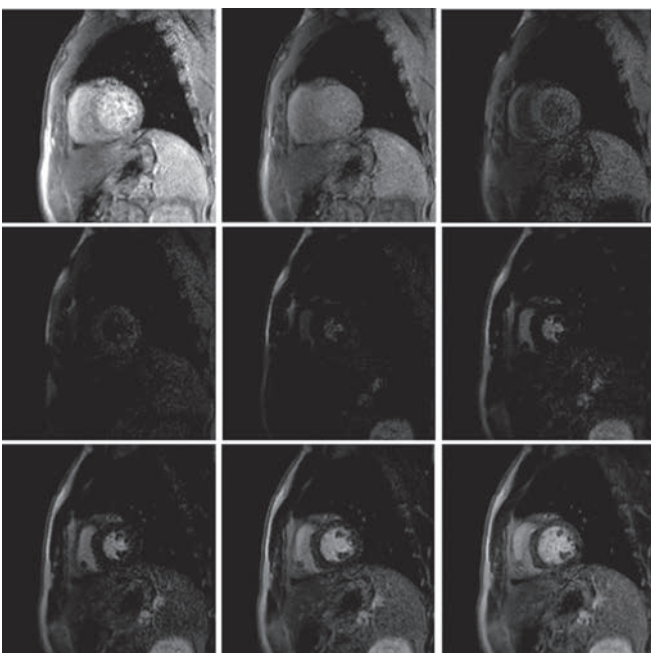
where $E_1 = \exp(-\text{TR}/T_1)$ and we have assumed a $\text{TE} \ll T_2^*$. This can be rearranged as

$$\frac{S(\alpha)}{\sin \alpha} = E_1 \frac{S(\alpha)}{\tan \alpha} + M_0(1 - E_1)$$

(a)



(b)



(c)

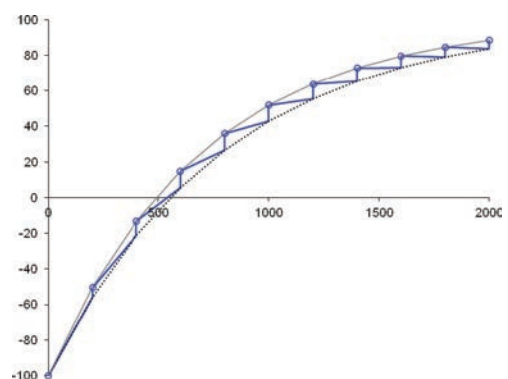


Figure 19.2 (a) Look-Locker pulse sequence. (b) Series of images of the heart using a LL sequence. (c) M_z recovery curve in the LL technique (blue line). Blue circles indicate the measurement points at each α° flip angle. Note that the relaxation time T_1^* appears to be shorter (solid grey line) than the true T_1 (dotted black line).

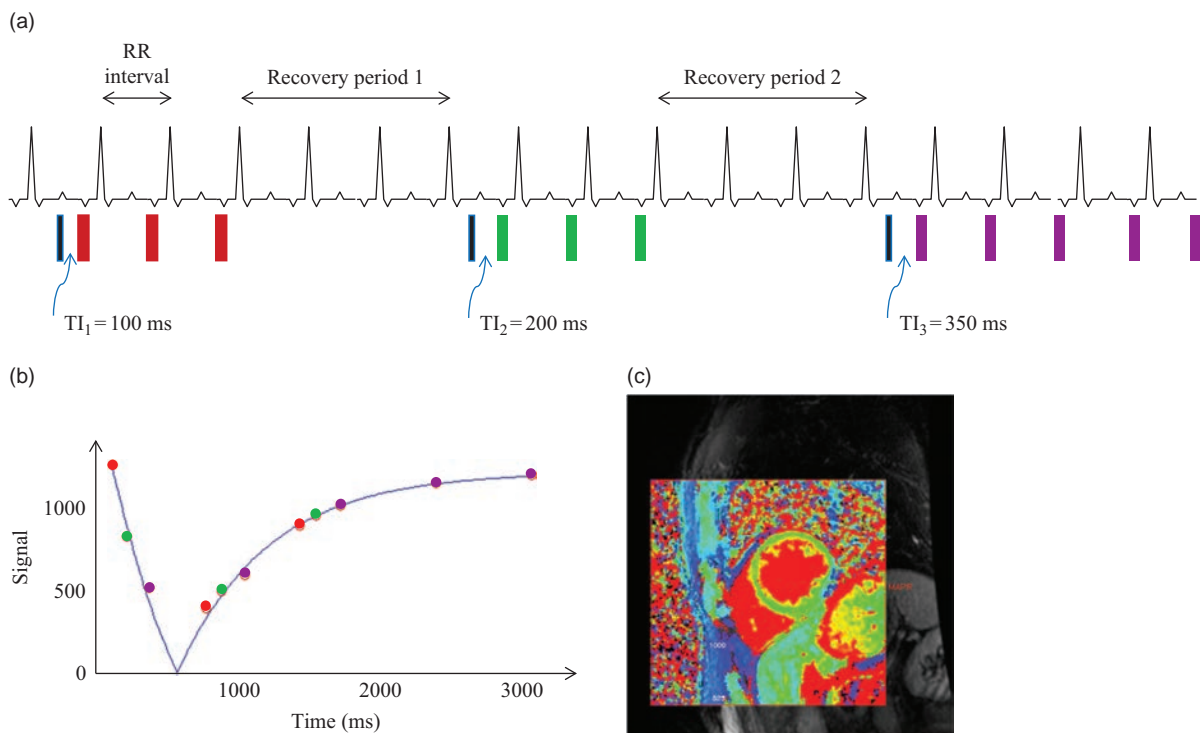


Figure 19.3 (a) Modified Look-Locker Imaging (MOLLI) with a 3(3)3(3)5 scheme. Blue bars are inversion pulses, red bars are bSSFP images with α excitation pulses. See text for other details. (b) The relationship of the bSSFP acquisitions to the T_1 recovery curve; purple points, first inversion set; green dots, second inversion set; orange dots, third inversion set. A magnitude inversion recovery model is fitted to the data points to determine the T_1 , yielding (c) a T_1 map.

which is a straight line of the form $y = mx + c$. We plot $S(a)/\sin \alpha$ against $S(a)/\tan \alpha$, and fit a straight line to the data. The slope m of the plot is equal to E_1 , from which we can obtain T_1 :

$$T_1 = -\frac{TR}{\ln(m)}$$

A Light Heart? Cardiac T_1 Relaxometry

Conventional imaging methods are excellent for detecting focal defects in the heart and great vessels, but systemic myocardial disease is harder to detect. T_1 relaxometry is proposed as a bio-marker for diffuse cardiac fibrosis, myocarditis and other diseases. Apart from measuring the myocardial T_1 directly (so-called 'native T_1 mapping'), T_1 measurements can also be used to estimate the extracellular volume (ECV) of fluid in the myocardium, as we will see at the end of this box. At the time of writing, it is unclear whether native T_1 or ECV measurements will be the most useful in diffuse cardiopathies.

The Look-Locker method is the basis for quantitative T_1 measurements in the myocardium, using an ECG-triggered variant known as MOLLI (**M**odified **L**ook-**L**ocker **I**maging). MOLLI uses single-shot bSSFP readouts after each of the low flip angle α pulses, and is of course fast enough to be done in a breath-hold. There are several ways to organize the bSSFP readouts between heartbeats, to allow for measuring the T_1 recovery curve properly. The original MOLLI implementation has three inversion pulses and 11 readouts distributed over 17 heartbeats, as shown in Figure 19.3a. The first inversion pulse is followed by bSSFP readouts in the first three heartbeats, giving three inversion times of T_{I1} , $T_{I1} + RR$ and $T_{I1} + 2 \times RR$. The next three heartbeats are empty, to allow full relaxation. Another inversion pulse is applied followed by three more bSSFP readouts, providing three more inversion times at T_{I2} , $T_{I2} + RR$ and $T_{I2} + 2 \times RR$. After another three-beat relaxation period, the final inversion pulse is applied followed by five bSSFP readouts, giving a total of 11 inversion times. This scheme is called either MOLLI 3-3-5 or 3(3)3(3)5.

When the 11 images are placed in the correct T1 order, the apparent T_1^* and then the 'true' T_1 can be calculated on a pixel-by-pixel basis.

There have been shorter MOLLI variants proposed, the most common of which is Shortened MOLLI (ShMOLLI) involving a 5(1)1(1)(1) acquisition. However, the data processing is more involved and is conditional upon the heart rate. All cardiac quantitative T_1 techniques may require motion correction/registration of the individual images to improve accuracy.

To extend from measuring the native T_1 to estimating the ECV, T_1 mapping is performed at two time-points: one before a bolus injection of Gd, and the second approximately 15 min after the bolus injection. The relaxation rate is measured in the myocardium and in the blood-pool, and the ECV is then estimated as follows:

$$\text{ECV} = (1 - Hct) \cdot \frac{\Delta R_{1,\text{myo}}}{\Delta R_{1,\text{blood}}}$$

where Hct is the haematocrit, $R_1 = 1/T_1$ and ΔR_1 is the change in R_1 at the pre- and post-Gd time-points. Literature values for Hct can be used (0.45 for men and 0.40 for women), but it is preferable to take the patient's true Hct value since this also varies with disease. The normalization by the blood-pool T_1 is necessary to avoid confounding factors such as Gd clearance rate. The typical ECV of normal myocardium has been shown to be around 20–30%.

19.2.2 T_2 and T_2^* Relaxation Times

To measure T_2 , you might intuitively use a series of spin-echo sequences and measure the signal height at each TE. Plotting a graph of signal against TE would show an exponential decay and allow us to find T_2 . Unfortunately we can't use separate scans: the diffusion of protons through an inhomogeneous magnetic field adds an irreversible dephasing which reduces the signal much faster than the true T_2 . It's also very inefficient, since we can acquire several echoes after each 90° pulse. Back in the 1950s it was shown that a series of equally spaced 180° pulses on the $+x'$ axis creates a train of spin echoes alternating between negative and positive signs. This is known as a Carr–Purcell echo train, and the signal at time t is given by

$$S(t) = M_0 \left[\exp\left(\frac{-t}{T_2}\right) \cdot \exp\left(\frac{-2\gamma^2 \Delta B^2 D \tau^2 t}{3}\right) \right]$$

where ΔB is the magnetic field inhomogeneity, 2τ is the echo spacing, D is the diffusion coefficient and t is the overall time from the excitation to a particular echo we are measuring. Provided the echo spacing is small, the second term is almost equal to 1, and we are left with an exponential decay due to T_2 . A further modification known as the Carr–Purcell–Meiboom–Gill (CPMG) sequence compensates for imperfections in the 180° echo which would otherwise accumulate over the echo train. In CPMG, the initial 90° pulse is on the $+x'$ axis, the train of 180° pulses is on the $+y'$

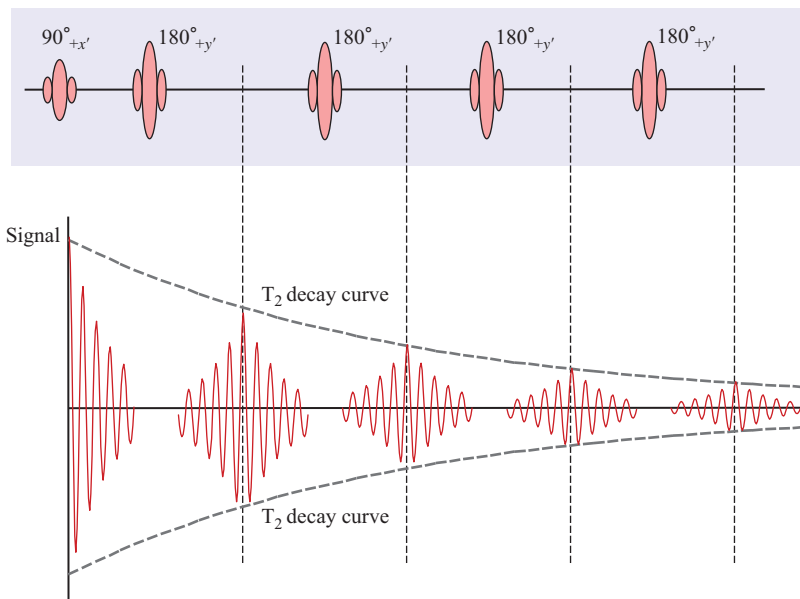


Figure 19.4 The Carr–Purcell–Meiboom–Gill sequence showing four echoes.

axis and all the echoes are positive (Figure 19.4). If the 180° pulse is imperfect, the first and every odd-numbered echo will be slightly too small, but the even echoes will be the correct height, and the errors do not accumulate. To measure T₂, we should therefore use the echo height from only the even echoes. At least five echo heights should be used (implying an echo train of at least ten) with a range of echo times up to about three times T₂.

For *in vivo* relaxometry, we need to make sure the TR is long enough for complete T₁ relaxation between the 90° pulses. The T₂ scan must be a classic SE sequence – we cannot use the echo train for phase encoding – and the rather long echo train puts limits on the number of slices that can be acquired. Scan times are typically 8–10 min, which is reasonable. An alternative method for T₂ relaxometry is called Driven Equilibrium Single Pulse Observation of T₂ (DESPOT₂), which uses a series of 3D fully rewound gradient-echo scans with different flip angles α . See Box ‘Big Brother is Measuring T₂’ for more details.

Measuring T₂^{*} is almost identical to measuring T₂, except that we use a multi-echo gradient-echo scan. We simply fit the multi-echo signal heights to a mono-exponential decay curve to derive T₂^{*}:

$$S(t) = M_0 \exp\left(\frac{-t}{T_2^*}\right).$$

However, there are some critical issues about measuring T₂^{*}, related to the main field inhomogeneity. Since all modern scanners perform automatic shimming per patient, often with no way for the user to control the process, it is difficult to know if changes in T₂^{*} are due to changes in the tissue itself, or independent changes in ΔB₀. Accuracy and precision are particularly influenced by ΔB₀, especially if comparing between different field strengths. Finally, there is no real ‘gold’ standard to use as a reference measure.

As with T₁ relaxometry, T₂ and T₂^{*} relaxometry methods suffer from problems related to the imaging method, in particular flip angle variations across the slice profile and B₁ inhomogeneity effects.

Big Brother is Measuring T₂

The signal equation for DESPOT₂ is based on the equation for fully rewound gradient echo:

$$S(\alpha) = \frac{M_0(1 - E_1) \sin \alpha}{1 - E_1 E_2 - (E_1 - E_2) \cos \alpha}$$

where E₁ = exp(-TR/T₁) and E₂ = exp(-TE/T₂). As before, this can be recast as a linear equation:

$$\frac{S(\alpha)}{\sin \alpha} = \frac{E_1 - E_2}{E_1 E_2} \cdot \frac{S(\alpha)}{\tan \alpha} + \frac{M_0(1 - E_1)}{E_1 E_2}$$

T₂ can be found from the gradient m of a plot of S(a)/sina against S(a)/tana:

$$T_2 = -TR / \ln\left(\frac{m - E_1}{mE_1 - 1}\right)$$

Notice that it is necessary to know the tissue T₁ in order to find the T₂. This limits the application of DESPOT₂ as a standalone sequence, so most often it is done in combination with DESPOT₁.

Conceptually, once we know both T₁ and T₂ for all the tissues, we can use the signal equations to generate images with any contrast we desire. Over the years there has been intermittent interest in ‘synthetic’ imaging, but it has suffered from limitations; the signal equations generally do not include flow or diffusion effects, and cannot predict how Gd will affect the images. Recently this interest has resurfaced, based on a new magnetization-prepared SE acquisition method which compensates for non-uniformities in B₁. It has been commercialized by GE Healthcare under the name of MAGIC (**MAG**netic resonance **I**mage **C**ompilation) and is also supported on Philips systems.

Too Many Irons in the Fire: Monitoring Iron Overload With MRI

Excess iron in the body is stored in the liver, in the form of ferritin or haemosiderin, and can also accumulate in the cardiac muscle. This occurs in patients with hereditary or idiopathic haemochromatosis, and those who have had repeated transfusions for chronic anaemias such as thalassaemia. Iron overload can lead to liver fibrosis, cirrhosis, hepatocellular carcinoma and heart or liver failure.

In the liver, either T₂ or T₂^{*} relaxometry can be used to assess liver iron concentration. Empirically it has been shown that the iron load is correlated to the inverse of relaxation time, i.e. the relaxation rates R₂ or R₂^{*}. The FerriScan method is a commercially available service which is FDA approved for measuring liver iron content. It uses motion-corrected R₂ maps calculated from a series of single spin echoes and results are processed offline at FerriScan’s offices (Figure 19.5). It requires careful calibration of the scanner using a standard phantom. Other methods use R₂^{*} calculated from a multi-echo gradient-echo

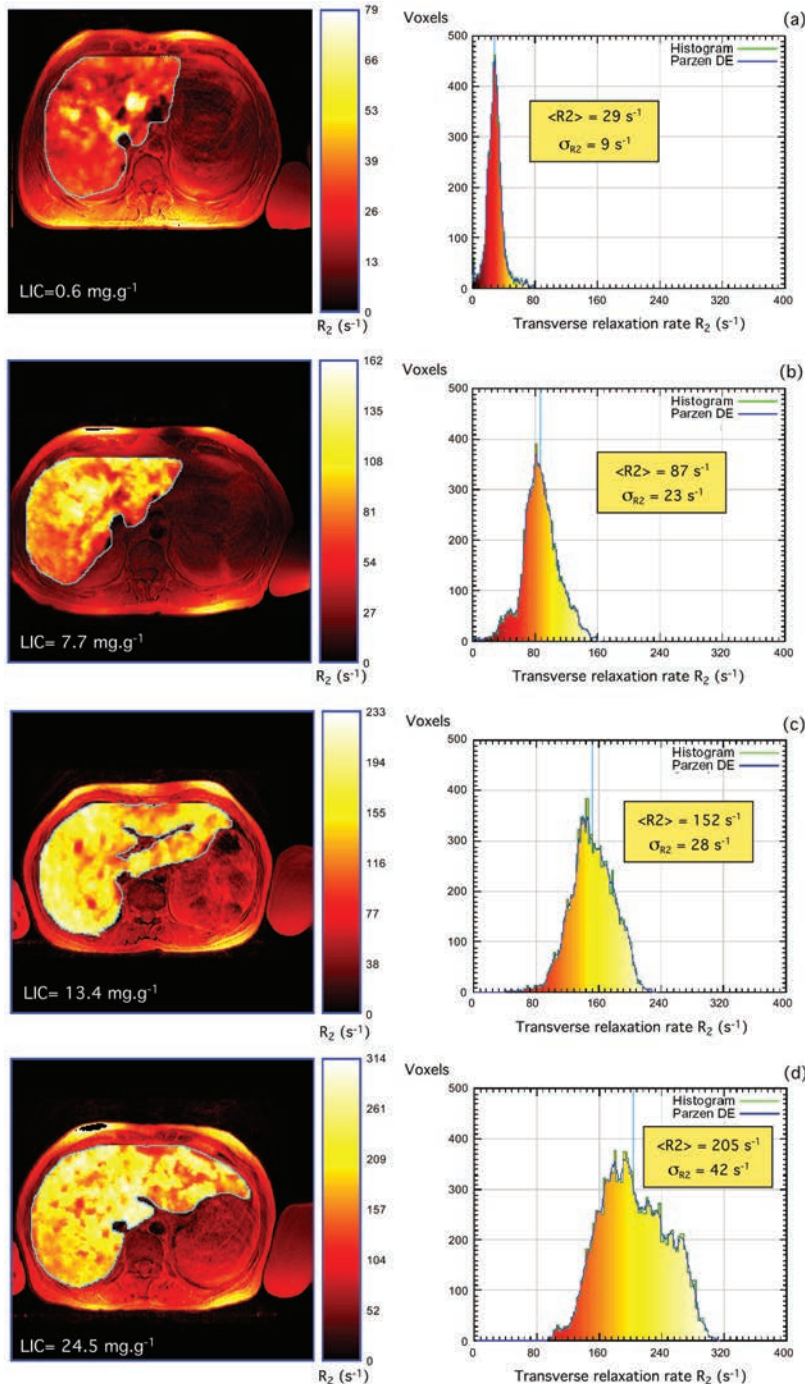


Figure 19.5 R₂ maps and histograms demonstrating different levels of liver iron concentration: (a) healthy liver, (b) mild overload, (c) moderate overload, and (d) severe overload. Images courtesy of Resonance Health Ltd, providers of FerriScan R2-MRI www.resonancehealth.com

sequence. However, care is required for there are scanner-specific errors (from ΔB_0), the measurement of high R₂^{*} (short T₂^{*}) is prone to errors due to very low SNR and there is no universal calibration. With careful measurement methods, a linear relationship

between iron content from liver biopsy results and R₂^{*} can be obtained.

In the heart, quantitative T₂^{*} measurement has been proposed to monitor progression of iron overload in these patient populations. An ECG-gated

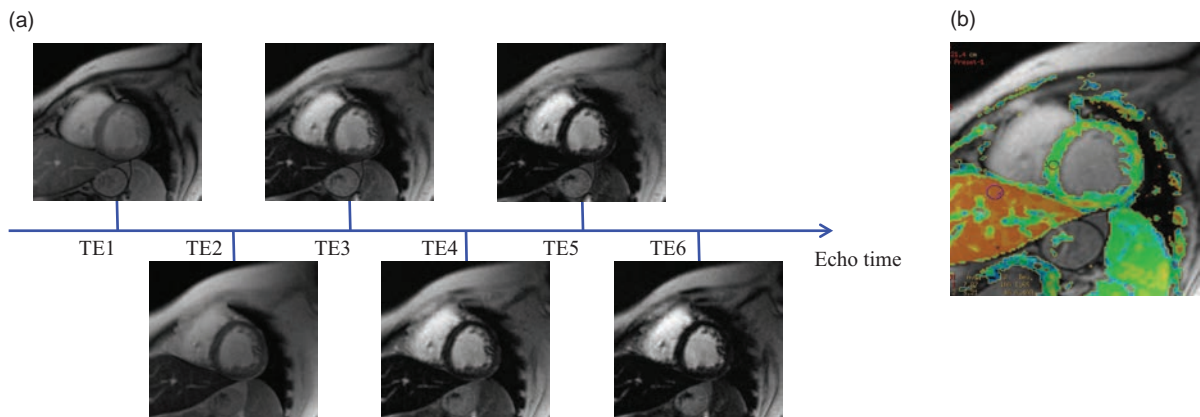


Figure 19.6 (a) A series of cardiac images acquired at increasing TE. (b) Quantitative T_2^* data overlaid on an anatomical image. The myocardial ROI shows a T_2^* of 8 ms, while the liver ROI shows a T_2^* of 3 ms. These values are typical for a patient with iron overload.

breath-hold multi-echo gradient-echo imaging technique is used, followed by T_2^* calculation on a pixel-by-pixel basis. The choice of TEs is very important: in cases of severe iron overload, the T_2^* may be so short that the signal has decayed before the first echo is acquired. Conversely, in cases of low iron overload, selecting a range of TEs that are too short will only show the first part of the decay curve, reducing accuracy. The practical answer is to use the shortest possible echo spacing, but with at least five echoes. Various research studies have suggested that T_2^* values higher than 20 ms can be considered normal, while lower T_2^* 's indicate iron loading (see Figure 19.6).

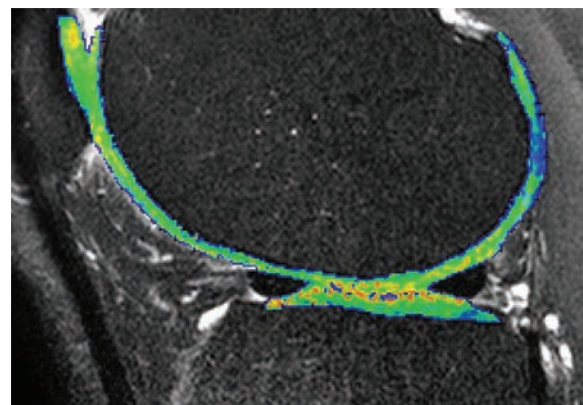


Figure 19.7 T_2 cartilage map.

19.2.3 Sources of Error in In Vivo Relaxometry

Apart from all these problems, there are still others which introduce significant errors in in vivo relaxometry. These include poor sequence parameter choice, particularly too short a TR for the PD-weighted image, inhomogeneous RF pulses, unwelcome magnetization transfer effects in multiple-slice acquisitions arising from selective (therefore off-resonance) pulses intended for other slices, and slice profile distortions. It is extremely important to understand these error sources, especially when trying to compare relaxometry results between different systems or in a multi-centre study.

Knee-Jerk Reactions: Cartilage Relaxometry

Osteo-arthritis (OA) is a chronic disease which results in degeneration of the joints and is a major cause of

pain and morbidity among the ageing population. It has been proposed that T_2 relaxometry is a biomarker for cartilage degeneration. T_2 is sensitive to changes in the collagen matrix, increasing significantly both locally and globally in osteoarthritic joints. In patients who have had transplanted chondrocytes, monitoring of T_2 can identify cartilage repair (Figure 19.7). T_2 cartilage measurements suffer from poor precision due to low SNR, noise floor bias (because we use magnitude reconstruction, giving a non-Gaussian noise distribution) and partial volume effects.

T_1 relaxometry is also useful in cartilage assessment. As a precursor to OA, glycosaminoglycan (GAG) molecules break down. Since both GAG molecules and gadolinium are negatively charged, gadolinium will penetrate articular cartilage in inverse proportion to the local GAG concentration. T_1 quantification follows an injection of a Gd-based contrast

agent intravenously. After 30–90 min of exercise post-injection, the Gd penetrates the cartilage. T_1 relaxometry will give an indication of GAG concentration and hence cartilage integrity. As GAG decreases, the Gd concentration increases and T_1 decreases, so shorter T_1 s indicate a more advanced disease process. This technique is often known as dGEMRIC (**d**elayed **G**adolinium-**E**nhan**C**hed **M**RI of Cartilage).

Other less common quantitative investigations of cartilage include $T_{1\rho}$ (pronounced ‘tee wun roh’, sometimes written as T_1 -rho) or sodium (^{23}Na) imaging. $T_{1\rho}$ refers to spin-lattice relaxation in the rotating frame, and requires specialist pulse sequences. Sodium has extremely short T_2 in vivo, so ultra-short TE imaging sequences are required. Since the gyromagnetic ratio of ^{23}Na is 11.27 MHz T^{-1} , special RF transmission and reception hardware and coils are also required.

19.3 Diffusion Parameters

The apparent diffusion coefficient ADC is routinely calculated in clinical practice, in order to separate true diffusion effects from T_2 shine-through (see Section 18.2.2). Since tumours appear very bright on diffusion-weighted images, they obviously have reduced ADCs compared with normal tissue. Regions of interest on the ADC map can easily provide the ADC of various tissues. Numerous studies have been conducted using ADC in various cancers (breast, liver, prostate, brain, etc.); however, there is significant diversity in the results. It turns out that we need a better model of the diffusion process.

In practice, what we measure in normal DWI is related to the actual diffusion coefficient but also contains contributions from other sources of tissue

motion. Microcirculation in pseudo-random capillary systems is one such source of so-called IntraVoxel-Incoherent Motion (IVIM). Bulk flow and motion will also seriously degrade the measurements and lead to image artefacts.

An implicit assumption in the simple ADC calculation is that there is a single diffusion coefficient. By collecting multiple b -factor DW-images, it is possible to see that the signal decay is not mono-exponential, and in most organs it is in fact bi-exponential (Figure 19.8). The signals from the multi- b -factor scan can be fitted to this two-compartment model, which is shown mathematically as

$$S(b) = S_0 \cdot [f_{\text{perf}} \cdot \exp(-bD^*) + (1 - f_{\text{perf}}) \cdot \exp(-bD)]$$

where f_{perf} is the volume fraction of the perfusion compartment, which has pseudo-diffusion coefficient D^* .

This is known as the IVIM model, where the shorter diffusion coefficient is actually due to capillary perfusion, and only the longer one is due to true diffusion of water. These two compartments have different sizes, depending on the organ, but also depending on any pathology that may be present.

Bi-exponential fitting, especially when the sizes of the two compartments are not independent, is notoriously difficult. So even using the IVIM model, it proves tricky to achieve good accuracy and reproducibility of diffusion quantification. As a workaround, some researchers revert to the mono-exponential calculation, but using a low b -factor (e.g. $b = 50$ –100) image instead of $b = 0$ in the calculation of ADC:

$$D = \frac{\ln S(b_2) - \ln S(b_1)}{b_1 - b_2}$$

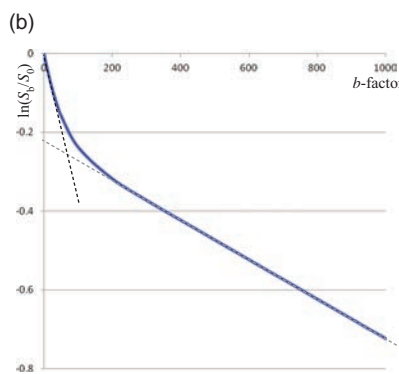
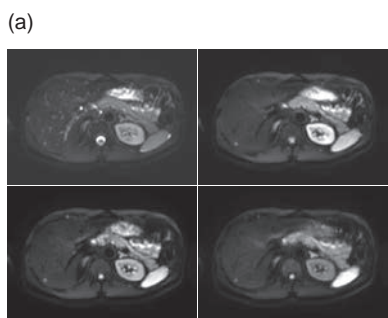


Figure 19.8 (a) Series of DW images of the liver with various b -factors. (b) Plot of $\ln(S_b/S_0)$ vs b -factor is bi-exponential, revealing two components: the true diffusion (dashed grey line) and the pseudo-diffusion, or perfusion fraction (dashed black line).

19.4 Tissue Perfusion and Permeability

Tissue perfusion, in particular for brain imaging, is important for vascular diseases like stroke and vascular dementia. Perfusion is the rate of blood flow per 100 g of tissue, and is critical to deliver sufficient oxygen and glucose to the cells. The average perfusion rate for the whole brain is $50\text{--}55 \text{ ml min}^{-1} 100\text{g}^{-1}$, measured using PET. It is widely accepted that if perfusion falls below $20 \text{ ml min}^{-1} 100\text{g}^{-1}$ tissue ischaemia will start to cause damage to cells, and eventually cell death will occur if perfusion is lower than $10 \text{ ml min}^{-1} 100\text{g}^{-1}$. Since these thresholds are well-established, quantification of perfusion is an important marker during the initial work-up of ischaemic stroke. Outside the brain, permeability is a more accessible parameter, particularly useful in cancer because most tumours have characteristically ‘leaky’ endothelial cells and an abundant capillary bed. So leaky, in fact, that many tumours show enhanced signal during the first pass of the Gd agent in the vascular system.

As we already saw in Chapter 18, there are two methods for measuring brain perfusion: first-pass Gd, also known as dynamic susceptibility contrast (DSC) imaging, and arterial spin labelling. Refer back to Box ‘Advanced Processing and Quantification’ to see how DSC data can be processed to derive the cerebral perfusion, and to Box ‘ASL Analysis’ for the ASL model processing. Chapter 18 also describes the processing to extract permeability parameters from dynamic contrast enhancement (DCE) imaging, in Box ‘Mathematical Modelling: The MRI Catwalk’. Since these models seem fairly straightforward, you might be wondering why quantitative perfusion and permeability are not part of the clinical routine.

In the case of DSC perfusion and permeability, there is a significant problem measuring the arterial input function (AIF) in the in-flowing blood. Arterial flow is typically very fast, so we need extremely high temporal resolution to capture the true shape of the Gd bolus as it passes – usually far higher than we can achieve in practice. The model also assumes a linear relationship between Gd concentration and blood signal, which is (probably) not valid at high concentrations such as the bolus peak. So we can assume that the AIF is underestimated, but we have no idea by how much. Some research groups have used calibration factors, e.g. comparing normal volunteers with DSC-perfusion and PET, to improve quantification, but this is unreliable in any pathological condition

where the arterial flow is different from normal. In DCE, there are attempts to use ‘model’ or population-averaged AIFs in the processing: even though this gives better results than trying to estimate the AIF each time, inevitably there will be unpredictable changes in some disease conditions.

That leaves ASL. Indeed this method is still considered ‘promising’ for quantification of brain perfusion, and researchers are starting to use it in other organs too. Many of the key difficulties can be overcome by careful tuning of the magnetic labelling pulses (adapting the pulse sequence) and by including exchange times in the model. ASL in the brain shows better accuracy and reproducibility than DSC perfusion, and is also showing good results when inter-site comparisons are made. It is too early to say that it ‘works’, but it is currently the favourite horse in this particular race.

19.5 Fat Quantification

The current obesity epidemic has led to considerable interest in methods for the quantification of fat as a marker of disease progression or to monitor therapeutic interventions. It has been shown that people with high abdominal visceral adiposity, sometimes referred to as the TOFI (Thin on the Outside, Fat on the Inside) phenotype, are at a substantially higher risk of developing so-called metabolic syndromes including type II diabetes and cardiovascular disease. MRI is an ideal modality for measuring SubCutaneous Adipose Tissue (SCAT) and Visceral Adipose Tissue (VAT), typically using a fast gradient-echo $T_1\text{w}$ sequence with good contrast between fat and other tissues. Quantification of SCAT and VAT then becomes an image analysis task, and there are several software tools available which calculate the volumes. Figure 19.9 shows a single-slice $T_1\text{w}$ image that has been semi-automatically segmented into SCAT and VAT. Dixon techniques are now offering a good alternative to $T_1\text{w}$ imaging.

The quantification of intra-organ fat, such as in the liver, is a little more complex since large vacuoles of triglyceride fat accumulate in the liver cells in a process known as steatosis. Since alcohol may also contribute to the disease, fatty liver is often categorized as either alcoholic or Non-Alcoholic Fatty Liver Disease (NAFLD). If inflammation is also present, then this is referred to as alcoholic steatohepatitis or Non-Alcoholic SteatoHepatitis (NASH). Measurement of liver fat fraction is becoming very important

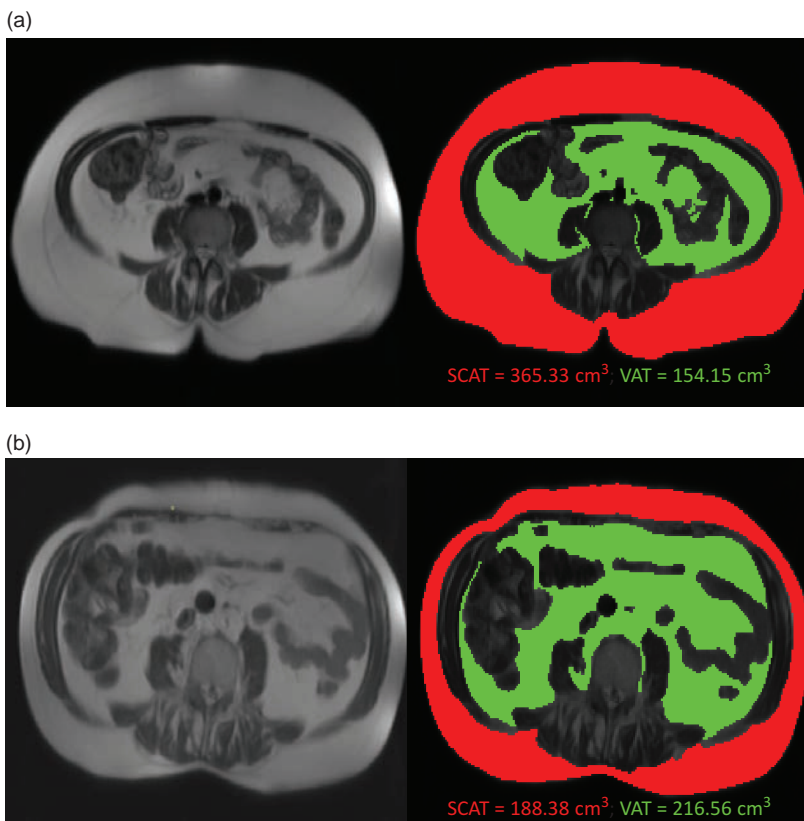


Figure 19.9 Measurement of subcutaneous adipose tissue (SCAT) and visceral adipose tissue (VAT) from two different subjects. (a) A subject with a large subcutaneous fat deposit. (b) A subject with the TOFI (thin on the outside fat on the inside) phenotype.

in the Western world as researchers investigate these ‘lifestyle’ diseases and potential therapies for them.

For the liver, it is simple to calculate a hepatic fat fraction (HFF) from a gradient-echo Dixon scan, using the signal in the magnitude water and fat images as follows:

$$\text{HFF} = \frac{|S_f|}{|S_f| + |S_w|}$$

However, this simple approach ignores several confounding effects. Remember that gradient-echo Dixon scans have at least two echoes, and often five or more. Clearly, the first echo is acquired at a different TE to the second or later echoes, so we have to take into account the effect of T_2^* in the signal model. We typically estimate T_2^* using a multi-echo acquisition, i.e. a scan with five or six echoes. This is particularly important in patients with high iron concentration in the liver, a condition which occurs in about 40% of patients with steatosis. Second, T_1 relaxation may also cause inaccuracies in the HFF measurement and fat-quantification scans use a low

flip angle, e.g. 5°. Although a small residual T_1 bias may exist, this can be corrected using literature values for the T_1 of fat and liver. Finally, accurate HFF measurements require a more sophisticated signal model with six or seven fat peaks, rather than just a single methylene peak (Figure 19.10). Commercial software packages provide not only the HFF maps (see Box ‘Swapping Notes: More Detail about Dixon Reconstruction’), but also T_2^* or R_2^* maps (see Figure 19.11). Clinically R_2^* maps are useful because shorter T_2^* values, that are usually associated with pathology, appear brighter.

Swapping Notes: More Detail About Dixon Reconstruction

The in-phase echo (S_{IP}) is the sum of water (S_w) and fat (S_f) signals, while the out-of-phase echo (S_{OP}) is the difference:

$$S_{IP} = (S_w + S_f) \cdot \exp(i\phi_0)$$

$$S_{OP} = (S_w - S_f) \cdot \exp(i\phi_0) \cdot \exp(i\phi)$$

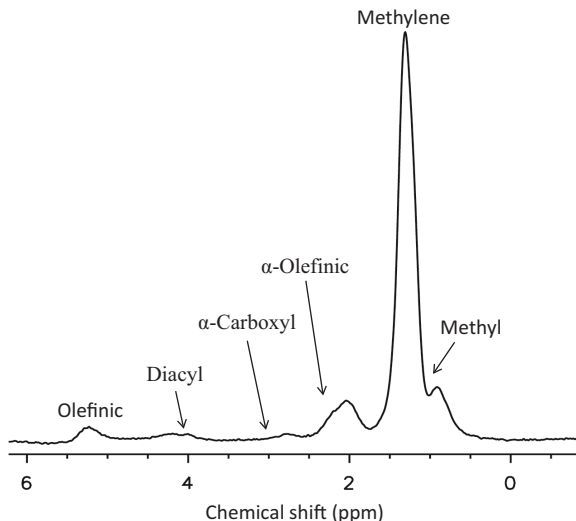


Figure 19.10 Water-suppressed spectrum of human subcutaneous fat, showing six different proton resonances. Courtesy of Dr Mary McLean, University of Cambridge, UK.

The term $\exp(i\phi)$ represents the phase shift, due to B_0 non-uniformity (ΔB_0), accumulated during the echo shift τ , i.e. it only applies to the out-of-phase image.

$$\phi = \gamma \Delta B_0 \tau$$

The term $\exp(i\phi_0)$ represents all other phase errors that are the same for both images. Ignoring the phase shifts and simply adding the two images would result in a water-only image, while subtracting the OP image from the IP image leaves a fat-only image:

$$S_{IP} + S_{OP} = (S_w + S_f) + (S_w - S_f) = 2S_w$$

$$S_{IP} - S_{OP} = (S_w + S_f) - (S_w - S_f) = 2S_f$$

This is the so-called two-point Dixon (2PD) technique and is often referred to as a $\{0, \pi\}$ technique reflecting the fact that there is a 0 and π (180°) phase shift between the two acquisitions. The main problem with this technique is that the assumption of zero background phase shifts ($\exp(i\phi) = 1$) is not valid in practice. Dixon originally attempted to circumvent this problem by dealing only with magnitude images, which ignore the phase of the signal:

$$S_w = 0.5 \times (|S_{IP}| + |S_{OP}|) \quad S_f = 0.5 \times (|S_{IP}| - |S_{OP}|)$$

However, this calculation is only valid when the relative fraction of water in a voxel is greater than or equal to the fat fraction. If the situation is reversed,

i.e. the fat fraction is greater than the water fraction in the voxel, then the pixel values will be swapped. The following worked example demonstrates this effect. First consider a voxel which contains 60% water and 40% fat, then

$$S_{IP} = (S_w + S_f) = 0.6 + 0.4 = 1.0$$

$$S_{OP} = (S_w - S_f) = 0.6 - 0.4 = 0.2$$

Using the magnitudes of the signals, Dixon's reconstruction gives:

$$S_w = 0.5 \times (|1.0| + |0.2|) = 0.6$$

$$S_f = 0.5 \times (|1.0| - |0.2|) = 0.4$$

which is the correct answer. However, if the voxel contains 40% water and 60% fat, then

$$S_{IP} = (S_w + S_f) = 0.4 + 0.6 = 1.0$$

$$S_{OP} = (S_w - S_f) = 0.4 - 0.6 = -0.2$$

This time Dixon's method gives

$$S_w = 0.5 \times (|1.0| + |-0.2|) = 0.6$$

$$S_f = 0.5 \times (|1.0| - |-0.2|) = 0.4$$

which is wrong! The water image is allocated the fat fraction and the fat image the water fraction, i.e. the pixel is misclassified as being predominantly water and not fat. The Dixon reconstruction algorithms attempt to ensure that this error does not occur but sometimes, particularly in areas of large phase shift such as the dome of the liver, water-fat swaps can occur. Figure 19.12 shows an example of a Dixon water-fat swap artefact.

The difficulty with not knowing the background phase shifts led to the development of three-point Dixon (3PD) techniques where three separate acquisitions are performed, each with different echo shifts τ , resulting in $\{0, \pi, 2\pi\}$ phase shifts. The 0 and 2π acquisitions, in which water and fat are both in-phase, can then be used to calculate $\exp(i\phi)$. We now have three equations:

$$S_0 = (S_w + S_f) \cdot \exp(i\phi_0)$$

$$S_\pi = (S_w - S_f) \cdot \exp(i\phi_0) \cdot \exp(i\phi)$$

$$S_{2\pi} = (S_w - S_f) \cdot \exp(i\phi_0) \cdot \exp(i2\phi)$$

We can then calculate ϕ from

$$\hat{\phi} = 0.5 \cdot \tan^{-1}(S_0 \cdot S_{2\pi}^*)$$

where $*$ represents taking the complex conjugate. In this equation, we use the symbol $\hat{\phi}$ rather than ϕ because it is only possible to determine the result within the range $-\pi$ to $+\pi$, i.e. any phase shift less

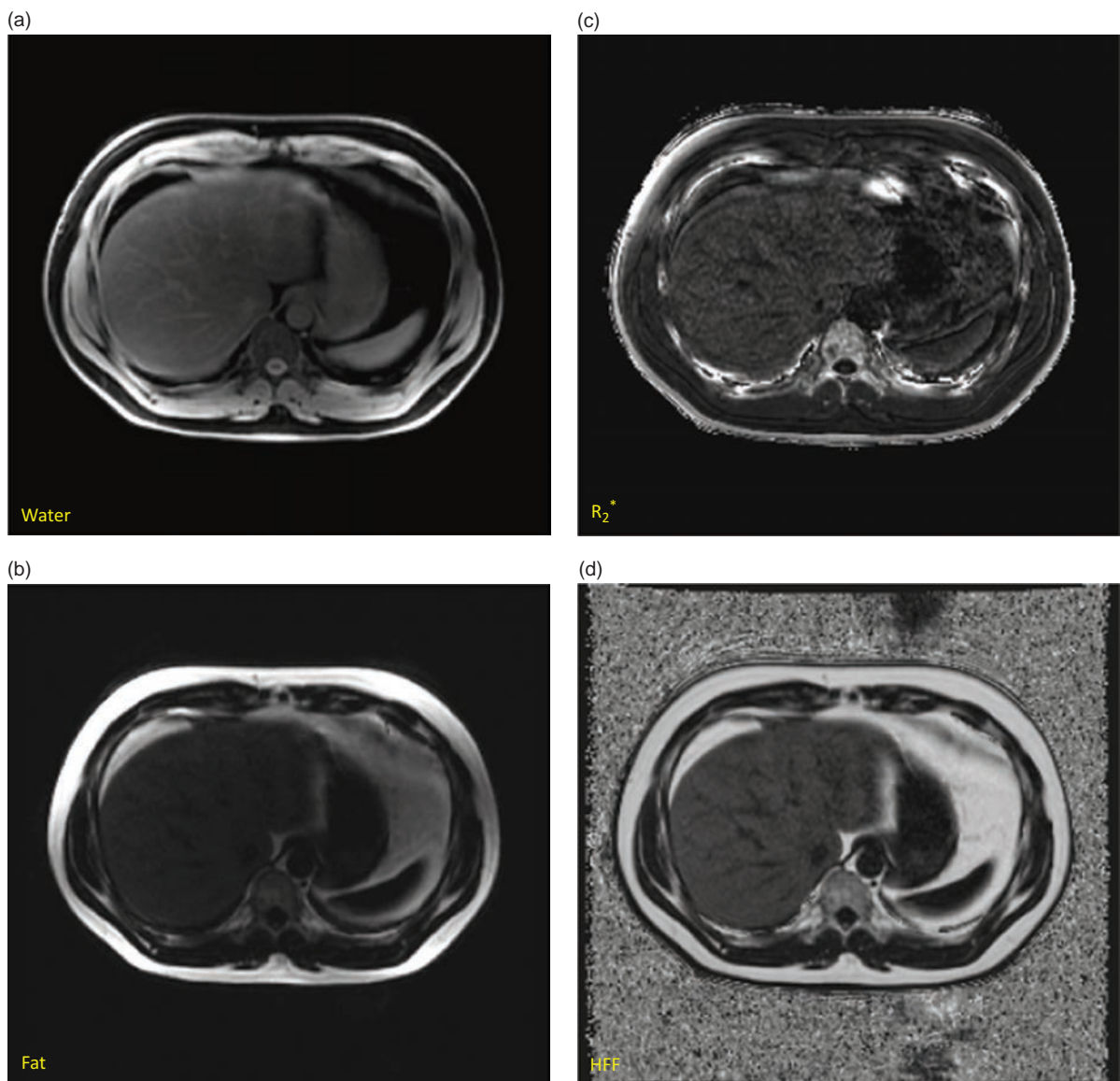


Figure 19.11 Quantitative hepatic fat fraction (HFF) imaging using a six-echo gradient-echo acquisition obtained in a single breath-hold. (a) Water-only image. (b) Fat-only image. (c) Quantitative R_2^* map obtained by a pixel-by-pixel fit to the T_2^* exponential decay curve. (d) Quantitative HFF map. A region of interest in the liver measures approximately 20% HFF in this subject.

than $-\pi$ or greater than π will have a multiple of 2π added or subtracted to bring the phase back into the range $-\pi$ to $+\pi$. This means that in the regions where the phase is wrapped, the signals from fat and water can be swapped. Fortunately, this problem of phase wrapping exists in many branches of physics and engineering and there is an extensive literature on phase-unwrapping algorithms that can be used to extract the correct sign of the signal.

19.6 MR Elastography

MR Elastography (MRE) is a method for quantitatively assessing the mechanical properties of tissue, primarily the tissue stiffness. For centuries, physicians have used palpation as a diagnostic method to determine an organ's size, shape, position and stiffness. The stiffness is particularly important since many disease conditions can increase the stiffness of an organ either

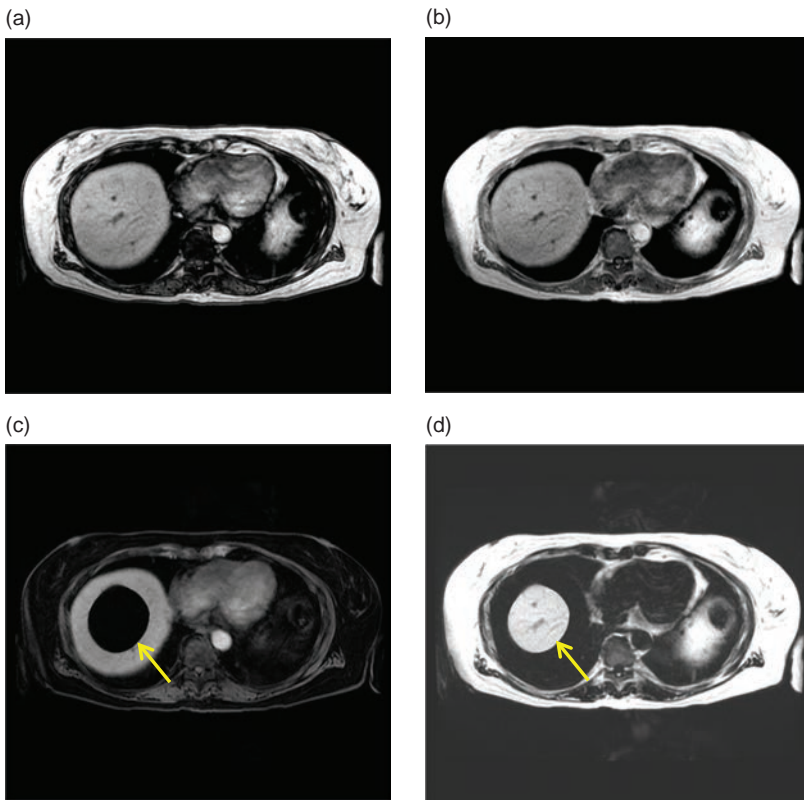


Figure 19.12 Dixon water-fat swap artefact. The figure shows images from a dual-echo gradient-echo acquisition with the (a) first OP echo image acquired at TE = 2.3 ms and the (b) second IP echo acquired at TE 4.6 ms. Following Dixon processing separate (c) water and (d) fat images are reconstructed, but in this case the Dixon reconstruction algorithm has incorrectly classified water and fat (arrows).

globally or focally, and the difference between normal and pathological tissues may be as high as five orders of magnitude. For example, fat has a shear modulus of 10^2 Pa while that of bone is more than 10^7 Pa. Creating non-invasive ‘maps’ of tissue stiffness may therefore offer some unique insights into disease characterization and therapeutic interventions.

MR elastography was first proposed in 1995 by Ehman’s research group at the Mayo Clinic. MRE uses an external driver system to create mechanical waves that propagate through the body, and generates quantitative images, known as elastograms, displaying the shear modulus of the tissue. Since 2012 this technology has been commercially available on conventional MRI systems, for the important clinical application of assessing hepatic fibrosis, a condition linked to alcohol-related disease and to obesity.

Stretch Your Imagination: Quantifying Elasticity

From school, you probably remember that the stiffness of a material is called the elastic modulus or Young’s modulus. Young’s modulus is the ratio of stress, i.e. the force per unit area applied to the

sample, to strain, i.e. the linear deformation of the sample. Conventionally given the symbol E (for elastic), the modulus is calculated from the equation

$$E = \frac{\text{stress}}{\text{strain}} = \frac{F/A_0}{\delta l/l_0}$$

where F is the force applied in the direction of L_0 , A_0 is the cross-sectional area perpendicular to L_0 , and δl is the deformation. As well as measuring Young’s modulus via a static experiment (like you did at school), it can also be measured by setting up a series of longitudinal waves in the material, and then measuring the speed c of the waves:

$$c = \sqrt{\frac{E}{\rho}} \Rightarrow E = \frac{(\lambda f)^2}{\rho}$$

where ρ represents the mechanical density of the material (instead of proton density), and λ and f are the wavelength and frequency respectively for the longitudinal waves. There are other elastic moduli which describe other types of elastic deformation, and in MRE we actually measure the shear modulus. This describes the tissue stiffness when force is applied parallel to one of its surfaces, while the

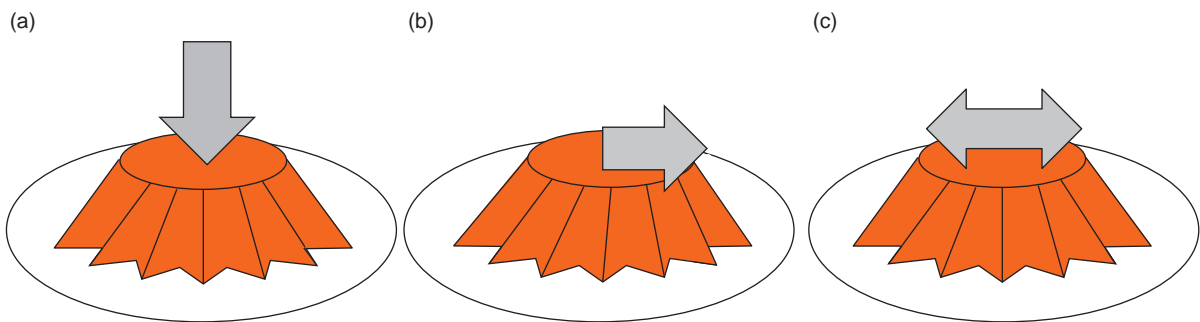


Figure 19.13 Young's modulus of a jelly: (a) push down on the top. (b) Shear modulus of the jelly: pull the top surface to one side. (c) Shear waves in a jelly.

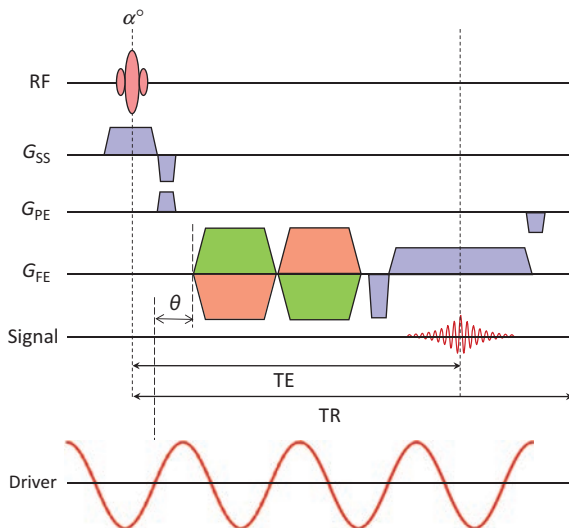


Figure 19.14 Gradient-echo-based MRE sequence showing the bipolar motion encoding gradients (MEGs) in red and green for the two polarities. The driver waveform and its temporal relationship with the MEG is given by.

opposite surface remains static. If you think about a jelly on a plate, you can measure E by pressing down on the top of the jelly (Figure 19.13a); to measure the shear modulus you need to pull the top surface of the jelly to one side (Figure 19.13b).

Like Young's modulus, the shear modulus μ can be measured using a static deformation, or by setting up shear waves in the medium and again measuring the speed or wavelength of the waves:

$$c = \sqrt{\frac{\mu}{\rho}} \Rightarrow \mu = \frac{(\lambda f)^2}{\rho}$$

where again ρ is the mechanical density of the tissue, and now μ is the shear modulus (not the magnetic moment of the proton, or the average of a set of

measurements). To set up shear waves in the jelly, you need to wobble the top surface of the jelly back and forth (Figure 19.13c) – or pick up the plate and shake it horizontally!

The MRE pulse sequence is essentially a variant of phase contrast velocity imaging: refer back to Section 15.3.2 for a refresher course. A pair of bipolar gradients is inserted in the pulse sequence, known as Motion Encoding Gradients (MEGs, Figure 19.14). The external driver creates mechanical vibrations in the body, and the MEGs encode the tiny tissue displacements as the phase of the MR signal. Since the displacements are truly tiny, typically 10^{-7} mm, the MEGs are applied at the same frequency as the mechanical wave driver and with a controlled phase relationship θ . The gradient limits of typical MR systems means that the MRE sequence is 'tuned' to a frequency which matches shear waves in tissue; longitudinal waves travel much faster and are 'invisible' with our current technology. Just as with PC angio, the MEGs are applied twice with opposite polarities, and the signal phases are subtracted to remove non-motion-related background phase shifts.

In order to calculate the tissue stiffness, we need to measure the speed of the shear wave propagation through the tissue. This can be done by repeating the acquisition but changing the phase offset (θ) between the driving waveform and the MEGs. Typically, four phase offsets are acquired, spaced equally over a period of the wave motion. If these four images are displayed as a movie, it gives an impression of the wave propagation through the tissue.

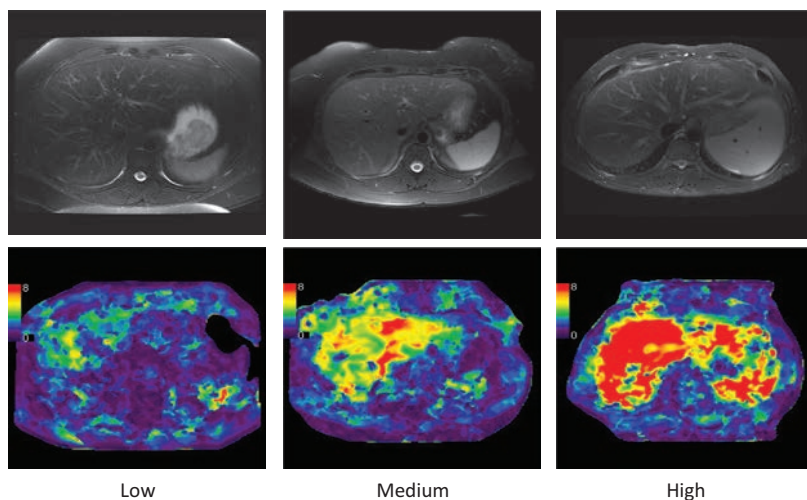


Figure 19.15 T₂w images (top row) and MR elastograms (bottom row) in three patients with low (normal), medium and high liver stiffness. The elastograms are in the range 0–8 kPa. Note that there are no noticeable differences in the T₂w images, but the elastograms show clear differences in liver stiffness.

Remembering that the shear modulus is found from the relationship $(\lambda f)^2/\rho$, we assume ρ is 1000 kg m⁻³ and we know f , the operating frequency of the driver unit. We just need to determine λ from the wave images, something which turns out to be rather difficult, but possible if we use a number of simplifying assumptions. Following the MRE acquisition, an MR elastogram is produced (Figure 19.15).

In theory, MEGs can be used with several conventional MRI pulse sequences; however, for the clinical application of liver imaging it needs to be fast – achievable in a breath-hold. Typical commercial protocols are gradient echoes, with a limited number of slices and rather low spatial resolution matched to the driving frequency of the MRE device. Each phase offset θ is acquired in a separate 15 s breath-hold acquisition. The liver MRE images shown here were acquired using a pneumatic driver at a frequency of 60 Hz. The driver is essentially an acoustic speaker positioned outside the magnet room, with an alternating current at the driver frequency applied to the speaker magnets. This causes the cone to oscillate, creating variations in air pressure. A length of plastic tubing transmits this pressure variation into the magnet room and ends with a small circular drum-like paddle which is positioned in close contact with the patient's abdomen, just overlying the liver. The surface of the drum vibrates, creating the mechanical waves that propagate through the tissue. Although the driver is sending longitudinal waves into the body, the internal boundaries (diaphragm, ribs, etc.) convert them into a mixture of longitudinal and shear waves.

While not painful, it is certainly a weird experience, particularly the first time!

Clinical Applications of MRE

MRE has primarily been used to quantify liver stiffness as a marker of hepatic disease progression. A number of studies have shown good correlations of mean liver stiffness with histopathological assessment of tissue obtained from liver biopsy. Hepatic disease characterization is currently the only commercially available application. However, researchers are exploring other clinical applications, e.g. the breast, where tumours are known to be stiffer than benign lesions; and the brain, where tissue stiffness may help in neurodegenerative diseases as well as brain cancers. New applications may need different mechanical devices to induce shear waves, and areas like the brain can be particularly difficult because the skull strongly attenuates the waves.

19.7 Accuracy, Precision, and Diagnostic Confidence

The move towards more quantitative MR methods is valuable for the whole community, as it improves objectivity and supports evidence-based medical decisions. Of course it is critical to know more about the measurement methods in order for them to reach widespread adoption, in particular accuracy and precision. This section will provide a short introduction to medical statistics; see Further reading at the end of the chapter for more detailed explanations.

Suppose we have a tissue sample which has a true T_1 of 446 ms, measured by some gold standard technique. Now we make a T_1 measurement using one of the methods described in Section 19.2.1: we hope that the result will match, but you will not be surprised if it is not exactly the same. If we make many measurements in the sample, we can find the accuracy of the technique: how close its results are to the true value provided by the gold standard method. We can also define the precision of the technique: sometimes called the test-retest reliability or repeatability.

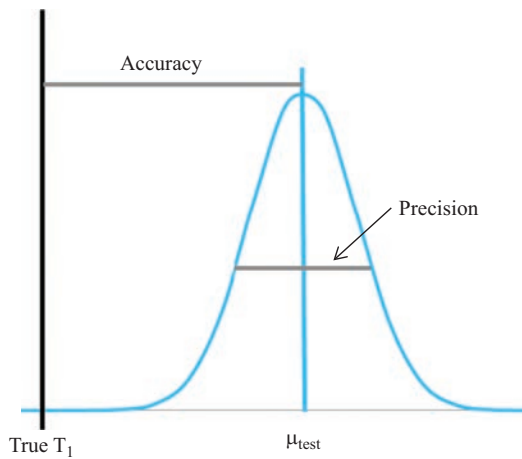


Figure 19.16 Accuracy and precision.

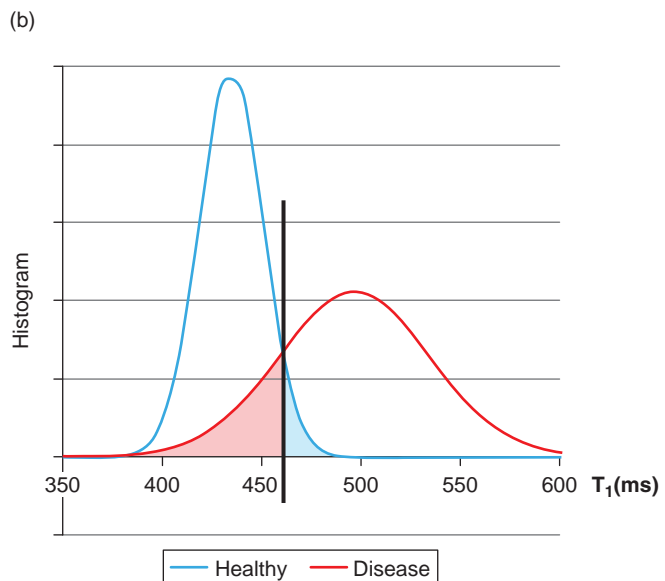
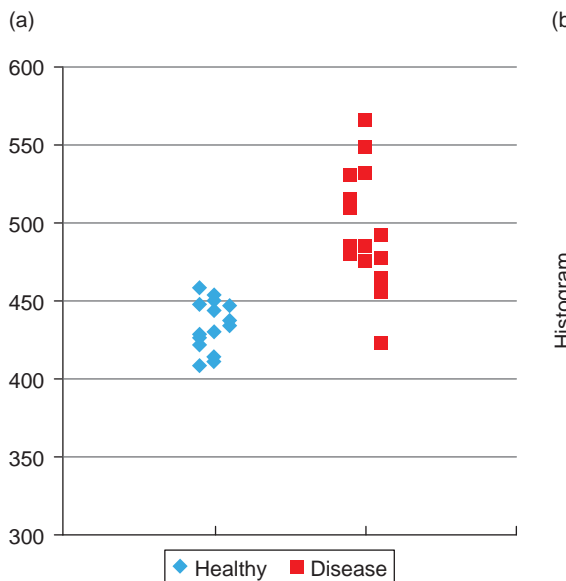


Figure 19.17 (a) Hypothetical T_1 results for healthy subjects and patients with a disease. (b) Histogram of results, showing the cut-off T_1 to distinguish between healthy and disease groups. Blue shaded area = false positive results, red shaded area = false negative results.

Mathematically, the accuracy or *bias* is given as the difference between the mean of the sample measurements, 435 ms in our experiment, and the true value: $\mu_{\text{test}} - T_{1,\text{true}}$. (Note that μ in this section is used for the mean or average of the set of measurements – not the magnetic moment of the proton, nor the shear modulus. Sorry for any confusion!) The precision is usually measured by finding the standard deviation of the sample measurements, assuming there is a Gaussian distribution of measurements about the mean: $\sigma_{\text{test}} = 16$ ms in our experiment. Precision can also be described using the 95% confidence limits. Once again assuming a Gaussian distribution, the 95% confidence limits are at $\mu_{\text{test}} \pm 1.96 \times \sigma_{\text{test}}$, e.g. taking the data shown in Figure 19.16 the 95% confidence limits are 405 ms and 467 ms.

Suppose we now extend our testing, and measure the T_1 s in a series of healthy subjects and in a group of patients with a particular disease. We assume that both groups have Gaussian distributions, so we can define the mean and standard deviation of T_1 in each group. If the T_1 s are well separated (Figure 19.17), we can have high confidence that a T_1 measurement in a single subject will be able to distinguish between healthy and diseased tissue. We generally use Student's *t*-test to test the separation of the two results:

$$t = \frac{\mu_1 - \mu_2}{\sqrt{(\sigma_1^2/n_1) + (\sigma_2^2/n_2)}}$$

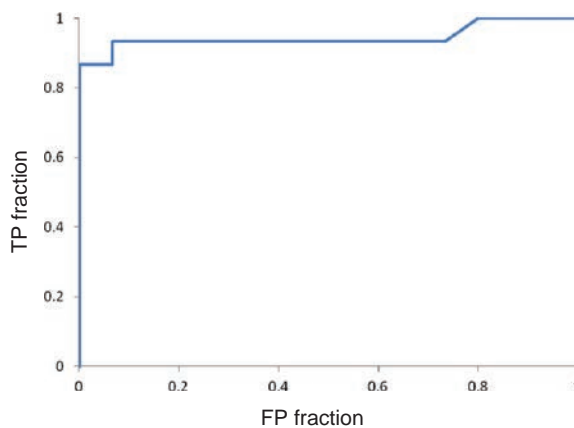


Figure 19.18 ROC (receiver operating characteristic) curve for our hypothetical T_1 experiment.

Statistics software can convert the resulting t -score into a probability p , which tells us the probability that the two samples are actually measuring the same thing (the null hypothesis). The smaller the p -value, the higher our confidence in the T_1 measurement as a quantitative tool. Many research papers use thresholds of $p < 0.05$ (5%), $p < 0.001$ (0.1%), etc. to describe *significant differences* between the two sample groups. You can translate this as ‘there is only N% probability that our experiment is showing separation of the means when it should show them overlapping’. In our example, $p < 0.00001$, a result which can be considered extremely promising – it shows that T_1 measurement can easily distinguish between healthy and disease groups.

However, we need to take this one step further if we want to consider using our T_1 technique to make a clinical decision in a single patient. You can see from Figure 19.17 that if we have overlapping distributions for normal and disease, we are going to have trouble if a patient’s result lands in the overlap region. As well as true positive (TP) and true negative (TN) results, there would be some false positive (FP) and false negative (FN) results. We can define two new metrics for our set of results: sensitivity and specificity.

$$\text{Sensitivity} = \frac{\text{TP}}{\text{TP} + \text{FN}}$$

$$\text{Specificity} = \frac{\text{TN}}{\text{TN} + \text{FP}}$$

In our example with a threshold of 460 ms, sensitivity = 0.86, and specificity = 1.00. Notice that if we change the threshold for T_1 , we will also change the sensitivity and specificity. This can be mapped as an ROC (receiver operating characteristic) curve, as shown in Figure 19.18.

Finally, if the disease prevalence (Prev) is known, we can calculate the positive and negative predictive value of the test. The prevalence has to be estimated from population studies, not from our small sample experiment. The predictive values are found as follows:

$$\text{PPV} = \frac{\text{Sens} \cdot \text{Prev}}{\text{Sens} \cdot \text{Prev} + (1 - \text{Spec}) \cdot (1 - \text{Prev})}$$

$$\text{NPV} = \frac{\text{Spec} \cdot (1 - \text{Prev})}{\text{Spec} \cdot (1 - \text{Prev}) + (1 - \text{Sens}) \cdot \text{Prev}}$$

Using our T_1 example again, if the disease has a prevalence of 1% in the general population, we have PPV = 12.3% and NPV = 99.9%. In words, this suggests that around 12% of patients who have a positive result from the T_1 measurement actually have the disease; on the other side, nearly all the negative results are true negatives. Once again, the PPV and NPV are dependent on the choice of threshold to distinguish between healthy and disease.

As you can see from this brief introduction, quantitative MR is only the first step towards a truly useful diagnostic test, and you should be wary of results which only show the means of two groups. Our advice: always challenge yourself to measure the confidence intervals or sensitivity and specificity to get a better idea of the potential diagnostic value of your exciting new method!

See also:

- Fat suppression techniques: Section 7.3

Further Reading

Bernstein MA, King KF and Zhou XJ (2004) *Handbook of MRI Pulse Sequences*. London: Elsevier Academic Press, chapter 17.

Bland M (2000) *An Introduction to Medical Statistics*, 3rd edition. Oxford: Oxford University Press.

Crema MD, Roemer FW, Marra MD, et al. (2011) ‘Articular cartilage in the knee: current MR imaging

techniques and applications in clinical practice and research’. *RadioGraphics*, 31:37–61. Available online at <http://pubs.rsna.org/toc/radiographics/31/1> [accessed 1 April 2015].

- Delfaut EM, Beltran J, Johnson G, Rousseau J, Marchandise X and Cotten A. (1999) 'Fat suppression in MR imaging: techniques and pitfalls'. *RadioGraphics* 19:373–382.
- Deoni SCL, Rutt BK and Peters TM (2003) 'Rapid combined T₁ and T₂ mapping using gradient recalled acquisition in the steady state'. *Magn Reson Med* 49:515–526.
- Eggers H and Börnert P (2014) 'Chemical shift encoding-based water–fat separation methods'. *J Magn Reson Imaging* 40:251–268.
- Leenders KL, Perani D, Lammertsma AA, et al. (1990) 'Cerebral blood flow, blood volume and oxygen utilisation: normal values and effect of age'. *Brain* 113:27–47.
- Thomas Dixon WT (1984) 'Simple proton spectroscopic imaging'. *Radiology* 153: 189–194.
- Wood JC, Enriquez C, Ghurgre N, et al. (2005) 'MRI R₂ and R₂^{*} mapping accurately estimates hepatic iron concentration in transfusion-dependent thalassaemia and sickle cell disease patients'. *Blood* 106:1460–1465.

But is it Safe? Bio-effects

20.1 Introduction

For centuries magnets have been attributed with alleged healing and hypnotic powers despite a lack of scientific evidence or plausible hypotheses on mechanisms. Magnets may not make you better, but are they harmful? In the course of undergoing a clinical MR examination, the patient will be exposed to the static field, time-varying gradient fields and RF fields as shown in Table 20.1. Staff normally will only be exposed to the fringe field from B_0 . In 35 years of MR, there have been 16 documented fatalities related to magnet safety, 13 of these involving persons with cardiac pacemakers, one involving displacement of an aneurysm clip, one involving a projectile and the other from an unknown cause. Practical MR safety was considered in Chapter 2; you must thoroughly know your institution's safety practices and patient screening procedures, and carrying out a metal check on yourself and others will be second nature to you by now. The purpose of this chapter is to provide

background on the underlying potential biological effects of magnetic fields, in particular:

- the main effect of RF exposure is tissue heating, restricted to less than 1 °C by monitoring and limiting the SAR (specific absorption rate);
- peripheral nerve stimulation (PNS) is the main bio-effect of the time-varying magnetic fields generated by the gradients, and may cause discomfort but it is not harmful;
- at high B_0 (i.e. 3 T and above) mild and transient sensory effects, associated with movement in the static field, may be experienced;
- caution is required for staff and patients who are pregnant, although there is no evidence of any deleterious effect on the fetus;
- occupation exposure limits for MR staff are low, and within sensible limits.

In addition we briefly review the safety of Gd-based contrast agents.

20.2 Radiofrequency Effects

RF effects arguably give the greatest cause for concern in terms of potential bio-effects, partly because they are under the operator's control. The principal physical effect is deposition of energy, leading to tissue heating with possible physiological effects including changes in cardiac output. Of particular concern are heat-sensitive organs such as the eyes and testes, although there is no evidence of any deleterious effect of MR on either. Caution is required where the patient has a metallic (but non-ferromagnetic) implant that may result in localized heating (see Figure 20.1). The use of inappropriate physiological monitoring leads can also result in heating of the electrodes and the possibility of skin burns. Other implant safety issues are addressed in Chapter 2 and elsewhere. See Further reading at the end of this chapter.

Table 20.1 The range of magnetic field exposures for patients in MRI; staff are normally only exposed to the B_0 fringe field and its spatial gradient

	Amplitude	Frequency/ slew rate	Typical duration
Static field B_0	0.2–7 T	0 Hz	Always present
Static fringe field spatial gradient	0–25 T m ⁻¹	Movement acts as dB/dt < 1 Hz	Always present
Imaging gradients G_x, G_y, G_z	0–50 mT m ⁻¹	0–10 kHz 0–200 T m ⁻¹ s ⁻¹	0–10 ms
RF transmit field B_1	0–50 µT	8–300 MHz	0–1 ms

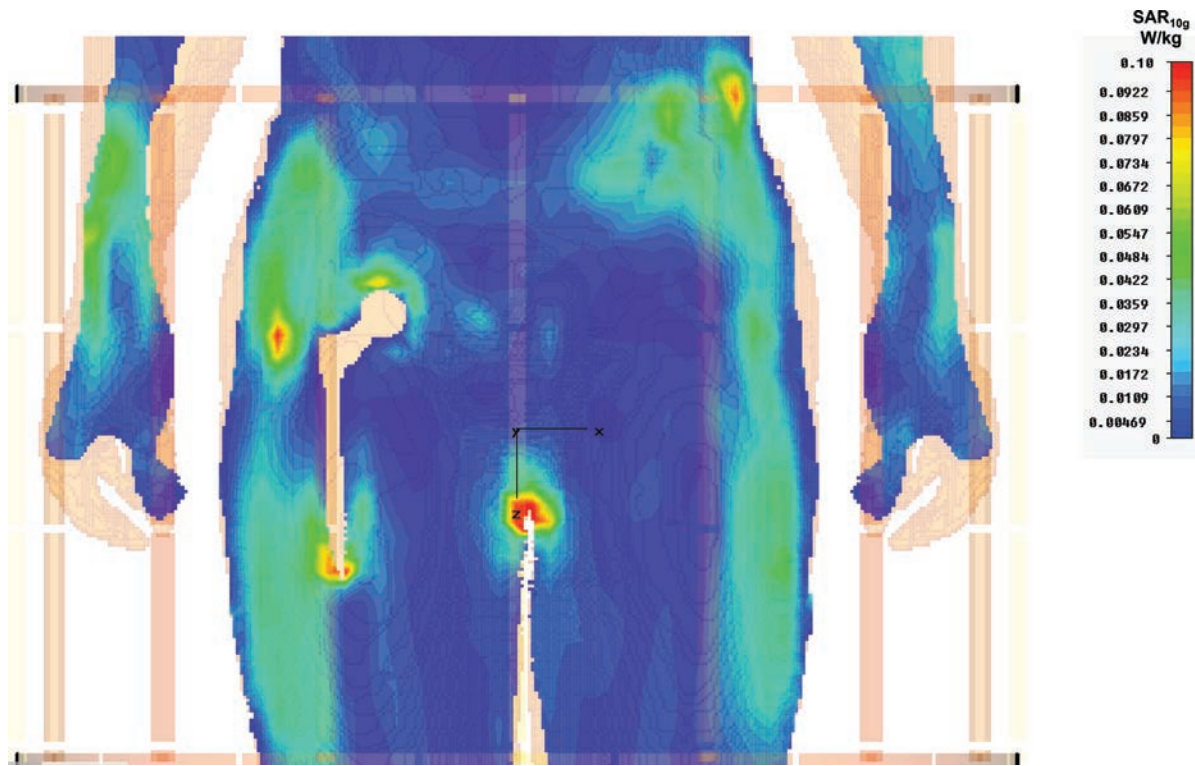


Figure 20.1 SAR hotspots occurring at the tip of non-ferromagnetic implants. Note that the groin region has higher SAR than the implant. Image courtesy of Prof J. Hand, King's College, London.

20.2.1 Specific Absorption Rate

The RF exposure is measured in terms of the specific absorption rate (SAR), defined as the total transmitted power in watts (W) per kilogram of tissue. This is why you need to enter the patient's weight when registering them. The scanner will estimate the SAR for each sequence before scanning begins. During the scan the scanner may monitor its RF transmitter output and compute an average SAR (see also 'SAR Maths'). Normally two levels of RF exposure are accessible. The lower (Normal Mode) level can be applied without restriction. Exposure to the First Level (Controlled Mode) requires positive confirmation from the operator. The Second Level is only available in research mode operating under research governance guidelines.

SAR Maths

For a uniform conducting medium of conductivity σ the SAR can be calculated as follows. The energy deposition is given by the product of induced current

density J and induced electric field E (this is just 'power = voltage times current', but for a volume conductor)

$$P = \mathbf{J} \cdot \mathbf{E} = \sigma E^2$$

and then

$$\text{SAR} = 0.5\sigma \frac{E^2}{\rho}$$

where ρ is the density of tissue and the factor 0.5 comes from time-averaging the alternating electric field (just as in AC power calculations). Thus SAR has units of W kg^{-1} .

From Faraday's law (see Box 'Faraday Induction') and allowing for a sinusoidal B_1 (and for simplicity assuming rectangular, i.e. hard, pulses) we get an average SAR

$$\text{SAR} = 0.5\sigma \frac{\pi^2 r^2 f^2 B_1^2 D}{\rho}$$

where D , the duty cycle, is the fraction of total scan time for which the RF is present. This shows that:

- SAR increases with the square of Larmor frequency or B_0 ;

- SAR increases with the square of flip angle;
- SAR increases with the patient size;
- SAR increases with the number of RF pulses in a given time.

Of course, this calculation is a huge simplification. The details of anatomical geometry can change the power levels. The occurrence of local hotspots has led to the development of localized SAR limits for partial body exposure. At 3 T local SAR is often the limiting factor.

Some scanners also compute the total energy imparted in joules.

20.2.2 Staying Cool: Reducing SAR

SAR is under the control of the MR operator. Some factors that help to reduce the SAR are:

- using quadrature transmit coils (this is standard) or parallel transmission, if available, on high-field systems;
- using a localized transmit coil for certain examinations, e.g. using a transmit–receive head or extremity coil if available;
- increasing TR;
- using fewer slices;
- reducing echo train length (ETL, turbo factor) in TSE sequences;
- reducing the refocusing pulse flip angle, especially in TSE sequences and also fully rewound gradient-echo sequences (bFFE, True-FISP, FIESTA).

Reducing the refocusing pulse is by far the most effective as SAR depends upon B_1^2 which determines the flip angle – a reduction to 150° reduces SAR by 30% but barely affects image quality. Scanning at lower field, e.g. 1.5 T rather than 3 T, also results in lower heating, as SAR is proportional to the Larmor frequency squared, i.e. proportional to B_0^2 (see Box ‘Standing Waves’). Using parallel imaging may also help in some instances by reducing the number of RF pulses used. Alternating between higher and lower SAR sequences can help to spread the thermal load.

Table 20.2 RF temperature limits

Operating mode	Core temperature rise (°C)	Maximum temperature limits (°C)	
		Core	Local
Normal	0.5	39	39
First-level controlled	1	40	40
Second-level controlled	>1	>40	>40

Standing Waves

The wavelength λ for a medium of dielectric constant ϵ_r is

$$\lambda = \frac{c}{\sqrt{\epsilon_r} f}$$

where c is the speed of light, 3×10^8 m s⁻¹. This gives the nominal ‘wavelength’ of the B_1 field in air as 4.8 m at 63 MHz (1.5 T), or 2.4 m at 126 MHz (3 T) – remember we are dealing with fields not waves – strictly the ‘near’ field zone. However, the dielectric constant of tissue (basically water) of 80 gives wavelengths of 0.52 m and 0.26 m at 1.5 T and 3 T. If the dimension of the patient or a metallic implant is equal to half a wavelength then standing waves can be established. These will lead to B_1 non-uniformities (signal non-uniformity) and increased RF heating.

20.2.3 RF Exposure Standards

The IEC 60601-2-33 standard is based upon limiting RF-induced core temperature rises to 0.5 °C or 1 °C for normal and first-level controlled operations respectively. This translates into whole-body SAR limits of 2 and 4 W kg⁻¹ averaged over 6 min. The IEC 60601-2-33 standard gives the following limits for the temperature rise (Table 20.2) and SAR limits (Table 20.3) for the first and second-level controlled modes.

20.3 Gradient Effects

The time-varying fields generated by the gradients fall in a part of the frequency spectrum known as extremely low frequency (ELF). There is much controversy about the effect of chronic exposure to ELF fields from high-voltage power lines and household appliances. However, in MRI we are concerned with acute effects. There is no evidence of MR switched gradient fields causing carcinogenic or teratogenic (literally, the production of monsters!) effects.

Table 20.3 SAR limits

Operating mode	SAR (W kg^{-1})					
	Whole body		Partial body		Local transmit coils	
	Any	Head	Head	Trunk	Extremities	
Normal	2	2–10	3.2	10	10	20
First-level controlled	4	4–10	3.2	20	20	40
Second-level controlled	>4	>4–10	>3.2	>20	>20	>40
Short-term SAR	The SAR limits over any 10 s period should not exceed three times the stated SAR average					

Note: The averaging time is 6 min for all except the short term SAR limit.

20.3.1 Stimulation Effects

The switching of the gradients induces electrical fields and currents in conducting tissues according to Faraday's law (see Box 'Faraday Induction') which may exceed the nerve depolarization threshold and cause peripheral nerve stimulation (PNS). The possibility also exists, at least theoretically, of stimulating cardiac muscle, thus presenting a hazard. Stimulation of motor nerves and skeletal muscle may be disconcerting to the patient (discomfort being reported for levels 50–100% greater than the sensation threshold) but is not itself hazardous and will not normally occur in routine clinical scans. Animal research (with dogs) has shown that respiratory stimulation occurs at exposure levels of the order of three times that required for PNS, while cardiac stimulation requires about 100 times the PNS threshold. In addition to the strength of the stimulus, the rate of change of the gradient fields (dB/dt), the likelihood of stimulation is related to the membrane time constant of the tissue, requiring a stronger stimulus for shorter pulse durations. See Box 'The Strength–Duration Curve'.

Faraday Induction

Faraday's law gives the EMF (or voltage) induced in a conducting loop of area A from a uniform time-varying field as

$$\text{EMF} = A \frac{dB}{dt} = \pi r^2 \frac{dB}{dt}$$

for a circular loop (see Figure 20.2).

The induced electric field round a circular loop is given by volts/distance (strictly $\int E \cdot dl$ for the mathematically unchallenged) or

$$E = \frac{1}{2} r \frac{dB}{dt}$$

around the circumference of the circle. We can work out the maximum induced E by assuming a loop radius (r) of 0.25 m around the torso at the point of peak value of the gradient, where the field generated by the gradient is highest:

$$E_{\max} = \frac{1}{2} r^2 S R_{\max}$$

where $S R_{\max}$ is the maximum slew rate in $\text{T m}^{-1} \text{s}^{-1}$.

$$E_{\max} = 0.03125 \times S R_{\max}$$

A slew rate of $64 \text{ T m}^{-1} \text{s}^{-1}$ (or $\text{mT m}^{-1} \text{ms}^{-1}$) is required to give an electric field on the order of 2 V m^{-1} , the lower limit for stimulation. This is well within the capabilities of modern gradients. In practice the stimulating slew rate is also determined by the pulse duration, as in Box 'The Strength–Duration Curve'.

In older publications current density (J) in A m^{-2} is considered. This is given by

$$J = \sigma E$$

('Ohm's law' for volume conductors) and σ is the electrical conductivity measured in siemens per metre (S m^{-1}).

PNS is most likely to occur in echo planar imaging. In particular we have to be careful when oblique slices are used and it is possible to have a greater slew rate by summing the contributions from two or three sets of gradient coils. In all cases the scanner will calculate dB/dt and advise on the likelihood of stimulation, requiring positive confirmation to proceed to the first-level controlled mode.

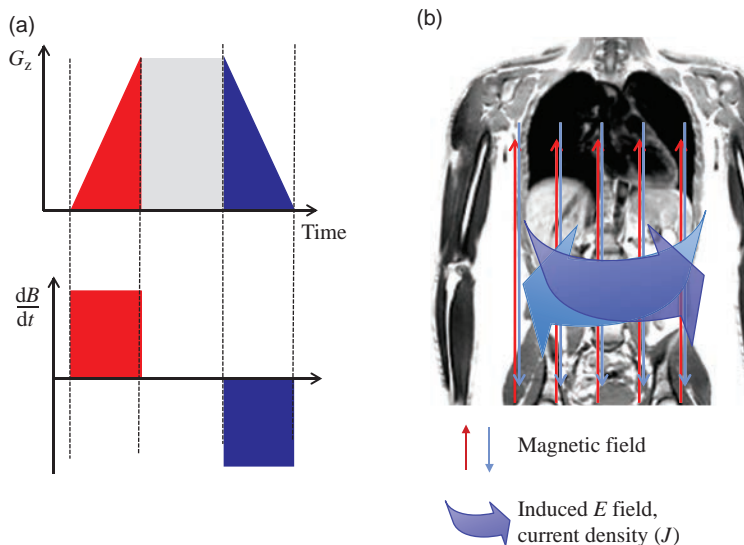


Figure 20.2 Faraday induction in a time-varying magnetic field. (a) With a trapezoidal gradient waveform dB/dt only exists during the ramp-up and ramp-down periods. (b) An electric field is induced in loops around the patient, with circulating currents in conductive tissues. The direction of these reverses for the down-ramp periods.

Another well-documented effect is magneto-phosphenes, or experiencing the harmless sensation of flashes of light. This is thought to originate from retinal stimulation by the induced electric field. Phosphenes occur most readily in the frequency range 10–100 Hz and are not commonly encountered in MRI.

The Strength–Duration Curve

Both the gradients and the RF are examples of time-varying magnetic fields and both induce electrical currents in tissue. So why are their associated bio-effects so different? The reason lies in the strength–duration (SD) curve, a plot of the threshold for stimulation against the duration of the stimulating pulse. In MRI terms, the duration of the pulse refers to the duration of the leading and trailing slopes of the gradient pulses, the part during which tissue currents are produced (Figure 20.2a).

Each type of muscle fibre or nerve may have a different time constant that determines the shape of the SD curve. For MRI the following hyperbolic relationship is considered to apply

$$\left(\frac{dB}{dt}\right)_{\text{threshold}} = C \cdot rb \cdot \left[1 + \frac{\tau_{\text{chron}}}{\tau}\right]$$

where $(dB/dt)_{\text{threshold}}$ is the threshold for peripheral nerve stimulation (about 20 T s^{-1}), τ is the duration of the gradient field change (i.e. the time to ramp from maximum negative to maximum positive) and τ_{chron} (the chronaxie) is a type of tissue electrical time

constant. Typical values for τ_{chron} are 0.5 ms for a peripheral nerve and 3.0 ms for cardiac muscle. rb is known as the ‘rheobase’, the lowest threshold for long stimulus durations. The constant C accounts for the tissue radius and the gradient orientation. Theoretical hyperbolic SD curves for cardiac stimulation and the PNS limits for the IEC Normal level and first-level controlled operating modes are illustrated in Figure 20.3. The lowest thresholds occur for the longest ramp times and therefore gradients that switch faster, i.e. have very short rise times, actually allow much greater amplitude changes as well. Cardiac stimulation requires a lengthy duration of switching, and is not possible on any real MR system. In any event, owing to the different likely conduction paths or loops, the patient would almost always experience severe peripheral muscular stimulation first, which would serve as adequate warning.

In an alternative formulation of the SD curve, the step-size change in B , ΔB , is considered as the stimulus (this is analogous to electrical charge) giving

$$\Delta B_{\text{stim}} = \Delta B_{\min} \left(1 + \frac{\Delta t}{\tau_{\text{chron}}}\right)$$

where ΔB and Δt are the maximum change in B (including negative portions) and the duration of the change. This gives a linear SD relationship and also shows that there is a minimum value of ΔB below which no stimulation can occur. In whole-body MR gradient systems this value is around 9 mT.

20.3.2 Gradient Noise

The characteristic knocking or drilling noise heard when an MRI sequence is in progress arises from the Lorentz force generated by the coils when a current is pulsed through them in the presence of the static magnetic field. The noise is caused by the movement of the coils against their mountings, and can be in excess of 100 dB(A) for some manufacturers' sequences. This is why hearing protection is recommended for patients during MRI scanning. The reduction of gradient noise is an active area of development for system manufacturers, with various approaches including acoustic shielding or the use of non-Cartesian spiral or radial acquisitions that minimize gradient switching (see Chapter 14).

20.3.3 Gradient Exposure Standards

The principle behind the IEC 60601-2-33 standard gradient exposure limits is to prevent cardiac stimulation and minimize PNS at any operating mode. IEC standard thresholds for normal and the first-level controlled operating mode for PNS and for cardiac stimulation are shown in Figure 20.3. The limit of the normal mode is set as the 80% median perception threshold for PNS, while the first-level limits at 100%. Further details are considered in Box 'Crossing the Threshold'.

The risk to hearing is also addressed by the IEC, which states that the system manufacturer must issue a warning on the system console if a particular pulse

sequence is likely to exceed 99 dB(A). The FDA advice is effectively the same. Note that the threshold for instantaneous acoustic trauma is 140 dB and that properly fitting ear-plugs offer about 20 dB(A) attenuation. dB(A) is a unit of sound pressure level which takes into account the normal hearing curve for most people.

Crossing the Threshold

In IEC 60601-2-33, cardiac stimulation is assumed to be avoided when the combined gradient output of all gradient units of the gradient system satisfies

$$\frac{dB}{dt} < 20/1 - \exp\left(\frac{-ts}{3}\right)$$

where dB/dt is in $T s^{-1}$ and ts is the duration of the gradient field change (i.e. the time to ramp from maximum negative to maximum positive) in ms.

PNS limits for the normal operating mode (L01) and the first-level controlled operating mode (L12) are

$$L01 = 0.8 \cdot rb \cdot \left(1 + \frac{0.36}{ts}\right)$$

$$L12 = 1.0 \cdot rb \cdot \left(1 + \frac{0.36}{ts}\right)$$

where again ts is the effective stimulus duration and rb is the rheobase, the threshold below which no further excitation is possible, independent of the stimulus duration. Manufacturers may choose to derive experimental threshold limits to use for L01

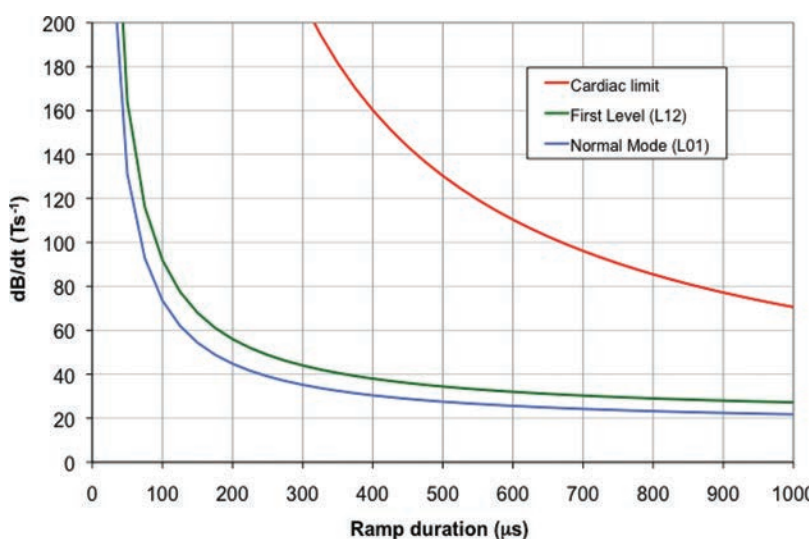


Figure 20.3 Derived strength–duration (SD) curves for the IEC 60601-2-33 limits for cardiac stimulation and the normal (L01) and first-level controlled (L12) operating modes for peripheral nerve stimulation (PNS).

Table 20.4 Rheobase values for different types of gradient system

Type of gradient system	rb expressed as dB/dt	rb expressed as E
Whole-body gradient system (cylindrical magnet)	2.2 V m^{-1}	20 T s^{-1}
Special-purpose gradient system	2.2 V m^{-1}	(not applicable)

and L12, setting them at 80% and 100% of the median threshold experienced by a cohort of volunteers. These are shown in Figure 20.3.

The IEC 60601-2-33 rheobase values are given in Table 20.4 and may be expressed either as the electric field $E (\text{V m}^{-1})$ induced in the patient or as the time rate of change of the magnetic field in the patient $\text{dB}/\text{dt} (\text{T s}^{-1})$.

20.4 Static Field Effects

There is evidence for some mild sensory effects of static magnetic fields, including vertigo (sometimes called ‘magnet sickness’), nystagmus (involuntary eye movement) and taste sensations, with the suggestion of a dose–effect relationship for 1.5, 3 and 7 T whole-body magnets. Other effects, namely headache, tinnitus, vomiting and numbness, have not been substantiated, with some subjects claiming the effect with the magnet switched off! Recently mild transient neuro-cognitive effects in humans have been reported, although in some psychometric tests the participants did better when the field was present. At very high fields the possibilities exist of altering nerve conduction characteristics at least theoretically (e.g. for a field of 450 T), of changing the rate of ion transport across cell membranes and of altering chemical reactivities. None of these hypothetical effects has been demonstrated experimentally.

Published animal-based experiments have been beset by contradictory evidence, failure to be reproduced, poor control and lack of exposure details. For example, prolonged exposure to 9.4 T fields had no effect on numbers of offspring, growth rates, feeding patterns, blood and urine biochemistry and behavioural development for male and female adult and fetal rats. In another study on mice at 4 T (although with combined RF and switched fields and ultrasound) small changes in fetal weight, birth

rates, delayed motor skill learning and adult sperm production rates were reported. At 10 T some behavioural changes in laboratory animals have been noted. Whatever the final conclusions of these experiments, any acute physiological effects of static field exposure from MRI are extremely subtle or of a mild nature.

Remember that the exposure of human subjects in MRI is for short periods only and that these effects cease with the exposure. Epidemiological studies on female magnet workers have shown no deleterious effects on fertility, pregnancies or children. A cautious approach should nevertheless be adopted for both patients and staff who are pregnant.

So what about ‘mag lag’, the idea that cognitive function or memory is affected by exposure to fringe fields? There is no evidence for it. It simply doesn’t exist. (That loss of short-term memory you are experiencing is simply old age!)

20.4.1 Flow Effects

One well-established bio-effect is the generation of electric potentials in moving, conducting tissue, e.g. across blood flowing in vessels, particularly the aorta (the magneto-hydrodynamic effect was covered in Chapter 16). Although this is not known to be hazardous, the possibility exists, at least theoretically, of the induced potential exceeding the threshold for depolarization of cardiac muscle (about 40 mV).

Magneto-Hydrodynamic Effect

The magneto-hydrodynamic effect is illustrated in Figure 20.4, where charged particles moving at velocity v within and at an angle θ to a magnetic field B generate an electric field E

$$E = vB \sin \theta$$

Flow along the field direction will produce no effect, the maximum occurring for flow perpendicular to the field. In an idealized case, the voltage across a vessel of diameter d containing conducting fluid (e.g. blood) will be

$$V = dvB \sin \theta$$

The above expression estimated for aortic flow gives a voltage of about 40 mV at 2.5 T. Although these voltages have been demonstrated *in vivo*, there is no evidence of any consequent ill-effects.

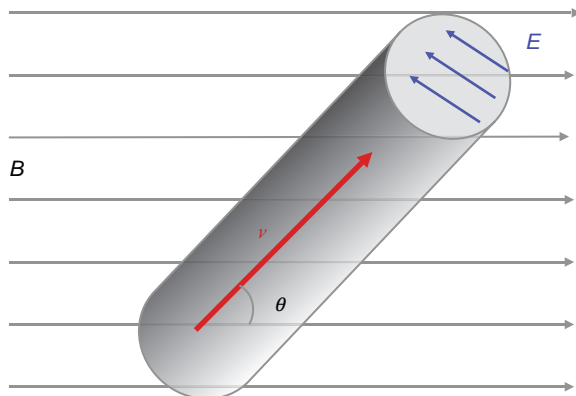


Figure 20.4 Magneto-hydrodynamic effect. An electric field E is induced across the moving conducting fluid, giving an EMF (voltage) across the vessel. v is velocity.

20.4.2 Force Fields

Static fields also pose hazards through the displacement of ferromagnetic implants (clips, coils, stents, etc.). The field will exert both a translational force and a torque (twisting force) on magnetic objects (see Box 'Of Frogs and Forces'). The field may disrupt the function of cardiac pacemakers. Of the sixteen reported deaths in MR incidents, thirteen resulted from the inadvertent scanning of persons with pacemakers. In specialist centres, under strict protocols, it has become possible to scan patients with certain newer kinds of MR conditional pacemakers. However, we strongly recommend that you don't do this unless you happen to be working in one of those centres and have appropriate local policies and procedures.

Of Frogs and Forces

Biological tissue is diamagnetic, which means it is essentially, but not entirely, non-magnetic. A diamagnetic material responds to an applied magnetic field by generating fields that oppose the applied field, i.e. generating a repulsive force. This effect has been demonstrated dramatically by magnetically levitating frogs in the spatial gradient of the fringe field of a 16 T magnet (we always thought frogs were repulsive).

Forces and torques were examined in Section 2.3.1. Aside from floating frogs, the theoretical effect of these forces on biological tissues *in vivo* is negligible compared with the normal mechanical and haemodynamic forces involved with life. Although

red blood cells in sickle cell anaemia have shown displacement *in vitro* in a 0.5 T field, this has not been replicated in patients, or for normal blood cells.

20.4.3 Static Field Exposure Standards

The IEC 60601-2-33 standard gives the following static magnetic field limits:

- normal operating mode: equal or lower than 3 T;
- first-level controlled operating mode: higher than 3 T and equal to or lower than 8 T;
- second-level controlled operating mode: higher than 8 T.

20.5 MR Exposures and Pregnancy

Although there is no convincing biological, physiological or epidemiological evidence that the magnetic field exposures encountered in MRI are harmful to the fetus, it is usual to practice caution for patients in the first trimester, delaying the scan if feasible, or using alternative (but not ionizing) investigations. There is now so little concern that one organization (the HPA) forgot to advise on magnetic field exposure during pregnancy in their current guidelines! There is a call for caution (again without direct evidence) concerning the sensitivity of fetal hearing, so quieter sequences should be used if possible. Scanning should be restricted to the normal mode. Gadolinium contrast should only be used if clinically justified.

For staff who may be pregnant, there is no need to specifically alter their duties. The American College of Radiology (ACR), and the UK Society and College of Radiographers (SCoR) guidelines recommend that, on account of the theoretical risk to fetal hearing, pregnant staff should not enter the scanner room during scanning, but all other routine activities are okay.

20.6 Occupational Exposure

The patient exposure limits are very well controlled in MRI, but what about the staff? This has been a major focus recently on account of the European Union (EU) Physical Agents Directive (Electromagnetic fields) of 2004 which has generated a decade's worth of controversy.

Studies of static field exposure have shown that, in general, the peak B field exposure to staff is around 40% of B_0 (unless you crawl into the magnet), with a time-averaged exposure (over an eight-hour working day) of around 5 mT. In most instances this is the only magnetic field exposure staff will experience. Exposure to RF and dB/dt time-varying fields will only occur in close proximity to the bore entrance

during scanning – for example, when monitoring an anaesthetized patient or comforting an anxious or vulnerable patient, or during interventional procedures. Studies, including those commissioned by the EU, have shown that the exposure limits set by ICNIRP in 2010 and adopted in the 2012 EU Directive are unlikely to be exceeded. Indeed the Directive allows for its own limits to be exceeded in the special

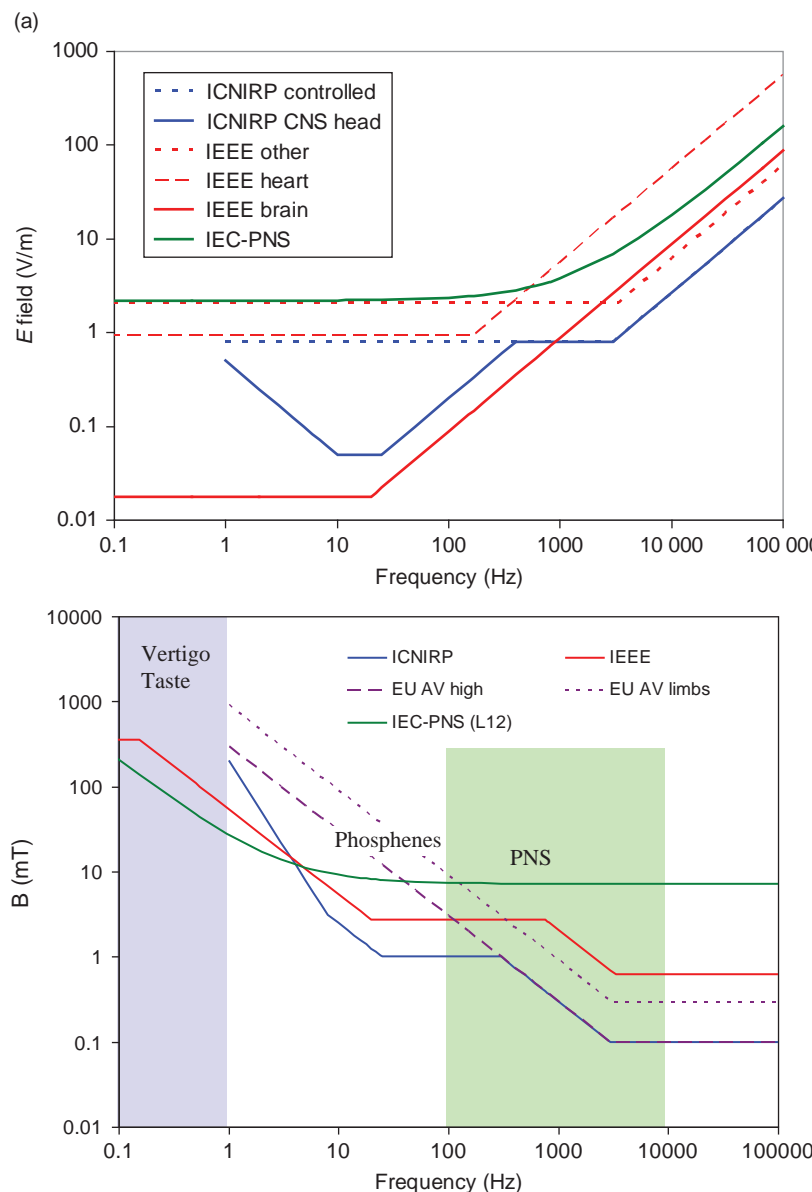


Figure 20.5 (a) Basic restrictions for occupational exposure for 1 Hz to 100 kHz and (b) corresponding Reference Levels. The blue shaded area represents the frequency range relevant to the static field (and movement within it), while green represents the imaging gradient region. These are defined as RMS values. The approximate regions of known bio-effects are also indicated.

case of clinical or research MR and MR engineering. More details are contained in Box 'Occupational Exposure Limits'.

Occupational Exposure Limits

Outside of the EU, we are not aware of any legislated occupational limits affecting MRI. Instead most countries apply guidelines set by international bodies such as ICNIRP (the International Commission on Non-Ionising Radiation Protection). There is no shortage of organizations wishing to protect you from the 'harmful' effects of electromagnetic fields. In our

Table 20.5 Occupational exposure limits for static magnetic fields

	Trunk and head instantaneous ceiling (T)	Limbs (T)
IEC ^a	8	8
ICNIRP ^b	2	8
IEEE ^c	0.5	0.5

^a International Electrotechnical Commission (2013) *Medical Electrical Equipment – Part 2-33: Particular Requirements for the Safety of Magnetic Resonance Equipment for Medical Diagnosis*, 3rd edition. Geneva: IEC.

^b International Commission on Non-Ionising Radiation Protection (2009) 'Guidelines on limits to exposure from static magnetic field'. *Health Physics* 96:504–514.

^c The Institute of Electrical and Electronics Engineers (IEEE) (2002) *IEEE Standard for Safety Levels with Respect to Human Exposure to Radio Frequency Electromagnetic Fields. 0–3 kHz*. New York: IEEE.

opinion (and that of the MR community) their definition of 'harmful' seems overly cautious, and some limits lack scientific basis.

The structure of these guidelines usually encompasses two limits shown in Figure 20.5. The Basic Restriction (BR) or Exposure Limit Value (ELV) is most often expressed in terms of the electric field induced in a tissue which is related to the physiological effect of the exposure. As the internal induced field is very difficult (i.e. impossible) to measure, Reference Levels (RL), Maximum Permissible Exposures (MPE) or Action Values (AV) are derived in terms of the incident field, usually B , which can be readily measured. Compliance with the RL (MPE, AV, etc.) is sufficient to ensure compliance with the Basic Restriction or equivalent. Tables 20.5 and 20.6 contain static field and RF occupational exposure limits relevant to MRI. Relevant references are listed in Further reading at the end of the chapter.

The IEC occupational limits (which apply only for MRI) are the same as the patient exposure values, except for RF, where the limit is 0.4 W kg^{-1} .

20.7 Contrast Agent Safety

There are several different formulations available commercially with various osmolalities and safety profiles (Table 20.7). In general, gadolinium is a safe drug well tolerated by subjects, and apart from NSF (see Box 'Gadolinium and NSF Case History') there are only a handful of serious adverse effects noted in the literature. In 2010 the European Medicines Agency (EMA) published definitive advice

Table 20.6 Occupational exposure limits for RF magnetic fields

	Frequency (MHz)	Reference Level, Limit or Maximum Permissible Exposure			
		SAR (W kg^{-1})	$E (\text{V m}^{-1})$	$H (\text{A m}^{-1})$	$B (\mu\text{T})$
IEC ^a	Any	4			
ICNIRP ^b	10 to 400	0.4	61	0.16	0.2
IEEE ^c	0.1 to 100	0.4	61.4	0.163	
	127.7		61.4	0.128	
	298.0		61.4	0.0547	

^a International Electrotechnical Commission (2013) *Medical Electrical Equipment – Part 2-33: Particular Requirements for the Safety of Magnetic Resonance Equipment for Medical Diagnosis*, 3rd edition. Geneva: IEC.

^b International Commission on Non-Ionising Radiation Protection (2010) 'Guidelines for limiting exposure to time-varying electric, magnetic, and electromagnetic fields (up to 100 kHz)'. *Health Physics* 99:818–836 and Erratum: *Health Physics* (2011) 100:112.

^c The Institute of Electrical and Electronics Engineers (2005) *IEEE Standard for Safety Levels with Respect to Human Exposure to Radio Frequency Electromagnetic Fields, 3 kHz to 300 GHz*. New York: The Institute of Electrical and Electronics Engineers.

Table 20.7 Commercially available Gd-based contrast agents, ordered by Gd concentration. The European Medicines Agency (EMA) classified all available agents according to their risk profile for NSF in 2010; Ablavar was subsequently withdrawn from all EU countries in 2011. All trade names are registered trademarks of their respective manufacturers

Active ingredient	Ligand structure	Trade name	EMA risk class	Gd conc'n (mmol mL ⁻¹)	Indications for use							
					Adults >2yo		Children		Lesions with abnormal vascularity		Evaluate vessels	
					Brain, spine, associated tissues	Head and neck	Body/liver	Heart	Aorto-iliac	Iliac-femoral	CNS	
Gadoxetate disodium	Linear, ionic	Eovist, Primovist	Medium	0.25	X				X			
Gadofosveset trisodium	Linear, ionic	Ablavar (US) previously Vasovist	N/A	0.25	X					X	X	
Gadoterate meglumine	Cyclic, ionic	Dotarem	Low	0.5	X	X	X					X
Gadoteridol	Cyclic, non-ionic	Prohance	Low	0.5	X	X	X	X				
Gadobenate dimeglumine	Linear, ionic	Multihance	Medium	0.5	X	X	X		X		X	X
Gadopentetate dimeglumine	Linear, ionic	Magnevist	High	0.5	X	X	X	X	X			
Gadobenate dimeglumine	Linear, ionic	Magnegita (some EU countries)	High	0.5	X		X	X	X	X	X	X
Gadobenate dimeglumine	Linear, ionic	Gado-MRT, RatioPharm (Germany only)	High	0.5	X		X	X	X	X	X	X
Gadoversetamide	Linear, non-ionic	Optimark	High	0.5	X		X		X			X
Gadodiamide	Linear, non-ionic	Omniscan	High	0.5	X		X		X			
Gadobutrol	Cyclic, non-ionic	Gadavist (US), Gadovist (EU)	Low	1	X	X	X					X

Source: FDA website.

concerning NSF and Gd, classifying all Gd agents as either high, medium or low risk. In the USA, the FDA published new guidelines for manufacturers of Gd agents, requiring the information label to include warnings about NSF. The FDA requires the same warning for all formulations, even though there is good scientific evidence that some agents are much higher risk than others.

The main contraindications are poor renal function (with glomerular filtration rate $<30 \text{ ml min}^{-1}$) and pregnancy. The gadolinium complex crosses the placenta into the fetal circulation and there is insufficient safety data about fetal exposure to gadolinium. Gadolinium also crosses into breast milk, so lactating mothers should not breastfeed for 24 h following gadolinium administration. Full details of contraindications and clinical applications can be found on the information insert in any preparation of gadolinium.

Starting in 2014 there have been reports that gadolinium may be deposited in the brain following repeated Gd contrast agent administration. It is not yet clear whether it is free Gd or still chelated, but it is well known that unbound Gd is toxic. Although Gd-based contrast agents still have a better safety profile than X-ray contrast media and radioisotope tracers, companies and radiologists should be aware of the potential risk and stay abreast of the latest research.

Gadolinium and NSF Case History

The first reports of Nephrogenic Systemic Fibrosis (NSF) appeared in 1997. In patients with severe kidney dysfunction, NSF may develop over a period of days to several weeks. The first symptoms are red or dark patches or papules that develop on the skin. The skin thickens and feels 'woody', and

the skin surface can have an orange-peel texture. In addition patients may experience pain in the affected areas. In many cases, skin thickening prevents joint movements, and other organs might be affected. About 5% of patients have very rapid and progressive disease development, and some patients may die.

In 2006 a pivotal study reported that five of nine patients with NSF had received a gadolinium-based contrast agent 2–4 weeks before reporting symptoms. Shortly after, several more studies confirmed the link between Gd and NSF; higher risk was shown with high-dose administration (e.g. double-dose or bolus injection for contrast-enhanced MRA), and with one particular formulation, gadodiamide. By 2010 around 250 cases had been reported linking NSF in patients with renal failure with administration of Gd agents. (Note that NSF has never been reported in patients with normal renal function.)

20.8 So is MRI Safe?

With hundreds of millions of people having been scanned over the last four decades, it seems unlikely that some unthought-of detrimental effect from the field exposures should appear now. Caution is required concerning the use of gadolinium-based contrast agents. Aside from the NSF issue, there is some evidence that gadolinium ions may accumulate in very small concentrations in the brain. However, that is an issue for pharmaceutical safety, not magnetic fields. Ultimately the everyday dangers arise from the magnetic attractive and twisting forces and from implant heating or malfunction. Unfortunately accidents are usually caused by people, not machines. MRI is only as safe as you are in your practice.

See also:

- Safety first: Section 2.3

Further Reading

American College of Radiology Expert panel on MR Safety (2013)' ACR guidance document on MR safe practices: 2013'. *J Magn Reson Imaging* 37:501–530.

Capstick M, McRobbie D, Hand J, et al. (2008) 'An investigation into occupational exposure to electromagnetic fields for personnel working with and around medical

magnetic resonance imaging equipment'. Report on Project VT/2007/017 of the European Commission Employment, Social Affairs and Equal Opportunities DG. Available from www.myesr.org/html/img/pool/VT2007017FinalReportv04.pdf [accessed 8 May 2015].

Health Protection Agency (2008) *Protection of patients and volunteers*

undergoing MRI procedures.

Chilton: Health Protection Agency.

Institute of Electrical and Electronics Engineers (IEEE) (2002) *IEEE Standard for Safety Levels with Respect to Human Exposure to Radio Frequency Electromagnetic Fields. 0–3 kHz*. New York: IEEE.

International Commission on Non-Ionising Radiation Protection (2009) 'Guidelines on limits to

- exposure from static magnetic field'. *Health Physics* 96:504–514.
- International Electrotechnical Commission (2013) *Medical Electrical Equipment – Part 2-33: Particular Requirements for the Safety of Magnetic Resonance Equipment for Medical Diagnosis*, 3.2 edition. Geneva: IEC.
- Kanal E and Tweedle MF (2015) 'Editorial: residual or retained gadolinium: practical implications for radiologists and our patients'. *Radiology* 275(3):630–634.
- Kanal E, Gillen J, Evans JA, Savitz DA and Shellock FG (1993) 'Survey of reproductive health among female MR workers'. *Radiology* 187:395–399.
- Kanda T, Osawa M, Oba H, et al. (2015) 'High signal intensity in dentate nucleus on unenhanced T1-weighted MR images: association with linear versus macrocyclic gadolinium chelate administration'. *Radiology* 275:803–809.
- McRobbie DW (2012) 'Occupational exposure in MRI'. *Br J Radiol* 85:293–312.
- Medicines and Healthcare products Regulatory Agency (2014) 'Magnetic resonance imaging equipment in clinical use: safety guidelines, version 4'. Available from www.gov.uk/government/publications/safety-guidelines-for-magnetic-resonance-imaging-equipment-in-clinical-use [accessed 26 March 2015].
- Shellock FG (2015) *Reference Manual for Magnetic Resonance Safety 2015*. Salt Lake City, UT: Amirsys Inc. (new edition published annually).
- Shellock FG and Crues JV (eds) (2013) *Magnetic Resonance Procedures: Health Effects and Safety*. Los Angeles, CA: Biomedical Research Publishing.

Where Are We Going Now?

21.1 Introduction

To quote the old human rights song, we've come a long, long way – both since the genesis of modern MRI and since the start of the book. We started with an allusion to rocket science. In this last chapter we delve into what may have been regarded as science fiction, or mere star-gazing, a few years ago. What will tomorrow's MR scanner be like, and what will it do – or possibly, what won't it do? In the last edition we predicted:

- The use of interventional MRI will increase and expand, coupled with a proliferation of minimally invasive therapies, including gene therapies. *These are still on the way.*
- Interventional MR systems may use high-temperature superconducting flat magnets (like fridge magnets) incorporated into the operating room couch. *We're not there yet.*
- For screening we may see walk-through magnets. *Ha ha! We were probably watching Star Trek!*
- New extensions to parallel imaging will render EPI unnecessary except in some functional neurological examinations (i.e. just like the present!). *No comment.*
- Field strengths will of course keep increasing, and 3 T will become the norm for state-of-the-art clinical scanning. *This part is true.*
- There will be new 'intelligent' contrast agents for molecular-specific proton imaging. *Keep watching this space ...*
- Finally, spectroscopy will be deployed as a routine clinical application. *Hooray, we got this one right too!*

21.2 7 Tesla Systems

In the last edition of this book we predicted (cautiously) that 'Field strengths will of course keep increasing, and 3 T will become the norm for state-

of-the-art clinical scanning.' By 2014 the second part of this prediction was certainly true. By solving specific 3 T issues related to B_1 homogeneity, 3 T systems are able to provide high-quality images for all clinical applications, and they are economically within reach for most healthcare institutions. What about the first part, that field strengths will keep increasing? Well certainly, the first 7 T whole-body scanner was developed at the University of Minnesota in 1999 for research purposes; by 2003, all three major manufacturers launched their own 7 T systems to meet the growing demand from research centres around the world. The logical extension of clinical MRI from 3 T to 7 T has not yet happened – and may take several more years, for technical reasons that we will explain below.

The obvious attraction of going to 7 T is the improved SNR – just like the shift from 1.5 T to 3 T in the late 1990s. As we already saw, SNR scales approximately with B_0 , so 7 T systems offer slightly more than double the SNR of a clinical 3 T system. The extra SNR is typically traded for much higher resolution. There are other differences of course: T_2 s become shorter, and T_1 s longer (see Table 21.1). SAR (specific absorption rate) also increases with B_0^2 ; together with the long T_1 s, this means longer TRs and therefore longer scan times.

Of course, there are also disadvantages with going to higher field (apart from the costs). Due to the shorter wavelength, standing waves cause severe B_1 inhomogeneity even in small FOVs used for brain imaging, and the centre of the brain is often significantly brighter than the cortex (see Section 10.4.2). Overall image quality for clinical diagnosis is barely equal to the image quality available at 3 T. To overcome this, 7 T systems require multi-transmit coils and RF chains, probably with eight channels. Although the multi-transmit problem is 'solved' for 3 T, the extra work to develop eight-channel transmit systems, with the necessary safety controls, is

Table 21.1 Brain relaxation times at three field strengths

Tissue	T ₁ (ms) ^a			T ₂ (ms) ^b		
	1.5 T	3 T	7 T	1.5 T	3 T	7 T
White matter	646	838	1126	72	62	37
Grey matter	1197	1607	1939	90	71	43

^a Wright PJ, Mougin OE, Totman JJ, et al. (2008) 'Water proton T1 measurements in brain tissue at 7, 3, and 1.5T using IR-EPI, IR-TSE, and MPRAGE: results and optimisation'. *Magn Reson Mater Phys* 21:121–130.

^b Zhu J, Klarhofer M, Santini F, et al. (2014) 'Relaxation measurements in brain tissue at field strengths between 0.35T and 9.4T'. *Proc Intl Soc Mag Reson Med* 22:3208.

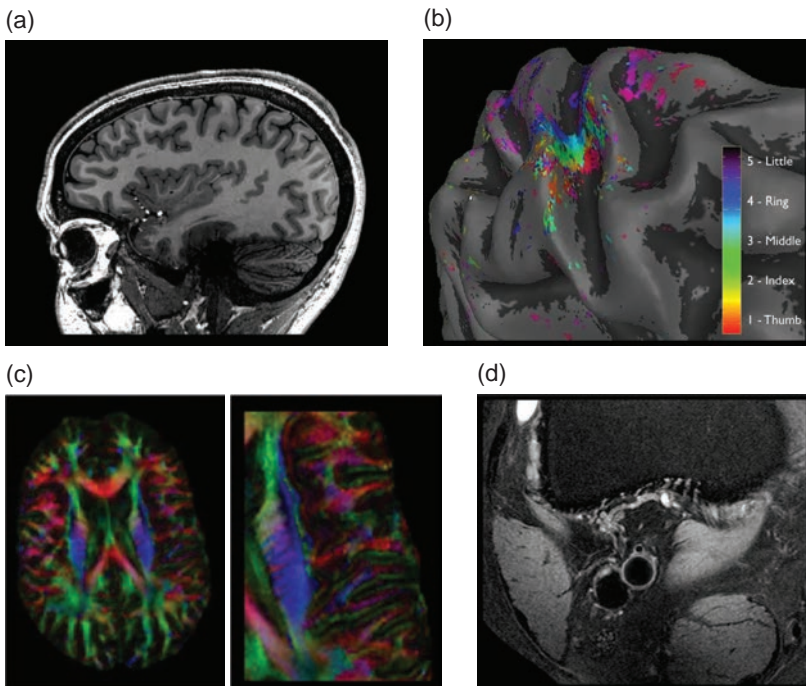


Figure 21.1 7 T imaging often uses the higher SNR to achieve much higher spatial resolution than clinical systems. (a) MP-RAGE with 0.6 mm isotropic voxels (courtesy of Utrecht Medical Centre, Netherlands); (b) finger-tapping fMRI with high resolution, distinguishing between individual digits (courtesy of Sir Peter Mansfield MRI Centre, Nottingham, UK); (c) high-resolution FA map (courtesy of Vanderbilt University, Nashville TN); (d) popliteal artery wall imaging (courtesy of Utrecht Medical Centre, Netherlands).

significant. The very high SAR deposition at 7 T is extremely limiting for standard pulse sequences. For example, TSE T₂w or T₁w scans with even a modest train of refocusing pulses requires a long TR to keep SAR under control, which leads to very long scan times to achieve whole-brain coverage. Therefore many 7 T scans are done using gradient echo.

Susceptibility effects also become very challenging at 7 T, and systems require extra B_0 shimming. The shimming involves not only first- and second-order shim coils, but also third order; these extra shim coils take up more space in the magnet bore, so the internal patient aperture is usually 55–60 cm, instead of the

more usual 70 cm in a clinical system. The susceptibility effect can also be an advantage, however, particularly for detection of the BOLD effect in fMRI. One of the main applications for 7 T scanning is high-resolution fMRI which can localize brain function with very high spatial resolution.

Today (early 2015) there are approximately 60 installations of 7 T MR systems worldwide. There is still significant development work to do to make these systems clinically useful and to improve diagnostic abilities. We need a wider range of RF receive coils, as well as the multi-transmit capabilities, and we need to guarantee safety, e.g. by developing special

low-SAR excitation and refocusing RF pulses. Will 7 T become clinically relevant in the next decade? These authors are not ready to place their bets, yet.

21.3 Hyperpolarization

Polarization in MRI refers to the number of excess nuclei in the low-energy state that contribute to the net or bulk magnetization. The polarization at thermal equilibrium for a spin $\frac{1}{2}$ nuclei is given by (see Box 'Population of Energy States' in Section 9.3)

$$P \approx 1 - \frac{\gamma \hbar B_0}{k_B T}$$

Hence P is approximately 5×10^{-6} at 1.5 T for ^1H which is at 80 M concentration in biological tissues. However, other NMR active nuclei that we may be interested in have either very low natural abundance, e.g. ^{13}C , or are not naturally occurring in the body, e.g. noble gases such as ^{129}Xe . The theoretically achievable SNR for a given nucleus is proportional to $C\gamma P$, where C is the concentration, γ is the gyromagnetic ratio and P is the polarization. Since we cannot increase C substantially and γ is a constant, the only option is to try to increase the polarization P . Increasing the static magnetic field strength B_0 is one way to increase the polarization, but also has a number of drawbacks, not least of which is cost. An alternative, and completely different, approach is to create an artificial, non-equilibrium distribution of the nuclei known as the 'hyperpolarized' state, which creates a several orders of magnitude increase in polarization. This hyperpolarized state is most effectively created by an external polarization of a suitable substrate, followed by rapid administration of the hyperpolarized agent. For example, hyperpolarization of noble gases such as ^{129}Xe or ^3He can be achieved using optical pumping while hyperpolarization of a wide range of organic molecules containing ^{13}C can be achieved using either parahydrogen-induced polarization (PHIP) or dynamic nuclear polarization (DNP).

In DNP the ^{13}C is hyperpolarized by transferring spin polarization from electrons to protons. This phenomenon was theoretically predicted by Albert Overhauser in 1953 and relies on the random interactions between an electron and a nucleus. The ^{13}C agent to be polarized is mixed with an organic radical with unpaired electrons, which is known as the electron paramagnetic agent (EPA). The sample is then placed in a polarizer which keeps it at a very

low temperature, <1 K, in a high magnetic field, typically 5 T. At these extreme physical conditions the EPA electrons are nearly 100% polarized. The sample is then irradiated with microwave energy at a frequency corresponding to the electron spin resonance of the EPA at that field strength. This transfers the polarization from the electrons to the ^{13}C nuclei. The polarization builds up over a period of 15–60 min, after which time the frozen sample is dissolved in heated water or buffer to produce a room-temperature solution, a process known as dissolution. Typically hyperpolarization with DNP can result in a more than 10 000-fold increase in SNR, making it possible to monitor real-time changes in metabolism.

Hyperpolarized nuclei have the advantage that they are either not naturally present in the body, such as ^{129}Xe or ^3He , or they have very small natural abundance, such as ^{13}C . The low background signal produces high levels of image contrast. The disadvantage is that separate transmit and receive coils tuned to the precessional frequency of the nuclei at the field strength of interest are required. Similarly larger gradient amplitudes are required for equivalent spatial resolution to proton imaging since the slice thickness and pixel sizes are all scaled by γ . The resolution of hyperpolarized imaging is therefore generally inferior to proton imaging. The hyperpolarization signal of most biological molecules decays with a T_1 of the order of a few tens of seconds, so it is critical to inject and image the agent as rapidly as possible after dissolution and to use a low flip angle imaging sequence to avoid consuming the hyperpolarized magnetization too quickly.

Hyperpolarized gases such as ^{129}Xe or ^3He have been used for imaging the lung since they can be readily inhaled by the patient and provide direct visualization of the airspaces (Figure 21.2). As such they are both suited to 'ventilation' imaging, i.e. demonstrating that the gas can reach the lung alveoli. This is important in monitoring diseases such as chronic obstructive pulmonary disease, cystic fibrosis and asthma. The self-diffusion (ADC) of the gases can also be measured to aid in the assessment of airway size, which can change due to diseases such as emphysema. In addition ^{129}Xe is also slightly soluble in tissue and blood, which means it can also be used for investigating diseases that impair the exchange of gas across the alveolar wall, e.g. fibrosis or certain interstitial lung diseases.

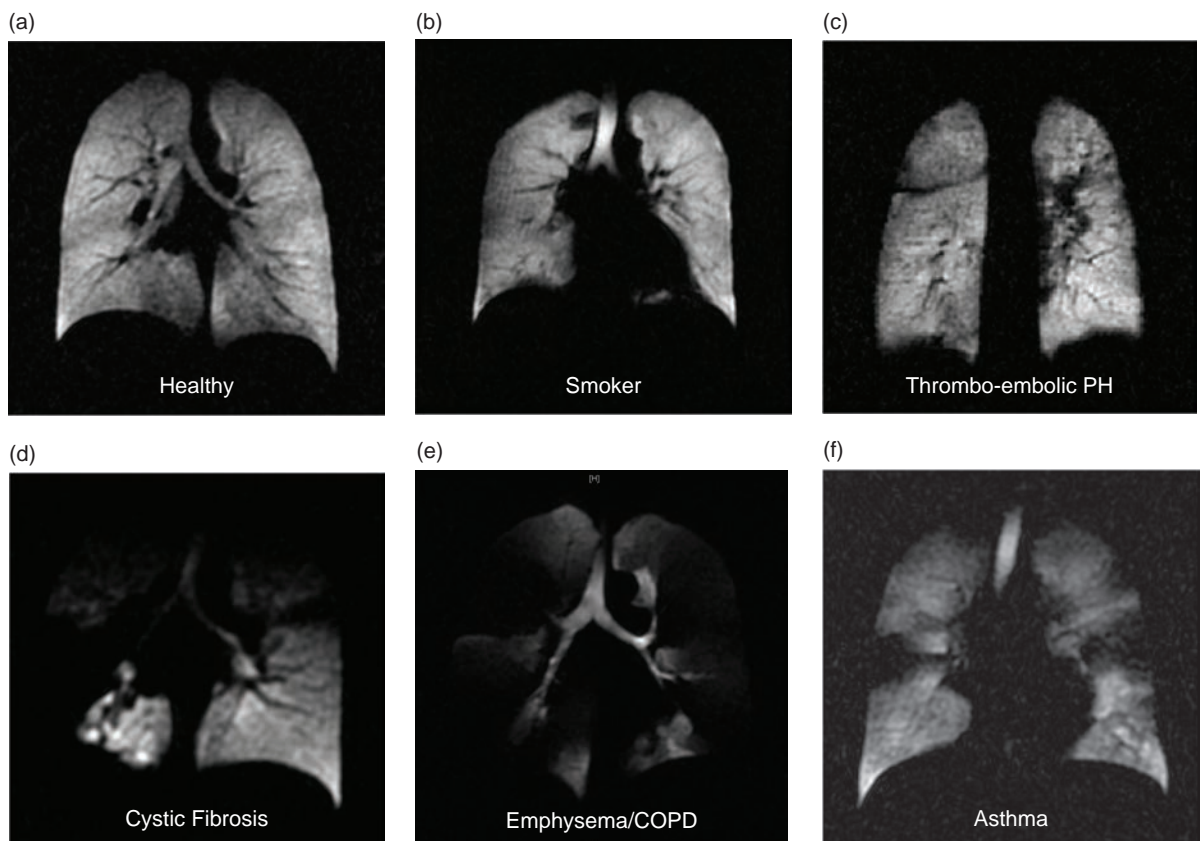


Figure 21.2 Hyperpolarized ^{3}He ventilation images acquired at breath-hold from subjects with different obstructive airway diseases. Courtesy of Prot. Jim Wild, University of Sheffield, UK.

Hyperpolarized ^{13}C Using DNP

Hyperpolarized ^{13}C is of particular interest for characterizing tumour metabolism. Malignant cancer cells have a metabolism some 200 times greater than normal cells, which is demonstrated by the high uptake of a radioactive form of glucose in Positron Emission Tomography (PET) imaging. In normal tissue, in the presence of oxygen, glucose is converted into pyruvate which in turn is metabolized in the tricarboxylic acid cycle (TCA) to produce ATP, the molecule that supplies energy for cell metabolism. This is a process known as oxidative phosphorylation. Without oxygen, pyruvate is converted to lactate in a process known as anaerobic, i.e. without oxygen, glycolysis catalysed by the enzyme lactate dehydrogenase (LDH). However, in cancer cells aerobic glycolysis occurs, i.e. the majority of the pyruvate is converted into lactate even in the presence of

oxygen. This is known as the Warburg effect. This conversion of glucose into lactate can be decreased in tumours undergoing cell death induced by chemotherapy.

The only hyperpolarized ^{13}C human study to date has used ^{13}C -labelled pyruvate which has a sufficiently long T_1 (approx. 30 s) to demonstrate elevated $[1-^{13}\text{C}]\text{lactate}/[1-^{13}\text{C}]\text{pyruvate}$ ratios in regions of biopsy-proven prostate cancer. Although used in a number of animal studies, the paucity of clinical studies is due to the challenges in producing a sterile hyperpolarized agent such as $[1-^{13}\text{C}]\text{pyruvate}$ that can be injected into patients. This first human study required a 'clean-room' adjacent to the MRI system in order to prepare the sterile fluid paths (SFP) containing the sample and then to rapidly quality control (QC) the agent between dissolution and injection. Recently a standalone DNP polarizer, designed for

sterile use, has become commercially available. Although the single-use SFP requires filling in a clean environment, afterwards it can be stored at -20°C (to keep the pyruvate frozen) prior to insertion into the polarizer. Once polarized the system also provides a non-contact QC system. The system automatically fills a standard power injector syringe which is then quickly passed into the magnet room and injected into the subject.

21.4 MR-PET

Combined MR-PET is a natural extension of the wide commercial availability of PET-CT. There is, however, a number of challenges and opportunities associated with MR-PET. The main issue is the PET detector assembly. In a PET-CT 511 keV γ -ray photons hit an inorganic scintillation crystal which creates tens of thousands of optical photons, a flash of light known as a ‘scintillation’. The scintillation crystal is coupled to a photo-detector, typically a photomultiplier tube (PMT) that converts the scintillation to an electrical current. In a PMT the optical photons strike a photocathode surface that releases a small number of electrons. These are then accelerated within a vacuum tube, hitting further electrodes (dynodes) that release more electrons, causing a massive cascade. After several dynode stages a large number of electrons hit the anode, resulting in a measurable current pulse. Unfortunately PMTs are very sensitive to magnetic fields. One manufacturer’s approach is to have a physical separation between the MRI magnet and the PET detector ring containing the PMTs. The common patient table can be directly moved out of the MRI scanner and into the PET detector, allowing for sequential imaging. Other manufacturers have opted for systems whereby the PET detector is positioned inside the MRI magnet for true simultaneous PET-MR (see Figure 21.3). This has required the development of magnetic field insensitive photo-detectors. The most widely used technology is that of the Avalanche Photo Diode (APD) which is essentially a semiconductor version of a PMT, although it has a much lower gain. More recently silicon photomultipliers have been developed which are essentially many APDs connected in parallel, resulting in a higher sensitivity and response speed.

A further challenge in PET-MR is the attenuation correction. PET works by coincidence detection of two γ -rays being produced 180° apart when an electron annihilates with a positron. Attenuation is when the two coincidence events do not get recorded within a very short period of each other due to either γ -ray getting absorbed in the body or scattering outside the detector FOV. This loss of photons increases the noise in the PET image as well as causing artefacts and distortions. The attenuation of photons can be corrected if the tissue density is known. In PET-CT the CT not only provides a high-resolution anatomic image, onto which the lower-resolution PET image can be overlaid, but it also provides a direct measurement of tissue radiodensity, i.e. the Hounsfield scale. The signal intensity in MRI, of course, has nothing to do with tissue radio-density, hence an active area of development for PET-MR is in deriving attenuation correction maps from MRI data. The main approaches to date have been to use different pulse sequences, e.g. Dixon techniques, to identify different tissues such as fat, water, lung and air and then assign them appropriate attenuation coefficients. Bone has a very high attenuation and some groups have attempted to register the MR data to CT bone atlases to derive a pseudo-CT for each patient. Ultra-short TE (UTE) sequences have been used in an attempt to identify bone directly from MR images. As well as



Figure 21.3 PET-MRI system: the Siemens Biograph with cutaway to show the PET detector ring. Courtesy of Siemens Healthcare.

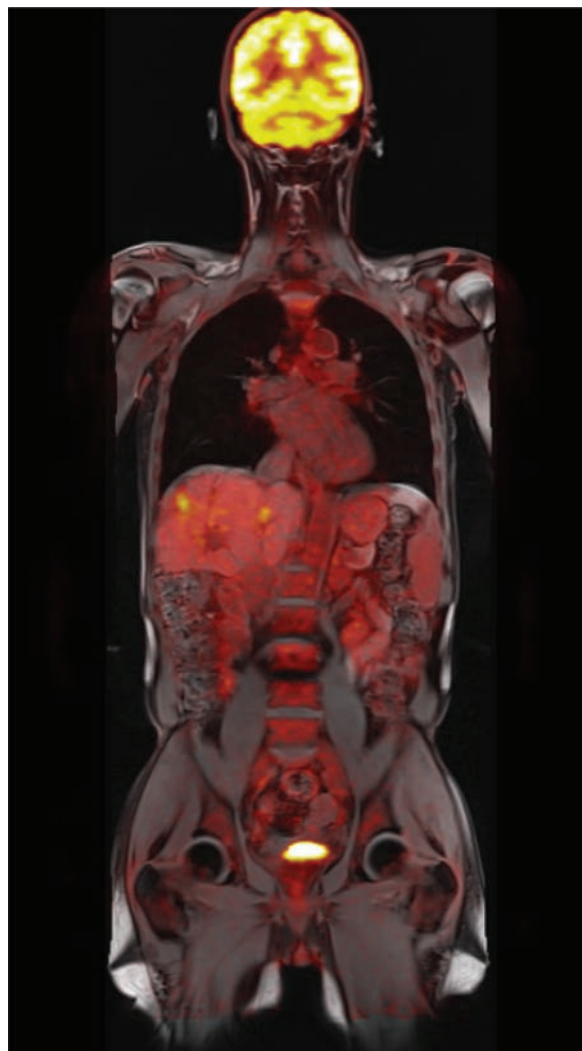


Figure 21.4 PET-MRI: ^{18}F -FDG injected dose 370 MBq, uptake time 60 min, overlaid on T_1 fat sat coronal showing established liver disease with multi-focal areas of increased FDG uptake along intrahepatic biliary ducts. Courtesy of Dr Anna Barnes, University College Hospital, London.

tissue attenuation it is also necessary to account for the attenuation caused by the RF coils and other high-density materials, e.g. the patient table. Rigid structures, like head coils, whose position is fixed in the scanner bore, can be imaged using CT and the attenuation maps incorporated into the patient-specific maps. Flexible coils that can be freely positioned present additional challenges in identifying their location. Again UTE sequences may help to identify coil structure in the FOV.

Finally patients in PET-CT are usually scanned with their arms above their head so that the arms do

not contribute to the tissue attenuation. The reduced bore size in PET-MR means that this is not generally possible. If the arms are not fully covered in the MR field-of-view then the attenuation maps may be incomplete: this is known as truncation artefact and the manufacturers have developed various methods to try to address this problem.

21.5 MR-LINAC

Conformal radiotherapy (RT) relies upon accurate 3D localization of the cancer and surrounding healthy tissue. Currently CT is the modality of choice for RT planning as it provides 3D images and information on the electron density required for accurate radiation dosimetry. However, its discrimination of soft tissue is inferior to MRI and, while fast, lacks some of the latter's advanced motion correction options such as navigator echoes. Internal organ motion, mainly from respiration, is a major problem in RT, as a larger volume of tissue has to be treated to ensure that the treatment area is fully covered. MRI's superior soft tissue information and motion correction options could enable a reduction in the treatment volume, thus sparing adjacent healthy tissue. Further benefit may derive from the ability to utilize advanced MR techniques to plan and monitor the response to treatment in real time.

The challenges of combining a Linear Accelerator (Linac) with an MRI scanner are significant, given the requirement for the fine control of high-energy (6 MeV) electron beams for accurate treatment. These are accelerated using microwave technology and then bent and field-shaped magnetically. Usually a Linac would be sited in a region of very low (earth's) magnetic field (see Table 2.1), so considerable modifications are required in order for it to operate in the region of the scanner's field! One feasible design is to use a split bore magnet, with the Linac mounted in the gap (see Figure 21.5), while in another, the Linac is mounted on the magnet axis. Some designs even have a rotating patient couch. Other challenges for the MR component are similar to those encountered in PET-MR – a need to be able to account for the attenuation of the tabletop and coils. Ultra-short TE (UTE) imaging may be useful in this respect and also in its ability to image bone directly.

At the time of writing a number of prototype systems are in existence and are currently undergoing pre-clinical commissioning.

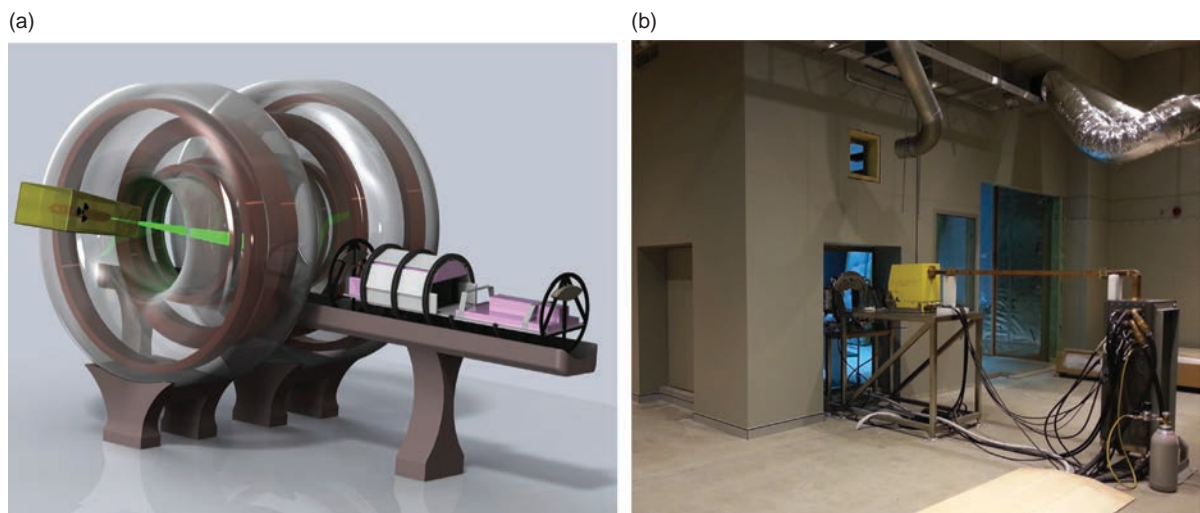


Figure 21.5 (a) Artist's impression of MR Linac; (b) the actual Linac bunker. Courtesy of Gary Liney and Brendan Whelan as part of the Australian MR-Linac program.

Further Reading

Feinberg DA and Yacoub E (2012) 'The rapid development of high speed, resolution and precision in fMRI'. *Neuroimage* 62:720–725.

Kauczor H-U (ed.) (2000) 'Special issue: hyperpolarised gases in MRI'. *NMR Biomed* 13(4):173–264.
Stafford RJ (2004) 'High field MRI: technology, applications, safety, and limitations'. American Association

of Physicists in Medicine, 46th Annual meeting. Available from www.aapm.org/meetings/04AM/pdf/14-2351-12342.pdf [accessed 8 May 2015].

Appendix: maths revision

Many people find maths challenging and are very happy to drop it after school. This appendix contains simple descriptions of the main mathematical concepts that will help you to understand MRI. These are:

- vectors;
- sine and cosine waves;
- exponentials;
- complex numbers;
- simple Fourier analysis.

A.1 Vectors

A vector quantity is one that has both magnitude and direction. For example, velocity describes the rate of movement in a particular direction (in comparison, speed is a scalar quantity which just measures the rate of travel). Vectors are commonly depicted using arrows with the length denoting the magnitude. They can be added together by putting the arrows end-to-end and then joining the start and end points, creating the resultant vector. Alternatively a vector may be divided into components along the x , y and z axes in any frame of reference (Figure A.1).

In equations vectors are either shown with little arrows over the top (like this \vec{M}) or in bold typeface (\mathbf{M}). In this book we have used the bold notation, but only in equations where the vector directions are important. Components of vectors can be denoted by their magnitude and unit vectors \mathbf{i} , \mathbf{j} and \mathbf{k} along the three directions. Vectors can be multiplied together using either the dot product (which has a scalar result) or the cross product (which has a vector result).

$$\mathbf{A} = A_x \mathbf{i} + A_y \mathbf{j} + A_z \mathbf{k}$$

$$\mathbf{A} \cdot \mathbf{B} = AB \cos \theta = A_x B_x + A_y B_y + A_z B_z.$$

$$\begin{aligned}\mathbf{A} \times \mathbf{B} = -\mathbf{B} \times \mathbf{A} &= (A_y B_z - A_z B_y) \mathbf{i} + (A_z B_x - A_x B_z) \mathbf{j} \\ &\quad + (A_x B_y - A_y B_x) \mathbf{k} = AB \sin \theta \mathbf{n}\end{aligned}$$

where θ is the angle between the two vectors, and \mathbf{n} is a unit vector perpendicular to both A and B .

A.2 Sine and Cosine Waves

The simplest waves are pure sine or cosine waves, which have the same shape but are shifted with respect to each other (Figure A.2a). They have three basic properties: the amplitude is the peak height (how large it is), the frequency, measured in hertz (Hz), describes how rapidly in time the magnitude of the wave is changing, and the phase describes where we are within the cyclic variation.

A unit vector rotating around a circle produces sine and cosine components along the x and y axes (Figure A.2b), and this gives us an easy way of thinking of phase, which is just the angle between the unit vector and the

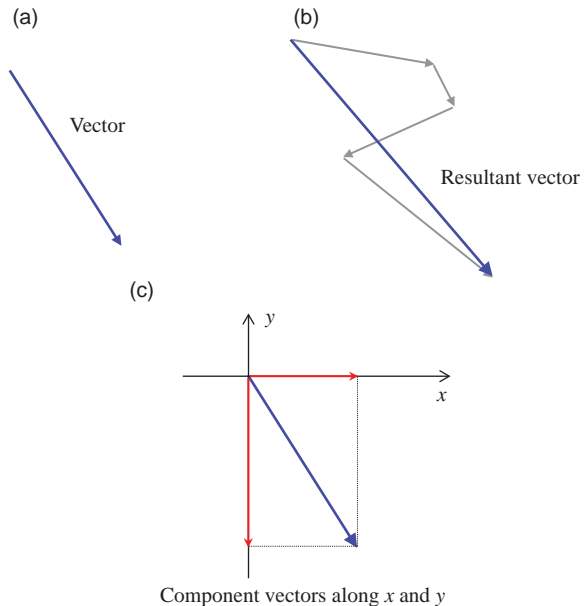


Figure A.1 (a) A vector is shown as an arrow. (b) Several vectors can be joined together end-to-end to create the resultant vector. (c) A vector can be broken down into components along principal axes.

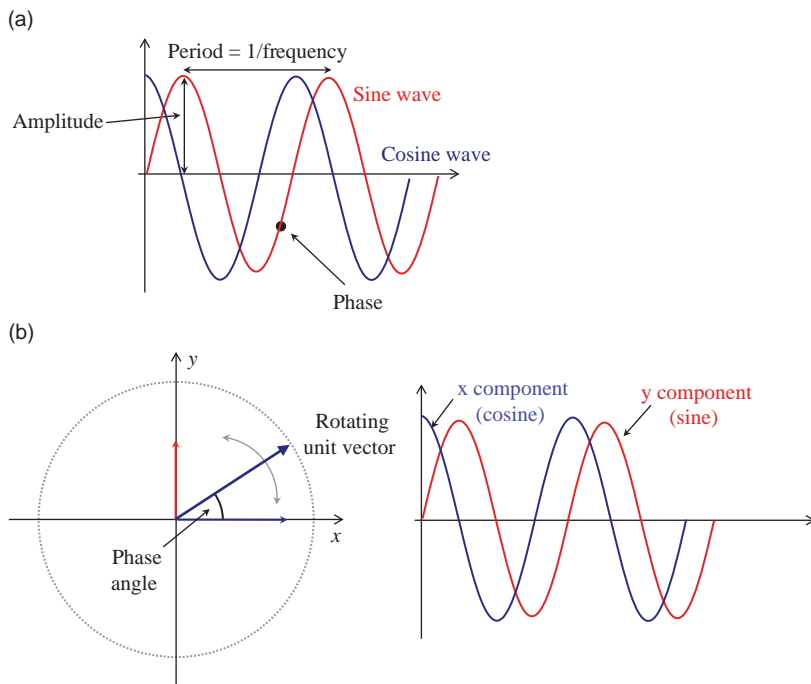


Figure A.2 (a) A wave has amplitude, frequency and phase. A cosine wave differs from a sine wave by a phase angle of 90° . (b) A rotating unit vector creates two waves along the x and y axes.

reference axis. Phase angles can vary from 0° to 360° , and angles larger than 360° just overlay themselves.

Angles around the circle can also be measured in radians, with the full 360° being equal to 2π rads. π (pronounced ‘pie’) is the ratio of the circumference of a circle to its diameter, and is approximately equal to 3.14. There are some important angles to know: $\pi/2$ is 90° , π is 180° , and in general $2n\pi$ is in line with 0° .

A.3 Exponentials

Exponentials are rather difficult to explain but you really only need to know some important properties of these useful numbers. They are based on the number e which is approximately equal to 2.718. In equations exponentials may be denoted either as e^x or $\exp(x)$ – we have used the latter in this book – and x is known as the exponent. Exponentials are the inverse of natural logarithms (denoted \ln), and in particular if $y = \exp(x)$ then $\ln(y) = x$.

Let’s start with some general results for exponentials:

$$\begin{aligned}\exp(-x) &= \frac{1}{\exp(x)} \\ \exp(x)\exp(y) &= \exp(x+y) \\ \exp(0) &= 1 \\ \exp(\infty) &= \infty \\ \exp(-\infty) &= 0\end{aligned}$$

In MRI we are particularly interested in exponential decays, $\exp(-x)$, which reduce down to zero (see Figure A.3). This not only describes radioactive decay and the free induction decay in MRI, it also shows how the temperature of a cup of coffee drops – fast at first but getting slower and slower until it is stone cold. In contrast, exponential growth, when the exponent is positive, just keeps getting bigger and bigger – like the world’s population!

A.4 Complex Numbers

Complex numbers have a real part and an imaginary part. The imaginary part is multiplied by i , the square root of -1 , so a complex number can be written as

$$A = R + iI$$

The complex conjugate of A is defined by

$$A^* = R - iI$$

so when A is multiplied by its complex conjugate the result is a pure real number

$$A \cdot A^* = R^2 - I^2$$

You may see j used instead of i , particularly in engineering textbooks. Of course in real life it is impossible to find the square root of a negative number, so the

imaginary parts don't really exist. However, complex numbers are useful for describing the rotational movement in MRI. We can define any point on the circle by a complex number

$$A = x + iy = \cos \theta + i \sin \theta$$

We can use a complex exponent to define the rotational operator $\exp(i\theta)$, so that

$$\exp(i\theta) = \cos \theta + i \sin \theta$$

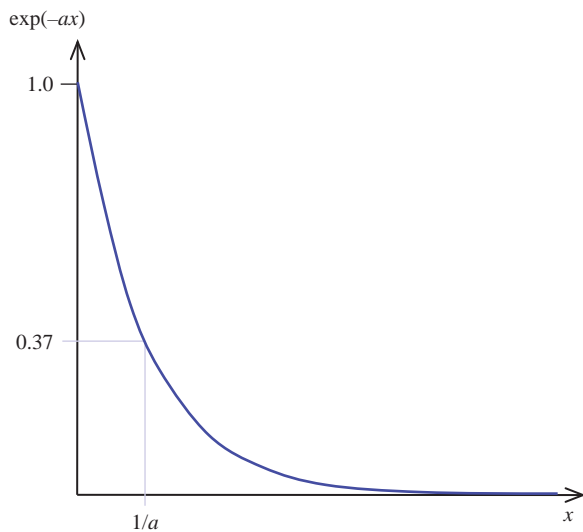


Figure A.3 Exponential decay describes spin–spin relaxation in MRI as well as radioactive decay.

and if we use $\theta = \omega t / 2\pi$, we can denote a rotating vector as $\exp(i\omega t / 2\pi)$, which allows us to combine any number of rotational movements simply by adding their exponents.

A.5 Simple Fourier Analysis

Fourier's theorem states that any complex waveform can be created from a sum of sine and cosine waves with appropriate frequencies and amplitudes. We write this as

$$s(x) = \frac{a_0}{2} + \sum_{n=1}^{\infty} (a_n \cos nx + b_n \sin nx) = \sum_{n=-\infty}^{\infty} a_n \exp(inx)$$

where a and b are the amplitudes and $i = \sqrt{-1}$. For MRI the most important feature of Fourier analysis is the Fourier transform, which is defined by the equations

$$S(k) = \int_{-\infty}^{\infty} s(x) \exp(-i2\pi kx) dx$$

$$s(x) = \int_{-\infty}^{\infty} S(k) \exp(i2\pi kx) dk$$

Although these integrals look nasty, you don't have to work them out, you just need to recognize them. $S(k)$ and $s(x)$ are functions of k and x respectively, called a Fourier transform pair, and k and x have an inverse relationship. Some important Fourier transform pairs are shown in Figure A.4. In MRI, x is real space and k

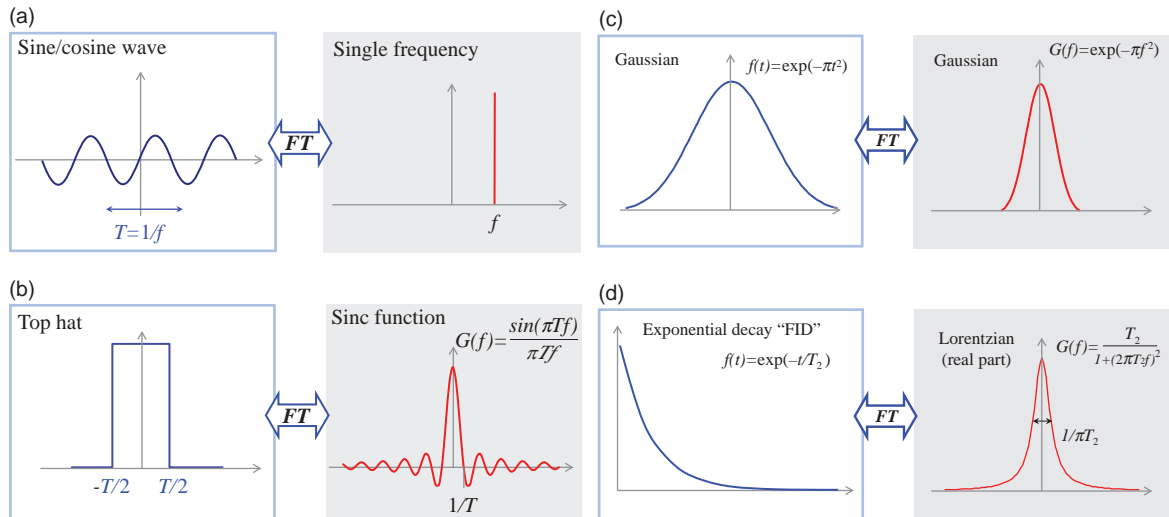


Figure A.4 Some important Fourier transform pairs. (a) A simple sine wave with frequency f has a period T , and its Fourier transform is a spike function at frequency f . (b) The FT of a top-hat function with width $2T$ is a sinc function, with the first zero crossing points at $1/T$. (c) A Gaussian function transforms to another Gaussian, and finally (d) an exponential decay transforms to a Lorentzian function.

is spatial frequency. Another useful Fourier transform pair is time t and frequency f . A two-dimensional Fourier transformation involves integration over two directions and 3D FT is over all three:

$$S(k_x, k_y) = \iint_{x,y} s(x, y) \exp(-i2\pi k_x x) \exp(-i2\pi k_y y) dx dy$$

$$S(k_x, k_y, k_z) = \iiint_{x,y,z} s(x, y, z) \exp(-i2\pi k_x x) \exp(-i2\pi k_y y) \exp(-i2\pi k_z z) dx dy dz$$

A.6 Some Useful Constants

The Boltzmann constant	k_B	$1.38 \times 10^{-23} \text{ J K}^{-1}$
Planck's constant	h	$6.63 \times 10^{-34} \text{ J s}$
	$\hbar = \frac{h}{2\pi}$	$1.05 \times 10^{-34} \text{ J s}$
Proton gyromagnetic ratio	γ	$2.68 \times 10^8 \text{ rad s}^{-1} \text{ T}^{-1}$
	$\gamma_1 = \frac{\gamma}{2\pi}$	42.57 MHz T^{-1}

Cambridge University Press

978-1-107-64323-9 — MRI from Picture to Proton

Donald W. McRobbie, Elizabeth A. Moore, Martin J. Graves, Martin R. Prince

Index

[More Information](#)

Index

Locators in *italic* refer to figures: Locators in **bold** refer to tables

Numbers are filed as spelled out e.g. 3D. *see* three dimensional

- abdominal imaging 52–53, 52, 78–80, 335
- absorption spectrum, MR spectroscopy 288
- access to MR suite, induction of new staff 12–13, 12
- accuracy, quantitative MRI 341–343, 342–343
- acoustic noise 15, 153–154, 350. *see also* hearing protection
- acronyms x–xix, 2, 41, 254, 255
- ACS (auto-calibration scans) 95, 229, 232–234, 233
- action values (AV), occupational exposure 354
- active implants, contraindications 18
- active shimming 148
- ADC. *see* analogue-to-digital converter
- ADC. *see* apparent diffusion coefficient
- adiabatic RF pulses 92, 192, 194–195, 195
- adverse patient reactions, contrast agents 15–16. *see also* safety
- AIF (arterial input function), dynamic CE-MRI 313, 319, 335
- AIMDs (active implants) 18
- air conditioning 163–164
- alcoholic steatohepatitis 335
- α (alpha) flip angles 27
- Alzheimer’s disease, MR spectroscopy 289. *see also* dementia patients
- American Association of Physicists in Medicine (AAPM), quality control standards 166–169
- American College of Radiology (ACR) guidelines, access to MR suite 12–13, quality control standards 166–169, 172, 172
- American Society for Testing and Materials (ASTM), medical implants risk categories 18–19, 19
- amide proton transfer (APT) 140, 141
- amplifiers 153–155, 155
- analogue-to-digital converter (ADC) 55, 56. *see also* signal digitization
- aneurysm clips, safety 17
- angiography. *see* magnetic resonance angiography
- animal experiments, bio-effects of MRI 351
- anisotropy, diffusion-weighted imaging 306–308
- anti-parallel, protons 125
- APD (avalanche photo diode) 362
- apodization, MR spectroscopy 288
- apparent diffusion coefficient (ADC) hyperpolarization 360–364
pulsed gradient spin-echo method 304, 304–305, 306
quantitative MRI 326, 334, 334
- apparent spin–spin relaxation time 27, 36, 330–331
- APT (amide proton transfer) 140, 141
- ARC (auto-calibrating reconstruction for Cartesian imaging) 229, 234–235
- arrays, radiofrequency coils 13–14
- arrhythmia rejection period (ARP), cine cardiac imaging 275–276, 276
- artefacts, image 101. *see also* motion artefacts
- cardiac MRI 269
- definitions 26, 81
- diagnostic flow chart 100, 101
- digital imaging 55, 60, 61, 81, 92–96
- echo planar imaging 203–204, 203–204
- equipment artefacts 98–101, 99
- fat-based tissues 88–92, 89–91
- Fourier imaging 119–120
- metal 16, 19, 31, 96–98, 96–98
- MR-PET 362–363
- parallel imaging 238
- quality control/assurance 178, 178–179
- rework gradient echo 215, 215
- susceptibility effects 96–98, 96
- turbo spin echo 48
- arterial input function (AIF), dynamic CE-MRI 313, 319, 335
- arterial spin labelling (ASL) 311, 314–316, 315–316, 335
- arterio-venous malformations (AVMs) 38, 323–324
- ASSET parallel imaging 227, 229
- astrocytoma, clinical fMRI 323–324
- attenuation, MR-PET 362–363
- auto-calibration scans (ACS) 95, 229, 232–234, 233
- ARC (auto-calibrating reconstruction for Cartesian imaging) 229, 234–235
- auto-SMASH (simultaneous acquisition of spatial harmonics) 232–234, 233
- AV (action values), occupational exposure 354
- avalanche photo diode (APD) 362
- averaging parameters, image optimization 73–76, 75
- B_1 transmit fields, mapping 155–156, 157
- babies, possible contraindications 18
- back-emf, eddy currents 152–153
- balanced FFE rework gradient-echo pulse sequences 53
- balanced steady-state-free-precession (bSSFP) 261–263, 262, 273
- bandwidth, image optimization 72, 74, 78
- baseline roll, MR spectroscopy 288, 297
- basic restriction (BR), occupational exposure 353, 354, 354
- bellows, motion artefacts 82, 83
- best practice 166. *see also* guidelines; quality control/assurance; standards
- bias, quantitative MRI 341–343, 342–343
- biliary system, MR cholangiopancreatography 48. *see also* liver
- binomial pulses, inversion recovery turbo spin echo 194

Cambridge University Press

978-1-107-64323-9 — MRI from Picture to Proton

Donald W. McRobbie, Elizabeth A. Moore, Martin J. Graves, Martin R. Prince

Index

[More Information](#)

Index

- bio-effects of MRI 345, 356. *see also* safety
 burns 15, 23, 345
 contrast agents 354–355, 355–356
 gradient field effects 347–351,
 349–350, 351
 induction of new staff 15–16
 magnetic field exposure 345
 occupational exposure 352–354, 353,
 354
 pregnancy 18, 345, 351–352, 356
 radiofrequency exposure 345–348,
 346, 347–348
 static field effects 351–352, 352
- Biomedical Informatics Research Network (BIRN) 179–180,
 180–181
- biopsy, image-guided 164
- birdcage transmitter coils 157–159,
 157
- black blood preparation, cardiac MRI
 272–273, 272
- black line artefacts 89–91, 90
- BLADE, radially-acquired TSE 48
- BLAST (broad-use linear acquisition speed-up technique) 240–242,
 242–243
- blipped single-shot GE-EPI 223
- Bloch, Felix 3–4, 5
- Bloch equations 136–137
- block design paradigms,
 fMRI 320–321, 321
- Bloembergen, Nicolaas 3–4, 5. *see also* BPP theory of relaxation
- blog, radiographer's 23
- blood flow. *see* flow effects; magnetic resonance angiography
- blood suppression, cardiac
 MRI 272–273, 272
- blurring, image 248, 248
- B_0 . *see* static magnetic fields
- body position. *see* positioning of patient
- body radiofrequency coils 13–14, 14
- BOLD (blood oxygenation level dependent) imaging 224, 303,
 319–325
- block design paradigms 320–321,
 321
- BOLD effect 320
- clinical 323–324, 324
- field strength 325
- haemodynamic delay and convolution 322–323
- interpretation 323, 323
- processing 321–322, 322
- Boltzmann constant 127, 129, 368
- bolus chase techniques, contrast-enhanced MRA 264, 265
- bore entrance, static field spatial gradients 16
- BPP theory of relaxation 3, 136, 139
- BR (basic restriction), occupational exposure 353, 354, 354
- brain imaging
 clinical examination 26
 clinical fMRI 323–324
 contrast 38
 dynamic susceptibility contrast MRI
 312–313
 high resolution 73
 image optimization 77, 77, 77
 MR spectroscopy 295, 296
 niche systems 164
 quantitative MRI 326
 spin-echo 46–47
 T₁-weighted imaging 29
 breast imaging 164, 297, 299
 breath-hold times 78–80, 79, 82, 240
 bridging gradients, acoustic noise 154
 broadband, digital radiofrequency transceivers 161, 162
 Brownian motion, diffusion-weighted imaging 304
 bSSFP (balanced steady-state-free-precession) 261–263, 262, 273
 bull's-eye plots, functional cardiac analysis 278
- burns, patient 15, 23, 345. *see also* heating of tissues
- CAIPIRINHA (controlled aliasing in parallel imaging results in higher acceleration) parallel imaging 235–236, 236
- calibration scans, sensitivity encoding 229
- cancer. *see* tumours
- carbon-13 301, 362–364
- cardiac gating, ECG monitoring 83–85,
 85, 85–86
- cardiac leads, contraindications 18
- cardiac MRI 5–6, 269. *see also* functional cardiac imaging
- coronary artery imaging 286–287
- k-t BLAST technique 242–243
- morphological imaging 272–273, 272
- motion artefacts 83–85, 85
- myocardial perfusion 282–284, 285
- myocardial viability 284–286, 286
- patient preparation 269–272, 270–271
- quantitative MRI 328, 329–330
- T₁-weighted 29
- tissue characterization 286
- cardiac pacemakers 18, 345, 352
- cardiac planes, functional cardiac imaging 273–274, 274
- cardiac viability 284–286, 286
- Carr-Purcell echo train, quantitative MRI 330
- Carr-Purcell-Meiboom-Gill sequence (CPMG) 186, 330, 330
- cartilage relaxometry, quantitative MRI 333, 333–334
- cavernous angiomas, time-of-flight angiography 257–258, 258
- CE-MRA. *see* contrast-enhanced magnetic resonance angiography
- cerebral blood flow (CBF), perfusion-weighted imaging 311
- cerebral blood volume (CBV), perfusion-weighted imaging 311
- cerebrospinal fluid (CSF) 26–28, 28
- checklists, staff safety questionnaire 16
- chemical exchange saturation transfer (CEST) imaging 140, 141
- chemical saturation 91–92, 91
- chemical shift artefacts 88–89, 89, 92,
 178–179
- chemical shift effect, MR spectroscopy 295
- chemical shift imaging (CSI) 295,
 297–302, 299–301
- chemical shift selective (CHESS) pulses 91–92, 291
- cholangiopancreatography 48, 196–198
- choline, MR spectroscopy 289, 289,
 299, 299
- chords, functional cardiac analysis 278
- cine cardiac imaging 273. *see also* functional cardiac imaging
- balanced steady-state-free-precession 273
- k-t BLAST technique 242–243
- myocardial viability 284–286, 286
- prospective and retrospective, 275–276, 276, 276
- real-time 277–278
- segmented k-space imaging 274,
 275
- cine phase contrast (CPC) 278–281, 280
- Circle of Willis, MR angiography 39
- circulation time, contrast-enhanced MRA 263, 264
- CISS (constructive interference in steady state) 218
- classical mechanics, nuclear magnetic resonance 124–125, 125
- claustrophobia, patients 22–23
- clinical applications
 magnetic resonance 6
 MR elastography 341, 341
 MR spectroscopy 295
 parallel imaging 240
 radial imaging 245, 246

Cambridge University Press

978-1-107-64323-9 — MRI from Picture to Proton

Donald W. McRobbie, Elizabeth A. Moore, Martin J. Graves, Martin R. Prince

Index

[More Information](#)

Index

clinical examples. *see specific organs/systems*
CNR. see contrast-to-noise ratio
 cochlear implants, contraindications 18
 coherence, gradient echo 207–211, 210–211, 217
 coils
 cardiac MRI 271
 image optimization 77
 quality control/assurance 172–173, 172
 selection 22
 complex numbers, mathematics of 366–367
 composite RF pulses, inversion recovery turbo spin echo 194
 compressed sensing (CS), parallel imaging 248–250, 249–250
 computed tomography (CT) 2, 242–243
 computer room, layout 11, 12
 computer systems, MR 162–163
 concatenations 76
 constants, mathematics of 368
 constrained spherical deconvolution 308
 constructive interference in steady state (CISS) 218
 continuous analogue signals 55, 55
 contraindications 11, 18–19, 356. *see also pregnancy*
 contrast 26–27, 26, 30, 40. *see also contrast-enhanced magnetic resonance angiography; dynamic contrast-enhanced MRA; dynamic contrast-enhanced MRI angiography* 38–39, 38–39
 clinical examinations 27, 30–31, 36, 38
 diffusion weighted images 39–40, 39
 FLAIR images 28, 28
 gradient-echo sequences 35–37, 35
 image optimization 68, 69, 71
 inversion recovery sequences 33–35, 34
 PD-weighted images 32–33, 33
 quality control/assurance 166, 177–178
 spin-echo images 33
 STIR images 30–31, 30
 T₁-weighted images 28–29, 29, 36
 T_{2*}-weighted images 36–37
 T₂-weighted images 27–28, 28
 technical information 30–31, 32–33
 terminology 27
 contrast agents 37. *see also gadolinium-based contrast agents*
 bio-effects/safety 15–16, 354–355, 355–356

contrast-enhanced MRA 267
 future of 358
 handling patients 22–23
 history 2
 manganese 141
 relaxivity 142–143
 super-paramagnetic iron oxide 37, 141
 contrast-detail detectability, test 178, 178
 contrast-enhanced magnetic resonance angiography (CE-MRA) 251, 255, 258–260, 260, 263–267
 contrast-to-noise ratio (CNR)
 image optimization 67, 67, 68–71, 71, 73–76
 quality control/assurance 166, 177–178
 control room, layout of MR suite 11, 12
 cooling systems, siting and installation 163–164
 corduroy artefacts 99–101, 99
 coronary artery imaging, cardiac MRI 286–287
 cosine waves, mathematics of 365–366, 366
 counselling, patients 21–23
 CPC (cine phase contrast) 278–281, 280
 CPMG (Carr–Purcell–Meiboom–Gill sequence) 186, 330, 330
 crash trolley, adverse patient reactions 15–16
 creatine, MR spectroscopy 289, 289, 299, 299
 cross-talk/cross-excitation artefacts 93, 93
 crusher gradients, inversion recovery turbo spin echo 193, 194
 cryogenic cooling fluids 13, 15
 CS (compressed sensing), parallel imaging 248–250, 249–250
 CSF (cerebrospinal fluid) 26–28
 CSI. *see chemical shift imaging*
 CT (computed tomography) 2, 242–243
 CUBE three dimensional spin echo 48, 43–44
 Curie, Marie and Pierre 1
 current changes, eddy currents 152, 152–153
 Damadian, Raymond 2, 2
 dark blood preparation, cardiac MRI 272–273, 272
 data acquisition systems (DAS) 120–121, 120, 162–163, 122
 data analysis, functional cardiac imaging 278, 278–279
 DE (driven equilibrium) 48, 49, 196, 197
 delayed interval echo train (DIET) 191
 dementia patients, MR spectroscopy 290, 293–294
 DENSE (displacement encoding with stimulated echoes) 282
 dephasing, spatial encoding 105–106, 105
 DESPOT. *see driven equilibrium single pulse observation*
 DESS (double echo steady state), gradient echo 218, 218
 diamagnetic materials 19, 21, 352
 diameter of a spherical volume (DSV) 148
 diamond SENSE (sensitivity encoding) 236
 DICOM. *see digital imaging and communications in medicine*
 DIET (delayed interval echo train) 191
 diffusion imaging 5
 diffusion parameters. *see apparent diffusion coefficient*
 diffusion-tensor imaging (DTI) 306–308, 307–308
 diffusion-weighted MRI (DW-MRI) 303–309, 309
 apparent diffusion coefficient 304, 306, 304–305
 clinical examinations 38
 contrast 39–40, 39
 diffusion-tensor imaging 306–308, 307–308
 echo planar imaging 310
 fractional anisotropy 307
 mathematics of 307
 molecular motion 303, 304
 pulsed gradient spin echo method 304–306, 305
 sequence options 308–309, 310
 tractography, constrained spherical deconvolution 308
 whole-body diffusion 310
 diffusion-weighted whole-body imaging with background suppression (DWIBS) 309, 310
 digital imaging artefacts 55, 60, 61, 81, 92–96
 digital imaging and communications in medicine (DICOM) 62–63, 169
 digital radiofrequency transceivers 155, 161, 161–162
 digitization of MR signal. *see signal digitization*
 DIR (double inversion recovery), cardiac MRI 272–273, 272
 direct signal digitization 57
 discrete data, signal digitization 55, 56

Index

- dispersion spectrum, MR spectroscopy 288
- distortion, quality control 173–174, 173–174
- Dixon, W. Thomas 213–214
- Dixon scans 336–338, 339, 362
- DNP (dynamic nuclear polarization) 360
- dobutamine 284
- Doppler effect 2
- double echo steady state (DESS), gradient echo 218, 218
- double inversion recovery (DIR), cardiac MRI 272–273, 272
- double oblique slices/orientations 108
- double-sideband excitation 237
- doublets, MR spectroscopy 288–289
- driven equilibrium (DE) 48, 49, 196, 197
- driven equilibrium single pulse observation (DESPOT) 327–329, 331
- DSC-MRI. *see* dynamic susceptibility contrast MRI
- DSV (diameter of a spherical volume) 148
- DTI (diffusion-tensor imaging) 306–308, 307–308
- dual-echo imaging sequences, spin echo 186–188, 187, 189
- dual-TR method, transmit field mapping 156, 157
- duty cycles, gradient 151
- DW-MRI. *see* diffusion-weighted MRI
- DWIBS (diffusion-weighted whole-body imaging with background suppression) 309, 310
- dynamic contrast-enhanced MRA 264, 266–267
- dynamic contrast-enhanced MRI 303, 316–319, 317–319
- dynamic nuclear polarization (DNP) 360
- dynamic susceptibility contrast MRI (DSC-MRI) 311–314, 317, 335
- ear defenders 22
- early gadolinium enhancement (EGE), myocardial infarction 286
- ECG. *see* electrocardiogram
- echo amplitude, gradient-echo pulse sequences 210–211
- echo formation, gradient-echo pulse sequences 207–211
- echo planar imaging (EPI) 5, 43–44, 54, 303
- diffusion-weighted imaging 310
- future of 358
- gradient-echo-based 222–224, 223
- manufacturer comparison chart 50–51
- multi-shot 204–205, 204–206
- parallel imaging 238–239, 239–240, 240
- peripheral nerve stimulation 348
- spin-echo-based 201–204, 202–204
- echo-spacing (ESP), segmented k-space imaging 274
- echo time (TE) 27, 30–31, 32–33, 41, 42, 44
- echo train, turbo spin echo 187, 187–188, 190, 190
- echo train length (ETL), functional cardiac imaging 274, 276–277, 276
- ECR (European Congress of Radiology) 164
- eddy currents, magnetic field gradients 152, 152–153
- Edelstein, W. A. 3
- edge response function (ERF), quality control 175–176, 175
- EGE (early gadolinium enhancement), myocardial infarction 286
- ejection fraction (EF), functional cardiac imaging 278
- elastic modulus 339–340, 340
- elastography. *see* magnetic resonance elastography
- electric potentials, flow effects of MRI 351
- electrocardiogram (ECG) monitoring 23, 83–85, 85, 85–86
- electrocardiogram (ECG) triggering 15, 260–261, 261, 269–271, 270
- electromagnets 13, 147. *see also* magnetic fields
- ELF (extremely low frequency), bio-effects of MRI 347
- ELV (exposure limit values), occupational exposure 354
- EMA (European Medicines Agency) 354, 355–356
- emergencies, medical 15–17
- EMI (company) 3
- encoding. *see* spatial encoding
- energy states, Boltzmann constant 127, 129
- enterology, motion artefacts 86
- EPI. *see* echo planar imaging
- epidemiology, bio-effects of MRI 345, 351–352
- equipment, MR 144, 164–165
- basic components/architecture 145
- computer systems 162–163
- gradient subsystems 149–154, 150–153
- less common/alternative MRI systems 164
- magnets 144–149, 146–147, 149
- phase images 148
- radiofrequency system 154–158, 155–157
- RF receiver subsystems 158, 158–162, 160–161
- siting and installation 163–164
- equipment artefacts 98–101, 99
- Ernst, Richard 3–4, 5
- Ernst angles, spoiled gradient-echo pulse sequences 212, 212
- ESP (echo-spacing), segmented k-space imaging 274
- ETL. *see* echo train length
- European Concerted Action Research Project 166–169
- European Congress of Radiology (ECR) 164
- European Medicines Agency (EMA) 354, 355–356
- European Union Physical Agents Directive (electromagnetic fields) 352
- examination rooms 11, 12, 13
- examinations (programs) 41–42
- excitation RF pulses, technical information 30–31
- exponentials, mathematics of 366, 367
- exposure limit value (ELV), occupational exposure 354
- extravascular extracellular space (EES) imaging 317
- extremely low frequency (ELF), bio-effects of MRI 347
- eye-movements, bio-effects of MRI 351
- FA (fractional anisotropy) 306–308, 307, 309
- FAIR (flow-sensitive alternating inversion recovery) 314–316, 315
- family tree/classification, pulse sequences 42–43, 43, 50
- Faraday cages 13–14, 163
- Faraday induction, bio-effects of MRI 348, 349
- fast field echo (FFE) 53, 215. *see also* gradient echo; rewound gradient-echo pulse sequences
- fast imaging with steady precession (FISP) 53, 214–216, 216, 218, 218. *see also* rewound gradient-echo pulse sequences
- fast spin echo. *see* turbo spin echo
- faster scanning, clinical benefits 240. *see also* parallel imaging
- fat quantification 335–338, 336–339
- fat suppression/saturation artefacts 88–92, 89–91
- contrast 26
- inversion recovery turbo spin echo 196

quality control/assurance 178–179
 sequence options 42
 spin echo 186
 spoiled gradient echo 213
 turbo spin echo 189, 191
 fatalities, MRI 345, 352
 FBI (fresh blood imaging),
 non-contrast MRA 260, 261
 fBIRN. *see* Functional Biomedical
 Informatics Research Network
 FDA (Food and Drug Administration)
 356
 FE. *see* frequency-encoding
 ferromagnetic materials 16–19, 21, 352
 FFE. *see* fast field echo
 fibre-optic cables 56
 FID. *see* free induction decay
 field echo. *see* gradient echo
 field focused nuclear magnetic
 resonance (FONAR) 2
 field of view (FOV) 60
 blood flow artefacts 87, 88
 gradient non-linearity 99
 image optimization 71, 72–73, 76,
 78, 79
 phase wrap-around artefacts
 93–94, 94
 phased array coils 159
 rectangular 121, 122
 spatial encoding 116–117, 118
 fields, magnetic. *see* magnetic fields
 FIESTA rewound gradient-echo pulse
 sequences 53
 filling factors, phantoms 169–171,
 170–171, 173
 filter roll-off, signal digitization 57
 first-order gradient moment nulling
 252–253, 253
 first-order phase correction, MR
 spectroscopy 296, 298
 FISP. *see* fast imaging with steady
 precession
 fixed parameter option, modes 15
 FLAIR. *see* fluid attenuated inversion
 recovery
 FLASH, gradient-echo 52
 flashes of light, bio-effects of MRI 349
 flip angles
 alpha 27
 gradient echo 212
 spin echo 190, 190
 flood field phantoms 169
 flow artefacts 252–254, 253
 flow compensation artefacts 87,
 252–254, 253
 flow effects 38, 38–39
 conventional imaging 251–254,
 252–253
 electric potentials 351

motion artefacts, 86–88, 87
 flow imaging 278–281, 280–283. *see*
 also magnetic resonance
 angiography
 flow-sensitive alternating inversion
 recovery (FAIR) 314–316, 315
 fluid attenuated inversion recovery
 (FLAIR) 43, 192
 contrast 28, 28
 half Fourier single-shot TSE 196
 pulse sequences 47
 slice interleaving 192
 fluorescent screens 2
 fluorine, MR spectroscopy 301–302
 fluoro-triggered contrast-enhanced
 MRA 255
 flux density. *see* magnetic field strength
 fMRI. *see* BOLD (blood oxygenation
 level dependent) imaging
 foldover suppression option, phase
 wrap-around artefacts 93
 FONAR (field focused nuclear
 magnetic resonance), history 2
 four dimensional (4D) contrast-
 enhanced MRA 255, 264, 266–267
 Fourier analysis 59–60
 mathematics of 367, 367
 MR spectroscopy 288, 296
 non-rectangular slice profiles 94
 spatial encoding 103, 106, 107,
 110–111, 116–120, 117–118
 FOV. *see* field of view
 fractional anisotropy (FA) 306–308,
 307, 309
 free induction decay (FID) 129, 130
 measuring 132–135, 133–134
 MR spectroscopy 288, 295–297,
 296–297
 frequency encoding (FE) 59–61, 61
 gradients 41, 102, 103
 spatial encoding 114–116, 115–116
 frequency-selective fat saturation
 91–92, 91
 fresh blood imaging (FBI), non-
 contrast MR angiography 260,
 261
 fringe magnetic fields 16, 144
 fringe field values/interference 17
 installation footprint 148–149
 magnetic field 16
 safety guidelines 20
 siting and installation 163–164
 full width at half maximum (FWHM)
 slice selection 93, 93, 175
 fully rewound gradient-echo pulse
 sequences 50–51, 255
 Functional Biomedical Informatics
 Research Network (fBIRN)
 179–180, 180

functional cardiac imaging 5, 7,
 273–282
 balanced steady-state-free-
 precession 273
 functional analysis 278, 278–279
 imaging planes 273–274, 274
 myocardial strain imaging 281–282,
 284
 prospective and retrospective cine
 imaging 275–276, 276
 quantitative velocity 278–281,
 280–283
 real-time cine imaging 277–278. *see*
 also cine cardiac imaging
 segmented k-space imaging 274, 275
 view sharing 276–277, 277
 functional MRI (fMRI). *see* BOLD
 imaging
 future of MRI 358
 hyperpolarization 360–362, 359,
 361
 MR-LINAC 363, 364
 MR-PET 362–363, 362–363
 7 tesla systems 358–360, 359
 FWHM. *see* full width at half
 maximum

gadolinium-based contrast agents
 15–16, 29, 37, 29
 bio-effects/safety 260, 354–355,
 355–356
 contrast-enhanced MRA 267
 handling patients 23
 resonance and relaxation 141–143,
 142
 spoiled gradient echo 52–53
 T₁-weighted 29, 29

gamma camera, history 2
 gating, cardiac MRI 269–271, 270
 gauss (G), magnetic field strength 13
 Gaussian function, MR spectroscopy
 296, 297

General Electric (company) 3
 geometric parameters, quality control
 166, 173–177, 173–177
 ghost artefacts 166, 178, 178. *see also*
 quality control/assurance
 ghost-to-signal ratio (GSR) 178
 Gibbs' artefact 94–95, 95, 119–120, 190,
 363

glioma
 dynamic susceptibility contrast MRI
 312–313
 T₁-weighted imaging 29
 glutamine/glutamate complex (Glx),
 MR spectroscopy 289, 289

GMN (gradient moment nulling) flow
 artefacts 87, 252–254, 253

gradient amplifiers 153, 153

Index

gradient and spin echo (GRASE) 191, 200–201, 43–44, 201, 202. *see also* spin-echo-based EPI; turbo gradient and spin echo
 gradient coils 14, 149–150, 150
 gradient duty cycles 151
 gradient echo (GE) pulse sequences 41, 49–53, 51, 207, 224. *see also* spoiled gradient echo
 abdominal clinical examination 52–53, 52
 amplitude of echo 210–211
 blood flow artefacts 87
 coherence and echo formation 207–211, 209–210, 210
 coherence pathways 211, 211
 constructive interference in steady state 218
 contrast 35–37, 35
 creating the echo 51, 52
 Dixon scan 336–338, 339
 double echo steady state 218, 218
 echo planar imaging 222–224, 223
 family tree/classification 50
 FID measurement 132–135, 133
 functional cardiac imaging 273
 image formation 207, 208
 manufacturer comparison chart 50–51
 rewound 53, 214–216, 215–216
 signal strength 68–69
 spatial encoding 102
 T_1 -weighted images 36
 T_2 -weighted images 27–28, 36–37
 technical information 30
 time-of-flight effect 252
 time-reversed GE 216–217, 217
 ultra fast 53, 218–222, 219–223
 gradient field bio-effects of MRI 347–351, 349, 350, 351
 gradient moment nulling (GMN) flow artefacts 87, 252–254, 253
 gradient moment spatial encoding 105
 gradient non-linearity, artefacts 99, 99
 gradient recalled acquisition in the steady state (GRASS) 214–216. *see also* rewound gradient-echo pulse sequences
 gradient recalled echo. *see* gradient echo pulse sequences
 gradient rise time 150–151
 gradient slew rate quadrupling, parallel imaging 225
 gradient spoiling. *see* spoiled gradient-echo pulse sequences
 gradient subsystems, MR equipment 149–154, 150–153
 gradients, imaging
 bio-effects of MRI 15

biological effects 15
 dephasing 105–106
 eddy currents 152, 152–153
 induction of new staff 14
 Larmor equation 103–104
 linearity 151, 152
 spatial encoding 104, 104–105
 spin echo 185, 186
 GRAPPA (generalized auto-calibrating partially parallel acquisitions) 238
 artefacts 229
 auto-calibration 229
 clinical benefits 241
 parallel imaging 229, 234–235, 235
 signal-to-noise ratio 238
 GRASE. *see* gradient and spin echo
 GRASS. *see* gradient recalled acquisition in the steady state
 grey matter, MR spectroscopy 294, 294
 gridding, radial imaging 244–245, 245
 GSR (ghost-to-signal ratio) 178
 guidelines. *see also* standards
 contrast agents 356
 noise 15
 occupational exposure 354
 safety 13, 15, 17–19, 19–21
 gyro-magnetic ratio 103
 Hadamard encoding, chemical shift imaging 298
 Hadamard excitation 237
 haemodynamic delay, BOLD imaging 322–323
 Hahn echo formation, gradient echo 207–211, 209–210
 half Fourier single-shot TSE (HASTE) 43, 43–44, 196–198, 197
 data acquisition 120, 120
 double inversion recovery scheme 273
 image quality 239
 pulse sequences 48, 52
 hard pulse 128
 hardware-related artefacts 81
 harmonics, spatial 232. *see also* SMASH
 HARP (harmonic phase), myocardial strain imaging 282
 HASTE. *see* half Fourier single-shot turbo-spin echo
 head coils 13–14, 14, 172
 head imaging, niche systems 164. *see also* brain imaging
 header, image 62
 healing powers of magnets, history 345
 hearing protection 153–154, 352. *see also* acoustic noise
 heart attack (myocardial infarction) 284–286, 286. *see also* cardiac MRI
 heart valves, prosthetic 18

heart viability 284–286, 286
 heating of tissues. *see also* bio-effects of MRI
 burns 15, 23, 345
 parallel imaging 240
 patient contraindications 18
 radiofrequency exposure 345–348
 helium (He), superconducting magnets 145–146
 hepatic fat fraction (HFF), liver 336, 338
 herring-bone artefact 99–101, 99
 high-intensity focused ultrasound (HIFU) ablation 181
 high-resolution brain scanning 73
 historical perspectives, NMR 1–5, 2–5, 345
 homogeneity. *see* magnetic field uniformity
 hot lips artefact 228
 Hounsfield, Sir Godfrey 2–3
 human head image, history 3
 Hutchison, J.M.S. 3
 hyperechoes, turbo spin echo 190, 190
 hyperpolarization, future of MRI 360–362, 361
 hypnotic powers of magnets, history 345
 IAM (internal auditory meatus), partial volume artefacts 92–93
 ICNIRP (International Commission on Non-Ionizing Radiation Protection) 12, 354, 354
 IEC. *see* International Electrotechnical Commission
 IEEE (Institute of Electrical and Electronics Engineers) 354
 image contrast. *see* contrast
 image display, signal digitization 61–63, 61, 62
 image formation
 gradient echo 207, 208
 sensitivity encoding 227–228
 image-guided biopsy 164
 image intensifiers, history 2
 image optimization 67, 67, 80
 brain scan examples 77, 77, 77
 contrast 68, 69, 71
 contrast and signal-to-noise ratios 69–71, 71
 definitions 67
 mathematics of 68–69, 72, 76
 practical hints/protocols 76–80, 77, 79
 resolution 70–71
 trade-offs 71, 72–76, 74, 75, 76
 image quality. *see* quality control/assurance

- imaginary components, MR spectroscopy 288
- imaging gradients. *see* gradients, imaging
- imaging planes, functional cardiac imaging 273–274, 274
- implants, medical 18–19, 31. *see also* cardiac pacemakers
- in vivo relaxometry, quantitative MRI 331, 333
- in vivo spectroscopy. *see* magnetic resonance spectroscopy
- India ink artefact 89–91, 90
- induction. *see* magnetic field strength
- induction of new staff. *see* staff induction
- infants, possible contraindications 18
- in-flow effect, blood flow artefacts 86–88. *see also* time-of-flight angiography
- inhomogeneity artefacts 81
- in-phase (IP) images
- gradient-echo 36, 52–53, 213–214
 - phase cancellation artefact 91
- in-plane localization, spatial encoding 110–117
- installation, equipment, MR 163–164
- Institute of Electrical and Electronics Engineers (IEEE) 354
- Institute of Physics and Engineering in Medicine (IPEM) 13, 166–169
- interleaved chemical shift imaging 298
- interleaved inversion recovery turbo spin echo 192, 192–193
- internal auditory meatus (IAM), partial volume artefacts 92–93
- International Commission on Non-Ionizing Radiation Protection (ICNIRP) 12, 354, 354
- International Electrotechnical Commission (IEC)
- medical implants risk categories 18–19, 19
- occupational exposure 354, 354
- quality control standards 166–169
- safety guidelines 15
- interventional therapy systems 164, 358
- intravoxel-incoherent motion (IVIM), quantitative MRI 334
- inversion recovery (IR) 48, 49, 191–196, 195–196
- adiabatic pulses 194
- real-valued inversion recovery 193
- and signal strength 68–69
- slice interleaving 192
- technical information 30, 33–35, 34
- water-only excitation 196
- inversion time (TI) 27, 30
- IPEM. *see* Institute of Physics and Engineering in Medicine
- iron overload, quantitative MRI 331–333, 332–333
- iron oxide contrast agents 37, 141
- isocentre landmarking 22
- isochromat of protons. *see* spin
- IVIM (intravoxel-incoherent motion), quantitative MRI 334
- J*-coupling 140–141
- JET radially acquired TSE 48
- joint imaging 164
- Joint Photographic Experts Group (JPEG) standards 248
- joint replacement implants, safety 31
- keyhole imaging, contrast-enhanced MRA 265, 266–267
- knee imaging
- blood flow artefacts 87
 - contrast 31
 - proton density-weighted images 33
 - radiofrequency coils 13–14, 14
 - sensitivity encoding 250
 - spin echo 48
 - T₁-weighted images 29
 - T₂-weighted images 28
- k-space 59, 110
- functional cardiac imaging 274, 275
 - gradient and spin echo 201, 202
 - gradient echo 220, 220
 - phase encoding 225–226
 - signal digitization 59–60, 59–60
 - simultaneous acquisition of spatial harmonics 232–233, 234
 - spatial encoding 117–120, 118
 - spiral imaging 247–248, 247–248
 - turbo spin echo 190, 190, 199–200, 199–200
- k-t BLAST (broad-use linear acquisition speed-up technique) 240–242, 242–243
- lactate (Lac), MR spectroscopy 289, 289
- laminar blood flow 253
- landmarking 22
- Langevin equation 171
- language, hemispheric dominance 323–324
- Larmor equation 103–104
- Larmor frequency 106
- classical mechanics 125, 125
 - digital radiofrequency transceivers 161–162
 - quality control/assurance 169
 - quantum mechanics 126
 - rotating frame of reference 127, 127–128
- late gadolinium enhancement (LGE), myocardial 284–286, 286
- Lauterbur, Paul 2–4, 5
- left ventricular functional cardiac analysis 279
- left ventricular outflow tract (LVOT) view, cardiac imaging 273
- Lenz's law 152–153
- level, image display 63, 63
- light flashes, bio-effects of MRI 349
- line broadening, MR spectroscopy 288
- line-pairs 111, 111, 114, 174
- line spread function (LSF) 175, 175
- linewidth, MR spectroscopy 288
- linear accelerators (Linac), 363, 364
- linearity, magnetic field gradients 151, 152, 173–174, 173–174
- liver imaging
- contrast 36
 - hepatic fat fraction 336, 338
 - image-guided biopsy 164
 - MR elastography 341, 341
 - MR spectroscopy 289, 297, 299
 - MR-PET 363
 - open MRI systems 164
 - phosphorus spectroscopy 301
 - quantitative MRI 326, 331–333, 332–333
 - T₁-weighted images 29
 - T₂-weighted images 28
- long TI inversion recovery, spin-echo pulse sequences 43–44
- Look-Locker (LL) technique 326–329, 328, 329–330
- look-up tables (LUTs), image display 61, 62
- Lorentz forces 153–154
- low-contrast-detail detectability 178, 178
- low-pass filters 57
- LSF (line spread function) 175, 175
- lung imaging, hyperpolarization 360–364, 361
- LUTs (look-up tables), image display 61, 62
- LVOT (left ventricular outflow tract) view, cardiac imaging 273
- mag lag 351
- magic angle/magic angle artefacts 138, 139
- magnet quenches 13, 17, 146–147
- magnet room 11, 12, 13
- magnet sickness 351
- magnetic field/s 17
- bio-effects 345, 347–352, 349–350, 351
 - safety 16–17, 16
- signal-to-noise ratio 171

Index

- magnetic field gradients. *see* gradients, imaging
- magnetic field strength 13, 144–147
 BOLD imaging 325
 future of MRI 358–360, 359
 magnet types 144–147
 units of measurement 13
- magnetic field uniformity
 (homogeneity) 22, 148
 parallel transmit technology 155, 156
 quality control/assurance 172–173, 172
- magnetic moment 124, 125
 classical mechanics 124–125, 125–126
 measuring 127–129, 127–128, 130
 quantum mechanics 125–127, 126–127
- magnetic properties, metals 19, 21
- magnetic resonance (MR) 1, 5. *see also* future of MRI
 clinical applications 6
 history 1–5, 2–5
 Nobel Laureates 3–4, 5
 picture of a modern scanner 1
- magnetic resonance angiography (MRA) 38–39, 39, 251. *see also* non-contrast MR angiography
- contrast 38–39, 38–39
contrast-enhanced 263–267, 263–266
flow effects in conventional imaging 251–254, 252–253
history 2
motion artefacts 86–88, 87–88
pulse sequences/acronyms 254, 255
susceptibility-weighted imaging 267–268, 267
- magnetic resonance
 cholangiopancreatography (MRCP) 48, 196–198
- magnetic resonance elastography (MRE) 338–341, 340–341
- magnetic resonance-guided
 interventional procedures 164
- magnetic resonance linear accelerator (MR-LINAC) 363, 364
- magnetic resonance positron emission tomography (MR-PET) 362–363, 362–363
- magnetic resonance spectroscopy (MRS) 6–7, 288, 302
 chemical shift effect 295, 295
 chemical shift imaging 297–302, 299–301
 chemistry 288–290, 289
 CHESS pulse 290, 291
 clinical applications 290, 293–295, 297, 299–300
 future of 358
- non-proton spectroscopy 301–302, 301
processing spectra 295–297, 296–298
quality control/assurance 179
single-voxel 291–295, 291–295
technical challenges 290–291, 300, 300
terminology 288
- magnetic resonance suite 11–13, 12
- magnetization 44, 45
magnetization preparation, sequence options 42
magnetization prepared rapid acquisition by gradient echo. *see* MP-RAGE
- magnetization restoration, sequence options 42
magnetization transfer (MT) 42, 139–140, 140
- magneto-hydrodynamic bio-effects of MRI 351
- magneto-phosphenes, bio-effects of MRI 349
- magnets 144
 commercial examples of different types 146
 cooling systems 145–146, 147
 healing powers of 345
 installation footprint 148–149
 quenches 13, 17, 146–147
 static magnetic field mapping 148, 149
 zero boil-off 145–146, 147
- manganese, contrast agents 37, 141
- Mansfield, Peter 3–4, 5
- manufacturer comparison charts
 gradient-echo pulse sequences 50–51
 spin-echo pulse sequences 43–44
- mapping, transmit field 155–156, 157
- mathematics 365
 complex numbers 366–367
 constants 368
 diffusion-tensor imaging 307
 dynamic contrast-enhanced MRI 318–319, 319
 exponentials 366, 367
 Fourier analysis 367, 367
 image optimization 68–69, 72, 76
 parallel imaging 228–229
 relaxation/resonance 127–129, 136–137, 142–143
 sine/cosine waves 365–366, 366
 spatial encoding 105, 107, 110–111, 117–120
 specific absorption rate 346–347
 vectors 365, 365
- matrix, image 55, 58–61
- matrix radiofrequency coils 13–14
- matrix size, image optimization 71, 72, 74–75, 76
- MAVRIC (multi-acquisition variable-resonance image combination) 97–98, 98
- maximum intensity projection (MIP) 38, 39, 255, 256
- maximum permissible exposures (MPEs) 354, 354
- mean transit time (MTT), perfusion-weighted imaging 311
- medical emergencies 15–17
- medical implants 18–19, 31. *see also* cardiac pacemakers
- Medicines and Healthcare Products Regulatory Agency (MHRA) 12
- MEGs (motion encoding gradients) 340, 340
- metal detectors 16
- metals
 artefacts 16, 19, 31, 96–98, 96–98
 magnetic properties 19, 21
 siting and installation of equipment 163–164
- microvascular obstruction (MVO) 286
- minimum intensity projection (mIP), susceptibility-weighted imaging 268
- MIP (maximum intensity projection) 38, 39, 255, 256
- modified Look-Locker imaging (MOLLI) 329, 329–330
- modified sensitivity encoding (mSENSE) 229, 230, 238
- modulation transfer function (MTF), quality control 175
- Moiré fringes 97
- molecular motion, diffusion-weighted imaging 303, 304
- MOLLI (modified Look-Locker imaging) 329, 329–330
- morphological imaging, cardiac MRI 272–273, 272
- mortality rates, MRI 345, 352
- MOSFET transistors 154–155
- motion artefacts 81
 blood flow 86–88, 87–88
 cardiac motion 83–85, 85, 269
 enterology clinical examination 86
 gross patient movements 81, 81–82
 peristaltic motion 86, 86
 respiratory movement 82–83, 82–84
- motion encoding gradients (MEGs) 340, 340
- MOTSA (multiple overlapping thin slab acquisition) 257–258, 258
- moving spins 251–254, 252–253. *see also* magnetic resonance angiography

- moving table contrast-enhanced MRA 264, 265
 MPR (multi-planar reformats) 43
 MPRI (myocardial perfusion reserve index) 283
 MP-RAGE (magnetization prepared rapid acquisition by gradient echo) 221–222, 221
 MR/MRI. *see* magnetic resonance angiography
 MRA. *see* magnetic resonance angiography
 MRCP (magnetic resonance cholangiopancreatography, 48, 196–198
 MRE. *see* magnetic resonance elastography
 MRS. *see* magnetic resonance spectroscopy
 MS (multi-slice) CAIPIRINHA 237–238
 mSENSE (modified sensitivity encoding) 229, 230, 238
 MT (magnetization transfer) 42, 139–140, 140
 MTF (modulation transfer function), quality control 175
 MTT (mean transit time), perfusion-weighted imaging 311
 multi-acquisition variable-resonance image combination. *see* MAVRIC
 multi-band sensitivity encoding (MBSENSE) 237
 multi-echo combined gradient-echo pulse sequences 50–51
 multi-planar reformats (MPR) 43
 multi-shot echo planar imaging 204–205, 204–206, 204
 multi-slice (MS) CAIPIRINHA 237–238
 multi-slice imaging signal digitization 64–66, 66 undersampling in parallel imaging 236–237, 237
 multi-slice interleaving, spatial encoding 109, 110
 multi-transmit systems 155
 multiple spin echo 186, 187
 multiple channel coil arrays, cardiac MRI 271
 multiple overlapping thin slab acquisition (MOTSA) 257–258, 258
 multiple sclerosis lesions 28, 290
 MultiVane radially acquired TSE 48
 musculoskeletal (MSK) imaging 30–31, 30
 musical analogy, spatial encoding 116
 MVO (microvascular obstruction) 286
 myelin breakdown, MR spectroscopy 289
 myocardial infarction 284–286, 286. *see also* cardiac MRI
 myocardial perfusion, cardiac MRI 282–284, 285
 myocardial perfusion reserve index (MPRI) 283
 myocardial strain imaging, functional cardiac imaging 281–282, 284
 myocardial viability 284–286, 286
 myo-inositol (mI), MR spectroscopy 289, 289
 N-acetyl-aspartate, MR spectroscopy 179, 289, 289, 299, 299
 National Electrical Manufacturers Association (NEMA), quality control standards 166–169, 170, 172
 navigator echoes, motion artefacts 83, 84
 navigators, respiratory 270–271, 271, 272
 NC-MRA. *see* non-contrast magnetic resonance angiography
 negative voxel values, inversion recovery turbo spin echo 193, 193
 neonates, possible contraindications 18
 nephrogenic systemic fibrosis 356
 Neptune superconducting system 3
 net magnetization, protons 126, 127
 neurological problems, spine clinical examination 30
 niche systems for particular applications 164
 niobium–titanium (NbTi) alloy, superconducting magnets, 145–146
 NMR (nuclear magnetic resonance). *see* magnetic resonance
 no phase wrap option, phase wrap-around artefacts 93
 Nobel Laureates 3–4, 5
 noise, acoustic 15, 153–154, 350
 noise break-through, parallel imaging artefacts 95
 noise, receive coils 158–159
 non-alcoholic fatty liver disease (NAFLD) 335
 non-alcoholic steatohepatitis (NASH) 335
 non-Cartesian acquisitions, parallel imaging 242–248
 non-contrast magnetic resonance angiography (NC-MRA) 251, 255–263
 balanced steady-state-free-precession 261–263, 262
 ECG-triggered TSE-based 260–261, 261
 phase contrast angiography 258–260, 259–260
 pulse sequences/acronyms 255
 time-of-flight angiography 255–258, 256–258
 non-rectangular slice profiles 93, 94
 nuclear magnetic resonance (NMR). *see* magnetic resonance
 number of signal averages (NSA), image optimization 77
 Nyquist ghosts 180, 203, 203–204
 Nyquist theorem, signal digitization 56, 56–57, 58
 nystagmus, bio-effects of MRI 351
 oblique slices/orientations 108
 occupational exposure 19, 352–354, 353, 354
 oedema 26–28, 28
 open MRI systems 164
 osteo-arthritis (OA), cartilage relaxometry 333, 333–334
 out-of-phase (OP) images 36, 52–53, 91, 213–214
 oversampling, signal digitization 57, 58
 pacemakers, cardiac 18, 345, 352
 PACS (Picture Archiving and Communications System) 11–12
 paediatric brain scanning contraindications 18 image optimization 77, 77
 paradigms, fMRI 320–321, 321, 325
 parahydrogen-induced polarization (PHIP) 360
 parallel imaging 13, 225, 250 artefacts 95–96, 96
 CAIPIRINHA 235–236, 236 chemical shift imaging 299 compressed sensing 248–250, 249–250
 gradient slew rate quadrupling 225 GRAPPA and ARC 229, 234–235, 235
 image quality 237–240, 241 k-t BLAST 240–242, 242–243 mathematics of 228–229
 non-Cartesian 242–248, 245–248 phase encoding 225–226, 226 phased array coils 159, 226, 226 sensitivity encoding 227–228, 227–229, 230 SMASH 230–234, 231–234 spin echo 185 undersampling by multi-slice excitation 236–237, 237 parallel state, protons 125 parallel transmit technology 155, 156

Index

- paramagnetic materials 19, 21, 37. *see also* gadolinium based contrast agents
- paramagnetic solutions, phantoms 169–171, 170–171
- paramagnetic susceptibility. *see* susceptibility effects
- parameters, sequence 41–42, 42
- parametric maps, dynamic susceptibility contrast MRI 311–314, 313, 314
- partial echo formation, gradient echo 207–211, 209–210
- partial volume effect 64, 65, 92–93
- passive implants, medical 18
- passive shimming 148
- patients. *see also* positioning of patient cardiac MRI preparation 269–272, 270–271
contraindications 11, 18–19
handling 21–23
movements, gross 81, 81–82. *see also* motion artefacts
- PCASL (pseudo-continuous arterial spin labelling) 315
- PD (proton density) 27, 32–33, 33, 49
- PE. *see* phase encoding
- perfusion, brain 326, 335
- perfusion fraction, quantitative MRI 334, 334
- perfusion, myocardial 282–284, 285
- perfusion-weighted imaging 303, 311–316, 312–316
- peripheral gating (PD), cardiac MRI 85–86, 271
- peripheral nerve stimulation (PNS) 15, 225, 345, 348–349, 349–350
- peristaltic motion artefacts 86, 86
- permanent magnets 13, 147
- permeability imaging. *see* dynamic contrast-enhanced magnetic resonance angiography
- PET (positron emission tomography) 2, 362–363, 362–363
- PGSE (pulsed gradient-spin echo) method 304–306, 305
- phantoms (test objects) 166, 167, 169, 172, 173–174. *see also* quality control/assurance
avoiding misleading results 173
filling factors 169–171, 170–171
- phase angles, radiofrequency 134
- phase cancellation artefact 89–91, 90
- phase contrast angiography. *see* contrast-enhanced MRA
- phase contrast velocity aliasing functional cardiac imaging 282
- phase correction, MR spectroscopy 288, 296, 298
- phase encoding (PE) 59–61, 61
gradient pulses 41
- parallel imaging 225–226, 226
- pulse sequences 102, 103
rewinding 188–189
spatial encoding 112–114, 113–114
- phase ghost artefacts 178
- phase images, MR equipment 148
- phase offset multi-planar (POMP) 236
- phase oversampling, phase wrap-around artefacts 93
- phase sensitive inversion recovery (PSIR) 285
- phase shift, velocity induced 252–254
- phase wrap-around artefacts 93–95, 94, 119–120
- phased array coils 159–160, 160
parallel imaging 226, 226
sensitivity profiles 231–232, 234
- Philips (company) 3, 4
- PHIP (parahydrogen-induced polarization) 360
- phosphorus MR spectroscopy 301, 301
- Picture Archiving and Communications System (PACS) 11–12
- pixel-limited resolution 116–117, 176
- pixels
chemical shift artefacts 89
signal digitization 55, 58, 60–64, 64
- Planck's constant 368
- planes, cardiac 273–274, 274
- pleths 271
- plug flow 253
- pneumatic bellows, respiratory triggering 270–271
- PNS. *see* peripheral nerve stimulation
- point-resolved spectroscopy (PRESS) 291, 292, 296, 298
- polarization 128–129, 361
- policies and procedures, induction of new staff 11
- POMP (phase offset multi-planar) 236
- positioning of patient
liver clinical examination 36
musculoskeletal clinical examination 31
positioning scans 22, 22
- positive voxel values, inversion recovery turbo spin echo 193, 193
- positron emission tomography (PET) 2, 362–363, 362–363
- post-Fourier transformation, sensitivity encoding 227
- Pound, Robert 3, 136, 139
- PP (pulse programmer) computer systems 162–163
- PR (projection reconstruction), non-Cartesian acquisition 242
- preamplification, RF receiver subsystems 160–161
- precession 124, 130
Larmor equation 103
magnetic moment 125, 125–126
quantitative MRI 341–343, 342–343
- pre-emphasis, gradient waveforms 152–153
- pre-processing filters, image optimization 78
- pregnancy 18, 345, 351–352, 356
- PRESS (point-resolved spectroscopy) 291, 292, 296, 298
- procedures, induction of new staff 11
- programs (examinations) 41–42
- projection reconstruction (PR), non-Cartesian acquisition 242
- PROPELLER (periodically rotated overlapping parallel lines with enhanced reconstruction) 48, 199–200, 199–200
- PROSET (principle of selective excitation technique) 196
- prospective cine cardiac imaging 275–276, 276
- prostate imaging 299–300, 300
- prosthetic heart valves, contraindications 18
- proton density (PD) 27, 32–33, 33, 49
- proton exchange 139
- proton gyromagnetic ratio 368
- proton spectroscopy. *see* magnetic resonance spectroscopy
- proton spectrum 288–290, 289
- proton spin 124–127, 125–127
- pseudo-continuous arterial spin labelling (PCASL) 315
- pseudo-diffusion, quantitative MRI 334, 334
- PSIR (phase-sensitive inversion recovery) 285
- pulse oximetry 23
- pulse programmer (PP) computer systems 162–163
- pulse sequences 41, 54. *see also* gradient-echo pulse sequences; spin-echo pulse sequences
contrast 26
echo planar imaging 54
examinations, protocols and parameters 41–42, 42
- family tree/classification 42–43, 43
- functions/basic structure 41, 42
- imaging gradients 14
- inversion recovery turbo spin echo 193–194, 194
- magnetic resonance angiography 254, 255
- manufacturer comparison chart 43–44

- respiratory navigators 272
 selection 54
 sequence options 42, 43
 spatial encoding 102–103, 102
 technical information 30
 pulsed arterial spin labelling 315
 pulsed gradient spin-echo (PGSE)
 method 304–306, 305
 pulse-width modulated (PWM)
 amplifiers 153, 153
 Purcell, Edward 3–4, 5, 136, 139
- quadrature 178, 288
 quality control/assurance 166, 167, 181
 artefacts 178, 178–179
 echo planar imaging 203–204,
 203–204
 geometric parameters 173–177,
 173–177
 parallel imaging 237–240
 relaxation parameters 166, 177–178,
 178
 signal parameters 169–173, 170–171,
 170–172
 specialist 181
 spectroscopy 179
 standards 166
 temporal stability 179–180, 180–181
 quantitative magnetic resonance
 imaging 326
 accuracy/precision 341–343, 342–343
 cardiac MRI 278–281, 280–283,
 283–284
 diffusion parameters 326, 334, 334,
 335
 fat quantification 335–338, 336–339
 MR elastography 338–341, 340–341
 relaxation times. *see below*
 quantitative MRI relaxation times
 326, 326–334
 cardiac MRI 328
 Carr–Purcell–Meiboom–Gill
 sequence 330
 liver iron concentration 332–333
 modified Look–Locker imaging 329
 T_1 326–330, 327–329
 T_2 330–331, 330
 T_2 cartilage map 333
 quantum mechanics (QM) 124–127,
 126–127, 129
 quenches, magnet 13, 17, 146–147
- radial fast spin-echo pulse sequences
 43–44
 radial imaging 243–245, 245–247
 radial k-space acquisition, turbo spin
 echo 199–200, 199–200
 radially acquired turbo spin-echo 48
 radiofrequency amplifiers 154–155
- radiofrequency break-through artefacts
 98–99, 99
 radiofrequency coils, induction of new
 staff 13–14, 14
 radiofrequency excitation 103. *see also*
 radiofrequency (RF) pulses
 radiofrequency field exposure
 bio-effects of MRI 15, 345–348,
 347–348
 heating of tissues 345
 occupational exposure 353, 354
 specific absorption rate 15, 346,
 346–347
 standards 347–348
 weight of patient 22
 radiofrequency inhomogeneity effects,
 metal artefacts 97, 97
 radiofrequency phase angles 134
 radiofrequency (RF) pulses 13, 41, 42,
 44. *see also* pulse sequences
 radiofrequency receiver subsystems
 158, 158–162, 160–161
 radiofrequency shielding 13–14,
 148–149, 163
 radiofrequency spoiling 213. *see also*
 spoiled gradient-echo (SPGR)
 radiofrequency systems 154–158,
 155–157
- radiographer's blog 23
 Radiological Society of North America
 (RSNA) 164
 RAGE (rapid acquired gradient echo)
 53
 ramped excitation, time-of-flight
 angiography 257
 random walk, molecular 304
 RARE (rapid acquisition with
 relaxation enhancement)
 185, 186–191, 187–188, 189, 191,
 190. *see also* turbo spin echo
 RARE driven equilibrium 43–44
 readout gradient pulse sequences 41,
 102, 103
 real components, MR spectroscopy 288
 real functions, Fourier transform
 120, 121, 121
 real-time cine cardiac imaging 277–278
 real-valued inversion recovery 193, 193
 receive bandwidth (RBW), signal
 digitization 57, 58
 receiver operating characteristic (ROC)
 curves 343, 343
 receiver radiofrequency coils 13–14,
 158–159, 158
 receivers (digitizers) 161, 161–162
 RECIST (response evaluation criteria
 in solid tumours) 318. *see also*
 dynamic contrast-enhanced
 magnetic resonance angiography
- rectangular field of view, data
 acquisition speed up 121, 122
 reduced matrix, data acquisition speed
 up 120–121
 reference levels (RL), occupational
 exposure 353, 354, 354
 refocused gradient echo. *see* rewound
 gradient-echo pulse sequences
 refocusing pulses 30–31, 45
 region of interest (ROI), quality control
 169, 170
 regional saturation technique (REST)
 slabs 87, 88
 re-gridding, radial imaging 244–245,
 245
 relaxation 3, 124, 143
 BPP theory 3, 136, 139
 free induction decay 132–135, 133–
 134
 gadolinium-based contrast agents
 141–143, 142
 magnetic moment 127–129, 127–
 128, 130
 mathematics of 127–129, 136–137,
 142–143
 quality control/assurance 166,
 177–178, 178
 rotating frame of reference 127–129,
 127–128
 sequence-dependent 68–69
 spin 124–127, 125–127
 technical information 30
 relaxation times 129–132, 130, 131,
 132. *see also* quantitative MRI
 relaxation times
 field strength 359
 mechanisms 135–141, 136–137, 139–
 141
- renal arteries 39, 262, 262–263
 renal function, and contrast agents 356
 repetition time (TR) 27, 30–31, 32–33,
 41, 44
 rephasing, spatial encoding 105–106,
 106, 109–110
 residual water peak, MR spectroscopy
 288
 resolution
 image optimization 70–76
 limits 176
 quality control/assurance 166,
 174–176, 174–175
 spatial encoding 116–117, 118
 RESOLVE multi-shot echo planar
 imaging 204–205, 206
 resonance condition, proton 125
 resonances, MR spectroscopy 288
 resonant frequencies
 acoustic noise 154
 Larmor equation 103

Index

resonant offsets 215–216, 215–216
 respiratory belts, motion artefacts 82, 83
 respiratory gating/triggering 82, 83, 270–271
 respiratory movement
 cardiac MRI 270–271
 motion artefacts 82, 82–83
 navigator echoes 84
 respiratory-ordered phase encoding 84
 respiratory navigators 270–271, 271, 272
 respiratory-ordered phase encoding (ROPE) 82–83, 83–84
 REST (regional saturation technique)
 slabs 87, 88
 restoration radiofrequency pulses, spin echo 185
 resuscitation, adverse patient reactions 15–16
 retrospective cine cardiac imaging 275–276, 276
 rewinding, phase-encoding 188–189
 rewound gradient-echo pulse sequences 53
 image formation 207, 208, 209–211, 210, 214–216, 216
 manufacturer comparison chart 50–51
 RF. *see* radiofrequency
 rheobase values, gradient field 351
 ringing artefacts 94–95, 95, 119–120, 190, 363
 risk assessment, medical implants 18–19
 RL (reference levels), occupational exposure 353, 354, 354
 ROAST (resonant offset averaging steady state) 215–216, 216
 ROC (receiver operating characteristic) curves 343, 343
 ROI (region of interest), quality control 169, 170
 root mean square (RMS) value, homogeneity of a magnetic field 148
 ROPE (respiratory-ordered phase encoding) 82–83, 83–84
 rotating frame of reference 106, 127–129, 127–128
 RSNA (Radiological Society of North America) 164
 runners on a track analogy, spin-echo pulse sequences 135
 safety 345, 356. *see also* bio-effects of MRI
 burns 15
 cryogens 15
 fatalities related to magnet safety 345, 352

fringe fields 17
 gadolinium-based contrast agents 260
 guidelines 13, 15, 17–19, 19–21
 induction of new staff 11, 14–18, 16
 joint replacement implants 31
 magnetic field 16–17, 16
 metal implants 97
 staff questionnaire 11, 16
 safety officers 13
 sampling, radial imaging 245, 247
 SAR. *see* specific absorption rate
 saturation 135
 saturation bands 87, 88, 186
 scan time
 motion artefacts 82
 image optimization 73, 78–80, 79
 scanner room 11, 12, 13
 SCAT (subcutaneous adipose tissue) 335, 336–337
 scintillation, MR-PET 362
 scout (positioning) scans 22, 22
 SE. *see* spin-echo pulse sequences
 screen brightness, image display 61
 second-order gradient moment nulling 252–253
 secondary coils, eddy currents 152–153
 security issues 11–12, 12
 segmented k-space imaging 274, 275
 selective excitation 3, 41, 106–110, 108–110
 SEMAC (slice encoding for metal artefact correction) 97–98, 98
 SENC (strain encoding), myocardial strain imaging 282
 SENSE (sensitivity encoding)
 CAIPIRINHA 236
 clinical benefits 241
 image quality 238–239, 238
 knee 250
 parallel imaging 159, 227–228, 227–229, 230
 signal-to-noise ratio 238
 sensitivity maps, parallel imaging 227
 sensitivity profiles, phased array coils 226, 226, 231–232, 234
 sequences. *see* pulse sequences
 shield coils, eddy currents 152–153
 shielding, radiofrequency 13–14, 148–149, 163
 shimming 144, 148
 field strength 359
 MR spectroscopy 288, 290–291, 294, 295, 300
 rewound gradient-echo pulse sequences 215
 short axis (SA) cine images, functional cardiac imaging 273

short TI inversion recovery. *see* STIR
 shoulder clinical examinations, contrast 31
 shoulder coils 13–14, 14
 side-bands, transmitters 154
 signal averaging, image optimization 73–76, 75
 signal digitization 55–57, 55, 64, 66
 DICOM 62–63
 display of images 61–63, 61, 63
 frequency and phase encoding axes 60–61, 61
 k-space 59–60, 59–60
 look-up tables 61, 62
 matrices 58–61
 multi-slice imaging 64–66, 66
 Nyquist theorem 56, 56–57, 58
 oversampling 57, 58
 partial volume effect 64, 65
 pixels 55, 58, 60–64, 64
 radiofrequency transceivers 155, 161, 161–162
 receive bandwidth 57, 58
 slices/orientations 61, 62
 signal-to-noise ratio (SNR)
 gradient echo sequences 35
 MR spectroscopy 294
 parallel imaging 238, 240
 phased array coils 226, 226
 quality control/assurance 67
 image optimization 67, 68–71, 77–78
 image optimization trade-offs 72–76, 75, 76
 receive bandwidth 57
 silent acquisitions, radial imaging 245, 246
 simultaneous acquisition of spatial harmonics. *see* SMASH
 sine waves 103, 365–366, 366
 Singer, R. J. 2
 single photon emission computed tomography (SPECT), history 2
 single-shot turbo spin echo (SS-TSE) 48. *see also* half Fourier single-shot TSE
 single-voxel MR spectroscopy 291–295, 296
 processing 295–297, 296–298
 siting of equipment, MR 163–164
 size parameters, image optimization 73–76. *see also* field of view
 slew rates, trapezoidal gradient pulses 150, 150–151, 154
 slice encoding for metal artefact correction (SEMAC) 97–98, 98
 slice-selective gradients, pulse sequences 102, 103
 slices
 image optimization 73, 76, 78

Cambridge University Press

978-1-107-64323-9 — MRI from Picture to Proton

Donald W. McRobbie, Elizabeth A. Moore, Martin J. Graves, Martin R. Prince

Index

[More Information](#)

Index

- interleaving, inversion recovery TSE 192–193, 192
 multi-slice imaging 65, 66
 number, turbo spin echo 189
 orientations 61, 62, 76, 78, 108–109, 109
 parameters, quality control 176–177, 176–177
 profiles, non-rectangular 93, 94
 selection 3, 41, 106–110, 108–110
 signal digitization 61, 62
 spatial encoding 108–109, 109
 thickness 59
 width 73, 93, 93
- SMASH (simultaneous acquisition of spatial harmonics) 159, 230–234, 231–234, 238
- SNR. *see* signal-to-noise ratio
- sodium, MR spectroscopy 302
- SPACE (three-dimensional turbo spin echo) 43–44, 48
- SPAIR (spectral adiabatic inversion recovery). *see* adiabatic pulses
- SPAMM (spatial modulation of magnetization) 281
- spatial encoding 102–122
 consequences of Fourier imaging 117–120, 118
 data acquisition speed up 120, 120–121, 122
 dephasing and rephasing 105–106, 105–106, 109–110
 Fourier transform 106, 107, 116, 117, 121–122, 122
 imaging gradients 104, 104–105
 in-plane localization 110–117
 Larmor equation 103–104
 mathematics of 105, 107, 110–111, 117–120
 musical analogy 116
 pulse sequences 102–103, 102
 rotating frame 106
 slice selection or selective excitation 106–110, 108–110
 spatial frequencies, spatial encoding 111–112, 111–112
 spatial frequency combs/filters 114
 spatial harmonics 232. *see also* SMASH
- spatial modulation of magnetization (SPAMM) 281
- spatial resolution. *see* resolution
- spatial saturation
 blood flow artefacts 87, 88
 sequence options 42
 spatial saturation bands, spin echo 186
- SPECIAL (spectral inversion at lipid)
 92
- specific absorption rate (SAR)
 handling patients 22
- radiofrequency exposure 346, 346–347
 radiofrequency fields 15
 safety guidelines 19
 standards 348
 turbo spin echo 190
- SPECT (single photon emission computed tomography), history 2
- spectral adiabatic inversion recovery (SPAIR) 92
- spectral attenuated inversion recovery (SPAIR). *see* adiabatic pulses
- spectral density function 137, 137
- spectroscopy. *see* magnetic resonance spectroscopy
- SPEEDER (Toshiba), parallel imaging 227, 229
- SPGR. *see* spoiled gradient-echo pulse sequences
- spherical deconvolution, tractography 308
- spike noise, artefacts 99–101, 99
- spin 124–127, 125–127
- spin-down 125
- spin-echo (SE) pulse sequences 41–48, 47, 185, 206. *see also* turbo spin echo
- brain clinical examination 46–47
 combined with gradient echoes 200–201, 201, 202
 contrast 33
 conventional technology 185–186, 189–191, 189
 creating the spin echo 45–46, 45
 diffusion-weighted imaging 308–309, 310
 driven equilibrium 196, 197
 family tree/classification 43
 fat saturation pulses and spatial saturation bands 186
 FID measurement 132–135, 134
 knee clinical examination 48
 magnetization 44, 45
 manufacturer comparison chart 43–44
 MR spectroscopy 293
 multiple 186, 187
 radial k-space acquisition 199–200, 199–200
 and signal strength 68–69
 simple sequence 45
 T_1 -weighted images 47
 T_2 -weighted images 27–28
 technical information 30–31, 32–33
 time-of-flight effect 251, 252
- spin-echo-based echo planar imaging (SE-EPI) 39, 43, 201–204, 204–206, 204–205
- spin labelling, perfusion-weighted imaging 303
- spin–lattice relaxation time 27, 30, 131–132, 131, 132. *see also* T_1 -weighted images
- BPP theory of relaxation 139
- contrast-enhanced MRA 264, 264–265
- mechanisms 135, 136, 137–138, 140–141
- quality control 177–178
 quantitative MRI 326–330, 327–329
- spin–spin relaxation time 27, 30, 129–132, 130, 131, 132. *see also* T_2 -weighted images
- BPP theory of relaxation 139
- mechanisms 135, 136, 138, 140–141
- quality control 177–178
 quantitative MRI 330–331, 330
- spin-up, proton 125
- spin warp, history 3
- spine clinical examination 30
- SPIO (super-paramagnetic iron oxide)
 contrast agents 37, 141
- SPIR (spectral inversion recovery), fat suppression 92
- spiral imaging 245–248, 247–248
- spoiled gradient-echo (SPGR) pulse sequences 52–53, 207, 208, 209–210, 210, 212–214
- flip angles 212
- manufacturer comparison chart 50–51
- two-point Dixon technique 214
- stack of stars 221, 222
- staff induction 11
 access to MR suite 12–13, 12
 burns to patients 15
 fringe field values/minimum distances to avoid interference 17
 handling patients 21–23
 imaging gradients 14
 magnet room 13
 MR suite 11–13, 12
 radiofrequency coils 13–14, 14
 safety 14–18, 16, 17–19, 19–21
 working conditions 19
- staff safety questionnaire 11, 16
- standards 166–169. *see also* guidelines; quality control/assurance
- compressed sensing 248
- gradient field 350, 351
- quality control 166–169, 170, 172, 172
- radiofrequency exposure 347–348, 347
- specific absorption rate (SAR) 348
- static field exposure 352
- Star-VIBE 222, 223
- static magnetic fields
 bio-effects of MRI 15, 351–352, 352
 mapping 148, 149
 occupational exposure 353, 354
 safety 16, 19, 20

Cambridge University Press

978-1-107-64323-9 — MRI from Picture to Proton

Donald W. McRobbie, Elizabeth A. Moore, Martin J. Graves, Martin R. Prince

Index

[More Information](#)

Index

- steady-state magnetization 135, 207, 208
 STEAM (stimulated echo acquisition mode), MR spectroscopy 291–292, 291, 293
 Stejskal and Tanner (PGSE) method 303–306, 305
 stimulated echoes. *see also* STEAM gradient echo 209, 209–210
 MR spectroscopy 291–292, 293
 STIR (short TI inversion recovery) 43, 192
 contrast 30–31, 30
 musculoskeletal clinical examination 31
 spin-echo pulse sequences 43–44, 196
 spine clinical examination 30
 streak artefacts, radial imaging 247
 strength-duration (SD) curves, bio-effects of MRI 349, 350
 stress testing, cardiac MRI 283
 stroke patients
 diffusion-weighted imaging 303, 305
 MR spectroscopy 290, 290
 subcutaneous adipose tissue (SCAT) 335, 336–337
 superconducting magnets 1, 13, 147
 history 2
 magnet types 145–147
 super-paramagnetic iron oxide (SPIO)
 contrast agents 37, 141
 surgical clip implants 18
 susceptibility effects 19, 29, 36
 susceptibility-weighted imaging (SWI) 267–268, 267
 field strength 359
 gradient echo 224
 pulse sequences/acronyms 255
 synovial fluid 26–28, 28
- T₁-weighted images 27. *see also* spin-lattice relaxation time
 contrast 28–29, 29
 gadolinium (Gd) contrast agents 29, 29
 gradient-echo (GE) sequence 36
 multi-slice imaging 64–66
 spin-echo (SE) pulse sequences 47
 T₂ cartilage mapping, quantitative MRI 333
 T₂ shine-through 304
 T₂-weighted images 27, 28. *see also* spin-spin relaxation time
 contrast 27–28
 gadolinium-based contrast agents 37
 gradient-echo sequences 36–37
 T₂* (apparent spin-spin relaxation time) 27, 36, 330–331
 Talairach Brain Atlas 321
- taste sensations, bio-effects of MRI 351
 tattoos, possible contraindications 18
 TE (echo time) 27, 30–31, 32–33, 41, 42, 44
 technical (computer) room, layout 11, 12
 temporal stability, signal fluctuation 179–180, 180–181
 temporally resolved imaging of contrast kinetics (TRICKS) 267
 terminology. *see also* acronyms
 contrast 27
 MR spectroscopy 288
 test objects. *see* phantoms
 TGSE. *see* turbo gradient spin echo
 thermoregulatory problems, contraindications 18. *see also* heating of tissues
 three-dimensional (3D)
 Fourier transform, spatial encoding 121–122, 122
 image optimization trade-offs 76
 phase contrast MRA 259–260, 260
 radial imaging 243–245, 245–247
 signal digitization 64–66
 spin echo 43–44, 48, 198–199, 198–199, 255
 time-of-flight angiography 255–258, 257–258
 ultra-fast gradient-echo manufacturer comparison chart 50–51
 VIBE gradient-echo pulse sequences 52
 VIEW 48, 198–199
 three-point Dixon (3PD) techniques 337
 TI (inversion time) 27, 30
 tilted optimized non-saturating excitation (TONE) 257
 time-of-flight (TOF) effect 87, 251–252, 252
 time-of-flight magnetic resonance angiography (TOF MRA) 38. *see also* contrast-enhanced MRA
 non-contrast 255–258, 256–258
 pulse sequences/acronyms 255
 time-resolved (4D) contrast-enhanced MRA 255
 time-resolved angiography with interleaved stochastic trajectories (TWIST) 266, 267
 time-reversed gradient-echo 207, 208, 209–211, 210, 216–217, 217
 manufacturer comparison chart 50–51
 tissue characterization, cardiac MRI 286
 tissue perfusion/permeability, quantitative MRI 326, 335
 tissue tagging, myocardial strain imaging 281–282
 TOF. *see* time-of-flight
- TOFI (thin on the outside, fat on the inside) phenotype 335
 Tofts model, dynamic contrast-enhanced MRI 317–319, 319
 TONE (tilted optimized non-saturating excitation) 257
 torque, safety issues 16–17
 TR (repetition time) 27, 30–31, 32–33, 41, 44
 tractography images, diffusion-weighted imaging 307–308, 308
 transmit field mapping 155–156, 157
 transmitter coils 13–14, 157–158, 157
 transmitters 154–155, 155–156
 trapezoidal gradient pulse 150, 150–151
 TRICKS (temporally resolved imaging of contrast kinetics) 267
 triggering, ECG 269–271, 270
 triggering, respiratory 270–271
 triplets, MR spectroscopy 288
 tru-FISP rewound gradient-echo pulse sequences 53
 truncation artefacts 94–95, 95, 119–120, 190, 363
 tumours
 hyperpolarization 362–364
 MR spectroscopy 290
 tuned electrical circuits, receive coils 158, 158–159
 turbo gradient spin echo (TGSE) 43, 54, 200–201, 201–202
 turbo chemical shift imaging 298–299
 turbo-FLASH spoiled gradient-echo sequences 219–221, 219–220
 turbo spin echo (TSE) 43, 46–48, 47, 49. *see also* RARE (rapid acquisition with relaxation enhancement)
 data acquisition (k-space) filling 187–188
 inversion recovery 191–196, 192–196
 radial k-space acquisition 199–200, 199–200
 single-shot 196–198, 197
 three-dimensional 198–199, 198–199
 TWIST. *see* time-resolved angiography with interleaved stochastic trajectories
 two-dimensional (2D)
 Fourier transform imaging 3
 image optimization trade-offs 76
 radial imaging 243–245, 245–247
 signal digitization 64–66
 spatial encoding 110–111, 116, 117
 time-of-flight angiography 255, 257
 turbo spin echo 48
 ultra-fast gradient-echo manufacturer comparison chart 50–51
 two-point Dixon technique 213–214

ultra-fast gradient echo 53, 218–222, 222–223
 ultra-short echo time (UTE)
 MR-PET 362
 radial imaging 245, 246
 ultra-small paramagnetic iron oxide (USPIO) nanoparticles 267
 ultrasound scanning, history 2
 undersampling, parallel imaging 236–237, 237
 uniform phantoms 169
 uniformity of magnetic field. *see* homogeneity
 uninterruptible power supplies (UPS) 163
 units of measurement, magnetic field strength 13
 variable view sharing. *see* view sharing
 vector cardiac gating (VCG) 269, 270
 vectors, mathematics of 365, 365
 velocity compensation. *see* gradient moment nulling
 velocity encoding (venc), cardiac imaging 260, 281, 282
 velocity-induced phase shift 252–254
 vertigo, bio-effects of MRI 351
 VIBE gradient echo sequence 222

view sharing
 contrast-enhanced MRA 265, 266–267
 functional cardiac imaging 276–277, 277
 visceral adipose tissue (VAT), quantitative MRI 335, 336
 voltage changes, eddy currents 152–153, 152
 volume interpolated 3D ultra-fast gradient-echo pulse sequences 50–51
 voxels (volume elements) 55, 61, 64
 image optimization 72
 inversion recovery turbo spin echo 193, 193
 MR spectroscopy 292–295, 294–295
 partial volume effect 64, 65
 susceptibility effects 97
 Warburg effect 361–364
 water binding 137, 137, 139
 water excitation 195, 196, 213
 water, properties 1
 water suppression
 contrast 26
 MR spectroscopy 288, 290–291, 291
 subcutaneous adipose tissue 337

weight of patient, and radiofrequency exposure 22
 white matter/white matter tracts
 diffusion-weighted imaging 306–308, 308
 MR spectroscopy 294, 294
 tractography images 307
 whole-body diffusion-weighted imaging 309, 310
 window width, display of images 63, 63
 working conditions. *see* occupational exposure
 Young's modulus 339–340, 340. *see also* magnetic resonance elastography
 zero boil-off magnets 145–146, 147
 zero-filling
 data acquisition speed up 121
 MR spectroscopy 288
 zeroth-order gradient moment nulling 252–253, 253
 zeroth-order phase correction, MR spectroscopy 298
 zeugmatography, history 2–3
 zipper artefacts 98
 zonal defence, security issues 12